TECHNISCHE UNIVERSITÄT MÜNCHEN

Department of Chemistry and Catalysis Research Center
Chair of Technical Electrochemistry

Determination of Physical and Electrochemical Parameters for Lithium-Ion Batteries and Advanced Electrochemical Impedance Analysis

Johannes Martin Landesfeind

Vollständiger Abdruck der von der Fakultät für Chemie der Technischen Universität München zur Erlangung des akademischen Grades eines

Doktors der Naturwissenschaften (Dr. rer. nat.)

genehmigten Dissertation.

Vorsitzende:	Prof. Dr. Corinna Hess
Prüfer der Dissertation:	1. Prof. Dr. Hubert A. Gasteiger
	2. Prof. Dr. Andreas Jossen
	3. Prof. Dr. Arnulf Latz
	4. Prof. Dr. Tom Nilges

Diese Dissertation wurde am 09.04.2018 bei der Technischen Universität München eingereicht und durch die Fakultät für Chemie am 16.05.2018 angenommen.

Abstract

The energy density of lithium-ion batteries in high power applications is limited. Due to the complexity of lithium-ion batteries, such high power limitations may have manifold causes. In consequence a profound knowledge about the underlying electrochemical and physical processes is required to understand limited power densities and to mitigate the bottlenecks in current lithium-ion technology. Correct electrochemical and physical parameters also enable predictive numerical models which allow distinct insights into a battery during operation. In this PhD thesis, novel electrochemical measurement techniques are introduced and applied to determine the rate limiting parameters for the operation of a lithium-ion battery at room temperature namely, the ionic transport properties of the liquid electrolyte and the transport path length in terms of the tortuosity of the porous media. It is demonstrated how ionic transport limitations will directly affect the power density of the battery on the electrode level and how previous reports of electrolyte transport properties oversimplify the temperature and concentration dependence of electrolyte properties. In addition to the electrolyte and porous electrode parameters, all other parameters required for numerical experiments have been measured or estimated and are presented in this thesis. The blocking configuration concept that is introduced for the AC impedance based determination of electrode tortuosities is furthermore developed into an in-situ cell characterization tool based on electrochemical impedance spectroscopy. It is shown that a careful experimental setup and measurement procedure allow to obtain a better understanding of the resistance build-up of lithium-ion battery electrodes during operation.

Kurzfassung

Die Energiedichte von Lithium-Ionen Batterien bei hohen Strömen ist begrenzt. Aufgrund der Komplexität von Lithium-Ionen Batterien können die Ursachen für diese Begrenzung vielfältig sein. Daher ist ein fundiertes Verständnis der zugrundeliegenden elektrochemischen und physikalischen Prozesse notwendig um die Limitierungen von heutigen Lithium Ionen Zellen zu verringern. Nur mit präzisen, elektrochemischen und physikalischen Parametern können prädiktive Batteriemodelle erstellt werden, die verlässliche Einblicke in eine Batterie während des Betriebs ermöglichen. In dieser Doktorarbeit wurden neuartige Messmethoden entwickelt und angewandt um die Raten limitierenden Parameter einer Lithium-Ionen Batterie bei Raumtemperatur zu bestimmen. Diese sind die ionischen Transporteigenschaften des Elektrolyten sowie die Pfadlänge des Ionentransports, bestimmt durch die Tortuosität der porösen Komponenten. Es wird gezeigt, dass diese ionischen Transportlimitierungen die Leistungsdichte einer Zelle auf Elektrodenebene bestimmen sowie dass die Temperatur- und Konzentrationsabhängigkeit des Ladungstransports im Elektrolyten in der Literatur zu sehr vereinfacht wird. Darüber hinaus wurden im Rahmen dieser Dissertation auch alle weiteren notwendigen Parameter zur analytischen Beschreibung einer Batterie bestimmt oder abgeschätzt, welche in dieser Arbeit zusammengetragen sind. Weiterhin wurde das Konzept einer blockierenden Elektrode, das für die Bestimmung der Elektrodentortuositäten verwendet wird, zu einer Impedanz-spektroskopischen in-situ Charakterisierungsmethode weiterentwickelt. Durch einen geeigneten experimentellen Aufbau und eine geschickte Messprozedur konnten hiermit neuartige Einblicke in den Widerstandsaufbau einer Lithium Ionen Zelle während des Betriebs erhalten werden.

Nomenclature

Abbreviations

A/An	Anode
C/Cath	Cathode
CA	Conductive additive
CC	Current collector
CCCV	Constant current constant voltage
CMC	Carboxymethyl dellulose
CT	Charge transfer
CV	Cyclic voltammogram
DBL	Double layer
DEC	Diethyl carbonate
DMC	Dimethyl carbonate
EC	Ethylene carbonate
EIS	Electrochemical impedance spectroscopy
Elyt	Electrolyte
EMC	Ethyl methyl carbonate
FEC	Fluoroethylene carbonate
FIB	Focused ion beam
GEIS	Galvano electrochemical impedance spectroscopy
GITT	Galvanostatic intermittent titration technique
Gra	Graphite
GWRE	Gold wire micro reference electrode
kin	Kinetic
LFP	Lithium iron phosphate
LIB	Lithium-ion battery
LNMO	Lithium nickel manganese oxide
NMC	Nickel manganese cobalt oxide
OCV	Open circuit voltage
PC	Propylene carbonate
PEIS	Potentio electrochemical impedance spectroscopy
PhD	Philosophiae doctor

PITT	Potentiostatic intermittent titration technique
PVDF	Polyvinylidene difluoride
SBR	Styrene-butadiene rubber
SEI	Solid electrolyte interphase
SEM	Scanning electron microscope
Sep	Separator
SOC	State of charge
SS	Solid state
TDF	Thermodynamic factor
VC	Vinylene carbonate
VGCF	Vapor grown carbon fibers

Symbols

α	Charge transfer coefficient	-
η	Overpotential	V
κ	Ionic conductivity	mS/cm
ϕ	Electrochemical potential	V
ρ	Density	g/cm³
σ	Electric conductivity	S/m
τ	Tortuosity	-
F	Faraday constant	C/mol
R	General gas constant	J/(mol K)
TDF	Thermodynamic factor	-
ε	Porosity	-
ε_{R}	Relative permittivity	-
A	Area	cm²
C	Capacitance	F
c_{l}	Electrolyte salt concentration	mol/L
c_{s}	Solid material lithium concentration	mol/m³
$D_{\pm}$	Binary diffusion coefficient	cm²/s
D_{SS}	Solid state diffusion coefficient	cm²/s
$f_{\pm}$	Mean molar activity coefficient	-
f_{bal}	Balancing factor	-
i	Current density	mA/cm²
i_0	Exchange current density	mA/cm²
k	Kinetic rate constant	m/s
L	Loading	mAh/cm²
m	Mass	g
N_{M}	MacMullin number	-
Q	Constant phase element capacitance	$\mathrm{mF} \cdot \mathrm{s}^{(\alpha-1)}$

R	Resistance	Ω
r	Particle radius	µm
S	Surface area	cm^2
T	Temperature	K
t	Thickness	µm
t	Time	s
t_+	Transference number	-
U	Potential	V
v_0	Convective flow velocity	m/s
x	Distance	µm

The scientist is not a person who gives the right answers, he's one who asks the right questions.

— Claude Lévi-Strauss

Contents

Chapter 1

Introduction

In 2016, the 25th anniversary of the lithium-ion battery was celebrated.[1] Since Sony's commercialization of lithium-ion batteries in 1991, the technology has penetrated every portable application, such as cellular devices and notebooks but also enables innovative application in, e.g., animal friendly submarines,[2] medical implants[3] and extra terrestrial applications.[4] Electromobility is attracting an increasing amount of interest due to the image campaigns of Tesla, BMW and others and makes electrical energy storage a recurrent subject in mass media. Caught in the strive for higher market penetration and energy density, the origins of electromobility are often overlooked. Between 1896 and 1939, over 500 producers for full-electrical vehicles existed,[5] with maximum velocities reaching 100 km/h and driving ranges of 130 km (at max. 20 mph).[6,7] Astonishingly, in 1912 a similar number of electrical vehicles were built in the USA (≈34000),[8] than registered in Germany in January 2017 (34022).[9] Around 1900 the market share for full electrical vehicles was nearly 40 % (another 40 % were steam powered, the remainder were combustion engines),[8] compared to 0.7 % in Germany as of early 2017.[9]

The current low market penetration of electrical vehicles is mainly due to range limitations and high costs of battery or fuel cell electrical vehicles.[10,11] These hurdles have to be overcome for electrical mobility to significantly reduce the amount of greenhouse gas emitted in the transportation sector. Even for the recent energy mix in Europe (50 % based on oil, natural gas and coal[12]) a significant reduction of tail-pipe CO_2 emissions may be achieved by moving from combustion engines (≈120 g_{CO_2}/km) to full electrical vehicles (≈0 g_{CO_2}/km).[13] The elaborate cell production of lithium-ion batteries as well as the increasing prices for necessary raw materials such as lithium and cobalt further drive the high cost. Even the political incentives for buying a full electrical vehicle in the European Union counteract the monetary barriers only partially; at the time of writing this thesis electrical cars bought in Germany are eligible for a 4000 € environmental bonus (half paid by the manufacturer, half by the government),[14] compared to the high purchase cost of ≈37000 €.[15] Concentrated research on cobalt-poor, nickel-rich NMCs demonstrates the pressure on battery manufacturers since the price for cobalt has nearly tripled since mid 2016 (≈24 €/t) till today (68 €/t).[16] Yet even these promising novel active materials, even in combination with silicon/graphite composite anodes will reach a limit in terms of energy density and are unlikely by themselves to break the barrier towards a high electrical vehicle market share (only a 33 % price reduction is expected

Figure 1.1: Forgotten history, an advertisement for the 1912 Detroit Electric Car, of which 13000 copies were sold, the production record for the entire 20th century.[7] (obtained from Wikimedia Commons)

by moving from graphite/NMC cell chemistry to silicon/manganese rich NMC)[17]. Thus it is not surprising that the Robert Bosch GmbH, one of the largest German engineering companies and automotive suppliers, announced its withdrawal from lithium-ion battery research in a recent press release.[18] The slow pace of incremental battery development by the lead suppliers (LG Chem, Samsung, Panasonic etc.) cannot be sustained by newcomers in the field and the focus has to be shifted towards innovative future technologies.

One possible solution to increase the energy density of a lithium-ion battery is to increase the active material loading, currently only representing ≈35 % of the battery weight on the system level.[10,19] An increase of the electrode thickness from 50 µm to 100 µm would, for example yield an increase of the mass fraction of active materials in the battery, effectively reducing its price on the cell level by ≈20 %.[20] The drawback of increasing the electrode thickness is the largely reduced power capability of the battery.[10] In a low loading electrode assembly (2 mAh/cm²), nearly 90 % of the cell capacity is accessible at a C-rate of 1 1/h (i.e., a discharge current corresponding to a complete discharge of the nominal capacity in 1 h), while for the high loading case (6 mAh/cm²), only a minor fraction of 25 % may be used reversibly at the same C-rate.[10] Mitigation of this power limitation would not only allow to increase the energy density of lithium-ion batteries, but also enable another innovative solution to the cost and range limitation of current electrical energy storage devices. An innovative future battery with a similar energy density as currently available lithium-ion batteries, but with largely reduced power limitations during charging could be refilled at much shorter times, thereby rendering larger battery packs unnecessary. If the power limitations of current lithium battery systems could be overcome, electrical mobility would become more affordable, not only because the battery could be smaller due to shorter recharging times, but also because the pricing pressure caused by the high demand of raw materials would be reduced. In

addition to reduced charging times, lithium-ion batteries with an improved rate capability will also show reduced tendencies for side reactions which may lead to accelerated cell aging or safety concerns.[21] Lacking profound characterization techniques of rate limiting parameters, manufacturers and users of current lithium-ion batteries can only avoid detrimental effects that result from too high currents with extensive and costly long-term cycling tests and the application of conservative safety margins for the cell operation. These approaches increase the price of the cells, limit their energy and power density and thereby hinder efficient use and higher market acceptance of lithium-ion batteries. To understand the origin of power limitations of lithium-ion batteries, their fundamental operating principle is shortly introduced in the following.

1.1 Operation of a Lithium-Ion Battery

Chemical energy is reversibly converted to electrical energy by redox reactions within a lithium-ion battery. In an outer electrical circuit, negatively charged electrons flow through the external load and are counterbalanced by Faradaic reactions yielding or consuming lithium ions, which are transported between the electrodes of the battery by the liquid electrolyte inside the pores of the porous electrodes. A porous plastic separator between the electrodes avoids an electrical short. The active materials inside the porous electrodes store lithium ions by reversible (de-)intercalation reactions. In addition, conductive additives may be used to enhance the electrical conductivity of the electrode, and polymeric binders provide mechanical stability. An example for an (de-)intercalation material is LFP, which can take up lithium ions in unoccupied interstitial sites of the crystal structure. During charge of an LFP electrode (positive electrode, commonly referred to as a cathode) lithium is deintercalated from the host structure and added to the electrolyte in form of lithium ions.

$$\mathrm{LiFePO_4} \rightleftharpoons \mathrm{FePO_4} + \mathrm{Li^+} + \mathrm{e^-} \tag{1.1}$$

The lithium ions are transported through the porous electrodes and the separator in the electrolyte phase until they are intercalated at the negative electrode (commonly referred to as anode), which typically consists of graphite as an active material.

$$\mathrm{Li^+} + \mathrm{e^-} + \mathrm{C_6} \rightleftharpoons \mathrm{LiC_6} \tag{1.2}$$

During intercalation the positively charged lithium ion combines with an electron provided by the outer electrical circuit. Figure 1 illustrates the ionic transport through a unit cell of an electrode assembly in a lithium-ion battery. Here the ion transport velocity is indicated by the movement of the lithium ion while the transport path through the porous electrodes and the separator is sketched as a red line.

The thermodynamics and the crystal structure determine the voltage and the energy density of the active materials. A large variety of anode and cathode active materials have been investigated for application in reversible batteries.[22] At the time of writing this thesis, NMC/graphite cells are the standard cell chemistry used, e.g., in the BMW i3, e-Golf by Volkswagen or the Fortwo EV by Smart.[23] The power capability, i.e., how much charge can be transported reversibly at which current, is determined by the cell geometry, the ionic transport properties of the electrolyte, the electrical conductivity

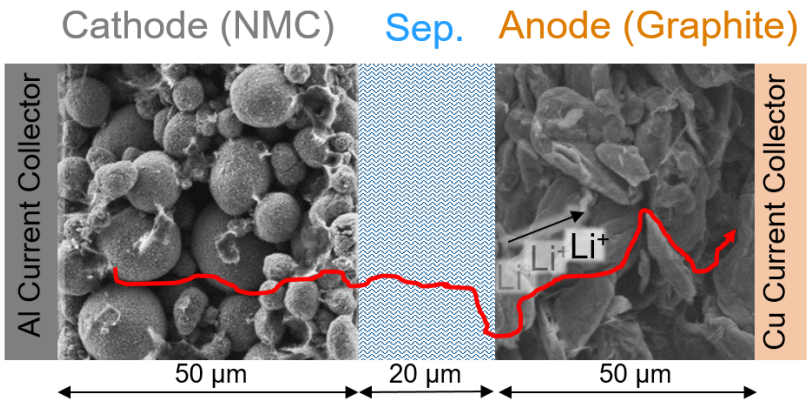

Figure 1.2: Cross section of a lithium-ion battery unit cell, with a NMC cathode supported on an aluminum current collector, with a porous plastic separator, and with a graphite anode, supported on a copper current collector. The pores of the electrodes and the separator are filled with the electrolyte which includes lithium ions. During charge, lithium is deintercalated from the cathode and the positively charged lithium ions are transported through the separator and are intercalated into the host material at the anode side.

of the current collectors and the electrodes, the lithium diffusion within the active materials, and the kinetics at the active material/electrolyte interface. In general, charge transport in a lithium-ion battery is only as fast as its slowest process, so that ideally the lithium ion transport between the electrodes, the lithium intercalation kinetics, the solid state diffusion within the bulk of the active material particles, and the electron conduction would have similar characteristic times. Consequently, to understand the origin of power limitations in lithium-ion batteries it is of utter importance to have a profound knowledge of all these transport processes and their characteristic times. Methods for the determination of all these parameters as well as reported values will be summarized in Chapter 2. It will be shown that it is largely charge transport in the electrolyte which limits higher power densities during charge/discharge operation (see Chapter 6).

When ionic charge transport is the rate limiting process during operation of a battery, concentration gradients of lithium ions will evolve within the pores of the electrode/separator stack. As motivated in the introduction (see Chapter 1), the fast-charge operation of a lithium-ion battery could have a pronounced impact for its future market acceptance. Additionally, detrimental side reactions, indirectly caused by concentration gradients, predominantly occur during fast cell charging. Therefore the following analysis refers to a battery charge, yet during discharge analogous concentration gradients will evolve and limit the cell's power. As shown in Eq. 1.2 and Eq. 1.1 during cell charging, lithium ions will be consumed in the electrolyte at the anode and at the same time the lithium ion concentration will increase within the pores of the cathode, where the lithium is deintercalated from the host structure. Ionic movement in the electrical field (migration) and due to the evolving concentration gradient (diffusion) counteracts the formation of concentration gradients and is described in the scope of the Newman

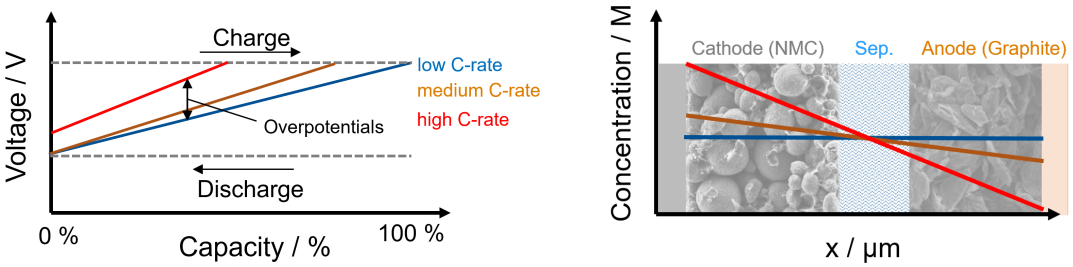

(a) Potential Transients **(b)** Concentration Gradients

Figure 1.3: Sketch of (a) potential transients evolving during operation and (b) concentration gradients at the end of charge of a lithium-ion battery. At low C-rates, i.e., small currents, the full capacity can be obtained and the potential follows the thermodynamically defined voltage/charge relationship (sketched schematically as a blue line in (a)), with the ion concentration remaining close to the initial concentration (blue line in (b)). For increasing C-rates (orange lines) concentration gradients evolve and lead to overpotentials during charging of the cell (see arrow in (a)). In this case the upper potential cut-off (upper dashed gray line in (a)) is reached before the full capacity is obtained (orange line in (a)). For even higher C-rates only a fraction of the full capacity can be obtained before the potential cut-off is reached and the ion concentration is depleted within the pores of the anode (red line in (b)).

model[24–26] for a binary electrolyte by

$$\frac{\partial(\varepsilon\, c_\mathrm{l})}{\partial t} + \vec{\nabla}\cdot(\varepsilon\, c_\mathrm{l}\, \vec{v_0}) = \vec{\nabla}\cdot\left(\frac{\varepsilon}{\tau}\, D_\pm\, \vec{\nabla} c_\mathrm{l}\right) - \frac{\vec{i}\cdot\vec{\nabla} t_+}{\mathrm{F}} \tag{1.3}$$

and

$$\vec{\nabla}\phi = -\frac{\vec{i}}{\kappa_\mathrm{Ion}\, \varepsilon/\tau} + \frac{2\mathrm{R}T}{\mathrm{F}}\left(1 + \frac{\partial \ln f_\pm}{\partial \ln c_\mathrm{l}}\right)(1 - t_+)\,\vec{\nabla}\ln c_\mathrm{l}. \tag{1.4}$$

Here ε is the porosity of the porous medium, c_l the ion concentration in the electrolyte, $\vec{v_0}$ the convective flow velocity (which is generally neglected for the microporous media), τ the tortuosity of the porous medium, $D_\pm$ the binary diffusion coefficient, $\vec{i}$ the current density, t_+ the transference number, F the Faraday constant, ϕ the electrochemical potential, κ_Ion the ionic conductivity, T the temperature, R the general gas constant and $f_\pm$ the mean molar activity coefficient. For small charge C-rates the ion concentration profile within the cell remains close to the initial salt concentration (see blue lines in Figure 1.3, commonly 1 M). For increasing C-rates steady state concentration profiles will evolve if the ionic charge transport can support the externally forced charging current (see orange lines in Figure 1.3). When the charging C-rate is too high to be supported by ionic charge transport in the electrolyte, the concentration gradient will further increase and lead to a significant depletion of lithium ions at the anode side (see red line in Figure 1.3b, analogously at the cathode side during discharge). Due to charge conservation the consumption of ions at the anode and the increase of the lithium ion concentration at the cathode have to counterbalance exactly.

In compliance with the principle of the Nernst equation further intercalation of lithium ions at the anode and deintercalation of lithium from the cathode active material is hindered. On the one hand the reversible potential of the active material

changes drastically when its SOC approaches 0 % or 100 %, on the other hand further (de-)intercalation in the low/high SOC regions is hindered kinetically. The Butler-Volmer equation is typically used to describe the correlation between the kinetic current density i and required kinetic overpotential η.[26]

$$i = i_0 \cdot \left[\exp\left(\frac{\alpha_\mathrm{a} \cdot \mathrm{F}}{\mathrm{R} \cdot T} \cdot \eta \right) - \exp\left(-\frac{\alpha_\mathrm{c} \cdot \mathrm{F}}{\mathrm{R} \cdot T} \cdot \eta \right) \right] \tag{1.5}$$

Here we use the nomenclature defined in COMSOL Multiphysics® with α_c and α_a the cathodic and anodic charge transfer coefficients (both typically assumed 0.5 for battery applications).[26] The exchange current density i_0 includes the dependence of the kinetic current on the concentration of products and educts and is defined by

$$i_0 = \mathrm{F} \cdot k_\mathrm{c}^{\alpha_\mathrm{a}} \cdot k_\mathrm{a}^{\alpha_\mathrm{c}} \cdot \left(c_\mathrm{s,max} - c_\mathrm{s} \right)^{\alpha_\mathrm{a}} \cdot c_\mathrm{s}^{\alpha_\mathrm{c}} \left(\frac{c_\mathrm{l}}{c_\mathrm{l,ref}} \right)^{\alpha_\mathrm{a}} \tag{1.6}$$

with the anodic and cathodic rate constants k_a and k_c, the current and maximum solid phase lithium concentrations c_s and $c_\mathrm{s,max}$, and the ionic lithium concentration c_l, made dimensionless by $c_\mathrm{l,ref} = 1$ mol/m³. Eq. 1.6 shows that the exchange current density decreases when either the lithium ion concentration is depleted or the solid phase degree of lithiation approaches 0 % or 100 %. I.e., if significant concentration gradients evolve during fast charging operation of a battery, the overpotentials necessary to maintain the same current have to increase.

A simple analysis of the potential transient during fast charge (and discharge) of a battery may help to understand its limitations. The overpotentials in the scheme in Figure 1.3a show two features for increasing C-rates, i) an increased overpotential at the beginning of charge, which is caused by the purely ohmic or kinetic contributions to the cell resistance, e.g., SEI resistance, electrolyte resistance or contact resistances and ii) for high C-rates, when concentration gradients evolve, the overpotential will increase over the course of charging/discharging of the cell due to the depletion of ions (see Eq. 1.5 and 1.6). I.e., whether the overpotential during cycling remains constant or is increasing during charge/discharge operation, serves as a first indicator to find if the cell performance is limited by ionic charge transport or by ohmic overpotentials. Independent of the origin of the overpotential, its existence will reduce the reversible capacity of the cell, as the typically set lower or upper cell potential limits are reached earlier (see gray dashed lines in 1.3a). One has to keep in mind that in two-electrode cells only the full-cell overpotential can be monitored and the overpotentials of the individual electrodes cannot be obtained independently. This poses a huge difficulty in full-cell battery operation as the commonly used graphite electrode potential is close to the lithium plating potential, an unwanted side reaction which poses not only a great safety hazard but also leads to accelerated aging of the cell.[21] In a well balanced cell, all the charge stored in the cathode may be intercalated into the anode during slow charge, as the anode is generally oversized slightly. However, during fast charging operation the ionic concentration gradient in the pores of the anode leads to inhomogeneous charging across the anode electrode thickness. Initially, at the interface to the separator, where lithium ions from the cathode arrive, the intercalation reaction may take place, as the necessary kinetic overpotential is small (see Eq. 1.6 for c_l high). However, once the initial lithium inventory in the electrolyte close to the anode current collector is depleted, the

intercalation reaction ceases quickly, as the supply of additional lithium ions is too small. As a result, the graphite particles close to the separator reach a higher degree of lithiation faster, than their counterparts sitting close to the current collector. This inhomogeneous charging does not pose a safety issue directly, yet once the degree of lithiation of the particles at the separator interface approaches 100 %, the intercalation reaction is hindered throughout the electrode (at the current collector because of $c_\mathrm{l} \to 0$, at the separator because $c_\mathrm{s} \to c_\mathrm{s,max}$, see Eq. 1.5). Further intercalation reactions of the not fully lithiated graphite particles at the current collector is only possible for an increased overpotential. Due to the high electrical conductivity of graphite electrodes (>10 S/cm)[27], the overpotential is not only applied at the not lithiated particles near the anode/current collector interface but also to the particles at the anode/separator interface which have a high state of charge already. Here the intercalation reaction is impossible and the applied overpotential drives the lithium plating reaction, enabled by the close potential of graphite particles at high SOC to the potential of metallic lithium deposition (≈10–50 mV). Depending on the plating current and the cell pressure, the metallic lithium may form mossy dendritic structures that only partially dissolve during the following discharge reaction,[28–30] leaving behind electrically not connected metallic lithium residue which reduces the cell's cycleable lithium inventory. Even if these metallic lithium dendrites are dissolved again reversibly, ongoing SEI formation on repeatedly forming, fresh lithium metal surfaces consumes active lithium and leads to a steady capacity decay.[21] The worst case scenario is the formation of an electrical short between the electrodes by continuous growth of metallic lithium dendrites which may locally perforate the separator. The resulting highly localized cell discharge may lead to a strong temperature increase which is a safety hazard, as the used organic electrolytes are flammable and the cathode active materials may release oxygen at high temperatures.[22] Because lithium plating reactions and ongoing SEI formation are not an issue during cell discharge, even at high rates, the charging operation of lithium-ion batteries mainly limits their performance and lifetime.

To avoid accelerated aging, safety concerns and capacity loss during the charge operation of two-electrode cells (in which the graphite potential cannot be monitored independently), conservative safety margins have to be used in battery control units such as battery management systems and the cut-off potential for the cell charge includes a carefully chosen safety margin. The reduction of concentration gradients in lithium-ion batteries by novel electrode designs or innovative electrolytes, may enable higher charge C-rates within the potential safety margins of the cell.

In addition to a quantitative knowledge about charge rate limiting transport parameters, novel in-situ characterization techniques will help to understand the cell behavior during operation. Such a methodology was developed as a part of this thesis and is based on electrochemical impedance spectroscopy (EIS).

1.2 Impedance Spectroscopy

Impedance spectroscopy is a powerful analysis method to investigate electrochemical systems. An impedance spectrum is recorded by application of frequency dependent sinusoidal potential or current excitations to the device under study. Analogous to the definition of the real resistance, the impedance is a complex resistance of the system

which can be obtained from the ratio of complex potential and the complex current flowing as a function of the excitation frequency. It thus follows the same rules for parallel (reciprocal addition) and serial (additive) connections. Every physical and electrochemical process can be described by single equivalent circuit elements such as, e.g., resistors, capacitors or inductors, or serial or parallel combinations of those circuit elements. Recorded impedance spectra are typically compared to calculated impedances of equivalent circuits which presumably describe the device under study. If the simulated and measured impedances agree well and the assumed equivalent circuit is motivated physically, the parameters of each equivalent circuit element should ideally represent defined physical-chemical properties of the experimental system. A great difficulty in impedance analysis is due to the fact that characteristic frequencies of some equivalent circuit elements are similar, such as, e.g., the charge transfer reactions at the anode and the cathode. The need for a sound physical equivalent circuit model is stressed, as generally multiple equivalent circuit models may allow for an equally well representation of experimental data, which unfortunately has given impedance analysis a rather negative image. For a detailed explanation of impedance spectroscopy the reader is referred to the pertinent literature.[31–34]

In the scope of this thesis, special focus is put on the so-called transmission line model equivalent circuit, which may be used to describe the effects of a porous electrode and is thus of great relevance for lithium-ion battery electrodes. In addition to the referenced books, the impedance documentation by Zahner, with its focus on transmission line models, was of great help for this work.[35–37]

In the following chapter an overview of the rate determining physical and electrochemical parameters of a lithium-ion battery is given. At the end of this thesis the obtained parameters and their experimental ranges are used in a numerical sensitivity analysis to highlight the limitations arising from the individual transport processes (see Chapter 6).

Chapter 2

Determination and Estimation of Lithium-Ion Battery Parameters

The behavior of a lithium-ion battery on the electrode level (see Figure 1.2) is determined by the current collectors (see Section 2.1), the separator (see Section 2.2), the electrolyte (see Section 2.3), the electrodes and their composition (see Section 2.4), the active material (see Section 2.5) and the interfacial kinetics (see Section 2.6). While the focus of this PhD thesis was on the characterization of porous electrode tortuosities and the analysis of novel techniques to find the electrolyte transport properties, all main parameters necessary to describe a lithium-ion battery on the cell level have been measured or estimated. The scope of this section is to review all measurement techniques and approaches used in this thesis to find physical and electrochemical parameters required for an isothermal 1D lithium-ion battery model (see Figure 2.1). At the end of this thesis, representative parameters given in the subsequent sections and their typical ranges are collected in Table 6.1. To demonstrate the significance of the experimental ranges found for each parameter they are furthermore used in a numerical sensitivity study using Comsol Multiphysics® in Chapter 6 which investigates the change of the critical C-rate and overpotential during discharge if individual parameters are changed to their upper or lower experimentally found limit.

The energy and power density obviously not only depend on the cell electrochemistry but also on the cell housing and on the system level engineering of the battery devices ehich must consider battery safety, cooling and monitoring regulations and requirements. These auxiliaries sum up to roughly half of the battery weight on the system level, with the remaining 50 % being distributed to active materials (35 %) as well as current collectors, electrolyte and separator (together ≈15 %).[19] The art of pack and system level engineering of lithium-ion battery assemblies is beyond the scope of this work, which in turn focuses on the electrode level effects in a lithium-ion battery.

2.1 Current Collectors

Copper and aluminum current collectors from MTI (MTI Corporation, USA) were used in this thesis. The current collector **thickness** $t_{\mathrm{Cu/Al}}$ was determined using a high precision measurement gauge (Mitotoyo, Litematic VL-50); the densities were assumed

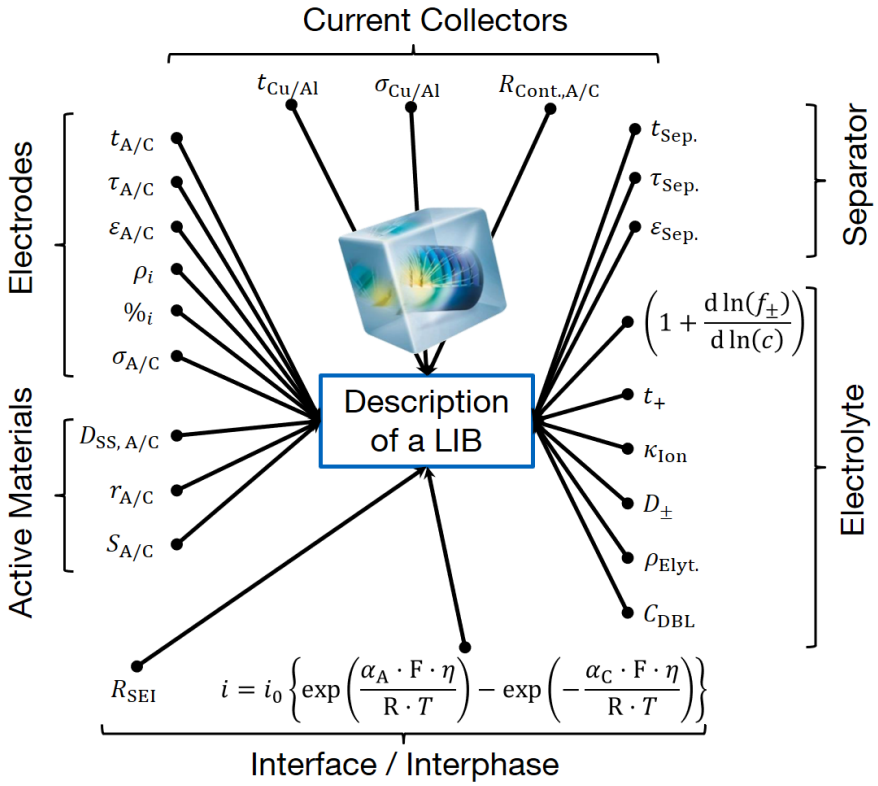

Figure 2.1: Overview of electrochemical and physical parameters determining the charge/discharge operation of a lithium-ion battery (subscript A refers to the anode, C to the cathode). For predictive battery models the parameters describing the current collectors, separator, electrolyte, kinetics, active material particles, and the electrodes are required. Representative values, measured or estimated within this thesis are collected in Sections 2.1 to 2.6 and summarized in Table 6.1 in Chapter 6. Starting from the separator and going clock-wise, the parameters are: separator thickness ($t_{Sep.}$), separator tortuosity ($\tau_{Sep.}$), separator porosity ($\varepsilon_{Sep.}$), thermodynamic factor (TDF), transference number (t_+), ionic conductivity (κ_{Ion}), binary diffusion coefficient ($D_\pm$), electrolyte density ($\rho_{Elyt.}$), areal double layer capacity (C_{DBL}), parameters for the Butler-Volmer kinetics equation (i_0, $\alpha_{A/C}$), areal film resistance (R_{SEI}), active material BET ($S_{A/C}$), particle radius ($r_{A/C}$), solid state diffusion coefficient ($D_{SS,A/C}$), electrical conductivity in the electrode ($\sigma_{A/C}$), electrode component weight fraction ($\%_i$), electrode component density (ρ_i), electrode porosity ($\varepsilon_{A/C}$), electrode tortuosity ($\tau_{A/C}$), electrode thickness ($t_{A/C}$), current collector thickness ($t_{Cu/Al}$), current collector electrical conductivity ($\sigma_{Cu/Al}$) and current collector/electrode contact resistance ($R_{Cont.,A/C}$).

to correspond to pure aluminum and copper.[38] Analogously, the electrical **conductivity** $\sigma_{Cu/Al}$ of the current collectors may be readily found in the literature.[38]

At the interface between current collector and porous electrode, mechanical adhesion is required to guarantee the stability of the electrode while being processed and handled. Additionally, this interface is required to transport electrons from the outer electrical circuit to the porous electrode, where the conductive carbon network distributes the electrons to all active material particles. The native Al_2O_3 passivation layer on the alu-

minum current collector has a low electrical conductivity and may yield a pronounced contact resistance. Especially when the active material has a low electrical conductivity, often found for cathode active materials,[39] or if the electrode is not calandered or too little conductive additive is used **contact resistances** can be significant. The contact resistance between a porous cathode electrode, and an aluminum current collector may be measured using the symmetric cell impedance approach introduced for the determination of porous electrode tortuosities (see Section 4.1). Using a *high* conductivity (reduces pore resistance) and non-intercalating electrolyte allows to easily and unambiguously observe a high frequency semicircle which results from such a contact resistance.[40] For details on the measurement procedure, the experimental setup as well as a clear assignment of the semicircle to the current collector/electrode interface using the capacitance of the semicircle the reader is referred to the original publication presented in Section 4.1.[41] In well prepared cathodes, i.e., with enough conductive carbon and a reasonable electrode compression, as well as for graphite anodes supported on copper foil, contact resistances should not be observable. On the other hand for mildly compressed LFP cathodes contact resistances up to 40 $\Omega\mathrm{cm}^2_{\mathrm{geo}}$ were observed.

2.2 Separator

An overview of porous plastic separators for application in lithium-ion batteries is given in the article presented in Section 4.1. The **porosity** $\varepsilon_{\mathrm{Sep.}}$ of a separator may be obtained gravimetrically from the separator layer **thickness** $t_{\mathrm{Sep.}}$, its areal mass and the bulk density of the separator material (e.g., polypropylene or polyethylene). Geometrical characteristics of porous separators, such as porosity, thickness and sometimes the areal resistance is given on the manufacturer's specification sheet.[42] In this study separator porosities from the manufacturer's specification sheet were validated from thickness (Mitotoyo, Japan, Litematic VL-50) and weight (Mettler Toledo, USA, XP6, ± 0.1 µg) measurements. **Tortuosities** of porous separators are obtained using the copper block setup introduced in Ref. [41]. A typical representative is the 20 µm thick trilayer separator H2013 from Celgard which has a porosity of $\varepsilon_{\mathrm{Sep.}} = 0.47$ and a tortuosity of $\tau_{\mathrm{Sep.}} = 3.2$.[41] Separator thicknesses, porosities and tortuosities range between 15–25 µm, 0.40–0.60, and 2.5–4, respectively (see Table II in Ref. [41] and Table 6.1 in Chapter 6).

2.3 Electrolyte

Charge transport in the liquid electrolyte is possible due to the dissociation of lithium salts (in this work $LiPF_6$, $NaPF_6$, and $LiClO_4$ are used) in the non-aqueous solvents EC, DEC, DMC, EMC, FEC and mixtures thereof. Predominantly the highly polar cyclic EC and FEC (or earlier PC)[43] molecules form a solvation shell around the small alkali ion and thereby determine its mobility and activity. To fundamentally understand the solvation structure around the alkali ion, a huge variety of experimental and theoretical investigations have been conducted.[44–46] Such analysis will help to obtain a physical understanding of, e.g., the solvation shell; however, the transfer of this knowledge to the electrolyte transport properties is purely qualitative, as validated theories are lacking.

Therefore this study focuses on the electrochemical determination of electrolyte parameters which has the advantage of not requiring a quantitative knowledge about ion pairing, the ion solvation shell, or the ionic mobility. Instead, these fundamental relations are implicitly included in our electrochemical measurements of effective transport quantities. In this approach, the conductivity of a nominally 2 M electrolyte is determined without including ion association effects, so that the *real* conductivity of the *free* ions might be higher. For an accurate electrochemical description of charge transport processes in a battery, however, the effective conductivity is sufficient. In the framework of the Newman Model,[24–26] ionic charge transport is defined by four transport properties: the ionic conductivity κ_{Ion}, the binary diffusion coefficient $D_{\pm}$, the transference number t_{+}, and the thermodynamic factor TDF.

In brief, the ionic conductivity relates to the ionic resistance of the electrolyte solution, the binary diffusion coefficient depends on the ionic mobility in a concentration gradient, and the transference number is defined by the ionic mobility in an electrical field.[26] The thermodynamic factor depends on the mean molar activity coefficient, which describes the energy required to free the ion from its solvation shell, referenced to the infinitely diluted state.[47]

The **ionic conductivity** κ_{Ion} can be determined using turn-key equipment which is commercially available. In this thesis, ionic conductivities were measured using a conductivity sensor from SI Analytics (LF 1100+) or a conductivity cell from rhd instruments (TSC 1600 Closed), which both include a temperature sensor. Calibration of the cell constants was done using commercially available conductivity standards (Sigma Aldrich). Due to the ease of determination, the ionic conductivity of lithium-ion battery electrolytes is well studied for a variety of electrolyte compositions.[48–50] For the sensitivity study in Chapter 6 the concentration dependent ionic conductivity of $LiPF_6$ in EC:EMC (3:7 w:w) at 25 °C is used and scaled (±3 %, see $f_{\kappa_{\mathrm{Ion}}}$ in Table 6 and 6.2), based on the experimental uncertainty observed in the temperature dependent study (see Section 3.4).

The **binary diffusion coefficient** $D_{\pm}$ may be analyzed individually using, e.g., pulsed field gradient NMR or electrochemical pulse experiments.[51–53] For the electrochemical determination from symmetric lithium cells, two different cell designs were used in this work. The measurement procedure, experimental artifacts and both cell designs are described in detail in the original publications (see section 3.1 and section 3.4).[54,55] For the sensitivity study in Chapter 6 the concentration dependent binary diffusion coefficient of $LiPF_6$ in EC:EMC (3:7 w:w) at 25 °C is used and scaled (±10 %, see $f_{D_{\pm}}$ in Table 6 and 6.2), based on the experimental uncertainty observed in the temperature dependent study (see Section 3.4).

Transference numbers t_{+} are hardly available in the literature. Apart from a widely applied work by Valøen and Reimers in 2005,[50] only few electrolyte studies fundamentally study the concentration dependence of the transference number.[56,57] The largest misconception in the literature is the adoption of the steady state polarization technique,[58] originally developed for solid electrolytes, to liquid electrolyte systems.[53] In the course of this thesis a variety of analytical derivations for the electrochemical determination of transference numbers were investigated (see Section 3.3). Experiments are based on pulse or steady state polarizations in symmetric lithium cells including a porous separator and concentration cell experiments (described in detail in Ref. [59] and

[55], see Chapter 3). For the sensitivity study in Chapter 6 the concentration dependent transference number of $LiPF_6$ in EC:EMC (3:7 w:w) at 25 °C is used and scaled (±20 %, see f_{t_+} in Table 6 and 6.2), based on the experimental uncertainty observed in the temperature dependent study (see Section 3.4).

In the simulation of lithium-ion batteries the **thermodynamic factor** TDF is often neglected, e.g., Ref. [60]. The reason for such simplification is the small effect of the thermodynamic factor on the modeled cell performance, and the fact that there are only very few studies reported in the literature.[50,56,57,61] For the direct electrochemical determination of thermodynamic factors a novel method was introduced in the beginning of this thesis (see Section 3.2). Only later it was found that one of the key assumptions is unfortunately invalid and thus renders the method unusable, which is discussed in the corresponding erratum (see Section 3.2). Alternatively, a novel approach, solely based on pulse experiments and concentration cells, is described in the temperature dependent study of electrolyte transport properties (see Section 3.4). For the sensitivity study in Chapter 6 the concentration dependent thermodynamic factor of $LiPF_6$ in EC:EMC (3:7 w:w) at 25 °C is used and scaled (±50 %, see f_{TDF} in Table 6 and 6.2), based on the experimental uncertainty observed in the temperature dependent study (see Section 3.4).

The solvation shell around the ions determines their minimum distance to the electrode surface. As the electron size in the metal is negligible, the **double layer capacity** C_{DBL} at the electrode/electrolyte interface is defined by the type of solvent and salt used. From the capacitive low frequency branch in a blocking electrode configuration (see, e.g., Section 5.2 or 4.1), the areal double layer capacitance may be obtained. E.g., Table I in Ref. [62] gives a constant phase element of $Q_{\mathrm{CT}} = 1\ \mathrm{mF} \cdot \mathrm{s}^{(\alpha_{\mathrm{CT}}-1)}$ for a porous LNMO electrode with a combined BET surface area of active material and conductive additive of $S = S_{\mathrm{LNMO}} + S_{\mathrm{CA}} \approx 600\ \mathrm{cm}^2_{\mathrm{BET}}/\mathrm{cm}^2_{\mathrm{geo}}$. Neglecting the constant phase element angle these values yield a double layer capacitance of 1.6 µF/cm². Analogously, the constant phase element of symmetric cells with a blocking electrolyte and two graphite anodes were investigated which yielded similar double layer capacitances of 1–5 µF/cm².

Although electrolyte densities do not affect the power capability of lithium-ion batteries, they play a role for gravimetric energy and power densities. In this work, **electrolyte densities** $\rho_{\mathrm{Elyt.}}$ are determined gravimetrically using a 10 ml measuring flask inside the glovebox (see supporting information for temperature dependent electrolyte properties study in Section 3.4).

2.4 Electrodes

Porous electrodes for lithium-ion batteries consist of the active material, mechanically stabilizing polymeric binder, and conductive additives to improve the electrical conductivity of the anode or cathode electrode layers $\kappa_{\mathrm{El.,A/C}}$. Their mass percentages $\%_i$ are defined by the slurry composition and allow to calculate the **porosity** of the electrode $\varepsilon_{\mathrm{A/C}}$ from its final, dry **thickness** $t_{\mathrm{A/C}}$ (Mitotoyo, Japan, Litematic VL-50) and its mass (both with current collector thickness and mass subtracted), with the bulk **densities** of all constituents. Densities ρ_i for conductive carbon, PVDF and some active materials are given in Table 6.1. Commercial electrode compositions contain >95 wt.% active material and similar mass ratios of binder and conductive additive.[63,64] For the

sensitivity study in Chapter 6 the electrode composition is fixed ($\%_{AM}/\%_{BI}/\%_{CA}$ = 95/3/2) and the electrode porosity is varied between $\varepsilon_{A/C} = 0.25$ and $\varepsilon_{A/C} = 0.35$. The electrode thickness used in the numerical sensitivity analysis in Chapter 6 is calculated based on a defined areal capacity of the anode of 3 mAh/cm², the cathode is undersized by 5 % (see Table 6.1).

Analogous to the separator case, and as briefly pointed out in Section 1.1, the length of the ionic transport path depends on the microstructure of the porous electrodes and is not only a function of their porosity $\varepsilon_{A/C}$ but also of their **tortuosity** $\tau_{A/C}$. Ionic transport around spherical particles, as illustrated in Figure 1.2 (compare NMC cathode example, left side of Figure 1.2) and is characterized by a comparably short extension of the actual ion transport pathway compared to the distance ions would travel in the absence of the particles (i.e., the tortuosity is comparably low). At the same time, due to the flake-like nature of commonly used graphite active materials, the direct path in graphite electrodes may require large detours (compare right side of Figure 1.2). In real electrodes, the extension of the effective ion transport length may increase by an order of magnitude (see $\tau_A = 10$ in Ref. [65]), effectively leading to increased concentration gradients and thus overpotentials (see Chapter 4). However, tortuosity values reported in the literature were mainly determined using large synchrotron facilities, by sophisticated and as will be shown often ambiguous analysis of 3D reconstructed X-ray tomographs or time consuming and not readily available FIB-SEM measurements.[66–68] In this study a novel method is introduced to measure the tortuosity of porous electrodes electrochemically using impedance spectroscopy (for details see Chapter 4). Depending on the electrode composition, particle morphology and the electrode preparation process, tortuosities of porous electrodes for lithium-ion batteries typically range between 2 and 5, while a tortuosity of 3.5 serves as a good representative. Interestingly, this value is generally ≈2-fold larger than what would be predicted by the commonly used Bruggeman equation, and the origin of this is discussed in Section 4.2 and Ref. [69].

As described above, depending on the intrinsic **electrical conductivity** $\sigma_{A/C}$ of the active material, additional conductive additives are used to enhance the electron transport to and from the active material and the current collector.[70] Branch-like 100–300 nm sized conductive carbons (e.g., SuperP C65, Timcal) with a primary particle size of 30 nm, µm-sized VGCF (vapor grown carbon fibers) or graphite particles are used to improve the electrical conductivity of the electrodes. Determination of the electrical conductivity of a porous electrode is challenging as it is supported on a metal foil and has a thickness of only around 50–100 µm. Two-point measurements are generally not feasible, as the contact resistance to the measurement equipment is on the same order of magnitude or larger than the electrical resistance of the electrode. Alternatively four-point probes allow to determine the in-plane electrical conductivity of electrodes prepared on a non-conductive substrate (e.g., a glass plate/separator), assuming isotropy of the electrical conductivity. The literature describes sophisticated measurement setups in combination with a numerical optimization approach[27] or microimpedance measurements.[71] Reported electrical conductivities for porous cathodes are ≈50 mS/cm, while for highly conductive anodes values of >10000 mS/cm are reported. A comprehensive overview of conduction phenomena in lithium-ion batteries is given in Ref. [39]. In the present thesis, the electrical conductivity was measured in in-plane direction for electrodes coated onto an insulating substrate (here a polymer sep-

arator) and typical values of 100 mS/cm for LFP cathodes with 5 % conductive additive and 20000 mS/cm for graphite anodes were found. Additionally, an impedance based approach is presented which allows to show under which circumstances the electrical resistance of the electrode can be neglected. For the determination of porous electrode tortuosities it is assumed that the electrical conduction resistance is negligible, i.e., the electrical conductivity across the electrode is typically at least a factor 10-100 higher than that of the ionic conductivity within the electrode pores (see Chapter 4 and the discussion in the article in Section 4.2). In consequence, tuning the ionic conductivity by using different salt concentrations will only yield a constant electrode tortuosity in impedance analysis if the electrical resistance is negligible (factor 10–100 smaller), which is shown exemplary in the article for graphite and NMC electrodes (see Section 4.2).[69] Based on this experience, namely our in-plane measurements and the reports in the literature, a typical electrical conductivity of 100 mS/cm is used for the sensitivity study in Chapter 6, with the lower and the upper boundaries given by the literature (50 mS/cm and 10000 mS/cm).

2.5 Active Material

The active material allows the reversible intercalation of lithium ions from the liquid electrolyte during battery operation.[22] Apart from the thermodynamics of the active material (storage capacity, potential profile), its physical properties determine the electrochemical charge and discharge behavior of a lithium-ion battery. The theoretical storage capacity of different active materials and their thermodynamic properties are not the focus of this work, and representative OCV curves and theoretical capacities of a NMC/graphite cell chemistry are used in the sensitivity analysis in Chapter 6.[72,73]

Particle size distributions of the active material may be determined quickly using laser scattering (Horiba LA-950V2, Retsch Technology, Germany), yet experimentally care has to be taken that all particles are well dispersed and not agglomerated during the measurement in order to obtain reliable results. Another problem with laser scattering is that the required refractive index of the active material is not commonly available and that assumptions must be made with regards to particle shape. However, particle size and shape are accessible from scanning electron micrographs. Using image analysis algorithms (e.g., ImageJ/Fiji),[74] particle size distributions may be obtained readily. Exemplary scanning electron micrographs in Figure 2.2 show the surface of a porous graphite (a) and a porous NMC (b) electrode. The graphite particles of the anode typically have a plate-like shape with ≈20 µm diameter and a thickness of ≈5 µm (not visible in Figure 2.2a, see, e.g., Ref. [41] for a cross section view of a graphite anode), i.e., the aspect ratio for the shown graphite material (SLP30, SGL Carbon GmbH) is around 4:1. On the other hand the NMC particles shown in Figure 2.2 are spherical with a 10 µm average diameter (see Figure 2.2b). It is important to note that in the sensitivity study in Chapter 6 the particle radius and shape is only used to describe the lithium diffusion within the active material and the BET surface area of the active material is used as active area for the intercalation kinetics and the double layer capacitance (here also the BET surface area of the conductive additive is used additionally).

The characteristic diffusion time of lithium within the active material depends on the particle size ($r_{\mathrm{A/C}}$, if assumed spherical) and shape, together with the **solid state**

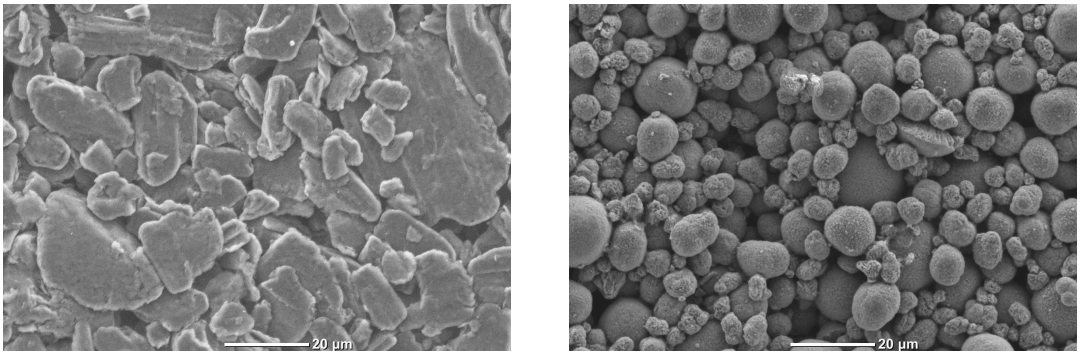

(a) Graphite **(b)** NMC

Figure 2.2: Top view scanning electron micrographs (Jeol, JCM-6000) of graphite (95/5/0) (a) and NMC (96/2/2) (b) electrodes. See article in Section 4.1 for electrode preparation process.

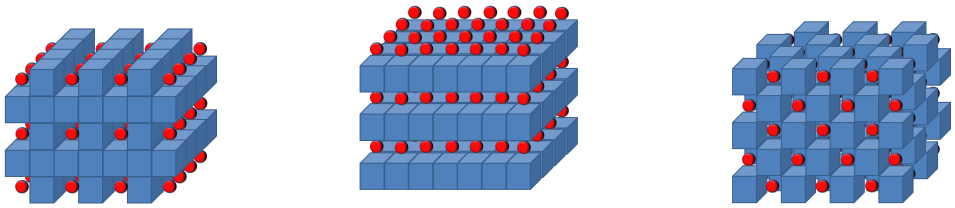

(a) 1D **(b)** 2D **(c)** 3D

Figure 2.3: Schematic crystal structures of intercalation materials used for lithium-ion batteries. A typical representative for the (a) 1D diffusion is LFP, for the (b) 2D diffusion NMC and (c) 3D diffusion occurs in, e.g., $LiMn_2O_4$. (adopted from Ref. [75])

diffusion coefficient $D_{SS,A/C}$. The crystal structure determines if the lithium diffusion is taking place mainly in 1D, 2D, or 3D (see crystal structures for lithium intercalation materials in Figure 2.3). It should be mentioned that the diffusion mechanism itself is still a highly disputed topic,[76–78] and here a simple Fickian process is assumed. In the literature the solid state lithium diffusion coefficient is investigated using, e.g., PITT/GITT,[79] CVs[80] or EIS and the reported diffusion coefficients for a range of anode and cathode active materials are summarized in a review on conduction phenomena in lithium-ion batteries by Park et al.[39] During this thesis it was necessary to estimate the solid state diffusion coefficient for lithium in $LiNi_{0.5}Mn_{1.5}O_4$ (LNMO), for the interpretation of impedance spectra in Section 5.2. The approach to obtain a lower boundary for the solid state diffusion coefficient, which is described in detail in the appendix of the corresponding study (see Section 5.2), is based on charging and discharging an electrode with a very low loading (<100 µAh/cm²) and thus also very low thickness at high C-rates versus a metallic lithium counter electrode and controlling the potential with a lithium reference electrode. In such an experiment the liquid ion transport is not limiting because the total amount of transported charge across a very thin electrode is

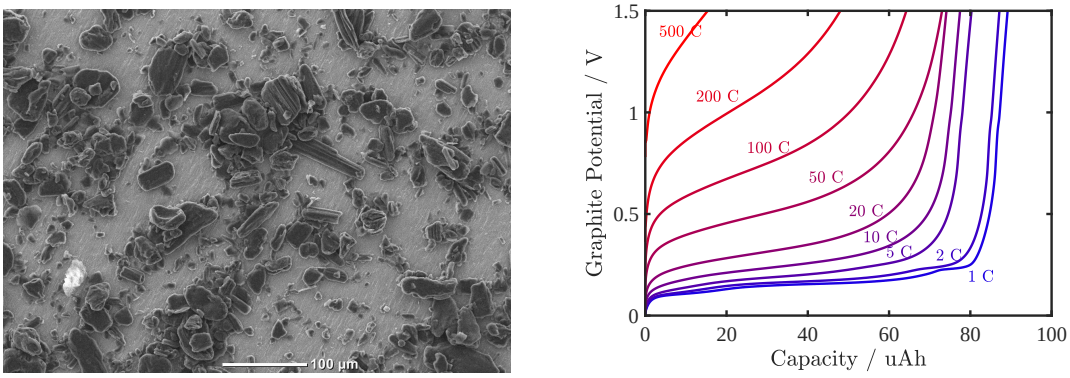

(a) Scanning electron micrograph **(b)** Potential curves

Figure 2.4: Discharge rate test (b) at 25 °C of a graphite electrode (a) with very low loading (90 µAh, $A = 0.95$ cm², current collector visible as light grey background in a) in a three-electrode T-cell setup, measured vs. a metallic lithium counter electrode and controlled with a lithium reference electrode. Two glass fiber separators and a standard electrolyte (1 M $LiPF_6$ in EC:EMC (3:7 w:w)) were used. The cell capacity was determined beforehand in three slow charge/discharge formation cycles at 0.1 C (assuming a gravimetrically estimated capacity of 100 µAh/cm²). Discharge C-rates of 1 C (blue) to 500 C (red) are tested until the upper cut-off potential of 1.5 V versus the reference electrode is reached.

small and thus no concentration gradients and accompanying overpotentials will form and limit the cell performance up to extremely large C-rates. An exemplary discharge rate test of a 90 µAh graphite electrode ($A = 0.95$ cm²) is shown in Figure 2.4b. The scanning electron micrograph of the corresponding graphite electrode which is shown in Figure 2.4a illustrates that the electrode mostly consists of single or few particles on top of the copper current collector (light grey area in Figure 2.4a).

The observed overpotential in the exemplary measurements shown in Figure 2.4b is solely due to the deintercalation kinetics. When the lithium concentration at the surface of the particles reaches the minimum concentration during deintercalation of lithium, the exchange current density approaches 0 mA/cm² (see Eq. 1.6 for $c_s \rightarrow 0$), which causes high overpotentials. Thus as long as the lithium transport within the active material is fast enough, the kinetic overpotential will not diverge and the theoretical capacity of the electrode will be obtained. On the other hand, if the kinetic overpotential becomes significant, the solid lithium concentration at the surface of the active material is depleted. All previously (de-)intercalated lithium must have traveled at least as far into/out of the particle so that the observed macroscopic capacity is obtained. Therefore, if the diffusion mechanism (here Fickian diffusion is assumed, even though this is certainly an oversimplification in the case of 2-phase materials) and its dimension (1D, 2D, 3D) is known, an upper boundary for the solid state diffusion coefficient may be obtained from

$$D_{\mathrm{SS,A/C}} = x^2/t \tag{2.1}$$

with t being the charge/discharge time and x the geometric travel distance in the re-

spective material which would correspond to the obtained capacity. As evident from Figure 2.4, roughly 50 % of the reversible discharge capacity of the low loaded graphite electrode may be obtained at 200 C, i.e., within 50 % of the nominal discharge time of 18 s (i.e., within $t = 9\ s$). Graphite particles are ellipsoidal and lithium intercalation predominately occurs at the basal planes at the outer perimeter (2D intercalation material).[22] Therefore the 3D problem may be simplified to the 2D diffusion into/out of an ellipse (aspect ratio roughly 20 µm : 10 µm $\rightarrow a : b = 10 : 5$, see Figure 2.2a). Fickian diffusion will yield faster intercalation at the vertices (due to a higher perimeter to area ratio) compared to the co-vertices, yet for the purpose of this study a rough estimate may be obtained by assuming a remaining, unaltered inner ellipse $A_{\mathrm{e,cent}}$ with axis lengths of $a - x$ and $b - x$, corresponding to half of the area of the entire ellipse $A_{\mathrm{e,full}}$.

$$A_{\mathrm{e,full}} = \pi \cdot a \cdot b = \frac{1}{2} \cdot \pi \cdot a^2 \tag{2.2}$$

$$A_{\mathrm{e,cent}} = \pi \cdot (a - x) \cdot (b - x) = \pi \cdot (a - x) \cdot \left(\frac{1}{2}a - x\right) \tag{2.3}$$

$$A_{\mathrm{e,cent}} = 50\% \cdot A_{\mathrm{e,full}} \rightarrow x \approx 0.2 \cdot a \tag{2.4}$$

For $a = 10$ µm, a diffusion distance $x = 2$ µm is obtained, yielding a minimum diffusion coefficient of $\approx 4 \cdot 10^{-9}$ cm²/s using Eq. 2.1. It is emphasized, that the presented estimation for the solid state diffusion coefficient only represents an order of magnitude estimate of the lower boundary of the solid state lithium diffusion coefficient, i.e., the lithium diffusion in the active material has to be at least as fast to accommodate the charge transported during the experiment. This is reasonably consistent with the literature values reported for graphite, which range between 10^{-7} cm²/s to 10^{-11} cm²/s.[39,81] Based on a similar analysis we previously found the lower boundary for the solid state diffusion coefficient of lithium in LNMO to be roughly $3.5 \cdot 10^{-10}$ cm²/s (see appendix in article presented in Section 5.2). Based on the estimated values and the broad range in the literature, solid state diffusion coefficients of 3.5, 10, and 40 $\cdot 10^{-10}$ cm²/s are used in the sensitivity analysis in Chapter 6.

It is noted that for low loaded electrodes the impedance at low frequencies is dominated by the solid state diffusion process in the active material and would thus also allow the estimation of this parameter. Preliminary measurements conducted during this PhD project did not yield the expected reflective diffusion impedance spectra (similar shape as a transmission line model, see [31]). For such measurements (lowest frequencies of 1 mHz), a perfectly stable reference electrode potential would be required, which might be the reason for the behavior observed in our experiments.

Additionally, based on the particle shape and size the electrochemically active geometric **surface area** S_{geo} can be estimated. For ellipsoidal particles, with the half-axis lengths a, b and c, the surface area can be approximated with

$$S_{\mathrm{geo}} = 4\pi \left(1/3 \cdot \left((ab)^{1.6} + (ac)^{1.6} + (bc)^{1.6}\right)\right)^{(1/1.6)}. \tag{2.5}$$

The geometric estimation of the active surface area however does not include the surface roughness and pores within the active material. Therefore more accurate active surface areas may be obtained from Brunauer-Emmett-Teller[82] surface adsorption isotherms

S_{BET}, which generally yield higher values compared to the geometric estimation. Typical BET values (m^2/g) for the electrode components are given in Table 6.1 and are used as active area for the intercalation reaction, film resistances and the double layer capacitance (here also the BET surface area of the conductive additive is included), as described in the following section.

2.6 Kinetics

At the interface from active material to liquid electrolyte, the intercalation and deintercalation reaction kinetics as well as the formation of surface films determine the efficiency of charge transport and the corresponding overpotentials. The well-studied solid electrolyte interface[83] forming at graphite anodes may be described as an ohmic contribution and is often investigated using impedance spectroscopy.[84,85] Using a gold wire micro reference electrode (GWRE),[86] the formation of the SEI during the first charge of a graphite anode is investigated in an ongoing project.[87,88] For details the reader is referred to the original publications and here only the found SEI resistance values are summarized. Depending on the type of solvent and additive, the **SEI resistance** after formation was found to be ≈200 $\Omega\mathrm{cm}^2_{\mathrm{BET}}$ (LP57) and SEI resistances between ≈100 $\Omega\mathrm{cm}^2_{\mathrm{BET}}$ and ≈400 $\Omega\mathrm{cm}^2_{\mathrm{BET}}$ were obtained when 1 % FEC and DiFEC was added, respectively.

The **intercalation kinetics** of lithium into the host crystal structure is investigated in the literature using, e.g., PITT experiments,[89] pulse experiments[90] or theoretical approaches,[91,92] yet the most frequent reports on the charge transfer kinetics are based on the analysis of electrochemical impedance spectra.[89,93–96] However one key requirement for the applicability of impedance spectroscopy is the linearity of the system under study, which directly invalidates the use of EIS to obtain the Butler-Volmer kinetics beyond the linear range at small overpotentials (see Eq. 1.5). This also includes state of charge regions in which the potential/capacity relation is not linear, e.g., for SOCs in which the solid state lithium concentration c_{s} approaches 0 M or $c_{\mathrm{s,max}}$. To obtain the kinetic charge transfer resistance R_{kin} from impedance measurements, it is necessary to disentangle it from additional effects overlapping in frequency space, such as the ionic pore resistance, the SEI resistance and possible contact resistances. The charge transfer resistance may, e.g., be obtained if the novel impedance measurement scheme, introduced in Section 5.2 is used. For small excitation amplitudes the exchange current density for the linearized Butler-Volmer equation may be obtained from the kinetic charge transfer resistance R_{kin}, observed in a Nyquist plot, and the electrochemically active surface area S_{BET} (see section 2.5). In its simplest form, the linearized Butler-Volmer equation given in Eq. 2.6 can be rewritten to obtain the exchange current density as a function of the sum of the anodic and cathodic exchange coefficients (α_{A} and α_{C}), of the linearized kinetic resistance from, e.g., impedance measurements and of S_{BET} (see Eq. 2.7).

$$i = \frac{i_0 \cdot \mathrm{F} \cdot \eta}{\mathrm{R} \cdot T} \cdot (\alpha_{\mathrm{A}} + \alpha_{\mathrm{C}}) \tag{2.6}$$

$$\rightarrow i_0 = \frac{i \cdot \mathrm{R} \cdot T}{\mathrm{F} \cdot \eta \cdot (\alpha_{\mathrm{A}} + \alpha_{\mathrm{C}})} = \frac{\mathrm{R} \cdot T}{\mathrm{F} \cdot R_{\mathrm{kin}} \cdot S_{\mathrm{BET}} \cdot (\alpha_{\mathrm{A}} + \alpha_{\mathrm{C}})} \tag{2.7}$$

With the known degree of lithiation c_s, the exchange current density can furthermore be used to obtain an effective rate constant k (assuming $k_A = k_C$ see Eq. 1.6) for assumed charge transfer coefficients of $\alpha_{A/C} = 0.5$ (see, e.g., Ref. [93, 97]). It is emphasized that the nomenclature from Comsol Multiphysics® is adopted here.[98]

$$k = \frac{R \cdot T}{F^2 \cdot \sqrt{c_{s,max} - c_s} \cdot \sqrt{c_s} \cdot \sqrt{\frac{c_l}{c_{l,ref}}} \cdot R_{kin} \cdot S_{BET}} \tag{2.8}$$

For an LNMO cathode the impedance deconvolution shown in section 5.2 yields an areal kinetic charge transfer resistance of $(R_{kin} \cdot S_{BET}) = 50 - 100\ \Omega cm^2_{BET,LNMO}$ which allows to obtain a kinetic rate constant of 10–20·10^{-11} m/s (measurement done for $c_l = 1$ M/L and at an SOC of ≈90 % of the nominal full capacity of $\rho_{LNMO} \cdot C_{LNMO}/F = 4.38\ g/cm^3 \cdot 170\ mAh/g/F \approx 28\ mol/L = 28000\ mol/m^3$). Analogously the kinetic rate constant for the graphite electrode may be obtained from its initial charge transfer resistance of $(R_{kin} \cdot S_{BET}) = 100\ \Omega cm^2_{BET,Gra}$ (see section 5.3) to be $9.8 \cdot 10^{-11}$ m/s. The difficulty in obtaining charge transfer resistances from impedance spectra may be reduced greatly by determining SOC dependent impedance spectra from ultra low loaded electrodes (such as used for the estimation of the solid state diffusion coefficient), thereby certainly avoiding porous electrode effects.

To overcome the intrinsic restriction of the impedance technique to the linear Butler-Volmer range, pulse experiments were conducted as a part of this study.[99] Three-electrode cells with an ultra-low loaded NMC cathode (≈155 µAh/cm²), a metallic lithium counter electrode and a gold wire micro reference electrode (see Section 5.1) were built inside an argon filled glovebox. After careful charge to 50 % SOC and a 1 h equilibration, a 2 s positive or negative galvanostatic pulse, corresponding to C-rates of 0.1 C to 30 C, was recorded. Experimentally it was found that a simple OCV phase before the pulse experiment will yield an additional potential offset which may be avoided by actively setting the current to zero before applying the pulse rather than starting the pulse from the open circuit condition (an instrumental artifact related to the circuity of the potentiostat). This effect may also be the reason for the finite potential offset during the potential relaxation after the pulse experiments used for the determination of electrolyte transport properties (see discussion in article presented in Section 3.4). The recorded potential transients during the pulse include double layer capacitance effects and the ohmic overpotential from the electrolyte in the separator. Concentration gradients and corresponding overpotentials in the liquid electrolyte are small due to the use of ultra-low loaded electrodes. In 1D simulations of the experimental setup, using reasonably chosen electrolyte transport properties (see Chapter 3) it was demonstrated that concentration gradients are negligible (<3 % at 30 C, see Ref. [99]) for such low loadings. Although the pulse duration is small, non-negligible changes of the electrode SOC are obtained for the 30 C pulses (≈1 %, which may correspond to >10 mV depending on the active material's thermodynamics and the SOC). Therefore experiments were repeated numerically using Comsol Multiphysics®, with all parameters determined beforehand, except for the solid state diffusion coefficient and the kinetic rate constant (see Ref. [99]). The solid state diffusion coefficient was assumed to be not limiting (based on fast cycling experiments with ultra-low loaded NMC electrodes,[99] analogous to the approach shown for graphite in Figure 2.4) and using Matlab - Comsol LiveLink all po-

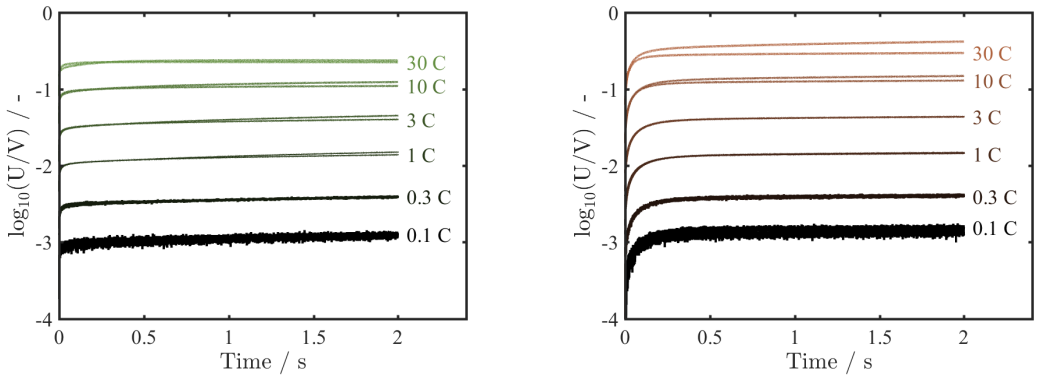

(a) Graphite **(b)** NMC

Figure 2.5: Positive and negative galvanostatic pulses at ultra-low loaded graphite (a) and NMC (b) electrodes at 50 % SOC, conducted in three electrode T-cells with a GWRE (see 5.1) and a lithium counter electrode. The potential transients of the positive and negative pulses are very similar and mostly lie on top of each other in the figure, apart from, e.g., the potential transients during the 30 C pulses with the NMC electrodes (see red lines in b). Cells were discharged completely (CCCV) and then charged at 1 C to the selected SOC. Pulses were applied only after a 1 h resting period to have reproducible starting conditions for each pulse. C-rates are calculated based on the reversible capacity obtained during three previous formation cycles at ≈0.1 C and span the range from 0.1 to 30 C (see labels in Figure). The experimental setup and procedure is similar to the measurements conducted in Ref. [99] and the reader is referred to the reference for details.

tential transients, i.e., all C-rate pulses were fitted simultaneously. Using this approach, a kinetic rate constant of $4.5 \cdot 10^{-11}$ m/s was found for NMC at 50 % SOC.[99]

Alternatively, the potential transients may be analyzed in a simplified manner. Based on the assumption of not limiting solid state diffusion and negligible ionic transport resistance (due to the small loading), the subtraction of the known potential loss due to the separator resistance (3 Ω) from the measured potential transients will yield only the kinetic overpotential. Exemplary measured potential transients during galvanostatic pulses are shown in Figure 2.5 for a low loaded graphite (0.21 µAh/cm²) and NMC (0.14 uAh/cm²) electrode, corrected for the OCV potential before the pulse (arithmetic mean of 100 data points recorded during 10 s directly before the pulse).

Figure 2.5 shows that the potential transients become fairly constant after 1 s and allow to extract the pulse overpotential. Only for pulse experiments at SOCs close to 0 % or 100 % (not shown), a distinct potential slope during the polarization can be observed for high C-rates. For the sake of comparability, the intercept of the linear extrapolation of the potential transients between 0.9 and 1.1 s with the y-axis is used as overpotential for the pulse. The time range for the extrapolation was chosen so that the potential change due to an SOC change of the electrode at high pulse currents (>1.5 s) is minimized and double layer capacitance effects (<0.5 s) are negligible. Obtained overpotentials are corrected for the electrolyte overpotential and are depicted for the C-rates from 0.1 C to 30 C in Figure 2.6 for two graphite and two NMC cells each. The obtained overpotential/current density relations agrees well with a linear trendline,

the slope of which allows to calculate the areal charge transfer resistance and thus the kinetic rate constant (see Eq. 2.8). To judge the linearity in Figure 2.6a and b multiple linear trendlines are shown. Linear trendlines through the experimentally found overpotentials for only the small C-rates (±0.1 C, see black lines in Figure 2.6a and b) are extended to the full C-rate range to be visible on the linear scale. For increasing C-rate ranges, e.g., for all overpotentials found for galvanostatic pulses corresponding to C-rates of 1 C and below, the color of the linear trendline becomes brighter (green for graphite in Figure 2.6a and orange for NMC in Figure 2.6b). It has to be noted that both NMC cells yield similar overpotentials at the same current densities, while the overpotentials of the graphite electrodes differ significantly. All linear trendlines in Figure 2.6a and b have similar slopes, independent of the underlying C-rate range used for the fit. The observed linear behavior differs from the Butler-Volmer relation. For $\alpha = 0.5$ a distinct difference from the linear slope would be expected for $\eta \gg 60$ mV if the kinetics follow a Butler-Volmer relation (see definition in Eq. 1.5). In consequence the (de-)intercalation reaction of lithium out of and into the graphite and NMC particles does either not follow a Butler-Volmer behavior or the measurements are dominated by an unaccounted and dominating ohmic (due to the linearity) overpotential. A reported Butler-Volmer relation for the active material LFP in the literature was also only found after correcting impedance based resistances for a dominant diffusion resistance.[93] The reader is reminded that in the presented experimental setup diffusion in the electrolyte phase was shown to be negligible and at the moment no definitive interpretation of the linear kinetic relation can be given. However, based on the linear trendlines in Figure 2.6 a mean kinetic charge transfer resistance of 633 ± 50 $\Omega\text{cm}^2_{\text{BET}}$ for graphite and 285 ± 28 $\Omega\text{cm}^2_{\text{BET}}$ for NMC is found from the pulse experiments at 50 % SOC from which the kinetic rate constants $1.0 \pm 0.1 \cdot 10^{-11}$ m/s and $1.2 \pm 0.1 \cdot 10^{-11}$ m/s are obtained respectively (using Eq.2.8).

Measurements were also conducted at SOCs of 10 %, 30 %, 70 % and 90 % and the kinetic rate constant were obtained accordingly. Although the kinetic charge transfer resistance increases at low SOCs, similar kinetic constants are obtained (see definition of exchange current density in Eq. 1.6). All areal kinetic charge transfer resistances and their corresponding kinetic rate constants are collected in Table 2.1. As the definition of the kinetic rate constant in the literature varies, kinetic charge transfer resistances are compared with the available literature. E.g., Ogihara et al.[100] report a very small kinetic charge transfer resistance of ≈15 Ωcm^2 for $LiNiO_2$, however it is not specified if the resistance is normalized to the BET area or the electrode area. Although reports for the kinetic rate constant for graphite exist, a direct comparison is hindered by the undefined nomenclature of the kinetic rate constant.[81] A reason for the focus on cathode active materials might be the additional complexity caused by the anode solid electrolyte interphase. Heubner et al.[93] report an exchange current density of 0.17 mA/cm^2 for LFP, from which a kinetic charge transfer resistance of 151 $\Omega\text{cm}^2_{\text{BET}}$ can be obtained which is similar to the values found in this study (see Table 2.1).

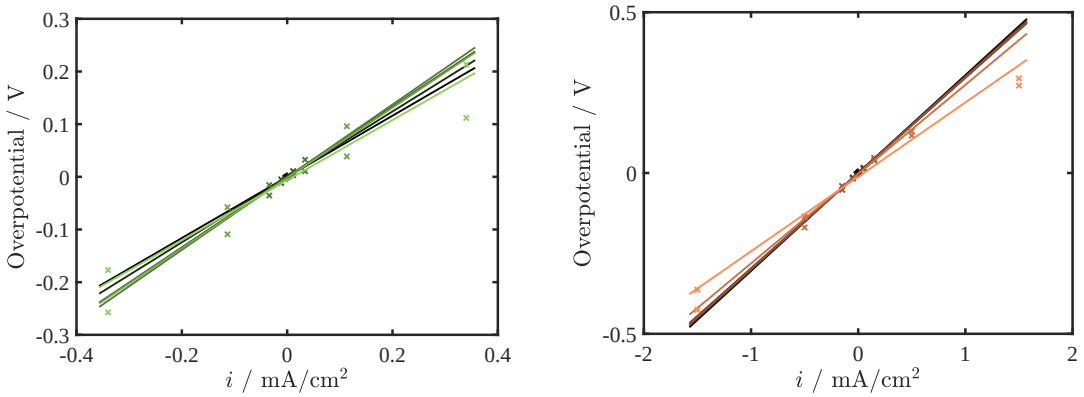

(a) Graphite **(b)** NMC

Figure 2.6: Kinetic overpotentials of positive and negative galvanostatic pulses at ultra-low loaded graphite (a) and NMC (b) electrodes at 50 % SOC, conducted in three-electrode T-cells with a GWRE (see 5.1) and a lithium counter electrode. Cells were discharged completely (CCCV) and then charged at a rate of 1 C to the selected SOC. Positive or negative pulses were applied only after a 1 h resting period to have reproducible starting conditions for each pulse. C-rates are calculated based on the reversible capacity obtained during three previous formation cycles at ≈0.1 C and span the range from 0.1 to 30 C. Kinetic overpotentials are obtained by linear extrapolation of the potential transients between $t = 0.9$ s and $t = 1.1$ s (see Figure 2.5) to the y-axis and subtraction of the ohmic potential drop from the separator (3 Ω). The experimental setup and procedure is similar to the measurements conducted in Ref. [99] and the reader is referred to the reference for details. Multiple linear trendlines are shown for the C-rate range from ±0.1 C (black lines, extrapolated to the full C-rate range) to ±30 C (green and orange lines for graphite in (a) and NMC in (b), respectively).

Table 2.1: Kinetic charge transfer resistances and rate constants (using the nomenclature of Eq. 2.8) for NMC and graphite electrodes, determined using pulse experiments with low loaded electrodes. Extrapolation of the potential transient between 0.9 and 1.1 s of the 2 s pulses allow to obtain the total overpotential as the intercept with the y-axis. Subtraction of the electrolyte potential loss throughout the separator yields the kinetic overpotential which is linear for C-rates from 0.1 C to 30 C. The obtained kinetic charge transfer resistances, given in the table, are normalized with the BET surface area of the active materials and are used to calculate the kinetic rate constant k by means of Eq. 2.8.

Active Material	SOC	$R_{\mathrm{kin}} \cdot S_{\mathrm{BET}} / \Omega \mathrm{cm}^2_{\mathrm{BET}}$	$k / 10^{-11} \mathrm{m/s}$
NMC	10 %	578 ± 132	1.18 ± 0.30
NMC	30 %	407 ± 79	1.03 ± 0.25
NMC	50 %	280 ± 29	1.22 ± 0.14
NMC	70 %	218 ± 26	1.46 ± 0.19
NMC	90 %	174 ± 14	1.82 ± 0.16
graphite	10 %	657 ± 45	1.46 ± 0.10
graphite	30 %	509 ± 62	1.25 ± 0.16
graphite	50 %	643 ± 48	0.90 ± 0.07
graphite	70 %	435 ± 60	1.46 ± 0.23
graphite	90 %	412 ± 41	2.34 ± 0.25

Chapter 3

Ionic Transport Properties in a Binary Electrolyte

During charge/discharge operation of a lithium-ion battery, charge is transported reversibly between the lithium ion host structures at the anode and the cathode. As indicated by the name, the charge is transported in the form of ions. At high charge/discharge currents, low temperatures, or for high energy cells with thick electrodes this ionic transport in the electrolyte phase becomes the rate limiting step. If the ion transport cannot support the applied/drawn current, ionic concentration gradients evolve yielding increased overpotentials (see Eq. 1.5), which eventually lead to reduced safety, reduced reversible capacity and reduced energy density in current lithium-ion batteries. For the development of improved cells and for predictive models and battery control units, the transport properties of the liquid electrolyte play an eminent role.

For the description of ionic transport phenomena in the commonly used Newman model for binary electrolytes,[24–26] the ionic transport properties, i.e., the ionic conductivity κ_{Ion}, the binary diffusion coefficient $D_{\pm}$, the transference number t_{+}, and the thermodynamic factor TDF (a derivative form of the mean molar activity coefficient $f_{\pm}$) are required (see Eq. 1.3 and 1.4). This chapter contains the journal articles presenting novel electrochemical measurement techniques, as well as a detailed comparison with existing techniques in the literature, for the binary diffusion coefficient (Section 3.1), the thermodynamic factor (Section 3.2) and the transference number (Section 3.3). Because the ionic conductivity may be obtained using turn-key equipment, it is not in the focus of this work (see Section 2.3). It has to be noted that not all initially made assumptions for the direct determination of the thermodynamic factor based on the ferrocene/ferrocenium redox couple were valid (compare erratum in Section 3.2). Hence the temperature and concentration dependent study of ionic transport properties (Section 3.4), as well as the comparison of ionic transport of $LiPF_6$ and $NaPF_6$ salts (Section 3.5), refrain from using the ferrocene cell method. Instead, while the diffusion coefficient is determined as described in Section 3.1, the transference number and the thermodynamic factor are found from pulse experiments and concentration cells with a further simplification of the concentration cell potential. In a comprehensive temperature and concentration dependent transport parameter study the methodology is described in detail, written as a manual for simple adoption (Section 3.4). The same technique is

then applied to a $LiPF_6$ and a $NaPF_6$ based electrolyte to investigate the influence of the cation size on the ionic transport phenomena (Section 3.5).

3.1 Binary Diffusion Coefficient

In this section the article *Determination of Transport Parameters in Liquid Binary lithium-ion battery Electrolytes I. Diffusion Coefficient*[54] is presented, which was submitted in December 2016 and published in the peer-reviewed Journal of the Electrochemical Society in February 2017. Parts of the article were presented at the 13$^{\text{th}}$ Symposium on Fuel Cell and Battery Modeling and Experimental Validation in Lausanne (Switzerland) in March 2016 and at the ECCOMAS 2016 in Crete (Greece) in June 2016. http://dx.doi.org/10.1149/2.1131704jes.

Our study on the electrochemical determination of binary diffusion coefficients is based on pulse experiments in a two-electrode cell configuration with two lithium metal electrodes. When a pulse current is applied to such a cell, concentration gradients will evolve in the vicinity of the electrodes and for long pulses a steady state concentration gradient will form. From the analysis of the potential and current transients during and after such current pulses, the binary diffusion coefficient may be obtained, as established in the literature for free-standing electrolyte solutions or polymer electrolytes.[51,101] The novelty of our approach is the use of a porous medium, first to be close to the final application, secondly to avoid convective effects, which may alter obtained diffusion coefficients to a large extent. In a separate experiment, where we apply positive and negative current pulses to an upwards facing cylindrical electrolyte volume we verified the necessity of a porous medium. Due to density gradients in such an experiment, the equilibration of the concentration gradient in the electrolyte takes place within minutes compared to hours for the different directions of current flow, which clearly shows that convective transport may generally not be neglected. In the publication we summarize three analytical solutions for the determination of the binary diffusion coefficient and challenge their accuracy in numerical experiments. Experimentally we investigate the binary diffusion coefficient of 0.01 M to 2.0 M $LiClO_4$ in EC:DEC (1:1 w:w) electrolytes with all three methods and find good agreement within the techniques. It is shown that short pulse experiments are the best method for the determination of binary diffusion coefficients, as side effects due to dendritic lithium formation are suppressed and the necessary assumption of a small concentration gradient is automatically fulfilled at long times after the pulse experiment.

Author Contributions

A.E., J.L. and H.G. developed the cell design. J.L. performed all electrochemical measurements, A.E. derived the analytical solutions for a 1D cell design and conducted numerical experiments. Data analysis was done by A.E. and J.L. and the manuscript was written by A.E. and J.L. and edited by W.W. and H.G. All authors discussed the data and commented on the results.

Determination of Transport Parameters in Liquid Binary Lithium Ion Battery Electrolytes

I. Diffusion Coefficient

Andreas Ehrl,[a,=,c] Johannes Landesfeind,[b,=,*,z] Wolfgang A. Wall,[a] and Hubert A. Gasteiger[b,]**

[a]*Institute for Computational Mechanics, Department of Mechanical Engineering, Technical University of Munich, Munich, Germany*
[b]*Chair of Technical Electrochemistry, Department of Chemistry and Catalysis Research Center, Technical University of Munich, Munich, Germany*

Various numerical methods for the simulation of ion-transport in concentrated binary electrolyte solutions can be found in the literature, whereas the corresponding transport parameters are rarely discussed. In this contribution, a polarization cell consisting of two electrodes separated by a porous separator is proposed to determine the concentration dependent binary diffusion coefficient of non-aqueous electrolyte solutions. Therefore, two different electrochemical methods are extended so that they can be applied to electrolyte solutions in a porous medium. Additionally, the different methods are compared with each other by means of numerical simulations. The proposed experimental setup is used to determine the concentration dependent binary diffusion coefficient of an exemplary electrolyte, lithium perchlorate dissolved in a mixture of ethylene carbonate and diethyl carbonate, and the data are compared to those available in the literature. It will be shown that the most reliable method to determine concentration dependent binary diffusion coefficients are long-term relaxation experiments in a two-electrode cell using a porous separator.

Manuscript submitted December 22, 2016; revised manuscript received February 2, 2017. Published February 22, 2017.

Advanced numerical simulation tools are important for the understanding of existing battery systems as well as the development and the optimization of future battery systems. For such numerical simulations, accuracy and reliability are key issues and depend on appropriate physical models, boundary conditions, and, most importantly, accurately determined physico-chemical parameters. For instance, the mathematical model for binary electrolyte solutions presented by Newman and Thomas-Alyea[1] is based on four different concentration dependent transport parameters, namely the conductivity $\kappa(c)$, the binary diffusion coefficient $D_{\pm}(c)$, the transference number $t_{+}(c)$, and the thermodynamic factor or the mean molar activity coefficient $f_{\pm}(c)$; in addition, for modeling porous battery electrodes, the concentration independent so-called tortuosity factor τ to describe the effective ionic conductivity in porous electrodes with a given morphology is required.[2] While the conductivity $\kappa(c)$ can be measured using turn-key conductivity sensors, the determination of the other three concentration dependent parameters is more elaborate. Experimental methods for the determination of the transference number and the thermodynamic factor are discussed, e.g., in Ehrl et al.[3] and Landesfeind et al.,[4] while the determination of a complete set of transport parameters can also be found in the literature.[5,6] An overview of the most popular experimental techniques for the determination of binary diffusion coefficients in lithium based electrolytes is given in the following.

In Castiglione et al.,[7] Sethurajan et al.[8] and Capiglia et al.,[9] pulsed-field gradient Nuclear Magnetic Resonance (NMR) is used to determine the self-diffusion coefficients of ions in an electrolyte solution, which describes the mobility of ionic species in the absence of an electrochemical potential gradient.[10] In Castiglione et al.,[7] the self-diffusion coefficients of all ions in an electrolyte composed of LiTFSI (lithium bis(trifluoromethanesulfonyl)imide) dissolved in the ionic liquid $PYR_{14}TFSI$ (N,N-dimethyl pyrrolidinium) at a molar ratio of 1:9 were determined, whereas Capiglia et al.[9] investigated $LiPF_6$, $LiBF_4$, and $LiN(C_2F_5SO_2)_2$ in ethylene carbonate (EC) ethyl-methyl carbonate (EMC) solvent mixture (EC:EMC at 2:8 v:v). A theoretical discussion of the experimental method is given in Price.[11] For this method, the major difficulty is to relate the ionic self-diffusion coefficients determined by NMR to the binary diffusion coefficients which are generally required for numerical simulations. Another method, based on Moiré patterns, was used to determine the binary diffusion coefficient $D_{\pm}(c)$ of $LiClO_4$ in PC (propylene carbonate).[12] This technique is based on the optical observation of the time-dependent relaxation of the concentration profile after two electrolyte solutions with different concentrations are brought into contact. Nishida et al. used the same technique to determine $D_{\pm}(c)$ for $LiPF_6$, LITFSI, and $LiBF_4$ in PC.[13] The binary diffusion coefficient can also be determined from limiting current measurements with a micro disc electrode, as was shown by Xu and Farrington[14] for 0.1 M $LiClO_4$ in PC, but this method does not allow to measure the concentration dependence of $D_{\pm}(c)$ and can only provide an average value between the chosen salt concentration and zero (the concentration at the surface of the electrode at the limiting current).

The most popular method for the determination of the concentration dependent binary diffusion coefficient $D_{\pm}(c)$ is the so-called restricted diffusion method introduced by Harned and French, which is based on the observation of the long-term relaxation behavior following an initially induced concentration profile.[15] The applicability of the method for concentrated electrolyte solutions was demonstrated by Newman and Chapman for potassium chloride in water.[16] The relaxation process can be observed by different methods. In Stewart and Newman, an optical device was used to record the relaxation of the $LiPF_6$ concentration profile in an EC diethylcarbonate (DEC) solvent mixture (EC:DEC at 1:1 w:w).[17] Limiting factors of this method are the spatial resolution of the optical measurement and the complexity of the required analysis equipment. Alternatively, the relaxation of an initially induced concentration profile can be observed indirectly via the measured potential.[6,18–23] In Hiller et al.,[18] the concentration and temperature dependent binary diffusion coefficients of LiTFSI and LiBOB (lithium bis(oxalato) borate) in polyethylene oxide (PEO) based polymer electrolytes were determined by analyzing the long-term potential relaxation following an initial current pulse in a restricted diffusion experiment. In addition, the binary diffusion coefficients

=These authors contributed equally to this work.
*Electrochemical Society Student Member.
**Electrochemical Society Fellow.
[c]Present address: Velling 4, 94374 Schwarzach, Germany.
[z]E-mail: j.landesfeind@tum.de

were also calculated based on the short-term relaxation behavior of steady-state concentration profiles. Unfortunately, the binary diffusion coefficients determined by the two methods differed significantly (by up to a factor of 6). Based on different relaxation experiments, the binary diffusion coefficient of $LiClO_4$ in PC electrolyte solution soaked into a glass wool filter was determined by a numerical optimization method by Georén and Lindbergh.[24] Their approach was based on a physical model including solvent effects, as introduced by Georén and Lindbergh[24] and Doyle,[25] whereby convective effects were neglected and the tortuosity of the glass wool filter was determined using the Bruggeman relation (the latter may introduce significant errors, as was demonstrated recently by Landesfeind et al.[2]). A similar approach based on a more elaborate optimization framework was used by Nyman et al.[19] and Lundgren et al.[26] for $LiPF_6$ in EC:EMC (3:7 w:w) and in EC:DEC (1:1 w:w), respectively. In both publications, solvent effects and convective transport due to the motion of ions are included in the physical model used for the numerical optimization and, in addition, the effective ionic conductivity of the used glass microfiber filters was determined experimentally. Recently, the influence of solvent effects on the determination of transport parameters was investigated numerically by Liu and Monroe.[27] Note that the experimental studies listed in this paragraph[6,19,24,26] obtained the binary diffusion coefficients by fitting the complete set of transport parameters to their numerical model (i.e., $D_{\pm}(c)$, $t_+(c)$, and $f_{\pm}(c)$) or rely on other transport parameters, which undoubtedly will compromise the accuracy achievable for each one of the parameters.

Although, as discussed above, there are various experimental methods for the determination of binary diffusion coefficients already available in the literature, these methods require either a conversion of self-diffusion coefficients into binary diffusion coefficients, an additional spectroscopic technique to independently monitor concentration vs. time, or a global fit involving all concentration dependent physicochemical transport parameters. For this reason, we believe, the simplicity of the here proposed experimental setup to determine $D_{\pm}(c)$ as a function of salt concentration, requiring no optimization framework and/or provision of additional parameters other than the tortuosity, which can be measured accurately in independent experiments,[2] constitutes a valuable alternative method, particularly in view of its here demonstrated accuracy and reproducibility. In the Theoretical background section, a comprehensive introduction to the volume averaged ion-transport equations for porous media is given, which is the theoretical basis for the determination of the concentration dependent binary diffusion coefficient. In the Experimental section, the experimental procedures as well as the used materials and devices are introduced. The analytical framework for the determination of binary diffusion coefficients are summarized in the section Mathematical derivation. In the latter two sections, the experimental and the theoretical differences between a cell setup with and without porous materials are highlighted. Validity and accuracy of the introduced techniques are analyzed and compared in the section Numerical validation. Because theoretically expected transients are more obvious in simulated experiments, this section aids the interpretation of experimental data. Finally, in the Results and discussion section, the concentration dependent binary diffusion coefficient of $LiClO_4$ in EC:DEC (1:1 w:w) obtained from our measurements is given and compared with data in the literature.

Theoretical Background

Many experimental methods for the determination of ion-transport parameters are based on analytical solutions of the component mass conservation law. For a cell consisting of a porous medium filled with an electrolyte solution, the more general case of the volume averaged mass conservation law has to be considered

$$\varepsilon \frac{\partial c}{\partial t} - \nabla \cdot \left(\frac{\varepsilon}{\tau} D_{\pm}(c) \nabla c \right) + \nabla \cdot \left(\frac{t_+(c)}{z_+ \nu_+ F} \bar{\boldsymbol{i}} \right) = 0 \qquad [1]$$

as introduced, e.g., in Newman and Thomas-Alyea.[1] Here, the *volumetric intrinsic phase average* of the concentration is denoted by c, the charge number of the positive ionic species by z_+, the stoichiometric coefficient of the cation by ν_+, and the volumetric phase average of the current density by $\bar{\boldsymbol{i}}$ (as usual, time is denoted by t and F denotes the faraday constant (96485 As/mol)). The terms *volumetric intrinsic phase average* and *volumetric phase average* result from the volume averaging approach used for the mathematical description of the porous medium. In this approach, the microscopic relations are averaged over a representative element volume to yield the macroscopic transport equations. In case of the volumetric intrinsic phase average, the averaging is performed only over the electrolyte phase within the representative element volume, whereas both the volume of the electrolyte and the solid phase within the representative element volume have to be considered in case of the volumetric phase average. The volumetric intrinsic phase average multiplied by the porosity thus corresponds to the volumetric phase average. The interested reader is referred to Bear and Bachmat[28] or Landstorfer and Jacob[29] for a detailed derivation of these macroscopic equations. The transport parameters used in the mass conservation law are the concentration dependent binary diffusion coefficient $D_{\pm}(c)$ and the transference number $t_+(c)$. The porosity ε and the tortuosity τ are parameters related to the morphology of the porous medium and are frequently used to obtain the so-called effective binary diffusion coefficient $D_{\pm,\mathrm{eff}} = \varepsilon\, \tau^{-1}\, D_{\pm}$.

The conservation of current is given by

$$\nabla \cdot \bar{\boldsymbol{i}} = 0 \qquad [2]$$

with

$$\bar{\boldsymbol{i}} = -\frac{\varepsilon}{\tau} \kappa(c)\ \nabla\Phi + \frac{\nu}{z_+ \nu_+} \frac{RT}{F} \frac{\varepsilon}{\tau} \kappa(c) \times \left[1 + \frac{\partial \ln f_{\pm}(c)}{\partial \ln c} \right] (1 - t_+(c))\ \frac{1}{c} \nabla c \qquad [3]$$

Here, Φ stands for the volumetric intrinsic phase average of the electric potential with respect to a lithium reference electrode. In addition, the concentration dependent conductivity $\kappa(c)$ and the thermodynamic factor $[1 + \partial \ln f_{\pm}(c)/\partial \ln c]$ are necessary to describe the current flow. The coefficient $\nu = \nu_+ + \nu_-$ is based on the stoichiometry coefficients ν_+ and ν_- resulting from the dissociation of a binary salt in its components (e.g., $\nu = 2$ for the typical 1:1 salts used in lithium ion batteries). The gas constant is denoted by R (8.314 J/(mol K)) and the temperature by T (in units of Kelvin).

In combination with Eq. 2, Eq. 1 can be simplified to a one-dimensional scalar transport equation

$$\frac{\partial c}{\partial t} - \frac{1}{\tau} D_{\pm}(c_0) \frac{\partial^2 c}{\partial x^2} = 0 \qquad [4]$$

with the volumetric phase average of the flux density $\bar{N}$ as the corresponding boundary condition

$$\bar{N} = -\frac{\varepsilon}{\tau} D_{\pm}(c_0) \frac{\partial c}{\partial x} + \frac{t_+(c_0)}{z_+ \nu_+ F} \bar{i} \qquad [5]$$

if the following assumptions are valid:

1. The experimental setup resembles an ideal geometrical configuration, as is for example satisfied for a setup consisting of two parallel and aligned flat electrodes separated by an electrolyte layer and completely enclosed by insulators. In this case, concentration and potential gradients are exclusively orientated in x-direction (i.e., normal to the electrodes). As a result, ion-transport in the electrolyte solution can be described by a one-dimensional partial differential equation. In reality, this ideal configuration can be approximated by a two electrode cell with a large radius to distance ratio.
2. The assumption of a zero order approximation for the concentration dependent binary diffusion coefficient $D_{\pm}(c)|_{c_o \pm \delta c} = D_{\pm}(c_0)$ and the transference number $t_+(c)|_{c_o \pm \delta c} = t_+(c_0)$ has to be valid. This assumption is fulfilled if the binary diffusion coefficient and the transference number are concentration independent or if the concentration variations δc around an initial concentration

c_0 are small. The same condition is required for the remaining ion-transport parameters, namely the conductivity and the thermodynamic factor. Typical concentration dependent transport parameters of various binary electrolyte solutions usually fulfill this assumption, as is demonstrated in the section Numerical validation.

3. The porosity ε and the tortuosity τ are constant with respect to time and space.

At the boundaries, the relation between the current density and the flux density $\bar{i} = z_+ \nu_+ \mathrm{F} \bar{N}$ can be used to reformulate Eq. 5.

$$\bar{i} = -z_+ \nu_+ \mathrm{F} \frac{\frac{\varepsilon}{\tau} D_\pm (c_0)}{1 - t_+ (c_0)} \frac{\partial c}{\partial x} \qquad [6]$$

A more detailed derivation of these equations is given, e.g., by Newman and Thomas-Alyea[1] or by Ehrl.[30]

The partial differential equation given in Eq. 4 can be solved analytically for different types of Boundary Conditions (BCs) and Initial Conditions (ICs). As a result, an expression for the concentration difference $\Delta c = c_\mathrm{A} - c_C$ between the Anode (A) and the Cathode (C) can be obtained, which for a given set of BCs/ICs correlates Δc with the concentration dependent binary diffusion coefficient and transference number, with the chosen salt bulk concentration, and the electrode morphology related porosity and tortuosity, in the general form Ref. 1

$$\Delta c = c_\mathrm{A} - c_C = \mathrm{f}\left(D_\pm (c_0), t_+ (c_0), \varepsilon, \tau, \mathrm{c}_0\right) \qquad [7]$$

If the concentration difference Δc for a specific set of BCs/ICs and the corresponding functional description of Eq. 7 with the remaining parameters are known, it is possible to calculate the binary diffusion coefficient $D_\pm(c)$. The functional description to calculate the binary diffusion coefficient from Eq. 7 with different experimental procedures is presented in the following. For polarization experiments, we further define the x-axis of the one-dimensional coordinate system to point from the electrochemical cathode with $x_C = 0$ toward the electrochemical anode with $x_A = l$, as a result of which, the concentration gradient will always be positive during the polarization experiment and the subsequent relaxation phase if Li^+ ions are the only reacting species in the system (i.e., the anode concentration $\mathrm{c_A} \geq$ the cathode concentration $\mathrm{c_C}$).

In this study, the concentration difference Δc is determined indirectly by utilizing its correlation with the measured cell potential $U = \Delta\Phi + \eta$, where the potential difference between anode and cathode $\Delta\Phi = \Phi_\mathrm{A} - \Phi_\mathrm{C}$ is the volumetric intrinsic phase average of the electric potential and η is the kinetic overpotential of the anodic and cathodic charge transfer reactions. To do so, Eq. 3 has to be reduced to its one-dimensional form as was demonstrated above for the ion-transport equation. This dimensional reduction is also only valid if the same conditions as for the ion-transport equation are fulfilled, especially the small concentration variation Δc between anode and cathode. In the absence of current flow (i.e., $\bar{i} = 0$) across the electrodes, the kinetic overpotential η term is zero and the integration of Eq. 3 along a one-dimensional path directed from the cathode to the anode gives

$$\mathrm{U} = \Delta\Phi = \frac{\nu}{z_+ \nu_+} \frac{\mathrm{R}T}{\mathrm{F}} \left[1 + \frac{\partial \ln f_\pm (c_0)}{\partial \ln c}\right] (1 - t_+ (c_0)) \ln \frac{c_\mathrm{A}}{c_\mathrm{C}} \qquad [8]$$

where the thermodynamic factor (TDF) is assumed to be constant for small concentration variations around the bulk concentration c_0, as was already assumed above for the binary diffusion coefficient and the transference number. In order to use the cell potential as a measure for the concentration difference Δc, it is necessary to introduce an additional linearization for the term $\ln c_\mathrm{A}/c_\mathrm{C}$. If the concentration difference $\Delta c = c_\mathrm{A} - c_C$ is small compared to the initial concentration c_0 ($\Delta c << c_0$), the logarithmic term in Eq. 8 can be approximated by

$$\ln \frac{c_A}{c_\mathrm{C}} \approx \frac{\Delta c}{c_0} \qquad [9]$$

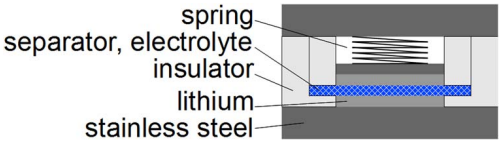

Figure 1. Schematic of two-electrode cell with symmetrical lithium electrodes and larger diameter, aligned separators, which was used for pulse experiments in the determination of binary diffusion coefficients.

as was shown, e.g., by Bruce and Vincent.[31] Under these conditions, the cell potential in the absence of current flow (s. Eq. 7) will be directly proportional to the concentration difference Δc between anode and cathode

$$U = \Delta\Phi \propto \Delta c \qquad [10]$$

This is one of the central aspects for the electrochemically based determination of transport parameters. The same method was also applied in, e.g., Ma et al.,[23] Zugmann et al.,[32] or Valøen et al.[6]

Experimental

Mixtures of ethylene carbonate (EC, 50% by weight, Sigma Aldrich, anhydrous, 99%) and diethyl carbonate (DEC, 50% by weight, Sigma Aldrich, anhydrous, >99%) were used as solvents for self-prepared electrolytes containing lithium perchlorate ($LiClO_4$, Sigma Aldrich, 99.99%) salt, mixed in an argon filled and temperature controlled glove box (MBraun, 25°C ± 1°C, water content <0.1 ppm, Ar 5.0, Westfalen, 99.999% Vol). $LiClO_4$ concentrations ranged from 0.01 to 2 M. Metallic lithium (Rockwood Lithium, 0.45 mm thickness, high purity) was used as counter electrode (CE) and working electrode (WE). The binary diffusion coefficient was determined by polarization experiments in a two electrode setup as shown in Figure 1.

All cell parts were cleaned by boiling them in a mixture of ethanol and water (Millipore, Elix, 15 M Ω), thoroughly rinsing them with water, followed by overnight drying at 70°C in a heating oven before bringing them into the glove box. Twenty circular layers of Celgard 2500 separator (porosity 55%, thickness 25 µm) with a diameter of 20 mm were placed between the two lithium electrodes with a diameter of 17 mm. A larger separator size ensured that no stray currents could flow around the porous separators through the bulk of the electrolyte. The electrode distance is determined by the thickness of the separators, which are incompressible in the pressure range induced by the mechanical spring (≈0.1 MPa). Due to the chosen setup, the geometrical distance between the electrodes (l) can be adjusted accurately to small values such as $l = 20 \cdot 25\,\mu\mathrm{m} = 0.5$ mm. As a result, a large radius to distance ratio was obtained, minimizing the influence of the edge effects of the electric field and thereby fulfilling the requirement of a one-dimensional concentration and potential gradient. It is emphasized that convective effects are also suppressed using this setup with a porous separator, which is supported by experimental data: after positive and negative polarizations of the two electrodes (aligned perpendicularly to the gravitational field), identical potential relaxation transients were observed, proving that convective transport can be neglected. After the cells were sealed with PTFE gaskets, measurements were conducted in a climate chamber outside the glove box. A Biologic VMP3 potentiostat/galvanostat was used for the electrochemical measurements and cell impedances were measured in a frequency range from 200 kHz to 1 Hz.

Experimental procedure used in polarization cells.—Potentiostatic steady-state and galvanostatic pulse polarization experiments were conducted using the two electrode symmetrical lithium cell shown in Figure 1. While after a long potentiostatic steady-state polarization a linear concentration profile is established between the electrodes (lower panels in Figure 2), the short galvanic pulse polarization procedure is designed such that the concentrations change

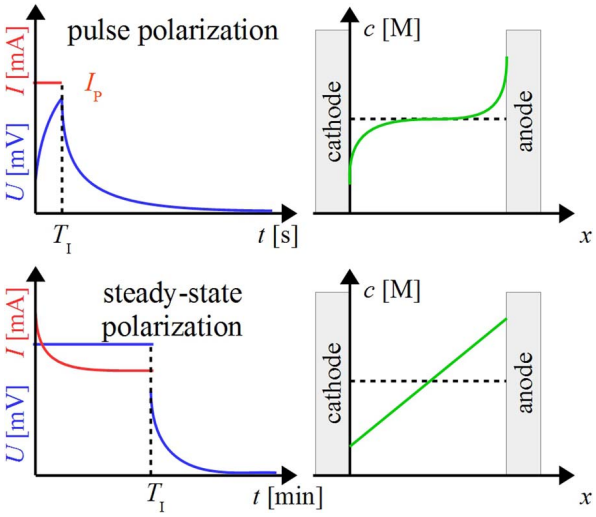

Figure 2. Schematic of the current/voltage profiles during the galvanostatic pulse polarization experiments (GPP; s. upper left panel) and of the potentiostatic steady-state polarization (SSPP; s. lower panel), together with the respective concentration profiles present at the current interruption time T_I.

only in the vicinity of the electrodes (s. upper panel in Figure 2). Measurements for each salt concentration were repeated at least two times in order to check for reproducibility.

In each cell, a 6 h rest period was followed by several galvanostatic pulse polarization (GPP) experiments with various polarization currents I_p and times T_I, whereby a pulse with a positive current flow was always followed by an identical pulse with a reversed current flow. After each individual polarization, an OCV (open circuit voltage) phase of at least 3 h was applied in order to ensure a complete relaxation of the concentration profile. In theory, the polarization time in a galvanostatic pulse experiment has no impact on the long-term relaxation behavior of the concentration profile. Due to the relaxation process, the requirement for small concentration differences between anode and cathode are automatically fulfilled for long times. However, due to the finite accuracy of the measurement equipment (100–200 μV noise with the VMP3 potentiostat/galvanostat), too short polarization times with correspondingly small logarithmic cell potential variations make a determination impractical. Following these galvanostatic pulse experiments, a steady state potentiostatic polarization (SSPP) experiment was conducted. For these experiments, the polarization phase was terminated manually for each cell once the current $I(t)$ remained stable for at least 2 minutes, resulting in potentiostatic polarization times on the order of 15 to 60 minutes. The high frequency resistance of the cell was measured before and at the end of each pulse experiment to evaluate the stability of the electrolyte and was found to vary less than 3% over the course of the experiments for the nominal electrolyte concentrations of 0.5 M to 2 M. Only for the smallest electrolyte concentration of 0.01 M, the high frequency resistance was found to decrease by 10% from the beginning to the end of the experiment (∼24 h). This decrease in the high frequency resistance implies an increase of the electrolyte conductivity, which must be due to an increase in ion concentration caused by SEI formation. Since the conductivity scales linearly with concentration at such low concentrations, the effective electrolyte concentration should be ca. 11 mM compared to the nominal concentration of 10 mM, which is a reasonably small error, particularly since the equations for the determination of the binary diffusion coefficient are not a function of the salt concentration (shown later on by Eq. 14 and Eq. 17). Table I summarizes the applied galvanostatic pulse and steady-state potentiostatic polarization parameters. The polarization currents in galvanostatic experiments and the potentials in potentiostatic experiments were selected such that the current density would always be below 0.3 mA/cm^2, as this assures the absence of lithium dendrite formation.[33]

Table I. Summary of the applied galvanostatic pulse polarization (GPP) steps and the subsequent steady-state potentiostatic polarization (SSPP) for different $LiClO_4$ concentrations in EC:DEC (1:1 w:w), used to determine the binary diffusion coefficient in the two-electrode cell setup shown in Figure 1.

Salt Concentration	GPP	SSPP
0.01 M	2 min, ± 50 μA 4 min, ± 50 μA 3 min, ± 75 μA	20 mV, ∼ 60 min
0.5 M, 1 M 1.5 M, 2 M	6 min, ± 500 μA 16 min, ± 500 μA 12 min, ± 750 μA	50 mV, ∼ 15 min

Mathematical Derivation

In this contribution, two different methods for the electrochemical determination of the binary diffusion coefficient from the potential relaxation after polarization are considered. In the first method, the observed long-term relaxation behavior of the cell potential after a galvanostatic pulse (GPP) or a steady-state potentiostatic polarization experiment (SSPP) is analyzed. The second method is based on the analysis of the short-term relaxation behavior of the cell potential following a steady-state potentiostatic polarization. The first method is frequently used in the literature to determine the binary diffusion coefficient of polymer electrolytes and non-aqueous electrolyte solutions.[6,18–23] However, when this method is applied to the evaluation of liquid electrolytes, most of the used experimental setups do not fulfill the ideal geometrical configuration which is required for simplification of Eq. 4. Additionally, convective effects influencing the ion transport equations in the polarization cell are not suppressed at all by these experimental setups, especially on long time scales. With regards to eliminating convective contributions to ion transport, the here proposed cell setup using porous separators is clearly superior (s. explanation in the Experimental section), but when using porous separators, the classical equations have to be adapted according to the volume averaged ion-transport equations, as will be shown in the following.

Analysis of the long-term relaxation behavior.—When using the long-term relaxation behavior for the determination of the diffusion coefficient, the two-electrode cell can be polarized by galvanostatic pulses or by potentiostatic steady-state polarization. For this method, the concentration profile $c(T_I)$ established at the interruption time T_I is considered as the initial concentration profile. The relaxation of the concentration profile (i.e., for I = 0) can be observed via the relaxation of the cell potential $U(t)$. Originally, the method was developed for dilute electrolytes by Harned and French.[15] The theoretical verification for concentrated solutions is given in Newman and Chapman.[16] It is important to realize that in both publications only bulk electrolyte solutions, i.e., without a porous separator are considered, so that they are not valid for experiments with porous separators. However, Eq. 4 can be simply rescaled to have the same form as Eq. 1 used by Newman and Chapman,[16] if we define a partial effective binary diffusion coefficient $D^*_{\pm,\mathrm{eff}}(c_0) \equiv \tau^{-1} \cdot D_{\pm}(c_0)$:

$$\frac{\partial c}{\partial t} - D^*_{\pm,\ \mathrm{eff}}(c_0)\,\frac{\partial^2 c}{\partial x^2} = 0 \qquad [11]$$

With this modification, the time dependent concentration at each electrode can now be determined by Eq. 2 in Newman and Chapman,[16] from which $\Delta c(t)$ can be obtained by taking the difference between $c_A(t)$ and $c_C(t)$ (i.e., evaluating Eq. 2 in Newman and Chapman[16] for cathode location $x_C = 0$ and the anode location $x_A = l$; note that

$x \equiv y$ and $l \equiv a$ in Reference 16):

$$\Delta c\,(t) = c_A\,(t) - c_C\,(t) = 2C_1 \exp\left(-\frac{\pi^2 D^*_{\pm,\mathrm{eff}}\,(c_0)}{l^2}t\right) + 2C_3 \times \exp\left(-\frac{9\pi^2 D^*_{\pm,\mathrm{eff}}}{l^2}t\right) + 2\sum_{n=3}^{\infty} C_{(2n-1)} \times \exp\left(-\frac{(2n-1)^2\pi^2 D^*_{\pm,\mathrm{eff}}\,(c_0)}{l^2}t\right) \quad [12]$$

It is important to note that the here used partial effective binary diffusion coefficient ($D^*_{\pm,\mathrm{eff}}(c_0) \equiv \tau^{-1} \cdot D_{\pm}(c_0)$) must be distinguished from the commonly used effective binary diffusion coefficient ($D_{\pm,\mathrm{eff}}(c_0) \equiv \varepsilon \cdot \tau^{-1} \cdot D_{\pm}(c_0) = \varepsilon \cdot D^*_{\pm,\mathrm{eff}}(c_0)$), which was defined in the Theoretical background section. In the derivation of Newman and Chapman,[16] a variable binary diffusion coefficient and convective effects as a result of a varying solution volume were also considered, resulting in a similar relationship as that of Eq. 12. Based on these results, the authors conclude that the variation in solution volume does not play a major role for small concentration variations. Convective effects as a result of natural or forced convection are not investigated in the latter publication, although the experimental setup uses a liquid electrolyte without porous separator, so that the absence of natural convection cannot necessarily be assumed. The different initial conditions resulting from the galvanostatic pulse and the steady-state potentiostatic polarization experiments do only have an influence on the prefactor C_n, but not on the exponential terms. A detailed derivation of this formula is given in Ehrl.[30]

For large times, i.e., $t \to \infty$, the first term of the analytical solution (Eq. 12) is dominating, yielding a linear relationship of the logarithmic concentration difference $\ln \Delta c(t)$ with respect to time t

$$\ln \Delta c\,(t) = \ln(2C_1) - \frac{\pi^2 D^*_{\pm,\mathrm{eff}}\,(c_0)}{l^2} \cdot t \propto \ln U\,(t) \quad [13]$$

Since the concentration difference Δc and the measured cell potential U are directly proportional (Eq. 10), the linear behavior can also be observed for the cell potential U (indicated at the right-hand-side of Eq. 13). Thus, when plotting $\ln U(t)$ vs. t, the slope of the line as $t \to \infty$ (denoted as $m_{\ln}$) corresponds to $\pi^2 \cdot D^*_{\pm,\mathrm{eff}}(c_0)/l^2$ (s. Eq. 13), so that the partial effective binary diffusion coefficient can be calculated from the linear slope $m_{\ln}$:

$$D^*_{\pm,\mathrm{eff}}\,(c_0) = \frac{l^2}{\pi^2} \cdot m_{\ln} \quad [14]$$

Advantageous in this approach is the fact that the initially imposed concentration difference by the galvanostatic pulse or the potentiostatic hold decreases with increasing time, which supports the requirement for small concentration variations introduced in the Theoretical background section.

Analysis of the short-term relaxation behavior.—In this second method, a linear concentration profile $c(T_\mathrm{I})$ from a preceding potentiostatic steady-state polarization is considered as an initial concentration profile established at the time T_I when the current is interrupted, which can be approximated by a linear function for small concentration variations. It should be noted, however, that whether the linear concentration profile is obtained galvanostatically or potentiostatically is irrelevant. For the short-term relaxation from a steady-state concentration profile, the time dependent concentration difference $\Delta c(t)$ is given by the relation

$$\Delta c\,(t) = \Delta c\,(T_\mathrm{I}) \cdot \left(1 - \sqrt{\frac{16 \cdot D^*_{\pm,\mathrm{eff}}\,(c_0)}{\pi \cdot l^2} \cdot t}\right) \quad [15]$$

showing that the short-term relaxation process is linear with respect to $\sqrt{t}$. Eq. 15 is derived by solving the partial differential equation given by Eq. 4, using a linear concentration profile as initial condition and no-flux conditions at both electrodes, which can be done by a Laplace transformation as shown, e.g., by Ehrl.[30] The same equation was presented by Hiller et al.[18] for a polymer electrolyte, the only difference being that in their equation $D^*_{\pm,\mathrm{eff}}(c_0)$ in Eq. 15 is replaced by $D_{\pm,\mathrm{eff}}(c_0)$, as there is no porous matrix/separator. For small concentration variations, Eq. 15 can also be expressed with Eq. 8 and Eq. 9 in terms of the cell potential

$$U\,(t) = U\,(T_\mathrm{I}) - U\,(T_\mathrm{I})\frac{\sqrt{16 D^*_{\pm,\mathrm{eff}}\,(c_0)}}{l\sqrt{\pi}}\sqrt{t} = U\,(T_\mathrm{I}) - m_{\mathrm{sqrt}}\sqrt{t} \quad [16]$$

where m_{sqrt} denotes the slope of a plot of cell potential U versus $\sqrt{t}$. As a result, the partial effective binary diffusion coefficient $D^*_{\pm,\mathrm{eff}}$ can be determined by

$$D^*_{\pm,\mathrm{eff}}\,(c_0) = \frac{\pi \cdot l^2}{16} \cdot \left(\frac{m_{\mathrm{sqrt}}}{U\,(T_\mathrm{I})}\right)^2 \quad [17]$$

Here, the cell potential $U(T_\mathrm{I})$ denotes the potential measured directly after current interruption.

For both methods, the tortuosity τ of the porous separator is required to determine the ultimately desired binary diffusion coefficient $D_{\pm}(c_0)$, which can be determined, e.g., by the method proposed in Landesfeind et al.[2] Alternatively, the effective binary diffusion coefficient $D_{\pm,\mathrm{eff}}(c_0) = \varepsilon \cdot \tau^{-1} \cdot D_{\pm}(c_0) = \varepsilon \cdot D^*_{\pm,\mathrm{eff}}$ for a specific porous medium/separator can be calculated from the determined value of $D^*_{\pm,\mathrm{eff}}$, if its porosity is known. In general, careful observation of the voltage versus time behavior always gives a good indication with regards to the quality of the experimental data, also if transport parameters are determined by a numerical fitting approach.

Numerical Validation

In the following, the analytical expressions for the determination of the binary diffusion coefficient $D_{\pm}(c_0)$ introduced in the Mathematical derivation section are analyzed by means of numerical simulations using typical transport parameters for lithium ion battery electrolytes and typical kinetic parameters for metallic lithium in order to evaluate their applicability for the experimental determination of binary diffusion coefficients, i.e., in order to verify the assumptions made in the Theoretical background section. All simulations are based on the Equations 1–3 and were performed with an in-house finite element research code. A detailed derivation of the used numerical methods is given in Ehrl.[30]

All numerical simulations are based on a one-dimensional domain representing a virtual electrode area $A = 227\ \mathrm{mm}^2$ (corresponding to the 17 mm diameter lithium electrodes used in this work). The simulation and transport parameters are summarized in Table II. The chosen parameters do not represent a specific material or electrolyte but should be somehow realistic. The values given for the porosity and the tortuosity are of the same order as for the Celgard 2500 separator characterized in Landesfeind et al.,[2] whereas the functional description of the transport parameters is guided by the transport parameter of an electrolyte solution consisting of lithium perchlorate $LiClO_4$ dissolved in EC:DEC (1:1 w:w).[3,4] In contrast to Landesfeind et al.,[4] the theoretically expected Debye-Hückel behavior is included in the description of the thermodynamic factor to demonstrate that even such a strong non-linearity at small concentrations does not influence the proposed measurement method. The exchange current density i_0 in the Butler-Volmer equation is chosen to correspond to a realistic value for the kinetic resistance of a porous electrode. The remaining parameters of the Butler-Volmer equation are assumed.

Numerical analysis of the polarization experiments.—Using a quasi-1D two-electrode cell (s. Figure 1), the binary diffusion coefficient $D_{\pm}(c_0)$ in this study will be determined by three different methods, which were summarized in the Mathematical derivation section. The binary diffusion coefficients $D_{\pm}|^{\mathrm{pulse}}_{\mathrm{long-term}}$ and $D_{\pm}|^{\mathrm{steady-state}}_{\mathrm{long-term}}$ refer to the values calculated from the long-term relaxation behavior after a pulse and a steady-state polarization experiment, respectively (in this

Table II. Simulation parameters for the quasi one-dimensional simulation using the finite element research code developed at the Institute for Computational Mechanics at the Technical University of Munich. The concentrations in the below given correlations are given in units of mol/L.

Computational domain [mm]	cathode at $x_C = 0$ and anode at $x_A = 0.5$
Virtual electrode area A [mm^2]	227
Porosity ε [-]	0.55
Tortuosity τ [-]	2.6
Initial concentration c_0 [M]	0.01 / 1.0 / 2.0
Binary diffusion coefficient $D_\pm$ [$\frac{mm^2}{s}$]	$2.84 \cdot 10^{-4} \exp(-0.45 \cdot c)$
Transference number t_+ [-]	$0.4 + 0.2 \cdot c - 0.125 \cdot c^2$
Thermodynamic factor [-]	$1 - \frac{1}{2} \cdot \frac{3.95 \cdot \sqrt{c}}{(1+63.05 \cdot \sqrt{c})^2} + 0.907 \cdot c$
Conductivity κ [$\frac{\mu S}{mm}$]	$\frac{3400 \cdot c - 4700 \cdot c^{\frac{3}{2}} + 2000 \cdot c^2}{1.0 + 0.2 \cdot c^4}$
Butler-Volmer equation/parameters	$i = i_0 \cdot \left(\frac{c}{c_0}\right)^\gamma \cdot \left[\exp\left(\frac{\alpha_A F}{RT}\eta\right) - \exp\left(\frac{\alpha_C F}{RT}\eta\right)\right]$ $i_0 = 3 \frac{\mu A}{mm^2}, \quad \gamma = 0, \quad \alpha_A = \alpha_C = 0.5$

Table III. Analytical methods for the determination of the binary diffusion coefficient $D_\pm(c_0)$ from the three different types of experiments.

$D_\pm\vert^{\text{pulse}}_{\text{long-term}}$, $D_\pm\vert^{\text{steady-state}}_{\text{long-term}}$	$\frac{l^2}{\pi^2} \cdot \tau \cdot m_{\ln}$	Eq. 14
$D_\pm\vert^{\text{steady-state}}_{\text{short-term}}$	$\frac{\pi \cdot l^2}{16} \cdot \tau \cdot \left(\frac{m_{\text{sqrt}}}{U(T_\text{I})}\right)^2$	Eq. 17

work, pulse polarization experiments were done galvanostatically and steady-state polarization experiments were done potentiostatically). In addition, the binary diffusion coefficient $D_\pm\vert^{\text{steady-state}}_{\text{short-term}}$ refers to values calculated from the short term relaxation behavior of a steady-state polarization experiment (done potentiostatically in this work). The relevant equations for determining these diffusion coefficients are given in Table III.

Figure 3 and Figure 4 depict exemplarily simulated potential relaxations after a simulated galvanostatic pulse (GPP) and steady-state

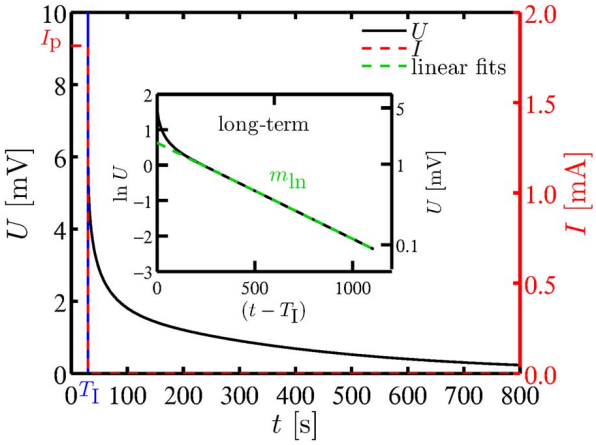

Figure 3. Simulation of a galvanostatic pulse polarization experiment (GPP) based on the parameters given in Table II and applying a polarization time of 30 s, a polarization current density of $i_\text{p} = 0.8$ mA/cm^2 (corresponding to a current of $I_\text{p} = 1.82$ mA), and an initial electrolyte concentration of $c_0 = 1$ M.

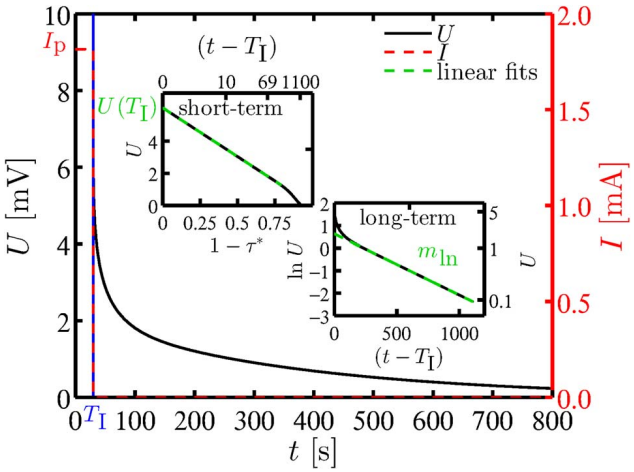

Figure 4. Plot of the relaxation phase of a simulated steady-state potentiostatic polarization experiment (SSPP) based on the parameters given in Table II, with a polarization time of $T_\text{I} = 3300$ s, a polarization potential of $U_\text{p} = 50$ mV, and an initial electrolyte concentration of $c_0 = 1$ M.

potentiostatic polarization (SSPP), respectively. The black and the red lines represent the numerical simulation results for the cell potential U and the current I, respectively. The green lines stand for the simplified analytical solution presented in the section Mathematical derivation and summarized in Table III. The insets in both figures show the linear long-term relaxation of the logarithm of the cell potential vs. time with the corresponding analytical solution (Eq. 13) and the linear short-term relaxation of the cell potential with respect to the square root of time with the corresponding analytical solution (Eq. 16). In both cases, the expected time behavior predicted by Eq. 13 and Eq. 16 can be observed. The slope $m_{\ln}$ obtained from the long-term relaxation behavior is proportional to the partial effective binary diffusion coefficient $D^*_{\pm,\text{eff}}(c_0)$ as shown in Eq. 14. Similarly, the slope m_{sqrt} obtained from the short-term relaxation of the cell potential allows to determine the partial effective binary diffusion coefficient as shown in Eq. 17. In this case, however, in addition to the known separator thickness l, the cell potential $U(T_\text{I})$ immediately after current interruption is necessary to calculate the partial effective binary diffusion coefficient from Eq. 17. In theory, $U(T_\text{I})$ is equal to the concentration overpotential resulting from the concentration difference Δc between anode and cathode. However, in actual experiments, the cell potential $U(T_\text{I})$ immediately after current interruption is usually affected by additional parasitic contributions as a result of the current interruption (SEI formation currents, capacitive currents), as shown later in Figure 9 in the Results and discussion section. To overcome this commonly encountered experimental problem, the linear relation of the concentration difference Δc (and thus of U) with respect to $\sqrt{t}$ (s. Eq. 15) can be used to extrapolate to the cell potential $U(T_\text{I})$, which would be solely due to the concentration overpotential immediately after current interruption (i.e., at $T_\text{I} + \delta t$). This is valid, if the relaxation process of the concentration difference Δc (diffusion process) proceeds on a slower time scale than the relaxation of potential parasitic processes as, e.g., capacitive effects. The extrapolation approach for determination of the cell potential $U(T_\text{I})$ at $T_\text{I} + \delta t$ is also demonstrated in Figure 4, but as the numerical simulations do not include parasitic effects, the extrapolated and the simulated value of $U(T_\text{I})$ are of course identical.

Validation of determination methods.—In Figure 5, the binary diffusion coefficients determined by the different approximation equations (s. Table III) are depicted with respect to the concentration difference $\Delta c(T_\text{I})$ at the current interruption time, which is determined from the simulation for a bulk salt concentration of $c_0 = 1$ M. In case of a pulse experiment, the concentration difference $\Delta c(T_\text{I})$ depends on the polarization time and the applied polarization current I_p while in

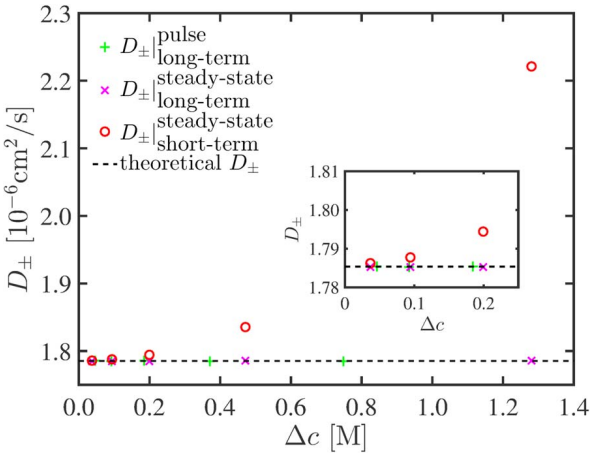

Figure 5. Binary diffusion coefficient $D_\pm$ with respect to the concentration difference $\Delta c(T_\text{I})$ between anode and cathode obtained from the simulation at the current interruption time for $c_0 = 1$ M ($T_\text{I} = 300\ s$ for pulse experiments, see Table II for other simulation parameters).

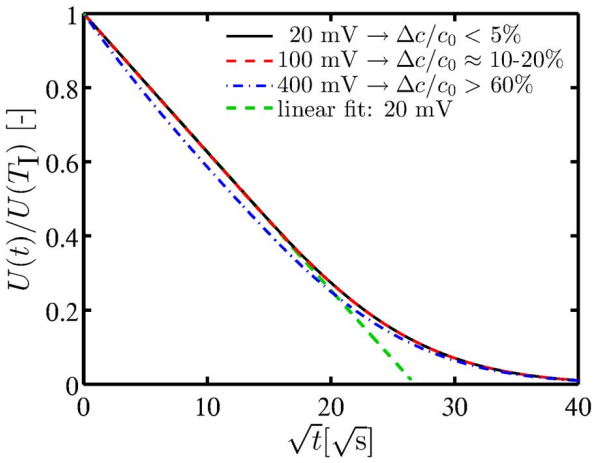

Figure 6. Relaxation behavior of the relative cell potential $U(t)/U(T_\text{I})$ with respect to $\sqrt{t}$ for different polarization potentials U_0 and for $c_0 = 1$ M. The data are fitted in the range from $t = 1$ s to $t = 10$ s (see Table II for simulation parameters).

case of a steady-state experiment it depends only on the polarization potential U_p.

The results presented in Figure 5 confirm that all three evaluation methods listed in Table III are reasonably accurate up to relative concentration differences $\Delta c/c_0$ of $\approx 20\%$ at the current interruption time. For the long-term relaxation behavior, the concentration difference $\Delta c(T_\text{I})$ at the current interruption time does not influence the quality of the obtained binary diffusion coefficient, since at the evaluated long times after the current interrupt, the concentration difference Δc is small enough to fulfil the requirement of small concentration variations, even though this is not satisfied for short times after the current interrupt. As already mentioned earlier, this is an obvious advantage of the analysis of the long-time relaxation behavior over that of the short-time relaxation behavior. These findings are also valid for all the other bulk concentrations c_0 investigated in this study, as shown in Table IV. It may be noted here, that evaluation of the long-term relaxation behavior requires the suppression of convective effects, which is generally valid for polymer electrolytes, but in case of liquid electrolytes is only really possible when using a porous matrix (separator) containing the electrolyte rather than a pure electrolyte phase.

Compared to the long-term relaxation behavior, the results of the short-term relaxation are clearly influenced by the concentration difference $\Delta c(T_\text{I})$ at the current interruption time, since high values of $\Delta c(T_\text{I})$ violate the requirement of small concentration variations (s. Theoretical background section). Additionally, the error for the determined binary diffusion coefficient $D_\pm|^{\text{steady-state}}_{\text{short-term}}$ increases for increasing bulk concentration c_0, since the absolute concentration difference $\Delta c(T_I)$ at current interruption is larger for a high salt concentration. The effect of the concentration difference $\Delta c(T_\text{I})$ on the linearity of the cell potential $U(t)$ vs. $\sqrt{t}$ is shown in Figure 6 for $c_0 = 1$ M.

As already indicated in Figure 5, a concentration variation of up to 20% with respect to the salt concentration c_0 does not significantly influence the linearity of the cell potential $U(t)$ vs. $\sqrt{t}$ behavior. For a higher relative concentration difference, a deviation of the linear behavior can be observed in Figure 6 (s. blue dash-dotted line). However, the differences between the linear and a non-linear behavior of the relative potential with time is quite small, which may make it difficult to distinguish between high and low quality results, especially in real experiments with limited signal to noise ratio. Two different effects are the reason for this deviation. First, the concentration dependence of the thermodynamic factor and the transference number $t_+(c)$ as well as the linearization of the natural logarithm in Eq. 9 violate the assumed proportionality between the concentrations difference $\Delta c(t)$ and the cell potential $U(t)$. Additionally, the concentration dependent binary diffusion coefficient $D_\pm(c)$ and transference number $t_+(c)$ in the ion transport equation violate the condition of constant transport parameters. This would be the only theoretical inaccuracy in case of a spectroscopic evaluation of the concentrations at cathode and anode. In case of the numerical simulation, the binary diffusion coefficient

Table IV. Exemplary influence of the relative concentration difference $\Delta c(T_\text{I})/c_0$ at the current interruption time on the determination of the binary diffusion coefficient $D_\pm$ from the equations listed in Table III. The relative errors are given in parenthesis.

c_0 [M]	$D_\pm(c_0)$ (s. Table II) $\times 10^{-6}$ [cm^2/s]		$\Delta c(T_\text{I})/c_0 \approx 5\%$	$\Delta c(T_\text{I})/c_0 \approx 20\%$	$\Delta c(T_\text{I})/c_0 > 60\%$
0.01	2.787	$D_\pm\|^{\text{pulse}}_{\text{long-term}}$	–	2.787 (0%)	2.787 (0%)
		$D_\pm\|^{\text{steady-state}}_{\text{long-term}}$	–	2.787 (0%)	2.787 (0%)
		$D_\pm\|^{\text{steady-state}}_{\text{short-term}}$	–	2.791 (0.1%)	3.106 (11%)
1	1.785	$D_\pm\|^{\text{pulse}}_{\text{long-term}}$	1.785 (0%)	1.785 (0%)	1.785 (0%)
		$D_\pm\|^{\text{steady-state}}_{\text{long-term}}$	1.785 (0%)	1.785 (0%)	1.785 (0%)
		$D_\pm\|^{\text{steady-state}}_{\text{short-term}}$	1.786 (0.1%)	1.794 (0.5%)	2.176 (21%)
2	1.138	$D_\pm\|^{\text{pulse}}_{\text{long-term}}$	1.139 (0.1%)	1.139 (0.1%)	1.139 (0.1%)
		$D_\pm\|^{\text{steady-state}}_{\text{long-term}}$	1.138 (0%)	1.138 (0%)	1.138 (0%)
		$D_\pm\|^{\text{steady-state}}_{\text{short-term}}$	1.141 (0.3%)	1.163 (2.1%)	1.973 (73%)

$D_\pm|^{\text{steady-state}}_{\text{short-term}}$ can also be determined directly from the relaxing concentration difference $\Delta c(t)$ rather than from the cell potential $U(t)$. The advantage of this approach is that potential non-linearities introduced by the concentration dependent thermodynamic factor and transference number as well as by the linearization of the natural logarithm are not included. As a result, the error in the binary diffusion coefficient $D_\pm|^{\text{steady-state}}_{\text{short-term}}$ reduces, e.g., from 21% (s. Table IV) to 7% for a simulation of a 1 M electrolyte solution and for the highest polarization potential $U_p = 400$ mV. These values are a good indication of the errors introduced by the indirect observation of the concentration difference $\Delta c(t)$ by the cell potential $U(t)$. Besides this exemplarily estimation, a more elaborate quantification of the errors is quite complex, since the error is strongly influenced by the concentration dependence of the transport parameters which are not known a priori.

In addition to choosing a polarization potential in SSPP experiments, the polarization time is an additional experimental parameter, since a steady-state concentration profile is strictly required. If the relaxation process starts from a non-linear concentration profile, a similar non-linear behavior of the relative cell potential with respect to the square root of time as shown in Figure 6 can also be observed. In consequence, the method based on the short-term relaxation behavior requires a true linear concentration profile at the current interruption time.

As a result of these considerations, the methods based on the long-term relaxation behavior of the potential are more reliable (reflected by the smaller errors shown in Table IV), since the results are not at all influenced by the initially established concentration profile. Additionally, the requirement of small concentration variations is automatically fulfilled for the methods based on the long-term relaxation behavior. Besides, both methods observing the long-term relaxation behavior depend only on a single parameter (viz., $m_{\ln}$ in Eq. 14), whereas it is necessary to determine the slope and the cell potential at current interruption time for the method based on the short-term relaxation behavior (viz., m_{sqrt} and $U(T_I)$ in Eq. 17). The effect of experimental uncertainties in these two parameters is furthermore magnified, since they appear in quadratic form in Eq. 17. Last but not least, the long-term linearity of the logarithmic potential is more distinct than the short-term linearity of the potential with respect to the square root of time, whereby it is critical to suppress convective effects at long times (s. above). This is of particular importance for experimentally determined data, which include experimental noise (the latter, of course, does not affect the numerical simulation of the experiments). Potential influences of experimental artefacts on the quality of the determination methods are discussed in detail in the next section.

Results and Discussion

In the following, the proposed methods are used to determine the partial effective binary diffusion coefficient $D^*_{\pm,\text{eff}}$ of an exemplary electrolyte ($LiClO_4$ in EC:DEC, 1:1 w:w). The tortuosity of the here used Celgard 2500 separator ($\tau = 2.5$) which is necessary for the calculation of the binary diffusion coefficient $D_\pm(c_0)$, is taken from Landesfeind et al.,[2] where it was determined from single separator layers. Because the experimental setup utilizes twenty layers of separators, it is necessary to prove the independence of the tortuosity from the number of separator layers, i.e., that the separator/separator interface does not alter the overall tortuosity of a stack of separators. Calculation of the tortuosity from the high frequency resistance measured before each pulse experiment (20 Ohm) of a cell filled with 20 layers of the Celgard 2500 separator (porosity 55%, active area 2.27 cm^2) and the 0.5 M electrolyte (conductivity 5.3 mS/cm) yields a tortuosity of 2.65, which is in good agreement with the value for an individual layer of the separator of 2.5. Because also contact resistances caused by, e.g., the spring in the experimental setup contribute to the high frequency resistance, we use the single layer tortuosity of 2.5 in the following analysis. As introduced in the Mathematical derivation section, the binary diffusion coefficient can be determined

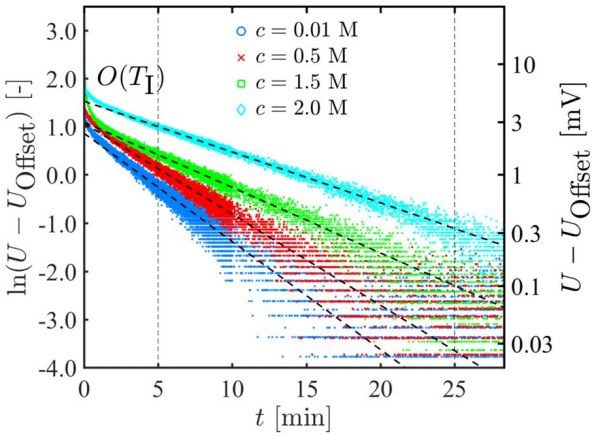

Figure 7. Experimental SSPP data (corrected for the long time offset potential) of the time relaxation of the natural logarithm of the potential (U in mV) after steady-state polarization (for polarization potentials and times see Table I), showing data for 0.01 M, 0.5 M, 1.5 M and 2.0 M $LiClO_4$ in EC:DEC (1:1 w:w) obtained in the two-electrode cell described in Figure 1. The binary diffusion coefficient is determined by the linear line fits (dashed black lines) via $D_\pm|^{\text{steady-state}}_{\text{long-term}}$ (see Eq. 14).

based on the long-term relaxation of the cell potential $U(t)$ after a pulse ($D_\pm|^{\text{pulse}}_{\text{long-term}}$, s. Table III) or after a steady-state polarization experiment ($D_\pm|^{\text{steady-state}}_{\text{long-term}}$, s. Table III) as well as based on the short-term relaxation of $U(t)$ after a steady-state polarization experiment ($D_\pm|^{\text{steady-state}}_{\text{short-term}}$, s. Table III). Figure 7 exemplarily shows the relaxation of the logarithm of the potential $\ln U(t)$ versus time t after a steady-state polarization experiment in a 0.01 M, 0.5 M, 1.5 M, and 2.0 M $LiClO_4$ electrolyte. While the cell potential $U(t)$ relaxes to a constant value at long times, it never relaxes exactly to zero, ending at a stable open circuit potential between −0.5 mV and +0.5 mV. This final value was found to be random in magnitude and sign and is attributed to changes of the lithium metal electrode surface state due to SEI formation (initiated during lithium deposition on one of the electrodes in each pulse) and roughness variation. In consequence, all relaxation curves are fitted with a free offset potential U_{Offset}, since the linear behavior of the open circuit potential $\ln U(t)$ with respect to time t can be only observed if the open circuit potential $U(t)$ approaches zero for long times. After offset correction, the linear behavior of $\ln(U)$ vs. t can be observed consistently over times ranging from 5 to 25 minutes (marked by vertical dashed lines in Fig. 7), which allows for a quantification of the binary diffusion coefficient according to Eq. 14.

The apparent increase in noise for long times is due to the logarithmic scale, ultimately showing the digital resolution of the potentiostat. In this study, the noise level of the potential measurement was ±100 µV. Applying the same analysis method, the binary diffusion coefficient can also be obtained from the long-term relaxation of the cell potential $U(t)$ after a pulse experiment ($D_\pm|^{\text{pulse}}_{\text{long-term}}$ method, s. Eq. 14) which is not shown explicitly.

The short-term relaxation of the cell potential $U(t)$ with respect to $\sqrt{t}$ after a steady-state polarization is the basis for the determination of the binary diffusion coefficient according to Eq. 17 ($D_\pm|^{\text{steady-state}}_{\text{short-term}}$ method). Exemplary current transients during steady-state polarization experiments with an applied potential of 50 mV, i.e., the current normalized by its initial value (I/I_0) vs. time are shown in Figure 8. In case of a 0.01 M, 0.5 M, and 2.0 M electrolyte (blue, red, and cyan lines in Figure 8), a reasonably stable current plateau was reached at the time when the current was interrupted (i.e., when switching to OCV). On the other hand, in the measurement with the 1.5 M electrolyte (green line in Figure 8), the current starts to increase after its initial decay, which is caused by the formation of high surface area lithium and an associated decrease in the charge transfer resistance for

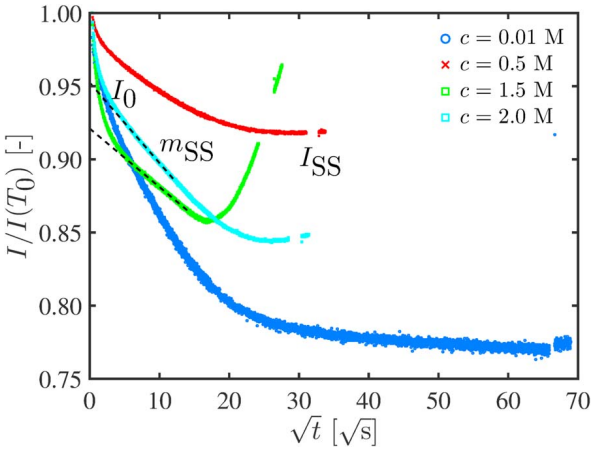

Figure 8. Exemplary steady state polarization current transients for 0.01 M, 0.5 M, 1.5 M, and 2.0 M $LiClO_4$ in EC:DEC (1:1 w:w) at constant polarization of 50 mV in the two-electrode cell shown in Figure 1. The gaps in the curves toward the end of the potentiostatic polarization procedure are due to impedance measurements which were conducted during that time.

lithium dissolution/plating. In this case, a linear concentration profile at current interruption cannot be guaranteed anymore as discussed in the following.

Figure 9 depicts the corresponding OCV decays after the potentiostatic polarization phases shown in Figure 8. For the experiments with 0.5 M and 2 M $LiClO_4$ (red and light blue curves) which exhibited a steady-state current (s. Figure 8), a potential relaxation phase where $U(t)$ is linear vs. $\sqrt{t}$ can be clearly discerned (between 25 and 225 s/400 s, i.e., between ca. $5/\sqrt{s}$ and $15/\sqrt{s}$ / $20/\sqrt{s}$) and is indicated by the dashed black lines in Figure 9. While the $U(t)$ vs. $\sqrt{t}$ behavior depicted in Figure 9 resembles its theoretically predicted response for $\sqrt{t}$-values exceeding $\approx 3\ s^{-0.5}$ (compare Figure 9 with Figure 6), the experimental data deviate dramatically at $\sqrt{t}$-values below $\approx 3\ /\sqrt{s}$, where the potential does not follow the predicted proportionality between $U(T_I)$ and $\sqrt{t}$. This behavior is commonly observed[32] and introduces two uncertainties in the evaluation of the diffusion coefficient based on Eq. 17: i) an ambiguity in defining the time frame over which the linear fit should be applied, which would be very straightforward if the response were to follow its theoretically predicted behavior (s. Figure 6); ii) the determination of the required

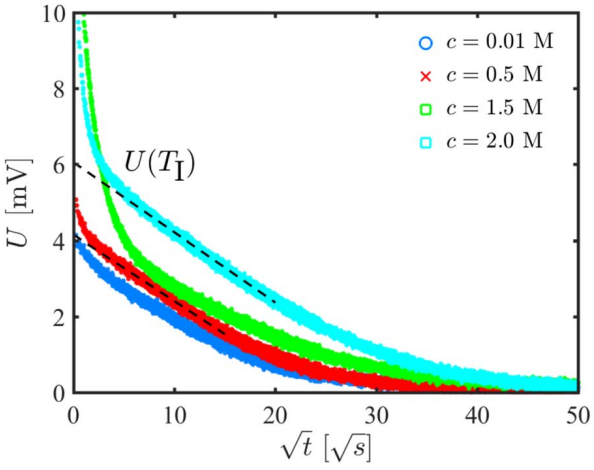

Figure 9. Short-term potential relaxation after the potentiostatic polarization experiments (SSPP) shown in Fig. 8. (0.01 M, 0.5 M, 1.5 M and 2.0 M $LiClO_4$ in EC:DEC (1:1 w:w)). The black dashed lines are a linear fit according to Eq. 16 in order to determine $D_{\pm}|^{\text{steady-state}}_{\text{short-term}}$.

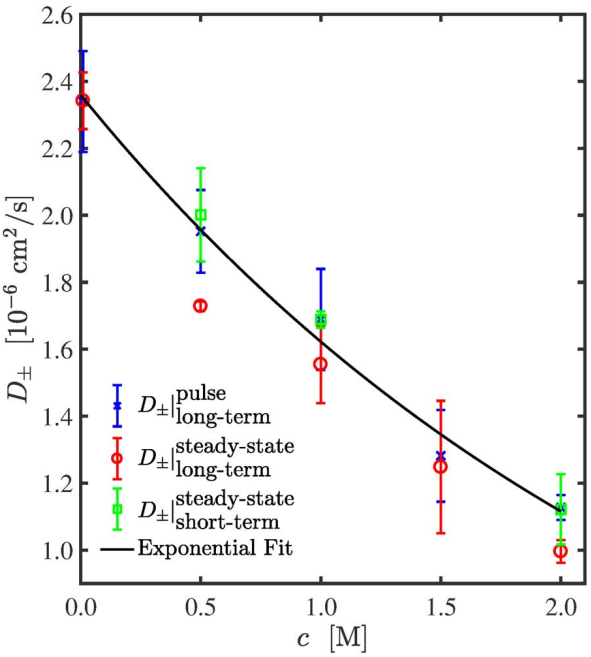

Figure 10. Concentration dependent binary diffusion coefficient $D_{\pm}$ of $LiClO_4$ in EC:DEC (1:1 w:w) measured in the two-electrode Li-Li cell shown in Figure 1. The error bars represent the standard deviations from at least two different cells; the relationships to determine $D_{\pm}$ are summarized in Table III.

initial potential just after current interruption ($U(T_1)$ in Eq. 17) is by no means straightforward and the value of $U(T_1)$ must be estimated by back-extrapolation of the linear segment to $\sqrt{t}= 0$, which would be the expected voltage response in the absences of parasitic currents (s. Figure 6). This deviation of the experimental short-time response from the theoretical short-term response (i.e., below $\sqrt{t}$-values of $\approx 3\ /\sqrt{s}$) is likely due to parasitic currents caused by the reformation of the SEI, particularly on the lithium electrode on which lithium plating occurred during potentiostatic polarization. Similar transients have been recorded by Odziemkowski when metallic lithium was cut while emerged in an electrolyte solution.[34] In summary, determination of the binary diffusion coefficient $D_{\pm}$ from short-term relaxation experiments is clearly more difficult and error prone than from long-term relaxation experiments.

In the case where no steady-state current is obtained during potentiostatic polarization (s. data for 1.5 M $LiClO_4$; green line in Figure 8), the conditions for an analysis of the short-term relaxation behavior are actually not fulfilled (i.e., it cannot be assumed that a steady-state linear concentration profile has been obtained). Nevertheless, the observed potential relaxation still displays a fairly linear segment (s. green line in Figure 9), so that one might be tempted to apply Eq. 17 to extract a binary diffusion coefficient. This would be clearly invalid, so that binary diffusion coefficients should only be determined from short-term relaxation experiments after having assured that a steady-state current was indeed obtained during polarization. In consequence, as the latter requirement is not met for the 1.5 M $LiClO_4$ experiment, our below summary of the concentration dependent binary diffusion coefficients of $LiClO_4$ in EC:DEC (1:1 w:w) obtained by the three different analysis methods used in this study (s. Table III) does not include any values for the short-term relaxation experiment for the 1.5 M $LiClO_4$ electrolyte. The same argumentation holds for the 0.01 M concentration due to ambiguous linear regions during polarization in Figure 8 (s. blue line) and relaxation (s. blue line in Figure 9).

Binary diffusion coefficients determined for a $LiClO_4$ in EC:DEC (1:1 w:w) electrolyte at five concentrations using the methods summarized in Table III and plotted in Figure 10 show a good

correlation between the three methods. The shown values are the mean values obtained from all pulses for all cells at a given concentration, and the error bars indicate their corresponding standard deviation. As already discussed in the Numerical validation section, the most reliable approach for determining the binary diffusion coefficient are the long-term relaxation methods (s. Eq. 14). Amongst these, the pulse polarization experiments ($D_{\pm}|^{\text{pulse}}_{\text{long-term}}$) have some advantage over steady-state polarization experiments ($D_{\pm}|^{\text{steady-state}}_{\text{long-term}}$): the much shorter polarization time for pulse experiments allows for higher polarization currents which result in larger potentials during relaxation, thus leading to a better signal to noise ratio and allowing for a longer time range over which Eq. 14 can be fitted. For the methodology based on the short-term relaxation after a steady-state polarization ($D_{\pm}|^{\text{steady-state}}_{\text{short-term}}$), the generally observed parasitic currents from SEI formation and the formation of high surface area lithium can lead to a non-constant concentration profile and render the method less reliable, in addition to the risk of analyzing data from conditions where the imposed concentration gradients were too large (s. Table IV).

Figure 10 also includes an exponential fit for the concentration dependence of the binary diffusion coefficient based on the $D_{\pm}|^{\text{pulse}}_{\text{long-term}}$ values, yielding

$$D_{\pm}(c) = 2.36 \cdot 10^{-6} \ \exp(-0.375\, c) \quad \left[\frac{\text{cm}^2}{\text{s}}\right] \qquad [18]$$

where the $LiClO_4$ salt concentration c is given in units of mol/l. A decrease in the binary diffusion coefficient $D_{\pm}(c)$ as observed in Figure 10 is expected theoretically. Upon increasing the salt concentration, ion-ion interactions become more prominent, leading to an increase of the viscosity of the electrolyte and thereby reducing the ionic mobilities. In addition, the binary diffusion coefficient $D_{\pm}$ determined by the described experimental method also includes additional factors such as the ratio between the total salt concentration and the solvent concentration, the thermodynamic factor, and potential volumetric effects as discussed, e.g., by Nyman et al.[19] or Georén and Lindbergh.[24] However, it is not necessary to separate these different effects from each other in order to use the determined binary diffusion coefficient in numerical simulations with a consistent physical model.

As discussed in the Introduction section, binary diffusion coefficients are reported based on rotating disc measurements,[14] numerical fitting procedures,[19,24,26] relaxations experiments with optical observation of the concentration gradient[17] as well as based on analysis of the Moiré pattern.[12] Similar trends are described by all publications, namely showing a decrease of the binary diffusion coefficient for increasing salt concentrations. Lundgren et al.,[26] Nyman et al.,[19] and Valøen et al.[6] get a very similar strong concentration dependence ranging from $5.5 \cdot 10^{-6}$ cm^2/s at infinite dilution to $0.5 \cdot 10^{-6}$ cm^2/s at 2 M salt concentrations for $LiPF_6$ dissolved in similar electrolyte solutions (s. red dotted and dashed lines in Figure 11). Although Stewart and Newman also investigated a similar electrolyte solution ($LiPF_6$ in EC:DEC 1:1 w:w), they reported a disproportionally strong concentration dependence, based on concentration gradient measurements with an optical cell[17] (s. solid red line in Figure 11). Using a numerical fitting method, Georén and Lindbergh[24] and Nishikawa et al.[12] determine the binary diffusion coefficient of $LiClO_4$ in PC (s. blue dashed and blue line with asterisks in Figure 11). Particularly at low concentrations, their results compare well with our binary diffusion coefficients (s. blue solid line in Figure 11). Xu and Farrington[14] obtained an average diffusion coefficient between 0 and 0.1 M $LiClO_4$ in PC using the rotating disc method (s. blue square in Figure 11). While generally larger diffusion coefficients are reported for $LiPF_6$ compared to $LiClO_4$ based electrolytes, similar ranges are obtained for each type, with our measurements being in good agreement with binary diffusion coefficients reported for similar electrolytes in the literature.

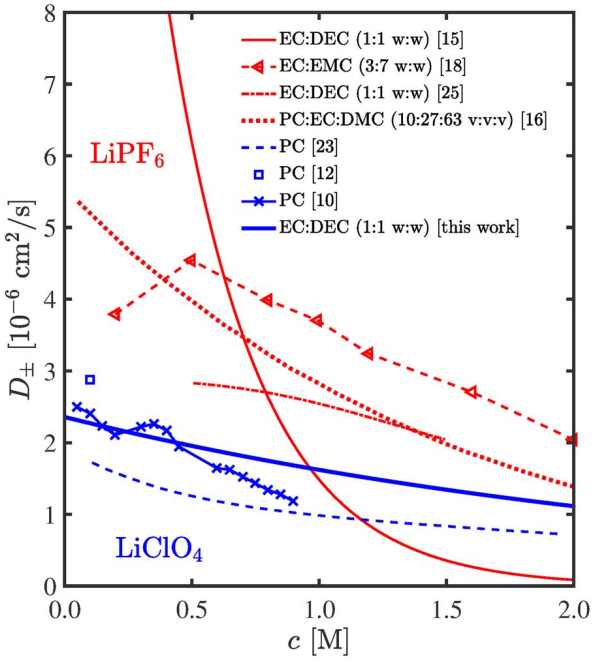

Figure 11. Literature comparison of binary diffusion coefficients for $LiClO_4$ (blue lines/symbols) and $LiPF_6$ (red lines/symbols) in electrolytes with different solvents with the $LiClO_4$ electrolyte investigated in this work ($LiClO_4$ in EC:DEC 1:1 w:w). The literature data are: Stewart and Newman[17] ($LiPF_6$ in EC:DEC 1:1 w:w, RT), Nyman et al.[19] ($LiPF_6$ in EC:EMC, 3:7 w:w, 25 ± 1°C), Lundgren et al.[26] ($LiPF_6$ in EC:DEC, 1:1 w:w, 25 ± 1°C), Valøen et al.[6] ($LiPF_6$ in PC:EC:DMC, 10:27:63 v:v:v, 21°C), Georén and Lindbergh[24] ($LiClO_4$ in PC, RT), Xu and Farrington[14] ($LiClO_4$ in PC, 25°C), Nishikawa et al.[12] ($LiClO_4$ in PC, 25°C).

Conclusions

In this work, the concentration dependent binary diffusion coefficient is determined from the short-term and the long-term relaxation behavior after a pulse or a steady-state polarization experiment in a new two-electrode cell design using lithium metal electrodes. In contrast to similar experimental procedures available in the literature, the distance between the lithium electrodes is kept small to ensure a large radius to distance ratio and thus reduces the influence of a non-homogenous electric field at the electrode edge. A small electrode distance is realized by 20 layers of polypropylene separators which effectively suppress convective effects which occur in experimental setups where a free electrolyte without porous matrix (separator) is used. For this new approach of using porous separators instead of free electrolyte, it was necessary to extend the analytical methods available in the literature to include the effect of the porous medium.

The accuracy of the various evaluation approaches was examined by numerical simulations, and experimental artefacts were examined by comparing simulations with the various experimental approaches using an exemplary electrolyte (0.01 to 2 M $LiClO_4$ in EC:DEC 1:1 w:w). The experimentally determined binary diffusion coefficients were in good agreement with those reported in the literature for similar electrolytes. Our analysis clearly shows that the most reliable and straightforward method for determining binary diffusion coefficients using a two-electrode cell is based on the long-term relaxation behavior after a galvanostatic polarization pulse using a porous separator which effectively suppresses convective effects.

Acknowledgment

We gratefully acknowledge the funding by the Bavarian Ministry of Economic Affairs and Media, Energy, and Technology for its financial support under the auspices of the EEBatt project.

List of Symbols

Symbol	Name	Unit
κ	conductivity	mS/cm
$D_{\pm}$	binary diffusion coefficient	cm^2/s
t_+	transference number of lithium ion	-
$f_{\pm}$	mean molar activity coefficient	-
c	volumetric intrinsic phase average of the concentration	$mmol/cm^3$
l	distance between electrodes	μm
ε	porosity	-
t	time	s
τ	tortuosity	-
z_i	ionic charge (neg./pos. for anions/cations)	-
ν_i	stoichiometry factor	-
$\bar{\boldsymbol{i}}$	spatial vector of the volumetric phase average of the current density	A/cm^2
$\bar{i}$	volumetric phase average of the current density	A/cm^2
$D_{\pm,\mathrm{eff}}$	effective binary diffusion coefficient	cm^2/s
ϕ	volumetric intrinsic phase average of the electric potential wrt. to a lithium electrode	V
U	cell potential	V
$D^*_{\pm,\mathrm{eff}}$	partial effective binary diffusion coefficient	cm^2/s
m_i	slopes of linear trends	various
A	electrode area	cm^2
I_i	current	mA
R_i	resistance	Ω
τ^*	artificial time	-

References

1. J. Newman and K. Thomas-Alyea, *Electrochemical Systems*, 3rd ed., Wiley Interscience, Hoboken, (2004).
2. J. Landesfeind, J. Hattendorff, A. Ehrl, W. A. Wall, and H. A. Gasteiger, *J. Electrochem. Soc.*, **163**, A1373 (2016).
3. A. Ehrl, J. Landesfeind, H. A. Gasteiger, and W. A. Wall, **in prep**. (2016).
4. J. Landesfeind, A. Ehrl, M. Graf, W. A. Wall, and H. A. Gasteiger, *J. Electrochem. Soc.*, **163**, A1254 (2016).
5. A. Nyman, M. Behm, and G. Lindbergh, *Electrochim. Acta*, **53**, 6356 (2008).
6. L. O. Valøen and J. N. Reimers, *J. Electrochem. Soc.*, **152**, A882 (2005).
7. F. Castiglione, E. Ragg, A. Mele, G. B. Appetecchi, M. Montanino, and S. Passerini, *J. Phys. Chem. Lett.*, **2**, 153 (2011).
8. A. K. Sethurajan, S. Krachkovskiy, I. C. Halalay, G. R. Goward, and B. Protas, *J. Phys. Chem. B*, **119**, 12238 (2015).
9. C. Capiglia, Y. Saito, and H. Kageyama, *J. Power Sources*, **81**, 859 (1999).
10. A. D. McNaught and A. Wilkinson, *IUPAC. Compendium of Chemical Terminology*, Blackwell Scientific Publications, Oxford, (1997).
11. W. S. Price, *Concepts Magn. Reson.*, **9**, 299 (1997).
12. K. Nishikawa, Y. Fukunaka, T. Sakka, Y. H. Ogata, and J. R. Selman, *J. Electrochem. Soc.*, **153**, A830 (2006).
13. T. Nishida, K. Nishikawa, and Y. Fukunaka, *ECS Trans.*, **6**, 1 (2008).
14. J. Xu and G. C. Farrington, *J. Electrochem. Soc.*, **143**, L44 (1996).
15. H. S. Harned and D. M. French, *Ann. N. Y. Acad. Sci.*, **46**, 267 (1945).
16. J. Newman and T. W. Chapman, *AIChE J.*, **19**, 343 (1973).
17. S. G. Stewart and J. Newman, *J. Electrochem. Soc.*, **155**, F13 (2008).
18. M. M. Hiller, M. Joost, H. J. Gores, S. Passerini, and H.-D. Wiemhöfer, *Electrochim. Acta*, **114**, 21 (2013).
19. A. Nyman, M. Behm, and G. Lindbergh, *Electrochim. Acta*, **53**, 6356 (2008).
20. I. V. Thorat, D. E. Stephenson, N. a. Zacharias, K. Zaghib, J. N. Harb, and D. R. Wheeler, *J. Power Sources*, **188**, 592 (2009).
21. M. M. Doeff, L. Edman, S. E. Sloop, J. Kerr, and L. C. De Jonghe, *J. Power Sources*, **89**, 227 (2000).
22. A. Ferry, M. Doeff, and L. DeJonghe, *Electrochim. Acta*, **43**, 1387 (1998).
23. Y. Ma, M. Doyle, T. F. Fuller, M. M. Doeff, L. C. Jonghe, and J. Newman, *J. Electrochem. Soc.*, **142**, 1859 (1995).
24. P. Georén and G. Lindbergh, *Electrochim. Acta*, **47**, 577 (2001).
25. C. M. Doyle, *PhD Thesis*, Berkeley (1996).
26. H. Lundgren, M. Behm, and G. Lindbergh, *J. Electrochem. Soc.*, **162**, 3 (2014).
27. J. Liu and C. W. Monroe, *Electrochim. Acta*, **167**, 357 (2015).
28. J. Bear and Y. Bachmat, *Introduction to Modeling of Transport Phenomena in Porous Media*, Springer Netherlands, Dordrecht, (1990).
29. M. Landstorfer and T. Jacob, *Chem. Soc. Rev.*, **42**, 3234 (2013).
30. A. Ehrl, *PhD Thesis*, München (2016).
31. P. Bruce and C. Vincent, *J. Electroanal. Chem.*, **225**, 1 (1987).
32. S. Zugmann, M. Fleischmann, M. Amereller, R. M. Gschwind, H. D. Wiemhöfer, and H. J. Gores, *Electrochim. Acta*, **56**, 3926 (2011).
33. D. Aurbach, E. Zinigrad, Y. Cohen, and H. Teller, *Solid State Ionics*, **148**, 405 (2002).
34. M. Odziemkowski and D. E. Irish, *J. Electrochem. Soc.*, **140**, 1546 (1993).

3.2 Thermodynamic Factor

In this section the article *Direct Electrochemical Determination of Thermodynamic Factors in Aprotic Binary Electrolytes*[102] is presented, which was submitted in January 2016 and published in the peer-reviewed Journal of the Electrochemical Society in April 2016. Parts of the article were presented at the 13$^{\text{th}}$ Symposium on Fuel Cell and Battery Modeling and Experimental Validation in Lausanne (Switzerland) in March 2016 and at the ECCOMAS 2016 in Crete (Greece) in June 2016.

A key requirement for the determination of the thermodynamic factor is to deconvolute it from the transference number. For example, concentration cell potential measurements depend on the concentration dependence of the thermodynamic factor and the transference number. In the literature the thermodynamic factor is determined from concentration cell experiments by assuming, e.g., a constant transference number.[50] While alternative optimization approaches exist,[56,57] no direct electrochemical measurement of only the thermodynamic factor is possible. *Physical* measurements of the vapor pressure lowering by salt addition exist and yield osmotic coefficients and activity coefficients without any assumptions on the other transport properties of the electrolyte.[103] In the presented publication we aimed at providing a novel *electrochemical* measurement technique for only the thermodynamic factor. The methodology is based on the assumption that the redox potential of the ferrocene/ferrocenium couple is independent of its surrounding. Careful measurements of the ferrocene/ferrocenium redox behavior in a range of supporting $LiClO_4$ electrolyte concentrations are referenced versus a metallic lithium electrode and analyzed analytically to yield the TDF of the supporting electrolyte. However, after publication of the study it was found that the ferrocene/ferrocenium redox potential is only independent of the type of solvent and strictly identical only for the same supporting salt and salt concentration. In consequence, and in agreement with the Debye-Hückel theory,[47] the ferrocenium activity coefficient and thus the redox potential of the couple is not independent of the surrounding salt concentration, especially at low salt concentrations, and the ferrocene method cannot be used to determine thermodynamic factors without further assumptions (now on the activity coefficient of the ferrocene/ferrocenium couple).

In order not to mislead the reader, we are in the process of publishing an erratum to the original manuscript which elaborates on the invalid assumption (see Section 3.2). Therein we also compare the thermodynamic factors obtained from the ferrocene cell method with an alternative approach introduced in our temperature dependent study (see Section 3.4) and suggest that the relative permittivity of the solvent determines the error of the ferrocene cell measurements.

Author Contributions

A.E., J.L. and H.G. developed the cell design. M.G. and J.L. performed all electrochemical measurements, A.E. derived the analytical solutions. Data analysis was done by A.E., J.L. and M.G. and the manuscript was written by A.E. and J.L. and edited by W.W. and H.G. All authors discussed the data and commented on the results.

Direct Electrochemical Determination of Thermodynamic Factors in Aprotic Binary Electrolytes

Johannes Landesfeind,[a,=,z] Andreas Ehrl,[b,=,z] Maximilian Graf,[a] Wolfgang A. Wall,[b] and Hubert A. Gasteiger[a,*]

[a] *Chair of Technical Electrochemistry, Department of Chemistry and Catalysis Research Center, Technische Universität München, Munich, Germany*
[b] *Institute for Computational Mechanics, Department of Mechanical Engineering, Technische Universität München, Munich, Germany*

We propose a novel method to determine the thermodynamic factor of binary salts dissolved in aprotic solvents as a function of salt concentration. The method is based on cyclic voltammetry experiments conducted in a three-electrode cell with the ferrocene/ferrocenium redox couple being used as an internal standard. The main advantage of this experimental setup is the direct electrochemical determination of the thermodynamic factor from a single type of experiment without the necessity of additional assumptions on other transport parameters. The theoretical derivation of the used relationship between peak/half-wave potentials and the thermodynamic factor as well as non-ideal effects which distort the experimental results, such as uncompensated resistances or concentration overpotentials are discussed in detail. Different strategies are suggested to avoid these non-ideal effects using the peak separation of the cyclic voltammograms as an inherent quality measure for the experimental data. Applicability of the experimental procedure is demonstrated for $LiClO_4$ in EC:DEC (1:1, w:w) in the range from 5 mM to 2 M and repeated for typical $LiPF_6$ containing electrolytes. At the end, the obtained results are compared to thermodynamic factors of similar electrolyte solutions published in literature.

 [DOI: 10.1149/2.0651607jes]

Manuscript submitted January 18, 2016; revised manuscript received April 4, 2016. Published April 19, 2016.

Advanced numerical simulation tools are important both for understanding existing battery systems such as lithium-ion batteries and for the development of future battery systems as, e.g., lithium-sulfur batteries. One beneficial aspect of computational methods is that they can provide insight into physical and chemical aspects, which sometimes cannot be probed by experimental methods. For such numerical simulations, accuracy and reliability are key issues and depend on appropriate physical models, boundary conditions, and accurately determined physico-chemical parameters. Standard ion-transport models for concentrated binary electrolyte solutions depend on three ion transport parameters, namely the conductivity, the transference number and the binary diffusion coefficient.[1,2] In addition to the transport parameters, the thermodynamic factor $(1 + \mathrm{d}\ln f_{\pm}/\mathrm{d}\ln c)$ which is derived from the mean molar activity coefficient $f_{\pm}$ is required for the correct description of the thermodynamic behavior of a binary electrolyte solution. In general, the focus in the literature is on the determination of ion transport parameters, while only few publications deal with the determination of mean molar activity coefficients or thermodynamic factors, especially in the case of non-aqueous electrolytes.

Some publications on activity coefficients and thermodynamic factors in non-aqueous electrolytes are summarized shortly in the following. In Bartel et al.,[3] the osmotic coefficient is determined based on the vapor pressure of lithium perchlorate ($LiClO_4$) in various alcohols. The data for the osmotic coefficients are well represented by the Pitzer equation with seven parameters. Two of the necessary parameters are assumed based on literature values, whereas the remaining parameters are determined by a regression model. In that publication, the mean molal (i.e., based on mol/$kg_{solvent}$) activity coefficient $\gamma_{\pm}$ rather than the mean molar activity coefficient $f_{\pm}$ (i.e., based on mol/$l_{electrolyte}$) is calculated from the osmotic coefficient by integration. Later on, the authors use the same approach for aprotic electrolyte solutions such as $LiClO_4$ dissolved in dimethylcarbonate (DMC).[4] In Stewart and Newman, the osmotic coefficient for lithium hexaflurophosphate ($LiPF_6$) in ethylene carbonate (EC) is determined by melting point depression.[5] However, this method may not be applicable to all solvent mixtures and the complete concentrations range since, according to the authors, it is limited by the eutectic point of the solvent mixture. In the same publication, the mean molar activity coefficient of $LiPF_6$ in EC:EMC (1:1, w:w) is also determined based on experiments in a concentration cell, whereby a constant, i.e., concentration-independent transference number was assumed. In Valøen et al., this approach is also used for $LiPF_6$ in PC:EC:EMC (10:27:63, v:v:v).[6] In addition, the temperature dependence of the mean molar activity coefficient is determined in the range from 263 K–333 K. The validity of a constant transference number is verified by experiments using the Hittorf method and data available in the literature. However, a theoretical explanation for the assumption of a constant transference number is missing in both contributions. In Nyman et al., the diffusion coefficient, transference number, and thermodynamic factor are determined for $LiPF_6$ in EC:EMC (3:7, w:w) by a numerical optimization approach, based on relaxation experiments in a polarization cell with a porous separator in combination with data from a concentration cell.[7] The numerical optimization algorithm is based on concentrated solution theory, incorporating the solvent velocity into the mass balance. Recently, the temperature dependence of $LiPF_6$ dissolved in EC:DEC (1:1, w:w) was investigated by the same method.[8] Binary diffusion coefficient, transference number, and thermodynamic factor can also be determined through a combination of three experimental setups. In this approach, the diffusion coefficient is measured by a galvanostatic relaxation experiment as presented, e.g., in Harned and French.[9] The concentration cell and a galvanostatic polarization experiment are then used to calculate the remaining two parameters.[10]

The basic objective of the present contribution is the *electrochemical* determination of the thermodynamic factor for aprotic binary electrolyte solutions within a *single* experimental setup. Therefore, cyclic voltammetry in electrolyte solutions containing small amounts of ferrocene are measured versus a lithium reference electrode, showing that the peak positions of the ferrocene redox couple can be related to the mean molar activity coefficient of the lithium salt. The use of the ferrocene redox couple as a quasi-reference is discussed in detail in the original contribution by Gritzner and Kuta.[11] In this context, the lithium salt is referred to as supporting electrolyte, since the ferrocene concentration is kept at least an order of magnitude lower concentration than the lithium salt. In the Experimental section, setup

=These authors contributed equally to this work.
*Electrochemical Society Fellow.
zE-mail: j.landesfeind@tum.de; ehrl-andreas@tum.de

Figure 1. Three-electrode glass setup with a Pt CE (left) and a Au WE (center) in EC:DEC (1:1 w:w) electrolyte containing $LiClO_4$ concentrations from 0.1×10^{-3} to 2 M and 50 μM Fc (ferrocene) as well as a metallic Li RE (right) in the same electrolyte without Fc.

and procedure are described in detail. The basic relation between the peak position and the mean molar activity coefficient is derived thereafter, and theoretical factors distorting experimental results are reviewed. Subsequently, experimental results are presented and experimental strategies are discussed which minimize errors caused by experimental constraint. Experimental data are selected depending on their peak separation and used to determine the parameters of an extended Debye-Hückel law. Obtained activity coefficients are then used to calculate the thermodynamic factor. By applying this procedure at various temperatures using a slightly modified cell design, meaningful values for the concentration dependent thermodynamic factor can be obtained.[12] Finally, the concentration dependent thermodynamic factors are compared to data available in the literature.

Experimental

Measurements and electrolyte preparations were performed in an argon filled and temperature controlled glove box (from MBraun, with temperature at 25°C ± 1°C, water content <0.1 ppm, and Ar 5.0 (Westfalen)). A custom made three-electrode glass setup (Figure 1) was used with a platinum (Advent, 99.99+% purity) counter electrode (CE), gold (Alfa Aesar, 99.999% purity) working electrode (WE), and a lithium (Rockwood Lithium, 0.45 mm, high purity) reference electrode (RE). Individual cell compartments were separated by porous glass frits. The distance between the electrodes was kept small (∼1 cm) to minimize ohmic drops in the electrolyte phase. To prevent electrolyte evaporation, the cell is sealed with PTFE sealing rings (Glindemann) at the glass joints and the electrodes are electronically connected with the potentiostat via fused-in tungsten wires. All glass cell parts were cleaned by boiling them in a mixture of ethanol and water (Millipore, Elix, 15 MΩ cm), thoroughly rinsed with water, and then dried at 70°C in a heating oven before bringing them into the glove box. Relative solvent permittivities were measured in a custom made coaxial stainless steel setup using impedance spectroscopy.

A mixture of ethylene carbonate (EC, 50 w%, Sigma Aldrich, anhydrous, 99%) and diethyl carbonate (DEC, 50 w%, Sigma Aldrich, anhydrous, >99%) was used as solvent for the investigated electrolytes with $LiClO_4$ (Sigma Aldrich, 99.99%) concentrations from 0.1×10^{-3} to 2 M. Ferrocene (Fc, Merck, >98%) was added to the electrolyte in the CE and WE compartment at equal concentrations of 50 μM or 100 μM. As usual, due to the small association constant of comparable electrolytes, 48 dm^3/mol for LiClO4 in PC/EMC,[13] ion pair formation is neglected in this work.[3–10] In consecutive measurement series with multiple $LiClO_4$ concentrations, smallest concentrations were measured first to avoid contaminations by salt remains from previous experiments. For repetitive measurements on different electrolytes, $LiPF_6$ (Sigma Aldrich, 99.99%), EMC (Sigma Aldrich, 99.99%) and DMC (Sigma Aldrich, >99.99%) were used for electrolyte preparations.

A Biologic VMP3 potentiostat/galvanostat was connected to the cell placed inside the glove box using actively shielded cables. The cell impedance was measured and the high frequency resistance between WE and RE was extracted by linear extrapolation of the high frequency part in a Nyquist plot. Recorded cyclic voltammograms (CVs) between 2.5 V and 4 V versus Li/Li^+ were online IR-corrected for different percentages of the determined WE-RE resistance, usually 85%. Always five consecutive scans were performed per analyzed scan rate (10 mV/s or 20 mV/s).

Theory

In this section, a general correlation between the cell potential U and the mean molar activity coefficient $f_\pm(c)$ of a binary salt is derived for cyclic voltammetry experiments. The used experimental setup is shown in Figure 1 and the meaning and units of each symbol are given in the List of Symbols/Constants at the end of this article. The cell potential U is the difference between the electrostatic potential of the Working Electrode (WE) Φ_{WE} and the electrostatic potential of the lithium Reference Electrode (RE) Φ_{RE}. The concentration dependence of the mean molar activity coefficient is expressed in terms of the concentration of a binary salt, which is defined as $c = c_+/\nu_+ = c_-/\nu_-$. Here, c_+ and c_- denote the molar concentration of the positive and negative ionic species, respectively. The coefficients ν_+ and ν_- describe the stoichiometry of the salt decomposition into its ionic components. In general, the mean binary activity coefficient of any salt is defined as

$$f_\pm^\nu \equiv f_+^{\nu_+} f_-^{\nu_-} \quad [1]$$

where ν is given by $\nu = \nu_+ + \nu_-$. Subsequently, the subscripts '+' and '−', indicating the positive and negative ionic species, are replaced by the names of their corresponding ions, namely lithium $Li^+$and perchlorate ClO_4^- for clarity. Generally the described framework can also be applied to any other binary salt. As mentioned before, the lithium perchlorate salt can also be thought of as a supporting electrolyte, whereas ferrocene (Fc) or its oxidized form ferrocenium (Fc^+) are the minor ionic species in the electrolyte solution.

Theoretical derivation.—The redox reaction at the Reference Electrode (RE) is defined as

$$Li \rightleftarrows Li^+ + e^- \quad [2]$$

and at the Working Electrode (WE) as

$$Fc \rightleftarrows Fc^+ + e^- \quad [3]$$

where Fc denotes the ferrocene and Fc^+ the ferrocenium ion. The reaction Gibbs energy $\Delta_R G$ for the lithium reaction at the RE is given by

$$\Delta_R G|_{RE} = 0 = \mu_{Li} - \tilde{\mu}_{Li^+} - \tilde{\mu}_{e^-} \quad [4]$$

and for the ferrocene reaction at the WE by

$$\Delta_R G|_{WE} = \mu_{Fc} - \tilde{\mu}_{Fc^+} - \tilde{\mu}_{e^-}. \quad [5]$$

Here, μ denotes the chemical potential of an uncharged component and $\tilde{\mu}$ the electrochemical potential of an ionic species. The reaction Gibbs energy of the RE is zero, since the reference electrode is always in an equilibrium state due to negligible current flow across its interface. As a result, the cell potential U expressed in terms of the electrochemical potentials of the electrons e^- in WE and RE

$$FU = F(\Phi_{WE} - \Phi_{RE}) = \tilde{\mu}_{e^-}|_{RE} - \tilde{\mu}_{e^-}|_{WE} \quad [6]$$

can be written as

$$FU = (\mu_{Li} - \tilde{\mu}_{Li^+})|_{RE} - (\mu_{Fc} - \tilde{\mu}_{Fc^+} - \Delta_R G)|_{WE}, \quad [7]$$

where the cell potential is determined by the reactions at the interfaces of WE and RE. The electrochemical potential of an arbitrary ionic species k for any electrolyte can be defined, according to Newman and Thomas-Aleya, as

$$\tilde{\mu}_k = z_k \mathrm{F}\Phi + \mathrm{R}T \ln c_k + \mathrm{R}T \left(\ln f_k - z_k z_n^{-1} \ln f_n\right) + \mathrm{R}T(\ln a_k^{\ominus} - z_k z_n^{-1} \ln a_n^{\ominus}), \quad [8]$$

where the electrostatic potential Φ in the electrolyte solution is defined with respect to an arbitrary negative ionic species n present in the electrolyte solution.[1] The anion of the supporting electrolyte is chosen as the reference species n, since it does not take part in any faradaic reaction at the electrodes in lithium ion batteries. Furthermore, the charge number of the ionic species k is denoted by z_k, the activity coefficient of the ionic species k by f_k, the Faraday constant by F, the gas constant by R, the temperature by T, and the proportionality constant for the secondary reference state of the ionic species k by $a_k^{\ominus}$. In addition, the following definition for the electrochemical potential of the reference species n is used according to Newman and Thomas-Aleya[1]

$$\tilde{\mu}_n = z_n \mathrm{F}\Phi + \mathrm{R}T \ln c_n. \quad [9]$$

In this framework, the activity coefficient and the proportionality constant of the reference species is included in the electrochemical potential of the ionic species k, as can be seen in Eq. 8, and thus does not occur in Eq. 9. In the following, the perchlorate ion ClO_4^- is chosen as reference species n. As a result, combining Eq. 1 and 8, the electrochemical potentials of lithium and ferrocenium ions can be written as

$$\tilde{\mu}_{Li^+} = z_{Li^+}\mathrm{F}\Phi + \mathrm{R}T \ln c_{Li^+} + \mathrm{R}T \ln f^2_{LiClO_4} + \mu^{\ominus}_{LiClO_4}, \quad [10]$$

$$\tilde{\mu}_{Fc^+} = z_{Fc^+}\mathrm{F}\Phi + \mathrm{R}T \ln c_{Fc^+} + \mathrm{R}T \ln f^2_{FcClO_4} + \mu^{\ominus}_{FcClO_4}. \quad [11]$$

The standard chemical potentials of lithium perchlorate

$$\mu^{\ominus}_{LiClO_4} = \mathrm{R}T \ln \left(a_{Li^+} a_{ClO_4^-}\right) \quad [12]$$

and ferrocene perchlorate $\mu^{\ominus}_{FcClO_4}$

$$\mu^{\ominus}_{FcClO_4} = \mathrm{R}T \ln \left(a_{Fc^+} a_{ClO_4^-}\right) \quad [13]$$

defined according to Newman and Thomas-Alyea, are independent of the electrolyte composition but are a function of additional state variables such as temperature and pressure. The mean binary activity coefficients of lithium perchlorate and ferrocene perchlorate are given by $f^2_{LiClO_4}$ and $f^2_{FcClO_4}$ as defined in Eq. 1. Therefore, using Eq. 10 and 11, Eq. 7 can be expressed as,

$$\mathrm{F}U = \mathrm{R}T \ln \left(c_{Fc^+} f^2_{FcClO_4}\right)|_{WE} + \Delta_R G|_{WE} - \mu_{Fc}|_{WE} - \mathrm{R}T \ln \left(c_{Li^+} f^2_{LiClO_4}\right)|_{RE} + \mathrm{F}(\Phi|_{WE} - \Phi|_{RE}) + \mu_{Cell}. \quad [14]$$

Here, the standard chemical cell potential μ_{Cell} includes the chemical potential of lithium μ_{Li} as well as the standard chemical potentials of lithium perchlorate $\mu^{\ominus}_{LiClO_4}$ and ferrocenium perchlorate $\mu^{\ominus}_{FcClO_4}$

$$\mu_{Cell} = (\mu_{Li}|_{RE} - \mu^{\ominus}_{LiClO_4}|_{RE} + \mu^{\ominus}_{FcClO_4}|_{WE}). \quad [15]$$

The potential drop in the electrolyte is described by the term $\Phi|_{WE} - \Phi|_{RE}$. From Eq. 14, the cell potential U can also be written as

$$U = U_{Ref} - \mathrm{R}T/\mathrm{F} \ln(c_{Li^+} f^2_{LiClO_4}), \quad [16]$$

where the reference potential U_{Ref} includes all remaining terms which are independent of the $LiClO_4$ concentration.

$$U_{Ref} = [\mathrm{R}T/\mathrm{F} \ln(c_{Fc^+}/c_{Fc}) + \Delta_R G + \mathrm{R}T/\mathrm{F} \ln(f^2_{FcClO_4}) - \mathrm{R}T/\mathrm{F} \ln(f_{Fc})]|_{WE} + \mu_{Cell} + \Delta\Phi. \quad [17]$$

If the ferrocene concentration is kept constant for different $LiClO_4$ concentrations, U_{Ref} can be shown to be constant as will be discussed in detail in section Reference potential.

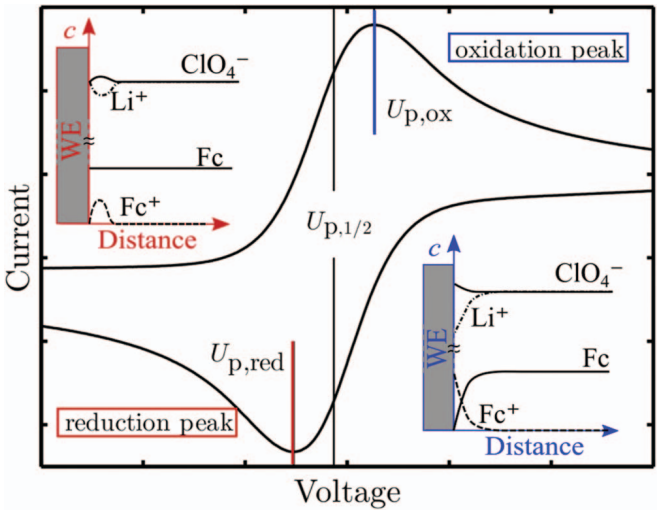

Figure 2. Concentration profiles in the vicinity of the Working Electrode (WE) for the components dissolved in the electrolyte solution at the oxidation peak (blue) and the reduction peak (red) of a cyclic voltammogram.

In summary, the relation given in Eq. 16 is the basis for the determination of the mean molar activity coefficient by cyclic voltammetry experiments which requires a constant ferrocene concentration throughout a measurement series while the $LiClO_4$ concentration is varied. As the obtained cell potential U is given by a constant U_{Ref} and an expression containing the activity coefficient of $LiClO_4$, the latter quantity can be determined mathematically.

Potential of oxidation and reduction peaks.—In the following, possible influences on the peak positions of a cyclic voltammogram are analyzed. While in the *Results and Discussion* part half wave potential $U_{p,1/2}$ versus the lithium reference electrode are used as reference point (U in Eq. 16), in this section we evaluate to which extent oxidation and reduction peak potentials may be affected by, e.g., the scan range. In general, the positions of oxidation and reduction peaks are defined by the ratio of ferrocenium to ferrocene at the WE. Idealized concentration profiles at both peaks are shown in Figure 2. At the oxidation peak, ferrocene is depleted at the WE while at the reduction peak the ferrocenium ion concentration approaches zero at the WE. In addition, this ratio is also the basic boundary condition for the boundary value problem as described, e.g., in Bard and Faulkner.[14] This becomes clearer, if Eq. 16 and Eq. 17 are reformulated to

$$c_{Fc^+}/c_{Fc} = \exp\left\{\mathrm{F}/\mathrm{R}T \left[(U - \Delta\Phi) - U_0'\right]\right\}. \quad [18]$$

with the formal potential U_0' of the WE with respect to the RE

$$U_0' \equiv \mu_{Cell} - \mathrm{R}T/\mathrm{F} \ln \left(f^2_{FcClO_4}/f_{Fc}\right) - \mathrm{R}T/\mathrm{F} \ln \left(c_{Li^+} f^2_{LiClO_4}\right). \quad [19]$$

Here, in a first approximation, it is assumed that the electrochemical reaction at the WE is always in an equilibrium state (i.e., following Nernstian behavior). In a cyclic voltammetry experiment with a RE, the potential between WE and RE is reduced by the potential drop $\Delta\Phi$ within the electrolyte solution. The cell potential U is time dependent and can be expressed as $U = U_{init} - st$, where s denotes the constant scan rate, U_{init} the initial cell potential and t the time. Based on this boundary condition, the following theoretical relations can be derived for the oxidation peak only in the first cycle.[14] The theoretical peak position $U_{p,ox}$ for the first cycle is given by

$$U_p = U_0' + \mathrm{R}T/\mathrm{F} \ln (D_{Fc}/D_{Fc^+})^{1/2} - 1.109\mathrm{R}T/\mathrm{F} \quad [20]$$

and the peak current by

$$I_{p,ox} = 2.69 \cdot 10^5 \mathrm{A} (D_{Fc})^{1/2} c^0_{Fc}\, s^{1/2}. \quad [21]$$

for a perfectly reversible Nernstian couple. The diffusion coefficient of ferrocene is denoted by D_{Fc} and the diffusion coefficient of the

Table I. Peak separation for Nernstian system with variable positive vertex potentials $U_{reverse}$.

$\lvert U_{p,ox} - U_{reverse}\rvert$ [mV]	171,5	271,5	∞
$U_{p,ox} - U_{p,red}$ [mV]	58,3	57,8	57,0

ferrocenium ion by D_{Fc^+}. The ferrocene concentration in the bulk of the electrolyte solution is indicated by c^0_{Fc}. Since ferrocenium ions are the minor species in the supporting electrolyte solution, they can be approximated by the pure diffusion problem with the ionic diffusion coefficient D_{Fc^+}.[1] The connection of the mean molar activity coefficient with the oxidation peak position for a single forward scan becomes clear in Eq. 16. If the measured potential U in Eq. 16 is only a function of the term $\ln(c_{Li^+} f^2_{LiClO_4})$ and if all other terms are constant, it is possible to determine the mean activity coefficient from the peak potential.

For a cyclic voltammogram of a reversible (i.e., Nernstian) redox couple, it is possible to derive a theoretical value for the peak separation defined by the potential difference between the peak potentials for oxidation $U_{p,ox}$ and reduction $U_{p,red}$. In general, the theoretical peak separation depends on the potential difference between the peak potentials $U_{p,i}$ and the vertex potentials at which the scan rate is reversed $U_{reverse,i}$. The theoretical values for a reversible Nernstian couple are shown in Table I.[14]

Concluding from Table I, a peak separation of 57 mV within 1 mV would be expected for reversible Nernstian couples if the difference between vertex and the peak potential is >300 mV. This theoretical value for the peak separation can be used to evaluate the quality of experimental data.

Reference potential.—To be able to use cyclic voltammetry in combination with the shown experimental setup for the determination of mean molar activity coefficients $f_{LiClO_4}(c)$, it is necessary that the reference potential U_{Ref} is independent of the supporting electrolyte salt concentration c. Therefore, it is important to get a detailed understanding of the characteristics of individual terms contributing to the reference potential U_{Ref} in Eq. 17. As discussed before, the logarithmic ratio of ferrrocenium to ferrocene at the WE, the first of the terms in Eq. 17, defines the theoretical positions of oxidation and reduction peaks and they are independent of the supporting electrolyte concentration.

Next, the $\Delta_R G$ term will be examined. For the derivation of the theoretical peak positions and the peak separation, it is assumed that the system is only limited by mass transport, i.e., infinitively fast kinetics are assumed. However, in reality, kinetic effects have to be considered, as they also influence the peak separation and, therefore, the peak positions. If the reaction Gibbs energy $\Delta_R G$ is not negligibly small, it can be approximated by the kinetic overpotential η, which describes the deviation from the equilibrium potential at the specific condition.[1] In this case, the peak separation is linked to the parameter Ψ defined and tabulated in Bard and Faulkner:[14]

$$\Psi = \frac{(D_{Fc^+}/D_{Fc})^{\alpha/2} k_0}{(\pi D_{Fc^+} \mathrm{F}/\mathrm{R}T\, s)^{1/2}}. \quad [22]$$

Here, α denotes the transfer coefficient in the Butler-Volmer equation and k_0 the standard rate constant of the electrochemical reaction. According to Eq. 22, the peak separation depends on the diffusion coefficient ratio and the standard rate constant, whereby both quantities may be a function of the supporting electrolyte concentration. A decrease of the value of the parameter Ψ due to slow kinetics, results in an increase in the peak separation, which is distributed symmetrically between oxidation and reduction peaks as shown, e.g., by Table 6.5.2 in Bard and Faulkner.[14] To decrease the influence of the non-Nernstian redox couple response (i.e., of finite kinetics), the half-wave potential $U_{p,1/2} = 1/2(U_{p,ox} + U_{p,red})$ can be used as a reference point instead of the oxidation or reduction peak positions (see Figure 2). For the half-wave potential, the symmetric potential shifts of oxidation and reduction peaks cancel out.

The next term in Eq. 17 is the mean molar activity coefficient of ferrocenium perchlorate $\ln(f_{FcClO_4})|_{WE}$, which is assumed to be constant in this work. This assumption is based on the original publication by Gritzner and Kuta.[15] In their publication, the authors argue that the activity of the ferrocene – ferrocenium species is independent of the surrounding solution. An even stronger argument for the constancy of the term $\ln(f_{FcClO_4})|_{WE}$ is its influence on oxidation and reduction peak positions. As ferrocenium ions only exist at the oxidation peak a possible contribution by the $\ln(f_{FcClO_4})|_{WE}$ term can only occur for this peak. Thus, when the $LiClO_4$ concentration is varied between experiments, a varying contribution to the oxidation peaks should be observable compared to the reduction peak. Experimental results shown later will prove that oxidation and reduction peaks behave in a completely identical manner. As the activity coefficient of the uncharged ferrocene is one, the fourth term in Eq. 17 can be assumed constant as well. The fifth term on the right-hand-side of Eq. 17, the chemical potential of the cell, μ_{Cell}, as defined in Eq. 15, depends on the used electrode materials and the electrolyte solution, which is generally constant for isothermal and isobaric conditions.

So far, all discussed terms deal with the electrolyte composition in the vicinity of the electrodes. In contrast to those, the last term in Eq. 17, the potential drop $\Delta\Phi$ describes the potential difference in the electrolyte between working and reference electrode. The potential field in such an electrolyte solution is described by

$$\nabla\Phi = \mathrm{R}T/\mathrm{F}\nabla \ln c_{ClO_4^-} - \boldsymbol{i}/\kappa - \mathrm{R}T/\mathrm{F}\xi, \quad [23]$$

with

$$\xi = t_{Li^+}\nabla \ln\left(c_{Li^+} c_{ClO_4^-} f^2_{LiClO_4}\right) + t_{Fc^+}\nabla \ln\left(c_{Fc^+} c_{ClO_4^-} f^2_{FcClO_4}\right), \quad [24]$$

which describes the current transport in concentrated electrolyte solutions derived from the Stefan-Maxwell approach

$$\mathrm{F}\boldsymbol{i}/\kappa = -\left(\sum_{k=1}^{n} t_k/z_k \nabla\tilde{\mu}_k\right) \quad [25]$$

using Eqs. 9–11.[1] Here, the current density is denoted by $\boldsymbol{i}$, the conductivity of the electrolyte solution by κ, and the transference numbers of lithium and ferrocenium ions by t_{Li^+} and t_{Fc^+}, respectively. A similar system is also discussed for example in Newman and Thomas-Alyea.[1] Using a one-dimensional approximation of the given setup and performing an integration along a path between RE and WE, it is possible to get an approximation for the potential drop between RE and WE

$$\Delta\Phi = \mathrm{R}T/\mathrm{F}\ln\left(c_{ClO_4^-}|_{WE}/c_{ClO_4^-}|_{RE}\right) - R_\Omega \boldsymbol{i} A - \mathrm{R}T/\mathrm{F}\int_{RE}^{WE}\xi \mathrm{d}x. \quad [26]$$

The ohmic resistance of the electrolyte solution is denoted by R_Ω and the current by $\boldsymbol{i}A$. In this formulation, the third term on the right-hand-side of Eq. 26 is not integrated, yet. The first term on the right hand side is zero since the perchlorate ion concentration is approximately constant in the entire electrolyte solution for oxidation as well as reduction peaks as indicated in Figure 2. The second term $R_\Omega \boldsymbol{i} A$ describes the potential drop within the electrolyte solution as a result of the current. Although the current between WE and RE is negligibly small, an ohmic potential is included in the cell potential U as a result of the current flowing between WE and CE. The so-called effect of uncompensated resistance between RE and WE thus also leads to an increased peak separation.[14] This effect is particularly pronounced for small supporting electrolyte concentrations since the resistance of the electrolyte solution is very large in this case. The increase in peak separation is not completely symmetric, since the peak currents at oxidation and reduction peak are usually not equal in a cyclic voltammogram. In order to reduce the effect of uncompensated resistance, the current between WE and CE electrode has to be minimized. Experimental parameters influencing the current are the scan rate and

the ferrocene concentration, as indicated in Eq. 21, so that low scan rates and/or ferrocene concentrations are desired. Furthermore, the potential drop $\Delta\Phi$ in the electrolyte is also influenced by the third term in Eq. 26, which describes the concentration overpotential resulting from concentration gradients within the electrolyte. In general, concentration gradients have to be considered only in the vicinity of the WE. The RE compartment is separated from the WE, thereby guaranteeing uniform lithium and perchlorate ion concentration profiles. Additionally, the polarization times are short enough (on the order of 10^2 s for the scan rates and potential windows used in our study), so that concentration gradients developing at the WE do not penetrate far into the bulk region of the electrolyte solution. As a result of small concentration variations within the electrolyte, it is valid to assume constant transference numbers for the integration of ξ in Eq. 26

$$\mathrm{R}T/\mathrm{F}\int_{\mathrm{RE}}^{\mathrm{WE}}\xi\mathrm{d}x = \mathrm{R}T/\mathrm{F}\Big[t_{\mathrm{Li}^+}\ln\left\{\left(c_{\mathrm{Li}^+}f_{\mathrm{LiClO_4}}^2\right)_{\mathrm{WE}}\left(c_{\mathrm{Li}^+}f_{\mathrm{LiClO_4}}^2\right)_{\mathrm{RE}}^{-1}\right\} + t_{\mathrm{Fc}^+}\ln\left\{\left(c_{\mathrm{Fc}^+}f_{\mathrm{FcClO_4}}^2\right)_{\mathrm{WE}}\left(c_{\mathrm{Fc}^+}f_{\mathrm{LiClO_4}}^2\right)_{\mathrm{RE}}^{-1}\right\}\Big] \quad [27]$$

whereby contributions of the perchlorate ions in the integral cancel out due to its uniform concentration profile (i.e., small changes in concentration compared to its overall concentration). The last term depending on the transference number of the ferrocenium ion in Eq. 27 can also be neglected, since the transference number of the minor species in a supporting electrolyte solution is approximately zero for a high ratio of supporting electrolyte to minor component. Such a high ratio also has a positive effect on the first term of the Eq. 27 since the concentration difference of lithium ions between WE and RE is also minimized. Concluding, a minimal ratio of ferrocenium ions, respective ferrocene, to supporting electrolyte is also advantageous to avoid concentration overpotentials. This is of course most critical for small concentrations of supporting electrolyte. It is emphasized that the concentration overpotential does not influence both peaks symmetrically. At the oxidation peak, the concentration difference for lithium as well as ferrocenium ions are the highest, resulting in a maximum concentration overpotential. On the contrary, the concentration differences of supporting electrolyte ions between RE and WE are negligibly small at the reduction peak. As a result, concentration overpotentials influence oxidation but not reduction peaks. As for all non-symmetric terms, this has to be considered if the half-wave potential is used for the determination of the mean activity coefficient, particularly for small supporting electrolyte concentrations.

Theoretical behavior of the mean molar activity coefficient of binary salts.—If all above mentioned theoretical assumptions are valid and if the experimental conditions are such that all of the above approximations are met, the reference potential U_{Ref} in Eq. 16 can be considered sufficiently independent of the lithium salt concentration, so that the logarithmic activity coefficient can be obtained from the variation of the cell potential U vs. the lithium salt concentration by means of Eq. 16. A well-known theoretical derivation for the logarithmic activity coefficient $f_{\mathrm{LiClO_4}}$ is the so-called Debye-Hückel law.[14,16] Thus, in the following paragraphs, different formulations as well as extensions of the Debye-Hückel law are compared. The listed approximations for the respective concentration regions provide a theoretical framework for a comparison with the measurements and thereby offers a means to validate the experimental results. According to the Debye-Hückel law, the theoretical behavior of the mean molar activity coefficient $f_{\mathrm{LiClO_4}}$ can be described by

$$\ln f_{\mathrm{LiClO_4}} = -\left|z_{\mathrm{Li}^+}z_{\mathrm{ClO_4^-}}\right| A\sqrt{I}\left(1+B\dot{a}\sqrt{I}\right)^{-1}, \quad [28]$$

where A, B, and $\dot{a}$ are defined below, and where I is the ionic strength of the electrolyte defined as

$$I = \frac{1}{2}\sum_{k=1}^{m} z_k^2 c_k \quad [29]$$

with $m = 3$ dissolved ionic species in our case (Li^+, ClO_4^-, and Fc^+). The parameters A and B are defined as

$$B = \left(2e^2\mathrm{N_A}\right)^{1/2}(\varepsilon_0\varepsilon_{\mathrm{R}}kT)^{-1/2} = \varepsilon_{\mathrm{R}}^{-1/2}\cdot 2.914\cdot 10^9\,\mathrm{dm}^{\frac{1}{2}}\,\mathrm{mol}^{-\frac{1}{2}}, \quad [30]$$

$$A = e^2(8\pi\varepsilon_0\varepsilon_{\mathrm{R}}kT)^{-1}B = \varepsilon_{\mathrm{R}}^{-3/2}\cdot 817.1\,\mathrm{L}^{\frac{1}{2}}\,\mathrm{mol}^{-\frac{1}{2}}. \quad [31]$$

In Eqs. 28–31, the minimal distance between two ionic species is denoted by $\dot{a}$, the relative permittivity by ε_{R}, the permittivity of vacuum by $\varepsilon_0 = 8.854\cdot 10^{-12}\,\mathrm{F,m^{-1}}$, the electronic charge by $e = 1.602\cdot 10^{-19}\,\mathrm{C}$, the Avogadro constant by $\mathrm{N_A} = 6.022\cdot 10^{23}\,\mathrm{mol^{-1}}$, and the gas constant by $\mathrm{R} = 8.314\,\mathrm{J\,mol^{-1}K^{-1}}$. Eq. 28 can also be approximated by the Debye-Hückel limiting law[17]

$$\ln f_{\mathrm{LiClO_4}} = -\left|z_{\mathrm{Li}^+}z_{\mathrm{ClO_4^-}}\right| A\sqrt{I} \quad [32]$$

applicable for low ionic strengths which will be discussed in detail in the Results and discussion section. For electrolyte solutions with higher ionic strengths, the Debye-Hückel law (Eq. 28) is often extended by a linear term[17]

$$\ln f_{\mathrm{LiClO_4}} = -\left|z_{\mathrm{Li}^+}z_{\mathrm{ClO_4^-}}\right| A\sqrt{I}\left(1+B\dot{a}\sqrt{I}\right)^{-1} + x_1 I. \quad [33]$$

This is an empirical extension accounting for effects like short range interactions between ions and the solvent, dispersion forces between ions, or ion association. A detailed discussion of this topic can be found, e.g., in Wright.[17] An n^{th} -order polynomial with respect to the concentration instead of ionic strength is frequently used by Newman and Thomas-Alyea to account for effects which are not included in the Debye-Hückel theory[1]

$$\ln f_{\mathrm{LiClO_4}} = -\left|z_{\mathrm{Li}^+}z_{\mathrm{ClO_4^-}}\right| A\sqrt{I}\left(1+B\dot{a}\sqrt{I}\right)^{-1} + y_1 c + y_2 c^{3/2} + y_3 c^2 + \ldots. \quad [34]$$

In this work, the extended form of the Debye-Hückel law given by Eq. 33 is used. Fits with higher order terms according to Eq. 34 were found to over-interpret experimental results.

Results and Discussion

Selection of experimental procedure.—As the parameters of the CV measurements influence the validity of theoretical assumptions and simplifications, it is necessary to identify a proper set of measurement conditions to fulfil the requirements described in the theoretical part of this work, mostly the small ferrocene concentration in comparison with the $LiClO_4$ salt. Figure 3 shows the steady-state CVs ($\geq 2^{\mathrm{nd}}$ scan) with 0.05 and 0.10 mM concentrations of ferrocene in 2 mM $LiClO_4$ at scan rates of 10 and 20 mV/s. All curves show reversible oxidation and reductions peaks of the ferrocene/ferrocenium couple at ~3.51 and ~3.43 V, respectively. Following the arguments in the *Theory* section, the smaller ferrocene concentration of 0.05 mM was used for the following experiments in order to satisfy the requirement of a small c_{Fc} to $c_{\mathrm{LiClO_4}}$ ratio, thereby avoiding parasitic effects such as diffusion overpotentials. Additionally, small ferrocene concentrations result in small currents and thus small ohmic drops in the electrolyte phase; they also allow that the ionic strength can be described sufficiently accurately by the concentration of the lithium salt only. Extraction of oxidation and reduction peak potentials was done by calculation of maxima and minima of fifth order polynomials which were fitted through data points in a range of ± 50 mV around the peaks. Due to the sensitivity of this procedure on the peak sharpness, the larger scan rates of 20 mV/s, showing higher oxidation and reduction currents, are used subsequently. For the same reason, the ferrocene concentration is not reduced below 0.05 mM. All following experiments have been conducted using the just determined set of measurement conditions, viz., a scan rate of 20 mV/s and a ferrocene concentration of 0.05 mM.

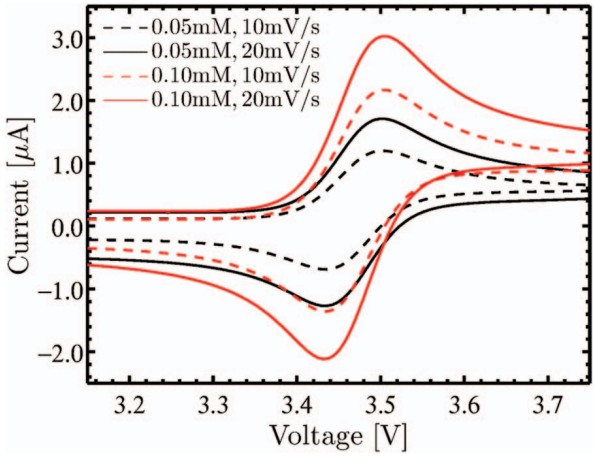

Figure 3. Steady-state CVs at two different scan rates (10 mV/s, dashed line and 20 mV/s, solid line) for two different ferrocene concentrations ($c_{Fc} = 0.05$ mM, black and $c_{FC} = 0.10$ mM, red) in 2 mM $LiClO_4$ in EC:DEC (1:1, w:w) with positive and negative potential limits of 2.5 and 4 V (85% online IR correction were used).

Ohmic drop compensation and correction.—In this Section, the goal is to find a method to best correct the CVs for IR losses, which is required for the later detailed analysis. Figure 4 shows an example for the influence of different types of IR correction on the peak positions. Without IR correction, oxidation and reduction peak potentials in a 1 mM $LiClO_4$ electrolyte with 0.05 mM ferrocene are 3.550 and 3.428 V respectively. Ferrocene oxidation and reduction peak potentials of 3.531 V and 3.443 V are obtained if the raw data are IR corrected after the measurement according to

$$U_{i,\text{corr}} = U_{i,\text{meas}} - I_{i,\text{meas}} \cdot R_{\text{RE-WE}}. \quad [35]$$

whereby $R_{\text{RE-WE}}$ was obtained by impedance measurements prior to the CV scans. In the following, this method is called *post IR correction*, according to its execution after the measurement. As oxidation and reduction currents are different (2.8 μA and 2.3 μA respectively), the post IR correction has different impacts on oxidation and reduction peak potentials, resulting in a non-symmetric behavior which can be observed in Figure 4.

For electrolyte solutions with RE-WE resistances in the kΩ range, the effective potential in the cyclic voltammogram is not truly linear with time anymore. This behavior can be circumvented by online IR correction, i.e., during the CV scans, using a certain percentage of the uncompensated resistance as explained by Bard and Faulkner.[14] Essentially, the scan rate is adjusted continuously during the scan, resulting in a linear effective potential vs. time behavior, although the applied potential is non-linear.[18] As oscillations occur for online IR corrections close to 100% of the total uncompensated resistance, $R_{\text{RE-WE}}$, caused by the measurement hardware, it was only possible to correct for 85% of the ohmic drop. As a result, a combined IR correction, consisting of an online IR correction and a subsequent post IR correction is introduced in the following and will be referred to as *85/15 combined IR correction*, where 85 denotes the percentage of online IR corrected resistance and 15 the percentage of post IR corrected resistance. Figure 4 shows the effect exemplarily for a 75/25 combined IR correction, giving a peak potential of 3.526 V for oxidation and 3.447 V for reduction peak potentials, respectively. Although both cases, 100% post IR correction and a 75/25 combined IR correction, theoretically account for the same total ohmic drop, a difference in peak positions of ∼5 mV is observed between both methods. This shows the importance of online over post IR correction and raises the question of remaining uncertainties for the combined IR correction.

As a full online IR correction, i.e., 100/0 combined IR correction, cannot be realized, CVs with four different percentages of online IR correction were measured in a 0.1 mM $LiPF_6$ electrolyte (Figure 5)

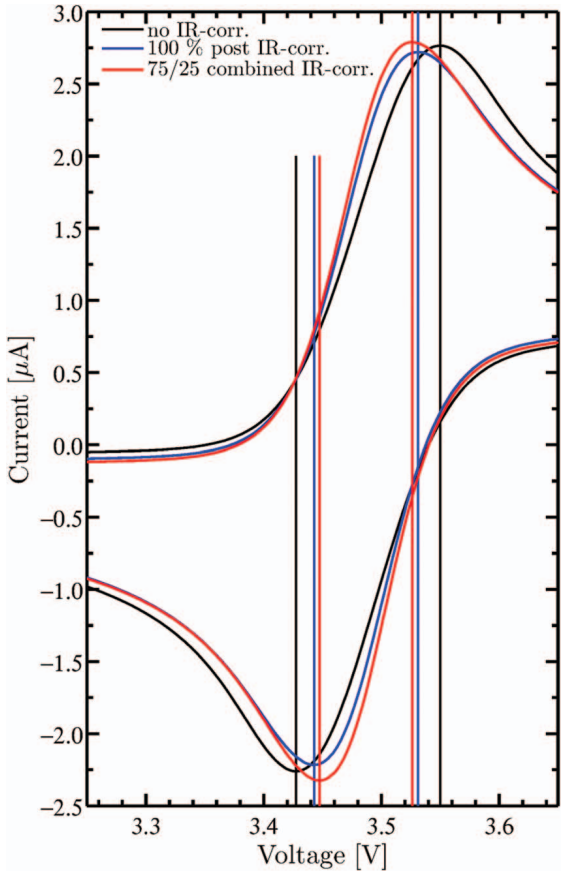

Figure 4. CVs showing the influence of IR correction on oxidation and reduction peak positions with 0.1 mM ferrocene at 20 mV/s in 1 mM $LiClO_4$ in EC:DEC (1:1, w:w) with positive and negative potential limits of 2.5 and 4 V: no IR correction (black), 100% post IR correction (blue), and 75/25 combined online/post IR correction (red). The value of $R_{\text{RE-WE}}$ determined by AC impedance was 6.9 kΩ.

to validate the following analysis procedure. This small concentration with the highest solution resistance is chosen to best illustrate the effect. Cross and plus symbols in Figure 5 correspond to oxidation and reduction peak potentials which are only online IR corrected. Subsequent post IR correction of these potentials by the remaining resistance, referred to as combined IR correction, results in oxidation and reduction potentials indicated by circles and triangles, respectively. The peak potentials resulting from a pure online IR correction and the combined IR corrections are extrapolated in Figure 5 to the theoretical 100% online IR correction based on the peak potential values for 25%, 45%, 65% and 85% online correction. The data are well represented by linear extrapolation lines as shown in Figure 5, with an interception point close to 100% online IR correction. For the extreme example shown in Figure 5, the peak potentials obtained from a 85/15 combined IR correction still show a small deviation of ∼3.5 mV from the extrapolated 100% online IR corrected value. Therefore, for all the following measurements, at least two different ratios of combined IR correction were used to determine peak potentials by extrapolating to 100% online IR correction; this methodology will be referred to as *100% extrapolated IR correction*. It should be noted, however, that for concentrations above 5 mM, the latter correction leads to negligibly small differences compared the value obtained from a 85/15 combined IR correction (<1 mV).

Data selection.—A quality measure for the obtained oxidation and reduction potentials is the peak separation. For reversible processes with fast electrode kinetics (Nernstian behavior), the theoretical peak

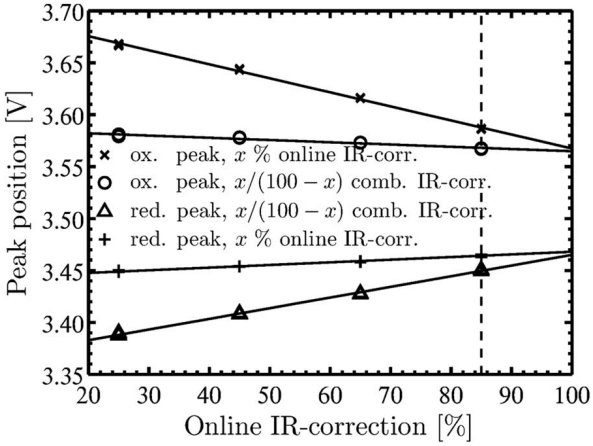

Figure 5. Oxidation/reduction peak potentials versus different applied percentages of online IR corrections without remaining post IR correction (cross/plus symbols) and with additional post IR correction (circle/triangle symbols) corresponding to the combined IR correction method. Conditions: 0.1 mM $LiPF_6$ in EC:DMC (1:1, w:w) with 0.05 mM ferrocene at 20 mV/s with positive and negative potential limits of 2.5 and 4 V ($R_{RE\text{-}WE} = 72$ kΩ).

separation as given by Table I should be 57–58 mV, as the difference between peak and the vertex potentials are larger than 300 mV.

For all measured $LiClO_4$ concentrations, the potential differences between oxidation and reduction peaks are plotted in Figure 6. To show reproducibility, the peak separation data are shown for three independent measurement series. In the measurement series three (red symbols), extrapolated values exist only for concentrations between 0.5 and 20 mM and above 20 mM only combined IR corrections are shown. Figure 6 depicts constant and identical peak separations for each series at concentrations above 5 mM, independent of the IR compensation method. For concentrations below 5 mM $LiClO_4$, the peak potential increases to 90–100 mV for the extrapolated IR correction values at the lowest concentration of 0.1 mM $LiClO_4$. From the constant peak separation of all measurement series for concentrations above 5 mM it is concluded, that all non-ideal effects discussed in the Theory section which influence the peak potentials are negligible. The first measurement series (green symbols) shows a shift of all measured peak separations by ∼5 mV compared to measurement two and three. This was identified as an experimental artefact caused by not flame annealing of the Au working electrode, thereby not removing thin oxide layers on the working electrode. The latter reduces the rate constant k_0 of the outer electron transfer[19] of the ferrocene/ferrocenium couple, which depends on the electron tunneling length, i.e., the thickness of

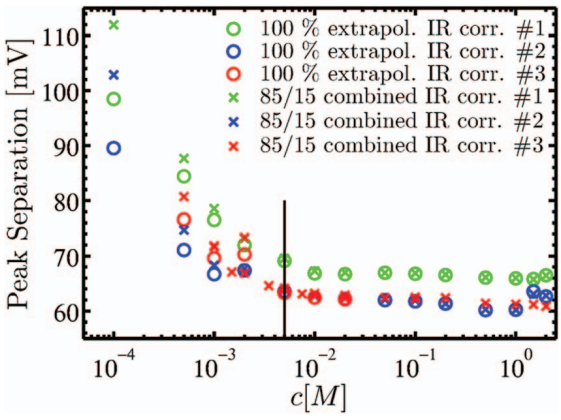

Figure 6. Peak separation of three measurement series with extrapolated values of series two and three, according to method depicted in Figure 5. The solid line indicates a concentration of 5 mM. Conditions: $LiClO_4$ of specified concentration in EC:DEC (1:1, w:w) with 0.05 mM ferrocene at 20 mV/s with positive and negative potential limits of 2.5 and 4 V.

the oxide layer on the gold surface. A smaller rate constant k_0 results in an increased peak separation according to Eq. 22. Nevertheless, even for the experiments conducted with properly annealed Au working electrodes (red and blue symbols in Figure 5), a deviation of ∼5 mV from the expected peak separation (57–58 mV according to Table I) remains even at $LiClO_4$ concentrations of ≥5 mM, which we believe is due to a limited rate constant k_0, leading to a deviation from the ideal Nernstian behavior. For example, according to Bard and Faulkner,[14] the here observed peak separation of ∼63 mV would be expected for $\Psi = 7$ (see Eq. 22). Based on the measurements by Scholl and Sochaj on the ferrocene/ferrocenium couple on a gold electrode in acetonitrile ($D_R = 2.43 \cdot 10^{-5}$ cm²/s, $D_O = 2.31 \cdot 10^{-5}$ cm²/s, $k_0 = 0.088$ cm/s), Eq. 22 would yield a value of $\Psi = 11.6$, which indeed is reasonably consistent with the peak separation of ∼63 mV at ≥5 mM $LiClO_4$ shown in Figure 5.[20]

For $LiClO_4$ concentrations below 5 mM (at a ferrocene concentration of 0.05 mM), the observed increase in peak separation may be due to several effects and is currently not understood. The kinetic rate constant k_0 and the ratio of diffusion coefficients of ferrocene and ferrocenium depend on the concentration of $LiClO_4$ as explained in the theoretical part of this work. Thus, the ratio between ferrocenium and ferrocene diffusion coefficients which affects the peak separation (see Eq. 22), was shown to depend on the supporting electrolyte concentration by Wang et al.[21] and Ruff et al.[22] However, a quantitative estimation is not possible, as no literature values exist for our electrolyte. Similarly, the dependence of the reaction rate constant k_0 was shown to depend on the concentration of the supporting electrolyte by Peter et al. for the ferro/ferri-cyanide couple.[23] In the same publication, the effect of ion pairing is also mentioned as an explanation for the non-ideal behavior of a cyclic voltammogram. A similar concept is discussed in Redepenning et al.[24]

In addition, the ratio of ferrocene to supporting electrolyte may introduce a diffusion overpotential, which would affect oxidation and reduction peak potentials asymmetrically (compare Eq. 27). The concentration overpotential estimated by Eq. 27, however, only partly explains the increase in peak separation. For example, a decrease in peak separation of ∼2 mV is expected for a 1 mM $LiClO_4$ concentration, if the concentration overpotential is subtracted from the oxidation peak potential. This low value is a result of the chosen experimental setup with a minimal ferrocene to $LiClO_4$ concentration ratio (1/20 at 1 mM $LiClO_4$). An obvious trend is only visible for the smallest $LiClO_4$ concentration of 0.1 mM $LiClO_4$, where the half peak potential is clearly shifted towards the oxidation peak as a result of the non-symmetric behavior of the concentration overpotential as explained in the Theory section.

We believe that the most likely explanation for the increase in peak separation is a supporting electrolyte concentration dependence of the rate constant k_0. Nonetheless, for concentrations below 5 mM, a combination of all of the described effects may be the case. As a consequence of this uncertainty, we will only consider concentrations above 5 mM $LiClO_4$ for the below described evaluation of the thermodynamic factor from our data, even though data derived from smaller concentrations are still plotted for comparison.

Parameter extraction.—In Figure 7, the negative values of the measured oxidation peak, reduction peak, and half-wave potentials, U, recorded at a series of $LiClO_4$ concentrations are subtracted by $RT/F \ln(c_{Li^+})$ and are plotted versus the square root of the $LiClO_4$ concentration. Based on Eq. 16, the thus defined y-axis would correspond to:

$$y_{Axis} \equiv -U - RT/F \ln(c_{Li^+}) = -U_{Ref} + 2\,RT/F \ln\left(f_{LiClO_4}\right) \quad [36]$$

In Figure 7, the previously mentioned constant peak separation as well as its increase for concentrations below 5 mM $LiClO_4$ can be observed, i.e., the difference between oxidation peak potentials (red symbols) and reduction peak potentials (blue symbols) remains constant at ≥5 mM $LiClO_4$ and increases at <5 mM $LiClO_4$. Therefore, for $LiCLO_4$ concentrations of ≥5 mM, the data in Figure 7 can be fitted using Eq. 36 together with Eq. 34 which describes $\ln(f_{LiClO_4})$ versus

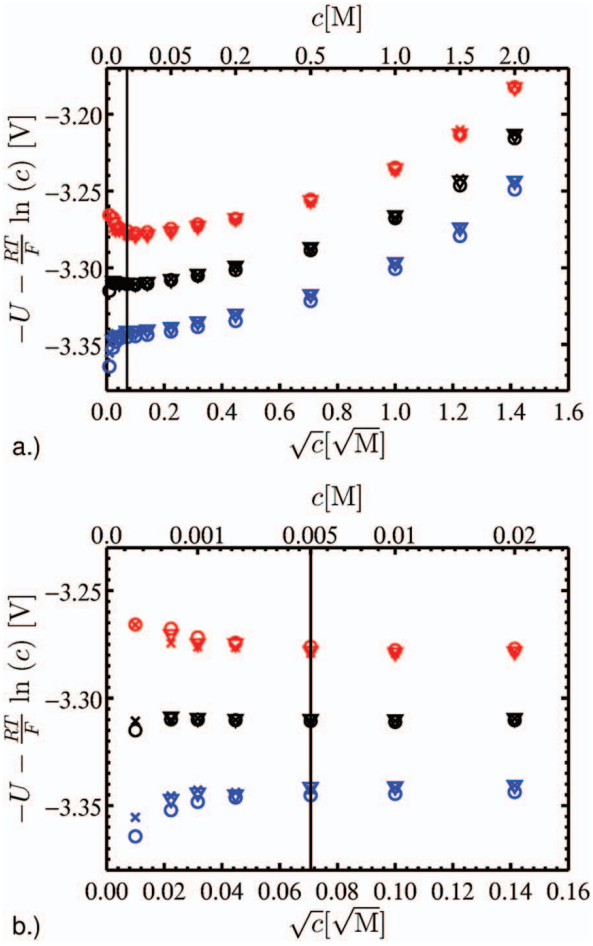

Figure 7. a. Potentials, extrapolated to 100% online IR correction, of reduction peaks (red), half wave positions (black) and oxidation peaks (blue) for three repeat measurement series (circles, crosses, and triangles) versus $LiClO_4$ concentration; b. zoom into the small concentration region; the vertical line marks the concentration of 5 mM $LiClO_4$. Conditions: $LiClO_4$ of specified concentration in EC:DEC (1:1, w:w) with 0.05 mM ferrocene at 20 mV/s with positive and negative potential limits of 2.5 and 4 V.

the $LiClO_4$ concentration, whereby either the oxidation peak, half-wave or reduction peak potentials can be used (each one would result in a different but constant reference potential, U_{Ref}).

For very low concentrations, Eq. 33 simplifies to the Debye-Hückel limiting law given by Eq. 32, which predicts a negative linear slope of the logarithmic mean molar activity coefficient over the square root of concentration. As the concentration is equivalent to the ionic strength as long as the ferrocenium concentration is much smaller than the $LiClO_4$ concentration (note that at 0.001 M $LiClO_4$, the molar ratio of Fc/$LiClO_4$ is 1/20 so that Fc^+/$LiClO_4$ must be <1/20), the slope of the tangent at concentration zero in Figure 7 should be negative and proportional to the Debye Hückel parameter A. Inspecting Figure 7b, it is clear that this expected behavior is only observed for the oxidation peak potentials, but not for the reduction peak potentials or the half-wave potentials, probably caused by the unknown peak separation at ≤5 mM $LiClO_4$ (see Figure 6), which as discussed above does not allow a meaningful analysis of the data at concentrations substantially below 5 mM $LiClO_4$. Nevertheless, this raises the question below which concentration the Debye-Hückel limiting law behavior would be expected to occur in the here used aprotic electrolytes. A way to estimate the concentration range in which the simplified Debye-Hückel behavior is expected is the comparison of the two terms in the denominator of the first term on the right-hand-side of Eq. 33: the Debye-Hückel limiting behavior is expected as long as $B\dot{a}\sqrt{I} \ll 1$. To approximate up to which concentration the limiting law and the Debye-Hückel equation give the same result, we assume a maximum deviation between both descriptions of 5%, which corresponds to $B\dot{a}\sqrt{I} = 0.05$. Parameter $\dot{a}$ in Eq. 33 corresponds to the distance of closest approach[16] and parameter B simply depends on the relative permittivity of the solvent (see Eq. 30). The relative permittivity of the electrolyte ($LiClO_4$ in EC:DEC, 1:1 w:w) was measured in a coaxial cell setup using impedance spectroscopy, yielding a value of $\varepsilon_R \approx 35 \pm 3$, which is consistent with that reported for a similar electrolyte ($LiClO_4$ in PC:DEC, 1:1 w:w) reported by Ding et al.[25] A reasonable estimate for the distance of closest approach in our aprotic solvent is $\dot{a} \sim 1$ nm.[16] It follows, that for $\dot{a} \sim 1$ nm and $\varepsilon_R \approx 35$ the approximate concentration up to which the Debye-Hückel limiting law deviates at most by 5% from the Debye-Hückel equation is ~0.1 mM $LiClO_4$, which is way below the range of our measurements. In comparison, the Debye-Hückel limiting law should be observable up to concentrations of ~2–3 mM for aqueous systems ($\varepsilon_R \approx 80$, $\dot{a} \sim 0.3$ nm).[16]

Table II. Fitting parameters and their standard deviation extracted from the fits of the measured half-wave potentials with Eq. 36 and Eq. 33, as shown in Figure 8, illustrating the influence of the chosen relative permittivities of 35 and 40.

ε_r [−]	U_{Ref} [V]	$\dot{a}$ [nm]	x_1 [−]	R^2 [−]
35	3.3079 ± 0.0042	12.8 ± 23.4	0.907 ± 0.016	0.996
40	3.3077 ± 0.0047	13.7 ± 25.6	0.907 ± 0.016	0.996

In summary, for the investigated non-aqueous aprotic electrolyte and within our experimental constraints ($c_{LiClO_4} \geq 5$ mM), it is not possible to get into the range where the Debye-Hückel limiting behavior is expected to apply. Thus, rather than verifying our experimental approach with the Debye-Hückel limiting law, as originally intended, the data points were fitted with Eq. 36, assuming the logarithmic activity coefficient according to Eq. 33 and using a calculated slope A (Eq. 31) based on the measured relative permittivity of the solvent.

Resulting fits of the reformulated half-wave potentials are depicted in Figure 8 with fixed relative permittivities ε_R of the solvent of 35 or 40. A second relative permittivity is shown to analyze the sensitivity of the fit towards the relative permittivity. Although half-wave potentials are used in all further analysis, essentially identical results can be obtained for a fit utilizing the oxidation or reduction peak potentials, as long as the $LiClO_4$ concentrations are ≥5 mM, which is the range in which the peak separation is constant and closely corresponds to its expected value. The extracted fitting parameters are the distance of closest approach $\dot{a}$, the reference potential U_{Ref}, and the slope x_1 of the linear term of the extended Debye-Hückel equation (Eq. 33), all of which are listed in Table II.

For both relative permittivity values, Table II and Figure 8 show an equally good fit, with R^2 values close to 1. Within reasonable error, the same constant reference potentials U_{Ref}, distances of closest approach $\dot{a}$, and linear slope values x_1 are determined. However, while the standard deviations for U_{Ref} and x_1 are quite small (~1.5%), this is not true for $\dot{a}$, which has standard deviations of nearly 200%, indicating the invariance of the fit with respect to $\dot{a}$. Therefore, under the given experimental constraints that data can only be considered trustworthy at $LiClO_4$ concentrations of ≥5 mM, the value of $\dot{a}$ cannot be determined from the fit of measured half wave potentials in EC:DEC based electrolyte and probably in none of the commonly used organics electrolytes. Interestingly, concentrations below 5 mM, even though they have not been used for the fit, are still reasonably well described by the fit. This implies that oxidation and reduction peak potentials are affected more or less symmetrically by the observed increase in peak separation at low $LiClO_4$ concentrations, as was discussed in detail above. It has to be added that an extension of Eq. 33 to higher orders than its linear correlation does not improve the quality of the fit significantly.

Discussion of results.—The methodology to determine the mean molar activity coefficient $f_\pm$ by fitting measured potentials of a

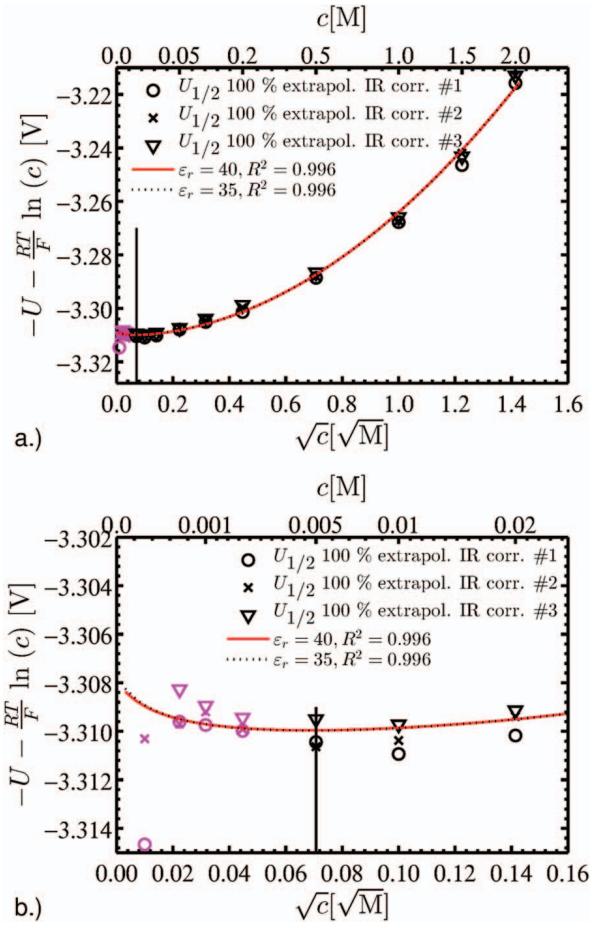

Figure 8. a. Fit of the measured half-wave potentials, U, in the concentration range from 5 mM to 2 M obtained from the 100% extrapol. IR correction (for measurement series three 85/15 combined IR correction values are used above 20 mM 85/15), with Eq. 36 and Eq. 33 to describe the activity coefficient. C; concentrations below 5 mM $LiClO_4$ (magenta symbols) are neglected for the fit. b. Zoom into the low-concentration region. Conditions: $LiClO_4$ of specified concentration in EC:DEC (1:1, w:w) with 0.05 mM ferrocene at 20 mV/s with positive and negative potential limits of 2.5 and 4 V.

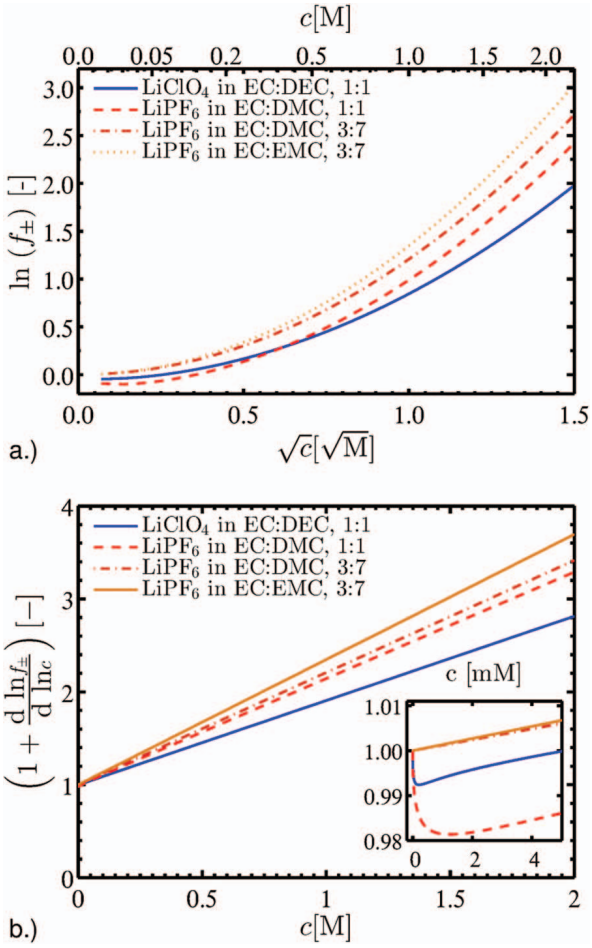

Figure 9. a. Concentration-dependent mean molar activity coefficients of $LiClO_4$ in EC:DEC (1:1, w:w), $LiPF_6$ in EC:DMC (1:1, w:w), $LiPF_6$ in EC:DMC (3:7, w:w), and $LiPF_6$ in EC:EMC (3:7, w:w), obtained from the fitting parameters in Table III for data obtained in a salt concentration range from 5 mM to 2 M, b. Corresponding thermodynamic factors, with a zoom-in view at the low-concentration region.

lithium reference electrode versus half-wave potentials of the ferrocene/ferrocenium redox couple was described in great detail for an exemplary electrolyte with $LiClO_4$ dissolved in a mixture of EC:DEC (1:1, w:w). The same methodology was applied to several more electrolytes in order to generate data which could be compared to the literature: $LiPF_6$ in EC:DMC (1:1, w:w), $LiPF_6$ in EC:DMC (3:7, w:w), and $LiPF_6$ in EC:EMC (3:7, w:w) in a concentration range from 5 mM to 2 M. These electrolytes are representatives of frequently used electrolytes for lithium ion batteries. An overview of measured and fitted parameters of the four electrolytes is given in Table III.

While the fitted parameters U_{Ref} and x_1 yield meaningful values and standard deviations, the fitted $\dot{a}$-values have unreasonably large values and they are plainly nonsensical for $LiPF_6$ in EC:DMC (3:7, w:w) and $LiPF_6$ in EC:EMC (3:7, w:w). This is a result of the insensitivity of the fit to the $\dot{a}$-value, caused by the fact that the lowest considered salt concentration of 5 mM is much too large to observe the Debye-Hückel behavior (see above discussion). Consequently, the natural logarithm of the activity coefficient vs. concentration obtained by inserting the parameters listed in Table III in Eqs. 30, 31, and 33, for the electrolytes with the excessively large and clearly incorrect $\dot{a}$-values depicted in Figure 9a (dotted and dash-dotted red lines), does not go negative at low salt concentrations as would be expected according to the Debye-Hückel limiting law. Owing to the insufficient fitting accuracy of the $\dot{a}$-value, our here presented method does not allow for an accurate description of the value of the activity coefficient, since this would require precise measurements at salt concentrations much less than 5 mM, which experimentally is not possible. This is true not only

Table III. Measured values of ε_r and fitted values for U_{Ref}, $\dot{a}$, and x_1 for four lithium ion battery electrolytes. The salt concentrations ranged from 5 mM to 2 M and the ferrocene concentration was 0.05 mM; CVs were recorded at 20 mV/s between 2.5 and 4 V. Parameters of the LiClO4 containing electrolyte are identical to Table II, parameters for the LiPF6 electrolytes were obtained using the 100% extrapolated IR correction method of two measurement series. The activity coefficient was fitted using Eq. 33.

Electrolyte	ε_r [−]	U_{Ref} [V]	$\dot{a}$ [nm]	x_1 [−]	R^2 [−]
$LiClO_4$ in EC:DEC (1:1, w:w)	35 ± 3	3.3079 ± 0.0042	12.8 ± 23.4	0.907 ± 0.005	0.996
$LiPF_6$ in EC:DMC (1:1, w:w)	38 ± 6	3.2941 ± 0.0001	4.5 ± 1.1	1.146 ± 0.012	0.995
$LiPF_6$ in EC:DMC (3:7, w:w)	23 ± 3	3.3030 ± 0.0005	$3.5 \cdot 10^4$	1.207 ± 0.010	0.996
$LiPF_6$ in EC:EMC (3:7, w:w)	22 ± 3	3.3101 ± 0.0003	$4.0 \cdot 10^4$	1.347 ± 0.006	0.998

for the low-concentration region, but also for the high-concentration region, as the obtained activity coefficients have an undefined offset throughout.

While our new methodology cannot provide activity coefficients, we will now show that it does provide accurate values for the so-called thermodynamic factor (TDF). In the equations of the concentrated electrolyte theory, the binary activity coefficient appears in the form of the TDF, defined as

$$\mathrm{TDF} = \left(1 + \frac{\mathrm{d}\ln f_{\pm}}{\mathrm{d}\ln c}\right) = \left(1 + c\frac{\mathrm{d}\ln f_{\pm}}{\mathrm{d}c}\right) \quad [37]$$

The TDFs shown in Figure 9b are based on an exact derivative of Eq. 33, with the parameters from Table III and inserted into Eq. 37. Only in the inset of Figure 9b, for concentrations below 5 mM, the impact of the Debye-Hückel behavior to the TDF can be seen, illustrating its negligible contribution at normal electrolyte concentrations (1 M). Mathematically this can also be shown with the ratio of TDFs based on Eq. 33 with and without the Debye-Hückel term. Using the parameters from Table III for the electrolyte with the largest Debye-Hückel behavior, $LiPF_6$ in EC:DMC (1:1, w:w), a ratio of 98% is found at a concentration of 5 mM.

$$\left[1 + c\cdot\frac{\mathrm{d}}{\mathrm{d}c}\left(-A\sqrt{c}\left(1 + Ba\sqrt{c}\right)^{-1} + x_1 c\right)\right] \Big/ \left[1 + c\cdot\frac{\mathrm{d}}{\mathrm{d}c}\left(x_1 c\right)\right] = 0.98 \quad [38]$$

In Eq. 38 the ferrocenium contribution to the ionic strength is neglected, i.e., $I = c$. We conclude, that due to the dependence of the TDF on the derivative of the logarithmic activity coefficient with respect to salt concentration, an exact knowledge of the low-concentration range and of the offset from the Debye-Hückel behavior mentioned above is not required. For most lithium ion battery applications the accuracy of the TDF at concentrations around and below 5 mM is not essential and an accurate value of the TDF between 5 mM and 2 M salt concentrations should be sufficient for most battery models. In this concentration range the TDFs can be well represented (error $< 2\%$ compared to full Debye-Hückel description) by a linear function as demonstrated with Eq. 38.

Our results for the TDFs are summarized in Figure 9b, showing similar trends for all $LiPF_6$ based electrolytes investigated (red colors) and slightly smaller values for the $LiClO_4$ containing electrolyte (blue). While former electrolytes range between a value of 2.15 and 2.35 for the TDF at 1 M salt concentrations, for the latter $LiClO_4$ electrolyte a value of 1.9 is found. A variation of the solvent ratio or replacement of the unpolar component only results in a small change of the TDF of the $LiPF_6$ electrolytes. Further investigations are necessary to quantify the individual salt and solvent contributions to the activity coefficient and the thermodynamic factor in order to give a precise description of the underlying principles.

Comparison with the literature.—A comparison of the TDFs of $LiPF_6$ containing electrolytes investigated by us, with those reported in the literature for similar electrolytes, is shown in Figure 10. All our $LiPF_6$ electrolytes, which were chosen as they represent standard electrolytes for lithium ion batteries, fall in a reasonably narrow range. Thus, they are represented by the red highlighted area in Figure 10, encompassing the red lines in Figure 9b. As the electrolytes investigated in literature are similar to ours, we would expect them to lie in or close to our range. A direct comparison with our data is possible for the electrolyte $LiPF_6$ in EC:EMC, 3:7 w:w, which was also analyzed by Nyman et al.[7] (brown). An excellent agreement is found at concentrations above 1 M; the values for the reported TDF lie within or are very close to our range of TDFs for $LiPF_6$ electrolytes. The deviation between our values and the values reported by Nyman et al.[7] (brown) at salt concentration below 1 M may be a result of the different determination technique used. Nyman et al.[7] determine the TDF, the transference number and the diffusion coefficient at once, based on experiments in a polarization cell and a concentration cell and assume polynomial functions for the parameters. The same procedure is

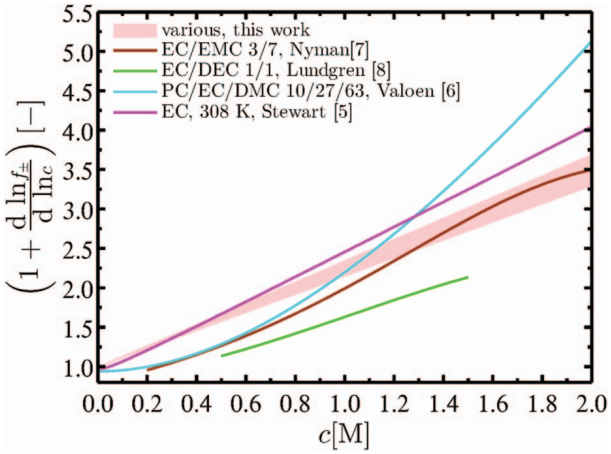

Figure 10. Comparison of determined thermodynamic factor for various $LiPF_6$ containing electrolytes (data from this work marked by red highlighted area) with TDFs published with similar solvents: Nyman:[7] $LiPF_6$ in EC:EMC, 3:7, w:w; Lundgren:[8] $LiPF_6$ in EC:DEC, 1/1, w:w; Valøen:[6] $LiPF_6$ in PC:EC:DMC, 10:27:63, v:v:v; Stewart:[5] $LiPF_6$ in EC:EMC, 1:1, w:w.

used by Lundgren et al.,[8] who also report smaller values for the electrolyte $LiPF_6$ in EC:DEC, (1/1, w:w) containing electrolyte (green) compared to our range. While in latter publications the behavior at low concentrations is neglected, Stewart and Newman[5] (magenta) and Valøen et al.[6] (turquoise) assume a Debye-Hückel behavior. In the publication by Stewart and Newman, a Debye-Hückel behavior as described by Eq. 33 is assumed for small concentrations.[5] In this case, the Debye-Hückel behavior also does not affect the curvature of the resulting TDF, but only imposes a small correction at the lowest concentrations. In the TDF determined by Valøen et al. a distinct, non-linear trend at low concentrations can be observed.[6] Valøen et al. assume the natural logarithm of the mean molar activity coefficient to be a series expansion of $\sqrt{c}$ terms. This formulation does not allow for a fast deviation from the linear Debye-Hückel behavior and thus leads to a pronounced negative feature in the TDF. We want to emphasize that in the literature generally more than one experiment was used to obtain the TDF.

In summary, we find the application of the presented methodology, i.e. determination of the thermodynamic factor based on the slope of the activity coefficient, shows good agreement with literature. We conclude, our analysis of reproducible measurements allows for a precise determination of the thermodynamic factor in a concentration range from 5 mM to 2 M.

Conclusions

In this contribution, we demonstrated the validity of determining the thermodynamic factor based on measurements conducted in a standard three electrode glass cell. Therefore we use cyclic voltammetry and measure the redox potentials of the ferrocene/ferrocenium couple vs. a lithium electrode immersed in electrolytes with variable lithium salt concentrations. The relation between the half-wave potentials and the mean molar activity coefficient of the lithium salt is derived in detail in order to unravel the underlying principles of the measurement and to understand the limits of the experimental methodology due to non-ideal effects caused by deviation from Nernstian redox behavior and from diffusion overpotentials. To evaluate the influence of non-ideal effects, the peak separation between the ferrocene/ferrocenium oxidation and reduction peak potentials is used as a quality measure for the experimental data. It is emphasized that correct ohmic drop compensation has to be performed in order to obtain reliable results. The half-wave potentials vs. lithium salt concentration were successfully correlated with an extended Debye-Hückel law by fitting. Extracted fitting parameters allow to precisely describe the trend of the activity coefficient at salt concentrations above 5 mM, but do not allow quantification of the absolute value of the activity coefficient.

However, the quantity of interest for battery simulations based on the concentrated solution theory, the thermodynamic factor, depends on the slope of the activity coefficient and can thus be calculated precisely by our new method from the parameters obtained by the extended Debye-Hückel fit. For better comparability with literature data, measurements were conducted in a concentration range from 5 mM to 2 M for three $LiPF_6$ containing electrolytes. Comparison of our TDF data with the literature shows the same qualitative, mostly linear trends and for similar electrolytes good agreement is found. The error made by assuming a linear TDF instead of the full description, including the Debye-Hückel behavior, is <2%. Within a ∼5% range, the TDF for the electrolytes $LiPF_6$ in EC:DMC (1:1, w:w), EC:DMC (3:7, w:w) and EC:EMC (3:7, w:w) can be described by $\mathrm{TDF}(c) = 1 + 1.25c$. Accordingly we find $\mathrm{TDF}(c) = 1 + 0.91c$ for the electrolyte $LiClO_4$ in EC:DEC (1:1, w:w). As mentioned in the introduction, also the temperature dependence of the thermodynamic factor should be investigated in detail. While this work provides a thorough description of the experimental setup and the measurement technique, the temperature dependence of the thermodynamic factor will be subject of a future study.[12]

Acknowledgment

We gratefully acknowledge the funding by the Bavarian Ministry of Economic Affairs and Media, Energy, and Technology for its financial support under the auspices of the EEBatt project. Many thanks to Qi He for the coaxial cell setup for measuring the relative permittivities. We thank Ram Subbaraman and Nathan Craig for valuable discussions.

Note added in proof.—The assumption of the redox potential of the Fc/Fc^+ couple not being strongly influenced by the $LiClO_4$ concentration made in the Theory section can also be verified by measurements conducted by Pendley et al., who showed a constant potential of the Fc/Fc^+ couple versus a sodium saturated calomel electrode in different concentrations of supporting electrolyte as long as the concentration ratio of ferrocene to supporting electrolyte is small.[26]

List of Symbols

Symbol	Name	Unit
$\gamma_\pm$	mean molal activity coefficient	-
$f_\pm$	mean molar activity coefficient	-
a_n^θ	prop. constant for the secondary ref. state	L/mol
$(1+\frac{\mathrm{d}\ln f_\pm}{\mathrm{d}\ln c})$	thermodynamic factor	-
U	cell potential	V
ϕ	electrostatic potential wrt. anionic species	V
c	concentration	mol/L
ν_i	stoichiometry factor	-
μ	chemical potential of uncharged species	J/mol
$\tilde{\mu}$	chemical potential of ionic species	J/mol
$\Delta_R G$	reaction Gibbs energy	J/mol
z_i	ionic charge (neg./pos. for anions/cations)	-
μ^θ	standard chemical potential	J/mol
μ_{Cell}	standard chemical cell potential	J/mol
U_0'	formal potential of WE wrt. RE	V
s	scan rate in cyclic voltammogram (CV)	mV/s
t	time	s
$U_{\mathrm{p.ox/red}}$	oxidation / reduction peak potential	V
$I_{\mathrm{p.ox/red}}$	oxidation / reduction peak current	A
D_i	diffusion coefficient of species i	cm^2/s
U_{reverse}	cyclic voltammogram (CV) vertex potential	V
η	kinetic overpotential	V
Ψ	dimensionless parameter relating CV peak separation with the rate constant	-
α	transfer coefficient in Butler Volmer eqn.	-
k_0	standard rate constant	1/s
$U_{\mathrm{p.1/2}}$	cyclic voltammogram half-wave potential	V
$\boldsymbol{i}$	current density	A/cm^2
κ	electrolyte conductivity	mS/cm
t_i	transference number of ionic species i	-
R	resistance	Ω
I	ionic strength	mol/L
$\dot{a}$	distance of closest approach	nm
ε_R	relative permittivity of electrolyte	-

Constants

F	Faraday constant	C/mole
R	gas constant	J/(mole K)
T	temperature	K
ε_0	vacuum permittivity	F/m
N_A	Avogadro constant	-
k	Boltzmann constant	J/K

References

1. J. Newman and K. Thomas-Alyea, *Electrochemical Systems*, 3rd ed., Wiley Interscience, Hoboken, (2004).
2. A. Latz and J. Zausch, *J. Power Sources*, **196**, 3296 (2011).
3. J. Barthel, R. Neueder, H. Poepke, and H. Wittmann, *J. Solution Chem.*, **27**, 1055 (1998).
4. J. Barthel, R. Neueder, H. Poepke, and H. Wittmann, *J. Solution Chem.*, **28**, 489 (1999).
5. S. Stewart and J. Newman, *J. Electrochem. Soc.*, **155**, A458 (2008).
6. L. O. Valøen and J. N. Reimers, *J. Electrochem. Soc.*, **152**, A882 (2005).
7. A. Nyman, M. Behm, and G. Lindbergh, *Electrochim. Acta*, **53**, 6356 (2008).
8. H. Lundgren, M. Behm, and G. Lindbergh, *J. Electrochem. Soc.*, **162**, 3 (2014).
9. H. S. Harned and D. M. French, *Ann. N. Y. Acad. Sci.*, **46**, 267 (1945).
10. Y. Ma, M. Doyle, T. F. Fuller, M. M. Doeff, L. C. Jonghe, and J. Newman, *J. Electrochem. Soc.*, **142**, 1859 (1995).
11. G. Gritzner and J. Kuta, *Pure Appl. Chem.*, **54** (1982).
12. J. Landesfeind, A. Ehrl, M. Frankenberger, W. A. Wall, and H. A. Gasteiger, *J. Electrochem. Soc.*, To be submitted.
13. C. Daniel and J. O. Besenhard, *Handbook of Battery Materials*, Wiley-VCH, (2011).
14. A. Bard and L. Faulkner, *Fundamentals and applications*, 2nd ed., John Wiley & Sons, Ltd, New York, (2004).
15. G. Gritzner, K. Danksagmüller, and V. Gutmann, *J. Electroanal. Chem.*, **72**, 177 (1976).
16. C. H. Hamann, A. Hamnett, and W. Vielstich, *Electrochemistry*, Wiley-VCH, Weinheim, (2007).
17. M. R. Wright, *An Introduction to Aqueous Electrolyte Solutions*, John Wiley & Sons, Ltd, Chichester, (2007).
18. A. M. Bond, K. B. Oldham, and G. A. Snook, *Anal. Chem.*, **72**, 3492 (2000).
19. W. Schmickler and E. Santos, *Interfacial electrochemistry*, Oxford University Press, New York, (1996).
20. H. Scholl and K. Sochaj, *Electrochim. Acta*, **36**, 689 (1991).
21. Y. Wang, E. I. Rogers, and R. G. Compton, *J. Electroanal. Chem.*, **648**, 15 (2010).
22. I. Ruff, V. J. Friedrich, K. Demeter, and K. Csillag, *J. Phys. Chem.*, **75**, 3303 (1971).
23. L. M. Peter, W. Dürr, P. Bindra, and H. Gerischer, *J. Electroanal. Chem.*, **71**, 31 (1976).
24. J. Redepenning, E. Castro-Narro, G. Venkataraman, and E. Mechalke, *J. Electroanal. Chem.*, **498**, 192 (2001).
25. M. S. Ding, *J. Electrochem. Soc.*, **150**, A455 (2003).
26. B. D. Pendley, H. D. Abruna, J. D. Norton, W. E. Benson, and H. S. White, *Anal. Chem.*, **63**, 2766 (1991).

Erratum

In the original publication it is assumed that the ferrocene/ferrocenium redox potential, and thus its activity coefficient, is independent of the supporting electrolyte salt and its concentration. This assumption is not fully supported; the references (e.g., Ref. [104]) only show that the activity coefficient is independent of the surrounding solvent, and assuming that it be independent of the salt concentration is definitely wrong for low permittivity solvents at low concentrations. This demonstrated in detail in the subsequently presented erratum.

Erratum: Direct Electrochemical Determination of Thermodynamic Factors in Aprotic Binary Electrolytes

Johannes Landesfeind,[az] and Hubert A. Gasteiger[a]

[a] Chair of Technical Electrochemistry, Department of Chemistry and Catalysis Research Center, Technical University of Munich, Munich, Germany

[z]corresponding author

Theoretical Considerations

One of the key assumptions in the original publication is a constant mean molar activity coefficient $f_{\pm}$ of the ferrocenium perchlorate, i.e., $\ln\left(f_{\mathrm{FcClO_4}}\right)|_{\mathrm{WE}} = \mathrm{const.}$ (compare Eq. 17 and the first paragraph on p. A1257) and thus independent of the surrounding electrolyte solution. Yet strictly speaking, the cited work by Gritzner and Kuta[1] (Ref. 15 in original publication) only shows a constant ferrocene/ferrocenium redox potential for different solvent systems, while maintaining the same salt and the same salt concentration. The solvent (but not necessarily salt and concentration) invariance of the ferrocene/ferrocenium redox couple is also demonstrated in Table 6.4 in *Electrochemistry in Nonaqueous Solutions* by Kosuke Izutsu, which gives the redox potentials of the ferrocene couple for a large range of solvents (always ~1.134 ± 0.1 V).[2] The assumed independence of the surrounding salt and its concentration however cannot be supported with published measurements. However, careful analysis of the Debye-Hückel theory shows, that the mean molar activity coefficient of *any* ionic species will depend on its ionic surrounding[3]

$$\ln f_{\pm} = -\frac{A\sqrt{I}}{1 + B\dot{a}\sqrt{I}} \qquad 1$$

indicated by the ionic strength *I*, rather than the concentration of the ionic species *c* (compare nomenclature of Eq. 28 in original publication for definition of electrolyte specific factors *A*, *B* and $\dot{a}$). While Eq. 1 only approximates the mean molar activity coefficient, it was found to agree well with experimental results from aqueous electrolytes, especially in the low concentration regime.[4] It is noted that the ionic size and possible shielding effects of the ferrocene molecular structure do not contradict the Debye-Hückel theory, i.e., Eq. 1 is only based on the charge number, which is the same for a single charged ferrocenium ion as for a single charged lithium ion. In conclusion the Debye-Hückel theory is valid for both ions in the electrolyte solutions studied in the original publication and $\ln\left(f_{\mathrm{FcClO_4}}\right)|_{\mathrm{WE}}$ cannot be constant at low supporting salt ($LiClO_4$) concentrations. Eq. 16 in the original publication should correctly read

$$U = U_{\mathrm{Ref}} - \frac{\mathrm{RT}}{\mathrm{F}}\ln\left(c_{\mathrm{Li^+}} f_{\mathrm{LiClO_4}}^2\right) + \frac{\mathrm{RT}}{\mathrm{F}}\ln\left(f_{\mathrm{FcLiClO_4}}^2\right) \qquad 2$$

with the third term originally assigned to the assumed constant reference potential U_{Ref}. I.e., in our analysis of $y_{\mathrm{Axis}} \equiv -U - \mathrm{R}T/\mathrm{F} \ln(\mathrm{c_{Li^+}})$ (compare Eq. 36 in the original publication) we are effectively analyzing the difference between the mean molar activity coefficients of $LiClO_4$ to $FcClO_4$. This also explains why the Debye-Hückel limiting law ($\ln f_{\pm} = -A\sqrt{I}$) cannot be observed at smallest concentrations, as in this concentration range (< 0.1 M) the magnitude of $\ln(f_{\mathrm{FcClO_4}})$ and $\ln(f_{\mathrm{LiClO_4}})$ only depend on the (same) solvent relative permittivity (A is only function of ε_{R}), their difference caused by higher order terms is negligibly small. In addition to the Debye-Hückel theory which definitely invalidates our assumption of a constant mean molar activity coefficient for the ferrocenium perchlorate at low concentrations, no statement about higher concentrations > 0.1 – 0.5 M can be made and the behavior of $\ln(f_{\mathrm{FcClO_4}})$ is entirely speculative in this case.

Experimental

In addition to the above definitive analysis of the theoretical Debye-Hückel behavior for the ferrocenium perchlorate we also tried to (in)validate the proposed direct determination method for the thermodynamic factor experimentally, which we briefly discuss in the following for the interested reader. The ferrocene/ferrocenium couple based methodology could be checked explicitly when applied to an electrolyte with a known mean molar activity coefficient. Data on mean molar activity coefficients in aprotic solvents is scarce though. Vapour pressure depression was used on some non-aqueous electrolyte systems, suitable for the ferrocene method, but the single reports are hard to verify as they cannot be compared to additional references.[5] However, highly reproducible results for the activity coefficients in aqueous systems exist and are based on numerous sources and measurement techniques. The intrinsic problem with applying the ferrocene cell method to a well-studied aqueous electrolyte is the very low solubility of Fc in water,[6] its interactions with water[7] and its decomposition.[8] Acetylferrocene (AcFc) can be easily dissolved in water,[9] yet we also found it decomposes with time and under UV light exposure yielding metallic iron (experimentally proven using a magnet). However, when dissolved in EC:DEC (1:1 w:w) AcFc does not decompose, yet when we repeat our measurements with AcFc instead of Fc (compare main article and Figure 1 below) largely different results are observed, suggesting that AcFc, due to its acetyl group, undergoes stronger interactions with the solvent and prohibits its use for the ferrocene method. Careful investigations of the mean molar activity coefficient of aqueous KCl electrolytes using the AcFc couple could thus not be interpreted conclusively and the observed discrepancy to literature values may also be related to the unsuited, strongly interacting redox couple.

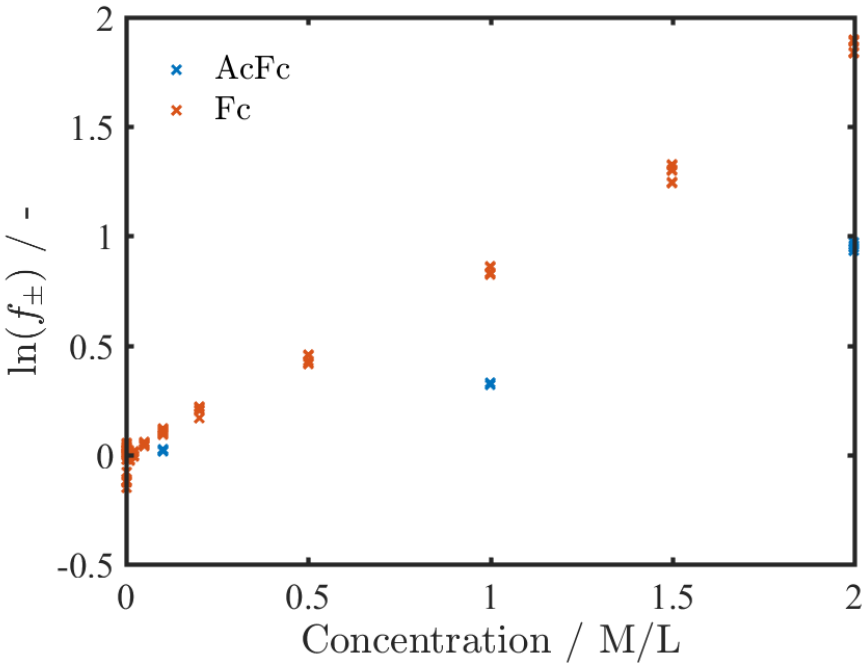

Figure 1. Comparison of logarithmic mean molar activity coefficients, obtained from application of the ferrocene cell method (see main article) to $LiClO_4$ in EC:DEC (1:1 w:w) with ferrocene/ferroceneium (orange crosses, same data as is original publication, shifted to y-axis intercept 0) and acetylferrocene/acetylferrocenium as redox couple (blue crosses at 0.1 M, 1 M and 2 M, shifted to y-axis intercept 0).

The best experimental evidence to proof the invalidity of the ferrocene cell method is the comparison of thermodynamic factors (TDFs) obtained using this method with an alternative approach, in which the TDF is determined from concentration cell and pulse experiments, for details on latter method the reader is referred to the literature.[10] Although generally similar trends are obtained (Figure 2), the ferrocene cell based TDFs cannot represent experimental results from concentration cell and pulse experiments, especially when a pronounced Debye-Hückel behavior can be observed (compare Figure 2c).

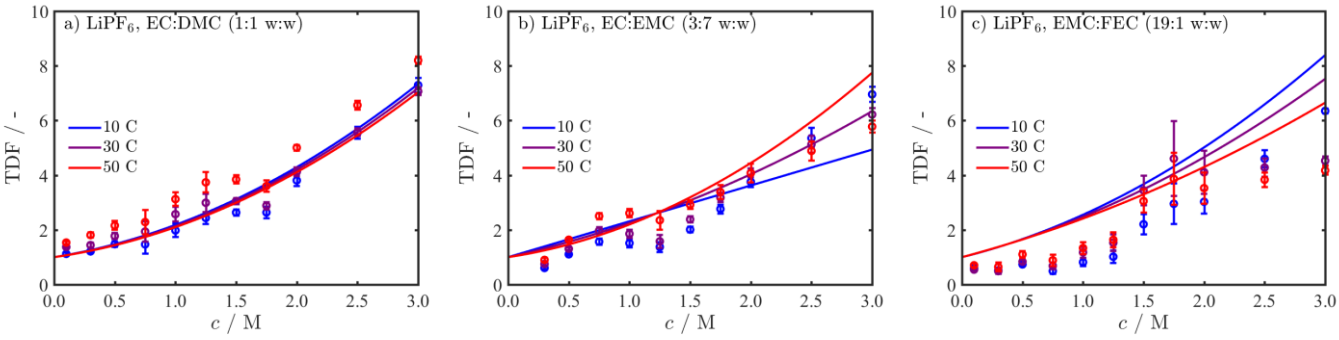

Figure 2. Temperature dependent thermodynamic factors for 0.1 M to 3 M $LiPF_6$ in a) EC:DMC (1:1 w:w), b) EC:EMC (3:7 w:w) and c) EMC:FEC (19:1 w:w) determined using the ferrocene cell approach with the Fc/Fc^+ redox couple (solid lines) and based on concentration cell potentials and pulse experiments in symmetric lithium cells (circles) at 10 °C (blue), 30 °C (purple) and 50 °C (red).

It is interesting to note, that best agreement is obtained with solvents of high relative permittivity (EC:DMC (1:1 w:w), $\varepsilon_R \approx 34$) compared to lower solvent permittivities (EC:EMC (3:7 w:w), $\varepsilon_R \approx 20$ and EMC:FEC (19:1 w:w), $\varepsilon_R \approx 3$), with the permittivities being approximated by the weighted means of the permittivities of the single components (compare Hall et al.[11] for similar compositions). Keeping in mind that the limiting law Debye-Hückel slope A is inversely proportional to ε_R ($A \approx 2,4$ and 76 for the electrolytes respectively at 25 °C), differences in the TDFs in Figure 2 are especially dominant at low salt concentrations and for electrolytes of low relative permittivitiy and explains why

remarkably similar trend are obtained for the high permittivity EC:DMC (1:1 w:w) system in Figure 2a. These results prove that a Debye Hückel behavior is also present for the ferroceneium ions at low concentrations when the solvent permittivity is low.

Conclusions

It is emphasized that the originally proposed methodology to determine thermodynamic factors in non-aqueous electrolytes based on the analysis of the ferrocene/ferrocenium redox potentials in three electrode cyclic voltammograms was based on not fully validated assumptions and should generally not be used for the analysis of thermodynamic properties. The theoretical considerations introduced above clearly show that the previously assumed mean molar activity coefficient of ferrocenium perchlorate cannot be assumed constant as it has to follow the Debye-Hückel behaviour at low concentrations, especially when low permittivity solvents are used. In the high concentration range the behavior of $\ln(f_{\mathrm{FcClO_4}})$ is purely speculative and found similarities with independently measured thermodynamic factors has to be interpreted as entirely incidental.

Acknowledgement

We thank Nathan Craig for motivating us to rethink the activity coefficient determination and Davide Menga, Hany El-Sayed and Robert Morasch for valuable discussions and support with troubleshooting the ferrocene cell setup.

References

1. G. Gritzner, K. Danksagmüller, and V. Gutmann, *J. Electroanal. Chem.*, **72**, 177–185 (1976).

2. K. Izutsu, *Electrochemistry in Nonaqueous Solutions*, Wiley-VCH, (2002).

3. M. R. Wright, *An Introduction to Aqueous Electrolyte Solutions*, John Wiley & Sons, Ltd, Chichester, (2007).

4. W. M. Haynes, *CRC Handbook of Chemistry and Physics*, 95th editi., CRC Press, (2014).

5. J. Barthel, R. Neueder, H. Poepke, and H. Wittmann, *J. Solution Chem.*, **28**, 489–503 (1999).

6. K. Aoki, Ouyang, Chen, Nishiumi, and Wang, *Reports Electrochem.*, 17 (2013).

7. G. Gritzner, *Handbook of Reference Electrodes* G. Inzelt, A. Lewenstam, and F. Scholz, Editors, p. 25-32, Springer, Berlin, Heidelberg, (2013).

8. J. K. Bashkin and P. J. Kinlen, *Inorg. Chem.*, **29**, 4507–4509 (1990).

9. F. A. Buryukin et al., *Russ. J. Phys. Chem. A*, **82**, 1545–1548 (2008).

10. J. Landesfeind and H. A. Gasteiger, in preparation (2018).

11. D. S. Hall, J. Self, and J. R. Dahn, *Phys. Chem. C*, **119**, 22322–22330 (2015).

3.3 Transference Number

In this section the article *Determination of Transport Parameters in Liquid Binary Electrolytes : Part II . Transference Number*[59] is presented, which was submitted in June 2017 and published in the peer-reviewed Journal of the Electrochemical Society in September 2017. Parts of the article were presented at the 13$^{\text{th}}$ Symposium on Fuel Cell and Battery Modeling and Experimental Validation in Lausanne (Switzerland) in March 2016 and at the ECCOMAS 2016 in Crete (Greece) in June 2016.

In analogy to the previous approach to analyze the binary diffusion coefficient, the electrochemical determination of the transference number is based on pulse experiments in a symmetric lithium cell setup. Additionally, the concentration potentials between differential electrolyte concentrations are measured in open glass-plate type concentration cells. However, as motivated before (see Section 3.2), the transference number cannot be obtained explicitly from neither the pulse experiments nor the concentration cell measurements alone. Therefore the publication compares two approaches, analysis of concentration cell potentials combined with a) the thermodynamic factor obtained in the ferrocene cell setup (see Section 3.2) and b) the analysis of the current and potential transients during and after galvanostatic pulses in the two-electrode setup. As the thermodynamic factor from the ferrocene cell setup is not reliable, which was not yet clear at the time of writing the article, the conclusion of the manuscript, the superiority of the concentration cell experiments coupled with the ferrocene cell, is unfortunately invalid. For the alternative determination of the transference number, based on concentration cells and pulse experiments, five different analytical solutions of the short and long term potential and current transients during steady state and pulse polarizations are described. As done previously for the determination methods for the binary diffusion coefficient (see Section 3.1), the analytical solutions are challenged in numerical experiments. In subsequent electrochemical experiments the results from the different methods are compared critically and a general agreement is found between four of them. The largest deviation was observed for the steady state polarization technique, introduced by Bruce and Vincent[58] for polymer electrolytes. It is noted that the transference numbers obtained with the thermodynamic factor from ferrocene cell experiments are in fair agreement with the analytical approaches discussed in the article, which has to be interpreted as purely incidental and may be motivated by the high relative permittivity of the solvent system used in the study (EC:DEC (1:1 w:w), $\varepsilon_{\text{R}} \approx 32$,[102] which is described in detail in Section 3.2).

Author Contributions

A.E., J.L., W.W. and H.G. developed the double glass plate cell design. J.L. performed all electrochemical measurements, A.E. derived the analytical solutions and conducted numerical experiments. Data analysis was done by A.E. and J.L. and the manuscript was written by A.E. and J.L. and edited by W.W. and H.G. All authors discussed the data and commented on the results.

Determination of Transport Parameters in Liquid Binary Electrolytes: Part II. Transference Number

Andreas Ehrl,[a,=,c] Johannes Landesfeind,[b,=,*,z] Wolfgang A. Wall,[a] and Hubert A. Gasteiger[b,]**

[a] *Institute for Computational Mechanics, Department of Mechanical Engineering, Technical University of Munich, Munich, Germany*
[b] *Chair of Technical Electrochemistry, Department of Chemistry and Catalysis Research Center, Technical University of Munich, Munich, Germany*

In the literature, various numerical methods for the simulation of ion-transport in concentrated binary electrolytes for lithium ion batteries can be found, whereas the corresponding transport parameters are rarely discussed. In this contribution, a novel method for the determination of the transference number in non-aqueous electrolytes is proposed. The method is based on data from a concentration cell and on the value of the thermodynamic factor obtained from independent measurements based on quantifying the redox potential of ferrocene. The concentration dependent transference numbers obtained by this new method are compared to values obtained by the classical approach, which is based on experiments in a polarization cell and a concentration cell. For the latter, a set of commonly used and some newly proposed analysis methods as well as their theoretical justification are discussed. Using an exemplary electrolyte (lithium perchlorate in a mixture of ethylene carbonate and diethyl carbonate), we will demonstrate that our newly proposed method based on concentration cell experiments and a thermodynamic factor derived from independent measurements is a more accurate approach for obtaining concentration dependent transference numbers. At the end, the experimentally determined concentration dependent transference numbers are compared to data available in the literature.

Manuscript submitted June 9, 2017; revised manuscript received August 8, 2017. Published September 9, 2017.

Numerical simulations are based on four different concentration dependent transport parameters, namely the conductivity $\kappa(c)$, the binary diffusion coefficient $D_{\pm}(c)$, the transference number $t_+(c)$, and the thermodynamic factor (TDF) or the mean molar activity coefficient $f_{\pm}(c)$, respectively. The accurate determination of these parameters is key for the reliable simulation of the charge/discharge performance of lithium ion batteries. The conductivity $\kappa(c)$, the binary diffusion coefficient $D_{\pm}(c)$,[1] and the thermodynamic factor[2] can be determined by a single experiment for each concentration. The determination of the concentration dependent transference number is more elaborate. In the following, an overview of various experimental techniques for the determination of transference numbers in lithium based electrolytes is given. In the context of this work the term transference number is used as defined in Newman and Thomas-Alyea.[3]

The transference number $t_+(c)$ can be determined directly by the Hittorf method which is discussed for polymer electrolyte solutions by Bruce et al.[4] An alternative version of the Hittorf method for liquid electrolytes was applied by Valøen and Reimers for $LiPF_6$ in PC:EC:DMC (10:27:63 v:v:v).[5] Since the influence of diffusion processes on mass transport is neglected in the derivation of the Hittorf method,[5] it can be not used for an accurate determination of the transference number in general. Additionally, the noise level observed with the Hittorf method as reported by Valøen and Reimers is too large for the determination of the transference number as a function of the concentration.[5] On the other hand, for dilute electrolyte solutions, the potentiostatic polarization method introduced in Bruce and Vincent[6] can be used for the direct determination of the transference number. In this work, as well as in Hiller et al.,[7] the method is used for polymer electrolytes, while Mauro et al.[8] and Zugmann et al.[9] applied the same method for liquid electrolytes such as $LiClO_4$ dissolved in PC and for $LiPF_6$ in various solvents, albeit at concentrations which cannot anymore be considered as dilute electrolytes. In Zugmann et al., three additional methods, namely the electromotive force method, the NMR method, and the galvanostatic polarization method are discussed.[9] The electromotive method is based on data from a concentration cell with transference,[10] including concentration overpotentials. In such an experimental setup, the transference number can be determined either in the dilute electrolyte limit,[5] where the thermodynamic factor can be assumed to be unity,[3] or the functional dependence of the thermodynamic factor on salt concentration has to be known or assumed. It would also be possible to use a concentration cell without transference,[10] but it is difficult to find appropriate salt bridges for aprotic lithium based electrolytes, which would satisfy the condition $t_+ = t_- = 0.5$.[9] The transference number can also be determined by measuring the ionic self-diffusion coefficients.[11,12] In Zhao et al.,[13] the method introduced by Bruce and Vincent[6] is compared to the NMR method, revealing that completely different values for the transference number are obtained, even for the smallest concentrations. In Sethurajan et al., the differences between transference numbers determined by NMR and other techniques are explained by the effect of ion-pairing.[14] In their publication, it is strictly distinguished between the transference number which is defined based on a current fraction versus the transport number which is defined based on the ionic diffusion coefficients. In the absence of ion-pairs, both definitions are equivalent, as can be concluded from the derivation of concentrated solution theory presented in Newman and Thomas-Alyea.[3] The most popular method to determine the transference number is the galvanostatic polarization method. It is used for polymer electrolytes in Ma et al.,[15] Ferry et al.[16] or Doeff et al.[17] However, the determination of the transference number by the galvanostatic polarization requires knowledge about the diffusion coefficient and thermodynamic factor. Therefore, it is necessary to perform three different experiments to determine the transference number, which usually results in an accumulation of inaccuracies from the errors in each experimental procedure and due to the necessity to use arbitrary functional relationships (e.g., assuming a concentration independent transference number in some cases). Alternatively, the diffusion coefficient, the transference number, and the thermodynamic factor can also be determined by a numerical optimization approach as shown in the publications by Georén and Lindbergh,[18] Nyman et al.,[19] and Lundgren et al.[20] In this approach, usually, the same or similar experiments as for the galvanostatic polarization are performed.

=These authors contributed equally to this work.
*Electrochemical Society Student Member.
**Electrochemical Society Fellow.
[c]Present address: Velling 4, 94374 Schwarzach, Germany.
[z]E-mail: j.landesfeind@tum.de

In the following, various of the aforementioned electrochemical methods for the determination of the transference number are reviewed regarding theoretical assumptions, experimental accuracy, and applicability. Additionally, an alternative method for the determination of the transference number based on the combination of measuring the redox potential of ferrocene/ferrocenium vs. lithium salt concentration[2] and a concentration cell is introduced. All discussed methods are also investigated experimentally before the final conclusion is presented. After presentation of the used materials and measurement setups in the Experimental section, the relevant theoretical framework is discussed in the Theory section, summarizing the equations used for the determination of the transference number used in the literature as well as newly introduced analysis methods. Validity and accuracy of the introduced techniques are analyzed and compared in the Numerical Validation section. Because theoretically expected transients are more obvious in simulated experiments, this section aids in understanding experimental data. In the Results and discussion section, the transference number is obtained from measurements in previously described cell setups. A short summary and a conclusion are given in the Conclusions.

Experimental

Ethylene carbonate (EC, 50%, by weight, Sigma Aldrich, anhydrous, 99%) and diethyl carbonate (DEC, 50%, by weight, Sigma Aldrich, anhydrous, >99%) were used as solvents for self-prepared electrolytes containing lithium perchlorate ($LiClO_4$, Sigma Aldrich, 99.99%) salt, whereby all components were mixed in an argon filled and temperature controlled glove box (MBraun, 25°C ± 1°C, water content <0.1 ppm, Ar 5.0, Westfalen, 99.999% vol). $LiClO_4$ concentrations ranged from 0.1×10^{-3} to 2 M. Metallic lithium (Rockwood Lithium, 0.45 mm, high purity) was used as counter electrode (CE) and working electrode (WE).

In this contribution, a polarization and a concentration cell are used for the determination of transference numbers. The polarization cell consists of two parallel and aligned lithium electrodes which are separated by porous separators, as described in detail in part I of this publication, where we presented the determination of diffusion coefficients.[1] The concentration cell consists of two parallel lithium stripes which are in contact with a stripe of glass fiber separator soaked with two electrolyte solutions which differ in their lithium salt concentration. To minimize electrolyte evaporation, separator and electrodes are sandwiched between two glass plates as depicted in Figure 1. Concentration cell potentials were measured over a time interval of four minutes using either a handheld voltmeter (Voltcraft VC830) inside the glove box or a potentiostat (Biologic VMP3).

Theory

In the following, the theoretical foundations of various methods for the determination of the transference number are discussed. First, the direct determination of the transference number for dilute electrolytes introduced by Bruce and Vincent[6] is embedded into the concentrated solution theory. Afterwards, the classical method for the determination of the transference number in concentrated electrolytes based on measurements in a polarization and concentration cell is shortly reviewed. A basic element of this method is the Sand equation. In the following, the same experimental setup is used to determine the transference number, but the Sand equation is replaced by several alternative analytical relations, which so far have not been used for the determination of the transference number. In the end of this section, a novel method for the determination of the transference number in concentrated electrolytes is introduced, which is based on measurements in a concentration cell and which makes use of the quantification of the thermodynamic factor in an independent experiment[2] based on measuring the redox potential of ferrocene/ferrocenium vs. lithium salt concentration (further on referred to as "ferrocene cell").

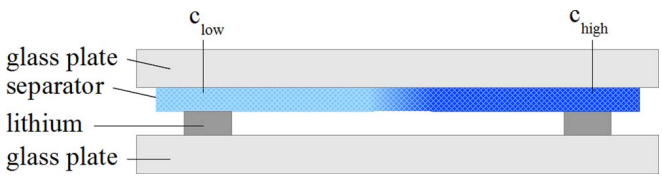

Figure 1. Concentration cell setup for the determination of concentration overpotentials between two lithium electrodes contacted by a glass fiber separator soaked with an electrolyte of two different salt concentrations (side view).

Direct determination of the transference number by steady-state polarization experiments.—The direct determination of the transference number t_+ for dilute electrolyte solutions is based on the application of a constant cell potential U_p until the steady-state current is reached. Theoretically, it is possible to calculate the transference number t_+ from the ratio between the initial current I_0 and the steady-state current I_s. However, a correction term for variable electrode kinetics as a result of, e.g., the SEI formation or the growth of mossy lithium has to be considered. In the original form introduced by Blonsky et al., the method was restricted to dilute electrolyte solutions with a constant diffusion coefficient.[21] Bruce and Vincent[6] extended it to electrolyte solutions with a variable ionic diffusion coefficient. In this extension, it is argued that the thermodynamic factor has to be close to unity in order to apply the dilute solution theory. However, it is also possible to derive the method from the more general framework of concentrated electrolyte solutions as discussed, e.g., in Doyle[22] and Ehrl.,[23] which is outlined in the following (Eq. 1 to 24). Comparison of the result obtained using this approach with the Bruce-Vincent equation will allow to obtain a mathematical condition which has to be fulfilled for the dilute solution theory to be applicable. The potential difference $\Delta\Phi$ between the anode A and the cathode C for a one-dimensional approximation of an electrochemical cell is given by the integration of Eq. 3 in part I of this publication (Ref. 1).

$$\Delta\Phi = I \int_C^A \left(\frac{1}{\kappa\,(c_0)} \frac{l}{A} \frac{\tau}{\varepsilon} \right) \mathrm{d}x + \frac{\nu}{\nu_+ z_+} \frac{RT}{F} \left[1 + \frac{\partial \ln f_\pm\,(c_0)}{\partial \ln c} \right] \cdot (1 - t_+\,(c_0)) \frac{\Delta c}{c_0} \quad [1]$$

The potential difference $\Delta\Phi$ denotes the volumetric intrinsic phase average of the electric potential, I the current, A the electrode area, l the distance between the electrodes, and c_0 the initial volumetric intrinsic phase average of the concentration.[1] The porosity ε and the tortuosity τ are parameters related to the morphology of the porous medium and are frequently used, e.g., to obtain the so-called effective binary diffusion coefficient $D_{\pm,\mathrm{eff}} = \varepsilon\,\tau^{-1}\,D_\pm$ or the effective conductivity $\kappa_{\mathrm{eff}} = \varepsilon\,\tau^{-1}\,\kappa_{\mathrm{eff}}$. While porosities can be measured gravimetrically the tortuosity of porous media may be determined from impedance measurements in symmetric cells.[24] The conductivity $\kappa(c_0)$, the transference number $t_+(c_0)$, and the thermodynamic factor $\left[1 + \frac{\partial \ln f_\pm(c_0)}{\partial \ln c}\right]$ are the first order approximations of the concentration dependent conductivity $\kappa(c)$, the transference number $t_+(c)$, and the thermodynamic factor $\left[1 + \frac{\partial \ln f_\pm(c)}{\partial \ln c}\right]$.[1] The coefficient $\nu = \nu_+ + \nu_-$ is based on the stoichiometry coefficients ν_+ and ν_- resulting from the dissociation of a binary salt in its components (e.g., $\nu = 2$ for the typical 1:1 salts used in lithium ion batteries). The gas constant is denoted by R (8.314 J/(mol K)), the Faraday constant (96485 As/mol) by F, and the temperature by T (in units of Kelvin).

In contrast to Eq. 8 in part I of this publication (Ref. 1) which is only valid in the absence of current flow, an additional ohmic contribution, accounting for the current flow through the cell, has to be considered for the potential difference $\Delta\Phi$. The integral in Eq. 1 is equivalent to the ohmic resistance R_{el} of the electrolyte solution. Therefore, the initial potential difference $\Delta\Phi_0$ during the polarization reads

$$\Delta\,\Phi_0 = R_{\mathrm{el},0}\;\; I_0 \quad [2]$$

since the concentration difference Δc is very small directly after the application of the cell potential U_p. The initial electrolyte resistance

is denoted by $R_{el,0}$. At the steady-state, the potential difference $\Delta\Phi_s$ is given by

$$\Delta\Phi_s = R_{el,s} I_s + \frac{\nu}{\nu_+ z_+} \frac{RT}{F} \left[1 + \frac{\partial \ln f_\pm(c_0)}{\partial \ln c}\right] (1 - t_+(c_0)) \frac{\Delta c_s}{c_0} \quad [3]$$

The initial and the steady-state electrolyte resistance measured by impedance spectroscopy (high frequency resistance) can be assumed to be identical

$$R_{el,0} = R_{el,s} = R_{el} \quad [4]$$

since the variation of the conductivity is negligible for small concentration variations. It is also assumed that the concentration difference Δc_S between the electrodes follows a linear concentration profile at steady-state. Due to the known concentration profile, Eq. 6 in part I of the publication (Ref. 1) can be used to express the concentration difference between anode and cathode.

$$\Delta c_S = c(T_I) = \frac{1}{z_+ \nu_+ F} \frac{1 - t_+(c_0)}{D_{\pm,eff}(c_0)} \frac{l}{A} I_s \quad [5]$$

In a next step, Eqs. 2 and 3 can be inserted into Eq. 4 and combined with Eq. 5 giving the following equation

$$\frac{I_0 \Delta\Phi_s}{I_s \Delta\Phi_0} = 1 + \frac{\nu}{\nu_+^2 z_+^2} \frac{R T}{F^2} \left[1 + \frac{\partial \ln f_\pm(c_0)}{\partial \ln c}\right] \frac{(1 - t_+(c_0))^2}{D_{\pm,eff}(c_0)} \cdot \frac{l}{A c_0 R_{el,0}} \quad [6]$$

Eq. 6 simplifies to the following equation for dilute electrolyte solutions

$$t_+ = \frac{I_s \Delta\Phi_0}{I_0 \Delta\Phi_s} \quad [7]$$

if the following approximations are made according to the dilute solution theory

$$1 + \frac{\partial \ln f_\pm(c_0)}{\partial \ln c} \approx 1 \quad [8]$$

$$\kappa_- \approx \frac{F^2}{R T} z_-^2 \nu_- D_- c_0 \quad [9]$$

in combination with the definitions for a binary electrolyte

$$(1 - t_+) \equiv t_- \quad [10]$$

$$\frac{\kappa_{eff}}{D_{\pm,eff}} \equiv \frac{\kappa}{D_\pm} \quad [11]$$

$$t_- \equiv \frac{\kappa_-}{\kappa} \quad [12]$$

$$D_\pm \equiv \frac{(z_+ - z_-) D_+ D_-}{D_+ + D_-} \quad [13]$$

$$t_+ = \frac{z_+ D_+}{z_+ D_+ - z_- D_-} \quad [14]$$

Here, κ_- is the anion contribution to the ionic conductivity and D_+/D_- are the diffusion coefficients of the cation/anion.

An alternative formulation of Eq. 7 can be found

$$t_+ = \frac{I_s \left(U_p - \left(R_{LF,0} - R_{el,0}\right) I_0\right)}{I_0 \left(U_p - \left(R_{LF,s} - R_{el,s}\right) I_s\right)} = \frac{I_s \left(U_p - \left(R_{LF,0} - R_{el}\right) I_0\right)}{I_0 \left(U_p - \left(R_{LF,s} - R_{el}\right) I_s\right)} \quad [15]$$

if the initial $\Delta\Phi_0$ (see Eq. 2) and steady-state potential difference $\Delta\Phi_s$ (see Eq. 3) are replaced by the following relation

$$\Delta\Phi_i = U_p - \left(R_{LF,i} - R_{el,i}\right) I_i \quad [16]$$

and if the assumption of a constant electrolyte resistance given in Eq. 4 is used. Here, R_{LF} denotes the low frequency (LF) resistance determined by impedance spectroscopy. The low-frequency resistance is the overall resistance of a serial equivalent circuit consisting of the electrolyte resistance R_{el} and additional resistances such as kinetic resistances or contact resistances. The subscript s indicates the steady state and 0 the initial state. Due to small concentration variations, the initial and steady-state electrolyte resistances $R_{el,s} = R_{el,0}$ can be assumed to be equal as indicated already in the beginning of the derivation. A similar formulation as given in Eq. 15 was introduced by Bruce and Vincent.[6]

The comparison of Eq. 6 and Eq. 7 gives a mathematical condition for the validity of the dilute solution theory and the corresponding transport parameter:

$$\underbrace{t_+ + t_-}_{=1} \left[\underbrace{\frac{\nu}{\nu_+^2 z_+^2} \frac{R T}{F^2} \left(1 + \frac{\partial \ln f_\pm(c_0)}{\partial \ln c}\right) \frac{t_+(c_0)(1 - t_+(c_0))}{D_\pm(c_0)} \frac{\kappa(c_0)}{c_0}}_{=1}\right] = 1 \quad [17]$$

The expression in the brackets has to be equal to one for the dilute solution theory to be applicable, since by definition the sum of the transference numbers t_+ and t_- is one.

Considering that the initial low frequency resistance corresponds to $R_{LF,0} = U_p / I_0$, and combining this with Eq. 4, allows a simplification of Eq. 15 to

$$t_+(c_0) = \frac{I_s R_{el}}{U_p - \left(R_{LF,s} - R_{el}\right) I_s} \quad [18]$$

which was introduced by Hiller et al.[7] The advantage of this formulation is that the number of parameters which has to be determined is reduced compared to Eq. 15. In addition, the steady-state current I_s is much easier to determine than the initial current I_0, which may include additional effects such as double layer charging and a non-uniform interface resistance.

The determination of the initial current I_0 can be improved by extrapolation of the initial time behavior of the current back to the start of the polarization. The theoretical time behavior of the current $I(t)$ in such an experiment can be derived from the partial differential equation of the form

$$\frac{\partial c}{\partial t} - D^*_{\pm,eff}(c_0) \nabla^2 c = 0, \text{ in } (0, l) \times (0, T_I) \quad [19]$$

with the current I as boundary condition (BC) at anode and cathode. This scalar transport equation results from the ion-transport equations given in part I of this publication (Ref. 1) by applying the one-dimensional approximation for the ion-transport equations (compare Ref. 1). The semi-infinite limit

$$\lim_{x \to \infty} c = c_0 \quad [20]$$

is used as an additional condition and can be interpreted as $c \to c_0$ for $x \to l/2$, which introduces a limitation for the time range in which the analytical solution is valid. A uniform concentration profile is assumed as an initial condition. This boundary value problem can be solved by Laplace transformation as shown in, e.g., Bard and Faulkner[25] (Responses based on linear diffusion and a planar electrode, chapter 5.5.1) or Ehrl.[23] As a result, the current $I(t)$ at the anode as well as the cathode can be expressed as

$$I(t) = \frac{U_p}{R_{LF,0}} \exp\left(H^2 t\right) \operatorname{erfc}\left(H t^{1/2}\right) \quad [21]$$

where $\mathrm{erfc}(H\sqrt{t})$ is the complementary error function defined as $1 - \mathrm{erf}(H\sqrt{t})$. The constant H is defined as

$$H = \frac{2\,\nu}{z_+^2\,\nu_+^2}\,\frac{\mathrm{R}\,T}{\mathrm{F}^2}\,\frac{1}{A\,\varepsilon\,c_0\,R_{\mathrm{LF},0}}\left[1+\frac{\partial \ln f_\pm(c_0)}{\partial \ln c}\right]\frac{(1-t_+(c_0))^2}{\sqrt{D^*_{\pm,\mathrm{eff}}(c_0)}} \quad [22]$$

According to Bard and Faulkner,[25] the factor $\exp(H^2 t)\mathrm{erfc}(H\sqrt{t})$ can be linearized for small values of $H\sqrt{t}$,

$$\exp\left(H^2\,t\right)\ \mathrm{erfc}\left(H\,t^{1/2}\right) \simeq 1 - \frac{2\,H}{\sqrt{\pi}}\sqrt{t} \quad [23]$$

In this case, Eq. 21 can be written as

$$I(t) = \frac{U_\mathrm{p}}{R_{\mathrm{LF},0}}\left(1-\frac{2\,H}{\sqrt{\pi}}\sqrt{t}\right) = I_0 - m_{\#3}\sqrt{t} \quad [24]$$

where $m_{\#3}$ denotes the slope of the current $I(t)$ with respect to $\sqrt{t}$. Thus at the beginning of a steady-state potentiostatic polarization, a linear relationship between the current flowing and the square root of time is expected.

Determination of the transference number based on the Sand equation, a concentration cell, and a known diffusion coefficient.— As already indicated in the literature survey, this method is the classical approach to determine the transference number of non-aqueous electrolytes. It is mainly used for polymer electrolytes as, e. g., in Ma et al.,[15] Ferry et al.[16] and Doeff et al.[17] In Zugmann et al., it is applied to a liquid electrolyte solution.[9] In contrast to the above described method, three experiments in two different experimental setups are necessary for the determination of the concentration dependent transference number $t_+(c)$. In a first step, the partial effective diffusion coefficient $D^*_{\pm,\mathrm{eff}}(c)$ ($\equiv \tau^{-1}\cdot D_\pm(c)$) is usually determined in a polarization cell as described, e.g., in Ehrl et al.[1] In a second step, the polarization cell can also be used for a second experiment, in which one can determine an additional factor of the form

$$f_1\left(f_\pm, t_+, D^{*\,0.5}_{\pm,\mathrm{eff}}\right) \equiv \left[1+\frac{\partial \ln f_\pm(c_0)}{\partial \ln c}\right]\frac{(1-t_+(c_0))^2}{\sqrt{D^*_{\pm,\mathrm{eff}}(c_0)}} \quad [25]$$

However, to determine the transference number from the factor $f_1(f_\pm,\ t_+,\ D^{*\,0.5}_{\pm,\ \mathrm{eff}})$ defined in Eq. 25 and the partial effective diffusion coefficient $D^*_{\pm,\ \mathrm{eff}}$, a third experiment is necessary. Thus, in order to close the system of equations, the factor $\left[1+\frac{\partial \ln f_\pm(c)}{\partial \ln c}\right](1-t_+(c))$ is determined in a concentration cell with transference[10] in a third step.

*Sand equation (method #1).—*The determination of the factor $f_1(f_\pm,\ t_+,\ D^{*\,0.5}_{\pm,\ \mathrm{eff}})$ in Eq. 25 is based on the analysis of the short-term potential relaxation after a galvanostatic pulse polarization in a two-electrode cell. In this method, the Sand equation for the concentration difference Δc between anode and cathode at the current interruption time T_I (derived, e.g., in Bard and Faulkner, chapter 8.2.2[25]) is used to determine the factor $f_1(f_\pm,\ t_+,\ D^{*\,0.5}_{\pm,\ \mathrm{eff}})$, i.e., the right-hand-side of Eq. 25 corresponds to

$$f_1\left(f_\pm,\ t_+,\ D^{*\,0.5}_{\pm,\ \mathrm{eff}}\right)\Big|^{\text{pulse–polarization}}_{\text{short–term relax.}} = \frac{z_+^2\,\nu_+^2}{4\,\nu}\sqrt{\pi}\,\frac{\mathrm{F}^2}{\mathrm{R}\,T}\,A\,\varepsilon\,c_0\,\frac{U(T_\mathrm{I})}{I_\mathrm{p}\sqrt{T_\mathrm{I}}} \quad [26]$$

where the superscript of the function f_1 indicates that the excitation phase is a short-term pulse polarization (rather than a steady-state polarization) and the subscript indicates that the function is defined by the short-term behavior during the relaxation phase. Here, the correlation between concentration and potential introduced in the first part of this study is used.[1] $U(T_\mathrm{I})$ is the cell potential measured directly after current interruption. Therefore, the quality of the method can be improved further if the theoretical short-term relaxation behavior after the pulse is used to evaluate the cell potential $U(T_\mathrm{I})$ exactly at the current interruption time T_I. According to Hafezi and Newman,[26] the cell potential $U(t)$ is proportional to the artificial time τ^*

$$\tau^* = \frac{\sqrt{T_\mathrm{I}}}{\sqrt{t}+\sqrt{t-T_\mathrm{I}}} \quad [27]$$

For the determination of the transference number $t_+(c)$, the tortuosity τ of the porous medium is not required. The tortuosity τ of the porous medium is only necessary to get the binary diffusion coefficient $D_\pm(c)$ from the partial effective binary diffusion coefficient $D^*_{\pm,\mathrm{eff}}(c)$ measured by the methods introduced previously.[1]

*Concentration cell.—*In a concentration cell as introduced in the Experimental section, the measured cell potential equals the concentration overpotential. In the absence of kinetic reactions at the electrode for $I = 0$, the measured cell potential U is defined as

$$U = \int_\mathrm{C}^\mathrm{A}\nabla\Phi\,\mathrm{dx} = \frac{\nu}{z_+\nu_+}\frac{\mathrm{R}\,T}{\mathrm{F}}\int_\mathrm{C}^\mathrm{A}\left[\left[1+\frac{\partial \ln f_\pm(c_0)}{\partial \ln c}\right](1-t_+(c))\right]\cdot \mathrm{d}(\ln c) \quad [28]$$

The theoretical background for the derivation of Eq. 28 is discussed in the Theoretical background section in part I of this publication.[1] In accordance with the concentration profile in a polarization cell, A denotes the electrode which is in contact with the higher concentrated electrolyte solution and C the electrode which is in contact with lower concentrated electrolyte solution. The measured cell potential U is independent of the porosity ε and the tortuosity τ of the interconnecting separator. Based on experiments with various combinations of electrolytes with high and low salt concentrations, the factor $\left[1+\frac{\partial \ln f_\pm(c)}{\partial \ln c}\right](1-t_+(c))$ is fitted continuously by an n^{th} order polynomial.

Alternative methods for the determination of the transference number.—The factor $f_1(f_\pm,\ t_+,\ D^{*\,0.5}_{\pm,\ \mathrm{eff}})$ cannot only be determined by the Sand equation, but also by alternative experiments in polarization cells. However, for some of these experiments, the factor $f_1(f_\pm,\ t_+,\ D^{*\,0.5}_{\pm,\ \mathrm{eff}})$ is replaced by an alternative form

$$f_2\left(f_\pm, t_+, D^*_{\pm,\mathrm{eff}}\right) \equiv \left[1+\frac{\partial \ln f_\pm(c_0)}{\partial \ln c}\right]\frac{(1-t_+(c_0))^2}{D^*_{\pm,\mathrm{eff}}(c_0)} \quad [29]$$

Some methods from the literature as well as some novel approaches will be summarized and introduced in the following sections.

*Long-term potentiostatic polarization (method #2).—*The same framework as used for the direct determination of the transference number in Direct determination of the transference number by steady-state polarization experiments can also be embedded into a more general framework which is also valid for concentrated electrolyte solutions as discussed, e.g., in Doyle[22] and Ehrl.[23]

Based on Eqs. 1–6 and Eq. 16 as well as the basic differential equations and reformulations as given in the first part of this paper,[1] the factor $f_2(f_\pm,\ t_+,\ D^{*\,0.5}_{\pm,\ \mathrm{eff}})$, i.e., the right-hand-side of Eq. 25 corresponds to

$$f_2\left(f_\pm,\ t_+,\ D^*_{\pm,\mathrm{eff}}\right)\Big|^{\text{ss polarization}}_{\text{transition period}} = \left[\frac{I_0\left(U_\mathrm{p}-\left(R_{\mathrm{LF,s}}-R_\mathrm{el}\right)I_\mathrm{s}\right)}{I_\mathrm{s}\left(U_\mathrm{p}-\left(R_{\mathrm{LF},0}-R_\mathrm{el}\right)I_0\right)}-1\right]\cdot\frac{\nu_+^2\,z_+^2}{\nu}\,\frac{\mathrm{F}^2}{\mathrm{R}\,T}\,\frac{A}{l}\,\varepsilon\,c_0\,R_\mathrm{el}. \quad [30]$$

where the superscript of the function f_2 indicates that the excitation phase is a steady-state polarization (rather than a pulse polarization) and the subscript indicates that the function is evaluated at the end of the polarization phase and at the beginning of the relaxation phase. An alternative formulation for Eq. 30 can be derived when the relation

for the initial low frequency resistance $R_{LF,0} = U_p / I_0$ is used:

$$f_2\left(f_{\pm},\ t_+,\ D^*_{\pm,\mathrm{eff}}\right)\Big|^{\text{ss polarization}}_{\text{transition period}} = \left[\frac{\left(U_p - \left(R_{LF,s} - R_{el}\right) I_s\right)}{I_s R_{el}} - 1\right]$$

$$\frac{\nu_+^2\, z_+^2}{\nu}\frac{F^2}{R\,T}\frac{A}{l}\varepsilon\, c_0\, R_{el} = \left[\frac{U_p}{I_s} - R_{LF,s}\right]\frac{\nu_+^2\, z_+^2}{\nu}\frac{F^2}{R\,T}\frac{A}{l}\varepsilon\, c_0 \qquad [31]$$

where the superscript of the function f_2 indicates that the excitation phase is a steady-state polarization and the subscript indicates that the function is defined by data from the very beginning of the polarization experiment and on the current/potential at the end of and after the steady-state polarization. As for the direct determination of the transference number, Eq. 31 is advantageous compared to Eq. 30, since less parameters have to be determined. Most important is this context is that the determination of the initial current flow I_0 which is required for Eq. 30 is challenging, as mentioned already before.

Initial time behavior of steady-state polarization (method #3).—The initial time behavior of the current following a steady-state polarization can also be used to determine the factor $f_1(f_{\pm},\ t_+,\ D^{*0.5}_{\pm,\ \mathrm{eff}})$ defined by Eq. 25. The basic derivation is given in Bard and Faulkner (chapter 5.5.1).[25] Based on the slope $m_{\#3}$ of the time dependent current given in Eq. 24, this factor, i.e., the right-hand-side of Eq. 25 corresponds to

$$f_1\left(f_{\pm},\ t_+,\ D^{*0.5}_{\pm,\ \mathrm{eff}}\right)\Big|^{\text{ss polarization}}_{\text{short-term pol.}} = \frac{z_+^2\ \nu_+^2}{4\ \nu}\sqrt{\pi}\frac{F^2}{R\ T}A\ \varepsilon\ c_0\ R_{LF,0}\frac{m_{\#3}}{I_0} \qquad [32]$$

where the superscript of the function f_1 indicates that the excitation phase is a steady-state polarization and the subscript indicates that the function is defined by the short-term behavior during the polarization phase. If the requirements for the linearization in Eq. 23 are not fulfilled, the additional information provided by Eq. 22 is limited, since the unknown factor H cannot be separated from the time t. The knowledge about the expected time behavior is also a good measure for the quality of experimental results.

Short-term relaxation from a steady-state concentration profile (method #4).—This method is based on the short-term relaxation behavior from a steady-state concentration profile as it has been used for the determination of the diffusion coefficient in the first part of this publication, starting with Eq. 16 in part I of this publication,[1] which can be reformulated to

$$U(t) = \underbrace{\frac{\nu}{Z_+^2\ \nu_+^2}\frac{R\ T}{F^2}\frac{l}{A\,\varepsilon\,c_0}\ I_s\ f_2(f_{\pm}, t_+, D^*_{\pm,\mathrm{eff}})}_{U(T_I)} \cdot \left(1 - \underbrace{\sqrt{\frac{16\ D^*_{\pm,\mathrm{eff}}(c_0)}{\pi l^2}}\sqrt{t}}_{m_{\#4}}\right) \qquad [33]$$

by means of Eq. 8[1] with Eq. 9[1] and Eq. 5 of this paper. The basic mathematical methods are given in Bard and Faulkner (chapter A.1, A.1.4).[25] Eq. 33 describes the linear relaxation of the cell potential $U(t)$ with respect to $\sqrt{t}$ from its initial value $U(T_I)$ at the current interruption time T_I. Therefore, the factor $f_2(f_{\pm},\ t_+,\ D^*_{\pm,\mathrm{eff}})$ described by the right-hand-side of Eq. 18 corresponds to

$$f_2\left(f_{\pm},\ t_+,\ D^*_{\pm,\mathrm{eff}}\right)\Big|^{\text{ss polarization}}_{\text{short-term relax.}} = \frac{z_+^2\nu_+^2}{\nu}\frac{F^2}{RT}\frac{A}{l}\varepsilon c_0\frac{U\ (T_I)}{I_s} \qquad [34]$$

where the superscript of the function f_2 indicates that the excitation phase is a steady-state polarization and the subscript indicates that the function is defined by the short-term behavior during the relaxation phase. Here, the cell potential $U(T_I)$ is the potential measured directly after current interruption. The idea behind it is that the cell potential U immediately reduces to $U\ =\ \Delta\Phi$ upon switching to open circuit, whereas the concentration difference Δc will not have changed significantly, since diffusion takes place on a slower time scale. However, it is also difficult to determine the correct potential $U(T_I)$ directly after current interruption, since parasitic contributions interfere with the signal as a result of the concentration difference Δc between anode and cathode. To overcome this problem, the linear relation of the cell potential $U(t)$ with respect to $\sqrt{t}$ as derived in Eq. 33 can be used to determine the cell potential $U(T_I)$ exactly at the current interruption time T_I by means of extrapolation. In addition, the observation of the time behavior gives a good indication for the quality of experimental data.

Long-term relaxation from a steady-state profile (method #5).—As for the determination of the diffusion coefficient described in in part I of this publication,[1] the long-term relaxation behavior of the steady-state concentration profile at current interruption time T_I provides information for the determination of the factor $f_2(f_{\pm},\ t_+,\ D^*_{\pm,\ \mathrm{eff}})$ defined by Eq. 18. In contrast to the determination of the diffusion coefficient, here a mathematical description for the prefactor C_1 is necessary (see Eq. 12 in Ref. 1). To be able to determine the prefactors C_{2n-1}, a steady-state concentration profile is required as initial condition, whereas it is arbitrary how the steady-state concentration profile is obtained. The derivation is discussed, e.g., in Polifke and Kopitz[27] (chapter 14.1) or in Ehrl.[23] As a result, the time dependent concentration difference $\Delta c(t)$ can be expressed as

$$\Delta c\,(t)\ =\ 8\frac{\Delta c\,(T_I)}{\pi^2}\exp\left(-\frac{\pi^2 D^*_{\pm,\mathrm{eff}}\,(c_0)}{l^2}t\right) \qquad [35]$$

Higher order terms are already neglected in Eq. 35. As usual, the expression for the concentration difference $\Delta c(t)$ given in Eq. 35 can be related to the potential U as explained in the section Theoretical background of the first part of this study:[1]

$$\ln U\,(t) = \ln\left(\frac{8\ \nu}{z_+^2\ \nu_+^2}\frac{R\ T}{F}\left[1 + \frac{\partial \ln f_{\pm}\,(c_0)}{\partial \ln c}\right](1 - t_+\,(c_0))\frac{1}{\pi^2}\frac{\Delta c\,(T_I)}{c_0}\right) - \frac{\pi^2 D^*_{\pm,\mathrm{eff}}\,(c_0)}{l^2}t\ =\ O\,(T_I)\ -\ \frac{\pi^2 D^*_{\pm,\mathrm{eff}}\,(c_0)}{l^2}t \qquad [36]$$

The long-term relaxation of the cell potential $\ln U(t)$ is proportional to the time t, whereas $O(T_I)$ stands for the first term on the right hand side of the equation, which corresponds to the value of $\ln U(t)$ extrapolated to time T_I in the relaxation phase (shown later in the lower inset of Figure 3b). Based on the constant factor $O(T_I)$ and Eq. 5, it is possible to find the following relationship for the right-hand-side of the factor $f_2(f_{\pm},\ t_+,\ D^*_{\pm,\ \mathrm{eff}})$ defined in Eq. 29

$$f_2\left(f_{\pm},\ t_+,\ D^*_{\pm,\mathrm{eff}}\right)\Big|^{\text{ss polarization}}_{\text{long-term relax.}} = \frac{z_+^2\ \nu_+^2}{8\ \nu}\ \pi^2\frac{F^2}{R\ T}\frac{A}{l}\varepsilon\ c_0\frac{\exp\ O\ (T_I)}{I_s} \qquad [37]$$

where the superscript of the function f_2 indicates that the excitation phase is a steady-state polarization and the subscript indicates that the function is defined by the long-term behavior during the relaxation phase.

Transference number based on data from a concentration cell and a ferrocene cell.—The transference number can also be determined by only two different types of experiments using a concentration cell and our previously described method for determining the thermodynamic factor $\left(\mathrm{TDF} \equiv \left[1 + \frac{\partial \ln f_{\pm}(c)}{\partial \ln c}\right]\right)$,[2] which is based on measuring the lithium concentration dependent potential of a lithium electrode versus ferrocene/ferrocenium as introduced in Landesfeind et al.[2] (further on referred to as ferrocene cell measurements). Based on a functional description of the TDF and the experimental data obtained by a concentration cell with transference[10] (see the above Concentration cell section), it is possible to solve for the

concentration dependent transference number from the relation given in Eq 28.

No restrictions regarding the concentration dependence of the transport parameters have been introduced so far. For a known functional description of the concentration dependent transference number $t_+(c)$ and for many experiments with different combinations of c_A and c_C covering the concentration range of interest, it is possible to determine the necessary functional parameters of the predefined function by numerical fitting. However, the functional description of the concentration dependent transference number $t_+(c)$ is usually not known a priori.

An alternative approach is to assume a constant transference number within a narrow concentration range centered about an average concentration of c_0, expressed as $c_0 \pm \delta c$ (with $\delta c \ll c_0$), so that one can determine an average transference number within a differential concentration range, i.e., $t_+(c_0 \pm \delta c)$. In this case, Eq. 28 can be approximated by

$$t_+(c_0 \pm \delta c) \approx 1 - \frac{z_+ \nu_+}{\nu} \frac{\mathrm{F}}{\mathrm{R}\,T} U \left[\int_{c_0-\delta c}^{c_0+\delta c} \left[1 + \frac{\partial \ln f_\pm(c)}{\partial \ln c} \right] \mathrm{d}(\ln c) \right]^{-1}$$

$$\approx 1 - \frac{z_+ \nu_+}{\nu} \frac{\mathrm{F}}{\mathrm{R}\,T} U \left[\int_{c_0-\delta c}^{c_0+\delta c} \mathrm{TDF}(c)\, \mathrm{d}(\ln c) \right]^{-1} \quad [38]$$

where TDF(c) represents the concentration dependent thermodynamic factor. Compared to all other methods introduced for the determination of the concentration dependent transference number $t_+(c)$, this last described approach requires no assumptions other than that the transference number can be assumed constant within a differential concentration range (i.e., that it be a smooth function with concentration). In the following this method is called the δc method.

Numerical Validation

In the following, the analytical expressions for the determination of the transference number t_+ introduced in the Theory section are analyzed in terms of their potential applicability for the experimental determination of the transference number by means of numerical simulations. Simulations are performed with a finite element research code developed at the Institute for Computational Mechanics at the Technical University of Munich. A detailed derivation to the used numerical methods is given in Ehrl.[23] The used governing equations as well as the corresponding boundary condition are given in the first part of this publication (Eq. 1 to 3 and Eq. 5) together with setup, boundary conditions, and parameters used for the simulation.[1]

Numerical analysis of the polarization experiments.—In the following, the transference number t_+ is calculated from the factors $f_1(f_\pm,\ t_+,\ D^*_{\pm,\mathrm{eff}})$ or $f_2(f_\pm,\ t_+,\ D^{*\ 0.5}_{\pm,\ \mathrm{eff}})$ defined in Eq. 25 and 29, respectively, the value of which be determined by the five different methods introduced in the Theory section and summarized in Table I. In contrast to the experimental approach introduced in the section Transference number based on data from a concentration cell and a ferrocene cell, in this section the transference number is not calculated based on data from a concentration cell but based on a given thermodynamic factor TDF(c). Our newly proposed method for the direct determination of the transference number will be discussed later on.

As shown in Figure 2, a pulse polarization experiment consists of a polarization and relaxation phase. During the short-term polarization phase, a short galvanostatic pulse with the current I_p is applied until the current interruption time T_I to establish a concentration gradient within the two-electrode cell. The concentration difference $\Delta c(t)$ between anode and cathode develops according to the Sand equation given in, e.g., Bard and Faulkner.[25] During this phase, the cell potential $U(t)$is influenced by the concentration difference $\Delta c(t)$, the current flow I_p, and kinetic effects at the electrode. At the time $t = T_I$, the current I_p is interrupted. During the following relaxation phase, the concentration difference $\Delta c(t)$ as well as the corresponding cell potential $U(t)$ slowly relax with time. In contrast to the polarization phase, the cell potential $U(t)$ is only influenced by the concentration difference $\Delta c(t)$. As long as the applied polarization current I_p is small, a linear relationship between the cell potential $U(t)$ and the concentration difference $\Delta c(t)$ can be assumed, as explained in the Theoretical background section in the first part of this publication.[1] In this case, the non-linearities introduced by the concentration dependence of the transport parameters and by the linearization of the natural logarithm are negligibly small.

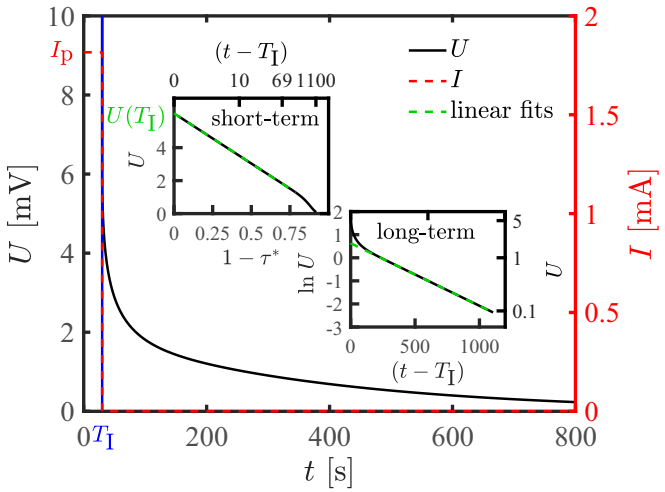

Figure 2. Simulation of a short-term galvanostatic pulse experiment according to the parameters given in Table I in Ref. 1 with a polarization time of 30 s, a polarization current density $i_p = 8 \cdot 10^{-3}$ mA mm^{-2} corresponding to the polarization current $I_p = 1.82$ mA and an initial electrolyte concentration $c_0 = 1$ M.

The expected linear behavior of the cell potential $U(t)$ with respect to the artificial time τ^* for the short-term relaxation as well as the linear behavior of the cell potential $\ln U(t)$ with respect to the time $(t - T_I)$ for the long-term relaxation are clearly observable for reasonable time periods in Figure 2. Since the determination of the factor $f_1(f_\pm,\ t_+,\ D^{*\ 0.5}_{\pm,\ \mathrm{eff}})|^{\text{pulse polarization}}_{\text{short-term relax.}}$ according to Eq. 26 (method #1) is based on the cell potential $U(T_I)$ at the current interruption time, the linearity in τ^* can be used to more accurately determine the cell potential $U(T_I)$ at current interruption time T_I. This is particularly important for experiments where the cell potential $U(t)$ is influenced by additional parasitic contributions as, e.g., the discharge of the double layer. While not evident from the upper inset in Figure 2 by eye, the simulated transient approaches the real axis for long times, i.e., $1 - \tau^* \to 1$, which is automatically fulfilled as the potential relaxes to 0 mV for long real times.

A steady-state polarization experiment also consists of two phases. In the first phase shown in Figure 3a, the two-electrode cell is polarized with a constant cell potential U_p (black line) until the steady-state current I_s is established (red dashed line). The steady-state current I_s is reached once a steady-state concentration profile within the cell is established. The electrode kinetics are modeled by a Butler-Volmer law without concentration dependence (i.e., $\gamma = 0$), resulting in a constant interface resistance R_I due to the linearity of the Butler-Volmer law for small surface overpotentials η. The initial current I_0 is the maximum current value obtained during polarization, since the concentration overpotential is negligibly small in the beginning. Due to an increasing concentration overpotential with time, the current $I(t)$ decreases with time until the steady-current I_s is reached. For concentrated electrolyte solutions, a steady-state experiment can be used to determine the factor $f_2(f_\pm,\ t_+,\ D^*_{\pm,\mathrm{eff}})|^{\text{ss polarization}}_{\text{transition period}}$ by method #2. The short-term relaxation of the current $I(t)$ is linear with respect to $\sqrt{t}$, with the slope $m_{\#3}$ (see inset of Figure 3a). As shown in the section Initial time behavior of steady-state polarization (method #3), this is already an approximation for the more complex function $\exp(H^2\, t)\mathrm{erfc}(H\,\sqrt{t})$ given in Eq. 23. Based on the here obtained

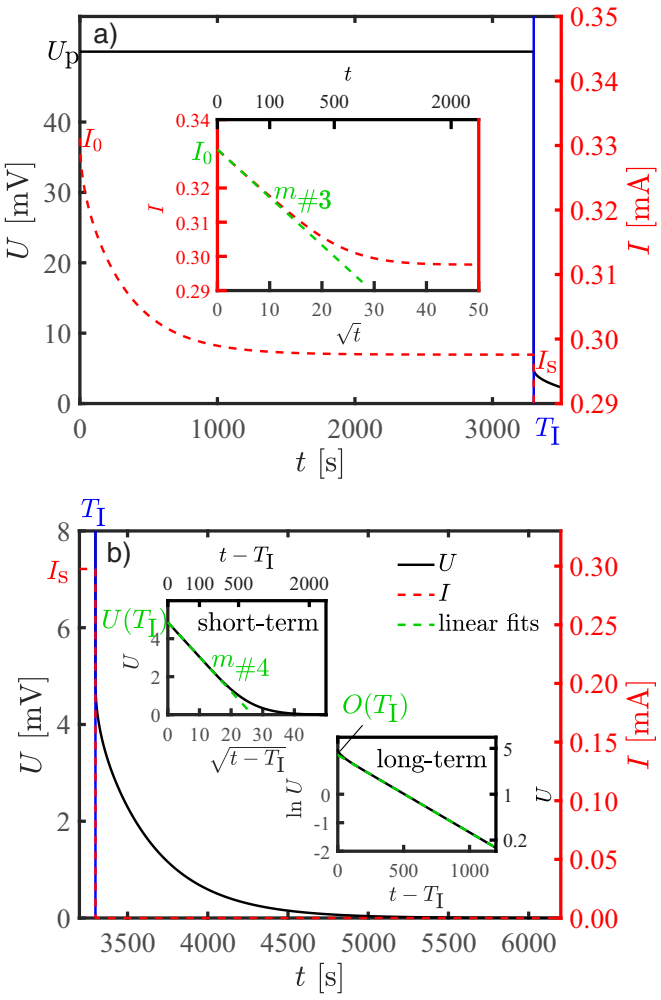

Figure 3. Simulation of a steady-state polarization experiment according to the parameters given in Table II in Ref. 1, with a polarization time $T_I = 3300$ s, a polarization potential $U_p = 50$ mV, and an initial electrolyte concentration $c_0 = 1$ M: a) polarization phase showing potential (black line) and current (red dashed line) vs. time as well as current vs. $\sqrt{t}$; b) relaxation phase showing potential (black line) and current (red line) vs. time, with the insets showing the short-term and long-term relaxation of the potential.

slope $m_{\#3}$, the factor $f_1(f_\pm,\ t_+,\ D^*_{\pm,\ \mathrm{eff}}{}^{0.5})|^{\text{ss polarization}}_{\text{short-term pol.}}$ can be calculated by Eq. 32.

Once the steady-state current I_s is reached, the polarization of the cell is interrupted and the relaxation phase of the steady-state experiment starts. During the relaxation phase, the cell potential $U(t)$ decreases continuously as shown in Figure 3b. The time for the relaxation process is much longer than in a pulse experiment because of the larger changes to the salt concentration profile. The long-term behavior of the relaxation process is characterized by a linear relationship between $\ln U$ and $(t - T_I)$ (see lower inset in Figure 3b), from which the value of $O(T_I)$ can be obtained by extrapolation to $(t - T_I) = 0$; from the latter, the factor $f_2(f_\pm,\ t_+,\ D^*_{\pm,\mathrm{eff}})|^{\text{ss polarization}}_{\text{long-term relax.}}$ can be calculated according to Eq. 37 (method #5). Different from a pulse experiment, the short-term relaxation behavior of the cell potential $U(t)$ in a steady-state experiment is proportional to $\sqrt{t}$, with the slope m_{sqrt} (see upper inset in Figure 3b). The extrapolated cell potential $U(T_I)$ at current interruption time T_I can be used to calculate the factor $f_2(f_\pm,\ t_+,\ D^*_{\pm,\mathrm{eff}})|^{\text{ss polarization}}_{\text{short-term relax}}$ with Eq. 34 (method #4).

Validation of the different parameter determination methods.— In the following, we numerically analyze how well the assumptions made in the theoretical part of this work are met when trying to determine the various transport parameters from simulated transients. For example, the influence of non-negligible concentration variations between anode and cathode and their impact on the determined diffusion coefficients and transference numbers will be evaluated in the following.

Influence of the magnitude of the concentration difference.—In Figure 4, the influence of the concentration difference $\Delta c(T_I) = c_A\ (T_I) - c_c(T_I)$ between the two electrodes at current interruption time T_I is investigated numerically for a bulk salt concentration of $c_0 = 1$ M. In the case of a steady-state experiment, the concentration difference $\Delta c(T_I)$ defined by the polarization cell potential U_p is the only design parameter influencing the quality of the determined transference number.

All methods summarized in Table I are capable to determine the correct transference number t_+ for a small concentration difference $\Delta c(T_I)$. For higher concentration differences $\Delta c(T_I)$, it is not possible to determine the transference accurately by the short-term transient of a steady-state polarization experiment (method #3; red diamond in Figure 4), which is based on the initial time behavior of the current $I(t)$ during the polarization phase in a steady-state experiment. In this case, the initial time behavior is not just influenced by concentration dependent transport parameters and the linearization of the natural logarithm introduced in Eq. 9 in part I of this publication (Ref. 1), but also by the basic characteristic of the electrode kinetics. For an increasing concentration difference $\Delta c(T_I)$ and therefore an increasing current flow, the Butler-Volmer law cannot be assumed linear anymore, which violates the linear boundary condition used for the derivation of Eq. 32. As a result, the linear behavior of the current $I(t)$ can only be observed clearly for the lowest polarization potential U_p (i.e., for the lowest concentration difference). For this method, the linearity of the current vs. $\sqrt{t}$ (see inset of Figure 3a) is a very good indication for the reliability of experimentally measured data, and therefore the method is only considered in the Results and discussion section, if a clear linear trend is observable. All remaining methods are accurate up to relative concentration differences $\Delta c(T_I)/c_0$ of about

Table I. Overview of the five analytical methods described in the text for the determination of the transference number from polarization cell experiments. Here, the right-hand-side of the definitions of the factors $f_1(f_\pm,\ t_+,\ D^*_{\pm,\ \mathrm{eff}}{}^{0.5})$ (Eq. 25) and $f_2(f_\pm,\ t_+,\ D^*_{\pm,\ \mathrm{eff}})$ (Eq. 29) equate to the terms shown in this table. The superscripts in the functions f_1 and f_2 refer the excitation phase (either pulse or steady-state polarization) and the subscripts refers to where the function is being evaluated (from the short- or long-term behavior during either the excitation or the subsequent relaxation phase).

method #1	$f_1(f_\pm,\ t_+,\ D^*_{\pm,\ \mathrm{eff}}{}^{0.5})\|^{\text{pulse polarization}}_{\text{short-term relax.}}$	$\frac{z_+^2\ \nu_+^2}{4\ \nu}\sqrt{\pi}\frac{\mathrm{F}^2}{\mathrm{R}\ T}\ A\ \varepsilon\ c_0\frac{U(T_I)}{I_p\sqrt{T_I}}$	Eq. 26
method #2	$f_2(f_\pm,\ t_+,\ D^*_{\pm,\mathrm{eff}})\|^{\text{ss polarization}}_{\text{transition period}}$	$\left[\frac{U_p}{I_s} - R_{\mathrm{LF,s}}\right]\frac{\nu_+^2\ z_+^2}{\nu}\frac{\mathrm{F}^2}{\mathrm{R}\ T}\frac{A}{l}\varepsilon\ c_0$	Eq. 31
method #3	$f_1(f_\pm,\ t_+,\ D^*_{\pm,\ \mathrm{eff}}{}^{0.5})\|^{\text{ss polarization}}_{\text{short-term pol.}}$	$\frac{z_+^2\ \nu_+^2}{4\ \nu}\sqrt{\pi}\frac{\mathrm{F}^2}{\mathrm{R}\ T}\ A\ \varepsilon\ c_0\ R_{\mathrm{LF},0}\frac{m_{\#3}}{I_0}$	Eq. 32
method #4	$f_2(f_\pm,\ t_+,\ D^*_{\pm,\mathrm{eff}})\|^{\text{ss polarization}}_{\text{short-term relax.}}$	$\frac{z_+^2\ \nu_+^2}{\nu}\frac{\mathrm{F}^2}{\mathrm{R}\ T}\frac{A}{l}\varepsilon\ c_0\frac{U(T_I)}{I_s}$	Eq. 34
method #5	$f_2(f_\pm,\ t_+,\ D^*_{\pm,\mathrm{eff}})\|^{\text{ss polarization}}_{\text{long-term relax.}}$	$\frac{z_+^2\ \nu_+^2}{8\ \nu}\pi^2\frac{\mathrm{F}^2}{\mathrm{R}\ T}\frac{A}{l}\varepsilon\ c_0\frac{\exp\ O(T_I)}{I_s}$	Eq. 37

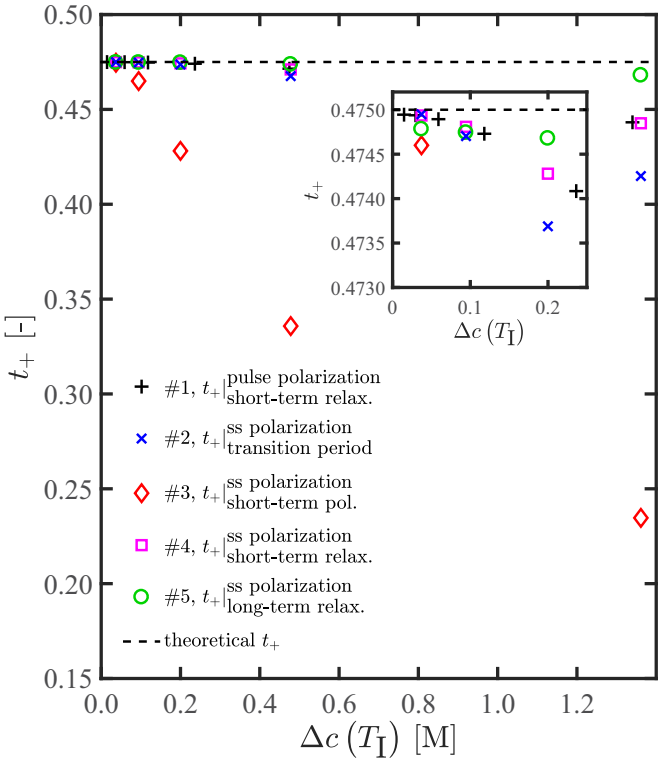

Figure 4. Influence of the concentration difference $\Delta c(T_\mathrm{I})$ at the current interruption time on the determined transference number for a $c_0 = 1$ M electrolyte solution (see Table II in Ref. 1 for other simulation parameters).

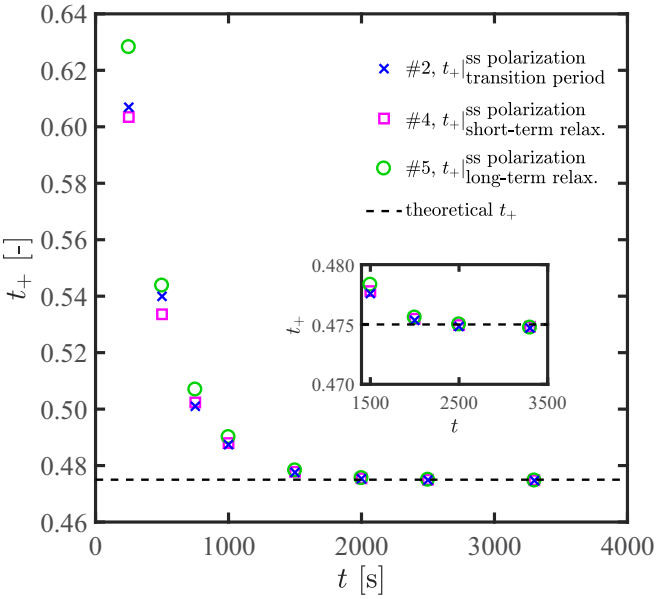

Figure 5. Influence of the polarization time in nominally steady-state polarization experiments on the determined transference number t_+ for a polarization potential $U_\mathrm{p} = 50$ mV and an initial concentration $c_0 = 1$ M (see Table II in Ref. 1 for simulation parameters).

20%. Particularly the method $f_2(f_\pm,\ t_+,\ D^*_{\pm,\mathrm{eff}})|^{\text{ss polarization}}_{\text{long-term relax.}}$ (green circles in Figure 4) is very accurate for higher polarization potentials, since it is based on the long-term relaxation behavior, where the requirement of a small concentration difference between the electrodes is automatically fulfilled at long times. Similar results are obtained for a bulk salt concentration of $c_0 = 0.01$ M and $c_0 = 2.0$ M which are not shown explicitly in this publication.

As explained under Direct determination of the transference number by steady-state polarization experiments, the transference number t_+ can also be calculated directly from Eq. 18 for dilute electrolyte solutions. The method is based on the steady-state current I_s, the steady-state low frequency resistance R_LF, the electrolyte resistance R_el and the polarization potential U_p. For the smallest polarization potential U_p, the calculated transference numbers t_+ are 0.32, 0.525 and 0.465 for the concentrations 0.01 M, 1 M and 2 M, respectively. For these concentrations the transference numbers resulting from the defined simulation parameter given in Table II in part I of this publication (Ref. 1) are 0.402, 0.475 and 0.3. Even for smaller concentrations c_0, the expected transference number t_+ cannot be determined correctly, since the mathematical condition given in Eq. 17 is not fulfilled for the used parameter set and for $c_0 \to 0$. Theoretically, Eq. 17 could be used as an additional condition for the determination of the parameter set for very dilute electrolyte solutions (i.e., as $c_0 \to 0$), but the experimental methods discussed in the first and the second part of this paper are not designed to determine the transport parameters at very dilute solutions, as will be explained in Results and discussion.

Influence of a non steady-state concentration profile on the determination of the transference number.—Although the concentration difference $\Delta c(T_\mathrm{I})$ at the current interruption time is the only design parameter in a steady-state experiment which can be influenced by experimental design, it is possible that a non-steady-state concentration profile at the current interruption time for an intended steady-state polarization experiments leads to an incorrect determination of the transference number. A non-steady-state concentration profile originates from too short polarization times or from the continuous variation of the interface resistance R_I during a steady-state experiment. The influence of a non-steady-state concentration profile as a result of too short polarization times on the determined transference number is depicted in Figure 5 for all corresponding methods. The method $t_+|^{\text{ss polarization}}_{\text{short-term pol.}}$ (#method 3) is not considered here since it does not rely on a steady-state concentration profile but only on the short-term behavior of the steady-state polarization experiment. The presented numerical data are the results for a bulk salt concentration of $c_0 = 1$ M polarized with a cell potential of $U_\mathrm{p} = 50$ mV. This applied cell potential results in concentration difference $\Delta c(T_\mathrm{I})$ at current interruption (steady-state) of 0.1 M, which corresponds to $\frac{\Delta c(T_\mathrm{I})}{c_0} = 10\%$. The error for the transference number t_+ based on a polarization time between 1000 and 1500 s is still below 5% (see Figure 5). For polarization times $t > 1500$ s, the correct transference number is obtained for all analysis methods. For short polarization times $t < 1000$ s, the error in the transference number t_+ increases rapidly (see Figure 5), because of the large deviation from the steady-state concentration profile.

The relaxation of the current $I(t)$ during the polarization is shown in Figure 6a, while Figure 6b shows the relaxation behavior of the relative cell potential $U(t)/U(T_\mathrm{I})$ with respect to $\sqrt{t}$ for differently chosen polarization times (indicated by the dashed vertical lines in Figure 6a). Only after a polarization time of $t \approx 1000 - 1500$ s, the current $I(t)$ approaches its steady-state value as shown in Figure 6a and the relative cell potential $U(t)/U(T_\mathrm{I})$ exhibits a clear linear behavior with respect to $\sqrt{t}$, as depicted in Figure 6b. While for shorter polarization times, the current is obviously still quite different from its steady-state value (see Figure 6a), the corresponding non-linearity of the relative cell potential $U(t)/U(T_\mathrm{I})$ during subsequent relaxation is unfortunately not very apparent, as is illustrated by the $U(t)/U(T_\mathrm{I})$ response for a polarization time of $T_\mathrm{I} = 500$ s (see blue dash-dotted line in Figure 6b). For longer polarization times of $T_\mathrm{I} = 1000$ s, $T_\mathrm{I} = 1500$ s, and $T_\mathrm{I} = 3000$ s, the shape of the scaled relaxation curve $U(t)/U(T_\mathrm{I})$ cannot be differentiated from Figure 6b (corresponding magenta, red and black lines overlap). Therefore, it is important for a steady-state experiment to carefully observe the relaxation behavior of the current $I(t)$ during polarization as well as the relaxation behavior of the cell potential $U(t)$ after current interruption in order to ensure a steady-state concentration profile. Numerical simulations indicate that a similar behavior can be expected for a concentration profile

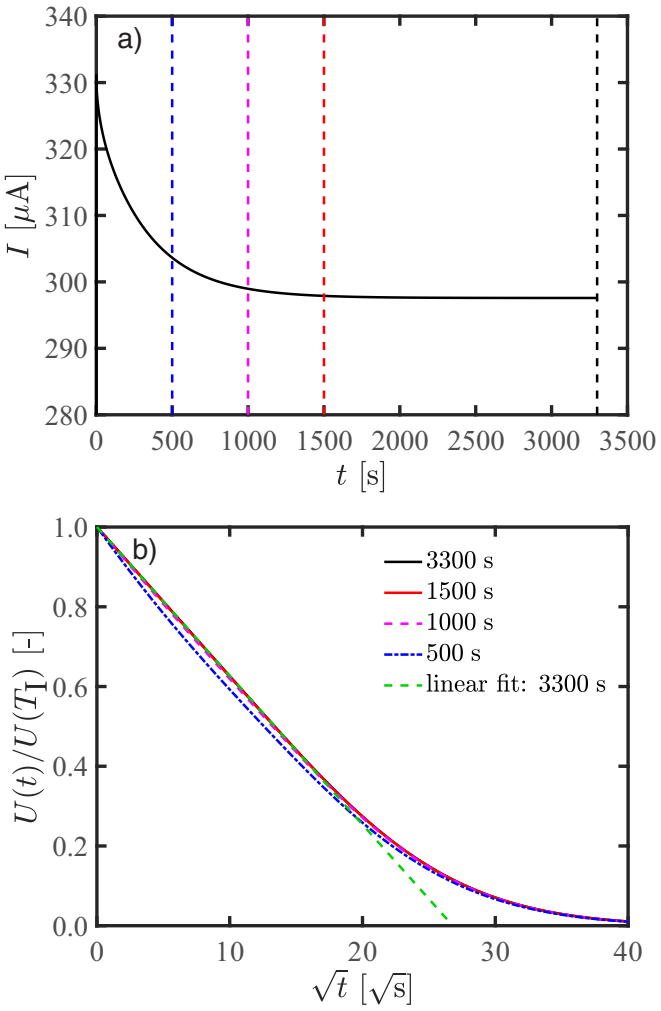

Figure 6. Polarization and relaxation phase of a nominally steady-state polarization experiment according to the simulation parameters given in Table II of Ref. 1 with the polarization potential $U_\mathrm{p} = 50$ mV and the intial concentration $c_0 = 1$ M: a) current I over time t during the initial polarization phase; b) relative cell potential $U(t)/U(T_\mathrm{I})$ vs. $\sqrt{t}$ during the relaxation phase following the initial polarization after different current interruption times T_I, indicated by the dashed vertical lines in a). Transients for T_I= 3300 s, 1500 s, and 500 s in b) overlap in the entire time range shown and are not distinguishable by eye.

deviating from its steady-state value as a result of a continuously varying interface resistance R_I.

Influence of the polarization time on the determined transference number in a pulse experiment.—For the determination of the transference number $t_+|^{\text{pulse polarization}}_{\text{short-term relax.}}$ (#method 1), a galvanostatic pulse experiment has to be performed as indicated in Figure 2. In this experimental setup, the concentration difference $\Delta c(T_\mathrm{I})$ is influenced by the polarization current I_p and the polarization time defined by the current interruption time T_I.[25] As shown discussed in the section Influence of the magnitude of the concentration difference, both design parameters have to be chosen so that the relative concentration difference $\Delta c(T_\mathrm{I})/c_0$ does not exceed 20%. Additionally, the current interruption time T_I has to be short enough to ensure that the semi-infinite boundary condition used for the derivation of Eq. 26 is not violated. For longer polarization times, the concentration profile will slowly approach the steady-state case, which must not happen for a pulse experiment. In Figure 7, the calculated transference number t_+ with respect to the polarization time for a 1 M electrolyte solution polarized with a current density of $I_\mathrm{p} = 0.454$ mA is depicted.

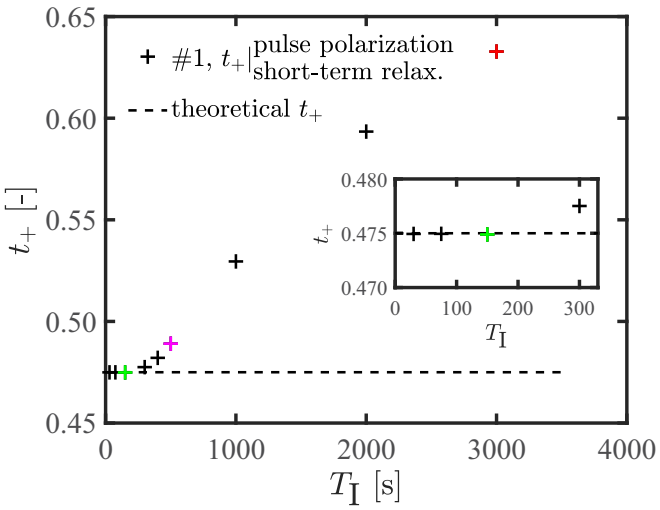

Figure 7. Influence of the polarization time in a pulse experiment on the determined transference number t_+ for a polarization current of $I_\mathrm{p} = 0.454$ mA and an initial concentration $c_0 = 1$ M (see Table II in Ref. 1 for simulation parameters). The colored crosses at times 150 s, 500 s, and 3000 s correspond to the coloring of the transients plotted in Figure 8.

As can be seen in Figure 7, for polarization times of about 500 s, the deviation of the determined transference number is below 5%. The corresponding relaxation behavior of the relative cell potential $U(t)/U(T_\mathrm{I})$ with respect to the artificial time $1 - \tau^*$ and the time $\sqrt{(t - T_\mathrm{I})}$ are shown in Figure 8a and Figure 8b, respectively. Figure 8b is added, since for longer polarization time the concentration profile approaches steady-state which results in a linear relaxation behavior of the cell potential with respect to time $\sqrt{(t - T_\mathrm{I})}$. Additionally, simulations with shorter and longer polarization times are shown to visualize the differences.

Figure 8a depicts the short-term relaxation of the potential after a pulse polarization which can be used for evaluation of the transference number according to method #1 (see Eq. 26). This method is valid for short polarization times, i.e., a steady-state concentration profile is not reached yet but only the electrolyte concentration at the vicinity of the electrodes is changed, which is the case for the 150 s polarization (green line in Figure 8). For this short polarization time, the linear behavior in Figure 8a is prominent and the typical S-shape can be observed (compare inset in Figure 2). This shape, i.e., an initial linear slope (green line between 0 and 0.5), followed by a steeper decline (green line between 0.7 and 0.8) eventually approaching the x-axis (green line beyond 0.8), cannot be observed for the longest polarization time of 3000 s. Note that the S-shape in Figure 8a and in Figure 2 is only partly visible as this would require much longer simulation times, the slow approach to the real axis will be automatically fulfilled as $U \to 0$ mV for $t \to \infty$. Although for all polarization times an initially linear behavior can be observed, the steeper section of the potential relaxation is missing for long pulse durations (compare Figure 8a for pulse duration of 3000 s, red line), making this part a distinguishable feature for whether or not the transference number can be determined by using method #1. Figure 8b also shows the short-term behavior of the potential relaxation, i.e., the same data as in Figure 8a but plotted on a different scale. Comparison of Figure 8b with the inset of Figure 3b shows that a steady state concentration profile is reached for the polarization time of 3000 s, evident through the linear potential relaxation with $\sqrt{(t - T_\mathrm{I})}$ (compare black dashed linear trend in Figure 8b). From Figure 8 it is concluded that method #1 yields the most accurate results for the transference number when the potential relaxation after a pulse polarization with $1 - \tau^*$ shows the typical S-shape and when the same relaxation data do not show a pronounced linear behavior with $\sqrt{(t - T_\mathrm{I})}$ which can be seen exemplarily for the shortest polarization time of 150 s in Figure 8. While

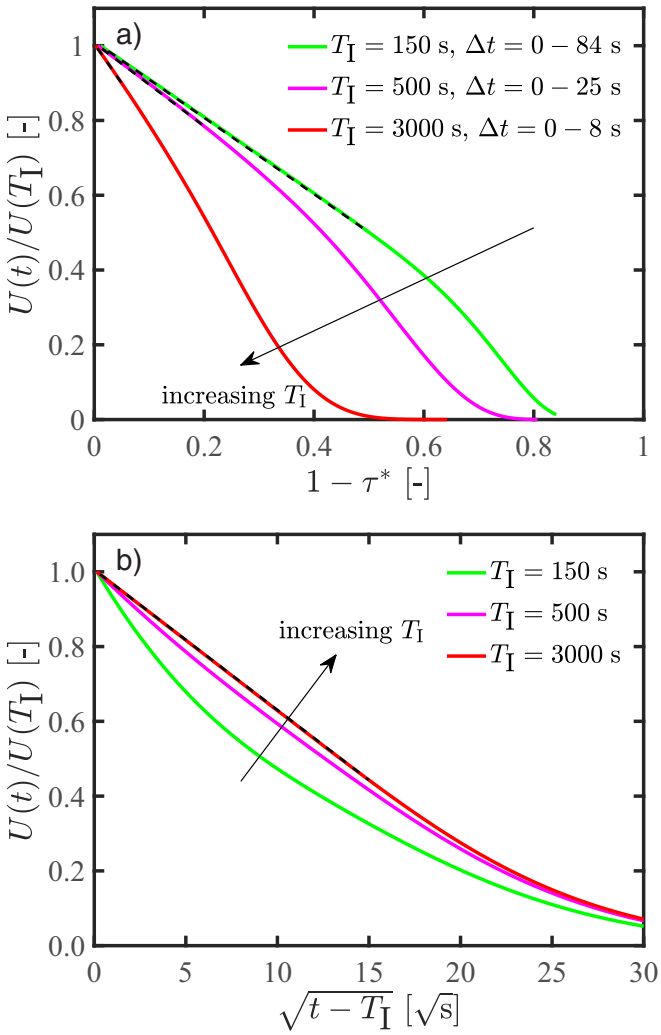

Figure 8. Relaxation behavior of the relative cell potential $U(t)/U(T_I)$ after pulse experiment with a polarization current of $I_p = 0.454$ mA and an initial concentration $c_0 = 1$ M (see Table II in Ref. 1 for simulation parameters): a) the artificial time $1 - \tau^*$ and b) the time $\sqrt{(t - T_I)}$. Black dashed lines indicate the linear ranges that would be used for analysis of experimental data. In a) the real times are given in the respective legends, in b) only the linear trend for $T_I = 3000$ s can be used for analysis.

in the computer simulations shorter polarization times yield smaller errors (compare Figure 7), in an experiment the experimental noise of, e.g., the potential measurement has to be considered and the pulse duration cannot be too short as the resulting concentration change would be too small to be measurable without large uncertainty.

Results and Discussion

In this section, we will present our new proposed method to determine the transference number from two sets of experiments: concentration cell measurements with a series of small concentration differences combined with the concentration dependent thermodynamic factor (TDF) obtained with a cell in which the potential of a lithium electrode vs. a ferrocene/ferrocenium reference electrode is measured for different lithium salt concentrations (referred to as "ferrocene cell").[2] The concentration dependence of the transference number obtained by this method will subsequently be compared with the values obtained by the various polarization methods (see Table I) in combination with a concentration cell.

Transference number based on data from a concentration cell and a ferrocene cell.—In the following, the transference number

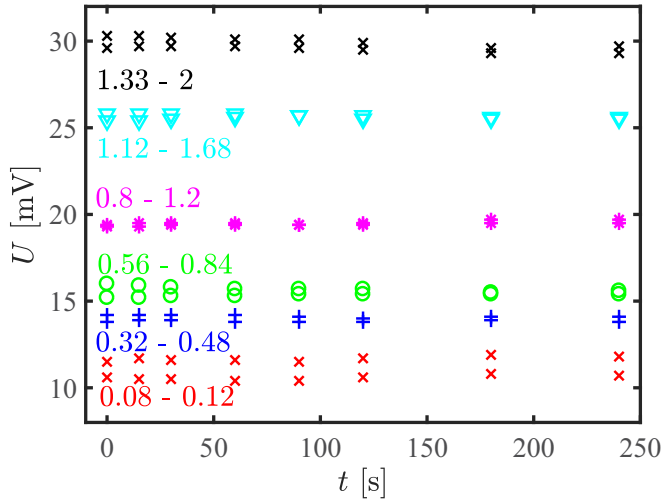

Figure 9. Exemplary concentration cell potentials for the δc method versus time for EC:DEC (1:1 w:w) based electrolytes, measured for differential $LiClO_4$ concentrations as given in the figure. Measurement were conducted in a temperature controlled glove box with the cell setup depicted in Figure 1. Two individual sets of measurements for each pair of concentrations (see legend in the figure) are depicted to illustrate the reproducibility of the measurements.

of the lithium ion will be determined from measurements with a concentration cell (see Figure 1) in combination with the concentration dependent thermodynamic factor obtained by ferrocene cell measurements for the same electrolyte taken from Figure 9 in the study by Landesfeind et al.[2] Exemplary concentration cell potentials (corresponding to concentration overpotentials) depicted in Figure 9 show the stability of the potential measurements over time and their reproducibility.

The measured concentration overpotentials are linearly extrapolated to t = 0 s and the obtained initial potentials were averaged. The variation between repeat measurements is <1.5 mV at the beginning of the measurement and differs by <1.5 mV over the course of the measurement period. As the standard deviations of latter averages are generally smaller than the accuracy of the potential measurement of 0.3 mV, only the error from the measurement device is considered in the following. Figure 9 shows exemplary measurements of our here proposed δc method, for which the concentration overpotentials between two electrolytes of similar concentrations centered about an average concentration $c_0 \pm \delta c$ are measured, whereby δc is a sufficiently small such that the transference number can be assumed constant. The advantage of this approach is that no functional for the transference number has to be assumed and that a pointwise calculation is possible to yield the average transference number $t_+(c_0 \pm \delta c)$ within a sufficiently small δc range as shown by Eq. 38. Analogously to Figure 9, also concentration cells with larger concentration differences were measured, with the results being displayed in Figure 11. As the concentration overpotential for larger concentration differences increases, the relative error gets smaller and exemplary data are thus not shown.

In combination with Eq. 38 and with the concentration dependent thermodynamic factor for this electrolyte (see Figure 9 in Reference 2), the values of $t_+(c_0 \pm \delta c)$ vs. concentration depicted in Figure 10 can be obtained, whereby the used values of δc are represented by the x-error bars. Additionally, Figure 10 shows a quadratic fit based on data from the δc method, with its 95% confidence interval as gray highlighted area. The obtained functional description is given by

$$t_+ \ (c \pm \delta c) = -0.117\, c^2 + 0.171\, c + 0.472 \qquad [39]$$

The transference number shows a peak around a concentration of 0.8 M $LiClO_4$, with a value of $t_+ \approx 0.53$. For $c \to 0$, we find a value of $t_+ \approx 0.47$, while at 2 M $LiClO_4$ concentration the transference number drops to $t_+ \approx 0.35$. For the following analysis, the transference number

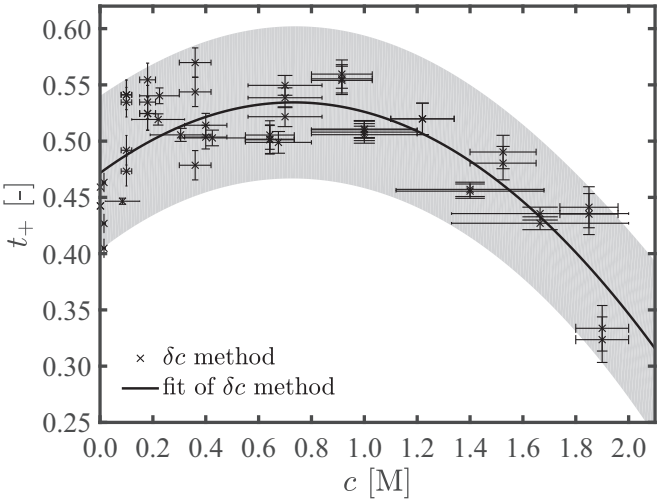

Figure 10. Concentration dependence of the transference number via the δc method, i.e., determined by Eq. 38 from concentration cell data based on small concentration variations ($c_0 \pm \delta c$) and from the concentration dependent thermodynamic factor obtained by ferrocene cell measurements (from Figure 9 in Ref. 2). Vertical error bars represent the effect of the 0.3 mV error of the concentration cell measurements, while the horizontal error bars indicate the experimentally chosen concentration variation δc. The black solid line is a quadratic fit (see Eq. 39) of all the depicted $t_+(c_0 \pm \delta c)$ data and the gray region indicates the 95% confidence interval. The electrolyte used is $LiClO_4$ in EC:DEC (1:1 w:w) and measurements are done inside a temperature controlled glove box.

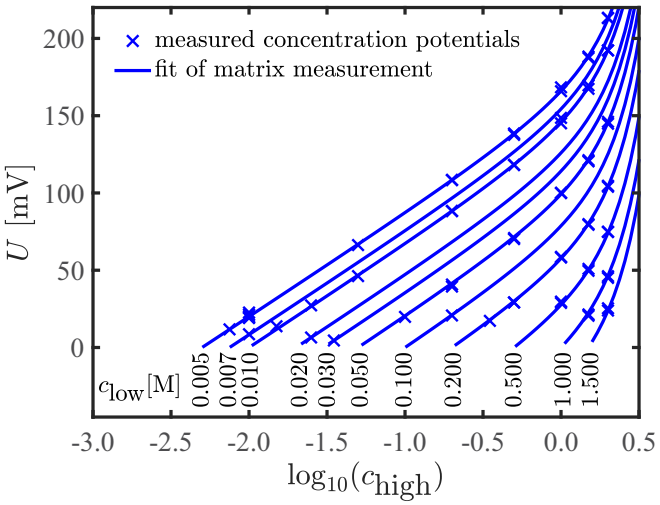

Figure 11. Concentration overpotentials U resulting from a set of permutations of low (c_{low}) and high (c_{high}) salt concentrations measured in the concentration cell setup (see Figure 1). Lower concentrations are indicated below the fit lines inside the figure, while higher concentrations are plotted logarithmically (base 10) on the x-axis. The electrolyte used is $LiClO_4$ in EC:DEC (1:1 w:w) and measurements are done inside a temperature controlled glove box. The solid lines are a numerical fit to Eq. 28.

determined with the δc method is used and shown for comparison. These data will be compared to the literature later on.

Transference number via polarization cell and concentration cell experiments.—In the following, the procedure for the determination of the concentration dependent transference number $t_+(c)$ based on polarization experiments in combination with concentration cell measurements, as outlined in the section Determination of the transference number based on the Sand equation, a concentration cell, and a known diffusion coefficient is investigated. The binary diffusion coefficient $D_\pm(c)$ is obtained from polarization cell experiments in symmetrical Li-Li cells as discussed in Ehrl et al.[1] The factors $f_1(f_\pm,\ t_+,\ D^{*}_{\pm,\ \mathrm{eff}}{}^{0.5})$ or $f_2(f_\pm,\ t_+,\ D^{*}_{\pm,\ \mathrm{eff}})$ given in Eqs. 25 and 29, respectively, are obtained by experiments in a polarization cell using the various methods discussed in the sections Sand equation and Alternative methods for the determination of the transference number (summarized in Table I). The factor $\left[1+\frac{\partial \ln f_\pm(c)}{\partial \ln c}\right](1-t_+(c))$ (see Eq. 28) is determined from concentration cell experiments in form of a continuous functional description. This will be described in the following.

The required concentration overpotential data were measured in a concentration cell as described in the Experimental section, with exemplary results shown in Figure 9. To be able to extract the factor $\left[1+\frac{\partial \ln f_\pm(c)}{\partial \ln c}\right](1-t_+(c))$, a set of concentration cell experiments was conducted (over 70 concentration cells were measured, of which most combinations were conducted at least twice). Figure 11 shows the recorded concentration cell potentials U for different lower salt concentrations c_{low} versus the higher salt concentration c_{high}, whereby each line corresponds to a fixed value of c_{low}.

The solid lines in Figure 11 represent the numerical fit of the measured concentration cell potentials using Eq. 28. As a result of the integral in Eq. 28, a functional description has to be assumed a priori for the factor $\left[1+\frac{\partial \ln f_\pm(c)}{\partial \ln c}\right](1-t_+(c))$. It is found that a third order polynomial represents the experimental data best, polynomials with a lower order result in a poor representation of measured data, while higher order polynomials improve the fit quality only insignificantly and may result in numerical oscillations. The solid lines in Figure 11 thus represent an overall third order polynomial fit of the concentration cell data with the following numerical result

$$\left[1+\frac{\partial \ln f_\pm(c)}{\partial \ln c}\right](1-t_+(c)) = 0.105\,c^3 + 0.042\,c^2 + 0.205\,c + 0.557 \qquad [40]$$

Based on this numerical fit, the transference number at infinite dilution is $t_+(c \to 0) = 0.44$, since the thermodynamic factor (i.e., the left-hand-term in square brackets) under these conditions approaches unity. This is in good accordance with the the δc method, which yields $t_+(c \to 0) = 0.47$ (see Figure 10 and Eq. 39). The factors $f_1(f_\pm,\ t_+,\ D^{*}_{\pm,\ \mathrm{eff}}{}^{0.5})$ or $f_2(f_\pm,\ t_+,\ D^{*}_{\pm,\ \mathrm{eff}})$ are determined based on experiments in a polarization cell. As presented in the section Numerical validation, five different analytical expressions based on pulse and steady-state experiments are considered for the determination of $f_1(f_\pm,\ t_+,\ D^{*}_{\pm,\ \mathrm{eff}}{}^{0.5})$ or $f_2(f_\pm,\ t_+,\ D^{*}_{\pm,\ \mathrm{eff}})$. The analytical expressions for these five methods are summarized in Table I and their accuracy was demonstrated by means of numerical simulations in the section Validation of the different parameter determination methods. In the following, the experimentally determined transients are shown exemplarily for the salt concentrations 0.01 M, 0.5 M, 1.5 M, and 2 M. Analysis of the high frequency resistance showed a steady decrease for the 0.01 M electrolyte over the course of the experiments, which we ascribe to side reactions which alter the electrolyte composition (mostly via continuous SEI formation caused by reaction with the freshly plated lithium during the polarization phase). In conclusion, because all factors in Table I depend on the initial salt concentration c_0, the recorded transients for the nominally 0.01 M electrolytes are only shown for the benefit of the reader and are not analyzed for their transference number in the case of polarization cell experiments. Physical vibrations, e.g. from glove box or temperature chambers, play negligible role as a porous medium rather than a free liquid electrolyte is used in the experimental setup. Gas generation is limited due to the small surface area of the lithium electrodes and at ambient temperatures, electrolyte evaporation plays no role in the tight two electrode cells and is negligible over the time of the transference number measurements (vapor pressure of linear carbonates <50 mbar). First of all, the factor $f_1(f_\pm,\ t_+,\ D^{*}_{\pm,\ \mathrm{eff}}{}^{0.5})$ can be determined from pulse experiments based on the Sand equation given in Eq. 26, which requires only the cell potential $U(\tau_I)$ at current interruption time. The accuracy of the method is improved by the observation of the short term relaxation

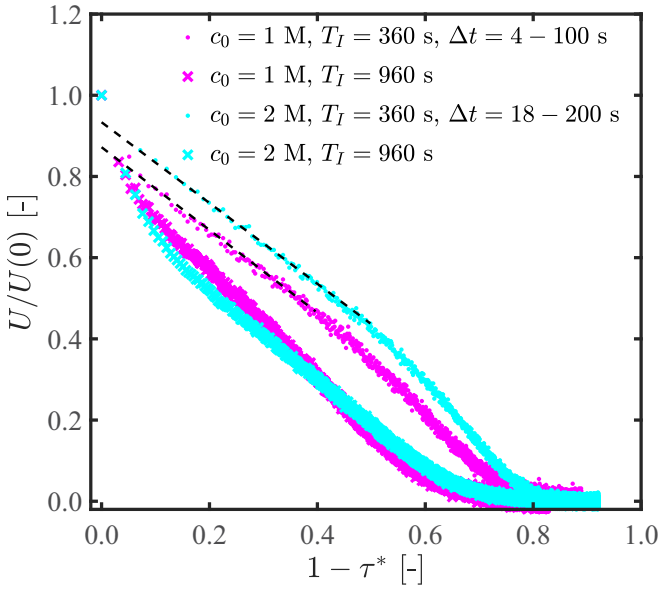

Figure 12. Exemplary relaxation after a current pulse of $i_p = 0.5$ mA (0.22 mA/cm^2) for T_1 values of 360 s or 960 s in either 1.0 M or 2.0 M $LiClO_4$ in EC:DEC (1:1 w:w). This was measured in the two-electrode setup shown in Figure 1 of Ref. 1.

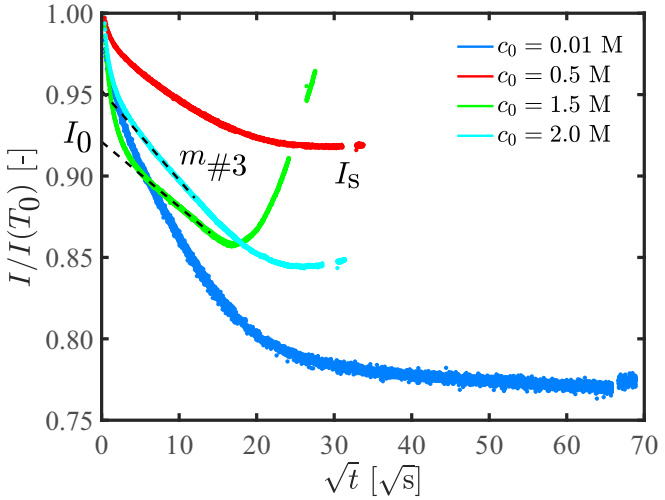

Figure 13. Exemplary steady state polarization current transients for 0.01 M, 0.5 M, 1.5 M, and 2.0 M $LiClO_4$ in EC:DEC (1:1 w:w) at constant polarization of 50 mV in the two-electrode cell shown in Figure 1. The gaps in the curves toward the end of the potentiostatic polarization procedure are due to impedance measurements which were conducted during that time.

after current interruption, which exhibits a linear relationship with respect to the artificial time τ^* defined in Eq. 27. In Figure 12, four normalized potential transients (two different $LiClO_4$ concentrations and interruption times) are depicted vs. the artificial time $1 - \tau^*$. The relaxation curves resulting from the shorter polarization time of $T_1 =$ 360 s (dots in Figure 12) exhibit the theoretically expected s-shape, which can also be observed in the numerical simulations, compare for example the green line in Figure 8a. The linear fits indicated by the dashed black lines correspond to real times between ≈10–150 s. The extrapolations of these fits to $(1 - \tau^*) = 0$ gives the desired cell potential $U(T_1)$ at current interruption time. While a linear relaxation behavior can also be observed for the longer polarization time of $T_1 =$ 960 s (crosses in Figure 12), the typical s-shape as depicted in Figure 8a is missing. This is an indication for a violation of the semi-infinite diffusion boundary condition resulting from too long polarization times, as discussed in the section Influence of the polarization time on the determined transference number in a pulse experiment. However, further reduction of the polarization time decreases the signal to noise ratio and is thus unsuitable for a precise determination of the cell potential at the polarization interruption time. The time transients for all potential relaxation curves in Figure 12 with respect to $\sqrt{(t - T_1)}$ show a non-linear behavior (data not shown), similar to the green line in Figure 8b, which may be caused by the higher sensitivity of the potential relaxation transient with $\sqrt{(t - T_1)}$ toward distortions from, e.g., SEI recreation effects and thus prohibit the dismissal of pulse polarization data. Thus the observation of the S-shape in Figure 12 is considered the best identifier for usability of experimental data and the factor $f_1(f_\pm, t_+, D^*_{\pm,\text{eff}}{}^{0.5})|^{\text{pulse polarization}}_{\text{short-term relax.}}$ (method #1) is only analyzed for pulses showing this shape, i.e., pulses of 360 s at 0.5 mA (0.22 mA/cm^2).

All other methods for the determination of the factors $f_1(f_\pm, t_+, D^*_{\pm,\text{eff}}{}^{0.5})$ and $f_2(f_\pm, t_+, D^*_{\pm,\text{eff}})$ are based on steady-state experiments. At first, the transient behavior of the current $I(t)$ during the potentiostatic polarization at U_p is analyzed. Exemplary current transients for a 0.01 M, 0.5 M, 1.5 M and a 2 M salt concentration are depicted in Figure 13.

While an initial linear current relaxation with respect to time $\sqrt{t}$ can be observed for salt concentrations 1.5 M (green) and 2 M (light blue) as is predicted by Eq. 21, this linearity is not apparent for the 0.01 M (dark blue) and the 0.5 M (red) electrolyte. This cannot be explained by the approximation of the term $\exp(H^2t)(1 - \text{erf}(H\sqrt{t}))$ with $\sqrt{t}$ as outlined in the theoretical part, since the values for H are of the same order for the depicted concentrations. However, since the theoretical relation between the current and $\sqrt{t}$ is derived based on the linearized Butler-Volmer law and therefore on a constant interface resistance, the observed curvature may result from parasitic effects, which may lead to the sometimes observed decrease of the total charge transfer resistance during the polarization time. The distinct drop of the current in the beginning of the polarization time may also be related to this effect. For larger concentrations, this effect may be restricted to a short time period in the beginning of the polarization, whereas it is distributed over a longer time period for the concentrations 0.01 M and 0.5 M, thereby interfering with the expected $\sqrt{t}$ relaxation. Extrapolation of the linear region in Figure 13 allows for the determination of the initial current I_0. As a result of Figure 13, the factor $f_1(f_\pm, t_+, D^*_{\pm,\text{eff}}{}^{0.5})|^{\text{ss polarization}}_{\text{short-term pol.}}$ (method #3, see Table I) is determined only for concentrations $c_0 \geq 1$ M by means of Eq. 32. In this case, the ratio $m_{\#3}/I_0$ is determined based on the linear fits indicated by the black dashed lines in Figure 13. Additionally, the required low frequency resistance $R_{\text{LF},0}$ is measured by impedance spectroscopy before each steady-state experiment.

While for this latter method, it is not necessary that a steady-state is reached at the end of the polarization period, for the remaining three factors $f_2(f_\pm, t_+, D^*_{\pm,\text{eff}})|^{\text{ss polarization}}_{\text{short-term relax.}}$ (method #4), $f_2(f_\pm, t_+, D^*_{\pm,\text{eff}})|^{\text{sss polarization}}_{\text{long-term relax.}}$ (method #5), and $f_2(f_\pm, t_+, D^*_{\pm,\text{eff}})|^{\text{ss polarization}}_{\text{transition period}}$ (method #2), a linear, steady-state current concentration profile is strictly required at the end of the polarization time, as discussed in the section Influence of a non steady-state concentration profile on the determination of the transference number. In a steady-state experiment, the steady-state is indicated by a distinct current plateau at the end of the polarization phase, which is observed for the 0.01 M, 0.5 M, 1 M (data not shown), and 2.0 M electrolytes (see Figure 13). A anomalous time dependence of the current at the end of the polarization phase as depicted, e.g., for $c_0 =$ 1.5 M in Figure 13 (green line) excludes this experiment from analysis based on methods #2, #3, and #5, because a linear concentration profile may not be present at the end of the polarization phase. The increase in the current may be explained by a decreasing interface resistance as a result of a modification of the lithium electrode/electrolyte interface (supported by the fact that the electrolyte resistance remains essentially unchanged over the time of polarization). The factor $f_2(f_\pm, t_+, D^*_{\pm,\text{eff}})|^{\text{ss polarization}}_{\text{transition period}}$ (method #2) defined

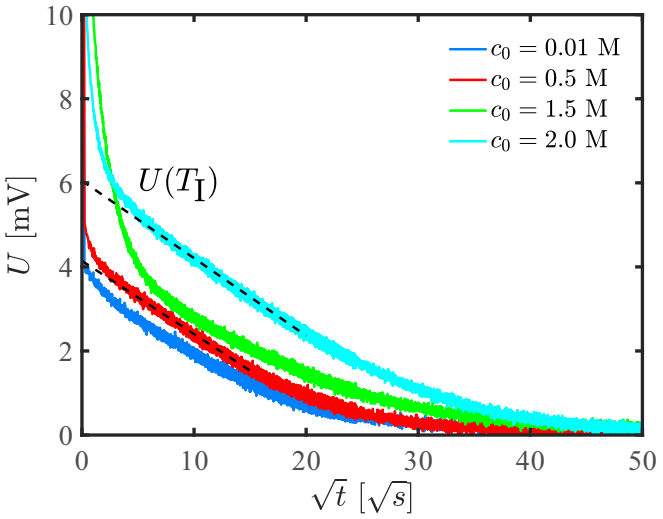

Figure 14. Exemplary fit of time behavior after 50 mV steady-state polarization for determination of the factor $f_2(f_\pm,\ t_+,\ D^*_{\pm,\mathrm{eff}})|^{\text{ss polarization}}_{\text{short−term relax.}}$ (method #4) for 0.01 M, 0.5 M, 1.5 M and 2.0 M $LiClO_4$ in EC:DEC (1:1 w:w) in a polarization cell. Dashed lines indicate linear fits used for determination of the transference number. The polarization times for the different concentrations can be found in the caption of Figure 13.

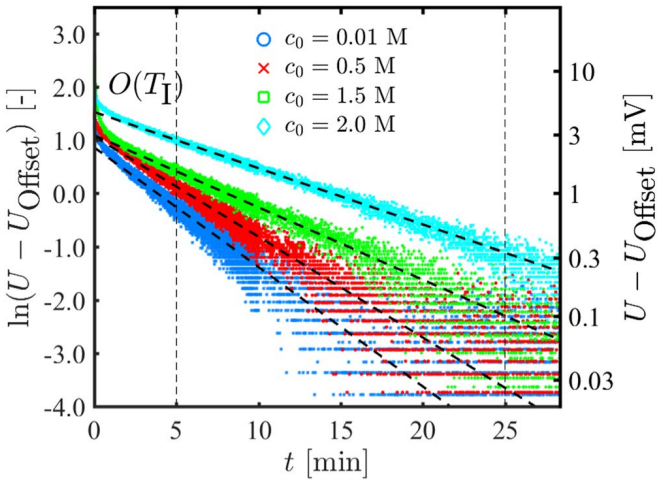

Figure 15. Exemplary fit of the logarithm of the potential vs. time during the relaxation phase after steady-state polarization (50 mV), from which the factor $f_2(f_\pm,\ t_+,\ D^*_{\pm,\mathrm{eff}})|^{\text{ss polarization}}_{\text{long−term relax.}}$ (method #5) can be determined for 0.01 M, 0.5 M, 1.5 M and 2.0 M $LiClO_4$ in EC:DEC (1:1 w:w) in two-electrode cells.

by Eq. 31 is based on the steady state current I_S and the low frequency resistance $R_{LF,S}$ at steady state which is determined by impedance spectroscopy at the end of the polarization time. The required steady state current I_s can be extracted from Figure 13. The short period with a constant steady state current in this figure is the result of the scaling with $\sqrt{t}$. The second factor $f_2(f_\pm,\ t_+,\ D^*_{\pm,\mathrm{eff}})|^{\text{ss polarization}}_{\text{short−term relax.}}$ (method #4) is based on the analytical solution for a steady state concentration profile at the end of the polarization phase. In this case, the cell potential $U(T_I)$ at current interruption time and the steady state current I_s has to be determined experimentally to calculate the factor by means of Eq. 34. As it was the case for the determination of the factor $f_1(f_\pm,\ t_+,\ D^{*\ 0.5}_{\pm,\ \mathrm{eff}})|^{\text{pulse polarization}}_{\text{short−term relax.}}$ (method #1), the short-term relaxation behavior of the cell potential can be used to extrapolate the exact cell potential $U(T_I)$ at the time of the potential interruption.

As shown in Figure 14, the expected linear relation with respect to $\sqrt{t}$ can be observed for $c_0 =$ 0.5 M and $c_0 =$ 2 M. On the other hand, the non-linear behavior with respect to $\sqrt{t}$ is a sign for experimental data either with dominating parasitic effects (side reactions in case of the 0.01 M electrolyte) or with instationary concentration profiles at the end of the polarization (as seen in Figure 13 for an initial salt concentration of 1.5 M). As a result, such experimental data are not used for the determination of the factor $f_2(f_\pm,\ t_+,\ D^*_{\pm,\mathrm{eff}})|^{\text{ss polarization}}_{\text{short−term relax.}}$ (method #4). In a steady-state experiment, also the factor $f_2(f_\pm,\ t_+,\ D^*_{\pm,\mathrm{eff}})|^{\text{ss polarization}}_{\text{long−term relax.}}$ (method #5) can be determined from the long-term relaxation behavior by means of Eq. 37. In this context, a linear fit of $\ln U(t)$ with respect to the time t is required, as it is shown for a steady-state experiment in Figure 15 and which can be observed for the relaxation phases for all concentrations investigated. This linear behavior of $\ln U(t)$ with respect to time does not depend on a steady-state profile as it is discussed in part I of this publication (Ref. 1). However, for the determination the transference number a steady-state profile is strictly required which means that although these linear trends are clearly visible in Figure 15 the corresponding relaxation periods cannot be used to calculate the transference number as side reactions (for the 0.01 M electrolyte) or instationary concentration profiles (as clearly visible in Figure 13) violate the theoretical assumptions (see Alternative methods for the determination of the transference number). The offset $O(T_1)$ of such a linear fit is the basis for the determination of the factor $f_2(f_\pm,\ t_+,\ D^*_{\pm,\mathrm{eff}})|^{\text{ss polarization}}_{\text{long−term relax.}}$.

In Figure 16, the transference numbers calculated from polarization experiments using the diffusion coefficient from the first part of this publication[1] are shown and compared to the transference number based on the δc method. Error bars indicate the variation between repeat experiments as well as the error of the diffusion coefficient. A qualitative agreement can be found when comparing the transference numbers determined by the δc method and the methods #1 (black), #3 (red), #4 (magenta) and #5 (green) utilizing the polarization cell. The only outlier is the transference number calculated from the factor $f_2(f_\pm,\ t_+,\ D^*_{\pm,\mathrm{eff}})|^{\text{ss polarization}}_{\text{transition period}}$ (method #2, magenta symbols/line in Figure 16), which is based on the polarization phase of a steady-state experiment. In this case, the qualitative behavior is in accordance with the other methods, but the absolute value is

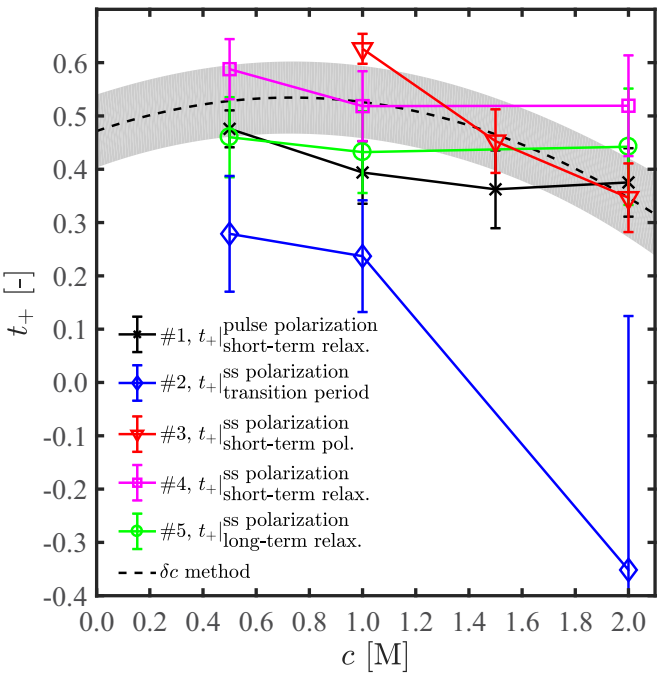

Figure 16. Overview and comparison of transference numbers determined from polarization experiments via factors summarized in Table I and comparison with transference numbers obtained from the δc method (see Figure 10).

significantly smaller, especially at higher concentrations. Unfortunately, there is no obvious reason for this behavior. For 10 mM concentrations, the electrolyte resistance measured in polarization cells by impedance spectroscopy is not constant over the entire experiment. No final assignment of latter effect was possible which is why polarization cell data with 0.01 M salt concentrations could only be used for the determination of concentration independent transport factors; at these low concentrations, only the diffusion coefficient could be determined, as shown in the first part of this study.[1] Thus, the only reliable method for the determination of the transference number at low concentrations is the δc method, as it requires no current flow at the lithium electrodes and thereby minimizes the effect of side reactions.

Although the qualitative results of the transference number determined by polarization experiments are comparable to the transference number determined by the δc method in a concentration cell, the method based on data from a concentration cell is clearly superior. It is much easier to perform experiments in the concentration cell than in the two-electrode cell. Another advantage of the concentration cell is that only the concentration overpotential resulting from two differently concentrated electrolyte solutions is measured. Therefore, additional physical phenomena such as mass and current transport do not influence the results. Also, the number of required experiments is reduced from three to two experiments, resulting in a decreased number of potential error sources. A similar result as shown in Figure 16 is obtained when the transference number is determined based on a known thermodynamic factor and polarization cell experiments (data not shown), rather than using the data from concentration cells (i.e., the data shown in Figure 11).

Although the direct determination of the transference number introduced in the section Direct determination of the transference number by steady-state polarization experiments has initially been developed for polymer electrolytes, it is also often applied for liquid electrolytes,[28–30] ionic liquids[31] or mixtures of both,[32] even though it strictly is valid only for dilute solutions and cannot be applied to concentrated solutions due to a violation of the underlying assumptions as indicated in the section Direct determination of the transference number by steady-state polarization experiments. It is also shown that the experimental setup of the polarization cell with two lithium metal electrodes and the $LiClO_4$ electrolyte, as used in this contribution, is not suitable for low salt concentrations, since a constant electrolyte resistance cannot be guaranteed. However, a constant electrolyte resistance is the basic requirement for the direct determination of the transference number.

Comparison with the literature.—In the literature a wide variety of transference numbers of liquid non-aqueous electrolytes is reported which are collected for similar electrolyte systems in Figure 17. Basically constant transference numbers of ∼0.4 for $LiPF_6$ in a PC/EC/DMC mixture E(10:27:63 v:v:v, red squares),[5] of ∼0.42 for LiTFSI in PC (green pluses),[14] or of ∼0.45 for LiDFOB in EC:DEC (3:7 w:w, magenta triangles)[9] are reported in the literature. While in all these reports, in which the transference number does not change more than 10% in the investigated concentration range, the salts and solvents differ, also strong concentration dependencies are reported for example for $LiPF_6$ electrolytes. Monotonically decreasing values for the lithium transference number are reported by Nyman et al.[19] for $LiPF_6$ in EC:EMC (3:7 w:w, red crosses) and Lundgren et al.[20] for $LiPF_6$ in EC:DEC (1:1 w:w, red diamonds). While comparison of the reports for $LiPF_6$ based electrolytes (compare red symbols in Figure 17) show the influence of the solvent on the transference number, direct comparison with the electrolyte investigated in this work is difficult due to the different salts, solvents, and measurement techniques. Although the only reference depicted in Figure 17 using $LiClO_4$ salt uses PC as solvent (blue stars),[18] it is closest to our electrolyte composition ($LiClO_4$ in EC:DEC, 1:1 w:w, black line) and to the authors best knowledge, no literature is available investigating exactly the same electrolyte as used in this work. In the latter publication the authors also use a second order polynomial to describe the concentration

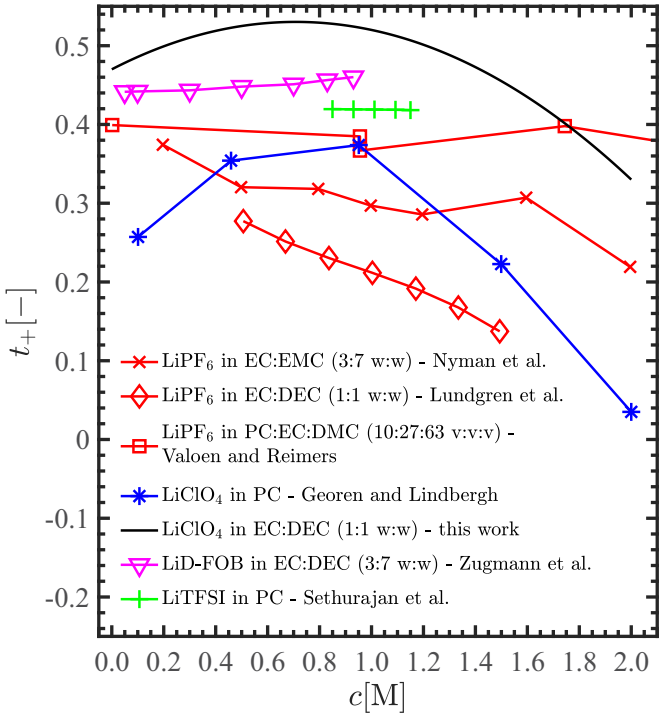

Figure 17. Literature comparison of transference numbers for a range of electrolytes: $LiPF_6$ in EC:EMC (3:7 w:w) - Nyman et al.,[19] $LiPF_6$ in EC:DEC (1:1 w:w) - Lundgren et al.,[20] $LiPF_6$ in PC:EC:DMC (10:27:63 v:v:v) Valøen et al.,[5] $LiClO_4$ in PC - Georén and Lindbergh,[18] $LiClO_4$ in EC:DEC (1:1 w:w) – this work, LiD-FOB in EC:DEC (3:7 w:w) - Zugmann et al.[9] and LiTFSI in PC - Sethurajan et al.[14]

dependence of the transference number resulting in a similar behavior compared to our results, only shifted to smaller values.

At low concentrations the transference number is defined by ion-solvent interactions, i.e., different mobility of anions and cations with their respective solvation shell within an excess of solvent molecules, and thus we expect different values for different solvent-salt combinations. In conclusion, the largely constant offset of ∼0.2 of the transference numbers for $LiClO_4$ in PC compared to EC:DEC (1:1 w:w) may be ascribed to the effect of the solvent. At concentrations above ∼0.8 M the transference number of the $LiClO_4$ electrolytes decreases (compare blue stars and black line in Figure 17). A decreasing transference number with an increasing salt concentration is explained by the formation of ion-pairs in the literature.[14,15] A similar effect was previously reported by Vatamanu et al.[33] Another explanation for the decrease of the transference number might be related to the ratio of moles of solvent to moles of salt. Depending on the solvation structure of the salt ions, a large fraction of the solvent (predominantly EC or PC) may be bound in the solvation shells around the ions. In consequence, the loosely solvated ion, generally the anion due to its large size to charge ratio, may still move mostly undisturbed through the electrolyte at high concentrations (small solvent to salt molar ratio) while movement of the strongly solvated cation is hindered by its solvation shell which includes an increasingly large fraction of the entire electrolyte. In the limiting case of very high molar ratios of salt/solvent, the cations may have to drag along the entire solvent (bound to its solvation shell), so that their mobility will decrease strongly compared to the anions, corresponding to a decrease of the cation transference number at high concentrations. The increase of the transference number, as evident from the $LiClO_4$ electrolytes for concentrations up to ∼0.8 M (compare blue stars and black line in Figure 17), may be explained by the coupled movement of ions at medium concentrations, while at high concentrations the effects of the solvation structure dominate.

Conclusions

In this work, a novel approach for the determination of the transference number is proposed. As a result of the direct determination of the thermodynamic factor introduced in Landesfeind et al.,[2] the transference number can be calculated based on data from concentration cells. The proposed procedure referred to as the δc method is based on small concentration variations and does not require a functional description for the concentration dependence of the transference number.

In addition to the determination via the concentration cell, the transference number is also determined by the classical experimental approach based on a known binary diffusion coefficient and data from polarization cell and concentration cell experiments. This work discusses five different experimental methods for the determination of the transference number based on polarization cell experiments, whereas three of the five methods have not yet been used in the literature for the determination of the transference number. These latter new methods are based on the initial relaxation behavior of the current in a potentiostatic polarization experiment and on the short-term and the long-term relaxation behavior of the cell potential after a potentiostatic polarization experiment. The basic principle of all electrochemical pulse experiments, the validity of the proposed methods as well as chances and potential risks are analyzed by numerical simulations.

In the end, experimental results of all discussed methods, obtained with an exemplary electrolyte solution ($LiClO_4$ in EC:DEC, 1:1 w:w) are compared. Resulting transference numbers based on polarization cell experiments and the δc method generally agree, however, experimental efforts and uncertainties are much higher in the approaches based on polarization cell experiments, since they require to combine results of three different experimental procedures. For a simple and accurate determination of the transference number, measurements of the thermodynamic factor in a ferrocene cell in combination with concentration cell data are superior to polarization cell experiments. It is also shown that the direct determination of the transference number by a steady-state potentiostatic polarization step is not suitable for concentrated binary electrolyte solutions.

List of Symbols

Symbol	Name	Unit
A	electrode area	cm^2
c	ionic concentration	mol/L
D_i	diffusion coefficient	cm^2/s
F	Faraday constant	C/mol
f_1	factor defined by Eq. 25	$\sqrt{s/cm^2}$
f_2	factor defined by Eq. 29	s/cm^2
$f_\pm$	mean molar activity coefficient	-
i_i	current density	mA/cm^2
I	current	A
l	distance between electrodes	µm
m_{ln}	slopes of $\ln U$ vs. t during relax. after steady state pot. pol.	1/s
$m_{\#3}$	slope of $I(t)$ vs. $\sqrt{t}$ during steady state pot. pol.	$A/\sqrt{s}$
$m_{\#4}$	slope of $U(t)$ vs. $\sqrt{t}$ during relax. after steady state pot. pol.	$V/\sqrt{s}$
O	constant factor in Eq. 36	-
R	gas constant	J/(mol K)
$R_{el,i}$	electrolyte resistance	Ω
$R_{LF,i}$	resistance	Ω
t	time	s
t_i	transference number of lithium ion	-
T	temperature	K
T_I	polarization time	s
TDF	thermodynamic factor	-
U_i	potential	V
ν_i	stoichiometry factor	-
x	space coordinate	µm
z_i	ionic charge	-

Greek

κ	conductivity	mS/cm
$\Delta\Phi$	difference of the volumetric intrinsic phase average of the electric potential	V
τ	tortuosity	-
ε	porosity	-
Δc	concentration diff. betw. electrodes	mol/L
τ^*	artificial time	-

Subscripts and Superscripts

Symbol	Name
A	anode
C	cathode
eff.	effective value of parameter with $x_{eff.} = \frac{\varepsilon}{\tau}\ x$
high	higher concentration in concentration cell
low	lower concentration in concentration cell
p	during polarization
s	steady state
0	initial state
+	cation
−	anion
±	of binary electrolyte

Acknowledgment

We gratefully acknowledge the funding by the Bavarian Ministry of Economic Affairs and Media, Energy, and Technology for its financial support under the auspices of the EEBatt project.

References

1. A. Ehrl, J. Landesfeind, W. A. Wall, and H. A. Gasteiger, *J. Electrochem. Soc.*, **164**, A826 (2017).
2. J. Landesfeind, A. Ehrl, M. Graf, W. A. Wall, and H. A. Gasteiger, *J. Electrochem. Soc.*, **163**, A1254 (2016).
3. J. Newman and K. Thomas-Alyea, *Electrochemical Systems*, 3rd ed., Wiley Interscience, Hoboken, (2004).
4. P. G. Bruce, M. T. Hardgrave, and C. A. Vincent, *Solid State Ionics*, **53–56**, 1087 (1992).
5. L. O. Valøen and J. N. Reimers, *J. Electrochem. Soc.*, **152**, A882 (2005).
6. P. Bruce and C. Vincent, *J. Electroanal. Chem.*, **225**, 1 (1987).
7. M. M. Hiller, M. Joost, H. J. Gores, S. Passerini, and H.-D. Wiemhöfer, *Electrochim. Acta*, **114**, 21 (2013).
8. V. Mauro, A. Daprano, F. Croce, and M. Salomon, *J. Power Sources*, **141**, 167 (2005).
9. S. Zugmann, M. Fleischmann, M. Amereller, R. M. Gschwind, H. D. Wiemhöfer, and H. J. Gores, *Electrochim. Acta*, **56**, 3926 (2011).
10. M. R. Wright, *An Introduction to Aqueous Electrolyte Solutions*, John Wiley & Sons, Ltd, Chichester, (2007).
11. F. Castiglione, E. Ragg, A. Mele, G. B. Appetecchi, M. Montanino, and S. Passerini, *J. Phys. Chem. Lett.*, **2**, 153 (2011).
12. C. Capiglia, Y. Saito, and H. Kageyama, *J. Power Sources*, **81**, 859 (1999).
13. J. Zhao, L. Wang, X. He, C. Wan, and C. Jiang, *J. Electrochem. Soc.*, **155**, A292 (2008).
14. A. K. Sethurajan, S. Krachkovskiy, I. C. Halalay, G. R. Goward, and B. Protas, *J. Phys. Chem. B*, **119**, 12238 (2015).
15. Y. Ma, M. Doyle, T. F. Fuller, M. M. Doeff, L. C. Jonghe, and J. Newman, *J. Electrochem. Soc.*, **142**, 1859 (1995).
16. A. Ferry, M. Doeff, and L. DeJonghe, *Electrochim. Acta*, **43**, 0 (1998).
17. M. M. Doeff, L. Edman, S. E. Sloop, J. Kerr, and L. C. De Jonghe, *J. Power Sources*, **89**, 227 (2000).
18. P. Georén and G. Lindbergh, *Electrochim. Acta*, **49**, 3497 (2004).
19. A. Nyman, M. Behm, and G. Lindbergh, *Electrochim. Acta*, **53**, 6356 (2008).
20. H. Lundgren, M. Behm, and G. Lindbergh, *J. Electrochem. Soc.*, **162**, 3 (2014).
21. P. Blonsky, D. Shriver, P. Austin, and H. Allcock, *Solid State Ionics*, **18–19**, 258 (1986).
22. C. M. Doyle, *PhD Thesis*, Berkeley (1996).
23. A. Ehrl, *PhD Thesis*, München (2016).
24. J. Landesfeind, J. Hattendorff, A. Ehrl, W. A. Wall, and H. A. Gasteiger, *J. Electrochem. Soc.*, **163**, A1373 (2016).
25. A. J. Bard and L. R. Faulkner, *Electrochemical Methods - Fundamentals and Applications*, 2nd ed., John Wiley & Sons, Inc., New York, (2001).

26. H. Hafezi and J. Newman, *J. Electrochem. Soc.*, **147**, 3036 (2000).
27. W. Polifke and J. Kopitz, *Wärmeübertragung: Grundlagen, analytische und numerische Methoden*, Pearson Deutschland GmbH, (2009).
28. C. L. Berhaut, P. Porion, L. Timperman, G. Schmidt, D. Lemordant, and M. Anouti, *Electrochim. Acta*, **180**, 778 (2015).
29. L. Niedzicki, M. Kasprzyk, K. Kuziak, G. Z. Zukowska, M. Marcinek, W. Wieczorek, and M. Armand, *J. Power Sources*, **196**, 1386 (2011).
30. G. A. Elia, J.-B. Park, Y.-K. Sun, B. Scrosati, and J. Hassoun, *ChemElectroChem*, **1**, 47 (2014).
31. C. Liu, X. Ma, F. Xu, L. Zheng, H. Zhang, W. Feng, X. Huang, M. Armand, J. Nie, H. Chen, and Z. Zhou, *Electrochim. Acta*, **149**, 370 (2014).
32. K. Kimura, J. Hassoun, S. Panero, B. Scrosati, and Y. Tominaga, *Ionics (Kiel)*,, 895 (2015).
33. J. Vatamanu, O. Borodin, and G. D. Smith, *Methodology*, **116**, 1114 (2012).

3.4 Temperature and Concentration Dependent Study

In this section the article *The Temperature and Concentration Dependence of Ionic Transport Properties*[55] is presented, which was not yet submitted at the time of submission of this thesis. Parts of the article were presented at the ECCOMAS 2016 in Crete (Greece) in June 2016, at the Electrochemistry 2016 in Goslar (Germany) in September 2016 and at the 14th Symposium on Fuel Cell and Battery Modeling and Experimental Validation in Karlsruhe (Germany) in March 2017.

As the direct determination of the thermodynamic factor from the ferrocene cell approach (see Section 3.2) is not valid (see Section 3.2), the presented concentration and temperature dependent study of the electrolyte transport parameters of three $LiPF_6$ based electrolytes is based on the analytical derivations developed for the determination of the transference number and on a further simplification of the concentration cell potential. While ionic conductivities and binary diffusion coefficients are found using turn-key equipment and our previously described approach,[54] respectively we here quantify transference numbers and thermodynamic factors from concentration cells and pulse experiments in symmetric lithium cells. Thus, these latter two parameters intrinsically show higher uncertainties, as they are based on the analysis of two, instead of one experiment. The manuscript explains the measurement procedure and data analysis steps in great detail, so that it may be used as a manual for the determination of ionic transport properties. In addition to its usability as a tutorial, the manuscript analyzes a wide concentration (0.1 M to 3 M) and temperature (-10 °C to 50 °C) range of two commonly used electrolytes in lithium-ion batteries ($LiPF_6$ in EC:DMC (1:1 w:w) and $LiPF_6$ in EC:EMC (3:7 w:w)) and one novel, EC-free electrolyte ($LiPF_6$ in EMC:FEC (19:1 w:w)). The vast number of experimental results (>900) as well as the functional approximations to the found transport parameters enables predictive simulations of ionic transport in porous media within the framework of the Newman model. It is emphasized that for the herein presented methodology on the ionic transport properties, no assumptions on their concentration and temperature dependence has to be made in order to obtain explicit values for each parameter, i.e., the transference number may be obtained for a set temperature and concentration without assuming a certain value or behavior of the thermodynamic factor, the binary diffusion coefficient, or the ionic conductivity. In contrast to the literature, in this study we are able to obtain transport properties explicitly, using simple, commonly used cell setups (here pouch cells and coin cells) and can show that the only large-range temperature and concentration dependent electrolyte study[50] oversimplifies the complexity of ionic transport in lithium-ion battery electrolyte solutions.

Author Contributions

J.L. developed the cell designs and measurement procedures. J.L. performed all electrochemical measurements and derived the analytical simplification to the concentration cell potential. Data analysis was done by J.L. and the manuscript was written by J.L. and H.G. All authors discussed the data and commented on the results.

The Temperature and Concentration Dependence of Ionic Transport Properties

Johannes Landesfeind,[az] and Hubert A. Gasteiger[a]

[a] Chair of Technical Electrochemistry, Department of Chemistry and Catalysis Research Center, Technical University of Munich, Munich, Germany

[z]corresponding author

Abstract

Lithium-ion battery performance at low temperatures or fast charge/discharge rates is determined by the intrinsic electrolyte transport and thermodynamic properties of the commonly used binary electrolytes. For predictive battery models and the development of future electrolyte solutions a profound understanding of the ionic conductivity, the binary diffusion coefficient, the transference number and the thermodynamic factor, over a large concentration and temperature range is mandatory. In this study we apply previously discussed and established methods for the determination of ionic conductivities and binary diffusion coefficients to two commonly used electrolyte systems (EC:DMC (1:1 w:w) and EC:EMC (3:7 w:w)) as well as one EC free electrolyte (EMC:FEC (19:1 w:w)). For the characterization of transference numbers and thermodynamic factors we introduce a novel analysis scheme and apply it to the electrolytes under study so that we are finally able to report temperature (-10 °C – 50 °C) and concentration (0.1 M – 3 M) dependent values as well as approximations to these experimentally obtained transport and thermodynamic properties. Comparison with the scarcely available literature highlights that reported concentration and temperature dependencies partially underestimate the complexity of ionic transport properties, possibly leading to imprecise predictions of, e.g., the cell's power limitation or the safety determining onset of lithium plating reactions.

Introduction

During the operation of lithium-ion batteries, ionic concentration gradients evolve in the liquid electrolyte, especially when the cell is cycled at high charge/discharge currents or at low temperatures. For a profound understanding of this rate limiting process and its detrimental side effects, such as lithium plating reactions during (too) fast charging operation, the ionic transport properties have to be known precisely. While the transport path length is largely determined by the tortuosity of the porous media,[1–3] the intrinsic ionic transport properties according to the widely applied Newman model[4] are the ionic conductivity, the binary diffusion coefficient,[5] the transference number,[6] and the thermodynamic factor.[7]

Despite its necessity, concentration and more importantly also temperature dependent studies of ionic transport in typical lithium-ion battery electrolyte solutions are scarce. Apart from the well-known groundwork by Valøen and Reimers only few additional studies are known to the authors which give a comprehensive set of transport properties in non-aqueous lithium-ion electrolytes over a reasonable concentration(and temperature range.[8–11] In a recent study by Farkhondeh et al.[12] an optimization approach for pulse experiments in a four electrode cell setup is presented and the transport parameters are reported for two 1 M $LiPF_6$ electrolytes at 25 °C. Although, with increased experimental effort, latter method may be applied to other salt concentrations and temperatures, the methodology requires experience in optimization routines and the simulation of battery cells which may prevent its wide application by electrolyte developers. In contrast, in this work we present simple experimental techniques that may be applied by the majority of laboratories working on lithium-ion batteries and guide through the straightforward analysis which does not require extensive model analysis but may be done using simple spreadsheet calculations. Building on our previous efforts to analyse various determination methods for the characterization of binary diffusion coefficients[5] and transference numbers[6] we analyse two typical battery electrolytes and one novel alternative containing no ethylene carbonate as proposed in the literature (see Experimental for electrolyte compositions).[13] Unfortunately, careful analysis of our previously introduced direct determination method for thermodynamic factors based on cyclic voltammograms of the ferrocene/ferrocenium couple identified partially invalid assumptions, discussed in more detail in the corresponding erratum for the interested reader.[14] Thus analysis of the transference number and the thermodynamic factor in the present study is not based on ferrocene cell experiments but we introduce a novel analytical method based on concentration cell potentials and galvanostatic pulse experiments in symmetric lithium cells to find transference numbers and thermodynamic factors. I.e. in total we determine the electrolyte transport properties in three cell setups, a conductivity cell impedance measurement, the open circuit potential recorded in a pouch concentration cell and the potential transient for short and long times after a galvanostatic pulse in symmetrical lithium cell. The finally obtained values for the ionic transport properties span the concentration range from 0.1 M to 3 M and were obtained at temperatures from -10°C to 50°C in 10°C steps for three electrolytes. We critically compare our results with suitable publications from the literature and highlight the partially oversimplified concentration and temperature dependencies reported.

In the following, we first introduce experimental procedures and setups used for the determination of transport properties in this work. Our previously presented methods[5,6] for the parameter determination are recapitulated briefly in the theory section and we introduce a simple scheme, useable as a manual for the measurement of ionic transport properties in battery electrolytes. Thereafter exemplary datasets show the data processing and analysis in great detail and help to judge the errors in the final results. The Results section summarizes the found temperature and concentration dependent values for the four transport properties and provides fit parameters and their errors to empirically and semi-empirically chosen temperature and concentration dependent functional approximations. To account for the complexity of

temperature and concentration dependent transference numbers and thermodynamic factors we additionally present individual analyses of those parameters on a per temperature basis for the benefit of the reader. The Supporting Information gives background analyses and measurements not required to follow the main study and is referred to at the appropriate sections in the main article.

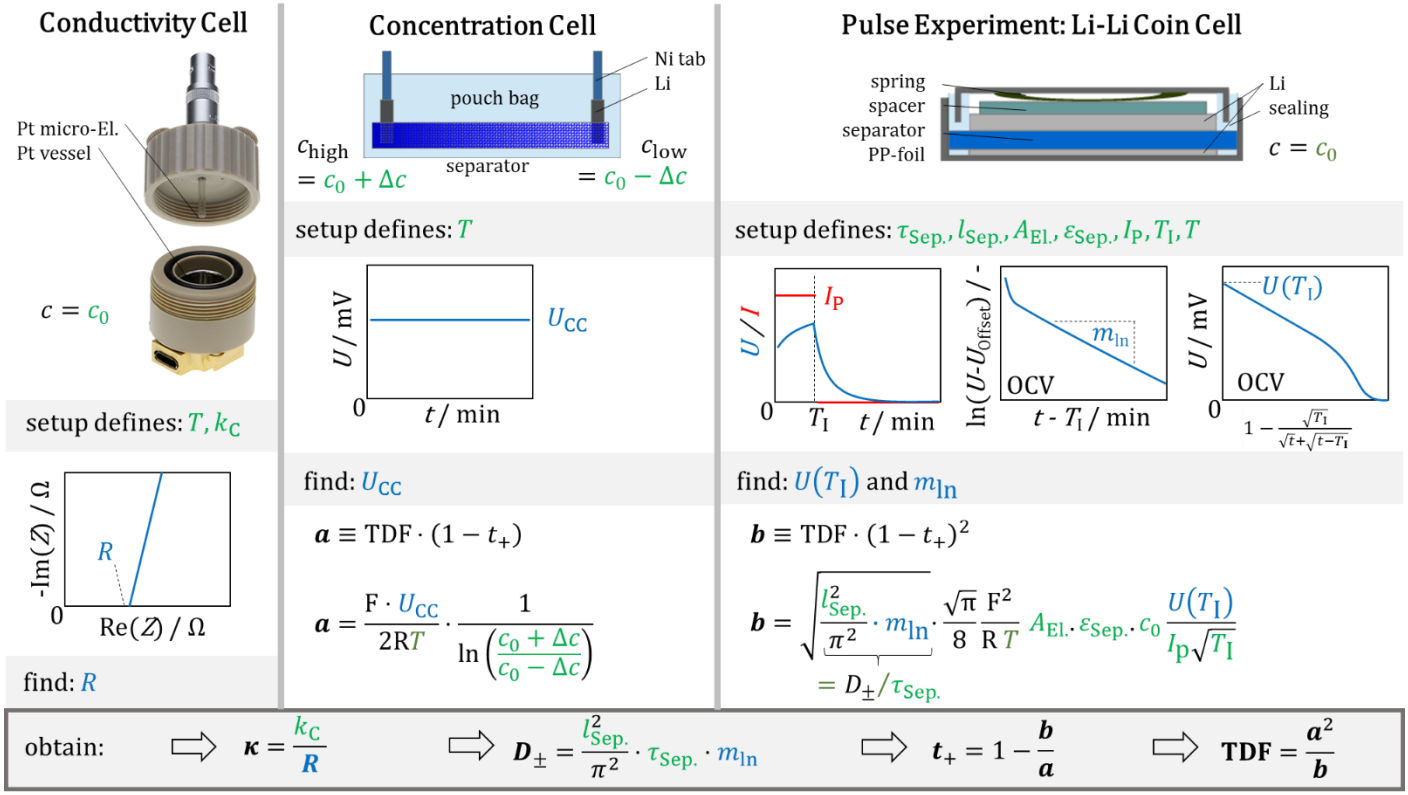

Figure 1. Determination scheme for the transport and thermodynamic parameters with measurements around a base salt concentration c_0. Slight modifications to this scheme are discussed in the main text (see section Data Analysis) due to the necessity to increase the concentration differences of the concentration cells to observe temperature effects. Analysis of the ionic conductivity is based on the conductivity cell depicted in the figure, thermodynamic factors (TDF) and transference numbers are obtained based on the analysis of the concentration potential in pouch cells and the short term potential behaviour after galvanostatic pulses in symmetric lithium coin cells and the binary diffusion coefficient is solely based on the long term relaxation of the potential after latter pulse experiments. The determination scheme allows to find individual values for all transport parameters without the necessity to make any assumptions on the remaining parameters (as done in the literature by assuming a constant transference number[8]).

Experimental

Mixtures of ethylene carbonate (EC, BASF, battery grade / Sigma Aldrich, anhydrous, 99%), ethyl-methylene carbonate (EMC, BASF, battery grade), dimethyl carbonate (DMC, Sigma Aldrich, anhydrous, 99%) and fluoroethylene carbonate (FEC, BASF, battery grade) were used as solvents for self-prepared electrolytes containing lithium hexafluorophosphate ($LiPF_6$, BASF, battery grade / Sigma Aldrich, 99.99%) salt, mixed in an argon filled and temperature controlled glove box (MBraun, 25 °C ± 1 °C, water content < 0.1 ppm, Ar 5.0, Westfalen, 99.999% Vol). $LiPF_6$ concentrations of 0.1, 0.5, 1, 1.5, 2 and 3 M are referred to as base concentrations subsequently. Additionally 0.01 M electrolytes were prepared for the use in concentration cells. Unless stated otherwise, throughout this manuscript we use M to denominate a volumetric concentration (moles per liter). For the interested reader we provide density measurements for the electrolytes used in this study, covering the used temperature and concentration range (see Supporting Information,

Figure 1, fit parameters to the linear concentration and temperature dependent function in Eq. 1, SI are given in Table 1, SI). Metallic lithium (Rockwood Lithium, 75 µm or 450 µm thickness, high purity) was used as counter electrode (CE) and working electrode (WE) in concentration cells and coin cells.

Due to residue hydrofluoric acid (HF) concentrations in the electrolytes the glass-fiber separators used before,[6] for short measurements at room temperature, could not be used in this study as ongoing gas evolution during the much longer and temperature dependent measurements will lead to an expansion of the pouch concentration cells and an inhomogeneous current distribution in symmetric coin cells. Therefore porous polyethylene films (PE, Nitto, Sunmap LC, 500 µm thickness, 30% porosity) were used as a separator in this study. To ensure good wettability of the PE separator, especially with the EC:DMC (1:1 w:w) electrolyte at high salt concentrations, all Nitto separators were nitrogen plasma treated for five minutes and assembled within the cells within one week (PlasmaFlecto 10, plasma technology, 0.3 mbar, 300 W).

All coin and pouch cell parts were dried overnight in a vacuum drying oven at 70 °C before bringing them into the glove box. Measurements were conducted outside the glovebox using a Biologic VMP3 potentiostat/galvanostat or a Biologic SP-300 potentiostat/galvanostat.

Conductivity Cell

The ionic conductivity of all electrolytes at their base concentrations was determined in a commercially available Pt microelectrode setup (rhd Instruments, TSC 1600 closed, Germany), consisting of a Pt beaker and a Pt microelectrode (see Figure 1), which can be temperature controlled automatically using an external Peltier element and controller unit (not shown in Figure 1). A small sample volume (1 mL), which allows for a fast temperature equilibration, was filled into the cleaned cell inside the glovebox and impedance measurements were done outside the glovebox between both Pt electrodes in a frequency range from 85 kHz to 1 kHz with an excitation amplitude of 100 mV. Prior to the electrolyte measurements the cell constant k_C was determined using 0.001, 0.01 and 0.1 M KCl calibration solutions at 25 °C (Sigma Aldrich, conductance standard A, B and C, k_C = 20 ± 0.2 1/cm). Lithium-ion electrolyte cell impedances were measured first at 50°C after a 10 min equilibration time, subsequently the cell temperature was decreased in 10°C steps down to −10 °C and 5 min equilibration times were used after the set-point temperatures were reached. Conductivity measurements were only done once for each concentration and temperature due to the very good agreement with values from the manufacturer (see Figure 2, Supporting Information) and the small error of the measurement (see 1 % uncertainty of cell constant).

Concentration Cell

Pouch cells for the temperature dependent measurement of concentration potentials were prepared inside the glovebox (setup depicted in Figure 1). Cell dimensions of ~5 cm (height) × ~13 cm (length) assured no mixing of electrolyte within the measurement time (diffusion time for $(5\ \text{cm})^2/(5\cdot10^{-6}\ \text{cm}^2/\text{s})$ ~60 days). Two 450 µm thick Li electrodes were attached to Ni tabs (MTI cooperation), which come with a sealing tape, and the cell was first sealed at the sides and the top to fix the tabs. A 1 cm x 10 cm stripe of Nitto separator was positioned on top of the lithium electrodes and two electrolyte solutions of differential concentrations (here pairs of adjacent base concentrations including the 0.01 M electrolyte, i.e., 0.01 – 0.1 M, 0.1 – 0.5 M etc.) were carefully added at the left and right ends of the separator. Care was taken that the electrolytes are soaked up by the porous separator and do not spill in the cell volume. The total electrolyte amount was calculated from the theoretically available pore space in the separator (150 µl) and was sufficient to see the

electrolyte wetted regions to contact in the middle of the separator before the cell was sealed at 50 mbar using a vacuum sealing device (C 70, multivac, Germany) inside the glovebox.

Multiple pouch concentration cells (up to eight) were stacked between copper plates of equal size each (~5 cm ×13 cm × 0.5 cm) and the entire stack was immersed into an ethylene glycol / water bath (~50:50 by weight) of a refrigerated circulator (Julabo FP 50, HL, Germany) with the Ni tabs facing upwards and positioned ~1 cm above the liquid level. The setup ensures a fast and very homogeneous temperature distribution of the pouch concentration cells, a condition not reached reproducibly before, when using a temperature convection chamber. Open circuit potentials of at least two cells for each temperature and concentration were measured for three minutes after reaching the set-point temperature (from -10 °C to 50 °C in 10 °C steps, starting a low temperatures to limit diffusion effects) using a potentiostat (Biologic, SP300) and the mean value during the full measurement period was taken as the final concentration potential.

Coin Cell

Pulse experiments in symmetrical Li-Li cells were conducted in coin cells (MTI cooperation, compare Figure 1) assembled inside a glovebox. A 17 mm Li electrode (75 µm thickness) and a 1 mm polypropylene foil ring (17 mm inner diameter, 19 mm outer diameter, ~80 µm thickness) were centrally positioned into the larger can of the coin cell before putting a 19 mm separator disc (plasma treated) on top. The cell assembly was finished by first adding the coin cell sealing ring, slowly adding the electrolyte (60 µL, ~150 % of separator pore volume) and then putting the second Li electrode (450 µm thickness, 17 mm diameter), a 1 mm thick stainless steel spacer (16 mm diameter) and the washer and crimping the cell inside the glovebox. As argued before the larger separator size (seed to the electrode area) avoids stray currents around the separator and the thick (500 µm), incompressible separator ensures long relaxation times after the current pulses.[5] The pulse experiments of two cells for each electrolyte concentration were conducted outside the glovebox in a temperature controlled climate chamber (PR15, ThermoTEC, Germany) at temperature set-points of -10°C to 50°C (in 10°C steps), i.e., different temperatures were measured using the same cell. Unfortunately the real cell temperatures were found later to differ from the set-point values, predominantly at low temperatures so that the actual measurement temperatures were -7.5 °C, 2.5 °C, 12 °C, 20 °C, 30 °C, 40 °C and 50 °C (all ± 1°C). As the analysis scheme (see Theory section and Figure 1) requires identical measurement temperatures for concentration cell and coin cell experiments we omit the slight temperature variations at temperatures below 20 °C and use the set-point temperature for calculation, thereby accepting slight inaccuracies. Measurement conditions for the pulse experiments, set with a Biologic VMP3 potentiostat, are listed in Table 1. The polarization time is chosen to ensure concentration gradients are only forming at the vicinity of the electrodes (the diffusion distance during a 15 minute pulse is ~500 µm ($3 \cdot 10^{-6} \frac{\mathrm{cm}^2}{\mathrm{s}}$), while here the distance through the porous medium is 500 µm x 4.8 (tortuosity) ≈ 2500 µm).

Table 1: Summary of the applied galvanostatic pulse polarization (GPP) steps for different $LiPF_6$ concentrations in the symmetrical lithium coin cell setup shown in Figure 1. The active electrode area in the coin cells was 2.27 cm², i.e., 100 µA correspond to ~45 µA/cm².

Salt Concentration	OCV + EIS	GPP	OCV
0.1 M	EIS measurement + 1 h for temp. equilibration	15 min, ± 100 µA	3 h 45 min measured ever 3 s
0.5 M		T_I =15 min, Ip =± 300 µA	
1 M			
1.5 M			
2 M			
3 M		15 min, ± 500 µA	

Alternating positive and negative pulse currents below 0.3 mA/cm² were chosen on purpose to avoid the unidirectional growth of lithium dendrites, all pulses were followed by ~4 h open circuit measurement. The measurement procedure was set up to take 5 h, so that for each electrolyte and concentration the temperature was held for 10 h to accommodate two pulses (positive and negative current). After the pulse experiment at 50°C the cell was cooled down to 20°C and a final pulse experiment was conducted to be compared to the 20 °C measurement during the increasing temperature cycle. Within the errorbars (see Section Results) no influence of the pulse direction could be observed, while repeat measurements at 20°C at the end of the procedure yielded slightly lower values (max. 10% lower) still within the measurement uncertainty of the first 20°C measurements.

In addition to the pulse experiments four separate coin cells were prepared analogously (incl. metallic lithium) for the determination of the Nitto separator tortuosity $\tau_{Sep.}$, containing 1 M and 2 M $LiPF_6$ in EC:EMC (3:7, w:w) and their impedance was measured at temperatures of -10 °C, 0 °C, 25 °C, 40 °C and 50 °C. In average a tortuosity of 4.8 ± 0.4 was found for the plasma treated Nitto film separator by analysis of the high frequency resistance with using the previously determined temperature dependent conductivities of the electrolytes, i.e., the same tortuosity was found to for 1 M and 2 M salt concentrations and independent of the temperature and is used below for the calculation of the binary diffusion coefficient.

Theory

In the following we briefly guide through the determination methods used in this work to obtain the transport properties of binary electrolytes, required for the application of the Newman model.[4] The measurement of the ionic conductivity does not require a separate introduction and was done using turn-key equipment in this work (see scheme in Figure 1). After finding the cell constant of the conductivity cell (k_C) using three conductance standards, the high frequency resistance R, obtained from impedance measurements of the cell, filled with the electrolyte of interest, can be used to calculate the ionic conductivity of the sample (see left column, Figure 1). Determination of the binary diffusion coefficient was described in detail in a previous publication and is applied analogously in this work.[5] While minor changes in the experimental setup and the measurement procedure are described in the Experimental the approach used in this study for the measurement of binary diffusion coefficients is based on the analysis of the long term potential relaxation after a galvanostatic polarization (see Eq. 14 in Ref. 5 and right column in Figure 1, galvanostatic pulse not

shown). In a symmetrical Li-Li cell with an active electrode area $A_{\mathrm{El.}}$, separated by a porous separator (thickness $l_{\mathrm{Sep.}}$, porosity $\varepsilon_{\mathrm{Sep.}}$) filled with the electrolyte of interest (concentration c_0) the slope of the logarithmic potential $m_{\ln}$ at long times after the current interrupt is determined. The effective binary diffusion coefficient $D^*_{\pm,\mathrm{eff}}$ can then be obtained from[5]

$$D^*_{\pm,\mathrm{eff}} = \frac{{l_{\mathrm{Sep.}}}^2}{\pi^2} \cdot m_{\ln}. \qquad 1$$

Measurement of the tortuosity of the porous separator $\tau_{\mathrm{Sep.}}$ allows to finally obtain the binary diffusion coefficient $D_\pm$

$$D_\pm = D^*_{\pm,\mathrm{eff}} \cdot \tau_{\mathrm{Sep.}} \qquad 2$$

Previously we suggested to find transference numbers (t_+) from concentration cell potentials when combined with a known thermodynamic factor from the analysis of the ferrocene redox potential versus metallic lithium by means of cyclic voltammograms (see Eq. 38 in Ref. 6). Unfortunately we had to accept that not all assumptions made in our previous publication on the determination of thermodynamic factors (TDF) are fulfilled automatically. Because the determination of the thermodynamic factor using the ferrocene cell setup is not reliable (especially at low concentrations) we refrain from using the ferrocene cell setup in this work, yet obtained thermodynamic factors are compared with the present analysis in the corresponding erratum for the interested reader, which also elaborates the issue in more detail.[14] Here we use concentration cell data in combination with the analysis of the short time behavior after the galvanostatic pulse experiments in symmetric Li-Li cells instead to acquire knowledge about the temperature and concentration dependent behavior of the thermodynamic factor and the transference number. The determination method is similar to the methodology introduced before (see Eq. 26 in Ref. 6) and is described in detail in the following.

First we introduce a further simplification to the analysis of concentration potentials (see middle column in Figure 1) which reduces the complexity of data analysis. In concentration cells with two identical (here Li electrodes), in contact with two different, but close, electrolyte concentrations ($c_0 \pm \Delta c$), the concentration potential U_{CC} can be described by[4]

$$U_{\mathrm{CC}} = \frac{2\mathrm{R}T}{\mathrm{F}} \int_{c_0-\Delta c}^{c_0+\Delta c} \frac{1}{c} \mathrm{TDF}(c) \cdot \big(1 - t_+(c)\big)\, \mathrm{d}c \qquad 3$$

and may be simplified to

$$U_{\mathrm{CC}} = \frac{2\mathrm{R}T}{\mathrm{F}} \mathrm{TDF}(c_0) \cdot (1 - t_+(c_0)) \int_{c_0-\Delta c}^{c_0+\Delta c} \frac{1}{c}\, \mathrm{d}c \qquad 4$$

$$U_{\mathrm{CC}} = \frac{2\mathrm{R}T}{\mathrm{F}} \mathrm{TDF}(c_0) \cdot (1 - t_+(c_0)) \ln\left(\frac{c_0 + \Delta c}{c_0 - \Delta c}\right) \qquad 5$$

under the assumption of a constant transference number and a constant thermodynamic factor between the two differential concentrations $c_0 - \Delta c$ and $c_0 + \Delta c$. Here R is the gas constant, F the Faraday constant and T the temperature. While latter assumption is only strictly valid for infinitely small concentration intervals, it provides a good approximation if reasonably small concentration differences are used and the transference number and the thermodynamic factor are well behaved in the respective concentration range. Once we determined functional approximations to experimental data for both parameters, the error of above simplification can be checked mathematically by comparing concentration potentials of Eq. 3 and Eq. 5. For the single temperature trends obtained below the error by simplification of Eq. 3 was found to be below 10% for all measurements (see Supporting Information

Figure 3). In consequence, rearrangement of Eq. 5 allows to determine a, the factor of thermodynamic factor (TDF) and $(1-t_+)$

$$a \equiv \mathrm{TDF}\cdot(1-t_+) = \frac{\mathrm{F}\cdot U_{\mathrm{CC}}}{2\mathrm{R}T}\cdot\frac{1}{\ln\left(\frac{c_0+\Delta c}{c_0-\Delta c}\right)} \qquad 6$$

for the arithmetic mean salt concentration c_0 (although the logarithmic mean would be more precise mathematically it only introduces a minor correction for the small concentration pairs and is neglected here). Additional analysis of the short term potential relaxation after galvanostatic pulses in symmetric Li-Li cells (see Eq. 26 in Ref. 6, with $z_+ = 1, \nu_+ = 1$ and $\nu = 2$) allows to obtain the factor

$$\mathrm{TDF}\cdot\frac{(1-t_+)^2}{\sqrt{D^*_{\pm,\mathrm{eff}}}} = \frac{\sqrt{\pi}}{8}\frac{\mathrm{F}^2}{\mathrm{R}\,T}A_{\mathrm{El.}}\cdot\varepsilon_{\mathrm{Sep.}}\cdot\ c_0\frac{U(T_\mathrm{I})}{I_\mathrm{P}\sqrt{T_\mathrm{I}}} \qquad 7$$

with $U(T_\mathrm{I})$, the potential at current interruption time T_I, i.e., directly after application of the constant current I_P. As described before $U(T_\mathrm{I})$ can be obtained by linear extrapolation of the potential versus the artificial time $1-\frac{\sqrt{T_\mathrm{I}}}{\sqrt{t}+\sqrt{t-T_\mathrm{I}}}$ (here t denotes the time from the beginning of the pulse).[6] Knowing the effective binary diffusion coefficient from previous analysis of the long term potential relaxation after the same pulses allows to rewrite Eq. 6 to yield b.

$$b \equiv \mathrm{TDF}\cdot(1-t_+)^2 = \sqrt{\frac{l^2_{\mathrm{Sep.}}}{\pi^2}\cdot m_{\ln}}\frac{\sqrt{\pi}}{8}\frac{\mathrm{F}^2}{\mathrm{R}\,T}A_{\mathrm{El.}}\cdot\varepsilon_{\mathrm{Sep.}}\cdot c_0\frac{U(T_\mathrm{I})}{I_\mathrm{P}\sqrt{T_\mathrm{I}}} \qquad 8$$

If the, herein called, transport factors a and b are determined for the same base concentration c_0 and temperature T, simple arithmetic allows to determine both, the thermodynamic factor and the transference number (see scheme in Figure 1). While this determination scheme has the advantage of requiring only two measurements (concentration cell and pulse polarization) it cannot be used to find single parameters from only one setup (TDF and t_+ require both cells) and thus intrinsically combines possible uncertainties of two experiments.

Figure 1 graphically summarizes the transport parameter determination scheme used in this study and depicts the experimental setups. Properties fixed by the experimental setup and materials (green letters) and the quantities determined from the experiments (blue letters), i.e., the high frequency resistance in the conductivity cell R, the concentration potential in the concentration cell U_{CC}, the slope of the logarithmic potential relaxation for long times after a galvanostatic pulse in a symmetric cell $m_{\ln}$ and the extrapolated potential at current interrupt $U(T_\mathrm{I})$, are marked to allow for an easy distinction.

Subsequently we show representative, exemplary datasets and their analysis so that the reader is able to follow step by step how the final values and their errors, presented in the Results section, are obtained.

Data Analysis

In the following we will present exemplary data and depict the data analysis used to obtain the transport properties shown in the subsequent Results section. In a step by step process we guide the reader through the data treatment which follows the outline sketched in Figure 1 and describe difficulties observed during the measurements. Correct

interpretation and evaluation of the found concentration and temperature dependencies of the electrolyte parameters is only possible when the analysis steps are understood in detail.

Conductivity Cell

Figure 2 shows exemplary Nyquist plots, recorded in the conductivity measurement cell (TSC 1600 closed, rhd Instruments), for 1 M $LiPF_6$ in EMC:FEC (19:1 w:w) at temperatures from -10 °C to 50 °C. The impedance spectra recorded in a frequency range from 85 kHz to 1 kHz using an excitation amplitude of 100 mV show a similar behavior, i.e., a partially visible semicircle at high frequencies followed by a linear capacitive branch at low frequencies. For the extraction of the cell resistances each individual spectrum was fitted automatically with a custom implementation of the modulus weighing[15] in Matlab employing the *fminsearch* algorithm.[16] An equivalent circuit is used consisting of an R/Q element to account for the partially visible, depressed, high frequency semicircle (from the ionic resistance of the electrolyte and the cell's geometrical capacitance) and a serially connected constant phase element to describe the capacitive behavior (from the double layer capacitance at the electrode/electrolyte interfaces) including the phase angle which is slightly below 1 (see not perfectly vertical at low frequencies in Figure 2). Fit curves of the R/Q + Q equivalent circuit model to the experimental data are found to be in excellent agreement and are depicted as solid lines in Figure 2 for the readers benefit. Analysis of the fit parameters allows to extract the resistance value *R* (circles on x-axis in Figure 2 with colors representing measurement temperatures according to legend), corresponding to the ionic resistance of the electrolyte under study and for the current temperature. Final values for the ionic conductivities are obtained with the cell constant (k_C = 20 ± 0.2 1/cm) previously determined using three conductance standards (see Experimental section) and are summarized in Figure 8a-c for all electrolytes, concentrations and temperatures. Error bars for the ionic conductivity correspond to 3 % to account for the error of the cell constant, cell filling and fitting. The obtained conductivities as well as their temperature and concentration dependence are discussed in the scope of all transport factors in the Results section.

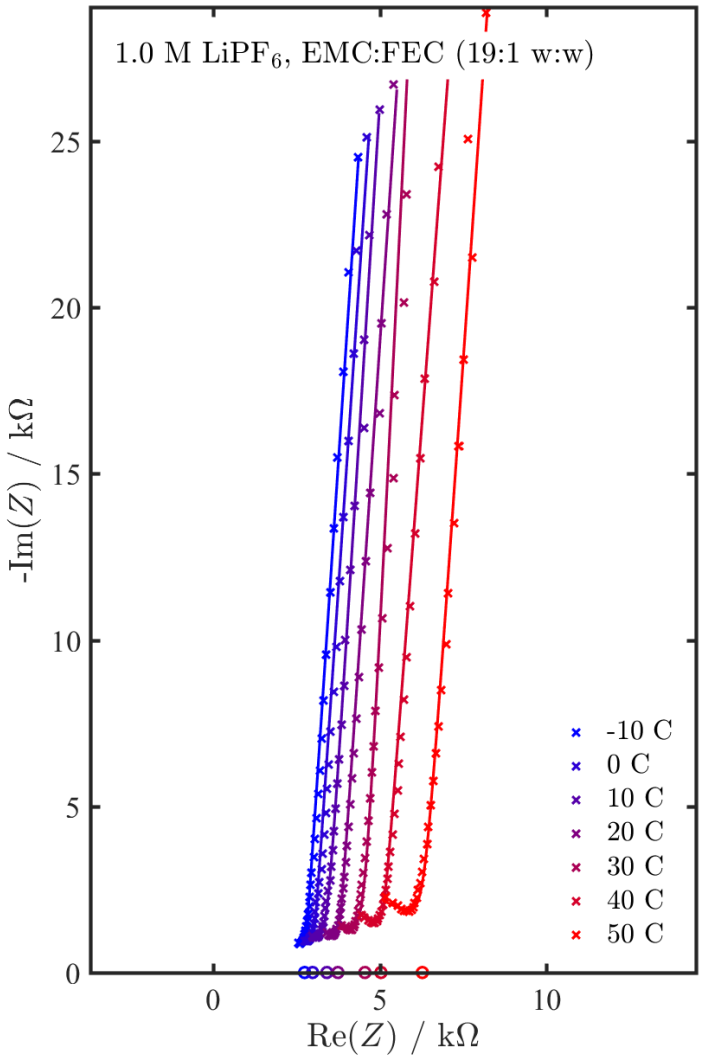

Figure 2. Exemplary data (1 M $LiPF_6$ in EMC:FEC, 19:1 w:w) for temperature dependent determination of ionic conductivity from -10 °C to 50 °C, measured in conductivity cell (rhd instruments, TSC 1600 closed, cell constant 20 ± 0.2 1/cm). Data points from impedance measurement from (85 kHz to 1kHz, 100 mV excitation) are indicated by crosses, the fit with the equivalent circuit (R/Q + Q) is shown as solid lines and the extracted resistance values *R* are marked on the x-axis (open circles), colors indicate measurement temperatures as described by the legend.

Concentration Cell

In contrast to the measurement scheme in the Theory section (Figure 1), where concentrations of $c_0 \pm \Delta c$ are given, the concentrations used with the pouch concentration cells are not symmetrically chosen around the main concentrations used in this work (0.1, 0.5, 1, 1.5, 2, 3 M) but we use adjacent base concentration pairs 0.01 – 0.1, 0.1 – 0.5, 0.5 – 1, 1 – 1.5, 1.5 – 2 and 2 – 3 M $LiPF_6$ in the respective solvents. The rationale behind the enlarged concentration ratios is the smaller signal to noise ratio as smaller concentration potentials would be obtained from smaller concentration differences. Especially with the pouch bag concentration cell setup introduced (see Concentration Cells in the Experimental section) the large distance between the electrodes, coupled with the low ionic conductivity (especially for low salt concentrations and temperatures) will yield very high cell resistances up to

$$R_{CC} = \frac{d \cdot \tau}{\kappa \cdot A \cdot \varepsilon} = \frac{10\ \text{cm} \cdot 5}{1\,\frac{\text{mS}}{\text{cm}} \cdot (500\ \mu\text{m} \cdot 1\ \text{cm}) \cdot 0.3} \approx 3\ \text{M}\Omega \qquad (9)$$

with the dimensions of the separator (10 cm x 500 µm x 1 cm), the porosity and tortuosity of the separator (30% and ~5, compare Coin Cell section in the Experimental) and a conductivity of 1 mS/cm. Open circuit potential measurements of such highly resistive cells might require specialized equipment and are very noise sensitive, e.g., when waling by the setup or when the circulator cooling is running. For that reason the circulator was completely switched of during the measurement period, the temperature however remained very stable during the measurement time (temperature difference prior to switching off and turning the device back on was <0.5 °C). With the setup used in this work, measurement of the concentration potentials in the pouch concentration cells was only possible as long as the two concentrations used differed significantly from each other. The interested reader is encouraged to further improve the noise sensitive setup and/or select suitable measurement devices for the potential determination of highly resistive cells. Figure 3 shows the concentration potentials for all electrolyte solutions, for the sake of completeness, with the used concentrations given next to the measurements inside the figure. Observed concentration potentials range between 20 ± 2 mV (0.5 – 1.0 M $LiPF_6$ in EMC:FEC (19:1 w:w) at -10°C, compare Figure 3c, pink squares) and ~105 ± 2 mV (2 – 3 M $LiPF_6$ in EC:DMC (1:1 w:w) at -10°C, compare Figure 3a, brown squares). For each concentration and temperature at least two cells were measured and the error bars are calculated according to the section Error Calculation using the mean potential during the measurement period as x_i and its standard deviation as Δx_i. Concentration potentials were found to depend fairly linear on the temperature (linear trendlines are added in Figure 3 as a guide to the eye). While for high concentrations a decreasing concentration overpotential is observed for increasing temperatures (~-10 – 20 % from -10 °C to 50 °C, compare brown squares and lines in Figure 3) the trend turns for decreasing concentrations, so that increasing concentration potentials are found for concentration pairs below 0.5 M (~+10 – 30 % from -10 °C to 50 °C, compare turquoise and orange squares and lines in Figure 3). The small temperature dependence of the concentration potentials observed in Figure 3 for all concentration ranges and electrolytes further supports the claimed necessity of enlarged concentration differences to be able to extract a significant temperature trend.

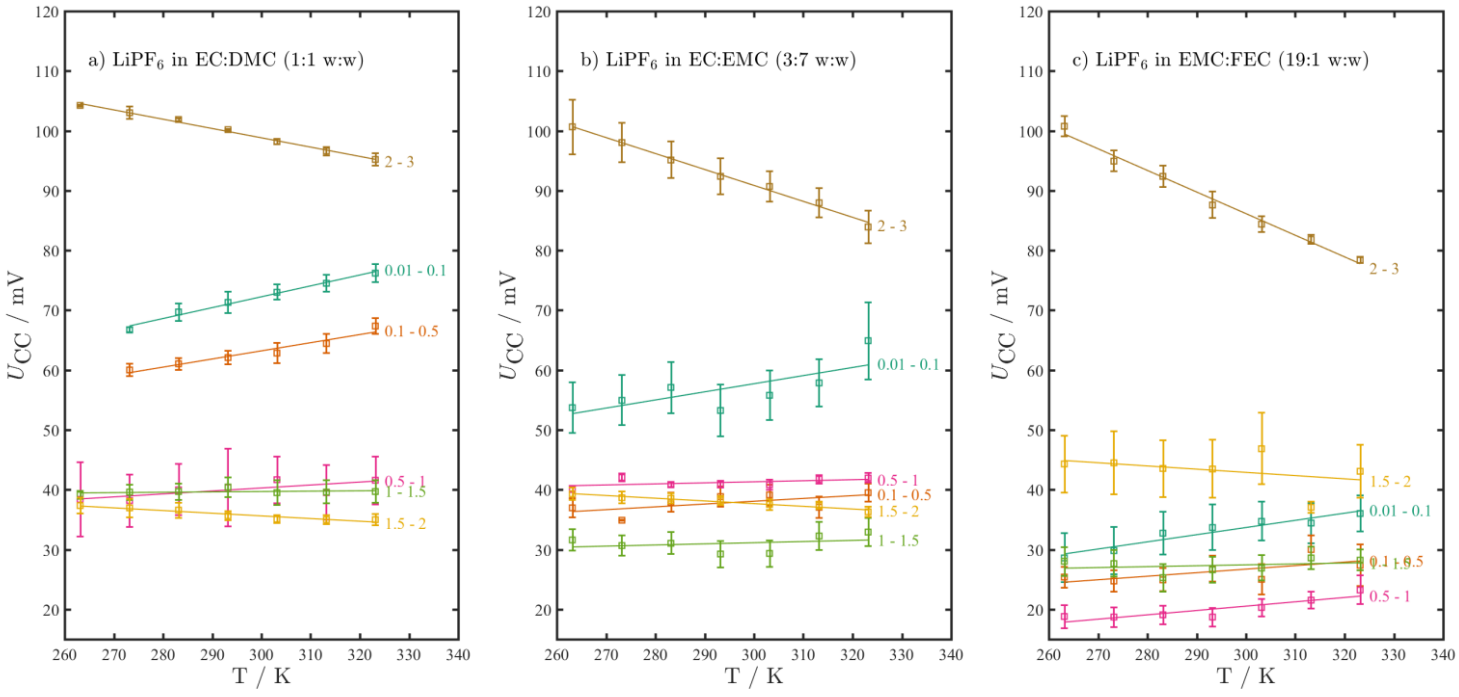

Figure 3. Concentration potentials measured in pouch bag concentration cells for 3 min, temperature controlled using a refrigerated circulator (switched off during measurement) to -10 °C to 50 °C outside the glovebox for $LiPF_6$ in a) EC:DMC (1:1 w:w), b) EC:EMC (3:7 w:w) and c) EMC:FEC (19:1 w:w) and the two concentrations as given in the figure. Errors are calculated as explained in the section Error

Calculation with the mean potential during the measurement period as x_i and its standard deviation as Δx_i, at least two cells were measured for each configuration.

As explained in the Theory section it is advantageous to convert the measured concentration potentials into the transport factors a ($\equiv \mathrm{TDF} \cdot (1 - t_+)$) by assuming a constant TDF and a constant transference number between the two electrolyte concentrations used in the pouch concentration cells (see Eq. 6). From the finally obtained temperature and concentration dependent transference number and thermodynamic factor the error due to the simplification of the integral was tested by comparison of Eq. 3 and Eq. 5 and the difference between both was found to be below 10 % (see Supporting Information, Figure 3). Figure 4 shows the factors *a*, calculated from the concentration potentials in Figure 3 (square symbols, with color corresponding to the temperature, see legend in figure). Here always the mean concentration is used as x-axis value (e.g., *a* for 1.5 – 2.0 M is plotted at *c* = 1.75 M). *a* is found to behave similar for all electrolytes under investigation. At mean concentrations of 0.055 M (mean between 0.01 M and 0.1 M) and for all temperatures values between 0.3 and 0.6 are obtained while for increasing concentrations the values increase (3.5 to 6 for mean concentration of 2.5 M, i.e., mean of 2 M and 3 M) and the difference between the temperatures becomes more prominent. For 2.5 M $LiPF_6$ in EC:EMC (3:7 w:w) we find values of ~4 at 50°C and ~5.8 at -10°C (see Figure 4b). When comparing the transport factor *a* reported in the literature for $LiPF_6$ in EC:EMC (3:7 w:w) at 25 °C to our measurements for the same electrolyte (at 20 °C or 30 °C) an excellent agreement can be found (see solid black line in Figure 4b). Additionally, although not representing exactly the same electrolyte composition, we depict the transport factor *a* for $LiPF_6$ in PC (propylene carbonate):EC:DMC (10:27:63 v:v:v)[8] in the temperature range from -10 °C (blue line, upper limit) to 50 °C (red line, lower limit) as the grey shaded area in Figure 4a. While the trends agree well at low concentrations, for increasing amounts of $LiPF_6$ the transport factor *a* found by Valøen and Reimers remains at lower values (in average 4 at 2.5 M compared to 5 for our measurements), likely due to the different electrolyte composition including PC. Additionally shown in Figure 4 are linear inter- and extrapolated points at the base concentrations used in this work, i.e., 0.1, 0.5, 1.0, 1.5, 2 and 3 M, which are necessary to follow the analysis scheme introduced in the Theory section (see Figure 1) and which will be explained below. The reader is reminded that in this work it was necessary to use enlarged concentration ranges for the measurement of concentration potentials due to high cell resistances and noise-prone measurements. An optimized setup for an accurate determination of concentration cell potentials might enable the use of differential concentrations around the base concentrations of interest ($c_0 \pm \Delta c$, compare Figure 1) and will vitiate the need for inter- and extrapolation.

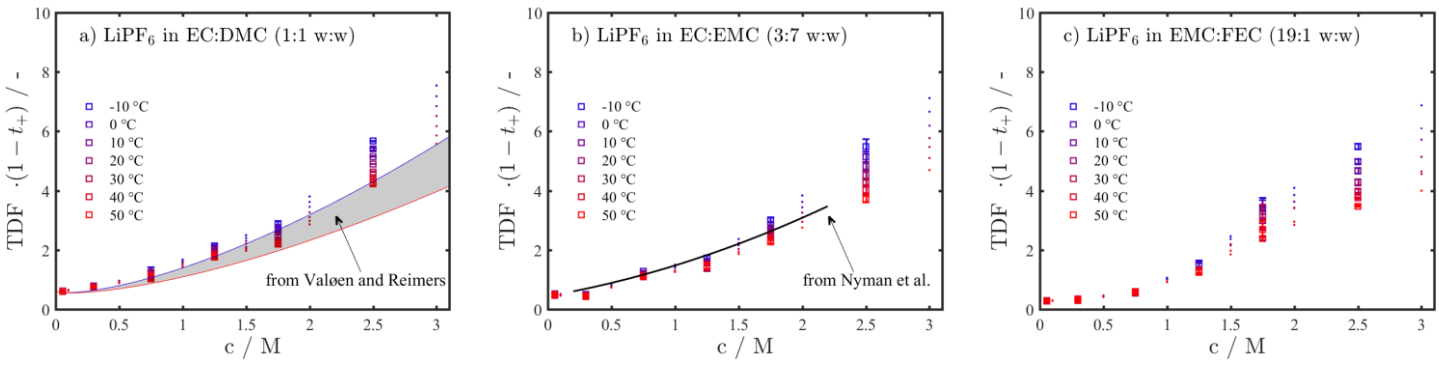

Figure 4. Transport factor *a* ($\equiv \mathrm{TDF} \cdot (1 - t_+)$), for $LiPF_6$ in a) EC:DMC (1:1 w:w), b) EC:EMC (3:7 w:w) and c) EMC:FEC (19:1 w:w) and from -10 °C to 50 °C, calculated from concentration potentials shown in Figure 3 by means of the simplification discussed in the Theory section (see Eq. 3-6). Data points are shown at the mean concentration of the concentration cell setup (squares, color according to measurement temperature, compare legend in the figure) including linear inter- and extrapolation points to the base concentrations used in this work (0.1, 0.5, 1, 1.5, 2 and 3 M, compare dots in the figure with color according to measurement temperature). Additionally depicted are the transport factors *a* reported

in the literature for $LiPF_6$ in PC:EC:DMC (10:27:63 v:v:v, grey shaded area from blue line upper limit at -10 °C to red line lower limit at 50 °C in Figure 4a)[8] and $LiPF_6$ in EC:EMC (3:7 w:w) at 25 °C (solid black line in Figure 4b).[17] Errors are calculated as explained in the section Error Calculation with the individual a values from repeat cells as x_i and their uncertainty, based on the standard deviation of the concentration potential during the measurement time, as Δx_i, at least two cells were measured for each configuration.

It is noted, that Figure 4 tempts to draw first conclusions on the absolute values of the transference. As, by definition, the mean molar activity coefficient, and thus also the thermodynamic factor, is 1 at infinite dilution the transference number could be estimated at the low concentration range. However, because the smallest concentration in Figure 4 is 55 mM (mean of 10 and 100 mM) and the Debye Hückel behavior of the activity coefficient suggests a steep decrease from 1 to smaller values in the small concentration range,[18] no reliable predictions can be obtained and the authors refrain from analyzing these measurements in order not to mislead the reader.

Pulse Experiments

To obtain the binary diffusion coefficient as well as the transport factor b ($\equiv \mathrm{TDF} \cdot (1 - t_+)^2$, compare Figure 1), which is necessary to deconvolute transference number and thermodynamic factor with the previously determined transport factor a, pulse experiments in symmetric lithium coin cells (see Experimental for measurement procedure and Figure 1 for cell setup) were conducted. For each base concentration (0.1, 0.5, 1, 1.5, 2 and 3 M) of the electrolytes under study ($LiPF_6$ in EC:DMC (1:1 w:w), $LiPF_6$ in EC:EMC (3:7 w:w) and $LiPF_6$ in EMC:FEC (19:1 w:w)) two coin cells were built, for a detailed overview of the measurement procedure the reader is referred to Table 1 in the Experimental.

In the following we first show the determination of the binary diffusion coefficient exemplarily, based on the long term potential relaxation after the galvanostatic pulses (for details on the method the reader is referred to Ref. 5). In this work the binary diffusion coefficient is obtained from the slope of the exponential potential relaxation after current interrupt at long times. Therefore we exemplarily show the logarithmic potential measured after application of the second (negative) current pulse in symmetric lithium cells containing 0.1 M $LiPF_6$ in EC:DMC (1:1 w:w) at temperatures from -10 °C to 50 °C (see Experimental for precise temperatures) in Figure 5. Even in the long time limit the potential of the coin cells did not relax to zero mV exactly, but a finite offset U_{Offset}, typically below 1 mV, remained and was subtracted from the measured potentials. In this work U_{Offset} is taken as the mean of the last 100 points (= last 5 min) recorded during the relaxation period. The ranges for the linear trends, marked for each temperature in Figure 5 (see black, dashed lines), are selected as follows. Due to a finite noise level of the potential measurement (~0.3 mV) we defined the endpoint for the linear trendline as the time for which the measured potential dropped below 0.3 mV for the first time (with U_{Offset} subtracted from the experimental data already). The start time for linear extrapolation was chosen as 15 % of the end time. Because different pulse currents were applied for different temperatures (see Table 1), in order to maximize the signal to noise ratio without driving too much lithium plating, the absolute starting potentials vary and the experimental data in Figure 5 is further shifted by y (chosen, so that the linear trendlines start at 1) to enable simple comparison. From the representative data shown in Figure 5 clear linear trends can be observed for all measurement temperatures over reasonably long periods of time (~10 to 60 min at 50 °C and -10 °C respectively). It is noted that a relaxation time of ~4 h (compare measurement procedure in Table 1) was necessary to allow for a full potential relaxation, especially for the concentrated, e.g., 2 and 3 M electrolyte solutions and at low temperatures.

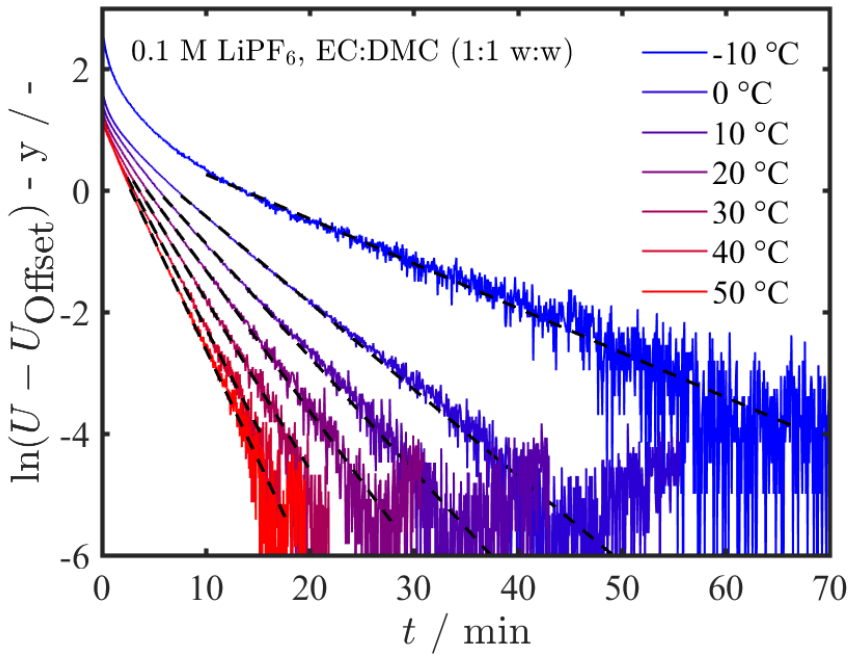

Figure 5. Exemplary data (0.1 M $LiPF_6$ in EC:DMC, 1:1 w:w) for temperature dependent determination of binary diffusion coefficient from -10 °C to 50 °C, measured in symmetrical lithium coin cell using a plasma treated Nitto separator as a porous medium (see Experimental for details on the setup and Table 1 for the measurement procedure). Potentials are offset corrected (mean of last 5 min, always below 1 mV) and shifted so that linear trendlines start at 1. Time ranges for the linear trendlines (shown as black dashed lines) are selected automatically, for details the reader is referred to the main text. Colors represent measurement temperatures as described by the figure legend, the reader is referred to the Experimental for a details on the precise measurement conditions.

When the cell potential U (subtracted by U_{Offset}) approaches 0 mV, the logarithmic representation starts to show high scatter due to the finite measurement accuracy (see -10 °C curve in Figure 5) and we only show data around the time range selected for linear extrapolation. To check the validity of the selected time range we also determine the linear trendlines of the time ranges shifted by ±50 % of the start time, i.e., in total, three values for the slope $m_{\ln}$ are obtained. From the slope value $m_{\ln}$, the separator thickness $l_{\mathrm{Sep.}}$ and its tortuosity $\tau_{\mathrm{Sep.}}$ (see Coin Cells in the Experimental) the binary diffusion coefficient $D_{\pm}$ can be obtained for the given electrolyte at the chosen salt concentration and temperature (see Eq. 1 and 2). Weighted mean diffusion coefficients and their error are calculated from the positive and negative pulse experiments of both repeat cells according to the Error Calculation section using the mean of the three $D_{\pm}$ values from the three time ranges as x_i and their standard deviation as Δx_i. Finally obtained values for the diffusion coefficient and their temperature and concentration dependence for the electrolytes under study are summarized in Figure 8 and will be discussed in the Results section in the scope of all transport parameters.

In addition to the determination of the binary diffusion coefficient from the potential relaxation after the galvanostatic pulses in symmetric lithium cells, the short time behaviour of the potential after current interrupt allows to determine the transport factor b ($\equiv \mathrm{TDF} \cdot (1 - t_+)^2$, compare Figure 1) by means of Eq. 8. For the evaluation of Eq. 8, known setup parameters (separator thickness $l_{\mathrm{Sep.}}$ and porosity $\varepsilon_{\mathrm{Sep.}}$, temperature T, salt concentration c_0 and active electrode area $A_{\mathrm{El.}}$), selected measurement characteristics (current interrupt time T_{I} and pulse current I_{P}), the previously determined slope of the exponential potential relaxation $m_{\ln}$ and the, so far unknown, potential at current interrupt $U(T_{\mathrm{I}})$ are required. Exemplarily we show the determination of $U(T_{\mathrm{I}})$ for the potential relaxation recorded in a symmetrical lithium coin cell filled with 2 M $LiPF_6$ in EC:EMC (3:7 w:w). Figure 6 shows the potential transients after the second (negative current) pulse recorded at temperatures from -10 °C to 50 °C, plotted versus the artificial time $\tau^* = 1 - \frac{\sqrt{T_{\mathrm{I}}}}{\sqrt{t}+\sqrt{t-T_{\mathrm{I}}}}$.[6,19] To allow

for a simple comparison the potential values are normalized by the finally obtained potential at current interrupt. In Figure 6 the typical s-shaped potential transients are observed for all temperatures (see Ref. 5 and 6), while the step appears later for smaller measurement temperatures. At -10 °C the step can be observed at $\tau^* = 0.75$ (≈ 1 h after current interrupt) while for the 50 °C measurements the step is clearly visible at $\tau^* = 0.4$ (≈ 4 min after current interrupt). It has to be noted that the observation of the s-shape is a necessary requirement for the applicability of the analysis method and thereby further fortifies our experimental results.[5] Also visible in Figure 6 is the pronounced deviation from the theoretically expected linear behavior for small times (see inset in Fig. 4 of Ref. 5), which might be caused by SEI recreation effects and predominately occurs at small measurement temperatures (see blue curves in Figure 6). In contrast to the automated selection of the linear time range for the determination of the binary diffusion coefficient, the time range (in terms of τ^*) for the linear extrapolation in Figure 6 was selected manually. The center of the linear range at the beginning of the s-shaped potential transient, excluding the deviations at small times, was selected by eye and linear extrapolations were done using a time range of ± 0.075 (in terms of τ^*) around that value. Although selected on an experiment by experiment basis the selected center points generally lie close to τ^*= 0.15 for measurements at 50 °C and around $\tau^* = 0.5$ at -10 °C, i.e., a consistent trend for the appearance of the step was found for all electrolytes under study. In Figure 6 the τ^* ranges used for the linear extrapolation are shown as range bars above the potential transients (colors corresponding to measurement temperatures, see legend in figure for details). The extrapolation of the measured potentials in the selected τ^* ranges to the y-axis yields the potential at current interrupt $U(T_\mathrm{I})$ (unity in Figure 6 due to normalization of potentials). The uncertainty of the obtained $U(T_\mathrm{I})$ values is taken as the 95% confidence interval of the fit parameter $U(T_\mathrm{I})$, which is calculated using the *confint* function in Matlab.[16]

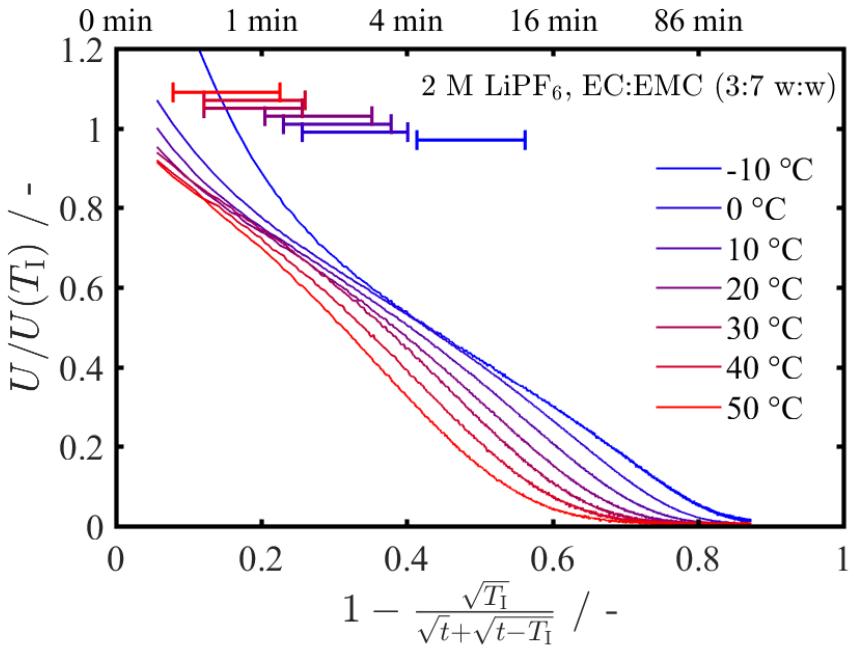

Figure 6. Exemplary potential transients recorded in symmetric lithium coin cells with a plasma treated Nitto separator as a porous medium after application of a current of 300 µA (~ 130 µA/cm²) for 15 min, filled with 2 M $LiPF_6$ in EC:EMC (3:7 w:w) in the temperature range from -10 °C to 50 °C (see figure legend for details), plotted versus the artificial time $\tau^* = 1 - \frac{\sqrt{T_\mathrm{I}}}{\sqrt{t}+\sqrt{t-T_\mathrm{I}}}$. S-shaped curvature, as required for application of the method,[5] is clearly visible at all measurement temperatures, while for small times deviations occur from the reconstruction of the SEI (see blue, -10 °C curve). Time for the linear extrapolation to the y-axis are shown above the potential transients (color corresponding to measurement temperature) and are selected manually, judged by eye. Real times indicated at the top x-axis correspond to the time after current interrupt, i.e., 0 min equals t = 15 min (since beginning of the pulse).

Analysis of the pulse experiments and extraction of the potentials at current interrupt times, as exemplarily shown for the electrolyte 2 M $LiPF_6$ in EC:EMC (3:7 w:w) in Figure 6, allows to calculate the corresponding transport factors b ($\equiv \mathrm{TDF} \cdot (1-t_+)^2$) for each electrolyte, concentration and temperature (see Eq. 8). In analogy to the previously discussed analysis of the concentration overpotentials, and the resulting values for the transport factor a ($\equiv \mathrm{TDF} \cdot (1-t_+)$) in Figure 4, we summarize b for $LiPF_6$ in EC:DMC (1:1 w:w), EC:EMC (3:7 w:w) and EMC:FEC (19:1 w:w) in Figure 7 a), b) and c) respectively. As before, values are calculated according to the section Error Calculation with the individual values for b (from positive and negative currents and both repeat cells) taken as x_i and their error, based on the confidence interval of $U(T_\mathrm{l})$, as Δx_i (note that we omit the error in m_ln here). Figure 7 closely resembles the qualitative behaviour observed for the transport factor a in Figure 4, increasing values for higher concentrations and lower temperatures. E.g., b ranges from 0.1 (50 °C) to 0.3 (-10 °C) for 0.1 M $LiPF_6$ in EC:EMC (3:7 w:w) and increases to ~4 (50 °C) to 14 (-10 °C) for the same electrolyte, compare Figure 7b. For all electrolytes investigated in this study steadily increasing values are found from 50 °C to 0 °C. Measurements conducted at -10 °C generally show an increased offset compared to the other temperatures, most pronounced at highest concentrations, which is accompanied by an increases error bar in Figure 7a and b. It is important to note, that only for the EC free electrolyte (see Figure 7c) and at 3 M $LiPF_6$ this spread is not observed.

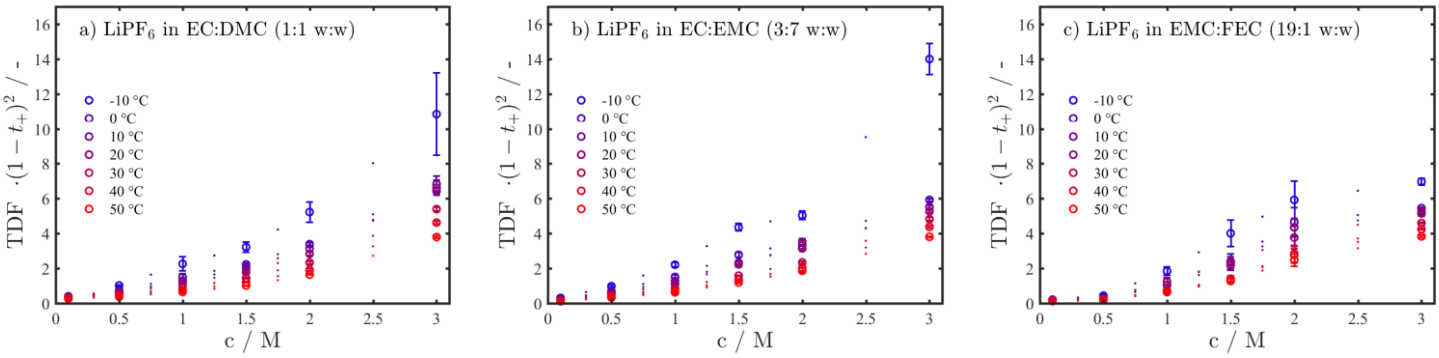

Figure 7. Transport factor b ($\equiv \mathrm{TDF} \cdot (1-t_+)^2$), for 0.1 to 3 M $LiPF_6$ in a) EC:DMC (1:1 w:w), b) EC:EMC (3:7 w:w) and c) EMC:FEC (19:1 w:w) and from -10 °C to 50 °C, calculated with the previously determined slope of the exponential potential relaxation for long times (exemplarily shown in Figure 5) and the potential at current interrupt (exemplarily shown in Figure 6) by means of Eq.8. Data points (circles, color according to measurement temperature, compare legend in the figure) as well as linear interpolations to the mean concentrations from the concentration cell (0.3, 0.75, 1.25, 1.75 and 2.5 M, compare dots in the figure with color according to measurement temperature) are shown. Errors are calculated as explained in the section Error Calculation with the individual b values x_i and their error based on the confidence interval of $U(T_\mathrm{l})$, as Δx_i, at least two cells were measured for each configuration and positive and negative current pulses are analyzed.

Error Calculation[20]

In this work error bars are given to indicate the accuracy of the n repeat measurements. Specifically we calculate the weighted mean $\bar{x}$ by

$$\bar{x} = \frac{\sum_{i=1}^{n} w_i \cdot x_i}{\sum_{i=1}^{n} w_i} \qquad 10$$

with the weighing factor w_i being defined as

$$w_i = \frac{1}{\Delta x_i^2}. \qquad 11$$

Here x_i is the measured value and Δx_i its uncertainty. Furthermore we determine the standard deviation of the weighted mean $\Delta\bar{x}$.

$$\Delta\bar{x} = \frac{1}{\sqrt{n}} \underbrace{\sqrt{\frac{1}{n-1}\sum_{i=1}^{n}(x_i - \bar{x})^2}}_{\text{std. dev.}} \qquad 12$$

Results

In the following we will discuss the obtained concentration and temperature dependent transport and thermodynamic parameters of ionic transport in binary electrolytes obtained for the three electrolyte solutions under study. Ionic conductivities and binary diffusion coefficients are determined as outlined in the section Data Analysis. Transference numbers and thermodynamic factors are calculated for each concentration and temperature with the transport factors *a* and *b* (see Figure 4 and Figure 7) using the equations given in the scheme in Figure 1, i.e.,

$$t_+ = 1 - \frac{b}{a} \qquad 13$$

and

$$\mathrm{TDF} = \frac{a^2}{b}. \qquad 14$$

Due to the necessity to measure the factor *a* for larger concentration differences to be able to detect temperature effects (see Figure 3) and the consequently different mean concentrations (0.055, 0.3, 0.75, 1.25, 1.75 and 2.5 M) compared to the base salt concentrations used in this work (0.1, 0.5, 1, 1.5, 2 and 3 M), Eq. 13 and 14 are always obtained from one measured (squares in Figure 4 and circles in Figure 7) and an interpolated (dots in Figure 4 and Figure 7) value of *a* and *b* or vice versa. For example the thermodynamic factor of 1 M $LiPF_6$ in EC:DMC (1:1 w:w) at 10 °C is obtained from the linearly interpolated transport factor a = 1.59 (from *a* values at 0.75 M, 1.18 and 1.25 M, 2.01) and the measured transport factor *b* (1.28 at 1 M) by means of Eq. 14 to 1.98. Analogously the transference number for, e.g., 2.5 M $LiPF_6$ in EMC:FEC (19:1 w:w) at 40 °C is calculated with Eq. 13 using the measured transport factor *a* (3.74 at 2.5 M) and the linearly interpolated transport factor b = 3.51 (from *b* values at 2 M, 2.78 and 3 M, 4.25) to be 0.06. Gaussian error propagation of Eq. 13 and 14 is used for the calculation of the errors of transference number and thermodynamic factor using the individual errors of *a* and *b* as obtained from the data analysis.

In addition to reporting our measurement results we aim at providing reliable concentration and temperature dependent descriptions of the thermodynamic and transport parameters. Yet, because the temperature and concentration dependence of especially the thermodynamic factor and the transference number lack a solid theoretical foundation, empirical functions (here polynomials) are used to approximate the real temperature and concentration dependence. It is emphasized that obtained functional descriptions serve as an approximation only and that better correlation with experimental data might be obtained for different types of base functions.

To give an overview we first analyse all parameters using functions to describe the temperature and concentration dependence simultaneously. As this multi temperature approach shows, that the complex temperature and concentration

dependence of the transference number and the thermodynamic factor make it challenging to obtain a comprehensive mathematical description, we subsequently analyse these two parameters on a per temperature basis.

Regression Analysis

Before introducing the results it is of absolute necessity to describe in detail how measured parameters are fitted to the functions given below. Without precise specification of the weighing factors and minimization algorithms used in this work somewhat different fit parameters may be obtained. Due to the complexity of data treatment and the large number of individual measurements (> 900) a thorough data management is required. In this work we use Matlab (Mathworks, V. R2017a) to manage experimental data and its built-in fitting algorithms for the regression analysis.

Specifically we use the *NonLinearLeastSquares* method of the *fit* function with the *Trust-Region-Reflective* algorithm.[16] Data points are weighed by $1/\Delta\bar{x}$ to get a significant fit. For the observant reader we note that the weighing for the weighted mean Eq. 11 was based on $1/\Delta x_i^2$ because there Δx_i describe *systematic* errors (e.g., noise during measurement time in case of concentration cell potentials) while for the fitting the *statistical* errors $\Delta\bar{x}$ from repeat measurements (the not-squared version) is used.[20] Obtained fit parameters are tabulated below (see Table 2 and Table 3) with their percental confidence intervals based on a 90 % standard deviation (in brackets) as well as the R^2 values for the individual fits.

Concentration and Temperature Dependent Analysis

Temperature and concentration dependencies of the ionic conductivity (a – c), the binary diffusion coefficient (d – f), the thermodynamic factor (g – i) and the transference number (j – l) for the three electrolytes under study (see figure legends) are summarized in Figure 8. In addition to experimental results and fit curves to be discussed below, Figure 8 also shows parameters reported in the literature. Although not exactly representing the EC:DMC (1:1 w:w) electrolyte used in this work we include (see Figure 8a, d, g, j) the evaluated fit functions for the transport and thermodynamic parameters at -10°C and 50 °C reported by Valøen and Reimers[8] (PC:EC:DMC 10:27:63 v:v:v) to our measurements as a reference due to its wide application in battery models. Nyman et al. reported trends for the EC:EMC (3:7 w:w) electrolyte also used in this work, and we show their 25 °C temperature curves as a reference in Figure 8 (b, e, h, k) as well.

The ionic conductivities determined from the conductivity cells increase with increasing temperature for all electrolytes and show a pronounced conductivity maximum. Highest conductivities are obtained between ~0.75 M (at -10 °C) and ~1 M (at 50 °C) in EC:DMC and EC:EMC, while the peak conductivities for the EC free electrolyte are shifted to higher concentrations (~1.25 M at -10 °C to ~1.6 M at 50 °C). Most ionic conductivities lie in the range of ~0.5 mS/cm (3 M $LiPF_6$ at -10 °C) to ~ 17 mS/cm (1 M $LiPF_6$ in EC:DMC (1:1 w:w) at 50 °C). Generally higher conductivities are obtained for the EC:DMC based electrolyte (Figure 8a) while lowest conductivities are obtained with the EC free electrolyte (Figure 8c). For 0.1 M $LiPF_6$ in EMC:FEC (19:1 w:w) the conductivities at all temperatures lie in the range from 0.05 mS/cm (-10 °C) to 0.1 mS/cm (50 °C) and thereby way below the conductivities found for the EC containing electrolytes at the same concentration (~2 – 5 mS/cm, compare Figure 8a and b) which may be due to a high degree of ion association. Also shown in Figure 8a-c are the fits of experimental data to[21]

$$\kappa(c,T) = p_1\left(1 + (T - p_2)\right) \cdot c \cdot \frac{\left(1 + p_3 \cdot \sqrt{c} + p_4 \cdot \left(1 + p_5 \cdot \exp\left(\frac{1000}{T}\right)\right) \cdot c\right)}{1 + c^4 \cdot \left(p_6 \cdot \exp\left(\frac{1000}{T}\right)\right)} \cdot \frac{\text{mS}}{\text{cm}} \qquad 15$$

with the free fitting parameters p_i. Here, as well as subsequently, the concentration c is used in units of molar concentrations (M/L) and the temperature in units of Kelvin (K). While Eq. 15 is empirically chosen it was selected to fulfil two theoretical limits, for infinite concentrations it approaches 0 (no negative values allowed)

$$\lim_{c\to\infty} \kappa(c,T) = 0 \qquad 16$$

and the Kohlrausch square root law can be obtained in the small concentration limit[22]

$$\lim_{c\to 0} \kappa(c,T) = p_a \cdot c + p_b \cdot c^{\frac{3}{2}}. \qquad 17$$

Very good agreement of the fits can be found for all three solvents (see R^2 values > 0.995 for all solvents in Table 2) and obtained fitting parameters are given in Table 2 including their percental confidence intervals based on a 90% standard deviation. Conductivities reported for EC:DMC (1:1 w:w) generally agree well with the similar electrolyte composition reported by Valøen and Reimers (PC:EC:DMC 10:27:63 v:v:v), as shown for reference in Figure 8a (grey highlighted region with the same upper and lower temperature limits as in this study (-10 °C to 50 °C).[8] In addition we show the conductivities measured by Nyman et al. for the same electrolyte composition used in this study (EC:EMC (3:7 w:w)) at 25 °C as a black solid line in Figure 8b.[17] The reported conductivities by Nyman et al. lie well between our 20 °C and 30 °C measurements, with slightly higher values (our measurement: 7.6 mS/cm at 30 °C, Nyman et al. 7.9 mS/cm at 25 °C) reported in the literature for 0.5 M $LiPF_6$ in EC:EMC (3:7 w:w, compare Figure 8b). Although not shown explicitly in Figure 8a our measurement for 1 M $LiPF_6$ in EC:DMC (1:1 w:w) also agrees well with the value reported by Farkhondeh et al. (11.9 mS/cm at 25 °C, this study 10.8 mS/cm at 20 °C and 12.9 mS/cm at 30 °C).[12] To further validate our measurements we compared the temperature dependence of the 1 M electrolyte conductivities for EC:DMC (1:1 w:w) and EC:EMC (3:7 w:w) with the specification sheet from BASF for their electrolytes of the same composition (tradenames LP30 and LP57) and obtain very good agreement (see Supporting Information Figure 2).

Figure 8d – f depict the concentration and temperature dependent binary diffusion coefficients we obtain from the analysis of the long term potential relaxation after galvanostatic pulses for the three electrolyte solutions (see Figure 5 in the section Data Analysis and Ref. [5]). The diffusion coefficients in Figure 8 are empirically fitted with

$$D_{\pm}(c,T) = p_1 \cdot \exp(p_2 \cdot c) \cdot \exp\left(\frac{p_3}{T}\right) \cdot \exp\left(\frac{p_4}{T} \cdot c\right) \cdot 10^{-6}\,\frac{\mathrm{cm}^2}{\mathrm{s}} \qquad 18$$

with four free fitting parameters p_1 to p_4. Eq. 18 was selected to be in accord with an Arrhenius type temperature dependence (i.e., $D_{\pm} \propto p_a \cdot \exp\left(\frac{p_b}{T}\right)$). In contrast to the clearly different ionic conductivities the diffusion coefficients of all three electrolytes are found to be almost identical. At 0.1 M $LiPF_6$ concentrations the diffusion coefficients lie between $\approx 2.3 - 7.4 \cdot 10^{-6}\ \mathrm{cm}^2/\mathrm{s}$ (EC:DMC (1:1 w:w) and EC:EMC (3:7 w:w)) and $\approx 2.7 - 8.0 \cdot 10^{-6}\ \mathrm{cm}^2/\mathrm{s}$ (EMC:FEC (19:1 w:w)) for temperatures of -10 °C and 50 °C respectively. For increasing salt concentrations the diffusion coefficients decrease, e.g., for the same temperature range at 3 M $LiPF_6$ to $\approx 0.2 - 2.4 \cdot 10^{-6}\ \mathrm{cm}^2/\mathrm{s}$ (EC:DMC (1:1 w:w), $\approx 0.2 - 1.6 \cdot 10^{-6}\ \mathrm{cm}^2/\mathrm{s}$ (EC:EMC (3:7 w:w)) and $\approx 0.2 - 2.0 \cdot 10^{-6}\ \mathrm{cm}^2/\mathrm{s}$ (EMC:FEC (19:1 w:w), compare Figure 8d – f). The observed decrease of the binary diffusion coefficient with increasing concentration is expected due to the increasing electrolyte viscosity.[22] In all cases temperature and concentration dependent fit functions represent experimental data well, while higher scatter is observed compared to the previously discussed ionic conductivity measurements. Both symmetric lithium coin cells filled 1.5 M $LiPF_6$ in EMC:FEC (19:1 w:w) yield somewhat higher diffusion coefficients than expected from the neighboring 1 M and 2 M electrolytes (see Figure 8f). The scatter and the simultaneously small error bars, based on the statistical variation of repeat measurements (here 2

cells with 2 pulses each) indicate that a systematic error due to, e.g., cell building effects or separator inhomogenities are not accounted for with the current error analysis and data quality might profit from a higher number of repeat cells. Still a reasonably well correlation of the experimental data with Eq. 18 can be obtained in all cases, yielding R^2 values of 0.97 and above (see Table 2 for R^2 values and fit parameters p_i). Reported diffusion coefficients in the literature[8,17] generally show similar values ($\approx 0.05 - 6.0 \cdot 10^{-6}$ cm^2/s for 1 M $LiPF_6$ in PC:EC:DMC (10:27:63 v:v:v) at -10 °C to 50 °C,[8] (see grey highlighted area in Figure 8d) and $4.5 - 2.0 \cdot 10^{-6}$ cm^2/s for 0.2 to 2 M $LiPF_6$ in EC:EMC (3:7 w:w) at 25 °C,[17] compare black crosses in Figure 8e) and the same trends, i.e., decreasing $D_{\pm}$ for increasing concentration and decreasing temperature. Yet stronger concentration dependencies are obtained when analyzing the functional descriptions reported in the literature, compared to the measurements in this study (see grey highlighted region in Figure 8d). In the calculation by Valøen and Reimers the diffusion coefficient is obtained based on their previously *determined* transference number and thermodynamic factor (see Eq. 13 in Ref. [8]). Because the authors assume a concentration and temperature independent transference number their diffusion coefficient will automatically incorporate these dependencies if the assumption on the transference number was imprecise. Because the diffusion coefficients determined in this study are obtained individually on a per concentration and per temperature basis (see scheme in Figure 1) without the necessity for any other transport properties we are confident that the increased diffusion and concentration dependence reported in the literature is due to the oversimplified transference number. Indeed Eq. 13 in Ref. [8] would predict smaller diffusion coefficients at elevated temperatures if the transference number is > 0.38 and higher diffusion coefficients at low temperatures if the transference number is < 0.38 which nicely correlates with our transference numbers, which will be discussed in detail below. For the 1 M $LiPF_6$ in EC:DMC (1:1 w:w) electrolyte Farkhondeh et al. report a binary diffusion coefficient of 2.7×10^{-6} cm^2/s at 25 °C, which is fairly close to our measurement (2.0×10^{-6} cm^2/s at 20 °C).[12] Diffusion coefficients reported by Nyman et al. (called apparent diffusion coefficients in the original publication, compare Figure 8e) at 25 °C lie between our values obtained at 30 °C to 40 °C (see solid black crosses in Figure 8e). Most likely the reason for this offset is caused by errors in the used cell geometry parameters, e.g., the uncertainty in the porous medium tortuosity or electrode distance.

Because the previously introduced direct measurement of the thermodynamic factor from cyclic voltammograms of the ferrocene/ferrocenium redox couple is not strictly valid, thermodynamic factors and transference numbers are calculated from the factors *a* and *b* (see Theory section as well as the scheme in Figure 1).[7,14] I.e., in contrast to the analysis of the ionic conductivity and the binary diffusion coefficient single parameters cannot be obtained from a single measurement anymore, yielding an intrinsically higher uncertainty. Yet it is emphasized that compared to the determination methods reported in the literature no assumptions on either transference number or thermodynamic factor has to be made (seed to assumed constant transference number in Ref. [8]) and obtained values for both parameters are explicit. In Figure 8g – l data points based on the measured factor *a* from concentration cell experiments are plotted as squares, data points based on the measured factor *b* from the pulse experiments are plotted as circles (i.e., analogously to Figure 4 and Figure 7). The thermodynamic factors we obtain from the analysis of the temperature and concentration dependent concentration potentials and the analysis of the short term behaviour after galvanostatic pulses in a symmetric lithium coin cell are depicted in Figure 8g – i. We deliberately start discussing the TDF rather than the transference number as it may be compared (at least partly) with theoretical considerations. By definition, the mean molar activity coefficient starts at 1, so that also the TDF $\left(\equiv 1 + \frac{\mathrm{d}\ln f_{\pm}}{\mathrm{d}\ln c}\right)$, theoretically should start at 1 at infinite dilution and initially decreases according to the Debye-Hückel theory,[23] thereby serving as a quality measure for experimentally obtained data. It is emphasized that the calculation of the TDF according to Eq. 14 is unbiased in terms of a fixed reference value and

obtained values close to 1 (0.5 to 1.5 for EC:DMC (1:1 w:w) and EMC:FEC (19:1 w:w), corresponding to the -10 °C and 50 °C boundaries respectively) in the small concentration limit as well as the decrease of the TDF at small concentrations as visible for EMC:FEC (19:1 w:w, ~0.3 – 0.5 at -10 °C from 0.35 to 0.75 M, compare Figure 8l) validate our results theoretically. TDFs for $LiPF_6$ in EC:EMC (3:7 w:w) lie well above the theoretical low concentration limit (~1 – 2.2 at 0.1 M, compare Figure 8h) and indicate erroneous measurements which we believe is due to unstable passivation of the metallic lithium electrodes. The reader is reminded that these data points are based on measured transport factors *b* from symmetric lithium coin cells nominally containing 0.1 M $LiPF_6$. Side reactions at low salt concentrations, due to, e.g., unstable SEI formation, may alter the electrolyte composition and invalidate the application of concentration dependent analytical solutions such as Eq. 8 (see also discussion in section "Transference number via polarization cell and concentration cell experiments" in Ref. [6]). The hypothesis of ongoing side reactions in these cells is further supported by analysis of the apparent separator tortuosity based on the impedance recorded of the symmetric cells prior to the pulse application. If the electrolyte was stable versus the metallic lithium electrodes the separator tortuosity, as a purely geometrical parameter, should be temperature and concentration invariant, a change in the obtained tortuosity indicating a change in electrolyte composition. The analysis of the high frequency resistances in the Nyquist plots recorded for all three electrolytes in the temperature range from 10 °C to 50 °C in symmetric coin cells filled with the 0.1 M electrolytes yield tortuosities of 4.7 for EC:DMC (1:1 w:w), 4.5 for EMC:FEC (19:1 w:w) but 2.6 for EC:EMC (3:7 w:w). I.e., for the first two cases the tortuosity in the symmetric lithium cell is equivalent to the separately obtained tortuosity value (4.8 ± 0.4, compare section Coin Cells in the Experimental), yet much smaller values are found for the EC:EMC based electrolyte at 0.1 M $LiPF_6$ which clearly shows the electrolyte's instability towards metallic lithium due to a constant change in electrolyte conductivity (and thus necessarily composition). In conclusion we refrain from including data points for 0.1 M $LiPF_6$ in EC:EMC (3:7 w:w) to our analysis of the thermodynamic factor and subsequently the transference number and only show the measurements for the interested reader as they serve as a convenient quality check for the experiments at low concentrations. Additionally -10 °C coin cell experiments of the EC:DMC based electrolytes below 1 M were inconclusive and are discarded in the following analysis of TDF and t_+. The largest errors of the TDF are observed for ~1.5 to 2 M $LiPF_6$ in EMC:FEC (19:1 w:w, compare Figure 8i) and coincide with the increased errors in the diffusion coefficients (see Figure 8f), which suggests an experimental artefact in the corresponding coin cells. Up to 2 M salt concentrations higher or similar TDFs are obtained for 50 °C and -10 °C with all solvents (see Figure 8g - i). At salt concentrations above 2 M the temperature dependence inverts, which is partially visible with EC:DMC (1:1 w:w) in Figure 8g and EC:EMC (3:7 w:w) in Figure 8h (0 °C at ~7.5, 50 °C at ~6) and which can clearly be observed for EMC:FEC (19:1 w:w) in Figure 8i. Latter inversion might be related to the amount of strongly solvating EC (or FEC) molecules which decreases from 50 wt.% (EC:DMC) to 30 wt.% (EC:EMC) and 5 wt.% (EMC:FEC). Especially at high salt concentrations the number of free, i.e., unsolvated, EC (or FEC) molecules will decrease and might drastically change the ion activity, yet a profound physical interpretation of this inversion is clearly beyond the scope of this work. Instead we focus on the discussion of the obtained fits and comparable literature reports. As briefly mentioned before no theoretical foundation for the temperature and concentration dependence of transference number and thermodynamic factor in non-aqueous electrolytes is known and we use polynomial functions to approximate our measurements. Specifically we use polynomials of the form

$$\mathrm{TDF}(c,T) = p_1 + p_2 \cdot c + p_3 \cdot T + p_4 \cdot c^2 + p_5 \cdot c \cdot T + p_6 \cdot T^2 + p_7 \cdot c^3 + p_8 \cdot c^2 \cdot T + p_9 \cdot c \cdot T^2 \qquad 19$$

for approximation of the thermodynamic factor as well as the transference number

$$t_+(c,T) = p_1 + p_2 \cdot c + p_3 \cdot T + p_4 \cdot c^2 + p_5 \cdot c \cdot T + p_6 \cdot T^2 + p_7 \cdot c^3 + p_8 \cdot c^2 \cdot T + p_9 \cdot c \cdot T^2 \qquad 20$$

with nine free fitting parameters p_i (see fit results in Table 2). As before the temperature is used in units of Kelvin and the concentration in units of M/L. In Eq. 19 and Eq. 20 the concentration dependence is described by a 3rd order polynomial, the temperature dependence by a 2nd order polynomial. Higher order polynomials were found to not improve the fit qualitatively. Reasonable agreement with experimentally obtained TDFs is found for EC:DMC (1:1 w:w, Figure 8g) and EMC:FEC (19:1 w:w, Figure 8i) as also indicated by the R^2 values of 0.99 in Table 2. Unfortunately the EC:EMC based electrolyte (see Figure 8h) shows highest experimental scatter and permits a high quality correlation with concentration and temperature simultaneously (R^2 value of 0.89 in Table 2). The reader is reminded that the temperature and concentration dependent functional descriptions as well as their fit parameters (as given in Table 2) only serve as an approximation and are provided for a simple, but not inconsiderate, use in temperature dependent battery models. For single temperatures the subsequently shown individually fitted concentration trends should be considered. Larger experimental uncertainties make it difficult to compare our results with the literature unambiguously. Within experimental variation, the TDFs for 0.35 M to 2 M $LiPF_6$ in EC:EMC (3:7 w:w) agree reasonably with the literature (see black line corresponding to 25 °C in Figure 8h).[17] The thermodynamic factor reported by Farkhondeh et al. for 1 M $LiPF_6$ in EC:DMC (1:1 w:w) of 2.3 at 25 °C is in good agreement with our results (2.2 at 20 °C and 2.6 at 30 °C).[12] Comparison of the TDFs of $LiPF_6$ in EC:DMC (1:1 w:w) with the widely applied, trends by Valøen and Reimers[8] for a similar electrolyte (see grey region in Figure 8g) yields two general differences. First, the TDFs start at 1 for all temperatures, which however was implicitly assumed in the analysis by the authors. Secondly, and more importantly, the temperature dependence is inversed compared to the measurements in this study (see blue upper boundary of grey highlighted region in Figure 8g corresponding to -10 °C and red lower boundary corresponding to 50 °C). Higher TDFs at higher temperatures, as found in this study, are also reported for $LiPF_6$ in EC:DEC (1:1 w:w).[9] Similar to our previous argumentation for the diffusion coefficient we are confident that the different temperature dependence of the TDF reported by Valøen and Reimers[8] directly follows from their concentration and temperature invariant transference number (TDF is calculated from $v(c,T) = (1 - t_+) \cdot \text{TDF}$ with $t_+ = \text{const.}$, compare Eq. 3 in Ref. [8]).

At last we discuss the concentration and temperature dependence of the transference numbers as shown in Figure 8j – l for the electrolytes under study. As before the transference numbers for 0.1 M $LiPF_6$ in EC:EMC (3:7 w:w) are only shown for the sake of completeness but are omitted in the analysis due to the above discussed electrolyte instability with metallic lithium. The found transference numbers decrease with decreasing temperature and increasing concentration. The transference number varies between 0.38 (0 °C) and 0.59 (50 °C) for 0.1 M $LiPF_6$ in EC:DMC (1:1 w:w), -0.25 (0 °C) and 0.51 (50 °C) for 0.35 M $LiPF_6$ in EC:EMC (3:7 w:w) and 0.29 (0 °C) and 0.59 (50 °C) for 0.1 M $LiPF_6$ in EMC:FEC (19:1 w:w). For typically used 1 M $LiPF_6$ concentrations we find transference numbers of 0.27 (fit suggests 0.28, compare Table 2 and Figure 8j) for EC:DMC (1:1 w:w), 0.16 (fit suggests 0.22, compare Table 2 and Figure 8k) for EC:EMC (3:7 w:w) and -0.34 (outlier with large error, fit suggests 0.11, compare Table 2 and Figure 8l) for EMC:FEC (19:1 w:w) at 20 °C. Our low temperature measurements, especially at -10 °C show a prominent error at all concentrations as well as negative values (see blue circles and squares in Figure 8j – l). Negative transference numbers were previously motivated in the literature with ion triplet formation.[24] Yet, as will be visible more clearly in the single temperature fits in Figure 9 our measurements from 0 °C to 50 °C mostly lie (within the error) inside the theoretically defined range for transference numbers (0 to 1). We rather assume that the statistical errors of the -10 °C measurements underestimate the experimental uncertainty. Qualitatively this is in accord with the analysis of the temperature and

concentration dependent transport factors *a* and *b* at -10 °C which shows an offset to the other temperatures (see Figure 4 and Figure 7). At 3 M salt concentrations the transference numbers are close to 0 for the EC:EMC (0.09 to 0.20, outlier at -10 °C at ~-1, compare Figure 8k) and the EMC:FEC electrolyte (-0.02 to 0.11, compare Figure 8l). When EC:DMC is used as a solvent the transference number remains surprisingly steady and values of 0.13 and 0.32 are measured for 3 M $LiPF_6$ at 30 °C and 50 °C respectively. Within experimental error the transference number reported by Nyman et al. at 25 °C agrees with our measurements (black line lies between our 20 °C and 30 °C values in Figure 8k).[17] The transference numbers found for 1 M $LiPF_6$ in EC:DMC (1:1 w:w, compare Figure 8j) at 20 °C (0.27) and 30 °C (0.41) are slightly below the reported value for the same electrolyte at 25 °C (0.42).[12] Due to the assumption of a concentration and temperature invariant transference number the value of Valøen and Reimers disagrees with our results, which is unlikely to be solely caused by the different solvent composition.[8] In their publication the authors argue that their fit of the transport factor *a* is independent of temperature at low concentrations and conclude that the transference number must be temperature invariant in this case, because the thermodynamic factor is defined as 1 for $c \rightarrow 0$. This conclusion however can hardly be verified as experimental data are only shown for one temperature (20 °C compare Figure 5 in the original publication) and smallest concentrations pairs are 77 µM to 0.4 M. The large concentration difference in the small concentration region permits to resolve the Debye-Hückel behavior (0 M to ~ 0.3 M), which theoretically predicts a strong change of the TDF with temperature at low concentrations due to the temperature dependence of the relative permittivity of the solvent.[23] To show the temperature invariance of the transport factor *a*, much smaller concentration differences in the small concentration range (< 0.1 M) and more measurements would be required to support the assumption made by the authors. We also note that a nearly temperature invariant transport factor *a* does not permit a temperature dependence of the transference number, e.g., for similar temperature dependencies of TDF and t_+ their effects might (at least partially) cancel out (remember $a \equiv \mathrm{TDF} \cdot (1 - t_+)$).

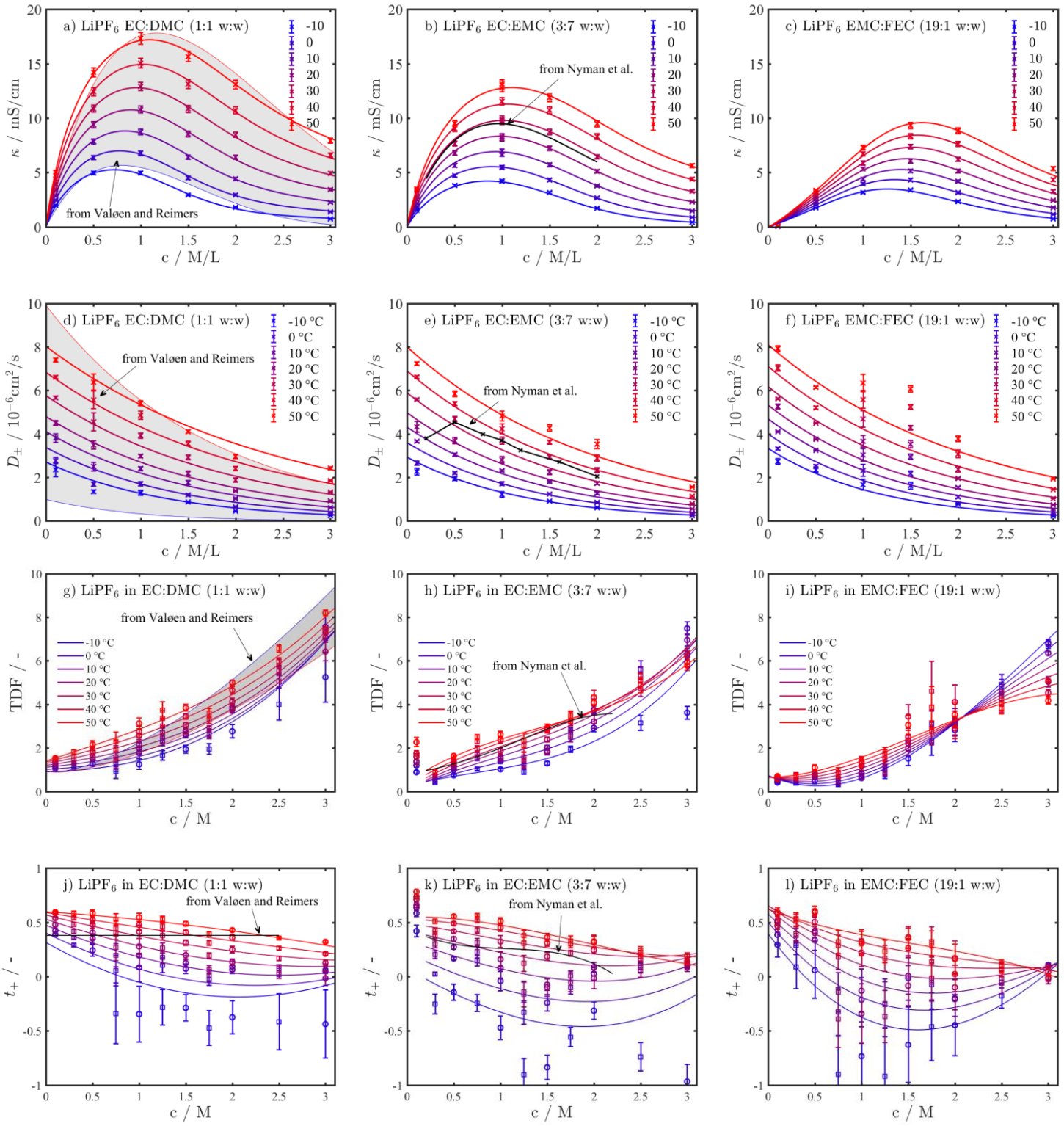

Figure 8. Ionic conductivity (a – c), binary diffusion coefficient (d – f), thermodynamic factor (g – i) and transference number (j – l) of 0.1 M to 3 M $LiPF_6$ in EC:DMC (1:1 w:w, a,d,g,j), EC:EMC (3:7 w:w, b, e, h, k) and EMC:FEC (19:1 w:w, c, f, i, l) in the temperature range from -10 °C to 50 °C (see legends for temperature scale). Parameters are determined using the analysis described in the scheme in Figure 1 and the section Data Analysis and are approximated (solid lines) with the functional descriptions given in Eq. 15 (κ), Eq. 18 ($D_{\pm}$), Eq. 19 (TDF) and Eq. 20 (t_+) with the fit parameters p_i and the goodness of fit values given in Table 2. Literature data from Valøen and Reimers are shown as grey highlighted area with -10 °C (blue) and 50 °C (red) boundaries as a reference within the EC:DMC panels although not comprising the same electrolyte composition ($LiPF_6$ in PC:EC:DMC (10:27:63 v:v:v)),[8] and temperature invariant parameters from Nyman et al. ($LiPF_6$ in EC:EMC (3:7 w:w), at 25 °C) are plotted as solid line in the EC:EMC panels.[17] Due to the complex behavior the concentration dependence of thermodynamic factor and transference number are analyzed on a per temperature basis in Figure 9 and Figure 10. Error bars for the ionic conductivity correspond to 3 % to account for the error of the cell constant, cell filling and fitting. Error bars for the binary diffusion coefficient depict the standard deviation of the weighted mean as described in the section Data Analysis and the section Error Calculation. Error bars for the thermodynamic factor and the transference number are calculated using Gaussian error propagation of Eq. 13 and Eq. 14 with the individual errors of *a* and *b* as described in the section Data Analysis.

Table 2. Parameters p_i of functional approximations of ionic conductivity (Eq. 15), binary diffusion coefficient (Eq. 18), thermodynamic factor (Eq. 19) and transference number (Eq. 20) for 0.1 M to 3 M LiPF6 in EC:DMC (1:1 w:w), EC:EMC (3:7 w:w) and EMC:FEC (19:1 w:w) in temperature range from -10 °C to 50 °C, their percental confidence intervals based on a 90 % standard deviation and the goodness of fit values R^2 for the individual fits, represented in Figure 8.

Parameter		EC:DMC (1:1 w:w)		EC:EMC (3:7 w:w)		EMC:FEC (19:1 w:w)	
$\kappa(c,T)$	p_1	7.98E-01	(5 %)	5.21E-01	(5 %)	2.51E-02	(54 %)
	p_2	2.28E+02	(1 %)	2.28E+02	(1 %)	1.75E+02	(22 %)
Eq. 15	p_3	-1.22E+00	(4 %)	-1.06E+00	(2 %)	1.23E+00	(117 %)
	p_4	5.09E-01	(10 %)	3.53E-01	(8 %)	2.05E-01	(329 %)
	p_5	-4.00E-03	(13 %)	-3.59E-03	(19 %)	-8.81E-02	(323 %)
	p_6	3.79E-03	(28 %)	1.48E-03	(42 %)	2.83E-03	(32 %)
	R^2	0.999		0.997		0.995	
$D_{\pm}(c,T)$	p_1	1.23E+03	(69 %)	8.36E+02	(81 %)	4.92E+02	(114 %)
	p_2	1.24E+00	(38 %)	9.35E-01	(80 %)	1.29E+00	(59 %)
Eq. 18	p_3	-1.63E+03	(13 %)	-1.50E+03	(16 %)	-1.33E+03	(26 %)
	p_4	-5.33E+02	(27 %)	-4.63E+02	(49 %)	-5.68E+02	(41 %)
	R^2	0.990		0.980		0.969	
TDF(c,T)	p_1	-2.78E+00	(460 %)	8.50E+00	(344 %)	2.24E+00	(596 %)
	p_2	1.47E+01	(86 %)	-3.19E+01	(112 %)	-7.22E+00	(190 %)
Eq. 19	p_3	1.93E-02	(453 %)	-6.91E-02	(291 %)	-1.13E-02	(809 %)
	p_4	2.18E+00	(50 %)	2.11E-01	(1161 %)	5.16E+00	(18 %)
	p_5	-1.19E-01	(74 %)	2.22E-01	(111 %)	1.70E-02	(553 %)
	p_6	-1.95E-05	(764 %)	1.40E-04	(247 %)	1.95E-05	(801 %)
	p_7	9.98E-02	(78 %)	2.35E-01	(81 %)	-7.29E-02	(146 %)
	p_8	-6.81E-03	(57 %)	-3.09E-03	(284 %)	-1.44E-02	(20 %)
	p_9	2.40E-04	(64 %)	-3.63E-04	(119 %)	2.10E-05	(766 %)
	R^2	0.990		0.890		0.990	
$t_+(c,T)$	p_1	-4.63E+00	(68 %)	-1.27E+01	(70 %)	-7.87E+00	(123 %)
	p_2	2.12E+00	(99 %)	-2.05E+00	(354 %)	-3.06E+00	(139 %)
Eq. 20	p_3	3.07E-02	(69 %)	8.46E-02	(71 %)	5.38E-02	(121 %)
	p_4	5.94E-01	(27 %)	1.56E+00	(36 %)	1.17E+00	(43 %)
	p_5	-2.21E-02	(64 %)	-1.95E-03	(2481 %)	7.42E-03	(364 %)
	p_6	-4.50E-05	(80 %)	-1.33E-04	(76 %)	-8.55E-05	(127 %)
	p_7	3.93E-03	(295 %)	-5.85E-02	(61 %)	3.27E-02	(106 %)
	p_8	-1.92E-03	(27 %)	-3.97E-03	(43 %)	-4.08E-03	(37 %)
	p_9	4.76E-05	(51 %)	2.08E-05	(391 %)	6.19E-06	(716 %)
	R^2	0.964		0.848		0.900	

Concentration Dependent Analysis at fixed Temperatures

While in the previous section comprehensive functional descriptions for the temperature and the concentration dependence of the ionic and thermodynamic parameters were presented, in this section we are investigating the concentration dependences of the thermodynamic factor and the transference number for each temperature individually. Because a detailed analysis as well as the comparison with the literature was already presented in the above discussion of the multi temperature fitting we mainly show single temperature fits for the benefit of the reader and only discuss the parameters concentration behavior briefl. As shown in Figure 8 g – i for the thermodynamic factor and in Figure 8 j – l for the transference number, experimental errors, the complex behavior (see e.g. Figure 8i) and the lack of a theoretical basis for the functional descriptions (Eq. 19 and 20) make the simultaneous interpretation of the concentration *and* temperature dependence challenging. Although these general approximations might serve as a coarse approximation to experimental results, experimentally found concentration dependences are represented more reliably on a per temperature basis. Thus in the following we approximate the experimentally obtained values for the thermodynamic factor and the transference number individually for each measurement temperature (-10 °C to 50 °C) using second order polynomials

$$\mathrm{TDF}(c) = p_1 \cdot c^2 + p_2 \cdot c + p_3 \qquad 21$$

$$t_+(c) = p_1 \cdot c^2 + p_2 \cdot c + p_3 \qquad 22$$

with three free fitting parameters p_i each and the concentration given in units of M/L. The individually shown values for each temperature (see separate panels in Figure 9 and Figure 10 with the measurement temperature given as legend) and their fit curves are shown in the figures while fit parameters, their percental confidence intervals and the goodness of fit values are given in Table 3 and allow for a distinct judgement of the individual concentration dependencies compared to the overarching depiction in Figure 8.

Thermodynamic factors for $LiPF_6$ in EC:DMC (1:1 w:w, Figure 9a), EC:EMC (3:7 w:w, Figure 9b) and EMC:FEC (19:1 w:w, Figure 9c) can be well approximated by their polynomial fit functions as judged by eye. However, the mathematically objective goodness of fit values are only above 0.94 for the EC:DMC and the EMC:FEC based electrolytes, while worse correlation ($R^2 > 0.81$) is found with the EC:EMC solvent system, in accord with the above discussion of generally larger errors for this electrolyte. Although the individual depiction of the concentration dependent transference numbers in Figure 10 make it much easier to follow its concentration dependence compared to Figure 8, the characteristic trends persist. From Figure 10 the very good correlation of the transference numbers with the selected second order polynomials for the EC:DMC based electrolyte can be observed clearly (Figure 10a). Starting from the linear behavior at 50 °C (uppermost panel in Figure 10a) the observed trend converges to 0 at high concentrations and for lower temperatures. Only the 10 °C measurements show negative transference numbers for all electrolytes (see Figure 10, panels for -10 °C). Because these measurements are based on potentials measured in the pouch concentration cells as well symmetric lithium coin cells, an experimental artefact due to the cell setup seems unlikely. We rather think that the observed sudden change (also visible for transport factors *a* and *b* in Figure 4 and Figure 7) has to be related to the electrolyte, which possibly restructures when the temperature approaches the electrolyte freezing temperatures (we note that we assured in a separate experiment that none of the electrolyte solutions froze at -10 °C as judged by eye). In summary we showed a reasonable description of the transference number for the EC:DMC solvent mixture and for temperatures above 20 °C for the EC:EMC and EMC:FEC cases. Although thermodynamic factor and transference number are both based on the same transport factors *a* and *b*, the transference number as

calculated from Eq. 13 is more sensitive towards errors (see generally larger errors for transference number in Figure 10 compared to thermodynamic factor in Figure 9). In conclusion a higher number of repeat measurements and an improved, less noise sensitive setup for the measurement of concentration potentials might enhance the experimental data quality and thus allows for a more rigid analysis than the herein presented qualitative trends.

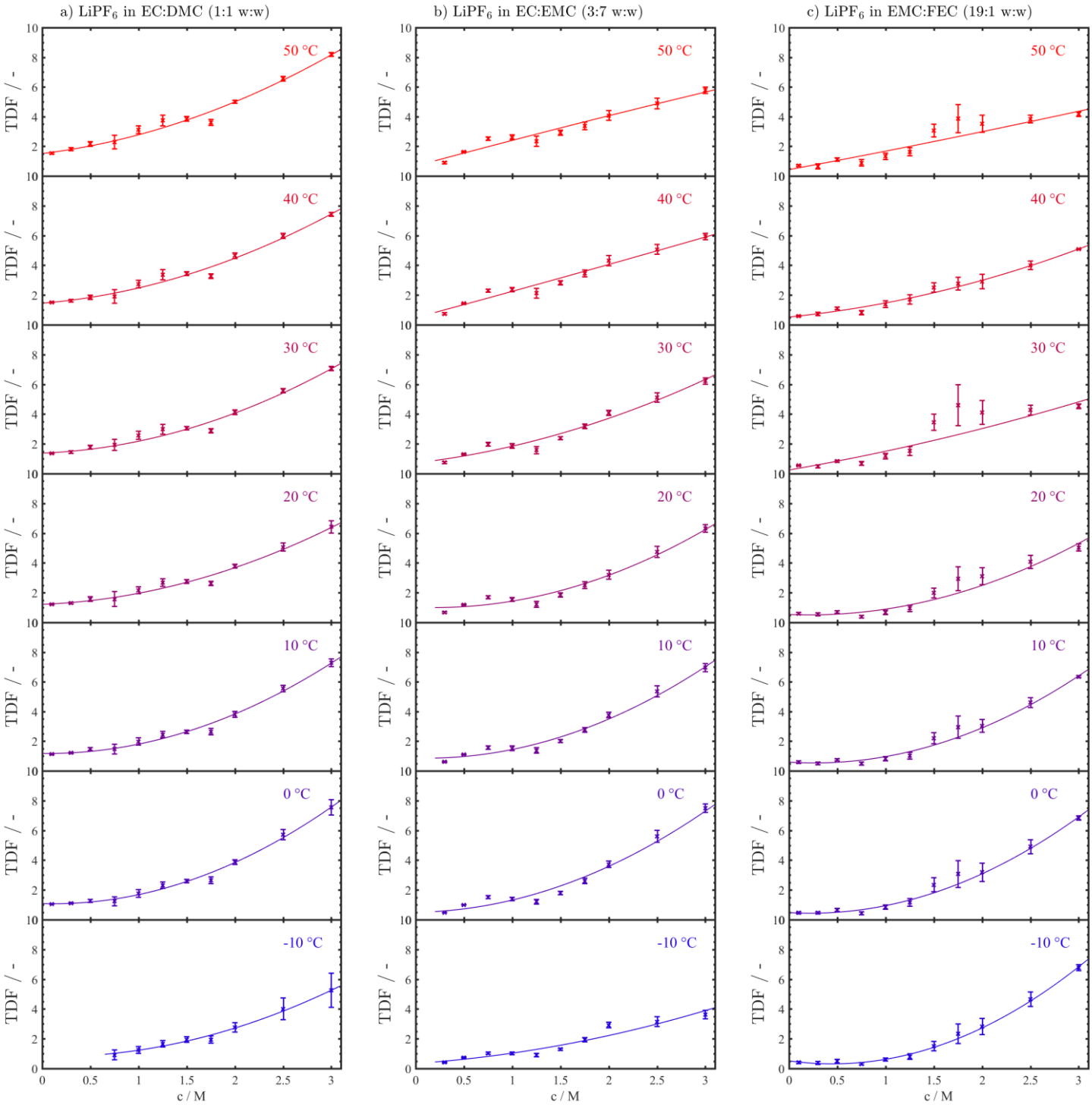

Figure 9 Individual thermodynamic factors of 0.1 M to 3 M $LiPF_6$ in EC:DMC (1:1 w:w, a), EC:EMC (3:7 w:w, b) and EMC:FEC (19:1 w:w, c) for the temperatures from -10 °C, 0 °C, 10 °C, 20 °C, 30 °C, 40 °C and 50 °C (see legends for temperature), i.e., same data as in Figure 8g - i but fitted individually. The thermodynamic factors are calculated from the transport factors *a* (Figure 4) and *b* (Figure 7) according to Eq. 14, compare scheme Figure 1 and are approximated (solid lines) with the functional description given in Eq. 21 with the fit parameters p_i and the goodness of fit values given in Table 3. Error bars are calculated using Gaussian error propagation of Eq. 14 with the individual errors of *a* and *b* as described in the section Data Analysis and the corresponding Error Calculation.

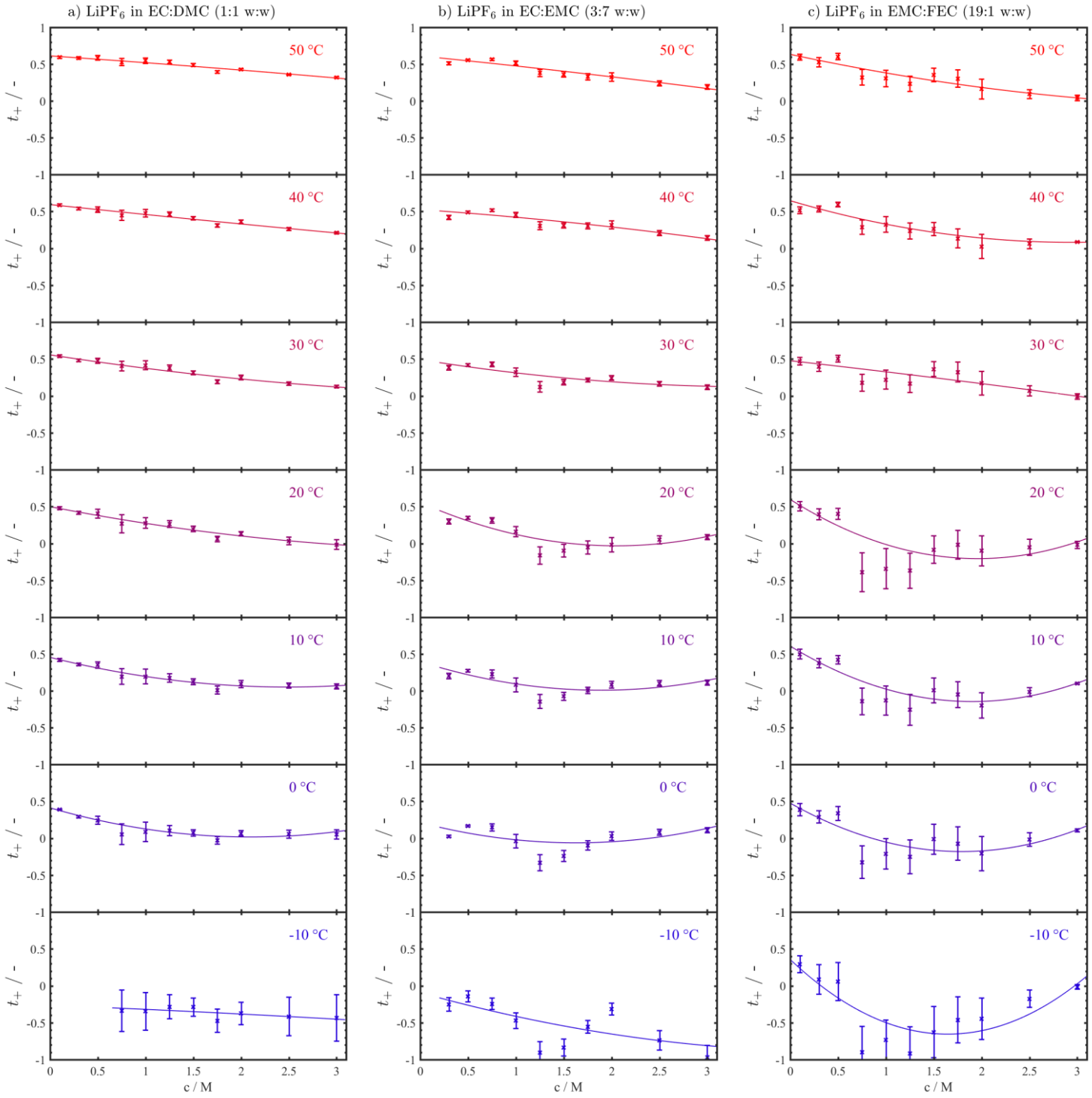

Figure 10 Individual transference numbers of 0.1 M to 3 M $LiPF_6$ in EC:DMC (1:1 w:w, a), EC:EMC (3:7 w:w, b) and EMC:FEC (19:1 w:w, c) for the temperatures from -10 °C, 0 °C, 10 °C, 20 °C, 30 °C, 40 °C and 50 °C (see legends for temperature), i.e., same data as in Figure 8j - l but fitted individually. The transference numbers are calculated from the transport factors *a* (Figure 4) and *b* (Figure 7) according to Eq. 13, compare scheme Figure 1 and are approximated (solid lines) with the functional description given in Eq. 22 with the fit parameters p_i and the goodness of fit values given in Table 3. Error bars are calculated using Gaussian error propagation of Eq. 13 with the individual errors of *a* and *b* as described in the section Data Analysis and the corresponding Error Calculation.

Table 3. Parameters p_i of functional approximations of the thermodynamic factor (Eq. 21) and the transference number (Eq. 22) for 0.1 M to 3 M $LiPF_6$ in EC:DMC (1:1 w:w), EC:EMC (3:7 w:w) and EMC:FEC (19:1 w:w), individually for each temperature in the measurement range from -10 °C to 50 °C, their percental confidence intervals based on a 90 % standard deviation and the goodness of fit values R^2. Fits for the thermodynamic factor and the transference number are graphically depicted for each temperature in Figure 9 and Figure 10 respectively.

Fitting Function			EC:DMC (1:1 w:w)		EC:EMC (3:7 w:w)		EMC:FEC (19:1 w:w)	
TDF(c,T)	-10 °C	p_1	4.75E-01	(108 %)	3.65E-01	(97 %)	1.01E+00	(8 %)
		p_2	1.96E-02	(8177 %)	8.20E-02	(970 %)	-9.36E-01	(22 %)
Eq. 21		p_3	7.59E-01	(159 %)	5.39E-01	(63 %)	5.18E-01	(18 %)
		R^2	0.943		0.825		0.996	
	0 °C	p_1	7.30E-01	(18 %)	1.71E-01	(386 %)	8.89E-01	(14 %)
		p_2	-6.64E-02	(397 %)	1.48E+00	(92 %)	-5.59E-01	(66 %)
		p_3	1.06E+00	(4 %)	5.42E-02	(748 %)	5.33E-01	(27 %)
		R^2	0.992		0.813		0.994	
	10 °C	p_1	6.62E-01	(23 %)	7.50E-01	(57 %)	8.29E-01	(16 %)
		p_2	3.16E-02	(1134 %)	-2.69E-01	(395 %)	-5.85E-01	(75 %)
		p_3	1.14E+00	(9 %)	9.85E-01	(45 %)	6.62E-01	(28 %)
		R^2	0.989		0.909		0.996	
	20 °C	p_1	4.86E-01	(49 %)	6.17E-01	(65 %)	7.15E-01	(27 %)
		p_2	2.53E-01	(206 %)	-1.65E-01	(636 %)	-6.25E-01	(85 %)
		p_3	1.20E+00	(12 %)	1.05E+00	(43 %)	6.65E-01	(35 %)
		R^2	0.977		0.875		0.956	
	30 °C	p_1	5.62E-01	(30 %)	4.82E-01	(82 %)	3.16E-01	(68 %)
		p_2	2.15E-01	(210 %)	3.84E-01	(274 %)	4.61E-01	(139 %)
		p_3	1.36E+00	(12 %)	9.56E-01	(50 %)	4.61E-01	(47 %)
		R^2	0.988		0.923		0.960	
	40 °C	p_1	4.99E-01	(30 %)	1.54E-01	(299 %)	2.95E-01	(44 %)
		p_2	5.03E-01	(81 %)	1.28E+00	(101 %)	6.28E-01	(67 %)
		p_3	1.46E+00	(10 %)	7.67E-01	(75 %)	5.48E-01	(28 %)
		R^2	0.993		0.886		0.998	
	50 °C	p_1	4.73E-01	(32 %)	-2.57E-02	(1827 %)	1.41E-01	(145 %)
		p_2	8.16E-01	(51 %)	1.72E+00	(80 %)	8.16E-01	(75 %)
		p_3	1.48E+00	(11 %)	7.50E-01	(83 %)	5.80E-01	(37 %)
		R^2	0.994		0.882		0.968	
$t_+(c,T)$	-10 °C	p_1	-1.68E-03	(8446 %)	2.24E-01	(101 %)	3.25E-01	(38 %)
		p_2	-7.24E-02	(727 %)	-9.73E-01	(60 %)	-1.10E+00	(38 %)
Eq. 22		p_3	-2.30E-01	(203 %)	3.64E-01	(78 %)	3.59E-01	(62 %)
		R^2	0.311		0.743		0.753	
	0 °C	p_1	9.57E-02	(33 %)	1.47E-01	(125 %)	1.83E-01	(46 %)
		p_2	-3.91E-01	(20 %)	-4.96E-01	(114 %)	-6.71E-01	(42 %)
		p_3	4.20E-01	(4 %)	3.26E-01	(70 %)	4.79E-01	(28 %)
		R^2	0.972		0.271		0.765	
	10 °C	p_1	6.24E-02	(32 %)	1.73E-01	(52 %)	1.77E-01	(43 %)
		p_2	-3.15E-01	(19 %)	-6.52E-01	(42 %)	-7.01E-01	(37 %)
		p_3	4.52E-01	(5 %)	5.75E-01	(23 %)	6.06E-01	(20 %)
		R^2	0.980		0.788		0.880	
	20 °C	p_1	2.75E-02	(116 %)	1.75E-01	(46 %)	1.65E-01	(62 %)
		p_2	-2.52E-01	(31 %)	-7.09E-01	(36 %)	-6.96E-01	(47 %)
		p_3	4.98E-01	(6 %)	6.61E-01	(17 %)	5.95E-01	(23 %)
		R^2	0.971		0.863		0.856	
	30 °C	p_1	2.10E-02	(90 %)	8.40E-02	(82 %)	-1.20E-02	(540 %)
		p_2	-2.07E-01	(28 %)	-4.11E-01	(50 %)	-1.32E-01	(161 %)
		p_3	5.56E-01	(5 %)	6.48E-01	(17 %)	4.93E-01	(21 %)
		R^2	0.980		0.839		0.903	
	40 °C	p_1	4.39E-03	(341 %)	4.84E-02	(139 %)	3.99E-02	(176 %)
		p_2	-1.42E-01	(32 %)	-3.17E-01	(65 %)	-3.05E-01	(79 %)
		p_3	5.96E-01	(4 %)	6.81E-01	(15 %)	6.40E-01	(17 %)
		R^2	0.983		0.820		0.957	
	50 °C	p_1	-2.20E-03	(651 %)	3.28E-02	(194 %)	1.90E-02	(264 %)
		p_2	-9.22E-02	(50 %)	-2.71E-01	(72 %)	-2.57E-01	(62 %)
		p_3	6.11E-01	(5 %)	7.11E-01	(14 %)	6.38E-01	(12 %)
		R^2	0.968		0.829		0.947	

Conclusions

In this study we apply established methods for the determination of ionic conductivities and binary diffusion coefficients to $LiPF_6$ solutions in EC:DMC (1:1 w:w), EC:EMC (3:7 w:w) and EMC:FEC (19:1 w:w) covering a concentration range from 0.1 M to 3 M and a temperature range from -10 °C to 50 °C. Additionally we introduce a novel analysis scheme for the unambiguous characterization of transference numbers and thermodynamic factors for the same electrolyte solutions and measurement conditions (concentration and temperature), based on the analysis of concentration cell potentials and the short term potential relaxation after galvanostatic pulses in symmetric lithium coin cells. We carefully describe the analysis procedure and the calculation of the final transport properties and their errors for exemplary data and thereby ensure that the presented methodology can be utilized for the characterization of novel electrolytes with low effort. Our stringent comparison with the (scarcely) available literature shows the qualitative agreement and highlights coarse assumptions partially made in widely adopted publications and their resulting prominent misinterpretation of electrolyte transport properties. For the use in predictive battery models we provide temperature and concentration dependent approximations to empirical and semi-empirical functions and report the obtained fit parameters as well as their errors in tabulated from. To address the observed complexity of concentration and temperature dependent thermodynamic factors and transference numbers we also report polynomial approximations for those, on a per temperature basis.

Acknowledgment

We gratefully acknowledges the funding by the Bavarian Ministry of Economic Affairs and Media, Energy, and Technology for its financial support under the auspices of the EEBatt project and the BMBF (Federal Ministry of Education and Research, Germany) for its financial support within the ExZellTUM II project (grant number 03XP0081). We thank rhd Instruments providing the conductivity measurement cell, Jörg Schuster for encouraging us to extent our measurements to 3 M concentrations, Askin Eldiven for electrolyte density measurements, Tobias Greese from the ZAE Bayern for plasma treating the Nitto separators and Andreas Ehrl for our previous, tireless team work, which is a key requirement for the present study. Special thanks also goes to Jürgen Höhn (glass compartment cells), Korbinian Schmidt and Simon Erhard (Peltier-element controlled temperature chamber) and Stefanie Neuner (16 channel multiplexer) for their valueable support and the manufacturing of cutom-made equipment, although finally not applicable for the current work. We also thank Nathan Craig for motivating us to rethink the activity coefficient determination and Davide Menga, Hany El-Sayed and Robert Morasch for valuable discussions and support with troubleshooting the ferrocene cell setup. Thanks goes to Bharatkumar Suthar for helpful comments on the manuscript.

List of Symbols

(alphabetical)

Symbol	Name	Unit
a	transport factor	-
α	constant phase exponent	-
$A_{\mathrm{El.}}$	electrode area	cm²
b	transport factor	-
c	concentration	mol/L
$D^{*}_{\pm,\mathrm{eff}}$	effective binary diffusion coefficient	cm²/s
$D_{\pm}$	binary diffusion coefficient	cm²/s
$\varepsilon_{\mathrm{Sep.}}$	separator porosity	-
$f_{\pm}$	mean molar activity coefficient	-
F	Faraday constant	As/mol
I_{P}	pulse current	µA
k_{c}	conductivity cell constant	1/cm
κ	electrolyte conductivity	mS/cm
$l_{\mathrm{Sep.}}$	separator thickness	µm
m_{ln}	slope of exp. pot. relaxation	1/s
n	number of measurements	-
p_{i}	fit parameter	-
Q	constant phase element (CPE)	$\mathrm{mF \cdot s^{\alpha-1}}$
R	gas constant	J/(mol K)
R	high frequency resistance in cond. cell	Ohm
R_{CC}	resistance of conc. cell	Ohm
t	time	s
τ^{*}	artificial time	-
t_{+}	transference number of lithium ion	-
T	temperature	K
T_{I}	current interrupt time	s
TDF	thermodynamic factor	-
U_{CC}	conc. cell potential	V
U_{Offset}	long term potential offset	V
w_i	weighing factor	various
$\bar{x}$	weighted mean	various
x_i	value	various
$\Delta\bar{x}$	error of weighted mean	various

References

1. J. Landesfeind, J. Hattendorff, A. Ehrl, W. A. Wall, and H. A. Gasteiger, *J. Electrochem. Soc.*, **163**, A1373–A1387 (2016).

2. J. Landesfeind, M. Ebner, A. Eldiven, V. Wood, and H. A. Gasteiger, *J. Electrochem. Soc.*, **165**, A469–A476 (2018).

3. J. Landesfeind, A. Eldiven, and H. A. Gasteiger, accepted (2018).

4. J. Newman and K. Thomas-Alyea, *Electrochemical Systems*, 3rd ed., Wiley Interscience, Hoboken, (2004).

5. A. Ehrl, J. Landesfeind, W. A. Wall, and H. A. Gasteiger, *J. Electrochem. Soc.*, **164**, A826–A836 (2017).

6. A. Ehrl, J. Landesfeind, W. A. Wall, and H. A. Gasteiger, *J. Electrochem. Soc.*, **164**, 2716–2731 (2017).

7. J. Landesfeind, A. Ehrl, M. Graf, W. A. Wall, and H. A. Gasteiger, *J. Electrochem. Soc.*, **163**, A1254–A1264 (2016).

8. L. O. Valøen and J. N. Reimers, *J. Electrochem. Soc.*, **152**, A882 (2005).

9. H. Lundgren, M. Behm, and G. Lindbergh, *J. Electrochem. Soc.*, **162**, 3–10 (2014).

10. A. Nyman, M. Behm, and G. Lindbergh, *Electrochim. Acta*, **53**, 6356–6365 (2008).

11. C. L. Berhaut et al., *Electrochim. Acta*, **180**, 778–787 (2015).

12. M. Farkhondeh, M. Pritzker, C. Delacourt, S. S. W. Liu, and M. Fowler, *J. Phys. Chem. C*, **121**, 4112–4129 (2017).

13. L. Ma et al., *J. Electrochem. Soc.*, **164**, 5008–5018 (2017).

14. J. Landesfeind and H. A. Gasteiger, in preparation (2018).

15. Andrzej Lasia, *Electrochemical Impedance Spectroscopy and its Applications*, Springer, (2014).

16. Mathworks, *Matlab Online Ref.*, **R2017b** https://mathworks.com/help/.

17. A. Nyman, M. Behm, and G. Lindbergh, *Electrochim. Acta*, **53**, 6356–6365 (2008).

18. C. H. Hamann, A. Hamnett, and W. Vielstich, *Electrochemistry*, Wiley-VCH, Weinheim, (2007).

19. H. Hafezi and J. Newman, *J. Electrochem. Soc.*, **147**, 3036 (2000).

20. M. Drosg, *Der Umgang mit Unsicherheiten: Ein Leitfaden zur Fehleranalyse*, 1st Ed., p. 232, Facultas, (2006).

21. A. Ehrl, *PhD Thesis*, München (2016).

22. A. J. Bard and L. R. Faulkner, *Electrochemical Methods - Fundamentals and Applications*, 2nd ed., John Wiley & Sons, Inc., New York, (2001).

23. M. R. Wright, *An Introduction to Aqueous Electrolyte Solutions*, John Wiley & Sons, Ltd, Chichester, (2007).

24. S. Stewart and J. Newman, *J. Electrochem. Soc.*, **155**, A458 (2008).

Supporting Information

To support the main article additional information is supplied for the benefit of the reader. This supporting information is presented subsequently.

Supporting Information: The Temperature Dependence of Ionic Transport Properties

Johannes Landesfeind,[az] and Hubert A. Gasteiger[a]

[a] Chair of Technical Electrochemistry, Department of Chemistry and Catalysis Research Center, Technical University of Munich, Munich, Germany

[z]corresponding author

Electrolyte Densities

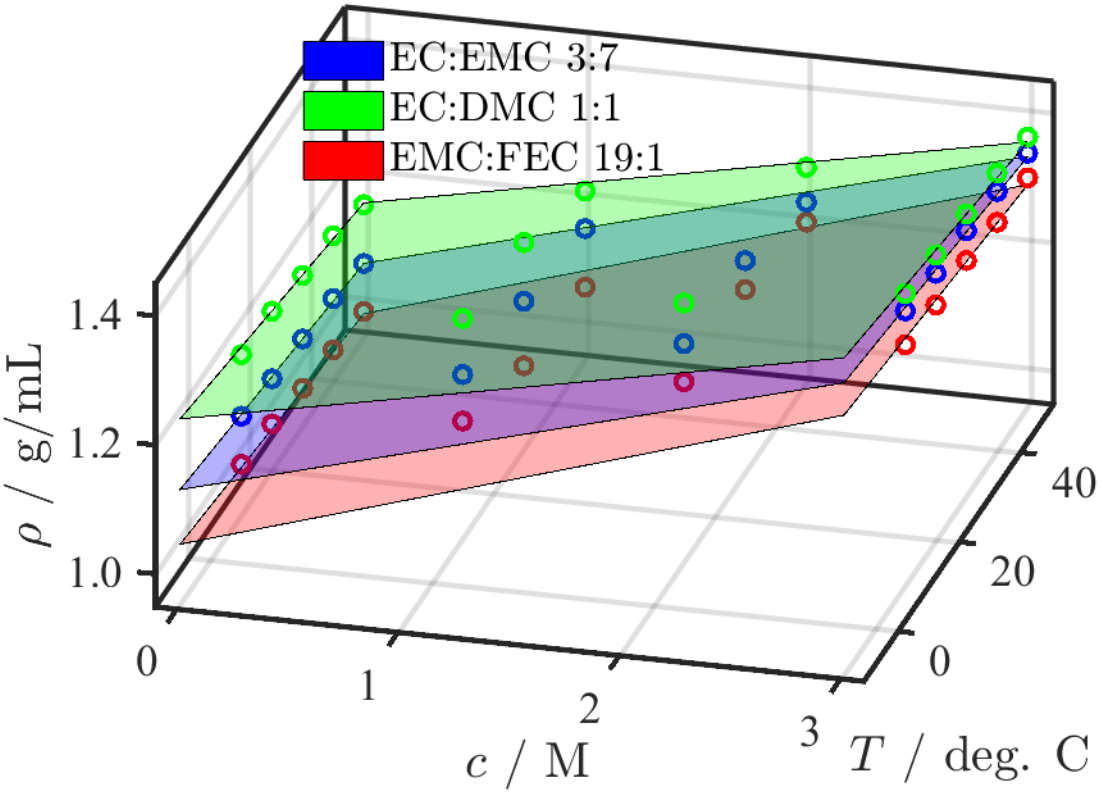

Figure 1. Temperature and concentration dependent densities of electrolytes used in this study ($LiPF_6$ in EC:DMC (1:1 w:w, green), $LiPF_6$ in EC:EMC (3:7 w:w, blue) and $LiPF_6$ in EMC:FEC (19:1 w:w, red)), measured gravimetrically using a 10 ml flask filled with the preheated/cooled electrolytes inside an argon filled glovebox. Experimental densities are fitted empirically to the empirical function given in Eq. 1 which assumes linear temperature and concentration dependences. Fit parameters and their uncertainty are given in Table 1 and allow the interested reader to convert our volumetrically based electrolyte parameter study (main article) to units of M/kg.

Based on the experimental data we selected a linear temperature and concentration dependence to approximate the electrolyte densities measured gravimetrically using 10 ml flasks filled with the corresponding preheated/cooled electrolytes.

$$\rho(c,T) = (p_1 + p_2 \cdot c + p_3 \cdot T)\frac{\mathrm{g}}{\mathrm{cm}^3} \qquad 1$$

The obtained three fitting parameters pi are given in Table 1 including their confidence interval based on a 95 % standard deviation. The concentration and temperature in Eq. 1 are used in units of M/L and K.

Table 1. Functional description of lithium ion battery electrolyte densities based on polynomial fit to measurements from 0°C to 50°C and 0.1 M to 3 M. Parameters are given including their confidence interval based on a 95% standard deviation.

Parameter		EC:DMC (1:1 w:w)		EC:EMC (3:7 w:w)		EMC:FEC (19:1 w:w)	
$\rho(c,T)$	p_1	1.59E+00	(7 %)	1.41E+00	(5 %)	1.30E+00	(12 %)
	p_2	6.74E-02	(7 %)	9.12E-02	(3 %)	1.03E-01	(6 %)
Eq. 1	p_3	-1.35E-03	(27 %)	-1.09E-03	(22 %)	-9.80E-04	(51 %)
	R^2	0.989		0.997		0.990	

Conductivity Comparison

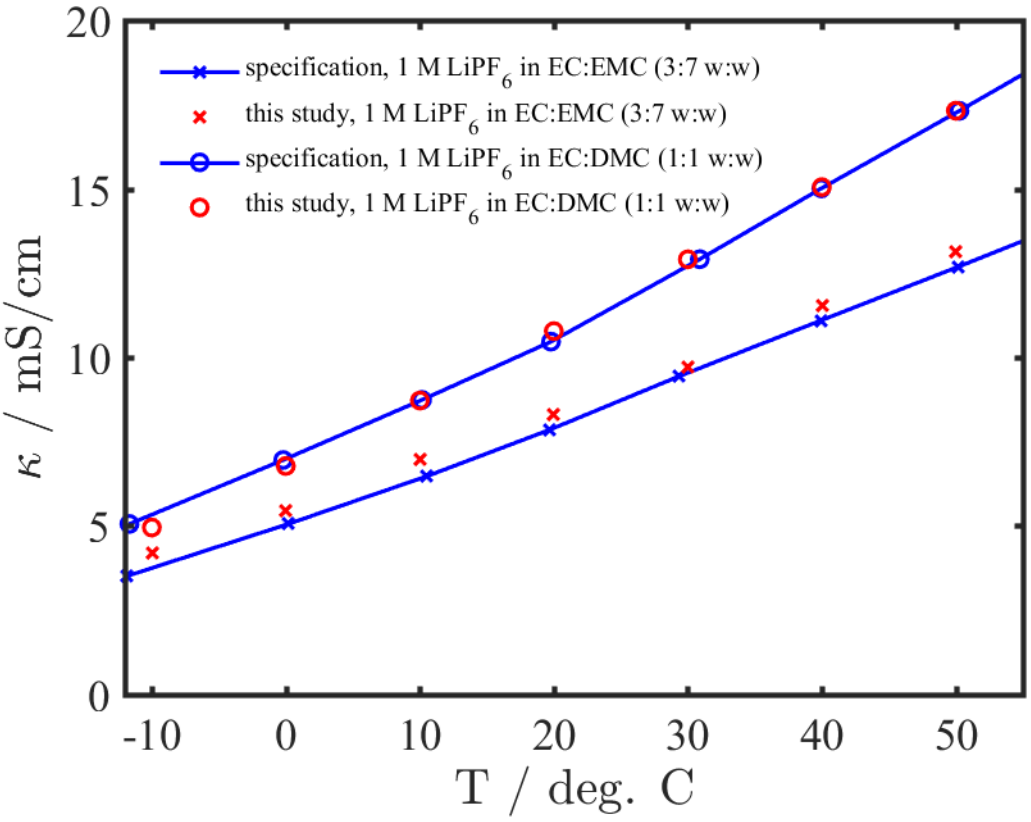

Figure 2. Ionic conductivities of 1 M LiPF6 in EC:DMC (1:1 w:w, circles) and 1 M LiPF6 in EC:EMC (3:7 w:w, crosses) in the temperature range from -10 °C to 50 °C of values obtained in this study (red) and the specification of commercially (BASF) available electrolyte solutions of the same composition.[1]

Error by Integral Simplification

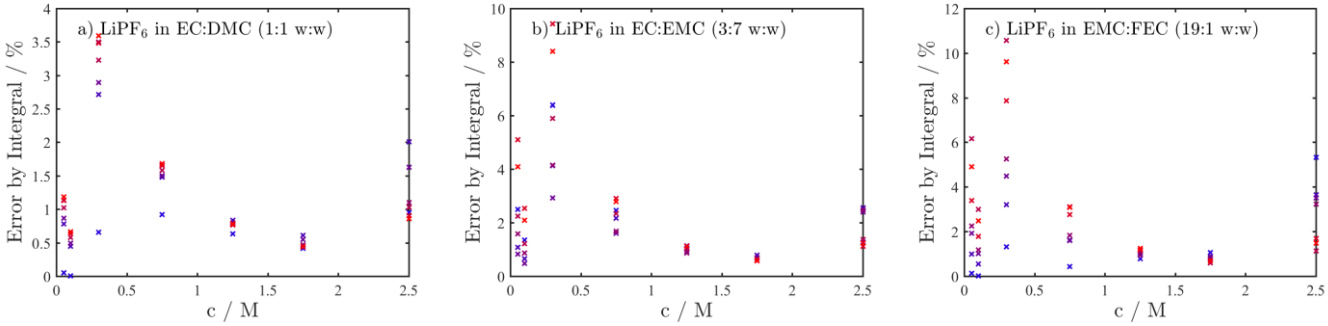

Figure 3. Percental errors by integral simplification, obtained by comparing calculated concentration potentials from Eq. 3 and Eq. 5 with inserting concentration dependent functional approximations found for individual temperatures (compare main article, Figure 9 and 10 as well as Table 3 and Eq. 21 and Eq. 22). Colors refer to the measurement temperatures (see main article legend), values are calculated for the same adjacent base concentrations used for experimental measurement of the concentration potential in the main article.

References

1. BASF, *Spec. Sheet.*, Specifications for Lithium-Ion Battery Electrolyte.

3.5 Comparison of a Lithium and a Sodium Electrolyte

In this section the article *Comparison of Ionic Transport Properties of Non-aqueous Lithium and Sodium Hexafluorophosphate Electrolytes*[105] is presented, which was not yet submitted at the time of submission of this thesis. Parts of the article were presented at the 231st Meeting of the Electrochemical Society in New Orleans (USA) in June 2017.

During charge/discharge operation of alkali batteries the ionic transport properties determine the efficiency of ionic charge transport and the extent of concentration gradients and overpotentials. A key feature, the mobility of the alkali ion, is determined by the ion's interaction with the surrounding solvent molecules. In addition to the dipolar moment of the solvent molecules, the electrical field of the alkali ion defines how strong the interaction between both species is. In the same solvent system (here EC:DEC (1:1 v:v)), the interaction of lithium ions, compared to sodium ions, are expected to be stronger due to the smaller ionic radius of lithium at the same overall charge (+1). The polar EC molecules from the solvent mixture are consequently expected to be more strongly coordinated around lithium and less weakly bound to the sodium ions. Thus the effective ion size in the electrolyte, which relates inversely to the ionic mobility, may be smaller for the larger sodium ion due to its weaker solvent interaction. I.e., the sodium ion mobility (incl. its solvation shell), could be higher than the lithium ion mobility, which in turn would suggest that the transference number of sodium may be larger than that of lithium. Transport properties for sodium battery electrolytes are hardly available in the literature.[106] In the manuscript we investigate the influence of the cation (lithium versus sodium) on the electrolyte transport properties and can show that indeed higher diffusion coefficients, cation transference numbers, and ionic conductivities are found for the sodium electrolyte. By means of 1D simulations using Comsol Multiphysics® we demonstrate the superiority of ionic transport for the sodium electrolyte, which shows smaller concentration gradients at the same C-Rate, smaller overpotentials and thus higher reversible capacities compared to the lithium electrolyte solution. Our results might help to mitigate some of the current drawbacks of future battery technologies such as the sodium ion battery and provides a new perspective for this cell chemistry.[107]

Author Contributions

M.G., T.H. and J.L. performed all electrochemical measurements and the data was analyzed by J.L. T.H., K.K. and S.K. provided valuable guidelines for handling metallic sodium. The manuscript was written by J.L. and edited by H.G. All authors discussed the data and commented on the results.

Comparison of Ionic Transport Properties of Non-aqueous Lithium and Sodium Hexafluorophosphate Electrolytes

Johannes Landesfeind,[a,z] Tomooki Hosaka,[b] Maximilian Graf,[a] Kei Kubota,[b]

Shinichi Komaba,[b] and Hubert A. Gasteiger[a]

[a] Chair of Technical Electrochemistry, Department of Chemistry and Catalysis Research Center, Technical University of Munich, Munich, Germany

[b] Department of Applied Chemistry, Tokyo University of Science, Tokyo, Japan

[z]corresponding author

Abstract

To bridge the gap between current lithium ion battery technology and alternative cell chemistries as, e.g., sodium ion or potassium ion batteries, the majority of the research focuses on the improvement of the cell's energy density by development of new active materials for reversible storage of sodium or potassium ions. On the other hand, the power density, which is determined by the ionic transport and thermodynamic parameters in the electrolyte, namely the conductivity, the thermodynamic factor, the transference number and the diffusion coefficient, is attracting little attention. In this contribution we determine these electrolyte properties for 0.1 M to 2 M $LiPF_6$ and $NaPF_6$ in EC:DEC (1:1 v:v) and use them in 1D simulations to show their impact on the cell discharge behavior and compare the theoretical rate performance of the lithium and sodium cell chemistry based on their electrolyte parameters. We show that the increased cation size of sodium and its corresponding weaker solvent interactions are beneficial for high power applications and that the improved ionic transport properties would allow for a substantial increase of either the (dis)-charge currents or the electrode loading compared to the well-established lithium system.

Introduction

Sodium ion and potassium ion secondary batteries, as alternatives to the currently utilized lithium ion technology, attract a growing interest in the research community.[1–6] The higher abundance of these alkali metals compared to lithium, their consequently lower cost, the possibility to replace the expensive copper current collector of lithium ion battery (LIB) anodes by cheaper aluminum and the reduced standard potential of potassium in non-aqueous solvents compared to lithium[7] make them a potential candidate for future electric storage applications in, e.g., electric cars or mobile phones. Established in 1988 with the first demonstration of a sodium ion full cell,[8] sodium ion batteries have been improved steadily and have been shown recently to be comparable to lithium ion batteries.[9] However comparative studies of the electrolyte parameters of lithium and sodium salts in aprotic solvents are scarce. Matsuda et al. study conductivity, viscosity and coordination number for $LiClO_4$, $NaClO_4$ and $KClO_4$ in PC:DME mixtures.[10] Similar studies were done by Kuratani et al.,[11] and, extended to a large range of different solvents, by Ponrouch et al.[12] In another publication the coordination numbers and desolvation energies of Li^+, Na^+, K^+ and Mg^{2+} ions for a large number of aprotic solvents are reported, based on DFT calculations and the found desolvation energies follows the order Li>Na>K, attributed to the decrease of cations' Lewis acidity.[13] An extensive study of the solvation structure of lithium and sodium hexafluorophosphate salts in various solvents by means of multiple experimental techniques including Raman spectroscopy and NMR spectroscopy analyses the extent of ion-ion and ion-solvent interactions and reports higher mobilities of $NaPF_6$ compared to $LiPF_6$ in EC:EMC.[14]

A profound understanding of the ion transport in the electrolyte can only be obtained from measuring all ionic transport and thermodynamic properties necessary to model ion movement in the electrolyte. I.e., in addition to the commonly reported conductivity, detailed knowledge about the thermodynamic factor (derivative form of the activity coefficient), the transference number and the diffusion coefficient is required as well. Because they are very "*cumbersome to attain*",[15] the literature lacks comparative studies of these electrolyte parameters in aprotic solvents which is particularly unsatisfactory as the different cation – solvent interactions of the lithium and sodium salts are likely to have a big influence. E.g., ion-ion interactions are reduced by 20% when switching lithium for sodium and coordination numbers and solvation structures differ due to the different charge/radius ratios of the cations and their different Lewis acidities.[16] The electrolyte parameters are directly or indirectly affected by the solvation shell around the cation as it modifies the cation's mobility (related to conductivity, transference number and diffusion coefficient) and impacts the energy required to remove the cation from its solvation shell (related to the thermodynamic factor).

Recently we introduced and applied novel and existing methods to determine all electrolyte parameters in non-aqueous electrolytes.[17–19] In addition to the straightforward measurement of the ionic conductivity, we described the determination of the binary diffusion coefficient from galvanostatic pulse experiments[17] and the measurement of transference numbers and thermodynamic factors based on concentration cell potentials and the short term potential relaxation after current pulses in symmetric lithium cells.[18,19] In this work we apply the same methodology to 0.1 M to 2 M $LiPF_6$ and $NaPF_6$ in EC:DEC (1:1 v:v). For a detailed description of theory and data analysis the interested reader is referred to the literature and we limit ourselves to a brief overview of the respective parameter determination methods, showing exemplary data in the supporting information.[19] The choice of salt and solvent is based on

commonly used electrolyte compositions in lithium ion batteries and recently reported stable cycling of sodium ion batteries for this electrolyte,[3] as well as the fact that only the PF_6^- anion provides long term stability towards cathodic oxidation.

In the *Experimental* all procedures, used materials and devices are introduced, if different to the original methodology, otherwise the reader is referred to the literature.[17–19] Obtained transport and thermodynamic parameters in the section *Results and Discussion* are compared to literature values of aqueous LiCl, NaCl and KCl electrolytes due to a lack of investigations in non-aqueous media. Concentration dependent functional descriptions of the parameters are fitted to experimental data and are summarized in Table 1. At last we use the determined electrolyte parameters to model the discharge behavior of a hypothetical NMC/graphite full cell and elaborate on the impact of the electrolyte parameters on the cell performance.

Experimental

A mixture of ethylene carbonate (EC) and diethyl carbonate (DEC, EC:DEC 1:1 v:v, Kishida Chemical, >99.5%) was used as solvent for self-prepared electrolytes containing 0.1 M, 0.5 M, 1.0 M, 1.5 M and 2.0 M lithium hexafluorophosphate ($LiPF_6$, BASF, battery grade) or sodium hexafluorophosphate ($NaPF_6$, Kishida Chemical, battery grade) salt, mixed in an argon filled glovebox (temperature 25 °C ± 1 °C, glovebox from MBraun, water content <0.1 ppm, Ar 5.0, Westfalen, 99.999% Vol). In this study we use M to denominate volumetric salt concentrations i.e., moles per liter. With the Karl-Fischer technique we found water contents below 12 ppm for the 2 M electrolytes. Metallic lithium (Rockwood Lithium, 75 µm thickness, high purity, 99.9%) or sodium (Sigma Aldrich, cubes, in mineral oil, 99.9%) was used for the electrodes. All cell parts were cleaned by boiling them in a mixture of ethanol and water (Millipore, Elix, 15 MΩ), thoroughly rinsing them with water, followed by overnight drying at 70 °C in a heating oven before bringing them into the glove box.

The electrolyte conductivities were measured at 25°C inside the glovebox using a commercially available conductivity sensor (SI Analytics, LF 1100 T+). Glass plate concentration cells were measured inside the glove box, as described in detail in Ref. [18]. The setup for galvanostatic pulse experiments only differs slightly from the symmetric lithium coin cells described in Ref. [19]. In this work metallic lithium was used as delivered and circular discs of 16 mm diameter ($A_{El.}$ = 2.01 cm²) were punched for use as counter and working electrodes (CE and WE). To obtain clean sodium electrodes, all sides of the sodium metal cube were cut, to avoid contaminations with mineral oil and the clean sodium metal piece was rolled inside a polypropylene plastic bag to prepare a flat foil, before punching 16 mm diameter sized electrodes. Instead of 20 layers of a conventional separator as described before[17] a circular disc (16 mm diameter) of a porous polypropylene sheet with $l_{Sep.}$ = 500 µm thickness (Sunmap LC, polypropylene, $\varepsilon_{Sep.} =$ 30 % porosity, 17 µm pore size, Nitto, Japan) was used as a porous medium. Compared to the setup described in our temperature dependent study the electrode and separator sizes are smaller, most importantly the separator is not larger than the electrodes and it was not plasma treated. While both improvements were only introduced after the electrolyte measurements for the present study we did not experience wetting issues of the Nitto separator. The tortuosity of the

porous medium, in the following called separator, was determined to be 4.8 ± 0.4 (compare experimental in Ref. 19). The coin cells were assembled inside the glovebox using two 0.5 mm spacers, a 1.4 mm washer and an electrolyte volume of 40 µl (corresponding to 4/3 of the separator void volume). After the coin cells were sealed, measurements were done at 25 °C in a climate chamber outside the glovebox. The measurement procedure consisted of a 30 min resting phase followed by an impedance measurement, a 15 min galvanostatic pulse and a 3 – 5 h OCV phase to observe the relaxation of the cell potential. In total four current pulses with alternating sign were applied to at least two cells for each electrolyte. Galvanostatic pulses of ± 150 µA/cm² for 0.1 M and ± 250 µA/cm² for 0.5 – 2 M were applied to the lithium electrolytes while ± 25 µA/cm² were used for 0.1 M and ± 65 µA/cm² for 0.5 – 2 M sodium electrolytes to avoid the formation of dendritic structures. A Biologic VMP3 potentiostat/galvanostat was used for the electrochemical measurement of concentration cells and pulse experiments.

Results and Discussion

In the following section we will present the measurement results for the ionic conductivity (using turn-key equipment), the binary diffusion coefficient (following the methodology introduced in Ref. [17]), the thermodynamic factor and the transference number (following the methodology introduced in Ref. [19]) for 0.1 M to 2.0 M $LiPF_6$ and $NaPF_6$ in EC:DEC (1:1 v:v) at 25°C. As the measurement techniques have been introduced in great detail in the given references this publication focuses on the observed differences of the ionic and thermodynamic transport properties for the two systems with different cations and the comparison with similar aqueous data. For the interested reader we show exemplary data and intermediate results (transport factors) in the Supporting Information. To simplify the comparison of transport properties of the aqueous and the non-aqueous systems we give the electrolyte concentrations in units of moles per liter in all plots, for the aqueous parameters from the literature,[20] partly calculated with the respective electrolyte densities.[21] At the end of this work, the found transport and thermodynamic properties of the lithium and the sodium electrolytes are used in a simulation of a hypothetical 1D NMC/graphite cell using COMSOL Multiphysics® to analyze the effect of the cation on the build-up of concentration gradients and overpotentials, as well as their impact on the discharge behavior of such cells.

Ionic Conductivity

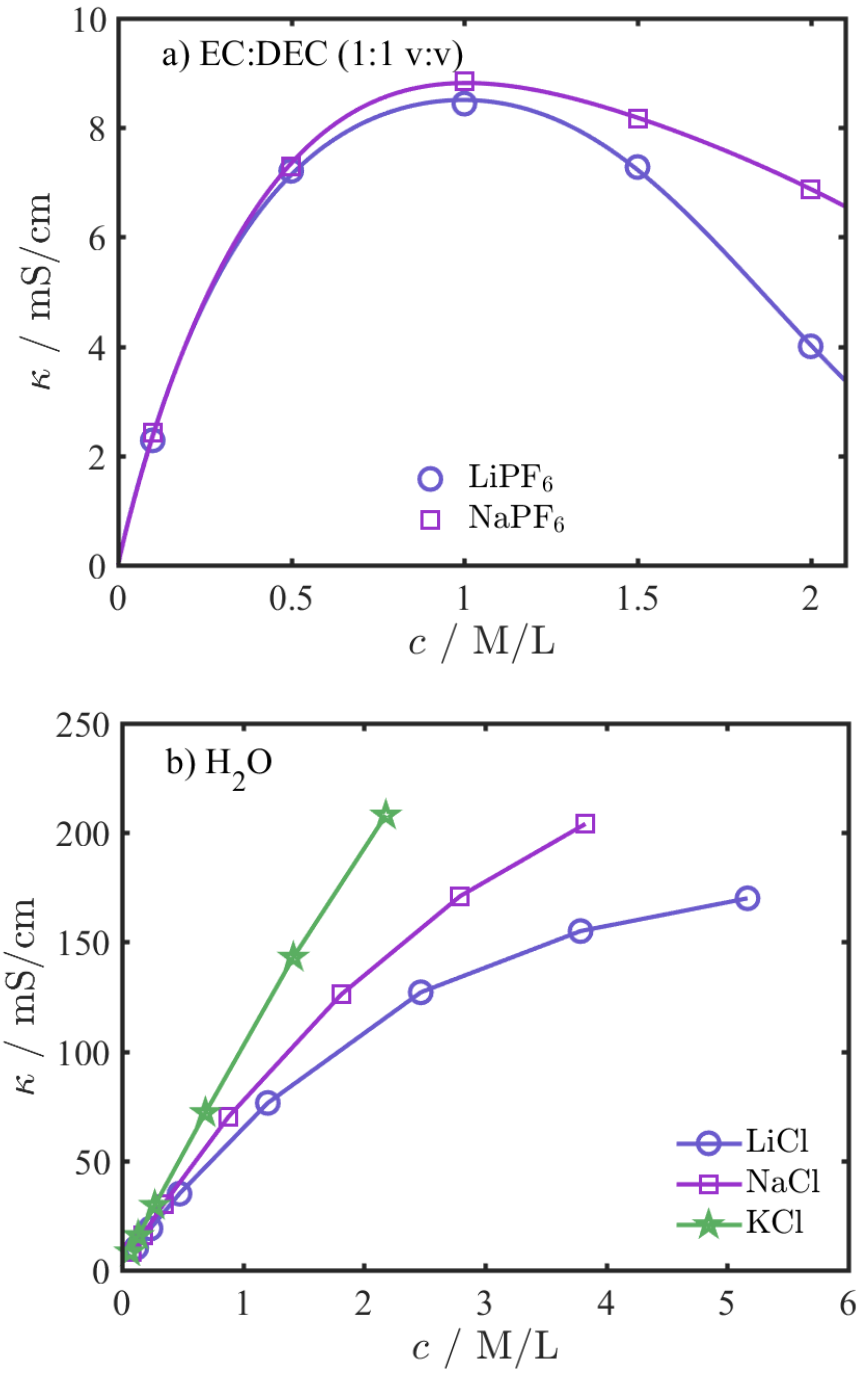

Figure 1. Ionic conductivity of: a) $LiPF_6$ (blue circles) and $NaPF_6$ (purple squares) solutions in EC:DEC (1:1 v:v) measured at 25°C, solid lines represent fits to the conductivity equation given in Table 1 (fitting parameters and their confidence intervals are also given in the table), b) aqueous LiCl (blue circles), NaCl (purple squares) and KCl (green stars) electrolytes at 25 °C (data taken from Ref. [20] and transformed into molarities with assumed linear densities from Ref. [21]), solid lines in b) serve as a guide to the eye.

In Figure 1a the ionic conductivities at 25 °C are shown for 0.1 M to 2 M $LiPF_6$ and $NaPF_6$ in EC:DEC (1:1 v:v). Up to ~1 M concentrations the electrolyte conductivities for both electrolytes are similar and differ by less than 10%. A maximum conductivity of ~8 mS/cm and ~8.5 mS/cm is obtained for the $LiPF_6$ and $NaPF_6$ electrolytes respectively, around 0.9 – 1.1 M salt concentrations. Only at concentrations above 1.3 M electrolyte conductivities differ

substantially, with higher values for the sodium compared to the lithium ion containing electrolyte (compare blue circles, and purple squares respectively). At 2 M, the conductivity of the lithium and the sodium electrolyte have decreased to ~4 mS/cm and 7 mS/cm respectively. Also shown in Figure 1a are the functional approximations of the experimental values to the conductivity equation given in the first column of Table 1. Figure 1b shows the conductivities for the aqueous electrolytes LiCl, NaCl and KCl (data from Ref. [22] and transformed into molarities with assumed linear densities from Ref. [21]). For concentrations below 0.3 M the conductivities are similar and only start to differ substantially above 0.5 M. At 1 M concentrations the electrolyte conductivities for the aqueous systems are ~65 mS/cm, ~75 mS/cm and ~100 mS/cm for LiCl (blue circles), NaCl (purple squares) and KCl (green stars) respectively and show an increasing spread for increasing salt concentrations (compare Figure 1b).

For both systems, aqueous and non-aqueous, the observed trend at high concentrations, i.e., higher conductivities for electrolytes containing the larger cation, are in agreement. This trend may be explained with different electrolyte viscosities. Reported, substantially higher viscosities of $LiClO_4$ compared to $NaClO_4$ above 1 M salt concentrations in PC support this argument.[11] In the same publication ~ 10 % higher conductivities of $LiClO_4$ are also obtained at lower salt concentrations (0.2 M – 0.5 M), compared to very similar values in this study, which may be due to different solvents and their relative permittivities (PC 65[23], EC:DEC ~30-40[24]).

The analysis of the conductivity showed that especially at high concentrations the larger sodium ion yield higher conductivities, i.e., smaller ohmic overpotentials would be expected for the $NaPF_6$ electrolyte especially at concentrations above 1 M.

Binary Diffusion Coefficient

In this section we will present concentration dependent binary diffusion coefficients for $LiPF_6$ and $NaPF_6$ in EC:DEC (1:1 v:v), obtained using the pulse polarization technique described in the literature.[17,25] The binary diffusion coefficient describes the coupled motion of anion and cation inside a concentration gradient.[26] Application of a short enough galvanostatic pulse to the symmetric cell setup described in the *Experimental* changes the salt concentration only at the vicinity of the electrodes, which equilibrates due to diffusion in a subsequent resting phase and can be monitored by measuring the cell potential. Exemplary data for the potential relaxation, shown in Figure 1 in the Supporting Information depict the exponential decay of the cell potential after a current pulse (pulse data not shown, measurement procedure described in the *Experimental*) for 1.5 M $LiPF_6$ and $NaPF_6$ in EC:DEC (1:1 v:v). From the slope $m_{\ln}$ in Figure 1 in the Supporting Information the binary diffusion coefficient $D_{\pm}$ can be obtained using

$$D_{\pm}(\mathrm{c}) = \frac{\tau_{\mathrm{Sep.}} \cdot l_{\mathrm{Sep.}}^2}{\pi^2} \cdot m_{\ln} \qquad 1$$

with the separator thickness $l_{\mathrm{Sep.}}$ (here 500 µm) and its tortuosity $\tau_{\mathrm{Sep.}}$ (here 4.8[19]). For more details about the method the interested reader is referred to the original publication.[17]

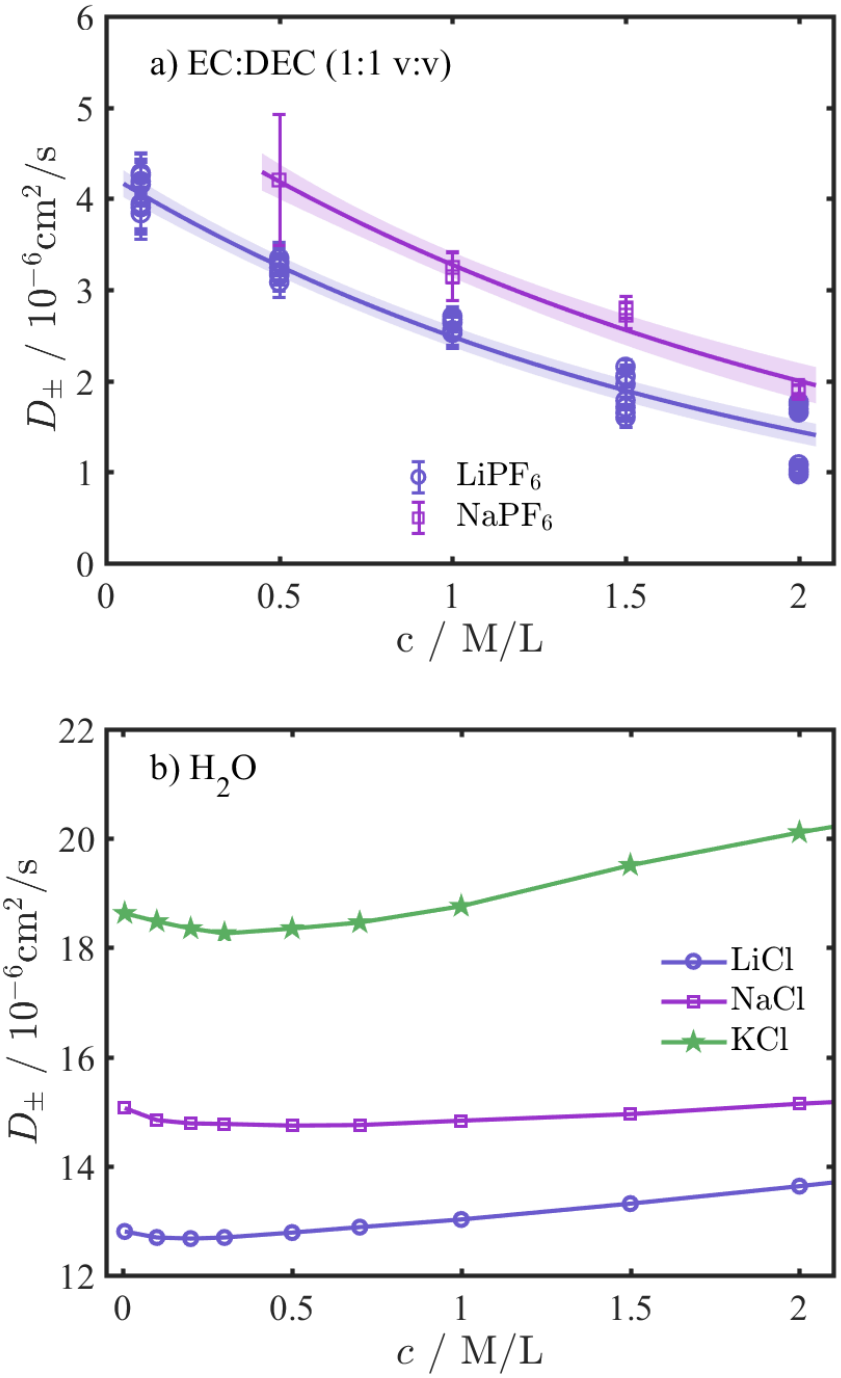

Figure 2. Diffusion Coefficients of a) $LiPF_6$ and $NaPF_6$ in EC:DEC (1:1 v:v) determined at 25°C in symmetric coin cells (as described in the *Experimental*) using the technique described previously,[17] the meaning of the errorbars is explained in the Supporting Information, with fits (solid lines) to the equation given in Table 1 and their confidence intervals, b) aqueous LiCl, NaCl and KCl electrolytes (data from Ref. [27]), solid lines in b) serve as guide to the eye.

From the slopes of the potential relaxation curves of repeat pulses and repeat cells we obtained the binary diffusion coefficients depicted in Figure 2a for the $LiPF_6$ (blue circles) and the $NaPF_6$ (purple squares) in EC:DEC (1:1 v:v) electrolytes. In case of the lithium electrolyte at least four measurements are shown at each concentration (resulting from the potential relaxation after four pulses, with alternating current), in case of the sodium electrolyte and the corresponding sodium metal electrodes only the relaxation after the first pulse(s) could be used, as later experiments showed increasing noise level or random potential jumps, which we ascribe to side reactions and/or the formation of

dendritic structures. For the same reason we were unable to obtain reliable measurements with the 0.1 M $NaPF_6$ electrolyte and exclude it from the data analysis. Figure 2a shows higher binary diffusion coefficients for the sodium salt compared to the lithium salt at all concentrations. At 1 M salt concentrations diffusion coefficients of $2.6 \cdot 10^{-6}$ cm²/s and $3.3 \cdot 10^{-6}$ cm²/s are found for $LiPF_6$ and $NaPF_6$ respectively. Similarly, in the aqueous LiCl, NaCl and KCl electrolytes the binary diffusion coefficients follows the same order, K > Na > Li (compare Figure 2b). In the aqueous case the diffusion coefficients are rather constant, while for the non-aqueous EC:DEC solvent mixture investigated in this work, a monotonic decrease is found, which however is in line with previous reports for binary diffusion coefficients in non-aqueous solvents in the literature.[17,28,29] The observed decrease of the binary diffusion coefficients may be explained with the increasing viscosity of the non-aqueous electrolytes for increasing salt concentrations, hindering ion movement as for example reported by Kuratani et al. for $LiClO_4$ and $NaClO_4$ in PC.[11] Higher viscosities of the lithium electrolyte yield lower diffusion coefficients compared to the sodium case. In the aqueous system the viscosity of the electrolyte may not be affected as strongly by the increasing salt concentration, at least not in the concentration range given in Figure 2b, explaining the fairly constant values.

During operation of a battery the formation of concentration gradients is unfavorable, as they are generally accompanied by increased overpotentials. The build-up of ionic concentration gradients is counteracted by ion diffusion and therefore higher diffusion coefficients reduce overpotentials during operation and are thus beneficial for thick electrodes and fast charge/discharge applications. In addition to diffusion effects also ionic migration in the applied electric field counteract the build-up of concentration gradients. The underlying property for ionic migration is the transference number, which will be analyzed in the following together with the thermodynamic factor.

Thermodynamic Factor

For the determination of thermodynamic factors and transference numbers (see next section) we analyze a) the short term potential relaxation after galvanostatic pulses in symmetric cells, i.e., the same transients of which the long term relaxation was used to determine the binary diffusion coefficient and b) the concentration potential measured in glass concentration cells. As argued in the corresponding erratum[30] the ferrocene cell method for the direct determination of thermodynamic factors may not be applied generally as not all necessary assumptions are valid and thus we follow the alternative scheme introduced in Ref. [19] (compare Figure 1 in the respective publication) and use two experimentally obtained transport factors[24] to mathematically extract transference number and thermodynamic factor. From concentration cell potentials, measured for differential salt concentrations, the transport factor $a \equiv \mathrm{TDF} \cdot (1 - t_+)$ may be obtained, while the transport factor $b \equiv \mathrm{TDF} \cdot (1 - t_+)^2$ is determined from the short term potential relaxation after the pulse experiment (for details compare Ref. [18,19]). Measured concentration potentials of the electrolyte concentration pairs 0.065 M – 0.1 M, 0.35 M – 0.5 M, 0.75 M – 1 M, 1.25 M- 1.5 M and 1.75 M – 2 M are shown in the Supporting Information and allow for the calculation of the transport factor a by simplification of the integral in the corresponding equation (see Eq. 3-5 in Ref. [19]), valid for small concentration differences. Transport factors a are obtained from concentration cell potentials and are assigned to their mean concentrations (e.g., a for 0.75 M – 1 M concentration pair is plotted at 0.875 M in the Supporting Information). Calculation of b requires to

find the potential at current interrupt from the analysis of the potential transient after the galvanostatic pulses using the artificial time $1-\frac{\sqrt{T_I}}{\sqrt{t}+\sqrt{t-T_I}}$. The typical s-shape for these potential transients, as observed in the exemplary data depicted for the 2 M electrolytes in Figure 3 in the Supporting Information serves as a quality measure for the applicability of the method. From extrapolation of the first linear section of the s-shaped curves (see range markers in Figure 3 in the Supporting Information) the potential at current interrupt, and thus the transport factor *b* can be obtained, requiring only geometrical parameters of the cell and the previously determined exponential slope of the long term potential relaxation m_{ln} (compare Eq. 8 in Ref. [19]). In addition to the found transport factors (marked by circle and square symbols in Figure 4 and 5 in the Supporting Information) we determine linear interpolations, shown as dots in the respective figures. For the calculation of transference number and thermodynamic factor the transport factors are required at the same salt concentration, so that linear interpolations of pulse and concentration cell experiments are required due to their slightly different concentrations (pulse experiments at 0.1, 0.5, 1, 1.5 and 2 M, but concentration cell potentials at 0.0825 M, 0.425 M, 0.875 M, 1.375 M and 1.875 M). Combination of one measured and one interpolated transport factor each allows to obtain explicit values for the transference number and the thermodynamic factor. With the transport factors *a* and *b*, as shown in Figure 4 and 5 in the Supporting Information the thermodynamic factors and transference numbers are determined.

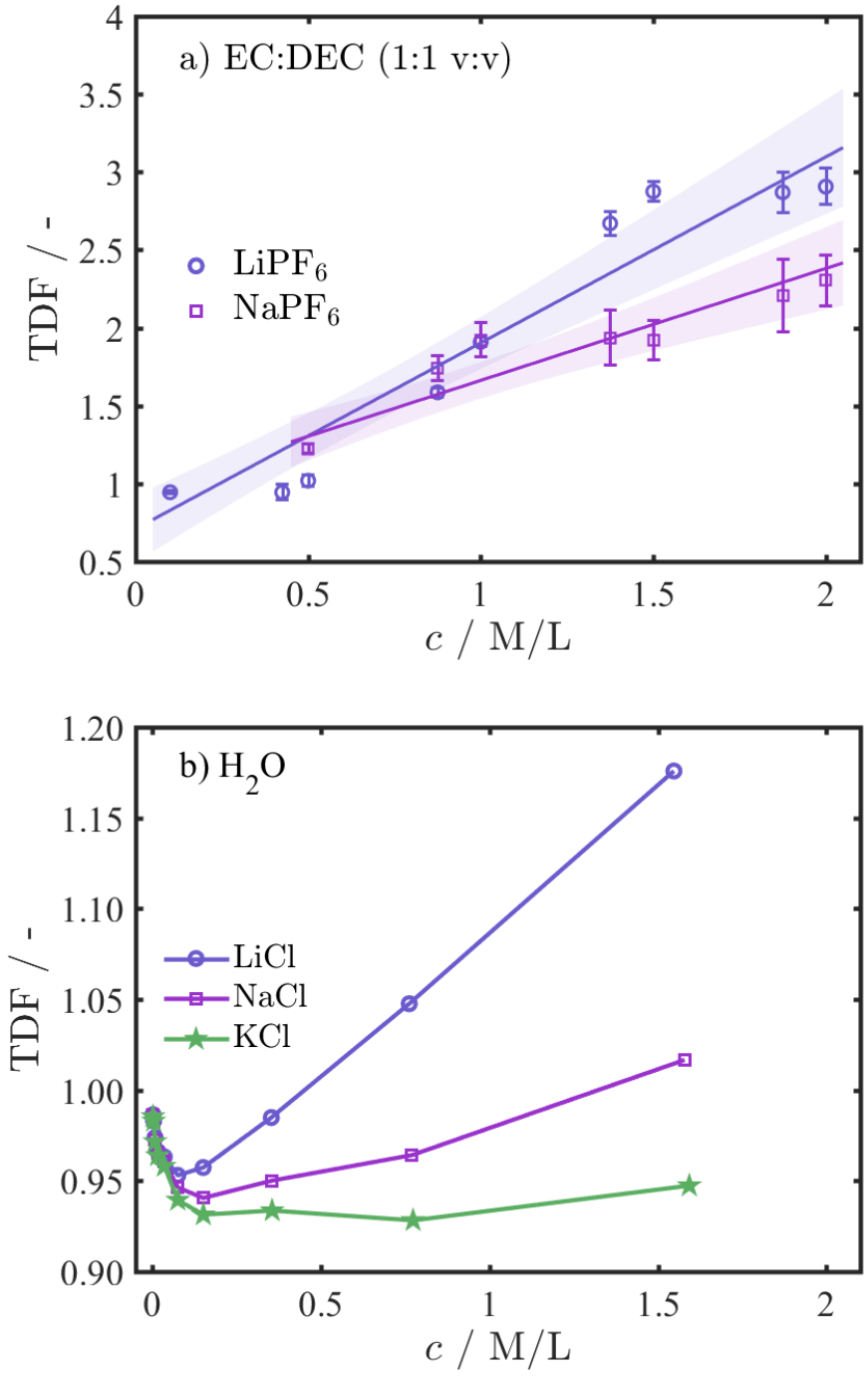

Figure 3. Thermodynamic factors of a) $LiPF_6$ and $NaPF_6$ solutions in EC:DEC (1:1 v:v) determined from transport factors *a* and *b* at 25°C (compare Figure 4 and Figure 5 in the Supporting Information) using the methodology described in Ref. [19] as well linear approximations (solid lines, parameters given in Table 1); error bars are based on Gaussian error propagation of the errors from the transport factors *a* and *b*, b) aqueous LiCl, NaCl and KCl electrolytes (data from Ref. [22] and transformed into molarities with assumed linear densities from Ref. [21]), solid lines serve as guide to the eye.

The thermodynamic factors ($TDF = \frac{a^2}{b}$) for $LiPF_6$ and $NaPF_6$ in EC:DEC (1:1 v:v) shown in Figure 3a increase with increasing salt concentration. In line with the theoretical definition of the thermodynamic factor the thermodynamic factor for the 0.1 M $LiPF_6$ electrolyte is close to unity. As argued before the 0.1 M $NaPF_6$ data from the pulse experiments is not reliable and could thus not be analyzed, however linear extrapolation from higher concentrations suggest a TDF around unity for $c \to 0$ as well. Experimental scatter in Figure 3a (and later Figure 4a) shows the

sensitivity of the technique for small variations in the transport factors (compare also fairly smooth transport factors in Figure 4 and Figure 5 in the Supporting Information) and suggests an improved accuracy with additional repeat measurements and might be (partially) related to the cell setup (same separator and electrode sizes, rather than larger separator, compare improved setup in Ref. [19]). In order to compare the low concentration range with the Debye-Hückel theory more measurements would be required. Instead we focus on the comparison with thermodynamic factors calculated from the activity coefficients of LiCl, NaCl and KCl in H_2O (activity coefficients from Ref. [22] and transformed into molarities with assumed linear densities from Ref. [21]), shown in Figure 3b. While for these aqueous electrolytes the thermodynamic factor changes by 10% from infinite dilution to 1 M, the thermodynamic factor of $LiPF_6$ and $NaPF_6$ in EC:DEC (1:1 v:v) shows a pronounced increase by ~100 – 200 % in the same concentration range. A general increase of the thermodynamic factor with decreasing cation size for concentrations > 0.2 M is found for both solvent systems (neglecting the small kink observed for ~0.4 M KCl in H_2O, green star in Figure 3b), the aprotic (Figure 3a) and the protic (Figure 3b) .

As the thermodynamic factor is a derivative form of the activity coefficient, which is normalized to infinite dilution by definition, the observed higher TDF for the smaller cation may be explained with the different relative change of the solvation structure at infinite dilution compared to higher concentrations. Due to the small size at same charge, the lithium ion interacts stronger with the solvent molecules, i.e., has the larger solvation shell at infinite dilution, and a (partial) loss of solvated molecules at increasing salt concentrations may yield a larger increase in reactivity (=increase in activity coefficient and TDF) compared to infinite dilution. At the same time the larger sodium cation shows a weaker coordination at infinite dilution due to its larger ion size and a (partial) loss of solvated molecules can only yield a smaller increase in reactivity. This is supported by theoretical studies showing a 20% smaller desolvation energy of Na^+ in different EC:DMC ratios at low concentration compared to Li^+.[16] In our understanding the increase of the TDF is mainly caused by the different activities at the reference state (infinite dilution) of the mean molar activity coefficient.

In the Newman model high TDFs lead to increased concentration overpotentials. Thus, based on the TDFs for $LiPF_6$ and $NaPF_6$ in EC:DEC (1:1 v:v) as well as the TDFs for the aqueous LiCl, NaCl and KCl electrolytes it is concluded that electrolytes with the smaller cations are beneficial in terms of ionic transport properties.

Transference Number

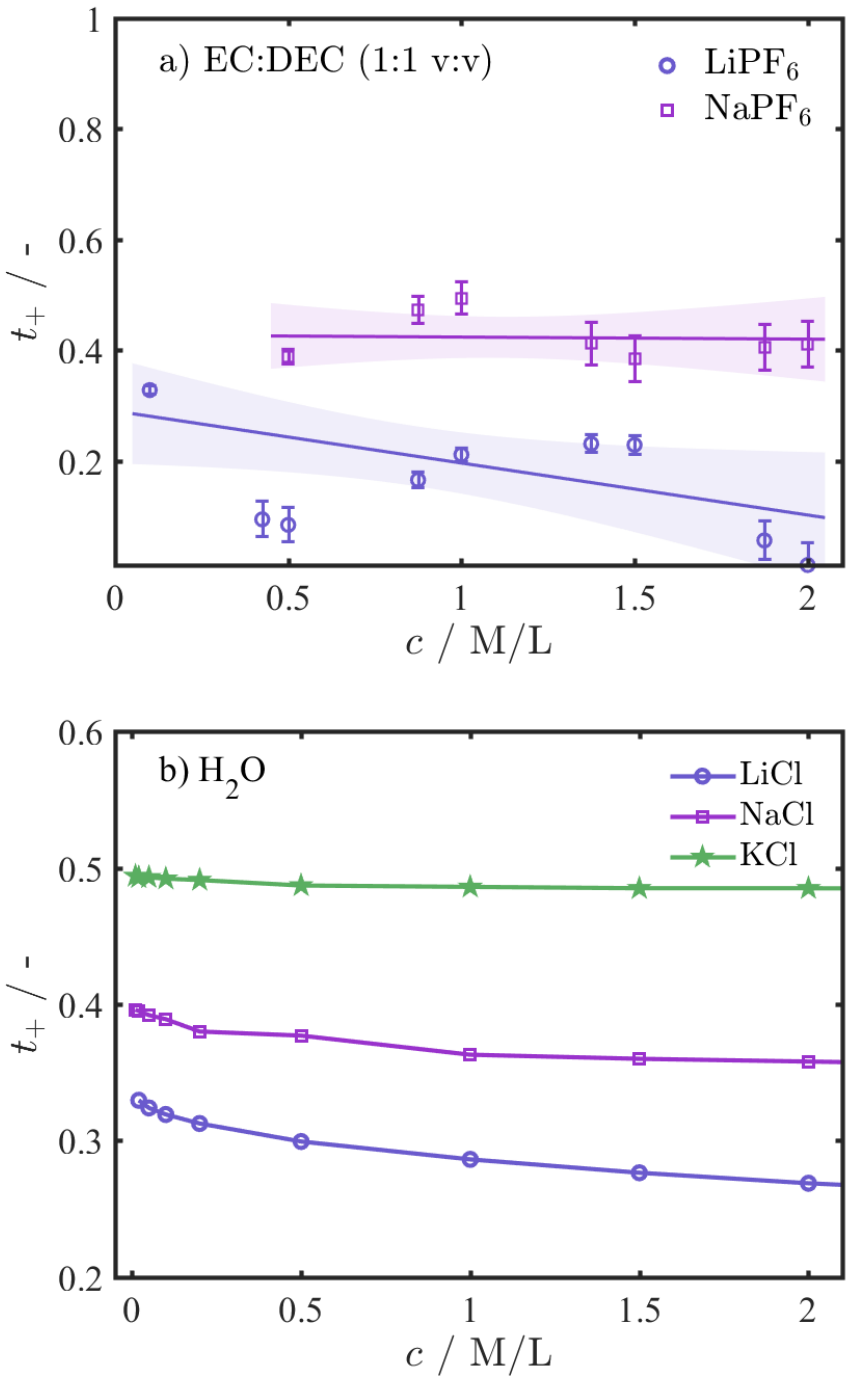

Figure 4. Transference numbers of a) $LiPF_6$ and $NaPF_6$ solutions in EC:DEC (1:1 v:v) determined from transport factors *a* and *b* at 25°C (compare Figure 4 and Figure 5 in the Supporting Information) using the methodology described in Ref. [19] as well linear approximations (solid lines, parameters given in Table 1); error bars are based on Gaussian error propagation of the errors from the transport factors *a* and *b*, b) aqueous LiCl, NaCl and KCl electrolytes (data from Ref. [31]), solid lines serve as guide to the eye.

In analogy to the determination of the thermodynamic factor, the transference numbers in Figure 4a are obtained from the transport factors *a* and *b* ($t_+ = 1 - \frac{b}{a}$) as shown in the Supporting Information (Figure 4 and Figure 5) for the $LiPF_6$ and the $NaPF_6$ in EC:DEC (1:1 v:v) electrolytes.[19] For $NaPF_6$ in EC:DEC (1:1 v:v) the transference numbers

are ~0.45 at all concentrations. At 0.1 M $LiPF_6$ in EC:DEC (1:1 v:v) the transference number is ~ 0.35 and decreases for increasing concentrations, which is a result of the similar transport factors *a* and *b* (compare Figure 4 and 5 in the Supporting Information), for $c \rightarrow 2$ M, $t_+ \rightarrow 0$ and $a \approx b$. Analysis of the aqueous data for transference numbers of LiCl, NaCl and KCl (data from Ref. [31]) shows a similar behavior, i.e., larger transference numbers for larger cations. The cation transference number is defined by the ratio of cation mobility to the sum of mobilities of anion and cation.[26] In the non-aqueous electrolyte, at high concentrations, the smaller cation, i.e., the one with the stronger interaction with the solvent molecules, has to drag along a large fraction of the solvent, bound to its solvation shell, which decreases the ion's mobility and in consequence also the transference number. Latter effect would be pronounced for non-aqueous solvent systems at high concentrations where strongly solvated ions, such as Li^+, may hold the majority of the large, polar EC molecules (moles of EC to moles of Li^+ at 2 M ~ 5 to 2). This is supported by similar ionic mobilities, reported for Li^+ and PF_6^- in DMC at infinite dilution while for increasing salt concentrations the PF_6^- mobility is larger than the mobility of Li^+.[32] As the sodium ion shows a lower interaction with the solvent (smaller charge to radius ratio), its mobility is less effected at high concentrations. Due to the different molar ratio of solvent to salt, caused by the small water molecule, this effect is not as pronounced in the aqueous case (moles of H_2O to moles of Li^+ at 2 M ~ 50 to 2, compare still larger decrease of the transference number for LiCl in H_2O compared to NaCl or KCl in Figure 4b).

Figure 4 shows higher transference numbers for the sodium system compared to lithium, especially at higher concentrations. The reader is reminded that concentration gradients forming during charge/discharge operation in the liquid electrolyte are counteracted by ionic diffusion *and* migration. As higher transference numbers equal higher mobilities in an electric field, lower concentration gradients and consequentially overpotentials would be expected with sodium. Before we adopt the found concentration dependent transport properties in a simple 1D Newman model to exemplarily show the influence of transport properties we summarize the functional approximations obtained for the ionic conductivity, the binary diffusion coefficient, the thermodynamic factor and the transference number as well as their fit parameters.

Overview of Transport Properties

All parameters found in the previous analyses, describing the concentration dependent ionic conductivity, thermodynamic factor, transference number and binary diffusion coefficient as well as their fit equations are given in Table 1 for $LiPF_6$ and $NaPF_6$ in EC:DEC (1:1 v:v). The functional description for the ionic conductivity is chosen to fulfill the Kohlrausch square root law at low concentrations and was selected similar to our temperature dependent study (compare Eq. 15 in Ref. [19] for constant temperatures).[26] It is noted that the number of measured ionic conductivities in this work is small and the high goodness of fit values (and at the same time large confidence intervals) are due to the high number of fit parameters (4) compared to the number of measurement points (5). Similarly the goodness of fit values for the linear transference number approximations are low and more measurements would be required to obtain more reliable concentration dependencies. In the present study the focus is on the qualitative difference between lithium and sodium ion transport properties, which can be separated clearly for all parameters (compare Figure 1a, Figure 2a, Figure 3a and Figure 4a). Although the accuracy of found functional approximations

in Table 1 could be improved by additional measurements they may be used to estimate the difference in ionic transport for $LiPF_6$ and $NaPF_6$ in EC:DEC (1:1 v:v).

Table 1. Fit equations and dimensionless parameters, including their confidence interval based on a 90 % standard deviation and the goodness of fit values, describing the concentration dependence of the transport and thermodynamic parameters for $LiPF_6$ and $NaPF_6$ in EC:DEC (1:1 v:v) as shown by the solid fit lines in Figure 1a, Figure 2a, Figure 3a and Figure 4a. Concentrations are used in units of moles per liter (M).

Functional Description		$LiPF_6$	$NaPF_6$
$\kappa(c) = p_1 \cdot \mathrm{c} \cdot \frac{1 + p_2 \cdot \sqrt{c} + p_3 \cdot c}{1 + \exp(p_4 \cdot c^2)} \cdot \frac{\mathrm{mS}}{\mathrm{cm}}$	p_1	6.30E+01(± 3.3E+01)	6.12E+01(± 1.6E+01)
	p_2	-7.77E-01(± 4.2E-01)	-7.32E-01(± 1.7E-01)
	p_3	2.02E-01(± 3.1E-01)	8.57E-02(± 1.8E-01)
	p_4	7.63E-01(± 4.0E-01)	3.74E-01(± 5.8E-01)
	R^2	0.999	1.000
$\left(1 + \frac{\mathrm{d} \ln f_{\pm}(c)}{\mathrm{d} \ln c}\right) = p_1 \cdot c + p_2$	p_1	1.19E+00(± 2.5E-01)	7.19E-01(± 2.3E-01)
	p_2	7.09E-01(± 2.1E-01)	9.43E-01(± 2.5E-01)
	R^2	0.921	0.890
$t_+(c) = p_1 \cdot c + p_2$	p_1	-9.40E-02(± 8.9E-02)	-3.73E-03(± 7.1E-02)
	p_2	2.90E-01(± 9.5E-02)	4.27E-01(± 8.6E-02)
	R^2	0.364	0.002
$D_{\pm}(c) = p_1 \cdot \exp(p_2 \cdot c) \cdot 10^{-6} \frac{\mathrm{cm}^2}{\mathrm{s}}$	p_1	4.28E+00(± 1.5E-01)	5.36E+00(± 4.8E-01)
	p_2	-5.43E-01(± 4.6E-02)	-4.93E-01(± 9.3E-02)
	R^2	0.951	0.978

Analysis of the electrolyte properties of both electrolytes showed higher conductivities, diffusion coefficients and transference numbers for the larger cation (sodium), i.e., for weaker interaction with the solvent molecules (compare Figure 1a, Figure 4a and Figure 2a) and thus suggest smaller overpotentials during cell operation. Only the thermodynamic factor suggests the opposite trend, i.e., smaller overpotentials and thus better cell performance for smaller cations (lithium). In the widely applied Newman model, used to describe the ionic transport and thermodynamics of battery cells in numerical experiments, the coupled transport and energy equations make it difficult to judge which of the above found trends dominates during cell operation. Therefore the found concentration dependent transport and thermodynamic parameters given in Table 1 for the two types of cations are used in the following section for 1D simulations of a cell discharge and to compare the effect of the found parameters on the battery performance.

1D Discharge Simulations with $LiPF_6$ and $NaPF_6$ Electrolyte Parameters

In the following 0.2 C to 20 C discharge rates of a theoretical 1D battery cell, described with the Newman model, are simulated using COMSOL Multiphysics®, using the functional approximations for the electrolyte parameters found for $LiPF_6$ and $NaPF_6$ in EC:DEC (1:1 v:v) in Table 1. As these parameters have been determined at 25°C only, the model is isothermal. Additional parameters resembling a typical battery setup with an electrode loading of 3 mAh/cm² are given in Table 1 in the Supporting Information for the reader's convenience. While the effects shown can also be observed with lower loadings, the comparably high loading of 3 mAh/cm² is used on purpose to highlight the different

behavior of the electrolytes at these challenging conditions. Because the goal of the subsequent analysis is the comparison of the effect of electrolyte parameters for the different chemistries, all parameters given in Table 1 in the Supporting Information are fixed and only the electrolyte parameters are changed between the two different sets given in Table 1. This also means that the same open circuit potentials for the electrodes (in this case graphite and NMC) are used, which is for academic reasons only and the authors are aware of the fact that the arbitrarily chosen NMC/graphite system would not be applicable for the sodium cell chemistry. Constant current discharge simulations are done at C-Rates of 0.2, 0.5, 1, 2, 3, 4, 5, 6, 7, 8, 10, 12, 15 and 20 C until the cell cut-off potential of 2.7 V is reached. An initial SOC of 3% (see Table 1 in the Supporting Information) was chosen on purpose to avoid numerical instabilities at the beginning of the discharge.

Depending on the current and the electrolyte parameters, larger or smaller concentration gradients may evolve. Exemplary concentration profiles for the electrolyte parameter sets given in Table 1 are shown in Figure 5a for a C-Rate of 1 1/h and Figure 5b for a C-Rate of 3 1/h at the end of discharge, i.e. when the cell potential reached 2.7 V, the last time step of the simulation. The corresponding full cell potential curves are shown in Figure 6a and b.

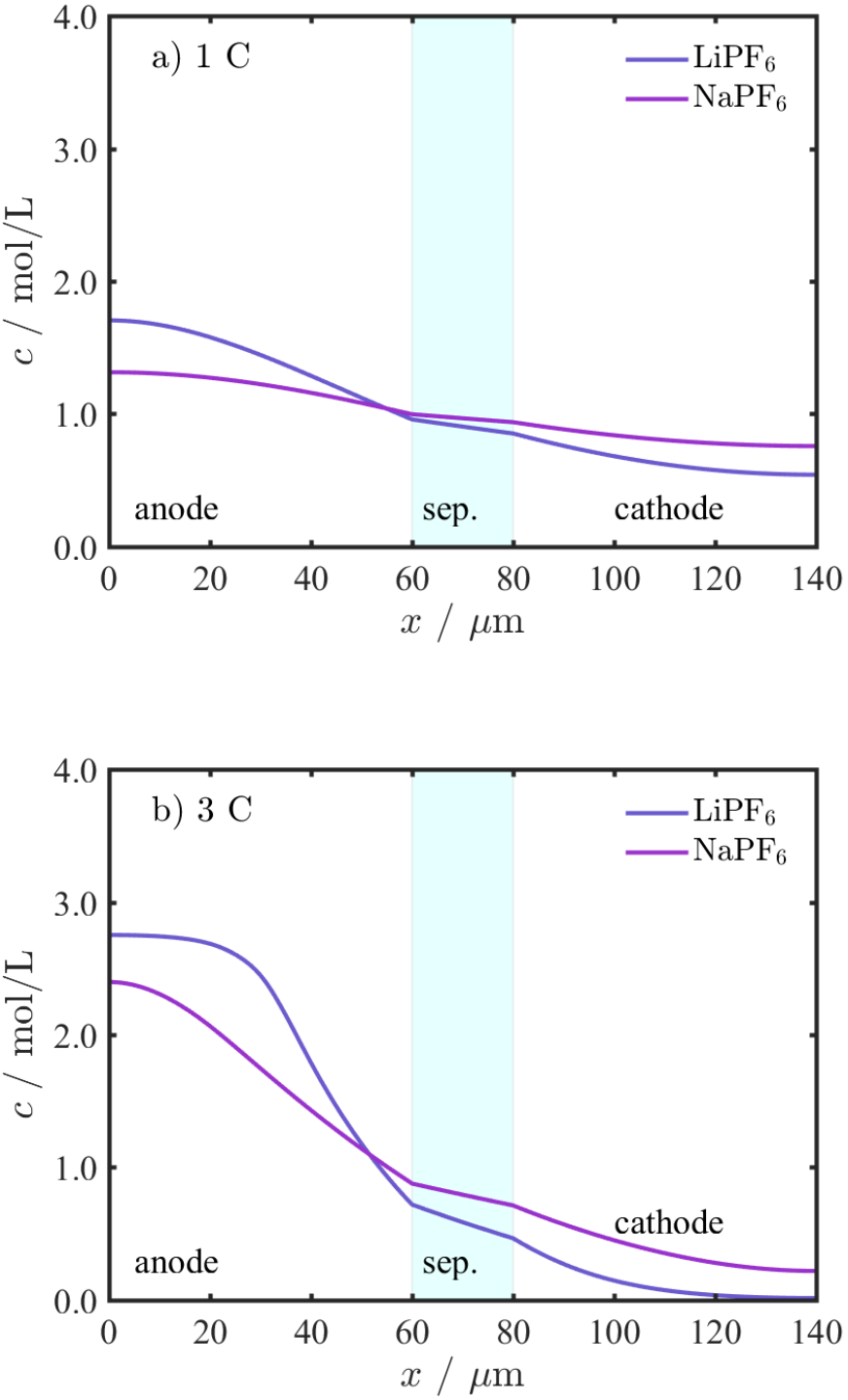

Figure 5. Electrolyte Concentration gradients at the end of a a) 1C and b) 3C constant current discharge, i.e., when the cell cut-off potential of 2.7 V is reached, in a hypothetical NMC/graphite cell. Solid lines for $LiPF_6$ (blue) and $NaPF_6$ (purple) in EC:DEC (1:1 v:v) are simulated with the measured transport and thermodynamic parameters given in Table 1. Additional simulation parameters are given in Table1. In the Supporting Information. The separator region is highlighted in cyan to easily discern it from the electrodes (see labels in figure).

At a C-Rate of 1 1/h, as shown in Figure 5a, the initial 1 M electrolyte concentration increases inside the pores of the anode (during discharge the alkali ion is deintercalated from the anode) and decreases inside the pores of the cathode (during discharge the alkali ion is intercalated into the cathode). While the $LiPF_6$ concentrations at the anode and the

cathode current collectors are 1.7 M and 0.5 M at the end of discharge, much smaller concentration gradients of 1.3 M and 0.8 M are found for $NaPF_6$ at the respective interfaces at the end of discharge. The consequential reduction of the cell overpotential can also be seen in Figure 6a when comparing the potential curves of the $LiPF_6$ (blue) and $NaPF_6$ (purple) simulations at 1C (higher mean discharge potential with $NaPF_6$ transport properties). Compared to the $NaPF_6$ simulation, the electrolyte parameters for $LiPF_6$ in EC:DEC (1:1 v:v) yield a ~50 mV higher overpotential (at 50% SOC, see Figure 6a), i.e., a 50 mV lower mean discharge potential. As long as the same capacity is obtained for both chemistries, it is straightforward to compare the influence of the transport parameters on the cell behavior. Figure 6a shows a clear trend, smaller concentration gradients for the electrolytes with the larger cation, demonstrating that the beneficial effect of higher conductivity at high concentrations, higher transference numbers and higher diffusion coefficients dominate over the found adverse behavior of the thermodynamic factor.

The concentration profile at the end of a 3 1/h discharge as well as the corresponding potential curves are shown in Figure 5b and Figure 6b. In contrast to the previously shown 1 1/h C-Rate, for the 3 1/h C-Rate the reached capacities differ largely between the different cell chemistries (compare Figure 6b), indicating that the difference in electrolyte transport parameters plays an important role and determines the maximum SOC during operation. For the high 3 1/h C-Rate the SOC after discharge is 61% and 93% for the $LiPF_6$ and $NaPF_6$ electrolyte parameters from Table 1 respectively (compare Figure 6b). As a result of the different capacities reached, the concentration gradients at the end of the 3 1/h discharge in Figure 5b correspond to different amounts of transported charge (= different times) and thus cannot be compared directly. Clearly visible is the increased magnitude of the concentration gradients for both cation types (Figure 5b) compared to the smaller C-Rate (Figure 5a), as well as the pronounced depletion of ions inside the pores of the cathode for the lithium electrolyte at the end of discharge (compare blue $LiPF_6$ concentration gradients in Figure 5b in the cathode, $x > 120$ µm). Aside from the concentration overpotential and the increasing ohmic overpotentials at high concentration gradients, this depletion of ions in the pores of either electrode (during discharge or charge in the porous cathode or anode) causes a large kinetic overpotential due to the dependence of the exchange current density in the Butler-Volmer equation on the ion concentration.[26] For small ion concentrations the kinetic resistance becomes very large, i.e., large overpotentials are necessary to draw/apply the same current. This depletion of ions inside the porous electrodes is the ultimate reason for the drop of usable discharge capacities at higher currents.[33]

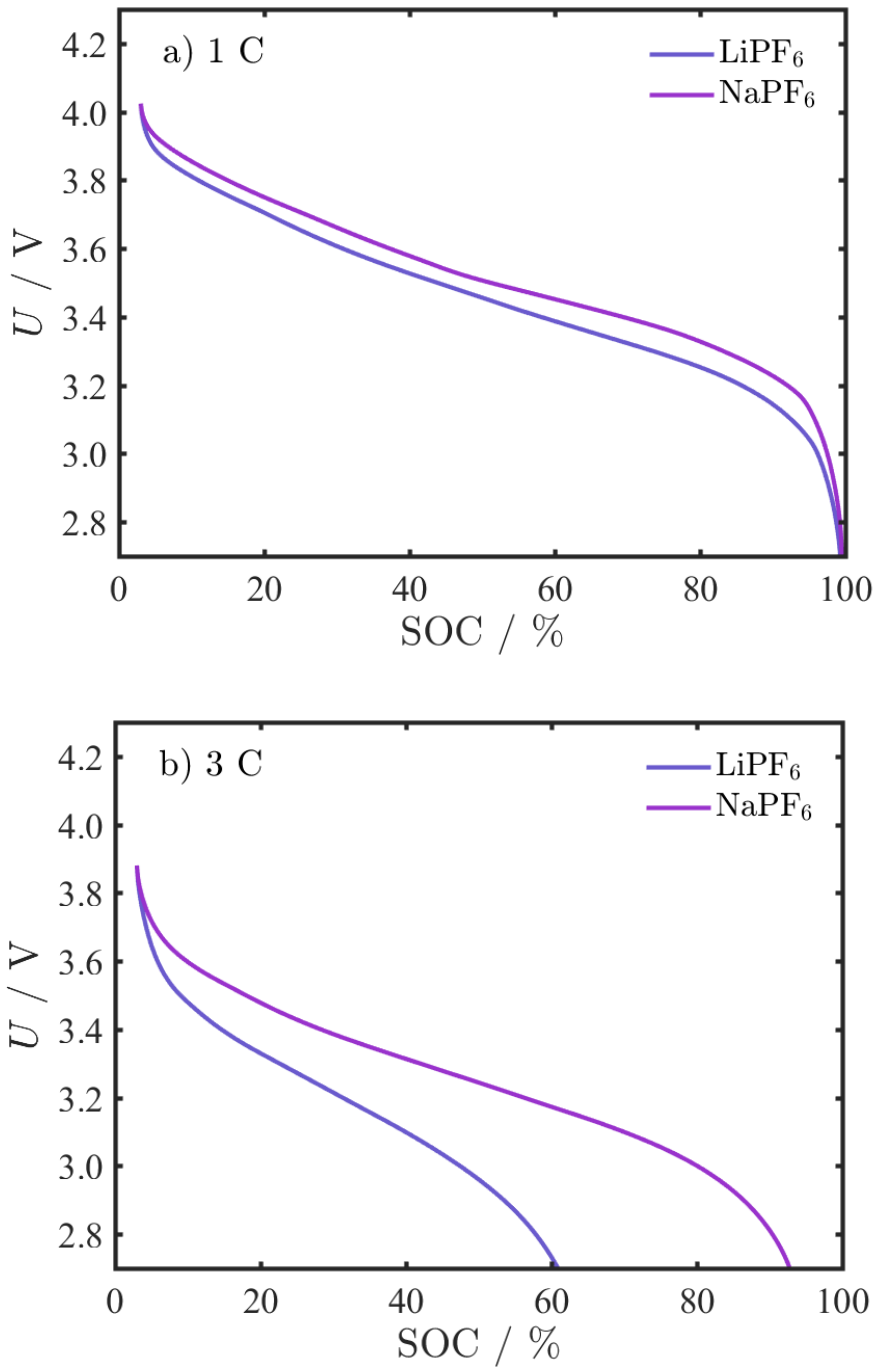

Figure 6. Cell potential curves during a) 1C and b) 3C constant current discharge of a hypothetical NMC/graphite cell. Solid lines for $LiPF_6$ (blue) and $NaPF_6$ (purple) in EC:DEC (1:1 v:v) are simulated with the measured transport and thermodynamic parameters given in Table 1. Additional simulation parameters are given in Table 1 in the Supporting Information. The initial SOC of 3% was chosen to avoid numerical instabilities at the beginning of the discharge simulations.

The percental discharge capacities for all simulated C-Rates are summarized in Figure 7. For C-Rates up to 1 1/h almost identical capacities are reached for both cell chemistries, although also in this case pronounced differences of the concentration gradients can be found (compare Figure 5a). With the $LiPF_6$ electrolyte parameters, the reached SOCs steeply drop from >80% to <20% for C-Rates of ~2 1/h to ~6 1/h, the same drop in SOC is observed only for higher C-Rates with the Na electrolyte (~4 1/h to ~8 1/h). The initial SOC of 3%, which was chosen to avoid numerical instabilities at the beginning of the discharge simulations, is the reason for the finite offset at high C-Rates.

In summary, Figure 7 illustrates the superiority of the electrolyte transport and thermodynamic parameters of the $NaPF_6$ compared to the $LiPF_6$ electrolyte. It is important to keep in mind that ion association is neglected in this work as reported electrolyte parameters are referenced versus the nominal ion concentration, i.e., even if the sodium salt would have a higher degree of association, the effective ion transport is still improved. As argued before, the difference between the salts is the structure of the solvation shell around the cation, caused by their different interactions with the solvent molecules. Larger cation sizes at the same charge result in weaker interactions with the solvent and lead to higher conductivities at high concentrations, higher transference numbers and higher diffusion coefficients. These trends are the result of the increased mobility of the cation with the weaker interactions with the solvent molecules. The drop of reached capacity shown in Figure 7 correlates with the magnitude of salt depletion inside the pores of the intercalating electrode (here the cathode) and also strongly depends on the intercalation kinetics, which was assumed identical for both cell chemistries in this work (compare Table 1 in the Supporting Information). Our results suggest that based on the electrolyte parameters higher currents can be drawn from/applied to sodium battery cells compared to lithium ion batteries without compromising the discharge capacity or alternatively higher loadings can be realized before salt depletion occurs within the electrolyte inside the pores of the porous coatings.

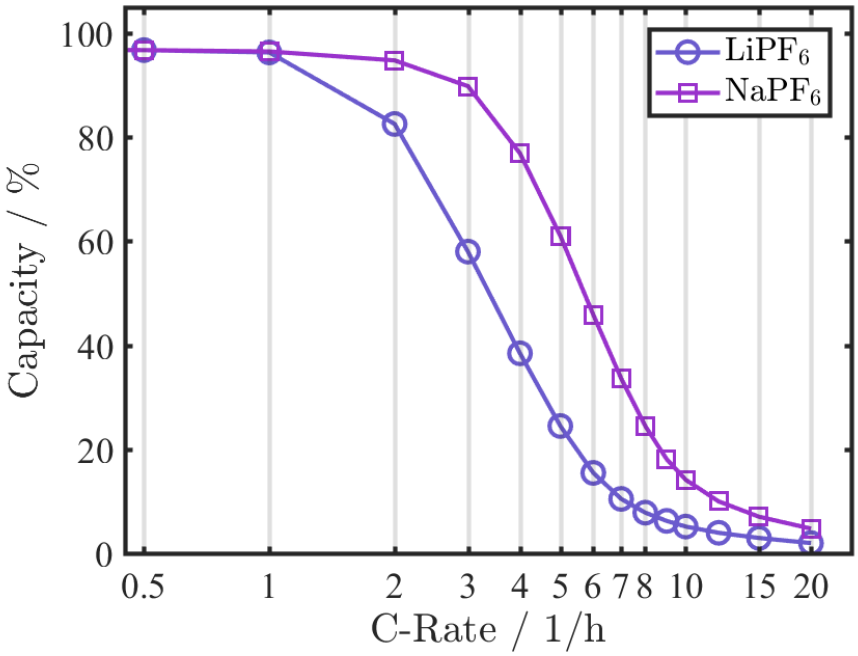

Figure 7. Simulated discharge capacities at C-Rates from 0.5 1/h to 20 1/h of theoretical NMC/graphite full cell with $LiPF_6$ and $NaPF_6$ in EC:DEC (1:1 v:v) using the parameters given in Table 1. Additional simulation parameters are given in Table 1 in the Supporting Information. The initial SOC of 3% was chosen to avoid numerical instabilities at the beginning of the discharge simulations and is the reason for the offset at low C-Rates (maximum discharge capacity is 97 %).

Conclusions

In this work the ionic conductivity, the thermodynamic factor, the transference number and the binary diffusion coefficient are determined for $LiPF_6$ and $NaPF_6$ in EC:DEC (1:1 v:v) by application of previously introduced measurement techniques.[17–19] The found increase of the ionic conductivity, transference number and diffusion coefficient of the sodium electrolyte compared to the lithium case can be explained with the weaker electrostatic interaction of the larger sodium cation. A qualitative agreement is found for the concentration dependent parameters when compared with literature values for aqueous electrolytes containing LiCl, NaCl and KCl. In a subsequent 1D cell simulation of a hypothetical NMC/graphite cell with an aerial loading of 3 mAh/cm², we use the two sets of electrolyte parameters to investigate their influence on the cell operation during constant current discharge operation. We show that concentration gradients and along-going overpotentials are decreased for the larger cation size. In addition the critical current, at which the depletion of the ion concentration within the cathode leads to large kinetic overpotentials, is shifted to higher discharge C-Rates when the sodium electrolyte parameters are used in the simulation compared to the lithium scenario. Although our work neglects different kinetics at the surface of respective Li and Na active materials as well as their different OCV curves, the presented results encourage research in alternative cell chemistries, possibly mitigating the rate or aerial loading limitations observed for current lithium ion batteries.

Acknowledgment

J. L. gratefully acknowledges the funding by the Bavarian Ministry of Economic Affairs and Media, Energy, and Technology for its financial support under the auspices of the EEBatt project. J. L. thanks Simon Erhard for his initial help with the simulation software COMSOL Multiphysics®.

References

1. N. Yabuuchi, K. Kubota, M. Dahbi, and S. Komaba, *Chem. Rev.*, **114**, 11636–11682 (2014).

2. V. Palomares, P. Serras, I. Villaluenga, K. B. Hueso, J. Carretero-González, and T. Rojo, *Energy Environ. Sci.*, **5**, 5884 (2012).

3. S. Komaba, T. Hasegawa, M. Dahbi, and K. Kubota, *Electrochem. commun.*, **60**, 172–175 (2015).

4. R. Dugas, A. Ponrouch, G. Gachot, R. David, M. R. Palacin, and J. M. Tarascon, *J. Electrochem. Soc.*, **163**, A2333–A2339 (2016).

5. N. Recham, G. Rousse, M. T. Sougrati, J.-N. Chotard, C. Frayret, S. Mariyappan, B. C. Melot, J.-C. Jumas, and J.-M. Tarascon, *Chem. Mater.*, **24**, 4363–4370 (2012).

6. C. Vaalma, G. A. Giffin, D. Buchholz, and S. Passerini, *J. Electrochem. Soc.*, **163**, A1295–A1299 (2016).

7. Y. Marcus, *Pure Appl. Chem.*, **57**, 1129–1132 (1985).

8. L. W. Shacklette, *J. Electrochem. Soc.*, **135**, 2669 (1988).

9. S. Komaba, W. Murata, T. Ishikawa, N. Yabuuchi, T. Ozeki, T. Nakayama, A. Ogata, K. Gotoh, and K. Fujiwara, *Adv. Funct. Mater.*, **21**, 3859–3867 (2011).

10. Y. Matsuda, H. Nakashima, M. Morita, and Y. Takasu, *J. Electrochem. Soc.*, **128**, 2552–2556 (1981).

11. K. Kuratani, N. Uemura, H. Senoh, H. T. Takeshita, and T. Kiyobayashi, *J. Power Sources*, **223**, 175–182 (2013).

12. A. Ponrouch, E. Marchante, M. Courty, J.-M. Tarascon, and M. R. Palacín, *Energy Environ. Sci.*, **5**, 8572 (2012).

13. M. Okoshi, Y. Yamada, S. Komaba, and A. Yamada, *J. Electrochem. Soc.*, **164**, 54–60 (2017).

14. A. V. Cresce, S. M. Russell, O. Borodin, J. A. Allen, M. A. Schroeder, M. Dai, J. Peng, M. P. Gobet, S. G. Greenbaum, R. E. Rogers, and K. Xu, *Phys. Chem. Chem. Phys.*, **19**, 574–586 (2017).

15. A. Ponrouch, D. Monti, A. Boschin, B. Steen, P. Johansson, and M. R. Palacín, *J. Mater. Chem. A*, **3**, 22–42 (2015).

16. E. Jónsson and P. Johansson, *Phys. Chem. Chem. Phys.*, **14**, 10774 (2012).

17. A. Ehrl, J. Landesfeind, W. A. Wall, and H. A. Gasteiger, *J. Electrochem. Soc.*, **164**, A826–A836 (2017).

18. A. Ehrl, J. Landesfeind, W. A. Wall, and H. A. Gasteiger, *J. Electrochem. Soc.*, **164**, 2716–2731 (2017).

19. J. Landesfeind and H. A. Gasteiger, in preparation (2018).

20. W. M. Haynes, *CRC Handbook of Chemistry and Physics*, 95th editi., CRC Press, (2014).

21. J. A. Gates and R. H. Wood, *J. Chem. Eng. Data*, **30**, 44–49 (1985).

22. J. Bockris and A. Reddy, *Modern Electrochemistry 1*, 2nd Editio., Kluwer Academic Publishers, (2002).

23. K. Xu, *Chem. Rev.*, **104**, 4303–4418 (2004).

24. J. Landesfeind, A. Ehrl, M. Graf, W. A. Wall, and H. A. Gasteiger, *J. Electrochem. Soc.*, **163**, A1254–A1264 (2016).

25. H. S. Harned and D. M. French, *Ann. N. Y. Acad. Sci.*, **46**, 267–284 (1945).

26. A. J. Bard and L. R. Faulkner, *Electrochemical Methods - Fundamentals and Applications*, 2nd ed., John Wiley & Sons, Inc., New York, (2001).

27. R. H. Stokes, *J. Am. Chem. Soc.*, **72**, 2243–2247 (1950).

28. A. Nyman, M. Behm, and G. Lindbergh, *Electrochim. Acta*, **53**, 6356–6365 (2008).

29. L. O. Valøen and J. N. Reimers, *J. Electrochem. Soc.*, **152**, A882 (2005).

30. J. Landesfeind and H. A. Gasteiger, in preparation (2018).

31. E. A. Kaimakov and N. L. Varshavskaya, *Russ. Chem. Rev.*, **35**, 89–105 (1966).

32. A. von Wald Cresce, M. Gobet, O. Borodin, J. Peng, S. M. Russell, E. Wikner, A. Fu, L. Hu, H.-S. Lee, Z. Zhang, X.-Q. Yang, S. Greenbaum, K. Amine, and K. Xu, *J. Phys. Chem. C*, **119**, 27255–27264 (2015).

33. K. G. Gallagher, S. E. Trask, C. Bauer, T. Woehrle, S. F. Lux, M. Tschech, P. Lamp, B. J. Polzin, S. Ha, B. Long, Q. Wu, W. Lu, D. W. Dees, and A. N. Jansen, *J. Electrochem. Soc.*, **163**, 138–149 (2016).

Supporting Information

To support the main article additional information is supplied for the benefit of the reader. This supporting information is presented subsequently.

Supporting Information: Comparison of Ionic Transport Properties of Non-aqueous Lithium and Sodium Hexafluorophosphate Electrolytes

Johannes Landesfeind,[a,z] Tomooki Hosaka,[b] Maximilian Graf,[a] Kei Kubota,[b]
Shinichi Komaba,[b] and Hubert A. Gasteiger[a]

[a] Chair of Technical Electrochemistry, Department of Chemistry and Catalysis Research Center, Technical University of Munich, Munich, Germany

[b] Department of Applied Chemistry, Tokyo University of Science, Tokyo, Japan

[z]corresponding author

Parameters for Comsol Simulation

Table 1. Overview of parameters used for simulation of the charging process of a theoretical NMC/graphite cell as implemented in a 1D battery model using the commercially available simulation software COMSOL Multiphysics® within the electrochemistry and battery module. Electrolyte parameters are separately listed in Table 1 in the main article for the $LiPF_6$ and $NaPF_6$ electrolytes.

Domain	Parameter	Value
general	temperature	25°C
	electrolyte concentration	1.0 mol/L
	cut-off potential	2.7 V
	Li inventory after formation	2.811 mAh/cm²
	1C current	2.811 mA/cm²
	electrolytes	see main article
graphite anode	thickness	60 µm
	volume fraction electrolyte	0.30
	volume fraction active material	0.60
	capacity	3.026 mAh/cm²
	tortuosity	4.8 (Ref. [1])
	particle radius	11 µm
	open circuit potential	from Ref. [2]
	solid state diffusion coefficient	$5 \cdot 10^{-13}$ m/s (Ref. [3])
	kinetic rate constant	$2.22 \cdot 10^{-11}$ m/s (Ref. 32, 33)
	kinetic symmetry exponent	0.5
	solid phase maximum concentration	31360 mol/m³
	initial solid phase concentration	28258 mol/m³ (=97% of inventory)
	electronic conductivity	1000 mS/cm (Ref. [3])
separator	thickness	20 µm
	volume fraction electrolyte	50%
	tortuosity	3 (Ref. [1])
NMC cathode	thickness	60 µm
	volume fraction electrolyte	0.30
	volume fraction active material	0.60
	capacity	3.123 mAh/cm²
	tortuosity	3.5 (Ref. [1])
	particle radius	5 µm
	open circuit potential	from Ref. [6]
	solid state diffusion coefficient	$1 \cdot 10^{-14}$ m/s (Ref. [3])
	kinetic rate constant	$6 \cdot 10^{-12}$ m/s (similar to Ref. [6])
	kinetic symmetry exponent	0.5
	solid phase maximum concentration	52501 mol/m³
	solid phase concentration at 4.3 V	20131 mol/m³
	initial solid phase concentration	874 mol/m³ (=3% of inventory) + 20131 mol/m³ (= at 4.3 V)
	electronic conductivity	100 mS/cm (Ref. [3])

Exemplary Data

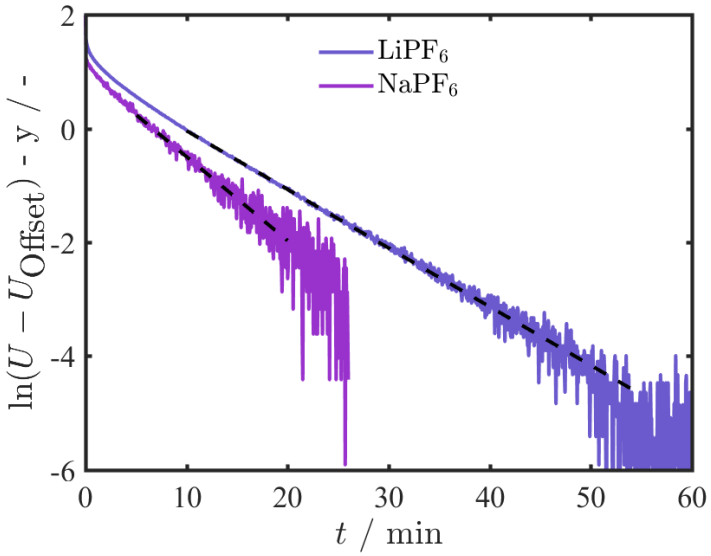

Figure 1. Potential relaxation after pulse polarization with current densities of 250 µA/cm² for 1.5 M $LiPF_6$ (blue) and 65 µA/cm² for 1.5 M $NaPF_6$ (purple) in EC:DEC (1:1 v:v) obtained in the symmetric coin cell setup described in the Experimental of the main article. Potentials are offset corrected (mean of last 5 min, always below 2 mV) and shifted for easy comparison so that linear trendlines start at 1. Dashed black lines indicate the time range used for linear regression and extraction of the diffusion coefficients with Eq. 14 in Ref. 7.

For the analysis of diffusion coefficients, the finite potential offset U_{Offset} observed for long relaxation times (not exactly 0 mV but constant and < 2 mV in absolute magnitude), is subtracted.[7] Then, very linear trends, indicated by the black dashed linear fit lines Figure 1, for the potential relaxation are found, exemplarily shown for the 1.5 M electrolytes. For better comparison the potential transients are shifted so that their linear slopes start at 1, which makes comparison easier, especially because the real magnitude of the logarithmic potential differs largely as a result of the different current densities applied in these cells (250 µA/cm² in the symmetric lithium cells, 65 µA/cm² in the symmetric sodium cells). The time ranges for the linear fit were selected manually as judged by eye. Fits were also done for the time range shifted by ± 50 % of the fit range starting time and the mean and its standard deviation are used for further analysis and are shown as data points Figure 2 in the main article. Although the slopes in Figure 1 appear similar, the numerical values yield diffusion coefficients of $2.1 \cdot 10^{-6}$ cm^2/s and $3.0 \cdot 10^{-6}$ cm^2/s for $LiPF_6$ (blue line) and $NaPF_6$ (purple line) respectively, as shown in Figure 2a in the main article. The noise visible at low potentials/for long times is due to the accuracy of the potentiostat (± 100 µV in this study). Therefore $NaPF_6$ data are only shown until 27 min in order for the noise not to overlap with the potential relaxation of the $LiPF_6$ cell.

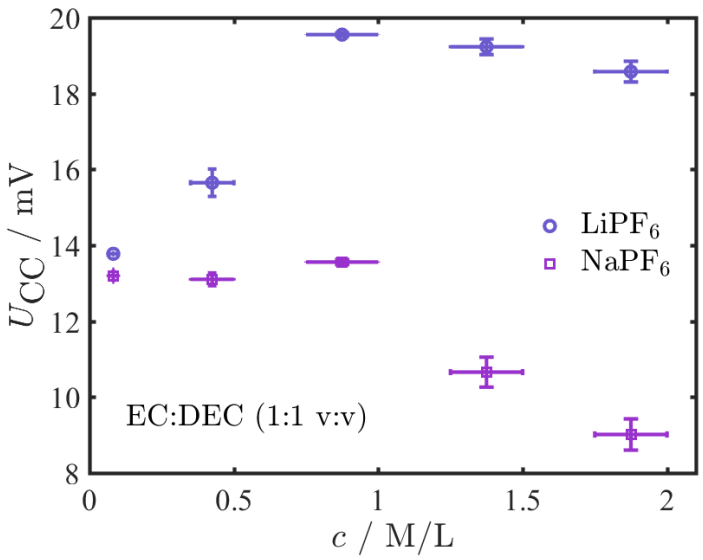

Figure 2. Overview of all measured mean concentration overpotentials of $LiPF_6$ and $NaPF_6$ electrolytes in EC:DEC (1:1 v:v) at 25°C. Data points represent the mean of the average potential during the 3 min measurement period of the repeat cells and their 95% standard deviation (vertical errorbars), horizontal errorbars indicate the lower and the higher concentration used for the measurement. The measurement setup is described in Ref. 8.

Concentration overpotentials for the $LiPF_6$ and $NaPF_6$ electrolytes are measured for three minutes inside an argon filled glovebox using the open glass plate setup shown in Figure 1 of Ref. [8] and the mean potentials over the measurement period as well as their standard deviation (vertical errorbars) are shown in Figure 2. Horizontal errorbars in Figure 2 indicate the lower and the higher concentrations used in the experiments, here, concentration pairs of 0.065 M – 0.1 M, 0.35 M – 0.5 M, 0.75 M – 1 M, 1.25 M- 1.5 M and 1.75 M – 2 M. For each concentration pair at least two cells were built for each electrolyte.

Figure 2 shows similar concentration overpotentials of 13 - 14 mV for both systems at the smallest concentration pair. For higher concentrations smaller concentration overpotentials are found for the sodium compared to the lithium electrolyte. While concentration overpotentials of ~ 14 mV are found for 0.75 M vs. 1 M $NaPF_6$ in EC:DEC (1:1 v:v, purple squares), ~ 20 mV are obtained for 0.75 M vs. 1 M $LiPF_6$ (blue circles). This trend is further pronounced at 1.75 M vs. 2 M salt concentrations and already suggests a different behavior of transference number and thermodynamic factor for both types of ions. Simplification of the concentration potential, as described in detail in Ref. [9] allows to calculate the transport factor a from the concentration potentials shown in Figure 2, which are depicted for the two electrolyte systems in Figure 4.

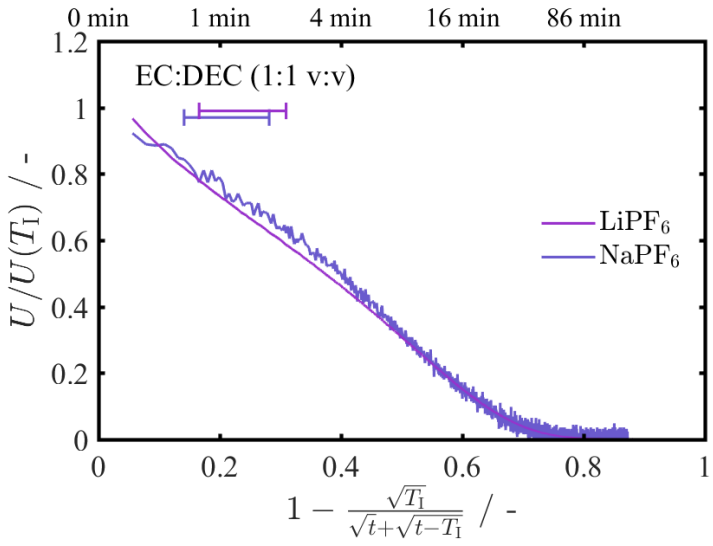

Figure 3. Potential relaxation after pulse polarization with current densities of 250 µA/cm² for 2 M $LiPF_6$ (blue) and 65 µA/cm² for 1.5 M $NaPF_6$ (purple) in EC:DEC (1:1 v:v) obtained in the symmetric coin cell setup described in the Experimental of the main article, plotted vs. the artificial time $1-\frac{\sqrt{T_I}}{\sqrt{t}+\sqrt{t-T_I}}$. Potentials are offset corrected (mean of last 5 min, always below 1 mV) and normalized for easy comparison so that linear trendlines start at 1. Range bars in the corresponding color indicate the time ranges used for the linear regression and the determination of the potential at current interrupt ($U(T_I)$). Different noise levels result from the normalization of the potential transients and the different current pulses applied in the cells. The necessary s-shaped curves are visible for both electrolytes and support our experimental procedure. With the potential at current interrupt, geometrical factors of the cell design and the separator and the previously determined slope of the exponential potential relaxation for long times (compare Figure 1) the transport factor *b* depicted in Figure 5 is obtained. For a detailed description of the analysis method the interested reader is referred to Ref. 9).

Transport Factors

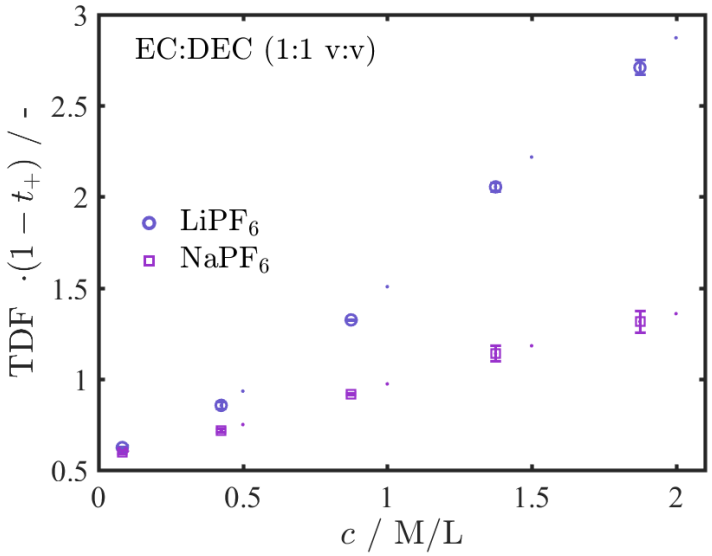

Figure 4. Transport factors *a* of $LiPF_6$ and $NaPF_6$ in EC:DEC (1:1 v:v) at 25°C, based on concentration cell potentials (see Figure 1 for raw data and concentration pairs) and the simplification of the concentration potential equation (compare Eq. 3-5 in Ref. 9), plotted at the mean concentration, e.g., the transport factor a, calculated for the concentration pair 0.75 M - 1 M is plotted at 0.875 M. In addition to the experimentally obtained values for *a* also linear interpolations to the base salt concentrations (0.1 M, 0.5 M, 1 M, 1.5 M and 2 M) used in this work are shown. Values and errors result from the mean concentration potential and its error as shown in Figure 1. For a detailed description of the analysis method the interested reader is referred to Ref.9).

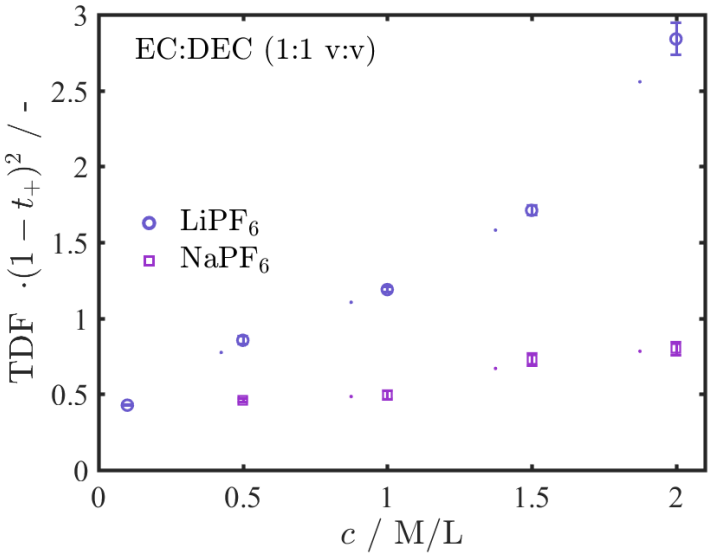

Figure 5. Transport factors *b* of $LiPF_6$ and $NaPF_6$ in EC:DEC (1:1 v:v) at 25°C, based on pulse experiments in symmetrical lithium / sodium cells (compare Figure 1 and Figure 3, compare Eq. 8 in Ref. 9). In addition to the experimentally obtained values for *b* also linear interpolations to the mean concentration cell concentrations (0.0825 M, 0.425 M, 0.875 M, 1.375 M and 1.875 M) are shown. Values and errors are the result of mean value and standard deviation of the transport factor *b* based on the repeat measurements done. For a detailed description of the analysis method the interested reader is referred to Ref. 9).

References

1. J. Landesfeind, J. Hattendorff, A. Ehrl, W. A. Wall, and H. A. Gasteiger, *J. Electrochem. Soc.*, **163**, A1373–A1387 (2016).

2. M. Safari and C. Delacourt, *J. Electrochem. Soc.*, **158**, 562–571 (2011).

3. M. Park, X. Zhang, M. Chung, G. B. Less, and A. M. Sastry, *J. Power Sources*, **195**, 7904–7929 (2010).

4. R. Chandrasekaran, *J. Power Sources*, **262**, 501–513 (2014).

5. Y. Idemoto and T. Matsui, *Solid State Ionics*, **179**, 625–635 (2008).

6. S. G. Stewart, V. Srinivasan, and J. Newman, *J. Electrochem. Soc.*, **155**, A664–A671 (2008).

7. A. Ehrl, J. Landesfeind, W. A. Wall, and H. A. Gasteiger, *J. Electrochem. Soc.*, **164**, A826–A836 (2017).

8. A. Ehrl, J. Landesfeind, W. A. Wall, and H. A. Gasteiger, *J. Electrochem. Soc.*, **164**, 2716–2731 (2017).

9. J. Landesfeind and H. A. Gasteiger, in preparation (2018).

Chapter 4

Tortuosity of Battery Materials

In lithium-ion battery electrodes and separators the direct straight-line transport path of lithium ions between two points is hindered by the microporous structure of cell components. The electrolyte volume fraction, i.e., the electrode porosity ε, and the tortuosity τ reduce the ionic conductivity and the binary diffusion coefficient in the Newman Model (see Eq. 1.3 and 1.4 in Section 1.1) to their effective values. This reduction to the effective transport properties in the liquid electrolyte limit the efficiency of ionic charge transport during battery operation and lead to the build-up of extensive concentration gradients, especially during low temperature operation even at low C-rates, during fast charge/discharge operation even at ambient temperatures, and for thick electrode layers, which are the consequence of trying to maximize energy density. While the electrode and separator porosities may be readily determined using weight and thickness measurements, the tortuosity of porous media (predominately electricalally conducting electrodes) is not easily accessible. For that reason the use of the so-called Bruggeman relation[108,109] is still widely applied in simulations of transport processes in porous media

$$\tau = \varepsilon^{-1/2}. \tag{4.1}$$

This chapter focuses on the electrochemical determination of the tortuosity of commercially available separators and laboratory prepared electrodes (article [41] in Section 4.1), using impedance spectroscopy. The underlying principles and the validity of the used transmission line model analysis is verified both theoretically and experimentally in Section 4.2 and the effect of the binder is shown exemplarily.[69]) In a separate study, the effect of the binder on the electrode tortuosity is studied in detail and a correlation to the charging power capability is drawn (article [69] in Section 4.3).

4.1 Tortuosity Determination using Electrochemical Impedance Spectroscopy

In this section the article *Tortuosity Determination of Battery Electrodes and Separators by Impedance Spectroscopy*[41] is presented, which was submitted in March 2016 and published in the peer-reviewed Journal of the Electrochemical Society in April 2016. Parts of the article were presented as Paper 202 at the 228$^{\text{th}}$ meeting of The Electrochemical Society in Phoenix (USA) in October 2015 and at the 8$^{\text{th}}$ International Workshop on Impedance Spectroscopy in Chemnitz (Germany) in September 2015. http://dx.doi.org/10.1149/2.1141607jes.

In this study we start with the definition of the tortuosity of a porous medium based on its effective transport properties. We use the MacMullin number[110] N_{M} for the definition of the tortuosity

$$N_{\text{M}} = \frac{\tau}{\varepsilon} = \frac{\kappa}{\kappa_{\text{eff}}} \tag{4.2}$$

and relate it to the different nomenclatures used in the literature. It is emphasized that in the context of this work the term tortuosity strictly refers to the definition in Eq. 4.2 and is not based on a geometric definition such as, e.g., the longest transport path or the average transport path length.[41] We always determine the tortuosity of the porous media from the ionic resistance ratio with and without the porous medium

$$\tau = \varepsilon \cdot \frac{R_{\text{porous}}}{R_{\text{free elyt.}}} \tag{4.3}$$

with the free-electrolyte resistance being defined by Ohm's law

$$R_{\text{free elyt.}} = \frac{t}{A \cdot \kappa_{\text{Ion}}}. \tag{4.4}$$

In the first part of the article we focus on the characterization of porous separator tortuosities for which a simple two-electrode copper block cell setup was developed. Analysis of the high frequency resistance of the copper block setup, with the separator of interest positioned between the circular copper electrodes, only allows to obtain reproducible tortuosities by means of Eq. 4.3 when the cell geometry is well defined. Otherwise, e.g., when the upper electrode is not ionically insulated, pronounced errors are obtained and demonstrate how small experimental details may have a detrimental impact on the obtained results.

In contrast to the simple determination of tortuosities of electricalally insulating separators, characterization of porous electrodes is more demanding. We assemble symmetric cells of nominally identical electrodes (same porosity, thickness, area and loading) and record impedance spectra. Analysis of such impedance spectra to find ionic resistances was known in the literature,[100,111] but no conclusion on the electrode tortuosity was drawn. In addition to the tortuosity calculation, our approach uses a non-intercalating electrolyte, i.e., not containing any lithium ions. This allows only capacitive currents to flow, due to the double layer capacity of the electrode's surface area, and thereby enables us to unambiguously ascribe observed semi-circles in the Nyquist plot, usually assigned

to charge transfer reactions, to contact resistances between the porous electrode and the current collector.

The determined tortuosities for porous separators as well as for electrodes with a range of typical anode and cathode active materials for lithium-ion batteries are mostly substantially longer than the tortuosity values obtained using the Bruggeman relation (4.1). The article highlights the effect of particle morphology (platelet graphite particles vs. spherical NMC particles), electrode composition (LFP cathodes with high and low carbon content) and compression (from $\approx$ 25 % to 70 %) and critically compares the found values with numerical results based on 3D reconstructions of battery electrodes using either FIB-SEM or X-ray tomography.

Author Contributions

A.E., J.L. and H.G. developed the measurement method using a non-intercalating electrolyte. J.L. and J.H. performed all electrochemical measurements. A.E. added the comparison of different tortuosity definitions and the literature overview. Data analysis was done by A.E. and J.L. and the manuscript was written by A.E. and J.L. and edited by J.H. and H.G. All authors discussed the data and commented on the results.

Correction

The following correction was published as erratum[112] to the main article.[41]

The caption for Fig. 10 on page A1380 should read:

Figure 10. Tortuosities of porous separators (Celgard is abbreviated with CG) and their standard deviations determined via high frequency resistance measurements (data from Table II). Fits with Eq. 6 using $\alpha = 1.5$ (dotted line, i.e., $\tau = \varepsilon^{-1.5}$) and $\alpha = 2.1$ (dashed-dotted line, i.e., $\tau = \varepsilon^{-2.1}$) vs. the conventionally used Bruggeman coefficient for spherical particles of $\alpha = 0.5$ (blue dashed line).

Tortuosity Determination of Battery Electrodes and Separators by Impedance Spectroscopy

Johannes Landesfeind,[a,*,z] Johannes Hattendorff,[a,*] Andreas Ehrl,[b] Wolfgang A. Wall,[b] and Hubert A. Gasteiger[a,]**

[a]*Chair of Technical Electrochemistry, Department of Chemistry and Catalysis Research Center, Technische Universität München, Munich, Germany*
[b]*Institute for Computational Mechanics, Department of Mechanical Engineering, Technische Universität München, Munich, Germany*

Lithium ion battery performance at high charge/discharge rates is largely determined by the ionic resistivity of an electrode and separator which are filled with electrolyte. Key to understand and to model ohmic losses in porous battery components is porosity as well as tortuosity. In the first part, we use impedance spectroscopy measurements in a new experimental setup to obtain the tortuosities and MacMullin numbers of some commonly used separators, demonstrating experimental errors of <8%. In the second part, we present impedance measurements of electrodes in symmetric cells using a blocking electrode configuration, which is obtained by using a non-intercalating electrolyte. The effective ionic resistivity of the electrode can be fit with a transmission-line model, allowing us to quantify the porosity dependent MacMullin numbers and tortuosities of electrodes with different active materials and different conductive carbon content. Best agreement between the transmission-line model and the impedance data is found when constant-phase elements rather than simple capacitors are used.
 [DOI: 10.1149/2.1141607jes]

Manuscript submitted March 3, 2016; revised manuscript received April 8, 2016. Published April 28, 2016.

Motivation.—Advanced battery models are a valuable tool for evaluating the performance, safety, and life-time of lithium ion batteries, since they can provide insight into the kinetics and the transport characteristics of batteries, which are not or only partially accessible by experiments. To obtain quantitative and meaningful numerical results, the choice of appropriate physical models and boundary conditions with the corresponding, accurately determined, kinetic and transport parameters are key issues. For numerical simulations of battery systems, the ion-transport model for concentrated electrolyte solutions introduced by Newman et al.[1] is frequently used. Since the microscopic geometry of actually used porous electrodes and separators are largely unknown, a homogenization approach is applied for the macroscopic description of porous media. In this case, the influence of the microstructure on the macroscopic behavior is modeled by additional geometric parameters such as the porosity ε and the tortuosity τ. The porosity ε is a well-defined property of a porous medium, which can be determined easily. In contrast, the effective tortuosity of separators and particularly of electrodes are more difficult to quantify, and, to further complicate the matter, many different definitions for the tortuosity τ are used in the literature. Thus, the different tortuosity definitions will be presented prior to reviewing the literature concerned with determining the tortuosity or the effective ionic conductivity of porous battery separators and electrodes.

Definitions of Tortuosity and MacMullin Number.—In the following, the most common definitions describing the influence of the microstructure on the macroscopic behavior are introduced. As explained in, e.g., Patel et al.,[2] the effect of a porous microstructure on the macroscopic conservation laws can be described by the MacMullin number N_M

$$N_M = \frac{\kappa}{\kappa_{eff}} \quad [1]$$

which relates the ionic conductivity κ of the electrolyte solution to the effective ionic conductivity κ_{eff} of a porous separator or electrode. The MacMullin number is the basis for many empirical laws established to describe the influence of the porous microstructure of separators and electrodes on the macroscopic conservation laws in terms of the porosity ε and additional parameters. One of the most famous empirical laws was introduced by Archie[3]

$$N_M = \varepsilon^{-m} \quad [2]$$

where a power-law relationship between the porosity ε of sandstone and the MacMullin number N_M with the exponent m (Archie's exponent) is used. Other empirical laws are given, e.g., in the review by Shen and Chen[4] or in Barrande et al.[5] As mentioned before, these empirical laws hold *"only for a series of samples from the same geological formation, because these rocks have similar microstructures*".[6] For a different type of microstructure, the exponential factor m may be quite different. The MacMullin number as well as the related empirical laws are based on a macroscopic view of the porous medium.

In contrast, it is also possible to use a microscopic approach to model a porous microstructure. In this case, the tortuosity is introduced as a measure of the elongation of the transport path due to the porous structure with respect to a straight line d. For example, the path-length tortuosity

$$\tau_{path} = \frac{d_{path}}{d} \quad [3]$$

is defined for a single channel with a constant cross-sectional area. The tortuosity can also be defined with respect to a physically motivated length definition. For instance, the path length of the electronic tortuosity τ_{el} is based on the gradient of the potential. Last but not least, the geometrical tortuosity τ_{geo} is defined as the shortest connection between two points x_1 and y_1 with respect to the length of the straight connection between these points. The path-length tortuosity τ_{path}, the geometrical tortuosity τ_{geo}, and the physically motivated tortuosity τ_{el} are not identical and may result in different numerical values. Until a few years ago, all microscopically motivated values for the tortuosity were usually based on simplified geometries such as channel networks or regular porous structures such as agglomerated spheres (see, e.g., Wyllie and Rose,[7] Cornell and Katz[8] or Zalc et al.[9]). More recently, realistic three-dimensional representations of complex porous structures can be provided by imaging technologies, enabling a numerical quantification of the mean geometrical tortuosity $\bar{\tau}_{geo}$,[10] which is based on an averaged value of the shortest path lengths d_{ij}

*Electrochemical Society Student Member.
**Electrochemical Society Fellow.
[z]E-mail: j.landesfeind@tum.de

between points x_i and y_j and is usually determined by numerical algorithms utilizing the random walk theory[11] or the graph theory.[10] Note that these numerical algorithms only consider the elongation of the transport path but do not include additional factors such as non-constant cross-sectional areas or the microscopic surface structure of the solids constituting the porous medium. Therefore, the constriction factor β is sometimes introduced to account for a non-constant cross-sectional area. The concept of the constriction factor and its theoretical motivation is, e.g., explained by Wiedenmann et al.,[10] using the following relation

$$N_M \equiv \frac{\overline{\tau_{geo}}}{\varepsilon\beta} \quad [4]$$

The big advantage of the microscopic approach is that it is based on a purely geometrical description of the microstructure, so that a basic understanding for a porous structure is generated which can be used for the design of future porous materials. However, the size of the reconstructed sample has to be considered as potential source of uncertainty, since it has to be large enough to be representative as, e.g., can be observed in Cooper et al.[12]

In the above discussion, macroscopic and microscopic approaches for the determination of tortuosity parameters were reviewed. In addition, it is also possible to simply apply the microscopic concept of tortuosity to the macroscopic description of a porous medium using an empirical approach

$$N_M = \frac{\tau}{\varepsilon} \quad [5]$$

in which the effective tortuosity τ is determined experimentally for each given porous medium. In this case, the effective tortuosity τ does not only describe the elongation of the transport path, but also includes other effects such as variable cross-sectional areas, surface morphologies, etc. As emphasized by Holzer et al.,[6] it is important to strictly distinguish between the effective tortuosity τ and the geometrical tortuosity τ_{geo}, since they are based on different definitions. The main advantage of the former is that all geometrical effects are automatically included in the effective tortuosity τ. However, its main disadvantage is that it is only accessible experimentally and therefore might include experimental artifacts and also does not allow to project values for other geometries (e.g., particle shapes, porosities, etc.). At this point, it is important to mention that the tortuosity τ in Eq. 5 appears often as τ^2, which is the result of different assumptions as, e.g., discussed in Clennell[13] or Djian et al.[14] The same macroscopic concept can be applied to reconstructed, three-dimensional microstructures. In this case, the McMullin number in Eq. 5 is not determined by experiments but by numerical simulation of the Laplace equation as discussed, e.g., in Ender et al.,[35] Joos et al.[15] and Cooper et al.[12] A similar concept is used in Ebner and Wood.[16] in which the effective tortuosity is computed numerically from top and cross sectional views of electrodes based on either NMC ($Li(Ni_xMn_yCo_z)O_2$; $x + y + z = 1$), LCO ($LiCoO_2$), or graphite. As for determination of the geometrical tortuosity based on reconstructed microstructures, the sample size has to be considered as a potential uncertainty.

The last important definition which is frequently used in battery applications results from the combination of Eqs. 2 and 5

$$\tau = \varepsilon^{1-m} = \varepsilon^{-\alpha} \quad [6]$$

This well-known equation with the exponent α is frequently called the Bruggeman relation[17] although the origin of this convention is unclear (see note added in proof). Unfortunately, in some cases the tortuosity is also defined differently, e.g., as $\tau = \epsilon^{(1-\alpha)}$.[18] The Bruggeman exponent relates to Archie's exponent by $-\alpha = 1 - m$. For spherical particles the Bruggeman exponents becomes $\alpha = 0.5$ (as defined in Eq. 6), corresponding to an Archie's exponent $m = 1.5$. This simplest case of the Bruggeman equation for spherical particles is used for comparison in the Results and discussion section. This case corresponds to the so-called Bruggeman approximation frequently used for porous electrodes as suggested in Newman and Thomas-Alyea[1] and implemented in commercial software packages (e.g., Comsol Multiphysics), where it is expressed terms of $\varepsilon/\tau = \varepsilon^{1.5}$. The validity of this relation was investigated experimentally as well as numerically, and reasonably close agreement was reported in the case of spherically shaped solids forming the porous medium.[2,19,20] For more complex structures, different α-values are obtained, whereby frequently Eq. 6 is modified by an additional proportionality factor f[18,19]

$$\tau = f\ \varepsilon^{-\alpha}. \quad [7]$$

In this work, we will examine the validity of the Bruggeman equation for spherical particles ($\tau = \varepsilon^{-0.5}$, i.e. $\alpha = 0.5$) by comparing it with tortuosities determined for separators and porous electrodes. The functional description of the tortuosity is analyzed by fitting experimental data for a variety of separators and electrodes with the general equation for the tortuosity used in literature (Eq. 7).

Literature Overview.—*Ionic Conductivity in Separators.*—In the literature, different values for the MacMullin number N_M, the coefficient α, or the tortuosity τ of various separators can be found.[2,14,22] In many publications, impedance based techniques are used to measure the effective conductivity. Unfortunately, the value of the MacMullin numbers vary quite significantly for the same separator material which, e.g., can be illustrated for the reported MacMullin numbers for Celgard 2500 separator of 8.5 (Patel et al.[2]), 13 (Djian et al.[14]) and of 18 (Abraham[22]). Quite clearly, this large scatter suggests the presence of experimental artifacts in at least some of the measurements, which still needs to be resolved. Gas transport resistance measurements are also commonly used to characterize separators, whereby the so-called Gurley number (the time in seconds it takes for 100 cm^3 of air to pass through a defined area at a defined pressure difference) is often assumed to be proportional to the effective ionic resistivity.[23] While useful for a rough benchmarking of separators, Gurley numbers cannot be quantitatively related to the effective ionic resistance.

Ionic Conductivity in Electrodes.—For electrodes, the determination of the MacMullin number is more elaborate, since now the porous medium is electronically conductive, so that the high-frequency resistance cannot be used as a measure of the ionic conductivity. The effective ionic conductivity of electrodes can in principle be determined by AC impedance using a transmission-line model (TLM).[24] This, for example, was used to quantify the proton conductivity of PEM (proton exchange membrane) fuel cell electrodes by Liu et al.,[25] where the charge transfer resistance in the TLM circuit model could be eliminated experimentally by removing the reacting gases. The resulting TLM circuit model is often referred to as being under *blocking conditions*. For lithium ion batteries, Ogihara et al. measured electrodes in a symmetric cell setup with a lithium salt electrolyte,[26,27] showing that they would obtain blocking conditions by conducting the impedance analysis at a state of charge (SOC) of 0% or 100%, where lithium intercalation/deintercalation is suppressed. Using the simplified TLM circuit model for blocking conditions, they could obtain effective ionic resistances of the electrodes from a fit.

An alternative method was used by Thorat et al.[18] and Holzer et al.,[6] who determined the MacMullin number of porous electrodes by the ratio of the effective binary diffusion coefficient in the electrode and the binary diffusion coefficient in the pure electrolyte. Here, polarization interrupt experiments allow the determination of the effective binary diffusion coefficient for a freestanding electrode sheet (prepared by delamination of the electrode from the current collector) placed between two separators by comparison with numerical simulations.[18,28] However, the two drawbacks of this method are that freestanding electrodes have to be prepared and that the numerical model requires knowledge of the concentration-dependent values of the transference number, the thermodynamic factor, and the diffusion coefficient. A more recently developed method by DuBeshter et al.[29] is based on measuring the pressure-dependent term of the gas diffusion coefficient through a porous electrode, which, however, is only valid

for isotropic electrode morphologies, i.e., if the in-plane permeability is equal to the through-plane permeability. This clearly is not satisfied for flake- or plate-like particles characteristic for many graphites.

Finally, the effective ionic conductivity can in principle also be determined numerically if the exact morphology and microstructure can be determined.[30,31] 3D reconstructions of porous electrodes can be obtained using X-Ray tomography[32,33] or focused ion beam scanning electron microscopy (FIB-SEM).[34] The tortuosity τ of many types of active materials, with a defined 3D-structure obtained from advanced imaging technologies, is often determined by numerical simulations as shown, e.g., for $LiFePO_4$[12,35] or for $La_{0.58}Sr_{0.4}Co_{0.2}Fe_{0.8}O_{3-\delta}$ (LSCF) cathodes.[15] For a reconstructed graphite electrode, the geometrical tortuosity τ_{geo} determined by the random walk theory was found to be consistent with the tortuosity τ determined by a physically motivated simulation.[11] Numerical investigations of 3D reconstructed electrodes based on X-Ray tomography data have shown the effect of particle anisotropy on the through-plane tortuosity, reporting increasing tortuosities when the particle shape is changed from spherical and non-spherical to platelet like graphite particles.[32] The limited spatial resolution of current 3D-imaging methods is still somewhat of a drawback, since detailed imaging of conductive carbons (primary particle diameters of ≈0.04 μm and primary particle agglomerates of ≈0.4 μm) would be required to include the effect of conductive carbon additives on the effective ionic conductivity of electrodes. This drawback can be mitigated by a combination of X-Ray tomography data with carbon binder modelling.[33]

The present work aims at quantifying the tortuosity of porous separators and electrodes used in lithium ion batteries using electrochemical impedance spectroscopy measurements. A new test setup will be shown to quickly and reproducibly determine the effective ionic conductivity of separators. To quantify the effective ionic conductivity of electrodes, a more general transmission-line model compared to that used by Ogihara et al.[26,27] will be used with symmetric electrodes, whereby measurement requirements to avoid experimental artifacts will be examined. To investigate whether the effective tortuosity of electrodes can be described by the power-law relationship of the Bruggeman equation and how it will vary across different electrodes, we will examine a number of electrodes composed of different electrode active materials at different compositions and compressions. Comparison of particle sizes, morphologies, and the electrode compositions are investigated toward their impact on the MacMullin number.

Theory

Ion transport through porous structures.—Charge transport in porous particle networks or structures such as lithium ion battery electrodes or separators is determined by the ionic resistance R_{Ion} inside the electrolyte phase. If the ionic resistance R_{Ion} through a cross-sectional area A of a material with porosity ε and a thickness d can be determined, and if the conductivity of the electrolyte κ is known, the MacMullin number N_M and the tortuosity τ can be calculated by rearranging Ohm's law using Eqs. 1 and 5

$$N_M = \frac{\tau}{\varepsilon} = \frac{R_{Ion} \cdot A \cdot \kappa}{d} \quad [8]$$

Note that the determination of the MacMullin number does not require knowledge of the electrode porosity, while it is required to determine the tortuosity. Techniques to measure ionic resistances R_{Ion} will be discussed in the next paragraphs for both separators and electrodes. For impedance based approaches, so-called *blocking electrodes* or *blocking conditions* are frequently used, which means that there is no charge transfer across the solid/liquid interface, i.e., that the surface is ideally polarizable.[36] Such conditions can be realized experimentally, if no charge transfer reaction can take place in the potential window under investigation. Implementation of blocking conditions may be realized by using a salt which cannot react electrochemically with the electrodes within the potential excitation of a few mV during an impedance measurement. In reality, surface roughness[37] or an inhomogeneous current distribution[38] may alter the ideally polarizable behavior of electrodes, and a blocking electrode is therefore generally described best by a constant-phase Element (CPE), the complex impedance of which is given as

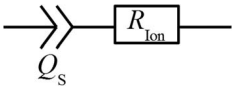

Figure 1. Equivalent circuit for non-electronically conducting porous separators in a blocking electrode configuration.

$$Z_{CPE} = \frac{1}{Q(i\omega)^{\gamma}} \quad [9]$$

where ω is the angular frequency, the parameter Q is related to the electrode capacitance, and γ is the constant phase exponent (for $\gamma = 1$, Z_{CPE} simplifies to the impedance of an ideal capacitor).

Ionic resistance of a separator.—Impedance measurements of electrolyte-filled electronically insulating separators, positioned between two electrodes in a blocking electrode condition can be described by an equivalent circuit consisting of a serial connection of two CPEs and an ionic resistance, whereby the CPEs can be lumped into one global CPE as depicted in Figure 1.

The impedance of the equivalent circuit in Figure 1 is given by

$$Z_{Sep.} = R_{Ion} + \frac{1}{Q_S(i\omega)^{\gamma}} \quad [10]$$

which allows for a simple determination of the ionic resistance R_{Ion} inside the porous separator by means of a high frequency extrapolation ($\omega \rightarrow \infty$) in the corresponding Nyquist plot.

Ionic resistance of a porous electrode.—The impedance of electrolyte filled pores in an electronically conductive particle network, such as in a lithium ion battery electrode, can be described by an equivalent circuit model referred to a transmission-line model (TLM).[36] Figure 2 depicts the equivalent circuit of the general TLM. Inside the solid phase, the electronic resistance is represented by a serial connection of ohmic resistors, r_{El}. Accordingly, the ionic resistances in the electrolyte phase are depicted by the ohmic resistors r_{Ion}. In addition, charge can be transferred between the solid and the liquid phase via faradaic or capacitive charge transfer reactions, which is described by the surface impedance elements z_S.

This equivalent circuit segment may then be connected ionically and/or electronically on either/or both ends. For example, for an electrode coated on a current collector and pressed against a separator, the electronic rail (upper brown rail in Figure 2) is connected only at one end and the ionic rail (lower blue rail in Figure 2) is connected only at the other end, as no ions can flow into the current collector (pure electron conductor) and now electrons can flow into the electrolyte (pure ion conductor). For practical purposes, the use of a separator is advantageous in order to prevent an electronic short-circuit between the two electrodes and to keep the electrodes in a plane-parallel configuration. For properly designed lithium ion battery

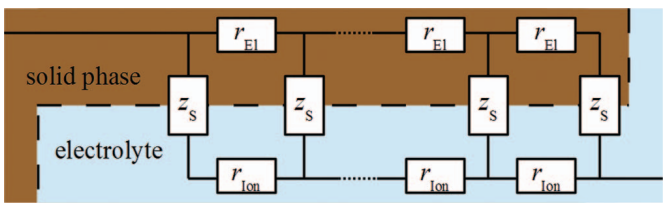

Figure 2. Equivalent circuit of the general transmission-line model for a porous electrode. The charge transfer process between the solid and the liquid phase through faradaic or capacitive charge transfer reactions is represented by z_S. Electrons are moving in the solid phase (brown region), while ions are moving in the electrolyte phase (blue region).

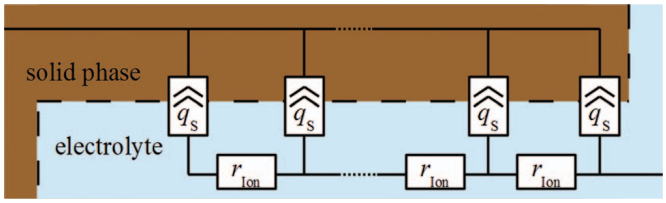

Figure 3. Simplified form of the transmission-line model for porous electrodes with $r_{El} << r_{Ion}$ and for blocking conditions.

electrodes, the electronic resistance in the solid phase r_{El} of the transmission-line model is negligibly small ($\kappa > 0.1$ S/cm due to the presence of conductive carbon additives[39,40]) compared to the resistance in the electrolyte phase r_{Ion} ($\kappa < 0.01$ S/cm). This means that the electronic resistances r_{El} are generally negligible compared to the ionic resistances r_{Ion}, so that the former can usually be omitted. Further simplifications can be made for blocking conditions, i.e., in the absence of faradaic charge transfer reactions, in which case the surface impedance elements z_S can be modeled by a capacitive behavior. The latter is modeled using constant-phase elements to account for geometric effects resulting from the materials surface roughness.[41] For lithium ion batteries, blocking conditions were shown to be approached at 0% and 100% SOC;[26,27] as we will show later, they can also be realized by using non-intercalating electrolyte salts, which are stable within the potential window of an impedance measurement (±10 mV). Thus, lithium ion electrodes in a blocking condition and with $r_{El} \ll r_{Ion}$, the general transmission-line model reduces to a form depicted in Figure 3.

An analytical electrode impedance $Z_{El.}$ can be derived for the simplified transmission-line model[36,42] in Figure 3, which we will refer to as TLM-Q:

$$Z_{El.} = \sqrt{R_{Ion} Z_S} \coth\left(\sqrt{\frac{R_{Ion}}{Z_S}}\right) = \sqrt{\frac{R_{Ion}}{Q_S (i\omega)^{\gamma}}} \coth\left(\sqrt{Q_S (i\omega)^{\gamma} R_{Ion}}\right) \quad [11]$$

where $R_{Ion} = \Sigma(r_{Ion})$ and $Q_S = \Sigma(q_S)$. If an ideal capacitive behavior would be assumed instead of the constant-phase elements, the constant-phase exponent γ becomes one and the $1/(Q_S(i\omega)^{\gamma})$ terms reduce to the impedance of a capacitor $1/(i\omega C)$. The transmission-line model with pure capacitive behavior of the surface impedance elements will be referred to as TLM-C. Exemplary Nyquist plots of the porous electrode transmission-line models with constant-phase exponents of $\gamma = 1$ (pure capacitor) and $\gamma = 0.9$ are shown in Figure 4 together with a 45° slope as a guide for the eye.

The Nyquist plot in Figure 4 shows that the TLM-C model (solid line) results in a vertical line toward low frequencies, while the TLM-Q model (dashed line) deviates toward lower angles from a vertical line at low frequencies. In addition, at high frequencies, the TLM-C model shows a 45° slope, while the TLM-Q model displays a slope with an angle smaller than 45°. One way to extract the electrode ionic resistance R_{Ion} of electrodes via impedance measurements is to fit Eq. 11 to experimental data. Exemplary fits are shown in the Results and discussion section. The ionic resistance can also be obtained via linear extrapolations of the low and high frequency regions to the x-axis in the Nyquist plots. While the latter extrapolation gives the high frequency resistance R_{HFR}, the extrapolation of the low frequency branch to the x-axis ($Z_{El.}|_{(\omega_{low} \to \infty)}$) gives the sum of the high frequency resistance and one third of the ionic resistance inside the pores, as already discussed by Ogihara et al.[26] or Liu et al.[25] for the transmission-line model with ideal capacitors:

$$Z_{El.}|_{(\omega_{low} \to \infty)} = \frac{R_{Ion}}{3} + R_{HFR} \quad [12]$$

Similarly, it can be shown, that if constant-phase elements instead of ideal capacitors are used in the transmission-line model, the same relation holds.

Experimental

Materials and electrodes.—Separators from Celgard (Celgard 3500, Celgard H2013, Celgard C480, Celgard 2320, Celgard 2500, Celgard 2325), Separion (S240P30), two commercial single-layer HDPE separators (#1 and #2) and Freudenberg (FS-3001-30) were punched to circular discs of at least 25 mm diameter and dried in a vacuum oven at 70°C overnight. Composite electrodes were prepared by doctor-blade coating of a slurry of active material (AM), binder (Kynar HSV 900, Arkema), conductive carbon (SuperC65, Timcal), and NMP (Sigma Aldrich, anhydrous, 99.5%) prepared in a planetary mixer (Thinky ARV-310), using a copper current collector foil (MTI, 19 μm) for anode active materials and an aluminum current collector foil (MTI, 15 μm) for cathode active materials. Coatings were dried in a self-built drying oven at 50°C under air and then punched to circular discs of 11 mm diameter. Compression to the desired electrode porosity was done in a hydraulic press (Mauthe, PE-011). Further drying was done in a vacuum drying oven at a minimum temperature of 95°C for at least 6 h. Commercially available active materials, electrode compositions, and the abbreviation by which the electrode will be referred to further on are listed in Table I.

Electrodes were characterized by measuring their weight (Mettler Toledo, XP6, 1 μg accuracy) and thickness (Mitutoyo, Lifematic, VL-50, 0.1 μm accuracy). These were used to calculate the electrode porosity, assuming the bulk active material densities listed in Table I as well as the bulk density of the conductive carbon of ∼2.2 g/cm^3. The absolute error in the thickness measurements is ca. ±2 μm (corresponding to ca. 4–10% for coating thicknesses ranging from 20–50 μm) and the absolute error in the weight measurements is estimated to be ±0.01 mg/cm^2. The resulting error in electrode porosity is represented by horizontal error bars in Figure 15, Figure 19 and Figure 20.

An argon filled and temperature controlled glove box (MBraun, 25°C ± 1°C, oxygen and water content <0.1 ppm, Ar 5.0, Westfalen, 99.999%vol.) was used for electrolyte preparation, the measurement of the effective ionic resistance of separators, and for cell assembly. All cell parts were cleaned thoroughly by boiling them in an ethanol water mixture, rinsing them with water (Millipore, Elix, 15 MΩ), and then drying them at 70°C in a drying oven before bringing them into the glove box. Mixtures of ethylene carbonate (EC, Sigma Aldrich, anhydrous, 99%), diethyl carbonate (DEC, Sigma Aldrich, anhydrous, >99%), and dimethyl carbonate (DMC, Sigma Aldrich, anhydrous, ≥99%) were used as solvents for self-prepared electrolytes containing tetrabutylammonium perchlorate ($TBAClO_4$, Sigma Aldrich, ≥99.0%) salt. Impedance measurements of separators were

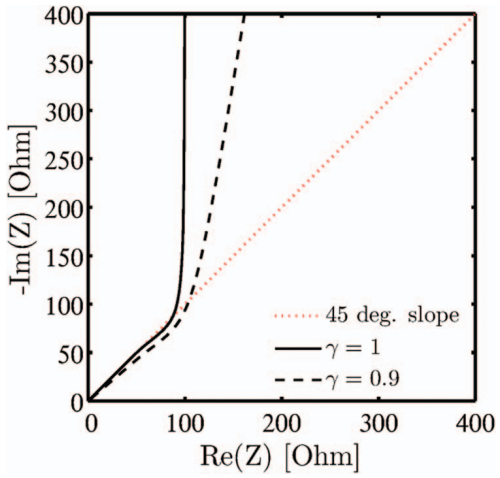

Figure 4. Simulated Nyquist plots of Eq. 11 with $R_{Ion} = 300\ \Omega$, $Q = 100\ \mu F \cdot s^{\gamma-1}$, and $\gamma = 1$ (solid) or $\gamma = 0.9$ (dashed); the dotted red line indicates a 45° slope.

Table I. Electrodes prepared for the determination of the MacMullin number and the tortuosity by the TLM-Q model. LFP, LNMO, and NMC were coated on aluminum current collectors, while LTO and graphite were coated on copper current collectors. Listed active material loadings are the mean loadings (±10%) of the electrodes shown in Figure 15.

Active Material (AM)	Loading	Density (AM)	%wt AM/binder/carbon	Referred to as
LFP (commercial)	8 mg_{AM}/cm^2	3.6 g/cm^3	90/5/5	LFP-lowC
LFP (commercial)	3 mg_{AM}/cm^2	3.6 g/cm^3	70/15/15	LFP-highC
LNMO (commercial)	7 mg_{AM}/cm^2	4.5 g/cm^3	96/2/2	LNMO
NMC 111 (commercial)	18 mg_{AM}/cm^2	4.7 g/cm^3	96/2/2	NMC
LTO (commercial)	9 mg_{AM}/cm^2	3.5 g/cm^3	90/5/5	LTO
graphite (SGL Carbon GmbH)	6 mg_{AM}/cm^2	2.3 g/cm^3	95/5/0	graphite-1
graphite (KS6L, Timcal)	4 mg_{AM}/cm^2	2.3 g/cm^3	91/9/0	graphite-2

conducted using commercially available LP572 electrolyte from BASF (EC:EMC (3:7 w:w) with 1 M $LiPF_6$ + 2% VC).

Measurement cells.—Three cell setups were used for the determination of the MacMullin number and the tortuosity of porous separators and electrodes. A turn-key conductivity sensor (LF 1100+, SI Analytics, with custom made ground glass fitting) with a built-in temperature sensor was used to measure the conductivity of the used electrolytes at 25°C.

First, the impedance of separators filled with electrolyte was measured inside a glove box in an open setup consisting of two cylindrical copper blocks, which were connected with actively shielded cables to a potentiostat outside the glove box. A schematic sketch of the copper block setup is shown in Figure 5.

An excess of electrolyte in the open copper block setup allows for good wetting and exact measurement of the ionic resistance as long as the measurement time does not exceed a few minutes, even if small amounts of solvent evaporate. In order to precisely confine the effective area, it is necessary to insulate the perimeter of the upper copper electrode. This was done with epoxy resin (EPO5.S200, Composite Technology), polished to a sharp edge with a polishing machine (Beta Grinder-Polisher, Buehler).

Second, symmetrical Swagelok type T-Cells (spring-compressed to ≈1 bar) were used to measure the impedance of porous electrodes (11 mm diameter) via the transmission-line model. Cells were assembled inside the glove box and then transferred into a temperature controlled climate chamber (25°C, Binder). In such a symmetrical setup, the measured impedance corresponds to the sum of the impedances of the individual electrodes. Therefore, care was taken to always combine two electrodes with closely matched loading and porosity. Two glass fiber separators (VWR, thickness 250 μm, borosilicate, binder-free, 1.2 μm pore size) with a diameter of 11 mm were used as separators.

Third, pouch bag cells were used, which consisted of a stack of a large electrode, a larger separator and a smaller counter electrode as schematically depicted in Figure 6. An uncoated/inactive part of the copper foil was led outside the pouch bag and used as a current collector tab. For measurements of the separator resistance, two copper foils were used as electrodes. Determination of the ionic resistance of porous electrodes in the pouch cell setup was done by placing a glass fiber separator between the electrodes under investigation. Precise determination of the active area in pouch cells was achieved by image analysis. Typical dimensions were 20 × 20 mm^2 for the larger electrode, 30 × 40 mm^2 for the separator and 15 × 15 mm^2 for the smaller electrode. The cells were filled with ≈50–200 μl electrolyte, depending on the size and the type of separator, and then vacuum sealed at 25 mbar. Four point electronic connections to the potentiostat (Biologic VMP3 potentiostat/galvanostat) were used to avoid contact resistances.

Electrochemical impedance spectra were measured around OCV. A frequency range of 200 kHz to 1 kHz with a 5 mV perturbation was used for determining ionic resistances of separators, and from 200 kHz to 0.5 Hz with a 10 mV perturbation for measurements of the transmission-line ionic resistance of electrodes.

Results and Discussion

Determination of separator tortuosities and macmullin numbers.—Ohmic resistances of porous lithium ion battery separators were determined with impedance measurements using the copper cell described in the Experimental section (Figure 5). In this setup, stray currents are avoided by electrical insulation around the upper copper electrode. The necessity of this insulation is demonstrated with Figure 7, where impedance spectra of 1, 2, or 3 separator layers were measured in the copper block setup with and without the insulation around the upper copper electrode. Measurements for each number of separator layers are repeated three times with fresh separators and a freshly cleaned cell. In total, this results in nine measurements with the insulated and nine measurements with the non-insulated upper copper electrode. Although shown for different separators and electrolytes, leading to different high frequency resistances, the very same trend would exist for a direct comparison of the same separator.

Figure 7a shows a large variation of the impedance spectra if the non-insulated upper copper electrode is used; note that repeated impedance spectra for any given assembled cell are reproducible, suggesting that the variability is not due to noise in the impedance measurements. This experimental scatter can be eliminated by electronically insulating the perimeter of the upper copper electrode as

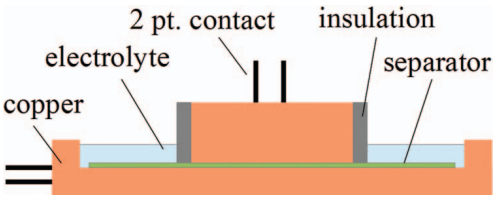

Figure 5. Sketch of copper block setup for the determination of the ionic resistance of electrolyte-filled separators. The upper copper electrode has a height of 10 mm and a diameter of 20 mm; the lower copper electrode has a height of 15 mm, a diameter of 50 mm, and the electrolyte reservoir has a depth of 5 mm (typically filled to a height of ≈2 mm) and an inner diameter of 45 mm; the diameter of the sandwiched separator is ≥25 mm.

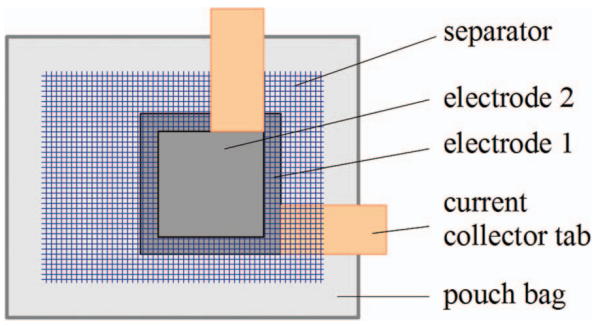

Figure 6. Schematic of pouch bag cell setup for symmetrical impedance measurements of transmission-line model of porous electrodes.

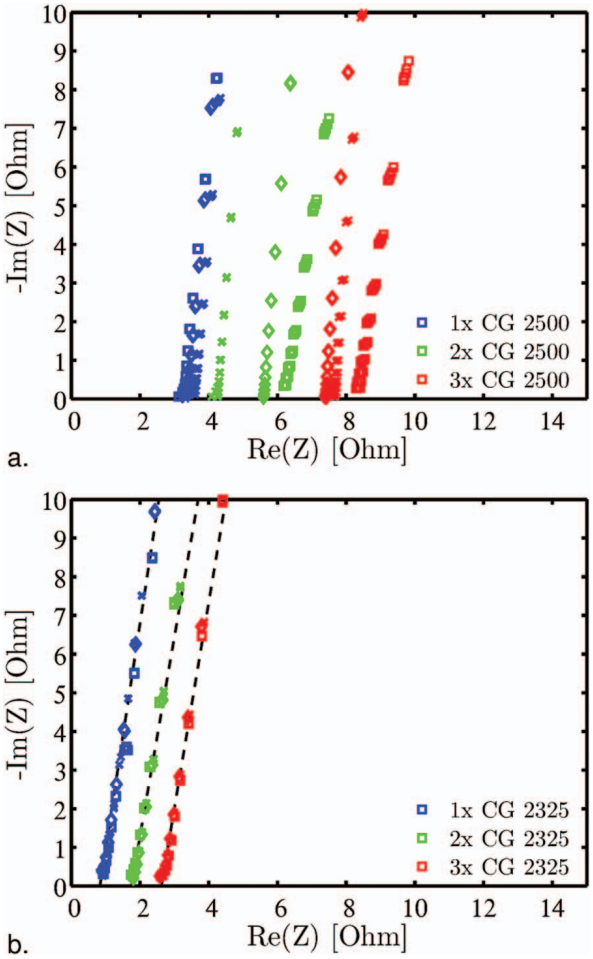

Figure 7. High frequency resistance of multiple layers of Celgard 2325 (with 1 M $LiPF_6$ in EC:EMC (3:7 w:w) + 2% VC) or Celgard 2500 (with 0.05 $MLiClO_4$ EC:DEC (1:1 w:w) separators, in copper block setup with a. non-insulated upper electrode and b. an insulated upper electrode to avoid stray fields and currents. Three independent repeat experiments (crosses, squares, diamonds) are shown for each experimental configuration (one, two and three separators, highlighted by colors).

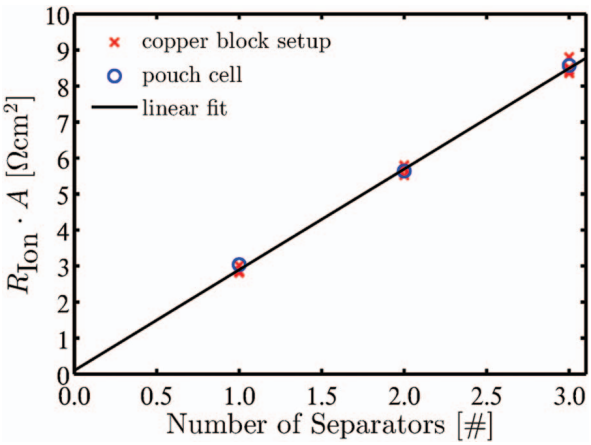

Figure 8. High frequency areal resistance of multiple layers of Celgard 2325 separators soaked with 1 M $LiPF_6$ in EC:EMC (3:7 w:w) + 2% VC using both the copper block setup (four repeat experiments per stacking) and pouch cells (one experiment per stacking). The line represents a least-squares fit of all the data to $R_{Ion} \cdot A = x_1 \cdot \#_{Sep} + x_0$, yielding $x_0 = 0.10\ \Omega cm^2$ and $R^2 = 0.998$.

shown in Figure 7b, where three independent repeat experiments (crosses, squares, diamonds) for each separator stacking yield identical impedance spectra (the remaining very small variations can be seen by regarding the rightmost red squares at the lowest frequencies). We conclude that the experimental scatter observed with the non-insulated upper copper block electrode (Figure 7a) is not due to unstable impedance measurements, but is caused by stray currents that bypass through the electrolyte and effectively increase the probed separator area by an unknown extent. By insulating the perimeter of the upper copper electrode, this effect can be eliminated, resulting in highly reproducible measurements (Figure 7b). Owing to in-plane ionic conduction in the separator, the effective separator diameter is larger than the upper copper electrode diameter (20 mm) by an effective length which is on the order of three separator thicknesses. Assuming a maximum separator thickness of ≈75 μm (stacking of three separators), this would correspond to an effectively sampled area of ≈3.28 cm^2 vs. the nominal sample area of 3.14 cm^2, which would introduce a maximum error in the determined areal resistance and effective conductivity of less than 5%.

Before application of this simple experimental setup to various battery separators, the accuracy of this new device will be verified by varying the separator thickness using multiple separator layers, by changing the electrolyte conductivity, and by comparing results obtained in pouch cells (see Figure 6) and in the copper block setup (see Figure 5). At first, the areal resistances of multiple layers of Celgard 2325 separators obtained from measurements with both the copper block setup and in pouch cells are compared and depicted in Figure 8.

Results from both pouch cells (blue circles in Figure 8) and from the copper block setup (red crosses in Figure 8) are in excellent agreement. The standard deviations for each separator count of measurements conducted in the copper block setup are below 3.5%, which is on the order of the assumed separator porosity and thickness variances. Furthermore, Figure 8 shows the expected perfectly linear relationship between areal resistance and the number of separators. The negligibly small y-intercept of $x_0 = 0.1\ \Omega\ cm^2$ of the least-squares regression line in Figure 8 demonstrates that no significant additional resistive contributions (e.g., from contact resistances) are present in either setup (i.e., x_0 is <3% of the overall resistance of a separator). Figure 8 also serves as a quality measure with regards to experimental artifacts which could arise from incomplete separator wetting. For different numbers of separators and in completely different cell setups, in which electrolyte is added either at ambient pressure (copper block setup) or the cell is sealed at an absolute pressure of 25 mbar (pouch bag setup), no difference in areal resistance could be observed.

In order to further verify the measurement setup, we also examined whether the measured tortuosity for a given separator is independent of electrolyte conductivity, as one would expect. Tortuosities were calculated for single layers of Celgard 2325 based on impedance measurements in the copper block setup and using porosity and thickness values specified by the manufacturer (see Table II). Data with five different electrolytes are compared in Figure 9, including the experimental data obtained with the copper block setup already shown in Figure 8 (data set at ∼9.5 mS/cm; light-blue symbols).

Independent of solvent, salt, or salt concentration, a tortuosity of 4.03 ± 0.24 is obtained from measured high frequency resistances as depicted in Figure 9. Compared to the standard deviation of ∼3% obtained from variation of the number of separators or the cell setup in Figure 8, an increased standard deviation of ∼6% is obtained from these experiments with different electrolytes. Part of this error is due to temperature fluctuations caused by the glovebox's temperature control (±1.0°C). In addition, very low electrolyte conductivities for electrolytes with small salt concentrations (left-hand side data set in Figure 9) are prone to errors from impurities, while high electrolyte conductivities (right-hand side data set in Figure 9) lead to small ionic resistances in which case signal contributions from cable inductivities and small contact resistances are more significant. Therefore, the best measurement conditions were found for electrolyte conductivities in the range of 3–10 mS/cm, with separator samples cut to a diameter of 25 mm or 40 mm. Such electrolytes are also closest to relevant

Table II. Tortuosities (τ) and MacMullin numbers (N_M) of porous separators determined by impedance measurements in blocking electrode configuration using the setups shown in Figure 5 and Figure 6, mainly using individual separator layers and 1 M $LiPF_6$ in EC:EMC (3:7 w:w) + 2% VC electrolyte (κ = 9.25 mS/cm). The listed separator porosity (ε) and thickness (d) values were taken from the manufacturers' specification sheets (separator parameters differing from the manufacturers' specification sheet are marked by an asterisk) and used in Eq. 8 to calculate τ and N_M values. The MacMullin number predicted by the Bruggemann relationship for spherical particles ($N_{M(B)} = \varepsilon^{-1-\alpha}$) based on Eqs. 5 and 6 with α = 0.5 and values from the literature ($N_{M(lit.)}$) are shown in the right-hand-most columns. Variations in τ and N_M indicate the standard deviations based on at least three independent repeat experiments.

Separator	Type	ε [-]	d[μm]	τ (meas.)	N_M (meas.)	$N_{M(B)}$	$N_{M(lit.)}$
commercial (#1)	monolayer HDPE	0.39	18.5	5.4 ± 0.4	14 ± 1.1	4.1	
commercial (#2)	monolayer HDPE	0.43	16	6.9 ± 0.1	16 ± 0.3	3.6	
Celgard H2013	trilayer	0.47	20	3.2 ± 0.2	6.9 ± 0.5	3.1	
Celgard 2320	trilayer	0.39	20	3.9 ± 0.0	10 ± 0.1	4.1	6.5*[23], 11*[44]
Celgard 2325	trilayer	0.39	25	4.1 ± 0.2	10 ± 0.6	4.1	7.0*[23]
Celgard 2500	monolayer PP	0.55	25	2.5 ± 0.2	4.5 ± 0.3	2.5	13*[14], 8.5[2], 18*[22]
Celgard 3500	coated PP	0.55	25	3.4 ± 0.1	6.1 ± 0.2	2.5	
Celgard C480	trilayer	0.50	21.5	3.6 ± 0.3	7.3 ± 0.5	2.8	
Freudenberg FS-3001-30	non-woven PET	0.60	28	2.7 ± 0.0	4.6 ± 0.1	2.2	14[43]
Separion S240P30	non-woven PET	0.46	28.1	4.3 ± 0.2	8.6 ± 0.3	2.8	

electrolytes for lithium ion batteries. The predicted tortuosity of τ = 1.6 for the Celgard 2325 separator based on the Bruggeman estimation for spherical particles (i.e., $\tau = \varepsilon^{-0.5}$ obtained from Eq. 6 with α = 0.5) and a porosity of ε = 0.39 (see lower dashed blue line in Figure 9) is only 40% of the experimentally obtained value, illustrating that the simple Bruggeman estimate for spherical particles but frequently applied to separator materials can lead to large errors. That this indeed seems to be the case for essentially all commonly used separators will be shown in the following.

Averaged results from impedance measurements on various separators in both setups (pouch cell and copper block setup) are summarized in Table II, listing porosity (ε) and thickness (d) values taken from the manufacturers' specification sheets, whereby our own thickness measurements were in excellent agreement with the specified values. Tortuosities (τ) and MacMullin numbers (N_M) were obtained from the measured ionic resistance (R_{Ion}) values and the specified separator properties using Eq. 8. While separator porosity and thickness values are needed to calculate τ, calculation of N_M only requires the easily measureable separator thickness, so that the latter will allow for a more straightforward comparison with the literature. For this reason, Table II also lists the literature values for the MacMullin number

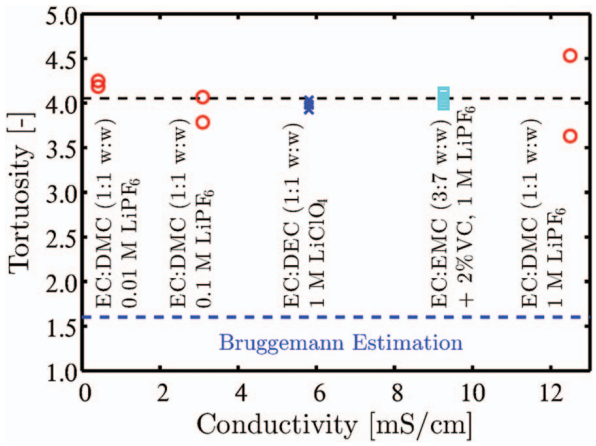

Figure 9. Tortuosities of a Celgard 2325 separator based on high frequency resistance measurements (copper block setup) versus electrolyte conductivity, spanning a range of 0.41 to 12.5 mS/cm (the specific electrolytes are listed in the figure). Tortuosities are based on a porosity of ε = 0.39 and a thickness of d = 25 μm as specified by the manufacturer, and are calculated using Eq. 8. The blue dashed line indicates the τ-value based on the Bruggeman estimation for spherical particles (Eq. 6, with α = 0.5).

($N_{M(lit.)}$) of various separators in addition to the MacMullin number predicted by the Bruggeman equation for spherical particles ($N_{M(B)}$), obtained by combining Equations 5 and 6 ($N_{M(B)} = \varepsilon^{-1-\alpha}$) and using α = 0.5. The standard deviations of the calculated tortuosities and MacMullin numbers in Table II are below 8% for each separator type, which suggests reasonably good reproducibility of the measurements. As already suggested above, the discrepancies between experimentally determined MacMullin numbers (N_M) and theoretical estimates based on the Bruggeman equation ($N_{M(B)}$) are substantial in all cases, consistent with previous literature reports.[2,18,21] Even the smallest discrepancy between N_M and $N_{M(B)}$, determined for the Celgard 2500 separator, amounts to a factor of ∼1.8, which in the most extreme cases increases to a factor of ∼4.5 (see Table II).

A comparison of the here determined values of N_M with the literature ($N_{M(B)}$) shows significant deviations. For example, based on the effective resistance values of Celgard 2320 and Celgard 2325 trilayer separators, the data reported by Arora and Zhang[23] correspond to N_M values of ∼6.5 and ∼7.0, which are substantially lower than our values of 10 ± 0.1 and 10 ± 0.6, respectively (see Table II). Likewise, a similarly large discrepancy is found when comparing the MacMullin numbers of 13 ± 1.5,[14] 8.5,[2] and 18[22] reported for Celgard 2500, in contrast to the value of 4.5 ± 0.3 obtained in our measurements. Finally, the product specification sheet[43] for the Freudenberg FS-3001-30 separator lists an ohmic resistivity which would correspond to a threefold larger N_M value compared to our measurements (second to last row in Table II). To a lesser degree, these discrepancies in MacMullin number may be due to variations in the separator microstructure, e.g., caused by modifications during production. An indication for different separator microstructures is the difference in reported separator thickness and porosity values by Djian et al.[14] for Celgard 2500 (23 μm and 0.47 respectively) compared to our Celgard product specification sheet, which lists values of 25 μm and 0.55 respectively. We believe, however, that the majority of these discrepancies are due to a combination of several effects: i) stray currents caused by the geometry of the conductivity measurement setup (e.g., an ionic bypass through the electrolyte between the cell wall and the separator could have led to the systematically lower MacMullin values reported by Arora and Zhang[23]); ii) substantial contact resistances in coin cell based two-point probe measurements (e.g., Patel et al.[2] subtracted a contact resistance of 0.35 Ω, while the expected separator resistance based on our results is of the same order of magnitude, viz., 0.57 Ω); iii) artifacts caused by the stacking of a large number of separators, often used to minimize contact resistance effects and/or to probe the effect of separator compression (e.g., Cannarella and Arnold[44] determined the separator resistance by stacking 32 separators, which for anisotropic materials may differ from measurements on a single separator); and/or, iv) uncertainties in

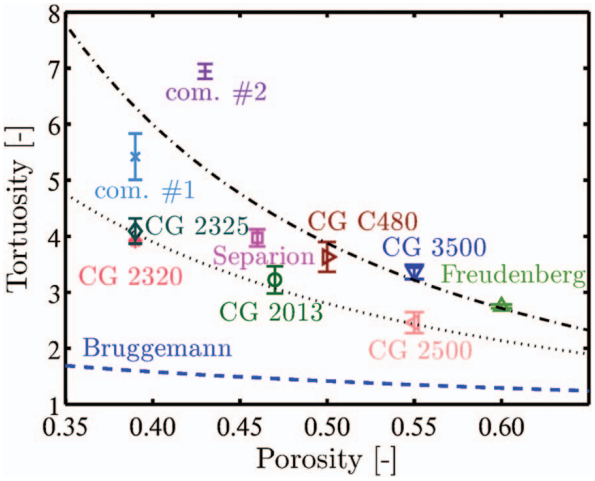

Figure 10. Tortuosities of porous separators (Celgard is abbreviated with CG) and their standard deviations determined via high frequency resistance measurements (data from Table II). Fits with Eq. 6 using $\alpha = 2.5$ (dotted line, i.e., $= \varepsilon^{-2.5}$) and $\alpha = 3.1$ (dashed-dotted line, i.e., $\tau = \varepsilon^{-3.1}$) vs. the conventionally used Bruggeman coefficient for spherical particles of $\alpha = 0.5$ (blue dashed line).

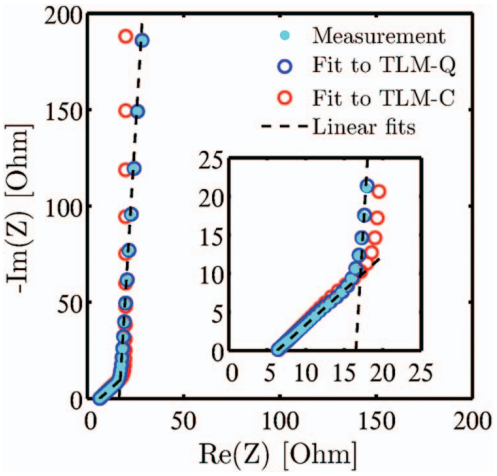

Figure 11. Exemplary impedance spectrum (200 kHz to 0.5 Hz) of two electrodes (graphite-1 (Table I) with thickness of 63.2 μm, porosity of 0.41, and effective area of 2.37 cm^2) assembled in a symmetrical pouch cell with one Celgard 2325 separator using 50 mM $TBAClO_4$ in EC:DMC (1:1 w:w) with a bulk conductivity of 1.74 mS/cm (light blue solid circles). The data are fitted to either the TLM-C model (red open circles) or the TLM-Q model (blue open circles); linear extrapolations to the high and low frequency branches of the TLM-Q model are indicated by the dashed lines. The inset is a magnified view of the high frequency range.

the effective geometric area of the separator probed in conventional conductivity-cells (likely the cause in the data reported by Abraham[22]). Although the MacMullin numbers reported in the literature scatter substantially, we believe that our here presented measurement setups and procedures provide a precise and reliable methods for determination of separator ionic resistances. While pouch cell measurements were used as a consistency check for our copper block setup, we believe that the copper block setup allows for equally precise results at reduced experimental effort (e.g., no vacuum sealing device is needed and experiments can be repeated quickly).

As seen above for a large variety of available separators, the Bruggeman equation (Eq. 6) with $\alpha = 0.5$ (i.e., $\tau = \varepsilon^{-0.5}$) is not valid for typical lithium ion battery separators (see N_M vs. $N_{M(B)}$ in Table II). Thus, we will compare obtained separator tortuosities with the generalized Bruggeman equation (Eq. 6 with free α) . Figure 10 depicts the separator tortuosities and their standard deviations listed in Table II as a function of porosity as well as two fits to Eq. 6 ($\alpha = 2.5$ and $\alpha = 3.1$) and a plot of the conventional Bruggeman equation for spherical particles with $\alpha = 0.5$.

The tortuosities of the separators Celgard H2013, Celgard 2320, Celgard 2325 and Celgard 2500 are well reproduced by $\tau = \varepsilon^{-2.5}$ ($\alpha = 2.5$), while the separators from Freudenberg, Separion, the commercial single-layer HDPE separators (#1 and #2) and the separators Celgard C480 and Celgard 3500 fit reasonably well to $\tau = \varepsilon^{-3.1}$ ($\alpha = 3.1$). An indication for the difference between these groups of separators may be gained by comparing Celgard 2500 and Celgard 3500. According to the manufacturer's specification sheet, these separators have identical materials properties (thickness, gurley number, porosity, pore size, TD and MD shrinkage, puncture strength, as well as TD and MD tensile strength),[45] and the only specified difference is that Celgard 3500 is surfactant-coated. For further identification of the differences between the two separator groups which can be discerned in Figure 10, more details on the preparation process, the detailed separator morphology and the presence and types of surfactant coatings would be necessary.

As a conclusion, from impedance measurements using the insulated copper block setup, precise tortuosity values and MacMullin numbers could be obtained for a wide variety of commonly used separators, with standard deviations of <8%. In all cases, the Bruggeman estimation for spherical particles (Eq. 6, with $\alpha = 0.5$), which is frequently used in battery models, largely underestimates the real ionic resistances through the porous separators.

Determination of electrode tortuosities and MacMullin numbers.—*Differentiation to literature.*—Prior to discussing our impedance measurements with porous electrodes, the methodology suggested in this work is compared with the work of Ogihara et al.[26] The differences between the two approaches are in the details of the used equivalent circuit model and in the realization of a blocking electrode configuration. While Ogihara et al.[26] used a transition-line model with pure capacitors to describe the surface impedance at the pore walls (TLM-C model, i.e., $\gamma = 1$ in Eq. 11), a constant-phase element is used in this work (TLM-Q model, i.e., $\gamma \neq 1$ in Eq. 11). The latter leads to a <90° slope in the low frequency branch of the Nyquist plot, as already shown for simulated Nyquist plots in Figure 4. To illustrate the influence of a constant-phase element versus a perfect capacitor, graphite electrodes (graphite-1, see Table I) were prepared as outlined in the Experimental section and assembled in symmetrical cells. An exemplary impedance spectrum of such a cell is shown in Figure 11.

The impedance spectrum in Figure 11 shows a TLM behavior starting at a high frequency resistance of $R_{HFR} = 6.35\ \Omega$, a value which corresponds to the ohmic resistance of the separator and which is consistent with the data shown in Table I (for the electrode area and electrolyte used in Figure 11, a resistance of 6.1 Ω would be predicted for the used Celgard 2325 separator). Figure 11 shows an excellent agreement between the experimental data (light blue solid circles) and the TLM-Q model fit according to Eq. 11 (blue open circles). According to Eq. 12, the difference between the x-axis values obtained from the linear extrapolations of the low and the high frequency branches of the TLM-Q model (dashed lines) corresponds to one third of the ionic resistance of both electrodes. From Figure 11, the thus determined ionic resistance for both electrodes equates to 31.6 Ω, which is in excellent agreement with the value of 31.0 Ω resulting from a fit of the experimental data to the TLM-Q model equation (Eq. 11). On the other hand, a more than 30% larger ionic resistance for both electrodes of 40.6 Ω is found when the same dataset is fitted to the TLM-C model as suggested by Ogihara et al.,[26] whereby this discrepancy is a result of the mismatch between the TLM-C model fit and the experimental data at low frequencies (see Figure 11). It should be emphasized that the experimental data neither in our work (see Figure 11) nor in the work by Ogihara et al.[26] (see Figure 6 of Ref. 26) show a perfectly vertical low frequency branch, so that the

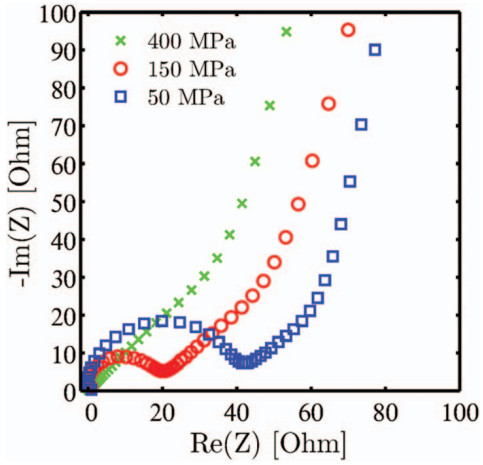

Figure 12. Exemplary Nyquist plots, subtracted by the HFR for better comparability, of LFP electrodes with low conductive carbon content (LFP-highC electrodes, see Table I) after different compressions: 50 MPa, 150 MPa, and 400 MPa, yielding porosities of 0.49, 0.34, and 0.27. The frequency maxima of the semi-circles are f_{max}(50 MPa) ≈ 4 kHz and f_{max}(150 MPa) ≈ 10 kHz. Measured in symmetrical T-cells with one glass fiber separator using 10 mM $TBAClO_4$ in EC:DMC (1:1 w:w) with a bulk conductivity of 0.46 mS/cm.

accuracy of the TLM-C model will largely depend on the selected low-frequency cutoff in the fitting procedure. For this reason, the TLM-Q model used in our work is preferred, as its fitting results are substantially less sensitive to the chosen low frequency cutoff value.

In addition to the different transmission-line circuit used by Ogihara et al.,[26] these authors also used a lithium ion containing electrolyte for their symmetrical cell measurements. In this case, blocking conditions were assumed to hold for freshly prepared electrodes at 0% and 100% state-of-charge (SOC), supported in their measurements by the absence of a semi-circle in the Nyquist plot, which would be expected if lithium intercalation/deintercalation were to occur. However, in our preliminary experiments with lithium ion containing electrolytes (not shown), semi-circles were observed for some of the electrodes listed in Table I, even at 0% and 100% SOC. As will be discussed below, this may be due to either an insufficiently suppressed charge-transfer reaction and/or electronic contact resistances. Since the use of a non-intercalating electrolyte ($TBAClO_4$) allows for an explicit assignment of an observed semi-circle feature to electronic contact resistances between coating and current collector, non-intercalating electrolytes were used in our work.

Current collector – coating contact resistances.—Prior to investigating the impact of active material particle size/morphology and electrode composition on the electrode's ionic resistance, impedance spectra of LFP cathodes will be analyzed after different compression steps. It will be shown that any compression-dependent contact resistances between current collector and electrode coating can be determined from an analysis of the impedance spectra obtained with a non-intercalating electrolyte.

Electrodes for lithium ion batteries are usually compressed or calandered to reduce their porosity, thereby enhancing the volumetric energy density while at the same time increasing the electronic conductivity across the electrode coating and across the current collector/coating interface. High carbon content LFP electrodes (LFP-highC, see Table I) were compressed to different porosities and assembled in symmetrical T-Cells, separated by two glass fiber separators. A high carbon content was chosen to ensure a high electronic conductivity within the coating in order to satisfy the assumption of negligible electronic resistances between the particles within the coating, which was made in the theoretical part of this work (see Figure 3).

Figure 12 shows the impedance spectra recorded of LFP-highC electrodes coated on an aluminum current collector and compressed by 50 MPa, 150 MPa and 400 MPa before assembly, shifted to the origin of the complex plane for better comparability. Although medium and low frequencies show the expected TLM for all compressions, a prominent difference can be observed at high frequencies. A distinct *R/Q* element dominates the high frequency region at a compression of 50 MPa, with the resistance of the high frequency semi-circle amounting to ∼40 Ω. Similar electrodes compressed at a three-fold higher pressure of 150 MPa also show a semi-circle, but with a lower resistance of ∼20 Ω. If a pressure of 400 MPa is applied, the semi-circle vanishes to a negligible size, indicating that it originates from electronic resistances which decrease upon compression. These might be caused by inter-particle electronic resistances within the electrodes and/or by a contact resistance between the current collector/electrode interface. Trying to distinguish between these two electronic resistance contributions, it is noteworthy that these additional semi-circles were only observed for electrodes coated on aluminum foil, but were never observed for graphite or LTO electrodes coated on copper foil. Considering that the intrinsic electronic conductivity of LTO (10^{-13} S/cm[46]) is lower than that of LFP (10^{-9} S/cm[47]) and considering that the LFP electrodes shown in Figure 12 were prepared with a high conductive carbon content (15%wt), the origin of the semi-circle in Figure 12 is most probably related to an electronic contact resistance between the current collector/coating interface rather than to inter-particle resistances within the electrode. This is further supported by estimating the effective capacitance of the semi-circle feature in Figure 12, obtained from its frequency at the semi-circle apex and its corresponding resistance, which amounts to 1 μF: at an approximate double layer capacitance of on the order of 10 μF/cm^2, this would equate to an effective interfacial area of about 0.1 cm^2, which is four orders of magnitude smaller than the electrode material surface area (∼980 cm^2 based on 2.58 mg_{LFP}/cm^2 at 24 m^2/g BET area and 0.58 mg_{carbon}/cm^2 at 62 m^2/g BET area).

The results and conclusions drawn here are in accordance with the work by Gaberscek et al.,[48] who argued that the semi-circle results from a parallel connection of the current collector/coating contact resistance and the current collector's double layer capacitance. Analogous to Figure 12, they also observed a reduced semi-circle resistance upon applying external pressure, whereby the magnitude of resistance change upon compression reported by Gaberscek et al. correlates well with our findings; in addition, they also showed a pronounced decrease of the contact resistance when copper instead of aluminum foil is used as a current collector. Current collector/coating contact resistances were also quantified by Illig[49] by analyzing the distribution of relaxation times of impedance spectra obtained with symmetrical cells.

In summary, our above measurements using a non-intercalating salt to realize a true blocking electrode configuration allow for a precise and unambiguous determination of potentially present contact resistances, without the interference from charge transfer reactions. In addition, as long as a transmission-line behavior can be observed, the ionic resistance through the electrode can still be determined, despite the serial addition of a contact resistance element (R_C/Q_{DBL}). From the results shown in Figure 12, it is apparent that a crucial step particularly during cathode electrode manufacturing is the reduction of the aluminum current collector/coating contact resistance by electrode compression/calandering. Measurements in symmetrical cells with a non-intercalating electrolyte as presented above offer a quick and reliable method to characterize the contact resistance of electrodes after the manufacturing process.

Reproducibility and validation.—In the following, the validity and reproducibility of the TLM-Q approach to determine the ionic resistance of electrodes will be demonstrated by varying electrolyte conductivity and electrode area. For this, impedance measurements in symmetrical pouch cells and T-Cells with graphite electrodes (graphite-1, see Table I) were done using an electrolyte containing 10, 50, 200, and 700 mM $TBAClO_4$ in EC:DMC (1:1 w:w).

Figure 13 shows the impedance spectra of symmetric graphite pouch cells (graphite-1, see Table I) and their excellent agreement with Eq. 11. As expected, the HFR increases together with the ionic

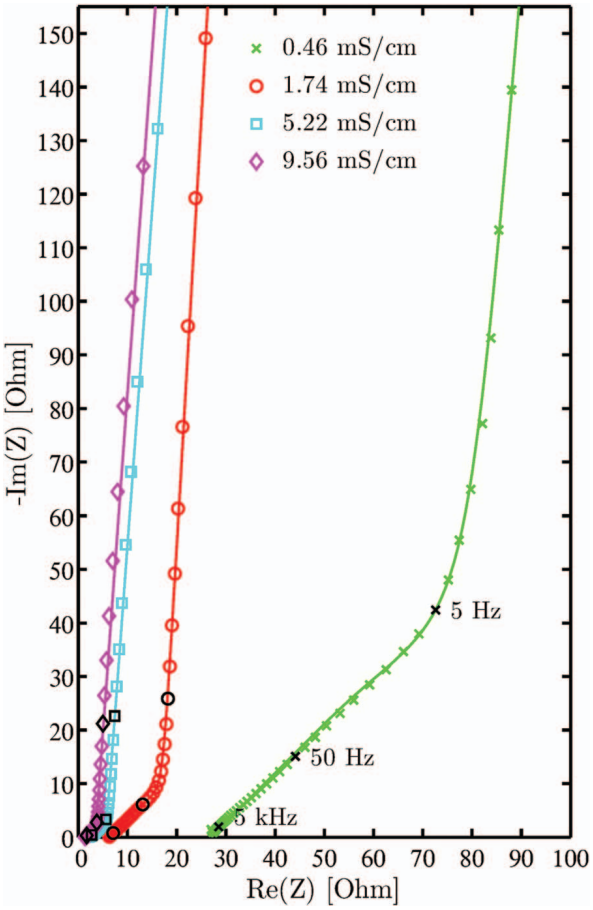

Figure 13. Impedance spectra and fits with Eq. 11 of four symmetrical graphite pouch cells (graphite-1 electrodes with $\varepsilon = 0.42 \pm 0.02$, see Table I) with EC:DMC (1:1 w:w) containing 10, 50, 200, and 700 mM $TBAClO_4$ (electrolyte conductivities κ are listed in the figure). Impedance data were recorded between 200 kHz and 0.5 Hz; the 5 kHz, 50 Hz, and 5 Hz data are indicated by the black symbols.

resistance (R_{Ion}) in the electrode when the electrolyte conductivity (κ) is decreased. The observed constant phase angle γ was found to be similar for each type of active material. In the case of graphite (compare Figure 13), constant phase angles in the low frequency range of 85° were found. For other active materials we found values ranging from 88° (LTO) to 80° (LFP). Due to the systematic correlation with the type of active material, we ascribe the constant phase behavior to the type and structure of the electrode surfaces.[41] After quantification of R_{Ion} from the impedance data, the tortuosity of the electrodes can be obtained by rearranging Eq. 8,

$$\tau = \frac{R_{Ion} A \kappa \varepsilon}{2\, d} \qquad [13]$$

where the porosity ε of the electrodes can be determined from the areal weight and the thickness of the electrodes (see Experimental section); the factor 2 accounts for the symmetry of the setup, where the sum of the impedances of two identical electrodes is measured.

To compare the possible influence of electrolyte conductivity and cell setup, the tortuosities calculated from Eq. 13 based on impedance measurements with symmetrical graphite electrodes (graphite-1, see Table I) from eight T-Cells (two for each salt concentration) and the four pouch cells shown in Figure 13 are plotted vs. electrolyte conductivity in Figure 14. For these graphite electrodes with a porosity of $\varepsilon = 0.43 \pm 0.02$, an average tortuosity of $\tau = 4.3 \pm 0.6$ is obtained, which is ~3-fold higher than the value of $\tau = 1.5$ which would be predicted by the Bruggeman equation for spherical particles with $\alpha = 0.5$ (Eq. 6), which is used quite frequently in battery models. It is emphasized

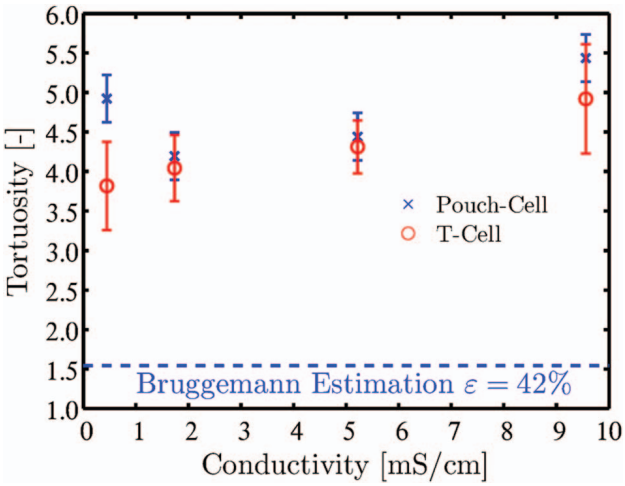

Figure 14. Influence of electrolyte conductivity on the determined tortuosities in symmetrical pouch and T-Cells with graphite electrodes (graphite-1, see Table I, with $d_{Coating} = 58 \pm 2$ µm, $\varepsilon \approx 0.43 \pm 0.02$) using four different electrolytes, viz., EC:DMC (1:1 w:w) with 10, 50, 200, and 700 mM $TBAClO_4$ (see Figure 13 for electrolyte conductivity values). The Bruggeman estimation for spherical particles with $\alpha = 0.5$ is represented by the dashed horizontal line. Error bars indicate the standard deviation of two T-Cells per electrolyte or a constant error of 0.3 for the pouch cells, which was estimated using the Gaussian variance with experimental deviations of effective area, electrolyte conductivity and determined electrode thickness and porosity.

that not all electrodes are 100% identical and a certain variance results from the laboratory scale electrode preparation process. Nonetheless, Figure 14 shows a reasonably good agreement between T-Cells and pouch cells with very different electrode areas and over a large range of electrolyte conductivities. In the following experiments with different electrodes, compressed to different porosities, we have chosen a $TBAClO_4$ concentration of 10 mM, which results in a tortuosity of $\tau = 4.2 \pm 0.7$ for the graphite electrodes shown in Figure 13. A 10 mM concentration was chosen to best fulfill the requirements for the simplification of the transmission line model (see Figure 3), i.e., negligible electronic resistance in the electrode compared to the ionic resistance inside the electrolyte. It should be noted that in comparison to the tortuosity determination of separators, small but finite contact resistances do not affect the determination of electrode tortuosities.

Drivers of the tortuosity of porous electrodes.—In this Section, we will investigate the effect of particle morphology, particle size, and electrode composition on the ionic resistance of porous electrodes. Where possible, the data will be compared to the literature. As typical electrode porosities in lithium ion batteries are adjusted to roughly 30% by calandering/compression of electrodes, we will first focus on electrodes prepared from different active materials which were compressed to porosities near 30% and which have an active material content of ≥90%wt (see Table I).

The MacMullin numbers for electrodes with different active materials shown in Figure 15 are calculated based on the ionic resistances obtained from the difference between the extrapolated x-axis intercepts of the low and the medium frequency regions in the impedance spectra as explained above (see Figure 11). Horizontal error bars indicate the uncertainty in the porosity (see Experimental section), while vertical error bars are based on the error on the thickness measurement (d), which affects the calculation of the MacMullin number calculated from a combination of Eqs. 5 and 13 (note that N_M thus is independent of ε). MacMullin numbers around 18-19 are obtained for the two examined graphite electrodes at porosities of ~29% (graphite-1) and ~35% (graphite-2). At a similar porosity, NMC electrodes have an almost 2-fold lower MacMullin number of 10-11. This difference is ascribed to the difference in particle morphology, which is illustrated by comparative top-view and cross-sectional-view scanning electron

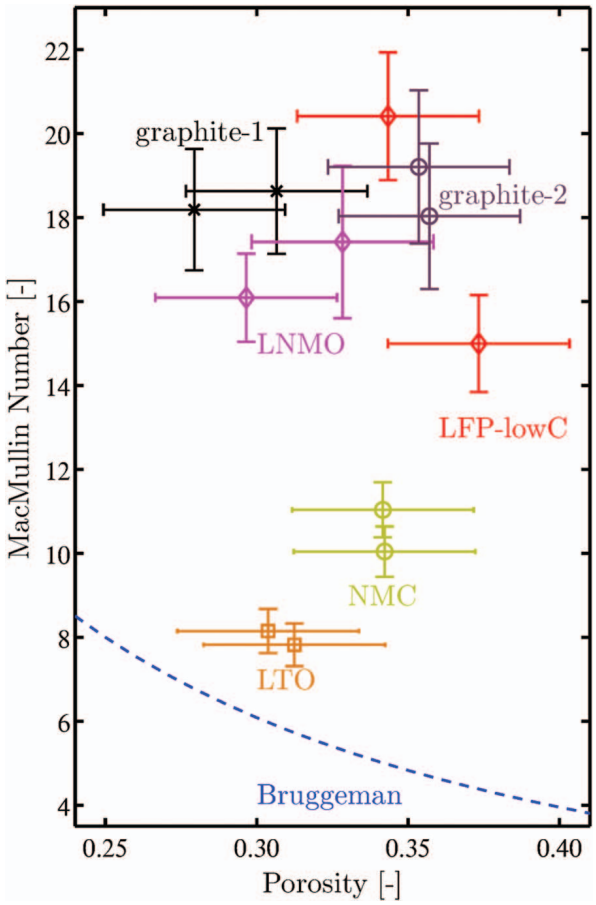

Figure 15. MacMullin numbers of electrodes with active material contents ≥90% as specified in Table I and compressed to porosities ranging between 0.27 and 0.37. Results are obtained from measurements in pouch cells and T-Cells using EC:DMC (1:1 w:w) with 10 mM $TBAClO_4$ as an electrolyte. The Bruggeman prediction for spherical particles ($\alpha = 0.5$, $N_{M(B)} = \varepsilon^{-1.5}$) is indicated by the blue dashed line.

microscope (SEM) images shown in Figure 16. Both active materials have large particles in the range of 10–30 μm, but while NMC particles are quite spherical, graphite particles have a plate-like morphology elongated in two directions. Since in the electrode coating process, graphite particles align preferentially horizontally (see Figure 16), it can be imagined easily, that ionic conduction will be hindered to a larger extent by the horizontally aligned graphite particles compared to spherical particles. This effect was also described by numerical evaluations of the tortuosity of graphite electrodes based on FIB-SEM derived morphologies, yielding ∼2-fold higher through-plane compared to in-plane tortuosities.[16] Similarly, two independent numerical evaluations of the tortuosity of spherical (like NMC) vs. plate-like particles (like graphite), yielded much higher values for the latter.[2,32] Thus, all three numerical evaluations are at least qualitatively consistent with the substantially lower tortuosities for NMC compared to graphite electrodes shown in Figure 15. Quantitatively, however, the numerical investigations based on 3D reconstructed geometries deviate substantially from our experimental results. For example, the analysis of 3D reconstructed electrodes of spherical NMC particles by Ebner et al.[32] yields through-plane tortuosity values very close to the Bruggeman equation for spherical particles ($\tau = \varepsilon^{-0.5}$) while our experimentally obtained values are two-fold larger than the latter prediction (see Figure 15). One reasonable explanation for this discrepancy can be the limited resolution of the used imaging technique, which will at best only partly resolve the conductive carbon and binder morphology, eventually assuming more empty pores than actually exist. In addition, the authors themselves state that their findings "are based on purely geometrical arguments"[32] which due to the different definitions of the tortuosity (geometrically, mathematically or physically; see very first section of this paper) may lead to different values compared to our electrochemical AC impedance spectroscopy measurements.

The influence of particle size can be demonstrated by comparing the MacMullin numbers of LNMO and LTO electrodes (composition see Table I), for which values of ∼17 and ∼8 are found, respectively (see Figure 15). Both active materials have a rather spherical morphology but the difference in particle size is obvious from Figure 17. LTO particles have a spherical/cube-like morphology with a size of about 1–2 μm, whereas LNMO particles have a particle size around 10–20 μm. We hypothesize that the observed difference in effective ionic transport resistance can be explained with a partial blockage of

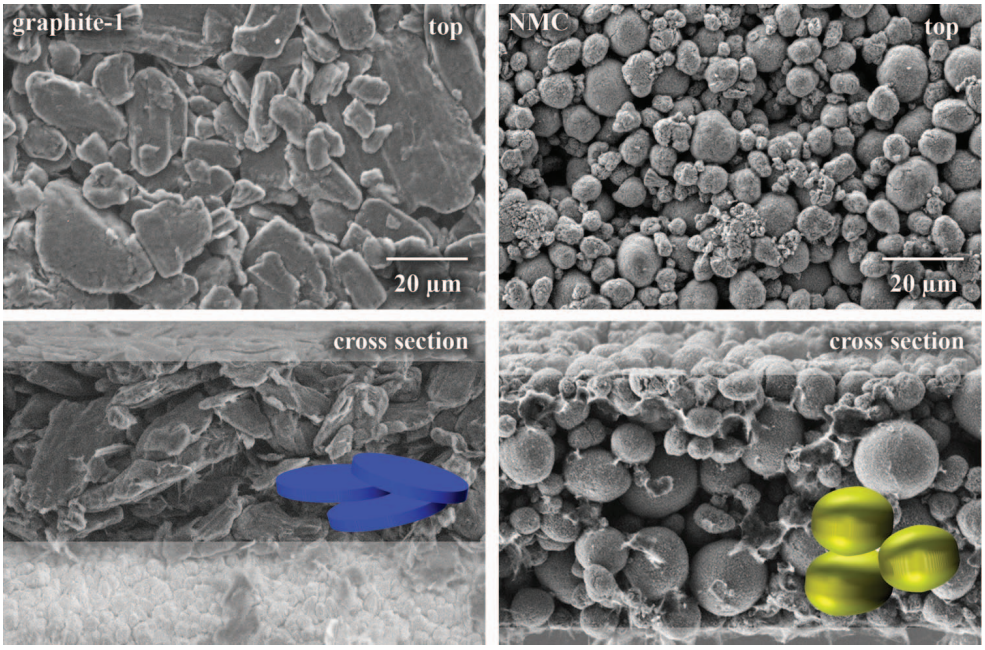

Figure 16. SEM top-view (upper figures) and cross-sectional-view (lower figures) micrographs of graphite-1 (ε ≈ 0.29) and NMC (ε ≈ 0.34) electrodes (composition see Table I), with a schematic representation of the particle morphology. The scale bar applies for both the top-views and the cross-sections.

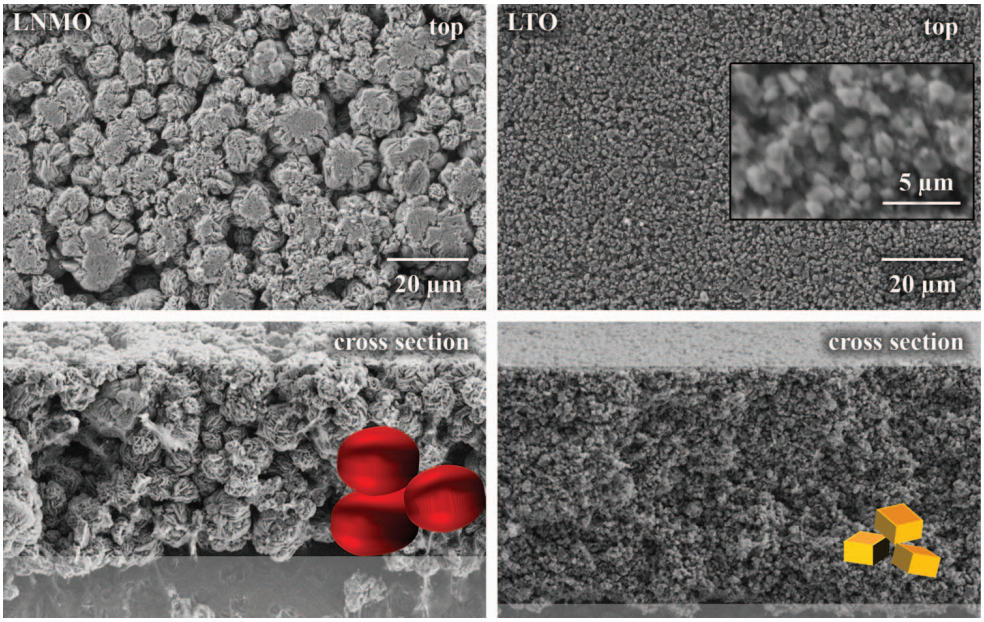

Figure 17. SEM top view and cross section micrographs of LNMO ($\varepsilon \approx 0.31$) and LTO ($\varepsilon \approx 0.30$) electrodes (composition see Table I), with schematic representation of particle morphology. The scale bar applies for both the top-views and the cross-sections.

the pores. Detours around a blocked pore are longer for large LNMO particles compared to small LTO particles.

The aforementioned effect of the particle size on the electrode tortuosity can also be observed if electrodes with the same active material but with different conductive carbon content are compared. This is seen best by examining their MacMullin numbers over a wider range of porosity, i.e., from ~25% to ~75%, which also allows to evaluate the functional relationship between tortuosity and porosity using Eq. 7. Figure 19 thus compares the MacMullin numbers of LFP electrodes with either low or high carbon content (LFP-lowC and LFP-highC see Table I) versus porosity. To understand the impact of the conductive additive on the electrodes' microstructure, we first have to compare the morphologies of the LFP active material and the conductive carbon. The conductive carbon used in this work, consists of very small primary particles (~40 nm diameter) which are fused together in branch-like structures of several hundreds of nm in length. On the other hand, the LFP active material consists of 4 to 20 µm sized weak agglomerates (see Figure 18) of primary LFP particles of <500 nm size.

Viewing the surface of the compressed LFP electrodes shown in Figure 18, broken LFP agglomerates can be easily spotted. Quite obviously, higher amounts of conductive carbon lead to a more effective separation of the LFP primary agglomerates, providing shorter ionic pathways into the center of the LFP agglomerates. In other words, we believe that owing to their high hardness, the conductive carbons function as incompressible scaffolds between the more compressible primary agglomerates of the LFP, which allows for a faster ionic transport.

As expected, the MacMullin numbers increase with decreasing ε, as shown in Figure 19, an effect which can be described by a fit of the data to a combination of Eqs. 5 and 7. To deconvolute the effect of porosity decrease and tortuosity change, MacMullin numbers of Figure 19 are multiplied with the porosity to obtain the tortuosity values depicted in Figure 20.

As tortuosities are calculated from MacMullin numbers using the experimentally determined porosities (see Experimental section), the y-errors increase compared to Figure 19. Also shown in Figure 19 and Figure 20 are fits of the experimentally obtained MacMullin numbers

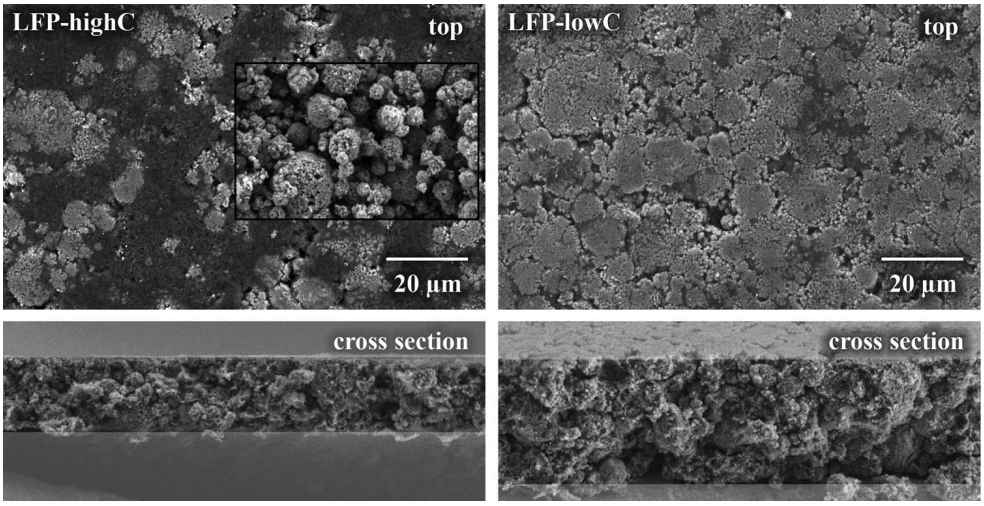

Figure 18. SEM top-view and cross-sectional-view of LFP-highC ($\varepsilon \approx 0.27$) and LFP-lowC ($\varepsilon \approx 0.27$) electrodes specified in Table I. Inset of LFP-highC depicts active material powder. The scale bar applies for both the top-views and the cross-sectional-views.

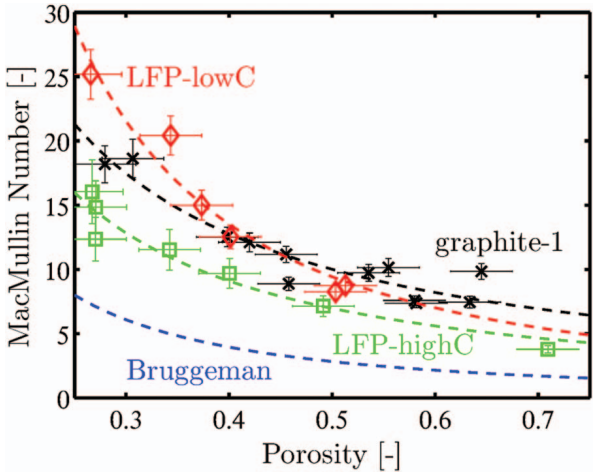

Figure 19. MacMullin numbers of LFP electrodes with an active material content of 70% (LFP-highC, see Table I) or 90% (LFP-lowC, see Table I) as well as of graphite electrodes (graphite-1, see Table I). Results are obtained from measurements in pouch cells and T-Cells using EC:DMC (1:1 w:w) with 10 mM $TBAClO_4$ as electrolyte. Data are fitted with a combination of Eq. 5 and Eq. 7: $N_M = 4.7\ \varepsilon^{-1.1}$ (graphite-1), $N_M = 3.1\ \varepsilon^{-1.6}$ (LFP-lowC), and $N_M = 3.0\ \varepsilon^{-1.2}$ (LFP-highC). The Bruggeman prediction for spherical particles ($\alpha = 0.5$, $N_{M(B)} = \varepsilon^{-1.5}$) is indicated by the blue dashed line.

and tortuosities with the generalized Bruggeman equation (Eq. 7). For all types of electrodes shown in these figures, the experimental data of N_M or τ vs. ε could only be properly represented when a variable prefactor f was used in the fits. We would like to emphasize that the experimental data could not be represented by a generalized Bruggeman equation with the prefactor $f = 1$, contrary to what was reported in studies with 3D reconstructed electrodes.[32] Comparison of the two plots show that the porosity dependence of the MacMullin number is mainly due to the decrease in available electrolyte pore volume, i.e., a decrease of the porosity. Tortuosities of graphite-1 and LFP electrodes with high conductive carbon content (LFP-highC) only show a small porosity dependence within the error bars, increasing from ~4.8 to ~5.2 and from ~3.5 to ~4.2, respectively, as the porosity decreases from ~70 to ~30%. While LFP electrodes with 5%wt conductive carbon (LFP-lowC) have a similar tortuosity as those with 15%wt conductive carbon (LFP-highC) at high porosity, the former

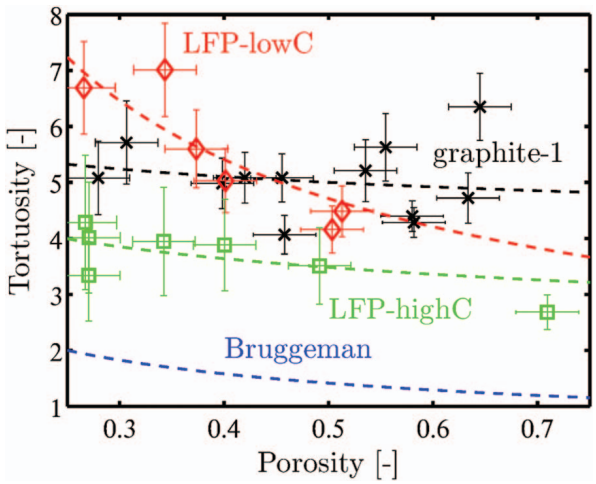

Figure 20. Tortuosities of LFP electrodes with 70% or 90% active material and graphite electrodes at different compositions and porosities. Results are obtained from measurements in pouch cells and T-Cells using EC:DMC (1:1 w:w) with 10 mM $TBAClO_4$ as an electrolyte. Dashed lines are based on the fitting results from Figure 19: $\tau = 4.7\ \varepsilon^{-0.1}$ (graphite-1), $\tau = 3.1\ \varepsilon^{-0.6}$ (LFP-lowC), $\tau = 3.0\ \varepsilon^{-0.2}$ (LFP-highC). The Bruggeman prediction for spherical particles ($\alpha = 0.5$, $\tau = \varepsilon^{-0.5}$) is indicated by the blue dashed line.

show a steep increase in tortuosity from ~4.5 at 50% porosity to ~7 at 30%. Comparison with the SEM micrographs given in Figure 18 shows, that the primary agglomerates of the LFP are broken at the higher compressive forces required to obtain low porosities. At least at the surface of these electrodes, this leads to a plate-like particle shape, from which an increase in ionic resistance is expected as argued before. As suggested by viewing Figure 18, the lateral dimensions of these compression induced plate-like particles is larger at lower conductive carbon content, so that the effect of primary agglomerate deformation of the LFP on the tortuosity and the MacMullin number is more pronounced at lower conductive carbon content.

Tortuosities of graphite electrodes (graphite-1) in Figure 20 show no dependence on the porosity. In our opinion, the open pores between the horizontally aligned graphite particles are unaltered upon electrode compression normal to the current collector plane so that the observed change in porosity has to be ascribed to a compression of the soft graphite particles. In stark contrast to our experimentally determined tortuosities of platelet-shaped graphite particles, very different results are obtained from an analysis of 3D reconstructed graphite electrodes.[32] While the reported tortuosity of ~5.5 at a porosity of 0.4 is in agreement with our experimental results, the reported tortuosity of 3 for an electrode porosity of 0.6 is very different from our data (see Figure 20). As argued above, the discrepancy may result from the inability to sufficiently resolve binder and carbon particles in the 3D reconstructed electrodes as well as from the purely geometrical nature of analysis of the tortuosity in the publication.[32] Additionally, as shown by our findings and also by the geometrical analysis of the influence of particle anisotropy on the electrode tortuosity,[32] a direct comparison might only be valid for electrodes of identical composition and, more importantly, the same particle size and shape.

Literature comparison.—From the above discussion, it is clear that the porosity dependence of the effective tortuosities and MacMullin numbers of porous electrodes even made of the same active material strongly depend on the amount and most likely the type of conductive carbon, which must be kept in mind when comparing τ and N_M values with the literature. Figure 21 depicts a comparison of the MacMullin numbers vs. porosity obtained in this work for LFP electrodes with those reported in the literature. Also shown in Figure 21 is the Bruggeman relation for spherical particles $N_{M(B)} = \varepsilon^{-1.5}$, which is frequently used in battery models.

The comparison in Figure 21 shows MacMullin numbers ranging from ~3-7 for electrodes at a porosity of 60-70%, in the porosity range of commercially used electrodes (~30–35%), the reported MacMullin numbers increase to ~7–20. The mismatch between the Bruggeman equation for spherical particles ($\alpha = 0.5$, dashed blue line in Figure 21) and the MacMullin numbers shown in Figure 21 (compare also Figure 15) is ~1.5 to ~3-fold, particularly at low porosities, an observation which has been made before.[18,21,29] For example, higher ionic resistances than suggested by the Bruggemann equation are reported by Thorat et al.[18] (brown line in Figure 21), who use Eq. 7 to fit tortuosities obtained from fits of polarization-interrupt experiments. Cooper et al.[12] used a synchrotron X-ray tomography to reconstruct a commercial LFP electrode and obtained MacMullin numbers between 6 and 10 from heat transport simulations (orange circles). In Ender et al.,[34] electrode morphology reconstruction using a FIB-SEM and subsequent solution of the Laplace equation was done for lab-scale LFP electrodes with a particle size of ~100 nm and with commercially prepared LFP electrodes with a secondary agglomerate LFP particle size of ~1.2 µm, obtaining MacMullin numbers of ~2.5 and ~5 respectively (green diamonds). In contrast to these reports on LFP based electrodes, somewhat higher MacMullin numbers are obtained in our study for the LFP electrodes with high conductive carbon content (LFP-highC, see green line in Figure 21), but the functional relationship between N_M and ε follows a similar trend. Unfortunately, owing to the strong dependence of active material morphology (see Figure 15) and conductive carbon content (see Figure 19), a rigorous comparison between the N_M values obtained by the methodologies used here and in the literature is not possible.

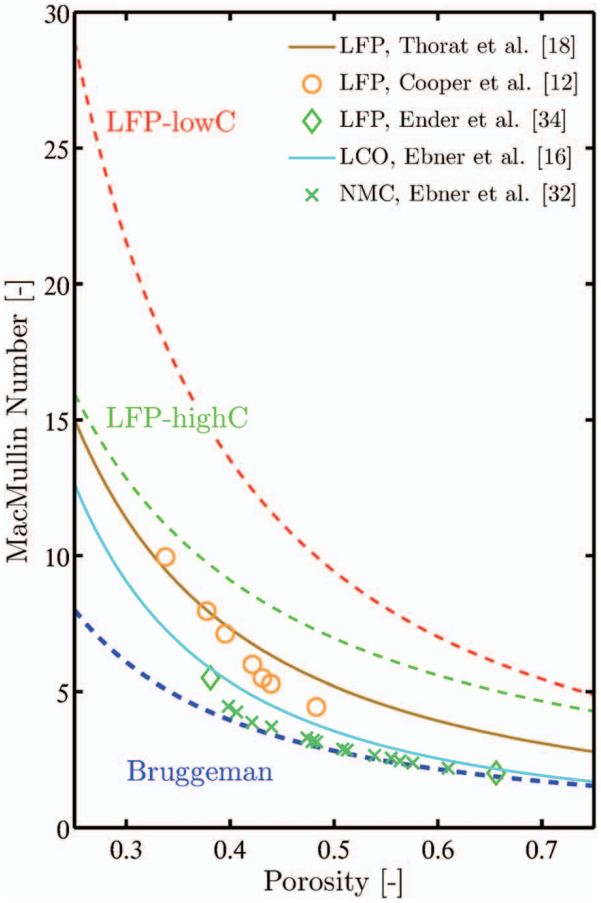

Figure 21. Comparison of the MacMullin numbers vs. porosity for the LFP electrodes studied in this work (LFP-lowC with 90/5/5 AM/binder/C and LFP-highC with 70/15/15 AM/binder/C, taken from Figure 19) with literature values from Thorat et al.[18] (LFP with 84/8/8 AM/binder/C, potato shaped, 300–600 nm length), Cooper et al.[12] (LFP, electrode composition unknown), Ender et al.[34] (LFP with 70/6/24 AM/binder/C, potato shaped, 200–600 nm length), Ebner and Wood[16] (LCO with ~94/3/3 AM/binder/C, non-spherical, 10 μm) and Ebner et al.[32](NMC with 96/2/2 AM/binder/C, spherical, 20 μm). The Bruggeman prediction for spherical particles ($\alpha = 0.5$, $N_{M(B)} = \varepsilon^{-1.5}$) is indicated by the blue dashed line.

Even though different active materials may result in very different MacMullin numbers (see Figure 15), we have added data on LCO and NMC electrodes in Figure 21, which were reported by Ebner and Wood[16] and Ebner et al.,[32] who developed a software called *Bruggeman Estimator* to obtain the tortuosity of porous electrodes from top and cross section SEM micrographs. The close relation of the MacMullin numbers of these NMC electrodes with the Bruggeman equation have been discussed critically above. For a LCO cathode, they report a Bruggeman exponent for the through plane tortuosity of $\alpha = 0.83$ (i.e., $\tau = \varepsilon^{-0.83}$), from which we calculated the MacMullin number data shown in Figure 21 (cyan line). The functional relationship between N_M and ε is again very similar to that observed for the literature data and for the LFP-highC data in Figure 21, whereby it is noteworthy that the conductive carbon content in the LCO electrodes is only 3%wt, which in the case of our LFP electrodes (LFP-lowC, see red line in Figure 21) yields ~2-fold higher N_M values.

Conclusions

MacMullin numbers as well as tortuosities of commonly used lithium ion battery separators measured in a custom made copper block setup are listed in the present study. The standard deviations for these measurements were shown to be below 8%. Our new measurement procedure was validated by systematic variation of experimental parameters like cell type, electrolyte conductivity, and number of separator layers.

We also showed an impedance based approach to quantify the ionic resistance in lithium ion battery electrodes, from which electrode tortuosities and MacMullin numbers can be determined. This method uses a simple transmission-line model in a blocking configuration, which is achieved by employing a non-intercalating electrolyte salt. We showed that an increased accuracy can be obtained when using constant-phase elements rather than ideal capacitors, as previously done in the literature. The invariance of the measured tortuosities with respect to electrolyte conductivity and electrode area was verified. Additionally while composite electrodes coated on copper current collectors always exhibited a perfect transmission-line model behavior, a distinct high frequency semi-circle was found for some LFP electrodes coated on aluminum current collector. In accordance with the literature, this semi-circle could be identified as a contact resistance between aluminum and the electrode coating, which was possible due to the absence of charge transfer reactions when using a non-intercalating electrolyte.

For all types of investigated electrodes, the MacMullin numbers are found to be ~1.5–3 times larger than suggested by the Bruggeman equation for spherical particles ($\alpha = 0.5$), which is frequently used in battery models. Furthermore, we showed the strong impact of active material particle size / morphology and conductive carbon content on the ionic conduction resistance.

Acknowledgment

We thank Daniel Pritzl and Simon Abendschein from our group for preparation of some of the electrodes. J. L. and A.E. gratefully acknowledge the funding by the Bavarian Ministry of Economic Affairs and Media, Energy, and Technology for its financial support under the auspices of the EEBatt project. Funding for J. H. was provided by the BMBF (Federal ministry of Education and research, Germany), ExZellTUM project, grant number 03X4633A. The authors thank SI Analytics for manufacturing the used custom made conductivity sensors.

Note added in proof.—A detailed discussion of the origin and the application of the Bruggeman relation in battery electrodes can also be found in Ref. 50.

List of Symbols

Symbol	Name	Unit
N_M	MacMullin number	-
κ	electrolyte conductivity	mS/cm
κ_{eff}	effective electrolyte conductivity in porous medium	mS/cm
ε	porosity of porous medium	-
m	Archie's exponent	-
τ	tortuosity of porous medium	-
α	Bruggeman exponent	-
f	proportionality factor	-
d	length	μm
β	constriction factor	-
R	resistance	Ω
A	area	cm^2
Z	complex impedance	Ω
Q	constant-phase capacitance	$F\ s^{\gamma-1}$
i	imaginary unit	-
ω	angular frequency	1/s
γ	constant phase exponent	-
r	resistances*	Ω
q	constant phase capacitance*	$F\ s^{\gamma-1}$
z	complex impedance*	Ω

*in a differential segment of the electrode/electrolyte.

References

1. J. Newman and K. Thomas-Alyea, *Electrochemical Systems*, 3rd ed., Wiley Interscience, Hoboken, (2004).
2. K. K. Patel, J. M. Paulsen, and J. Desilvestro, *J. Power Sources*, **122**, 144 (2003).
3. G. E. Archie, *Pet. Technol.*, 54 (1942).
4. L. Shen and Z. Chen, *Chem. Eng. Sci.*, **62**, 3748 (2007).
5. M. Barrande, R. Bouchet, and R. Denoyel, *Anal. Chem.*, **79**, 9115 (2007).
6. L. Holzer, D. Wiedenmann, B. Münch, L. Keller, M. Prestat, P. Gasser, I. Robertson, and B. Grobéty, *J. Mater. Sci.*, **48**, 2934 (2013).
7. M. R. J. Wyllie and W. Rose, *J. Pet. Technol.*, **2**, 105 (1950).
8. D. Cornell and D. L. Katz, *Ind. Eng. Chem.*, **45**, 2145 (1953).
9. J. M. Zalc, S. C. Reyes, and E. Iglesia, *Chem. Eng. Sci.*, **59**, 2947 (2004).
10. D. Wiedenmann, L. Keller, L. Holzer, J. Stojadinović, B. Münch, L. Suarez, B. Fumey, H. Hagendorfer, R. Brönnimann, P. Modregger, M. Gorbar, U. F. Vogt, A. Züttel, F. La Mantia, R. Wepf, and B. Grobéty, *AIChE J.*, **59**, 1446 (2013).
11. F. Tariq, V. Yufit, M. Kishimoto, P. R. Shearing, S. Menkin, D. Golodnitsky, J. Gelb, E. Peled, and N. P. Brandon, *J. Power Sources*, **248**, 1014 (2014).
12. S. J. Cooper, D. S. Eastwood, J. Gelb, G. Damblanc, D. J. L. Brett, R. S. Bradley, P. J. Withers, P. D. Lee, P. D. A., J. Marquis, N. P. Brandon, and P. R. Shearing, *J. Power Sources*, **247**, 1033 (2014).
13. M. B. Clennell, *Geol. Soc. London, Spec. Publ.*, **122**, 299 (1997).
14. D. Djian, F. Alloin, S. Martinet, H. Lignier, and J. Y. Sanchez, *J. Power Sources*, **172**, 416 (2007).
15. J. Joos, T. Carraro, A. Weber, and E. Ivers-Tiffée, *J. Power Sources*, **196**, 7302 (2011).
16. M. Ebner and V. Wood, *J. Electrochem. Soc.*, **162**, A3064 (2014).
17. D. A. G. Bruggeman, *Ann. Phys*, **24**, 636 (1935).
18. I. V. Thorat, D. E. Stephenson, N. A. Zacharias, K. Zaghib, J. N. Harb, and D. R. Wheeler, *J. Power Sources*, **188**, 592 (2009).
19. R. E. De La Rue and C. W. Tobias, *J. Electrochem. Soc.*, **109**, 827 (1959).
20. R. B. Macmullin and G. A. Muccini, *AIChE J.*, **2**, 393 (1956).
21. D.-W. Chung, M. Ebner, D. R. Ely, V. Wood, and R. Edwin García, *Model. Simul. Mater. Sci. Eng.*, **21**, 074009 (2013).
22. K. M. Abraham, *Electrochim. Acta*, **38**, 1233 (1993).
23. P. Arora and Z. J. Zhang, *Chem. Rev.*, **104**, 4419 (2004).
24. V. F. Lvovich, *Impedance Spectroscopy Applications to Electrochemical and Dielectric Phenomena*, p. 356, John Wiley & Sons, Ltd, New Jersey, (2012).
25. Y. Liu, M. W. Murphy, D. R. Baker, W. Gu, C. Ji, J. Jorne, and H. A. Gasteiger, *J. Electrochem. Soc.*, **156**, B970 (2009).
26. N. Ogihara, S. Kawauchi, C. Okuda, Y. Itou, Y. Takeuchi, and Y. Ukyo, *J. Electrochem. Soc.*, **159**, A1034 (2012).
27. N. Ogihara, Y. Itou, T. Sasaki, and Y. Takeuchi, *J. Phys. Chem. C*, 150209102507001 (2015).
28. N. A. Zacharias, D. R. Nevers, C. Skelton, K. Knackstedt, D. E. Stephenson, and D. R. Wheeler, *J. Electrochem. Soc.*, **160**, A306 (2013).
29. T. DuBeshter, P. K. Sinha, A. Sakars, G. W. Fly, and J. Jorne, *J. Electrochem. Soc.*, **161**, A599 (2014).
30. M. Ebner, F. Geldmacher, F. Marone, M. Stampanoni, and V. Wood, *Adv. Energy Mater.*, **3**, 845 (2013).
31. S. J. Harris and P. Lu, *J. Phys. Chem. C*, **117**, 6481 (2013).
32. M. Ebner, D. W. Chung, R. E. García, and V. Wood, *Adv. Energy Mater.*, **4**, 1 (2014).
33. L. Zielke, T. Hutzenlaub, D. R. Wheeler, I. Manke, T. Arlt, N. Paust, R. Zengerle, and S. Thiele, *Adv. Energy Mater.*, **4**, 1 (2014).
34. M. Ender, J. Joos, T. Carraro, and E. Ivers-Tiffee, *J. Electrochem. Soc.*, **159**, A972 (2012).
35. M. Ender, J. Joos, T. Carraro, and E. Ivers-Tiffée, *Electrochem. commun.*, **13**, 166 (2011).
36. Andrzej Lasia, *Electrochemical Impedance Spectroscopy and its Applications*, p. 1–117 (2004).
37. C. H. Kim, S. I. Pyun, and J. H. Kim, *Electrochim. Acta*, **48**, 3455 (2003).
38. J.-B. Jorcin, M. E. Orazem, N. Pébère, and B. Tribollet, *Electrochim. Acta*, **51**, 1473 (2006).
39. M. Ender, A. Weber, and E. Ivers-Tiffée, *Electrochem. commun.*, **34**, 130 (2013).
40. C.-W. C. Wang, A. M. Sastry, K. A. Striebel, K. Zaghib, and A. Marie, *J. Electrochem. Soc.*, **152**, A1001 (2005).
41. W. H. Mulder, J. H. Sluyters, T. Pajkossy, and L. Nyikos, *J. Electroanal. Chem. Interfacial Electrochem.*, **285**, 103 (1990).
42. M. Eikerling and A. A. Kornyshev, *J. Electroanal. Chem.*, **475**, 107 (1999).
43. Freudenberg, *Prod. Specif. Sheet* (2015).
44. J. Cannarella and C. B. Arnold, *J. Power Sources*, **226**, 149 (2013).
45. Celgard, *Prod. Specif. Sheet* (2014).
46. C. H. Chen, J. T. Vaughey, A. N. Jansen, D. W. Dees, A. J. Kahaian, T. Goacher, and M. M. Thackeray, *J. Electrochem. Soc.*, **148**, A102 (2001).
47. K. Zaghib, A. Mauger, J. B. Goodenough, F. Gendron, and C. M. Julien, *Chem. Mater.*, **19**, 3740 (2007).
48. M. Gaberscek, J. Moskon, B. Erjavec, R. Dominko, and J. Jamnik, *Electrochem. Solid-State Lett.*, **11**, A170 (2008).
49. J. N. Illig, PhD Thesis, Karlsruhe (2014).
50. B. Tjaden, S. J. Cooper, D. J. L. Brett, and D. Kramer, *Nanotechnology, Sep. Eng.*, **12**, 44 (2016).

4.2 Validation and Comparison with 3D Tomography

In this section the article *Tortuosity of Battery Electrodes – Validation of Impedance-Derived Values and Critical Comparison with 3D Tomography*[69] is presented, which was submitted in December 2017 and published in the peer-reviewed Journal of the Electrochemical Society in February 2018. Parts of the article were presented as Paper 268 at the 232nd meeting of The Electrochemical Society in National Harbor (USA) in October 2017.

To address the reason for the observed discrepancy between tortuosities from EIS and X-ray tomography,[41] further investigations were conducted. On the one hand all necessary assumptions for the originally introduced EIS based tortuosity determination technique were checked theoretically and experimentally. Previously it was assumed that a) the electrical resistance of the porous electrode can be neglected and b) the ionic resistance obtained from the transmission line model depends on the *real* tortuosity of the porous medium. Simulation of a generalized transmission line model equivalent circuit and a systematic variation of the electrical to ionic resistance contributions allowed to demonstrate the validity range of the introduced method. We show that correct ionic resistance values are obtained from the Nyquist plots if the electrical resistance is two orders of magnitude smaller than the ionic resistance in the porous electrode, which may be tuned by varying the salt concentration. Furthermore we conclude that repeat measurements of the same electrode using a range of electrolyte concentrations (10 mM to 1 M), and thus conductivities, allows to check for electrical resistance effects. Only for negligible electrical resistance the tortuosities obtained from experiments with different salt concentrations should remain constant. To prove the second assumption, namely the relation of the ionic resistance to the real tortuosity of the system, we apply the EIS method to a macroscopic setup of known tortuosity, here a dense packing of spherical ball bearings, for which the Bruggeman relation (Eq. 4.1) is valid. The tortuosity found from the ionic resistance of the transmission line model (1.56) agrees very well with the prediction of the Bruggeman relation (1.60 - 1.62) and establishes the EIS tortuosity method.

As a second part of the study we investigate the same electrodes using both approaches, EIS and X-ray tomography, which allows for a direct comparison of observed tortuosity values. In agreement with the literature, the EIS based tortuosities were found a factor of ≈2 larger than the X-ray tomography values. We argue that the finite resolution of the X-ray tomographs (here 325 nm voxel size) make it impossible to resolve the polymeric binder and conductive additive phases which on the other hand are likely to influence the tortuosity. To demonstrate this hypothesis we prepare electrodes with two different binder contents (1.5 % and 10 %) which, however, still present an overall small volume fraction. Although for these electrodes the overall composition only changed slightly (by 8.5 %), so that by means of X-ray tomography, as the binder cannot be resolved, similar structures would be obtained, we find large differences in EIS tortuosities (2.7 and 5.0 respectively). In a further study we build on this indication and study the influence of the binder on the tortuosity of porous electrodes in detail (Section 4.3).

Author Contributions

J.L. investigated the validity of the simplified transmission line model analytically. All electrochemical measurements were performed by A.E. and J.L. and were analyzed by J.L. X-ray tomography was done by Patrick Pietsch and analyzed by M.E. The manuscript was written by J.L. and edited by H.G. All authors discussed the data and commented on the results and the manuscript.

Tortuosity of Battery Electrodes: Validation of Impedance-Derived Values and Critical Comparison with 3D Tomography

Johannes Landesfeind,[1,*,z] **Martin Ebner,**[2] **Askin Eldiven,**[1] **Vanessa Wood,**[2,**] **and Hubert A. Gasteiger**[1,***]

[1]*Chair of Technical Electrochemistry, Department of Chemistry and Catalysis Research Center, Technical University of Munich, Munich, Germany*
[2]*Department of Information Technology and Electrical Engineering, ETH Zurich, Zurich, Switzerland*

Tortuosity values of porous battery electrodes determined using electrochemical impedance spectroscopy in symmetric cells with a non-intercalating electrolyte are typically higher than those values based on numerical analysis of 3D tomographic reconstructions. The electrochemical approach assumes that the electronic resistance in the porous coating is negligible and that the tortuosity of the porous electrode can be calculated from the ionic resistance determined by fitting a transmission line equivalent circuit model to the experimental data. In this work, we validate the assumptions behind the electrochemical approach. First, we experimentally and theoretically investigate the influence of the electronic resistance of the porous electrode on the extracted ionic resistances using a general transmission line model, and provide a convenient method to determine whether the electronic resistance is sufficiently low for the model to be correctly applied. Second, using a macroscopic setup with known tortuosity, we prove that the ionic resistance quantified by the transmission line model indeed yields the true tortuosity of a porous medium. Based on our findings, we analyze the tortuosities of porous electrodes using both X-ray tomography and electrochemical impedance spectroscopy on electrodes from the same coating and conclude that the distribution of the polymeric binder phase, which is not imaged in most tomographic experiments, is a key reason for the underestimated tortuosity values calculated from 3D reconstructions of electrode microstructures.
 [DOI: 10.1149/2.0231803jes]

Manuscript submitted December 28, 2017; revised manuscript received January 26, 2018. Published February 10, 2018.

In commercially relevant lithium ion battery cells operating at high currents or low temperatures and/or cells with thick and low porosity electrodes (i.e., electrodes with high areal capacity and high volumetric energy density), the ionic transport in the electrolyte throughout the thickness of the porous electrode becomes limiting, leading to the buildup of excessive electrolyte concentration gradients across the thickness of the electrode. Concentration gradients not only lead to increased overpotentials and thus lower accessible capacities, but also play an important role in battery aging caused by lithium plating reactions at the graphite anode/separator interface.[1] Along with the intrinsic transport parameters of the liquid electrolyte, the morphological properties of a porous electrode, quantified by the parameters porosity and tortuosity, are key to understanding the buildup of concentration gradients across the electrode thickness and the resulting performance limitations of porous electrodes.

In the battery community, there are currently two commonly used approaches to obtain values for the tortuosity of porous electrodes; however, they yield different results. One is based on numerical diffusion simulations on 3D reconstructions of the electrode obtained using X-ray (XTM) or focused ion beam scanning electron microscopy (FIB SEM) tomography.[2,3] The other approach is based on electrochemical impedance spectroscopy (EIS) measurements of the electrodes in a symmetric cell configuration.[4–6] Reported tortuosity values from the EIS method consistently yield larger tortuosity values compared to the ones reported from the numerical 3D approach.[5]

To obtain tortuosities of porous electrodes from impedance spectra of symmetric cells, it is assumed that a) the electronic resistance of the solid phase of the porous electrode is negligible, and, b) that the ionic resistance determined from fitting a transmission line model equivalent circuit to the impedance data represents the correct electrode tortuosity values. In this work, we investigate the validity of these two assumptions and then proceed to analyze the origin of the discrepancy between the tortuosity values derived from 3D reconstructions based on X-ray tomography compared to EIS-derived values.

Validation of the first assumption is important because the simplified transmission model used to analyze the EIS assumes electronic resistances are negligible. While for some electrodes, such as graphite, it is reasonable to assume good electronic conductivity, for cathodes with active materials having low electronic conductivity (e.g., LNMO ($LiNi_{0.5}Mn_{1.5}O_4$)), it is unclear whether the electronic resistance contribution within the electrode is negligible. We therefore use a general transmission line model to study the influence of the electronic conductivity of an electrode on the measured ionic conductivity of the electrolyte within the electrode pores and propose how to approach measuring the tortuosity of electrodes with unknown electronic conductivity via EIS.

To validate the second assumption that one can link the measured ionic resistance to the tortuosity, we apply the EIS method to a system of known tortuosity. Specifically, we construct a macroscopic model of an electrode, consisting of conducting spheres which are densely packed into a cylindrical tube and separated mid-way by a porous separator. We demonstrate that the EIS-derived tortuosity value in the macroscopic setup is indeed identical to the value predicted by the Bruggeman equation.

Finally, to resolve the origin of the observed discrepancy between the tortuosity values derived from 3D reconstructions based on X-ray tomography compared to EIS-derived values, both methods are applied to identical electrodes.

Experimental

Composite electrodes and cells used in this work were prepared and measured as described previously unless stated otherwise below.[5] To show the influence of the binder (Figure 6) a slurry of active material (T311, SGL Carbon, 3.0 m^2/g, D50 19 µm), PVDF binder (Kureha KF 1100) and NMP (Sigma Aldrich, anhydrous, 99.5%) was prepared in a planetary mixer (Thinky ARV-310) and doctor-blade coated on a copper current collector foil (MTI, 9 µm). All components were simultaneously loaded and mixed at 2000 rpm for 5 min. A 1:1 (by weight) mixture of ethylene carbonate (EC, Sigma Aldrich, anhydrous, 99%) and diethyl carbonate (DEC, Sigma Aldrich, anhydrous, >99%), was used as a solvent for the self-prepared electrolytes containing tetrabutylammonium perchlorate ($TBAClO_4$, Sigma Aldrich,

*Electrochemical Society Student Member.
**Electrochemical Society Member.
***Electrochemical Society Fellow.
zE-mail: j.landesfeind@tum.de

≥99.0%) salt. These graphite electrodes had a porosity of ε = 48%, a thickness of t = 90 μm, and an areal capacity of ∼3 mAh/cm^2 (8.6 mg/cm^2). Graphite, NCA, and NMC ($Li_1Ni_{0.33}Mn_{0.33}Co_{0.33}O_2$) electrodes for the comparison of EIS and XTM tortuosities were obtained from Custom Cells (specifications in Table II).

A turn-key conductivity sensor (LF 1100+, SI Analytics, with custom made ground glass fitting) with a built-in temperature sensor was used to measure the conductivity of the used self-mixed electrolytes at 25°C (Sigma Aldrich). Symmetrical Swagelok type T-cells (spring-compressed to ≈1 bar) were built outside the glove box using two porous glass fiber separators (binder free glass microfiber 691, thickness 200 μm, >90% porosity, VWR), then transferred into a temperature controlled climate chamber (25°C, Binder), and the impedance spectra were recorded around OCV after a resting period of at least 12 h in a frequency range of 200 kHz to 0.1 Hz with a 20 mV perturbation.

Effect of the Electronic Resistance in a Porous Electrode

First, we evaluate under which conditions the electronic resistance contributions in a porous electrode can be neglected when determining the electrode tortuosity from EIS, which is the assumption behind the use of the simplified transmission line model.[5]

To evaluate whether this assumption is valid for porous electrodes, we consider the general formulation of the transmission line model,[7] where the electronic resistance in the solid phase and the ionic resistance in the liquid electrolyte phase are considered, whereby both contributions impact the characteristic 45° mid-frequency section of the impedance in the associated Nyquist plot. Adopting the nomenclature of our previous work, the general transmission line model for a porous electrode ($Z_{El.}$) can be described by[7]

$$Z_{El.} = Z_{||} + Z^* \frac{1 + 2 \cdot p \cdot s\left[\sqrt{1 - \tanh(\nu)^2} - 1\right]}{\tanh(\nu)} \quad [1]$$

with

$$Z_{||} = \frac{Z_1 \cdot Z_2}{Z_1 + Z_2} \quad [2]$$

$$Z^* = \sqrt{(Z_1 + Z_2) \cdot Z_S} \quad [3]$$

$$p = \frac{Z_2}{Z_1 + Z_2} \quad [4]$$

$$s = \frac{Z_1}{Z_1 + Z_2} \quad [5]$$

$$\nu = \sqrt{\frac{Z_1 + Z_2}{Z_S}} \quad [6]$$

Here, Z_1, Z_2, and Z_S are the impedances of the electron conducting solid phase of the electrode ($Z_1 \equiv R_{El.}$), of the ionically conducting electrolyte phase within the pores of the electrode ($Z_2 \equiv R_{Ion}$), and of the solid/electrolyte surface impedance within the electrode Z_S. In general, the surface impedance element Z_S is described by an *R/Q* element, composed of the constant phase capacitance (Q_S) and the charge transfer resistance (R_{CT})

$$Z_S = \frac{R_{CT}}{R_{CT} \cdot (i\,\omega)^\gamma Q_S + 1} \quad [7]$$

with the angular frequency ω and the constant phase exponent γ. If no charge transfer reactions occur ($R_{CT} \rightarrow \infty$), only the capacitive coupling remains and Eq. 7 becomes (compare also Ref. 5)

$$Z_S = \frac{1}{(i\,\omega)^\gamma Q_S} \quad [8]$$

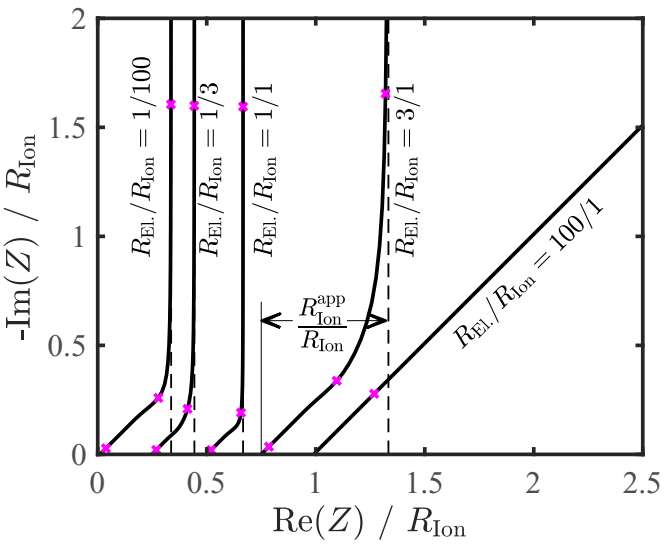

Figure 1. Simulated Nyquist plots (10 MHz to 1 Hz) of the general transmission line model (Eq. 1) for ratios of electronic to ionic resistances ($R_{El.}/R_{Ion}$) of 1/100 to 100/1 (indicated by the labels in the figure), whereby the axes are normalized to the ionic resistance of the porous electrode (R_{Ion}). Here, the absence of charge transfer reactions is assumed ($R_{CT} = \infty$), so that Z_S in Eq. 1 is described by Eq. 6, using an ideal capacitive behavior ($\gamma = 1$) and Q_S = 1 mF. Magenta crosses mark the frequencies 100 kHz, 1 kHz, and 100 Hz; dashed lines represent the extrapolation of the low-frequency capacitive behavior to the real axis (x-axis). The difference in x-axis intercepts of the solid lines (modeled impedance response) and the dashed black lines for each resistance ratio corresponds to 1/3 of the apparent ionic resistance (R_{Ion}^{app}).

Eq. 1 reduces to the simplified transmission line model (see Eq. 11 in Ref. 5) only if the electronic resistance ($R_{El.} \rightarrow 0$) is insignificant and if no charge transfer reactions are possible ($R_{CT} \rightarrow \infty$). For the simplified transmission line model, plotting the imaginary versus the real impedance in a Nyquist plot, one finds that the difference between the real axis (x-axis) intercept of the 45° mid-frequency section and between the x-axis intercept of the extrapolated low-frequency branch is equal to 1/3 of the ionic resistance (R_{Ion}).[5,8] Only under these conditions does the true ionic resistance of the electrolyte within the porous electrode result from the above described Nyquist plot analysis.

On the other hand, if these conditions are not fulfilled, the apparent ionic resistance analogously obtained from the Nyquist plot (R_{Ion}^{app}) is different from the true R_{Ion}-value, and an accurate determination of the tortuosity is only possible if the electronic resistance is known. To evaluate the influence of the electronic resistance contribution ($R_{El.}$) on the apparent ionic resistance (R_{Ion}^{app}) and the error this introduces into the calculated tortuosity values, we simulated Eq. 1 for varying ratios of the ionic to electronic resistances ($R_{El.}/R_{Ion}$). For the sake of simplicity, the absence of charge transfer reactions is assumed (i.e., $R_{CT} = \infty$), which is fulfilled when non-intercalating electrolytes are used.[5] In this case, the surface impedance elements Z_S of the general transmission line model (Eq. 1) are described by constant phase elements (Eq. 6). For simplicity, we use a constant phase exponent $\gamma = 1$ (ideal capacitive behavior) for the following analysis, but the same results would be obtained for other γ-values.

The simulated Nyquist plots are rescaled in terms of the real ionic resistance and plotted in Figure 1 for ionic to electronic resistance ratios of 100/1 to 1/100. For all ratios, the characteristic transmission line model behavior can be observed, i.e., a distinct 45° high/mid-frequency apparent ionic resistance section, followed by the capacitive behavior at low frequencies, with the phase angle approaching 90° (vertical line on Nyquist plot). For each spectrum, two characteristic resistances can be extracted from the Nyquist plots: a) the apparent high frequency resistance R_{HFR}^{app} from the intercept of the modeled high-frequency impedance with the x-axis, and, b) the low-frequency

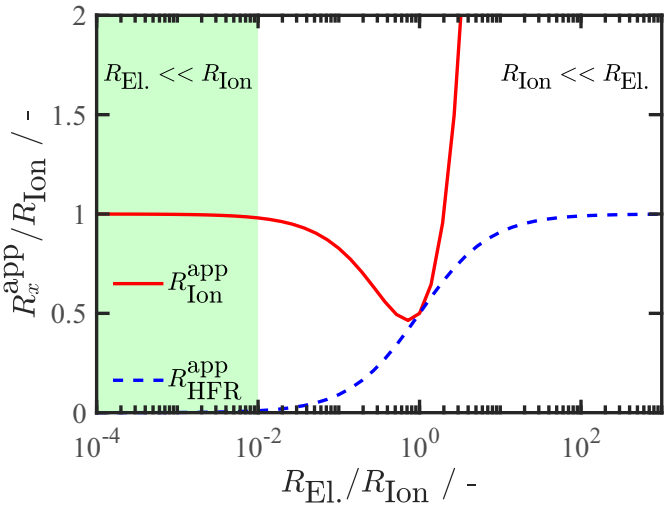

Figure 2. Apparent high frequency resistance (blue line) and apparent ionic resistance (red line) of the simulated Nyquist plots resulting from a general transmission line model (Eq. 1) for various ratios of electronic to ionic resistances ($R_{El.}/R_{Ion}$), normalized to the ionic resistance of the electrolyte in the pores of the electrode. The y-axis values of R_x^{app}/R_{Ion} represent R_{HFR}^{app}/R_{Ion} in case of the high frequency resistance (blue line) and R_{Ion}^{app}/R_{Ion} in case of the ionic resistance of the electrolyte (red line). Only for $R_{El.} \ll R_{Ion}$, the apparent ionic resistance and the apparent high frequency resistance approach their real values (indicated by green region).

resistance, represented by the x-axis intercept of the extrapolated low frequency impedance response (indicated by the dashed lines for each spectrum). The difference between the latter and R_{HFR}^{app} yields 1/3 of the apparent ionic resistance R_{Ion}^{app}.

We note that the Nyquist plots shown in Figure 1 are based on a general transmission line model only, which does not include a separate serially connected resistor, which would normally be added to represent electrolyte and cell contacting resistances. Therefore, the change of the apparent high frequency resistance is merely a result of the chosen $R_{El.}/R_{Ion}$-ratios, while by the conventional definition of the high frequency resistance in battery research, the real high frequency resistance should be zero (i.e., $R_{HFR}^{app} = 0$), as in the here used general transmission line model the separator and cell contacting resistances were omitted and thus effectively set to zero.

As shown by the left-most line in Figure 1, the apparent high frequency resistance approaches its real value of 0 Ohm only when the electronic resistance is small compared to the ionic resistance (i.e., $R_{El.}/R_{Ion} = 1/100$). Similarly, only under these conditions the apparent ionic resistance corresponds to the real ionic resistance, indicated by the fact that the x-axis intercept of the $R_{El.}/R_{Ion} = 1/100$ line in Figure 1 amounts to $Re(Z)/R_{Ion} = 0.33$. The deviation from this idealized case as the ratio of $R_{El.}/R_{Ion}$ increases, reflecting an increasingly important contribution from electronic resistances in the electrode, is illustrated in Figure 2, plotting the R_{Ion}-normalized apparent resistance vs. $R_{El.}/R_{Ion}$ for both the apparent high frequency resistance value and the apparent ionic electrolyte resistance in the electrode pores based on the general transmission line model. As shown at the left side of Figure 2, for $R_{El.}/R_{Ion} < 10^{-2}$ (green highlighted region), the apparent high frequency resistance (blue dashed line) approaches the real high frequency resistance of 0 Ohm and the apparent ionic resistance approaches its real value (i.e., $R_{Ion}^{app}/R_{Ion} = 1$). With an increasing $R_{El.}/R_{Ion}$ ratio, the apparent high frequency resistance increases (blue line, Figure 2) while the apparent ionic resistance initially decreases (red line). For $R_{El.}/R_{Ion} = 1/1$, the total charge at high frequencies is transported effectively through two parallel resistors (ionic and electronic) of the same value, resulting in an apparent high frequency resistance of $R_{HFR}^{app} = 0.5 \cdot R_{El.}$ (blue line), i.e., 50% of the electronic resistance of the electrode is added to the measured (apparent) high frequency resistance. At the same time, the apparent ionic resistance decreases to $R_{Ion}^{app} = 0.5 \cdot R_{Ion}$ (red line), so that the apparent ionic resistance determined from the Nyquist plot is only half the value of the true ionic resistance. For $R_{El.}/R_{Ion} \gg 1$, the apparent high frequency resistance approaches the ionic resistance, indicating that essentially all charges are now carried by ionic conduction, while the apparent ionic resistance approaches 1/3 of the electronic resistance (for $R_{El.}/R_{Ion} = 100/1$ the x-axis intercept of the low frequency extrapolation yields a value of ~33 Ω, not visible in Figure 1).

For the determination of the tortuosity (τ) of porous electrodes, the conductivity of the electrolyte (κ), the porosity (ε) of the electrode (easily determined by electrode thickness (t) and loading measurements) and the effective ionic resistance of the electrolyte within the pores of the electrode (R_{Ion}) are required (see Ref. 5).

$$\tau = \frac{R_{Ion} \cdot A \cdot \varepsilon \cdot \kappa}{t} \quad [9]$$

While electrochemical impedance spectroscopy (EIS) is a convenient tool to determine R_{Ion} via a simplified transmission model, the analysis depicted in Figure 2 shows precise R_{Ion}-values can only be obtained for $R_{El.}/R_{Ion} < 10^{-2}$ (green highlighted region) and that R_{Ion} would have an error of up to ~20% for $R_{El.}/R_{Ion}$ between 10^{-2} and 10^{-1}. For this reason, electrolytes with conductivities as low as possible should be used for the experimental determination of R_{Ion} via a simplified transmission line analysis. At the same time, higher electrolyte conductivities will lead to a different R_{Ion}^{app}/R_{Ion} value *only*, if the electronic contribution is non-negligible (i.e., if $R_{El.}/R_{Ion} \gg 10^{-2}$). As a consequence, if $R_{Ion}^{app} \cdot \kappa$ for identical electrodes remains constant for low (millimolar salt concentrations) and high (molar salt concentrations) electrolyte conductivities, the electronic resistance of the electrode must be negligible, as this condition is only fulfilled in the $R_{El.}/R_{Ion}$–region where R_{Ion}^{app}/R_{Ion} vs. $R_{El.}/R_{Ion}$ is constant, i.e., at $R_{El.}/R_{Ion} < 10^{-2}$ (see red line in the green highlighted region in Figure 2). Demonstration of the invariance of ($R_{Ion} \cdot \kappa$) over a wide range of electrolyte conductivities is thus a proof that electronic resistance contributions are negligible and that the extracted R_{Ion}^{app}-values indeed correspond to the true R_{Ion}-value.

The observant reader might be surprised by the diverging behavior of R_{Ion}^{app}/R_{Ion} for dominating electronic resistances (i.e., for $R_{El.} \gg R_{Ion}$). If one imagines this limiting case to be corresponding to the model of a separator, a characteristic impedance response of a pure capacitor would be expected (straight vertical line in Figure 1), shifted in the Nyquist plot by the ionic resistance of the separator. Although this might seem to contradict Figure 1 which still shows a 45° section as well as Figure 2, the capacitive behavior in such a separator cell only stems from the double layer capacitance at the metallic current collector, an interface not taken into account in the transmission line model described above. Further generalization of Eq. 1 allows to include the current collector/coating interface (compare Ref. 7), for which indeed the expected R-C behavior will be observed in the case of a dominating electronic resistance and a negligible double layer capacitance at the surface of the porous material. Because the focus of this work is on the understanding of the influence of the electronic to ionic resistance ratio in a Nyquist plot and for the sake of simplicity, the authors refrain from including interface effects into the above analysis. For the interested reader we note that further generalization will lead to the Nyquist plots in Figure 1, approaching the R-C behavior with the normalized high frequency resistance approaching unity, i.e., the ionic resistance of the porous medium. Correspondingly R_{Ion}^{app}/R_{Ion} in Figure 2 (red line) would not diverge but approach 0 (for $R_{EL.}/R_{Ion} \gg 1$). Up to ionic to electronic resistance ratios of 1/1 the analysis of the transmission line model as conducted above, as well as the generalized version including the contact element to the current collector yield identical results. I.e., in both cases constant R_{Ion}^{app}/R_{Ion} values can only be obtained for negligible electronic resistances (green highlighted region in Figure 2).

In our previous work, we indeed demonstrated the invariance of the measured R_{Ion}^{app}-values and thus the determined electrode tortuosity for porous graphite electrodes, varying the electrolyte conductivity range

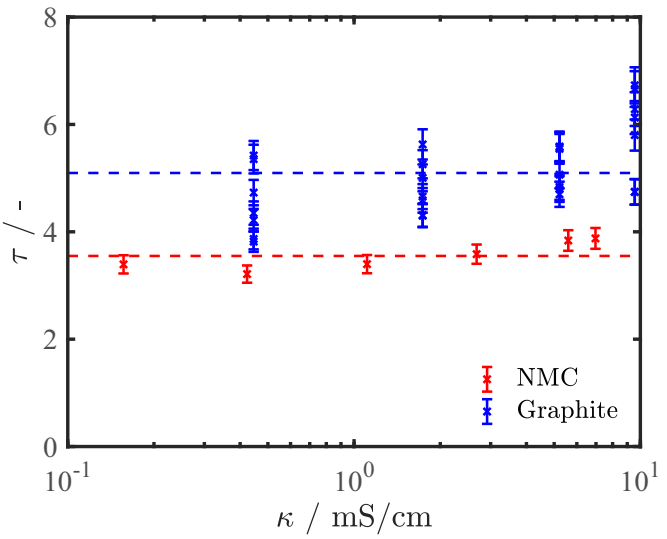

Figure 3. Tortuosity values obtained from simple transmission line model fits of the impedance response of symmetric T-cells using electrolytes with different conductivity. For graphite electrodes (blue symbols; same as in Figure 14 of Ref. 5, with $\varepsilon = 43\%$, $t = 58$ µm, and an areal capacity of 2.1 mAh/cm^2 (corresponding to 6 mg/cm^2), see Ref. 5 for details on electrode preparation and composition), EC:DMC (1:1 w:w) with 10–700 mM $TBAClO_4$ (conductivities from 0.46 – 9.56 mS/cm) was used. For NMC electrodes (red symbols; from Custom Cells with $\varepsilon = 42\%$, $t = 72$ µm, 86% active material fraction and an areal capacity of 2 mAh/cm^2 (corresponding to 13.8 mg/cm^2)), EC:DEC (1:1 w:w) with ∼4 mM - 1 M $TBAClO_4$ (conductivities from 0.156–6.97 mS/cm). The mean tortuosity values for each electrode are indicated by dashed lines. Error bars indicate a 5% uncertainty from fitting of the spectra and the conductivity error of the electrolytes.

from 0.45 mS/cm to 9.6 mS/cm (re-plotted in Figure 3, blue symbols using the data in Figure 14 of Ref. 5). This was certainly expected, since the electronic conductivity of graphite electrodes is on the order of > S/cm,[9] so that $R_{El.}/R_{Ion}$ quite clearly is $<10^{-2}$, However, for cathode electrodes based on oxide active materials with typically rather low electronic conductivities, e.g., LNMO,[10] and particularly for cathodes with a low amount of conductive carbon additive, the electronic resistance might not be negligible anymore and the measured value of $(R_{Ion} \cdot \kappa)$ could change when switching from low to high conductivity electrolytes. Such a variance of the apparent value of $(R_{Ion} \cdot \kappa)$ obtained by impedance analysis when changing the electrolyte conductivity would be a clear indication that the electronic resistance of the electrode cannot be neglected, and that the simple transmission line model would not yield the correct R_{Ion}-value (i.e., $R_{Ion}^{app} \neq R_{Ion}$). To investigate if the electronic contribution becomes significant for electrodes of unknown electronic conductivity, we measured the tortuosity of compressed NMC cathodes (from Custom Cells), using electrolytes based on EC:DEC (1:1 w:w) with different concentrations of $TBAClO_4$ with conductivities ranging from 0.156 mS/cm (∼4 mM $TBAClO_4$) to 6.97 mS/cm (∼1 M $TBAClO_4$). The obtained tortuosity values, depicted in Figure 3, are proportional to $(R_{Ion}^{app} \cdot \kappa)$ and take slight thickness and porosity variations between the cells into account. Tortuosity values calculated from the measured $(R_{Ion}^{app} \cdot \kappa)$ values for the NMC cathodes (red crosses) and the previously reported graphite anodes[5] (blue crosses) are essentially constant for electrolyte conductivities varying by a factor of ∼45 (0.156 to 6.97 mS/cm). The invariance of the NMC electrode tortuosity values obtained from a simple transmission line model analysis as the electrolyte conductivity is changed over ∼1.8 decades (Figure 3) demonstrates that for both types of electrodes the $R_{El.}/R_{Ion}$-ratio must be below ∼1/100, i.e., that it must lie within the green region of Figure 2. The resulting tortuosity values of the cathodes with spherical NMC particles are lower (3.6 ± 0.3) compared to the anisotropic graphite platelets (5.1 ± 0.8), which is in accord with previous observations.[5,11]

This analysis of the impedance response of porous electrodes over nearly two orders of magnitude in electrolyte conductivity constitutes a rigorous method to validate whether the R_{Ion}^{app}–values obtained from a simple transmission line model correspond to the true R_{Ion}-values (i.e., whether $R_{El.}$ contributions are indeed negligible). Experimentally, a further reduction of the electrolyte conductivity by reducing the $TBAClO_4$ concentration below 5 mM may lead to increased errors, as small impurities in the cell/porous electrode then could alter the effective ionic conductivity during the measurement. Similarly, the highest conductivity with typical battery electrolyte solvents is limited to ∼20 mS/cm. It should be noted that analogous to the experimentally determined R_{Ion}^{app}/R_{Ion} term (here represented in terms of tortuosity), the experimental R_{HFR}^{app} values should also be invariant when changing electrolyte conductivity under conditions where $R_{El.}$ can be ignored; an increase of R_{HFR}^{app} with increasing electrolyte conductivities would also indicate that the electronic resistance contribution starts to play a role (see blue line in Figure 2). However, changes in R_{HFR}^{app} with changing electrolyte conductivities can only be analyzed quantitatively if the cell compression can be controlled precisely (in the case of soft glass fiber separators) or if reasonably incompressible separators are used, so that the high frequency resistance contribution from the separator will be identical for each of the assembled symmetric cells.

In summary, our analysis of the general transmission line model shows that the electronic resistance can influence the apparent high frequency and the apparent ionic resistance obtained from EIS. These theoretical considerations demonstrate that the best condition to obtain the true high frequency resistance and the true ionic resistance is to use an electrolyte with very low conductivity, so that the ionic resistance dominates. Using graphite and NMC electrodes, we showed that if the product of electrolyte bulk conductivity times the apparent ionic resistance d $R_{Ion}^{app} \cdot \kappa$ (or $R_{HFR}^{app} \cdot \kappa$) is independent over a wide range of bulk electrolyte conductivities (tunable via salt concentration), the electronic resistance contributions are negligible. If the electronic resistance was non-negligible, it could be because the amount of conductive carbon additive is either insufficient or that it is poorly dispersed.

While we have shown above that for negligible electronic resistances in the electrode, the correct ionic resistance within the porous electrode can be extracted from the analysis of the impedance spectra obtained from symmetric cells, it yet remains to be proven that this ionic resistance value can be used to determine the real tortuosity of a porous electrode. Therefore, in the next section, we compare the tortuosity obtained by impedance analysis with the known tortuosity of an arrangement of spherical particles.

Transmission Line Equivalent Circuit Model Validation Using a Macroscopic Setup with Known Tortuosity

To validate that the tortuosity obtained from the above described EIS method is correct, we study a system with known tortuosity. For a porous medium of spherical particles, the mathematically derived Bruggeman relation allows the calculation of the tortuosity from the porosity of the porous medium[12]

$$\tau = \varepsilon^{-0.5}. \quad [10]$$

In order to apply the EIS method to a packing of spherical particles, a macroscopic symmetric cell setup is built, utilizing stainless chromium steel (type 1.3505) ball bearings of 1 mm diameter (TIS Wälzkörpertechnologie GmbH, Gauting, Germany) filled into a glass tube to produce a well-defined porous medium of densely packed spheres. As shown in the previous section, a key requirement for the EIS method to be applicable is that the electronic resistance in the porous medium be much smaller than its ionic resistance. For steel ball bearings between two current collectors and compressed using a manual clamp, we find an electronic resistance of 8 Ω, which is two orders of magnitude lower than the measured ionic resistance of 790 Ω (see below).

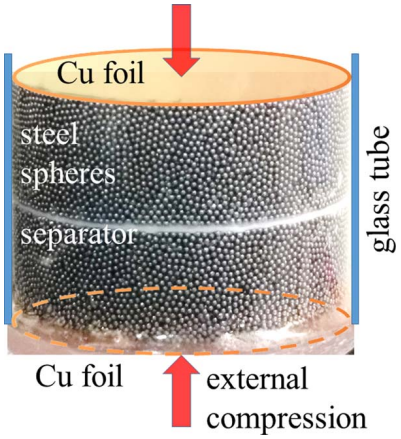

Figure 4. Photograph of the macroscopic symmetric cell setup composed of densely packed spherical steel ball bearings that serves as an idealized porous electrode with known tortuosity. The cell is compressed using a mechanical clamp to ensure a negligible electronic resistance compared to the electrolyte resistance. Experimental parameters of the macroscopic cell setup are given in Table I.

To perform the EIS measurement, the ball bearings are contacted at the top and at the bottom with two copper foil current collectors and are separated in the middle by a stack of glass fiber separators (see Figure 4), creating effectively two stainless steel ball bearing electrodes. The same mechanical pressure is then applied to ensure low electronic resistivity. EC:DMC:DEC with ∼30 mM $TBAClO_4$ is used as an electrolyte. The salt concentration is selected such that the ionic conductivity which was determined directly before the experiment, is small compared to the electronic conductivity in the porous medium. Table I lists the specifications for this experiment.

The porosity of the stainless steel ball bearing porous electrodes (SBBPEs) can be obtained from the full geometric volume of the electrodes and either the volume of the electrolyte phase or the volume of the steel ball bearings. With the measured mass of the electrolyte and steel spheres for each of the stainless steel ball bearing electrodes and their respective densities (see Table I), we find porosities of $\varepsilon = 38\%$ and 39%, resulting in tortuosities of $\tau = 1.62$ and 1.60, according to the Bruggeman relation (Eq. 10).

In analogy to the EIS based tortuosity determination for porous lithium ion battery electrodes,[5] we record an impedance spectrum (Figure 5) and fit it with the simplified transmission line model to extract the ionic resistance of the symmetric cell. An equivalent circuit similar to our previous work was used, i.e., a high frequency resistance from the separator and a serially connected transmission line model for which the electronic resistance was neglected (justified by the electrode compression and the low ionic conductivity, see Table I). From the macroscopic model electrodes composed of densely packed spheres and measured in a symmetric cell configuration, an ionic

Table I. Parameters of the macroscopic symmetric cell setup depicted in Figure 4.

Parameter	Value
thickness of one porous electrode	1.9 cm
radius of the electrode	2.64 cm
mass of electrolyte per electrode	16.8 g
mass of steel ball bearings per electrode	200.4 g
density of electrolyte*	1.065 g/cm^3
density of steel	7.9 g/cm^3
electrolyte bulk conductivity at $T_{exp.}$	0.892 mS/cm

*Measured by weighing 10 ml of electrolyte (∼30 mM $TBAClO_4$ in EC:DMC:DEC) directly before the experiment.

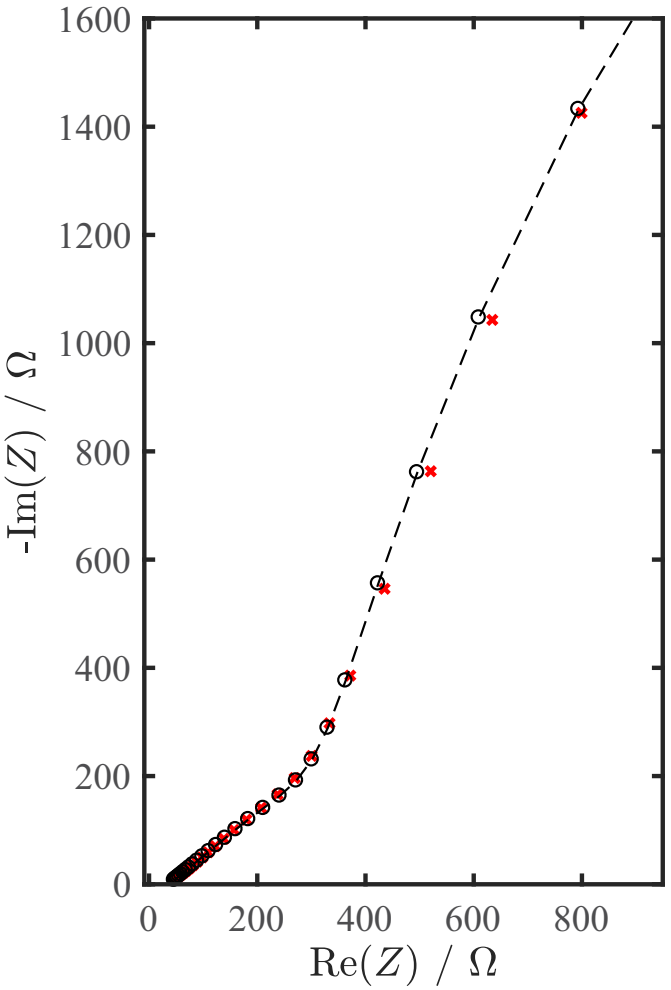

Figure 5. Measured (red crosses) and fitted (black circles) impedance spectrum of the macroscopic model electrodes composed of densely packed spheres shown in Figure 4, using an excitation amplitude of 10 mV in the frequency range from 200 kHz to 20 mHz (the fit and plot range are taken from 1 kHz to 30 mHz). The dashed line serves as guide to the eye connecting the measured data points. The fitted values are: $R_{HFR} = 37\ \Omega$, $R_{Ion} = 790\ \Omega$, $R_{CT} = 10200\ \Omega$, $Q_S = 2.8\ \text{mF} \cdot \text{s}^{(\alpha-1)}\Omega$, and $\alpha = 0.88$, yielding a tortuosity of 1.56 based on the measured electrode thickness (s. Table I) and an average porosity of $\varepsilon = 38.5\%$.

resistance of $R_{Ion} = 790\ \Omega$ for both electrodes is obtained. In this case, a large low-frequency semicircle in the Nyquist plot is observed indicating that the surface impedance elements between the liquid and the solid phase are not described by a constant phase element, but a parallel R_{CT}/Q_S connection. The large charge transfer resistance ($R_{CT} = 10200\ \Omega$) may be caused by minor parasitic reactions between the electrolyte and the stainless steel ball bearings. This, however, does not interfere with an accurate determination of the cell's ionic resistance, as is evident from the pronounced 45° section at high frequencies.

From the ionic resistance $R_{Ion} = 790\ \Omega$, the porosity of $\varepsilon = 38.5 \pm 0.5\%$, the thickness of $t = 1.9$ cm, and a bulk electrolyte conductivity of $\kappa = 0.892$ mS/cm (see Table I), we determine a tortuosity of 1.56 for the stainless steel ball bearing electrode. This experimentally determined value is in excellent agreement with the theoretical prediction of $\tau = 1.60$–1.62 from the Bruggeman relation.

The ∼3% lower experimental value is likely caused by edge effects in our macroscopic setup: while the Bruggeman relation assumes a perfectly homogeneous porosity throughout the porous medium, the porosity of our SBBPEs is slightly lower close to the surrounding glass cylinder walls where the packing is less dense, which effectively

Table II. Comparison of tortuosity values (τ) obtained for the same type of electrodes (Custom Cells) using 3D reconstruction with X-ray tomography (325 nm voxel size) vs. EIS measurements in a symmetric cell configuration. The uncertainty from the 3D reconstruction is a result of the threshold greyscale value for binarization. Values in brackets indicate the number of repeat measurements for calculation of the EIS-based mean tortuosity value and its standard deviation.

Electrode type	Porosity	Coating Thickness	τ from XTM	τ from EIS
NMC, 3.5 mAh/cm^2 / 24.1 mg/cm^2, 86% active material	40%	125 μm	1.77 ± 0.06	3.1 ± 0.3 (4)
NCA, 3.5 mAh/cm^2 / 21.6 mg/cm^2, 90% active material	40%	115 μm	1.73 ± 0.03	4.0 ± 0.05 (2)
graphite, 3.8 mAh/cm^2 / 10.9 mg/cm^2, 96% active material	51%	110 μm	2.18 ± 0.06	3.3 ± 0.05 (2)

reduces the overall measured ionic resistance (and thus the tortuosity) to a small degree.

In summary, the excellent agreement between the theoretically predicted tortuosity and experimentally determined value obtained from the simplified transmission line model equivalent circuit indicates that EIS is a robust method for measuring the tortuosity of porous lithium ion battery electrodes.

Discrepancies Between Tortuosities Obtained from EIS vs. 3D Tomography

Having demonstrated that neither electronic resistances in the porous electrodes nor the chosen equivalent circuit model introduce errors in the EIS determination of the tortuosity and that there is a good agreement between the tortuosity obtained both theoretically and experimentally for the macroscopic model electrodes, we must understand why the EIS-derived tortuosities are generally higher than the tortuosities obtained by performing numerical diffusion simulations on 3D tomography datasets (compare Figure 21 in Ref. 5).

Here we enable direct comparison between the techniques by analyzing the tortuosity of the same porous electrode using both EIS and numerical diffusion simulations on 3D reconstructions of the electrode microstructure. For details about the individual techniques, the reader is referred to the original publications (EIS: Ref. 5, X-ray tomography: Refs. 2,11).

Table II summarizes the tortuosities obtained for NMC, NCA, and graphite electrodes (Custom Cells, Itzehoe, Germany). In the case of the numerically calculated tortuosity, the reported values correspond to the value in the through-plane direction (i.e., the direction perpendicular to the separator and the copper foil). In accordance with the general trend in the literature,[5] even when using the same electrode coatings, a large discrepancy between the tortuosities obtained using both techniques is found (Table II). While XTM-derived tortuosities are in the range of 1.7 to 2.2 for all electrode types, the EIS-derived values are ∼2-fold larger, ranging between 3.1 and 4.0 (the largest discrepancy of a factor ∼2.3 is found for the NCA electrodes).

In the literature it was argued that interactions of the ions with the pore walls, e.g., porous separators, might affect the ionic transport.[13] It is important to note such interactions (i.e., an interaction between the ions and the surface of the solids) in the electrochemical measurements cannot account for the observed factor of ∼2 between EIS and XTM tortuosities. While generally finite interaction times of the ions may reduce the active ionic concentration in the pores of the coating, somewhere on the order of 50% of the ions would have to be lost for ionic transport to explain the difference between EIS and XTM tortuosities. However, as evident from Figure 3, stable EIS tortuosity values are observed from 10 mM to 1 M ion concentrations. For geometrical reasons, only a fraction of the ions from a 1 M electrolyte solution can interact with the limited surface area of a porous coating (∼100 cm^2/cm$^2_{El.}$): e.g., the necessary surface area for half of the ions of a 1 M concentration to be interacting with the pore wall of a 80 μm thick coating of 30% porosity (1.5 μM) would be >2500 cm^2/cm$^2_{El.}$ (conservatively assuming packing of ions without any void space, without solvation shell, and for an ionic radius of 0.3 nm). We conclude that any interactions of ionic species with the solid phase in the coating do not significantly alter the EIS tortuosity values (nor the effective ionic conductivity within the pores).

To explore the origin of the lower XTM-derived tortuosity values, it important to consider the origin of errors in the microstructural parameters. First, to measure statistically-relevant, with thousand particles, it is important to measure a volume on the order 1 mm^3. With this type of setup, it is not possible to resolve the carbon black and the binder which are generally present in the electrodes, so that only the morphology of the micrometer-scale active material particles can be imaged. The errors caused by the limited resolution (0.325 μm in the examples shown in Table II) have been discussed in the literature,[5,14] and in general similarly low XTM-derived tortuosities for graphite anodes have been reported (at an even larger voxel size of 0.56 μm).[15]

High resolution FIB-SEM images actually suggest an inhomogeneous distribution of the conductive carbon/binder phase in the electrode,[16] making it challenging to assume a distribution. Furthermore, the uncertainty of each tortuosity value derived from XTM stems from the choice of the thresholding greyscale value chosen for binarization of the tomographic information into solid and void space; in the case of EIS-derived tortuosities, the standard deviation of repeat measurements is given (the number of repeat measurements is indicated in Table III parentheses).

When high resolution 3D reconstruction techniques are used, higher tortuosities are found, e.g., values ranging from 2 to 7 are reported for MCMB (mesocarbon microbeads) anodes, but in this case the reconstructed volumes (15 μm sized cubes) are likely far too small to be representative for the entire electrode, due to the fact that the spherical MCMB particles already have a diameter of ∼8 μm.[17] Considering these difficulties, it is not surprising that 3D reconstructions of representative coating volumes only yield higher tortuosities, more in agreement with the electrochemical results, if the binder/carbon matrix is added computationally to the active material reconstruction.[18] An entirely different experimental approach is based on measuring the permeation rate of gas along the in-plane direction of an electrode (parallel to the current collector) using a flow-field setup, which also confirms the generally higher tortuosity values obtained by EIS. For example, a tortuosity of ∼6 for a graphite electrode with 30% porosity (50 μm thickness) is reported,[14] which is in good agreement with the EIS-derived tortuosity value of ∼5.5 which have been obtained for similarly compressed graphite electrodes.[5]

We conclude that the binder and carbon black phases are the most likely reason for the underestimation of the tortuosity of porous electrodes. To validate this hypothesis, we prepared anode coatings with graphite (T311, SGL Carbon, 3.0 m^2/g BET, D50 diameter of 19 μm) with different weight percentages of PVDF binder (Kureha KF 1100) in order to determine their tortuosity by EIS. We deliberately chose extreme binder weight percentages of 1.5% (minimum content to prepare stable electrodes) and 10% (highest reasonable content).

Figure 6 shows the Nyquist plots from symmetric T-cells (0.95 cm^2 area) with 10 mM $TBAClO_4$ in EC:DEC (κ = 0.423 mS/cm) for uncompressed graphite electrodes with 1.5% PVDF binder (blue; 109 ± 2 μm coating thickness, 51 ± 0.5% porosity) and with 10% PVDF (red; 85 ± 2 μm coating thickness, 50 ± 0.5% porosity). Two measurements are conducted for each electrode type, and the impedance response is shifted by the high frequency resistance to facilitate comparison. From the given experimental parameters (porosity, thickness, electrolyte conductivity, and area) and the EIS-derived ionic resistances of R_{Ion} = 145 ± 5 Ω and 213 ± 4 Ω, tortuosities of 2.7 ± 0.1 and 5.0 ± 0.2 are obtained for electrodes with 1.5% and

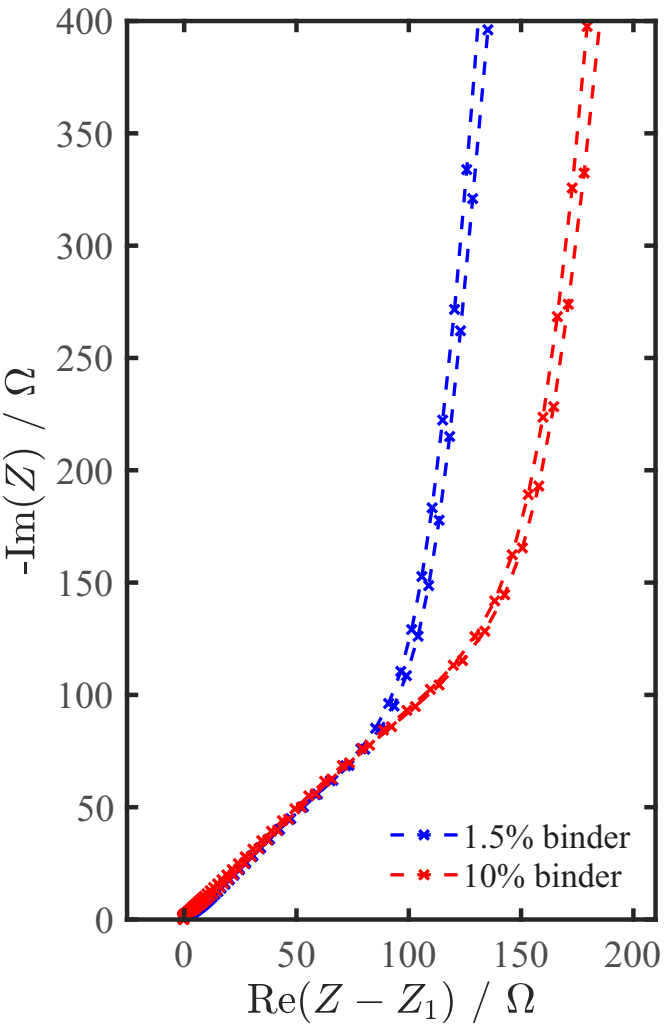

Figure 6. Nyquist plots of nominally identical symmetric T-cells (0.95 cm^2 area) with uncompressed graphite (T311, SGL Carbon, 3.0 m^2/g BET, D50 diameter of 19 μm) electrodes with 1.5% (blue) and 10% (red) PVDF binder (Kureha KF 1100). Measurements were conducted with 10 mM $TBAClO_4$ in EC:DEC (κ = 0.423 mS/cm), using an excitation amplitude of 20 mV in the frequency range from 200 kHz to 100 mHz. The spectra were shifted along the x-axis to the origin for easier comparability.

10% binder respectively. Thus, even though the binder is a small fraction of the coating mass and volume (1% – 5%), it has a pronounced effect on the effective ionic transport properties of the porous electrode and could explain the difference between the tortuosity measured by numerical diffusion of the 3D reconstructions and that measured by EIS.

In summary, this work highlights that tortuosity measured by numerical diffusion of the 3D reconstructions will only be as accurate as the 3D reconstructions themselves, i.e., for a large representative volume and if a high contrast allows to discriminate the binder/carbon matrix from the electrode void volume. Further experimental investigations about the influence of the binder on the electrochemically determined tortuosity for varying electrode compositions have been conducted and will soon be published in a detailed, separate study.

Conclusions

Previously reported tortuosities, determined by electrochemical impedance spectroscopy (EIS) measurements using a symmetrical cell configuration and a non-intercalating electrolyte, were based on the assumptions that the electronic resistance of the electrode is negligible and that ionic transport in the electrolyte phase within the pores of an electrode is represented correctly by a transmission line model. Under these conditions, the electrode tortuosity can be determined from the ionic resistance extracted from the impedance spectrum. In the present work, we validated both assumptions based on theoretical considerations and experiments. Thus, we demonstrated an experimental methodology by which the assumption of negligible electronic resistance contributions to the electrode impedance measured in symmetrical cells with a non-intercalating electrolyte can be verified: the assumption is fulfilled, if the product of the measured ionic resistance times the electrolyte bulk conductivity is independent of the bulk electrolyte conductivity, which can be adjusted by the salt concentration. This was illustrated for typical graphite anodes and NMC cathodes, both of which showed negligible electronic resistance contributions, allowing for the quantification of their tortuosity.

The validity of the transmission line model analysis was furthermore examined for a macroscopic representation of a porous electrode constructed from electronically conducting steel spheres which were densely packed into an electrolyte filled glass cylinder and separated mid-way by a porous separator. The impedance-derived tortuosity value was shown to be essentially identical with the value predicted by the Bruggeman relation, which was derived for this geometry. This unequivocally proves that the EIS-derived tortuosity values are indeed correct, as long as electronic resistance contributions can be neglected, whereby the latter assumption can be examined in a straightforward fashion (see above).

After having validated the accuracy of the EIS method, we investigated the reason for the ∼2-fold lower tortuosities derived from 3D reconstructions based on X-ray tomography compared to EIS-derived values, using identical electrodes cut from the same coating. From electrodes with deliberately chosen low and high binder contents, we conclude that the (at least partially) unresolved binder and conductive carbon phases due to the insufficient resolution of 3D reconstructions is the most likely cause for the pronounced underestimation of electrode tortuosities.

Acknowledgment

J. L. gratefully acknowledges the funding by the BMBF (Federal Ministry of Education and Research, Germany) for its financial support under the auspices of the ExZellTUM II project (grant number 03XP0081). M. E. and V. W. acknowledge the ERC (grant number 680070). Special thanks go to Andreas Ehrl for helpful discussions and Patrick Pietsch for help with X-ray tomography.

ORCID

Johannes Landesfeind https://orcid.org/0000-0003-0333-2185
Vanessa Wood https://orcid.org/0000-0001-6435-0227

References

1. X. G. Yang, Y. Leng, G. Zhang, S. Ge, and C. Y. Wang, *J. Power Sources*, **360**, 28 (2017).
2. M. Ebner, F. Geldmacher, F. Marone, M. Stampanoni, and V. Wood, *Adv. Energy Mater.*, **3**, 845 (2013).
3. J. Joos, T. Carraro, A. Weber, and E. Ivers-Tiffée, *J. Power Sources*, **196**, 7302 (2011).
4. N. Ogihara, S. Kawauchi, C. Okuda, Y. Itou, Y. Takeuchi, and Y. Ukyo, *J. Electrochem. Soc.*, **159**, A1034 (2012).
5. J. Landesfeind, J. Hattendorff, A. Ehrl, W. A. Wall, and H. A. Gasteiger, *J. Electrochem. Soc.*, **163**, A1373 (2016).
6. D. Cericola and M. E. Spahr, *Electrochim. Acta*, **191**, 558 (2016).
7. H. Göhr, in *Electrochemical Applications*, p. 2, ZAHNER-elektrik GmbH & Co. KG (1997).
8. Andrzej Lasia, *Electrochemical Impedance Spectroscopy and its Applications*, Springer, (2014).
9. M. Park, X. Zhang, M. Chung, G. B. Less, and A. M. Sastry, *J. Power Sources*, **195**, 7904 (2010).
10. H. Liu, J. Wang, X. Zhang, D. Zhou, X. Qi, B. Qiu, J. Fang, R. Kloepsch, G. Schumacher, Z. Liu, and J. Li, *ACS Appl. Mater. Interfaces*, **8**, 4661 (2016).

11. M. Ebner, D. W. Chung, R. E. García, and V. Wood, *Adv. Energy Mater.*, **4**, 1 (2014).
12. D. A. G. Bruggeman, *Ann. Phys.*, **416**, 636 (1935).
13. M. F. Lagadec, M. Ebner, R. Zahn, and V. Wood, *J. Electrochem. Soc.*, **163**, A992 (2016).
14. T. DuBeshter, P. K. Sinha, A. Sakars, G. W. Fly, and J. Jorne, *J. Electrochem. Soc.*, **161**, A599 (2014).
15. C. Lim, B. Yan, L. Yin, and L. Zhu, *Energies*, **7**, 2558 (2014).
16. L. Zielke, T. Hutzenlaub, D. R. Wheeler, C. Chao, I. Manke, A. Hilger, N. Paust, R. Zengerle, and S. Thiele, *Adv. Energy Mater.*, 1 (2014).
17. F. Tariq, V. Yufit, M. Kishimoto, P. R. Shearing, S. Menkin, D. Golodnitsky, J. Gelb, E. Peled, and N. P. Brandon, *J. Power Sources*, **248**, 1014 (2014).
18. L. Zielke, T. Hutzenlaub, D. R. Wheeler, I. Manke, T. Arlt, N. Paust, R. Zengerle, and S. Thiele, *Adv. Energy Mater.*, **4**, 1 (2014).

4.3 Binder Influence on Electrode Tortuosity and Performance

In this section the article *Influence of the Binder on Lithium-Ion battery Electrode Tortuosity and Performance*[65] is presented, which was submitted in February 2018 and accepted for publication in the peer-reviewed Journal of the Electrochemical Society in April 2018. Parts of the article were presented as Paper 268 at the 232nd meeting of The Electrochemical Society in National Harbor (USA) in October 2017.

Preliminary measurements of electrode tortuosities with different binder contents, presented as an outlook in the article in Section 4.2, are extended in this study to 3 mAh/cm² graphite anodes with different binder mass ratios (1.5 %, 3 %, 6 % and 10 %) and different binder types (PVDF binders from Kureha, Solef and Kynar as well as two water based systems, CMC/SBR and alginic acid sodium salt). For the first time we show how small volumetric binder contents determine the tortuosity of porous lithium-ion battery electrodes and thereby directly influence their high power behavior. For all systems studied we find increasing tortuosities for increasing binder contents, whereby for reasonable binder contents of 1.5 % to 6 % the EIS tortuosities lie between 3 and 10. Furthermore, we select three types of electrodes with different tortuosities (3.1, 4.3 and 10.2) and perform charge rate tests in a three-electrode configuration. Due to increased concentration gradients and therefore higher overpotentials, the high tortuosity electrodes are charged inhomogeneously and for increasing charge C-rates smaller capacities are obtained compared to the lower tortuosity electrodes: at 1 C roughly 80 %, 50 % and 30 % of the nominal capacity for the electrodes of increasing tortuosities (3.1, 4.3 and 10.2) are obtained. It is emphasized that the observed difference of the charge capacity is solely due to differences in electrode tortuosity as care was taken that electrode thickness, porosity and loading are comparable. The direct link between electrode tortuosity, here prepared by different binders and binder contents, with the electrochemical performance allows to draw conclusions about the electrode charging/discharge behavior before long term cycling experiments are conducted and may thus serve as a powerful tool to develop improved electrodes for future batteries.

Author Contributions

A.E. performed all tortuosity measurements, J.L. conducted the cycling experiments. Data analysis was done by A.E. and J.L. and the manuscript was written by J.L. and edited by H.G. All authors discussed the data and commented on the results.

Influence of the Binder on Lithium Ion Battery Electrode Tortuosity and Performance

Johannes Landesfeind,[az] Askin Eldiven,[a] and Hubert A. Gasteiger[a]

[a] Chair of Technical Electrochemistry, Department of Chemistry and Catalysis Research Center, Technical University of Munich, Munich, Germany

[z]corresponding author

Abstract

The electrochemical performance of porous graphite anodes in lithium ion battery applications is limited by the lithium ion concentration gradients in the liquid electrolyte, especially at high current densities and for thick coatings during battery charging. Beside the electrolyte transport parameters, the porosity and the tortuosity of the coating are key parameters that determine the electrode's suitability for high power applications. Here, we investigate the tortuosity of graphite anodes using two water as well as three n-methyl-2-pyrrolidone based binder systems by analysis of symmetric cell impedance measurements, demonstrating that tortuosities ranging from ~3-10 are obtained for graphite anodes of similar thickness (~100 μm), porosities (~50%) and areal capacity (~3.4 mAh/cm^2). Furthermore, selected electrodes with tortuosities of 3.1, 4.3, and 10.2 were cycled in cells with reference electrode at charging C-rates from 0.1-20 1/h, illustrating the clear correlation between electrode tortuosity and its rate capability.

Introduction

Understanding and predicting rate limitations in lithium ion batteries with porous electrodes requires profound knowledge of not only the electrolyte transport parameters (i.e., transference number, diffusion coefficient, conductivity) and the thermodynamic factor, but also the porosity and the tortuosity of the electrodes. The tortuosity of the electrode is particularly critical because the effective electrolyte conductivity and the effective diffusion coefficient in the electrolyte directly scale with the inverse of the tortuosity, so that care has to be taken to develop electrodes with minimized tortuosity. Using experimental approaches[1–4] or 3D tomography,[5,6] it was shown that the shape of active material particles distinctly influences the electrode tortuosity. For a given active material, however, electrode tortuosity and rate capability can also be improved by the design of the electrode layer such that short diffusion distances can be obtained across the electrode. For example, improved performance was demonstrated for graphite anodes when the platelet graphite particles were aligned normal to the current collector surface by means of a magnetic field[7] or when silicon/graphite anode electrodes were laser structured.[8] In this study we focus on the role of the electrode composition, specifically the role of the binder, on its tortuosity as well as on its implication for battery performance. While in the literature the link between binder and electrochemistry is frequently studied empirically using rate capability tests[9] and long-term cycling experiments,[10–13] we focus on the correlation of electrode tortuosity with binder content/type and its effect on rate capability.

In the following, the tortuosity of graphite anodes with different binders, different binder contents, and different amounts of conductive carbon additive will be determined by electrochemical impedance spectroscopy (EIS) of symmetric cells using the transmission line model approach.[3,14] In the first part of our analysis we will demonstrate the effect of binder and conductive carbon additives on electrode tortuosity and thereafter give an overview of the range of experimentally obtained tortuosities for two water and three NMP (n-methyl-2-pyrrolidone) based binder systems. Subsequently, charging rate performance tests in three-electrode cells for electrodes with largely different tortuosities are presented, illustrating the clear correlation between the tortuosity of the anode electrode and its rate capability.

Experimental

Electrode preparation **–** Composite slurries of graphite, binder, conductive carbon additive (material parameters and abbreviations given in Table 1) and NMP (Sigma Aldrich, anhydrous, 99.5 %) were prepared in a planetary mixer (Thinky ARV-310). As the mixing process is not at the focus of the current study, all solid components and half of the solvent were filled into the mixer at once and mixed at 2000 rpm for at least 2 min. The remaining solvent was added stepwise between subsequent mixing steps until similar slurry viscosities are obtained, as judged by eye. The prepared slurries were coated onto a copper current collector foil (MTI, 9 µm) using the doctor blade technique with a wet-film thickness of 200 µm. Coatings were dried in a self-built drying oven at 50°C under air and then punched (Hohsen Corporation) to circular discs of 11 mm diameter ($A_{El.}$ = 0.95 cm²) before assembly in

T-Cells without prior compression. Areal loading of the all graphite electrodes (thickness 98 ± 13 µm) used in this work were 9.6 ± 1.8 mg_{Gra}/cm^2 (corresponding to 3.4 ± 0.6 mAh/cm² or 3.2 ± 0.6 mAh/El. if referenced to the total electrode, using a theoretical graphite intercalation capacity of 350 mAh/cm²).

Table 1. List of the materials used for the preparation of porous graphite anodes, including supplier specifications, their BET surface area, and their density (* from manufacturer's specification).

Material	Abbreviation	BET Surface Area / m^2/g	Density / g/cm^3
Graphite, T311, Timcal, 19 µm D50	Gra	3*	2.26
SuperC65, Timcal	C65	62*	2.26
Sodium Carboxy Methylcellulose, Sigma Aldrich	CMC	-	1.59
Styrene-Butadiene Rubber, MTI	SBR	-	0.94
Alginic acid sodium salt, Sigma Aldrich	Alginate	-	1.60
PVDF, KF1100, homopolymer, Kureha	Kureha	-	1.78*
PVDF, Solef 5130, functionalized homopolymer, ultra-high molecular weight, Solvey	Solef	-	1.77*
PVDF, Kynar HSV 900, homopolymer, Arkema	Kynar	-	1.74*

Tortuosity determination – Tortuosities were determined for two nominally identical cells at each composition, using the same experimental procedure as described before (compare Experimental section in Ref. 3) unless stated otherwise. A 1:1 (by weight) mixture of ethylene carbonate (EC, Sigma Aldrich, anhydrous, 99%) and diethyl carbonate (DEC, Sigma Aldrich, anhydrous, >99%), was used as solvent for self-prepared electrolytes containing 12 mM tetrabutylammonium perchlorate ($TBAClO_4$, Sigma Aldrich, ≥99.0%) salt. A turn-key conductivity sensor (LF 1100+, SI Analytics, with custom-made ground glass fitting) with a built-in temperature sensor was used to determine the electrolyte conductivity (equating to 423 µS/cm at 25°C). Symmetrical Swagelok type T-Cells (spring-compressed to ≈1 bar) were built *outside the glovebox*, then transferred into a temperature controlled climate chamber (25°C, Binder) and impedance spectra were recorded (Biologic VMP3) around the open circuit potential (OCV) after a resting period of at least 12 h in a frequency range of 200 kHz to 0.1 Hz with a 20 mV perturbation using. No artifacts from the cell assembly under air were observed, which was confirmed by monitoring the electrolyte conductivity (no measurable change over period of 6 months) as well as by comparative measurements with cells assembled inside the glovebox.

Cycling Experiments – For charging rate performance measurements of selected composite graphite electrodes, for each composition three three-electrode Swagelok® T-cells utilizing a lithium reference and a lithium counter electrode (11 mm diameter; 450 µm thickness, Rockwood Lithium) were built inside an argon filled glovebox (MBraun, 25°C ± 1°C, oxygen and water content <0.1 ppm, Ar 5.0, Westfalen, 99.999 %vol.). All cell parts were cleaned thoroughly by boiling them in an ethanol water mixture, rinsing them with water (Millipore, Elix, 15 MΩ), and then drying them at 70°C in a drying oven before bringing them into the glovebox. Two porous glass fiber

separators (VWR, 250 µm thickness) and a commercially available battery electrolyte (1 M $LiPF_6$ in EC:EMC 3:7, w:w, LP57, battery grade, BASF) were used for the cycling experiment in a temperature controlled climate chamber (25°C, Binder) outside the glovebox using a potentiostat (BioLogic, VMP3). Without any additional formation cycle, three consecutive galvanostatic charging (i.e., lithiation) cycles with a lower cut-off potential of 5 mV versus the lithium reference electrode were recorded. For the charging and the discharging currents of the graphite electrodes a capacity value of 3 mAh/El. was used for all electrodes, corresponding to intercalation currents of 0.3, 0.6, 1.5, 3, 6, 15, 30 and 60 mA/El., corresponding to approximate C-rates of 0.1, 0.2, 0.5, 1, 2, 5, 10, 20 1/h (within ±10% due to minor loading variations), while the discharge (i.e., delithiation) current was held constant at 0.3 mA/El. (~0.1 1/h), with an upper cut-off potential of 1 V vs. the lithium reference electrode. For the sake of simplicity, the rounded C-rates are used in the text for reference, and the charging capacities of the third cycle at 0.1 1/h, given in Table 2 are used to calculate the exact C-rates used for the analysis shown in Figure 4 and Figure 5.

Table 2. Compositions and parameters of graphite anodes used for charging rate performance tests in three-electrode cells with metallic lithium counter and reference electrodes. Porosity, thickness and tortuosity values are taken from electrodes of the same coating which were used for the tortuosity measurement (errors indicate the standard deviation of 2 cells). Loading values are calculated based on the mass and composition of the electrodes used for the cycling experiments, using a theoretical intercalation capacity of 350 mAh/g_{Gra}. The charging capacity (i.e., the lithiation capacity) is given at the 3rd cycle at a C-rate of 0.1 h^{-1} and for a cut-off voltage of 5 mV vs. the lithium reference electrode potential, the error bar describes the standard deviation of three cells.

Electrode Composition Gra/Bi/C65 / wt.%	Binder	Porosity / %	Thickness / µm	Loading / mg_{Gra}/cm^2	$Q_{charging}$ at 3rd 0.1 C cycle / mAh/cm^2	Tortuosity / -
97/3/0	Alginate	56 ± 1	100 ± 2	9.8	3.20 ± 0.13	3.1 ± 0.1
97/3/0	Kynar	52 ± 2	95 ± 2	9.4	3.44 ± 0.21	4.3 ± 0.1
94/6/0	CMC/SBR 1:1	46 ± 1	101 ± 5	10.2	3.57 ± 0.21	10.2 ± 0.3

Results and Discussion

In the following, the effect of electrode composition on the tortuosity of porous graphite electrodes with different mass ratios of conductive additive (SuperC65) and binder will be demonstrated exemplarily with PVDF based graphite anodes. Figure 1 shows the tortuosities of different anode compositions, obtained from the transmission line analysis of the EIS response of symmetric cell measurements (details about this analysis technique and the tortuosity calculations can be found elsewhere[3,14]). Dashed lines in Figure 1 serve as guide-to-the-eye only; error bars indicate the error introduced by the electrode thickness measurement (2 µm) and the electrolyte conductivity (1%) and for all measurements two nominally identical cells yield very reproducible results.

At first we will discuss the results for anodes with *only* active material and Kureha PVDF binder, prepared as described in the Experimental section. For binder weight percentages of 1.5, 3, 6 and 10 wt.%, the tortuosity values increase linearly from 2.8 ± 0.1 to 5.2 ± 0.2 (compare Figure 1a, green crosses), an enormous, nearly 2-fold increase, although the electrode composition was altered only by a minor fraction of 8.5 wt.% (= 10 wt.% - 1.5 wt.%). This is

the more surprising, as all electrodes tested here are uncompressed and thus have very similar porosities (51 ±5 %) and are based on the same active material, so that one would expect little changes in tortuosity. The observed large tortuosity changes therefore suggest that the binder content strongly affects the effective transport properties in the electrolyte phases within the porous electrode, i.e., diffusion coefficient and conductivity. It is clear, of course, that the chosen binder weight ratios span a rather extreme range, as electrodes with only 1.5 wt.% of the Kureha PVDF are very brittle and have to be handled carefully, while 10 wt.% binder would substantially decrease the energy density of the electrodes and could clog the pores for electrolyte transport.[15]

Based on empirical studies by Marks et al., the best electrochemical performance while still maintaining good mechanical stability is obtained with an average binder layer thickness of ≈6 nm.[15] The binder layer thickness d_{Bi} corresponds to the thickness of the binder layer, if the binder were to be homogeneously distributed over the BET surface areas of active material ($\mathrm{BET_{Gra}}$) and the conductive carbon additives ($\mathrm{BET_{C65}}$; see BET values given in Table 1), and may be calculated by

$$d_{\mathrm{Bi}} = \frac{\sum\left(\frac{m_{\mathrm{Bi}}}{\rho_{\mathrm{Bi}}}\right)}{\mathrm{m_{Gra}} \cdot \mathrm{BET_{Gra}} + \mathrm{m_{C65}} \cdot \mathrm{BET_{C65}}} \qquad 1$$

where $\mathrm{m_i}$ represents the mass of component i per 100 g of electrode and ρ_{Bi} is the density of the binder (Bi = CMC/SBR/Kynar/Solef/Alginate/Kureha, values given in Table 1). Due to the low BET surface area of typical graphite active materials (generally in order to minimize irreversible SEI formation losses), really high binder layer thickness values are normally only obtained for composite electrodes of binder and active material *only*, i.e., without conductive carbon additives. This is illustrated in Figure 1b, which represents the same data as in Figure 1a, but re-scaled in terms of binder layer thickness rather than binder weight percentage. For electrodes without any conductive carbon additive (green crosses in Figure 1b), the binder layer thickness ranges from 2.9 to 20.8 nm, much higher than the reported sweet spot of 6 nm.[15] Closest to the suggested optimal ≈6 nm binder layer thickness are the electrodes with 3 wt.% binder.

Also shown in Figure 1 are the tortuosities of three electrode compositions (see figure for exact compositions) which additionally include different amounts of the conductive carbon C65. These electrodes were prepared by replacing a fraction of the active material of the 6 wt.% and 10 wt.% binder electrodes by C65 so that one obtains the same average binder layer thickness value of the electrodes without C65 and 3 wt.% binder have (5.8 nm, see Figure 1b). Analogously electrodes with 3 wt.% binder and C65 were prepared to obtain the same binder layer thickness of 2.9 nm as for the 1.5 wt.% binder electrodes without C65. In all these cases, due to the high surface area of C65, only a small mass fraction of C65 is necessary to adjust the binder layer thickness, and the resulting compositions are given in the figure. Figure 1a shows that the C65 containing electrodes with 6 wt.% and 10 wt.% binder yield much lower tortuosity values compared to their C65 free counterparts. With 10 wt.% Kureha PVDF binder, the tortuosity decreases from 5.2 ± 0.2 to 3.3 ± 0.1 by tuning the average binder layer thickness to 5.8 nm by addition of high surface area C65. Similarly, with 6 wt.% binder the tortuosity decreases from 3.9 ± 0.1 to 3.5 ± 0.1 by C65 addition (compare Figure 1a). In terms of binder layer thickness, Figure 1b shows that all electrodes with a binder layer thickness of 5.8 nm, with or without C65 have similar tortuosities. This suggests, that the calculated binder layer

thickness serves as a better indicator for the tortuosity of the electrodes than the binder amount, and that the high surface area conductive carbon additive behaves like a sponge, taking up a large fraction of the binder. By addition of C65 the binder layer thickness is reduced and (partially) blocked ionic conduction paths might become accessible, thereby reducing the coatings tortuosity. For the examples discussed so far, the electrode tortuosity increases with the average binder thickness (as calculated by Eq. 1), irrespective of whether conductive carbon is part of the electrode formulation (see Figure 1b). The nearly 2-fold tortuosity increase between the electrodes with 1.5 wt.% binder (Gra/Bi/C65=98.5/1.5/0, s. Figure 1b) and 10 wt.% binder (Gra/Bi/C65=95/10/0, s. Figure 1b) is quite striking, since even for the highest binder content of 10 wt.% the volume fraction of the binder ($\varepsilon_{binder} \approx 6$ %) is still nearly an order of magnitude lower than the void volume fraction of the electrode ($\varepsilon_{void} \approx 51 \pm 5$ %). Quite evidently, even small volume fractions of binder strongly affect electrode tortuosity.

The clear trend between average binder thickness and tortuosity, however, is not found for the 3 wt.% binder electrodes, for which the tortuosity increases from 3.2 ± 0.1 to 3.6 ± 0.1 when C65 is added to obtain a binder layer thickness reduction from 5.8 to 2.9 nm. Because both measurements for the composition 91.9:3:5.1 (Gra/Bi/C65, by weight) were done using electrodes from the same coating, these measurements were repeated using a newly prepared coating. However, also these repeat measurements yielded the same higher tortuosities compared to the C65 free electrodes using the same amount of 3 wt.% binder. This trend is in agreement with our previous publication for porous LFP cathodes at ~45% porosity (Ref. 3), where we reported higher tortuosities of ~5 with 5 wt.% binder and 5 wt.% C65 corresponding to a small average binder layer thickness of 1.2 nm, in contrast to a tortuosity of only ~3.5 with 15 wt.% binder and 15 wt.% C65 corresponding to a binder layer thickness of 3.3 nm. Thus, similar to the observations made with the graphite electrodes with low average binder layer thickness, C65 addition and the accompanying average binder layer thickness reduction leads to an increase in tortuosity. Currently we have no explanation of the detrimental effect from C65 addition on the electrode tortuosity for resulting average binder layer thicknesses of <<6 nm, and further investigations are necessary to check for example for an inhomogeneous carbon and binder distribution,[16] which was shown to negatively affect the C-rate capability of lithium ion battery anodes,[9] which we believe results from a lowering of the electrode tortuosity.

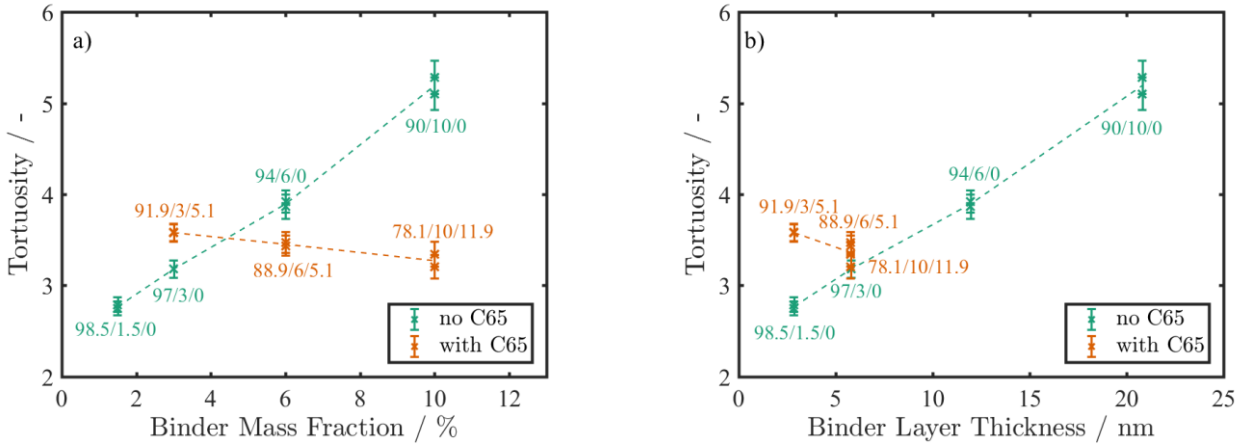

Figure 1. Tortuosities of graphite electrodes obtained from symmetric cell EIS measurements with (orange) or without (green) conductive carbon C65 plotted versus a) the binder mass percentage and b) the average binder layer thickness (according to Eq. 1). Exact electrode compositions of graphite active material (Gra), binder (Bi), and conductive carbon additive (C65) are given in terms of mass percentages in the figures using the nomenclature Gra/Bi/C65. Dashed lines serve as guide-to-the-eye only; error bars indicate the tortuosity uncertainty due to finite accuracy of the thickness (2 µm) and conductivity (1%) measurements, two measurements are shown for each composition.

In addition to the presented binder layer thickness versus tortuosity study utilizing the Kureha PVDF binder, four other binders were analyzed, namely two PVDF binders from different suppliers for use with NMP based inks, as well as CMC/SBR (here always in 1:1 mass ratio) and alginate for use with water based inks. This comparison was conducted with electrodes without conductive carbon and various amounts of binder content (1.5, 3, 6, and 10 wt.% for the Kureha PVDF and the CMC/SBR (1:1) binder, as well as 3 and 6 wt.% for the Kynar PVDF, Solef PVDF, and alginate binder). The electrode tortuosities obtained by the transmission line model EIS analysis are shown in Figure 2 versus the average binder thickness calculated from Eq. 1, whereby crosses and dashed lines indicate NMP based PVDF electrodes, while circles and solid lines represent the water based systems. The first thing to notice is that all porous graphite electrodes show the same general trend, viz., lower tortuosities for smaller amounts of binder. The measured tortuosities range from 2.7 ± 0.1 (Kureha, 1.5 wt.% binder) to 10.2 ± 0.3 (CMC/SBR 1:1, 6 wt.% binder); for 10 w.% of the CMC/SBR binder, the tortuosity increases to an extremely high value of 37 (indicated by the pink arrow in Figure 2). The grey rectangle in Figure 2 depicts the tortuosity range for platelet graphite obtained using X-ray tomography for the range of porosities used in this work (51 ± 5 %), which may be considered to be the theoretical lower tortuosity limit for the graphite active material if unaffected by the binder, as X-ray tomography cannot resolve the binder/conductive carbon phase and thus commonly ignores its effect on tortuosity.[5,14] By an approximate extrapolation of the tortuosities from the presented EIS measurements in Figure 2 to 0 wt.% binder, limiting tortuosity values for conceptually binder-free anodes between 2.4 and 4 can be projected, which is reasonably close to the tortuosity range for electrodes estimated from X-ray tomography (1.6 to 2.0), where the binder contribution is not considered. The remaining difference might be due to different aspect ratios of the graphite particles or to the inability to sufficiently extrapolate from 1.5-3 wt.% binder to 0 wt.% binder.

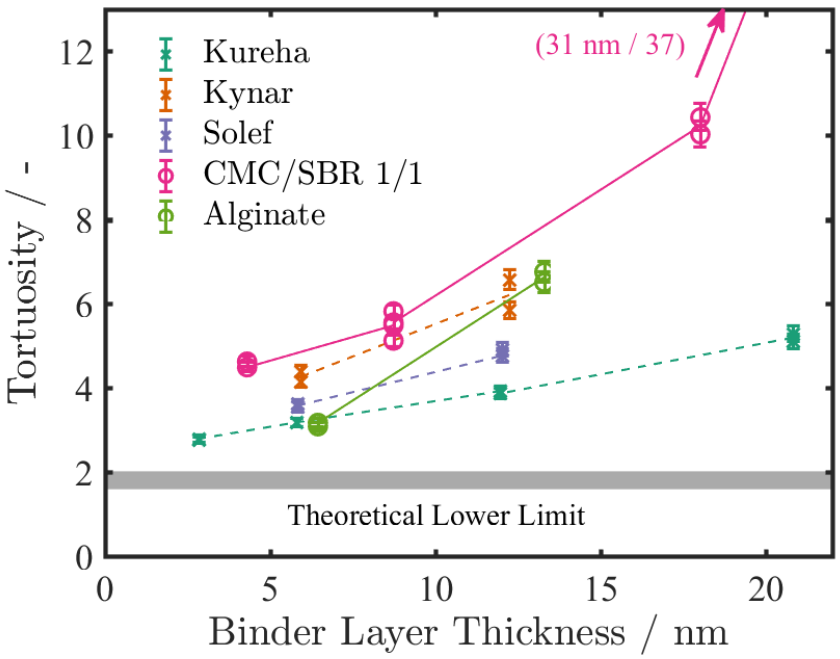

Figure 2. Tortuosities of porous graphite electrodes without conductive carbon and with different amounts of NMP based (Kureha, Kynar, Solef PVDFs; dashed lines) and water based (CMC/SBR and alginate; solid lines) binders, plotted versus the average binder thickness determined by Eq. 1. The binder contents were 1.5, 3, 6, and 10 wt.% for the Kureha PVDF and the CMC/SBR (1:1) binder, as well as 3 and 6 wt.% for the Kynar PVDF, Solef PVDF, and alginate binder. Tortuosities were measured using the transmission line model EIS analysis in symmetric cell configuration with 12 mM $TBAClO_4$ in EC:DEC (1:1 w:w) (see Ref. 3 for details). Lines serve as a guide-to-the-eye only; error bars indicate the tortuosity uncertainty stemming from the finite accuracy of the thickness (2 µm) and conductivity (1%) measurements, two measurements are shown for each composition.; the grey region gives an estimate for the likely lower tortuosity limit based analysis of X-ray tomography data (see text).

As proposed in the literature,[15] electrodes with a binder layer thickness of 5-10 nm have the highest relevance for practical consideration, representing a trade-off between sufficient adhesion and maximized active material content (see above), for which reason we will focus our comparison to graphite anodes with 3 wt.% binder, corresponding to average binder film thicknesses of ~6-9 nm (this variation is due to the variation in binder density, see Table 1). For this binder content, the lowest tortuosity is found for alginate (3.1 ± 0.1) and the highest tortuosity for CMC/SBR 1:1 (5.5 ± 0.1) binder. Even for electrodes with the same binder type (PVDF) with albeit different functionalized groups and molecular weights, the tortuosities differ substantially: 3.2 ± 0.1 for the Kureha PVDF binder, 3.6 ± 0.1 for the PVDF binder from Solvey, and 4.3 ± 0.1 for the PVDF binder from Kureha. Quite strikingly, the here prepared graphite electrodes with the CMC/SBR binder system show much larger ionic resistances compared to the other binder systems, especially for 6 wt.% and 10 wt.% binder (compare pink circles in Figure 2). While the average binder film thickness for the electrode with 6 wt.% CMC/SBR (~18 nm) is even lower than that for the electrode with 10 wt.% Kureha PVDF binder (~21 nm), the tortuosity of the former (10.2 ± 0.3) is substantially higher than that of the latter (5.2 ± 0.1). This could be due to an inhomogeneous distribution of the CMC/SBR binder across the electrode, leading to either the formation of a binder-rich surface layer/film at the electrode surface blocking ionic transport or to blocking the electronic pathway across the electrode, which would invalidate the

impedance analysis (in the here used transmission line model, the electronic resistance across the electrode is assumed to be low compared to the ionic resistance, which typically would be expected for graphite anodes).[14]

Further insights might be gained by a closer inspection of the Nyquist plots for graphite anodes with 6 wt.% binder, which is shown in Figure 3 (note that the EIS response is shifted to the origin for better comparability). The unique behavior of the CMC/SBR electrodes is reflected by the apparent inflections of its EIS spectrum (pink circles) in the mid frequency region (100 - 10 Hz) as well as in the low frequency region (10 – 0.1 Hz), in contrast to the nearly straight 45-degree lines for the electrodes with the other binders. This feature for the CMC/SBR electrodes, together with the much higher apparent tortuosity values may be caused by an inhomogeneous distribution of the binder,[17] which may result from the non-optimized slurry mixing and electrode drying steps.[18] Even for highly conductive graphite particles the required assumption for the applicability of the simplified transmission line model (i.e., neglecting the solid phase electronic resistance) might be erroneous if the binder agglomerates and/or is distributed inhomogeneously. As long as the electronic resistance is minor, the EIS tortuosity measurement is invariant towards ionic conductivity,[14] however repeat measurements for the electrodes with 6 wt% CMC/SBR with a higher electrolyte conductivity (2.5 instead of 0.423 mS/cm) yield much higher values for the tortuosity (>100 vs. ~10). Although, with optimized electrode preparation, the absolute values for the CMC/SBR binder system in this work may not be representative. Nevertheless, these electrodes demonstrate the sensitivity of electrode preparation and its pronounced effect on the effective ionic and electronic transport properties.

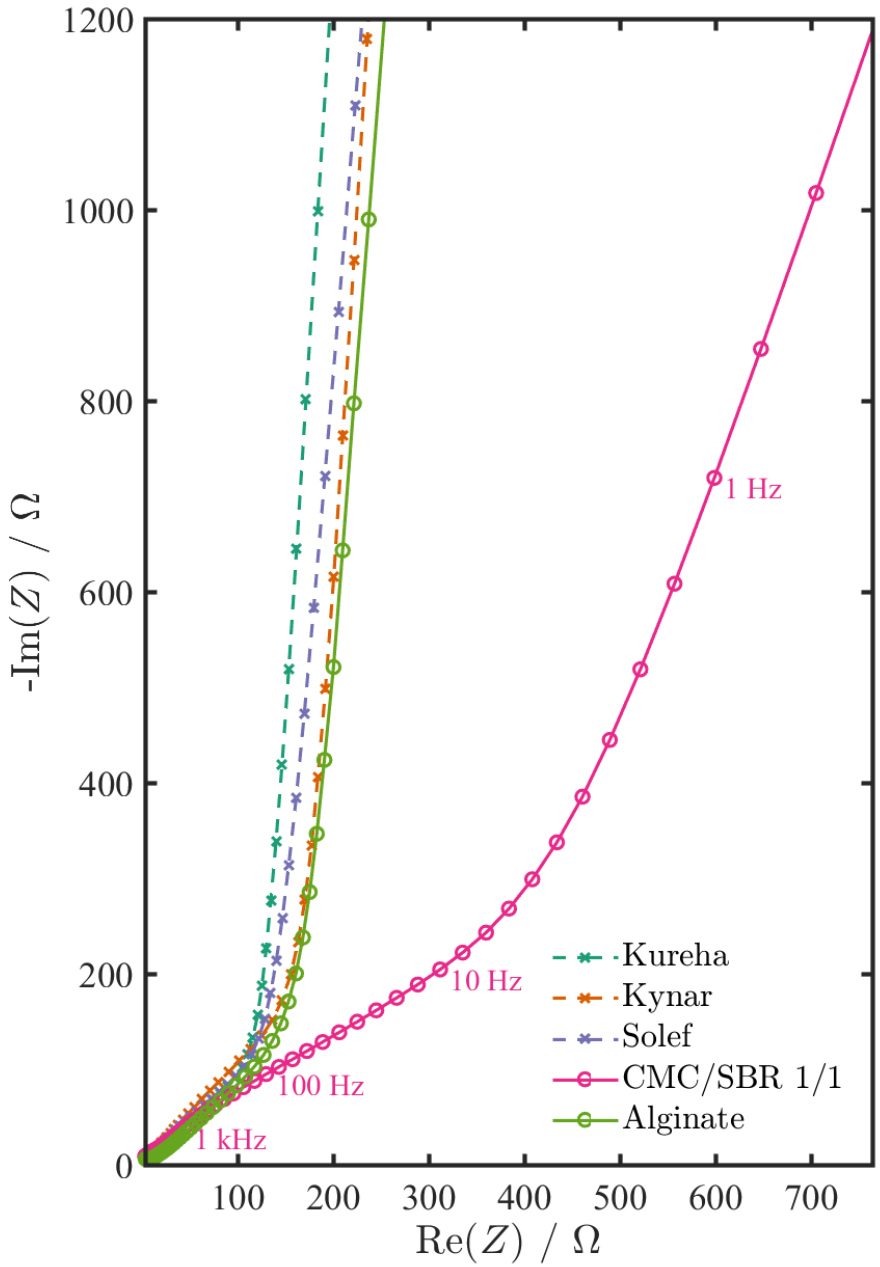

Figure 3. Nyquist plots of symmetric cells using graphite electrodes without conductive carbon additive and with 6 wt.% water based (solid lines, circles) and NMP based (dashed lines, crosses) binders. The EIS spectra are shifted to the origin for better comparability. A non-intercalating electrolyte with an ionic conductivity of 0.423 mS/cm was used (12 mM $TBAClO_4$ in EC:DEC 1:1) and impedance measurements were recorded from 200 kHz to 0.1 Hz with an excitation amplitude of 20 mV. The pink numbers next to the CMC/SBR data mark the frequencies in Hz at which the data were taken; lines serve as a guide-to-the-eye only.

In summary Figure 2 clearly shows the strong dependence of the tortuosity of porous anodes not only on the binder content and the average binder layer thickness, but also on the type of binder. Again, the reader is reminded that the here prepared electrodes have not been optimized in any way (i.e., the same mixing and drying procedures were used for all binders). Therefore, while we believe that the generally observed trend of increasing tortuosity with increasing binder content is correct for each binder, our data do not allow to make a quantitative comparison and

judgement between the tortuosities obtained with different binders and dispersing agents. It is emphasized that remarkably different tortuosity values (~3 - 10) are obtained for the graphite anodes under study although the binder volume fraction is minor (here between 0.8 and 5 % for binder mass fractions of 1.5 wt.% to 10 wt.%) compared to the void volume fraction of the electrodes (here 51 ± 5 %). The pronounced effect of the small volume fraction binder phase was previously shown for inhomogeneous binder distributions prepared by different drying procedures.[9] More detailed investigations of the electrode preparation steps and their influence on electrode tortuosity will be subject of a future work.[18]

Electrochemical Performance with Different EIS Tortuosities

After having determined the tortuosity value of the various electrodes, i.e., the scaling factor of the effective diffusion coefficient and the effective ionic conductivity,[19] we will now examine experimentally the relationship between tortuosity and electrochemical performance. To verify the expected behavior of better performance for low tortuosity electrodes,[20,21] we picked three electrode compositions with different tortuosities but similar areal capacity, thickness, and porosity in order to compare their electrochemical performance and their rate capability using three-electrode cells with a lithium counter and a lithium reference electrode. As the limiting operation mode for graphite anodes is the charging step, due to the proximity of the graphite intercalation potential to the lithium plating potential, we focus our analysis on the charging (i.e., lithiation) behavior of graphite anodes. From the set of the above investigated electrodes, electrodes with tortuosities of 3.1 ± 0.1, 4.3 ± 0.1, and 10.2 ± 0.3 were selected for electrochemical performance tests (the corresponding electrode compositions and parameters are given in Table 2). Again, it is important to note that all electrodes used in the following rate tests were uncompressed and had very comparable thicknesses of 98 ± 3 µm and porosities of 51 ± 5 %. For details on the rate test measurement procedure the reader is referred to the Experimental section.

Figure 4a and 4b show the galvanostatic charging curves for the 3rd cycle at a C-rate of 0.1 1/h and 1 1/h of graphite anodes with different tortuosities. The charging curves were measured versus the lithium reference electrode and are normalized to their charging capacity obtained in the 3rd cycle at 0.1 1/h (compare Figure 4a), which were essentially the same (3.4 ± 0.2 mAh/cm^2, see Table 2). In stark contrast to the behavior at low charging rate, at a C-rate of 1 1/h (compare Figure 4b) the highest capacity (given in terms of state-of-charge, SOC) is reached for the alginate based electrodes with 3 wt.% binder and the lowest tortuosity (τ = 3.1 ± 0.1), for which more than 80% of the lithiation capacity can be obtained until a cut-off potential of 5 mV (vs. the lithium reference electrode) is reached. For the 3 wt.% Kynar PVDF electrodes (τ = 4.3 ± 0.1), only 50% of the full capacity is accessible until the 5 mV cut-off potential is reached, while for the high tortuosity (10.2 ± 0.3) CMC/SBR based electrodes the capacity is limited to only 30% SOC. Thus, the accessible lithiation capacities at high C-rate (1 1/h) differ strongly amongst these electrodes, although their porosity, thickness, and areal capacities are comparable (see Table 2), clearly showing the significant effect of electrode tortuosity on the charging potential vs. SOC behavior, as would be expected based on theoretical models.[20,21]

In addition to the difference in lithiation capacities at 1 1/h, Figure 4b also illustrates two other distinctive features in the lithiation potential vs. SOC profiles for increasing tortuosities, namely an increasing overpotential and a smearing out or complete loss of the typical potential steps in the graphite lithiation process at high C-rates. At the slow charging rate of 0.1 1/h, the graphite lithiation plateaus (around SOC values of 10 %, 20 %, and 55 %) are clearly distinguishable and similarly well-defined for all graphite electrodes despite their vastly different tortuosities (compare Figure 4a). These plateaus are also still clearly visible at a C-rate of 1 1/h for the low tortuosity alginate based electrodes (τ = 3.1 ± 0.1, green, solid line). However, for electrodes with a higher tortuosity of 4.3 ± 0.1 (Kynar PVDF binder, dashed, orange line), the graphite potential plateaus are only partly visible and completely vanish for the electrode with the highest tortuosity (τ =10.2 ± 0.3, CMC/SBR, pink line, compare Figure 4b). Both effects, the increasing overpotentials (depending on SOC, compare Figure 4a and b) as well as the degree of observable lithium intercalation plateaus are a result of ionic concentration gradients within the electrolyte phase across the electrode thickness, which builds up during the charging process.[20,21] In this case lithium ions are intercalated into the graphite particles and are depleted in the electrolyte solution. At the same time, lithium ions generated at the counter electrode will be transported through the separator by migration and diffusion to the graphite anode / separator interface. If ionic transport through the electrode is fast compared to the selected charging time, i.e., if the electrode has a low tortuosity, the lithium ion concentration gradient across the graphite electrode remains low (i.e., the lithium ion concentration remains nearly constant) and the graphite electrode is charged homogeneously. In this case of nearly constant lithium ion concentration across the anode, the concentration overpotential also remains nearly constant across the anode thickness, so that the anode potential closely follows the graphite OCV curve or the charging curve a low C-rate (compare Figure 4a for low tortuosity alginate electrodes). On the other hand, for anodes with high tortuosity values, higher concentration gradients form across the anode electrode thickness, effectively leading to an inhomogeneous charging of the graphite electrode across its thickness. This, in turn, leads to the smearing out or the complete loss of the intercalation plateaus, as is best seen for the CMC/SBR electrode with the high tortuosity value (pink line in Figure 4b), an effect also reported from lithium ion battery simulations using different Bruggeman relations for the tortuosity of the electrode.[21]

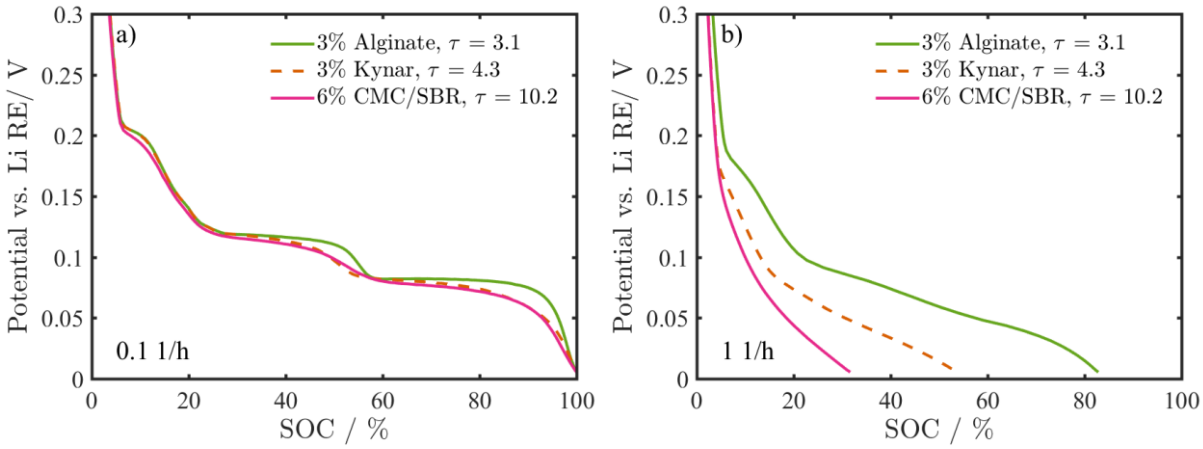

Figure 4. Third-cycle galvanostatic charging (lithiation) curves at C-rates of a) 0.1 1/h and b)1 1/h of porous graphite electrodes (see Table 2 for details) with three different tortuosities, recorded in three-electrode cells with lithium counter and lithium reference electrodes. Measurement were conducted using 1 M $LiPF_6$ in EC:EMC (3:7 w:w) as an electrolyte and at 25 °C. The upper and lower cut-off potentials were 1 V and 5 mV vs. the metallic lithium reference electrode, respectively. Capacities are normalized to the third-cycle capacity at 0.1 1/h (a); they are all within 3.4 ± 0.2 mAh/cm^2, and are given in terms of state-of-charge (SOC). Table 2 gives all parameters of the used electrodes.

The beneficial effect of lessened concentration gradients at 1C by reduced electrode tortuosities can also be seen from the capacities reached during a charging rate capability test. Mean values from three repeat cells for each electrode composition and their standard deviation (indicated by the error bars), are shown in Figure 5 for C-rates from ~0.1 1/h to 20 1/h (charging capacities are again normalized to the 3rd cycle charge capacity at 0.3 mA/$A_{El.}$ (C-rate ~0.1 1/h)). In line with the previously discussed potential transients at a C-rate of ~1 1/h, the graphite anodes with the lowest tortuosity show highest charge capacities at any given C-rate.

The fit of a mathematical description to describe the sigmoidal experimental rate capability behavior was added as dashed lines in Figure 5 in order to provide a smooth guide-to-the-eye. Empirically, i.e., not based on any physics-based derivation we found the mathematical description

$$y = \frac{y_{max}}{1 + \left(\frac{x}{x_0}\right)^{\text{slope}}} \qquad 2$$

to be well-suited to describe the accessible capacity $Q_{Acc.}$ for all tortuosities and C-rates R. Applied to our measurements, y_{max} corresponds to the theoretical charging capacity in the low C-rate limit ($R \to 0$), x becomes the C-rate R, and the symmetry point x_0, i.e., the point where only 50 % SOC are reversibly accessible is defined as critical C-rate, $R_{crit.}$. The slope s remains as a free fitting parameter.

$$Q_{Acc.} = \frac{Q_{Theo.}}{1 + \left(\frac{R}{R_{crit.}}\right)^{s}} \qquad 3$$

The fit parameters s and the obtained critical C-rates $R_{crit.}$ for the experimental data in Figure 5 are summarized in Table 3.

For a tortuosity of 10.2 ± 0.3, 50 % of the electrode's capacity can be utilized at a C-rate of $R_{\text{crit.}}$ = 0.6 1/h, while the same capacity is still accessible at $R_{\text{crit.}}$ = 0.9 1/h for a tortuosity of 4.3 ± 0.1, and at $R_{\text{crit.}}$ = 1.8 1/h for the lowest tortuosity of 3.1 ± 0.1. Thus, for electrodes of similar mass, capacity, thickness and porosity (compare Table 2), the C-rate at which the capacity drops below 50% can vary by a factor of three for electrode tortuosities ranging from 3.1 ± 0.1 to 10.2 ± 0.3. The experimentally found dependence of the critical C-rate on electrode tortuosity is in good agreement with the literature, where for a constant value of the accessible areal capacity the ratio of (dis)charge time for a full (dis)charge t_{d} over the tortuosity τ (i.e., t_d/τ) would be predicted to remain constant (compare Eq. 14 in Ref. 20). Applied to our measurements this would mean that the product of the critical C-rate $R_{\text{crit.}}$ (corresponding to the inverse of the full (dis)charge time) and the tortuosity should remain constant.

$$R_{\text{crit.}}^{\text{ideal}} = R_{\text{crit.}} \cdot \tau \qquad 4$$

Here we refer to the factor of critical C-rate times tortuosity as the critical C-rate ($R_{\text{crit.}}^{\text{ideal}}$) for an ideal electrode (in terms of tortuosity, this would mean an electrode with an ideal tortuosity of 1). Values for $R_{\text{crit.}}^{\text{ideal}}$, based on the critical C-rates and the tortuosity of the different electrodes are given Table 3 and are surprisingly similar. For the graphite electrodes with a tortuosity of 3.1 and 10.2, closely agreeing $R_{\text{crit.}}^{\text{ideal}}$ values of ~5.7 and ~5.8 are obtained, while a slightly lower value of ~3.9 is obtained for the Kynar PVDF based anodes with a tortuosity of 4.3 ± 0.1. A somewhat smaller $R_{\text{crit.}}^{\text{ideal}}$ for the Kynar based PVDF electrodes might due to the generally larger variance of the measured charging capacity of the three repeat cells compared to the other binders (compare error bars of C-rate of 0.1 1/h in Figure 5).

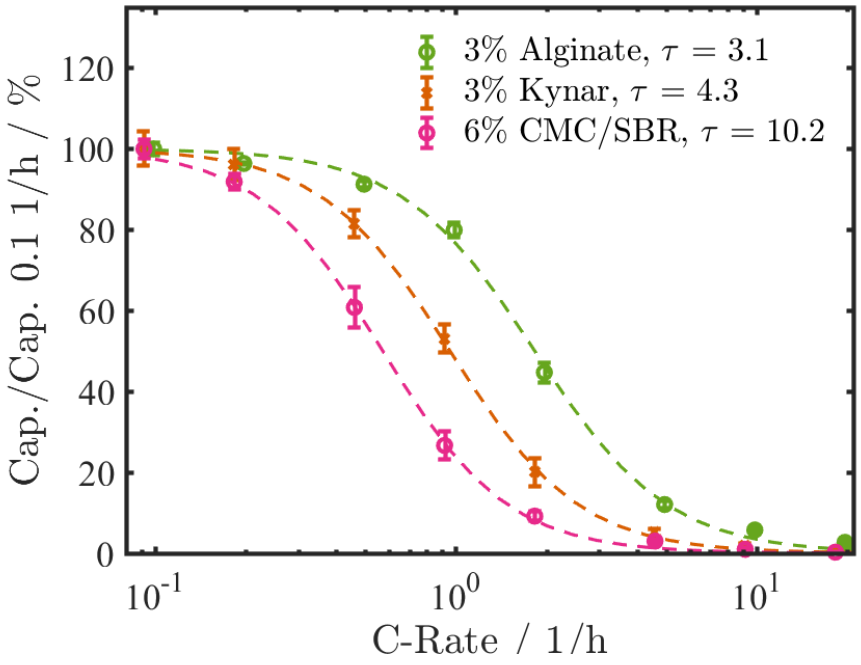

Figure 5. Mean charging (i.e., lithiation) capacities normalized to the capacity at 0.1 1/h of three types of electrodes with different tortuosities (see Table 2; all areal capacities within 3.4 ± 0.2 mAh/cm^2) vs. galvanostatic charging rates ranging from 0.1 1/h to 20 1/h, using a lower cut-off voltage of 5 mV vs. a metallic lithium reference electrode. The discharge rate was kept constant at 0.1 1/h and the experiments were conducted at 25 °C with 1 M $LiPF_6$ in EC:EMC (3:7 w:w). Error bars indicate the standard error of the mean of three independent measurements with electrodes of identical composition. The dashed lines are the fit curves to Eq. 3, with the fitting parameters listed in Table 3.

Table 3. Fitting parameters of Eq. 3 to the experimentally obtained capacities at C-rates from ~0.1 1/h to 20 1/h and the calculated critical C-rates for the ideal electrode (using Eq. 4). The fitting curves are shown as dashed lines in Figure 5.

Composition Gra/Bi/C65	Binder	Tortuosity / -	$R_{crit.}$ / 1/h	$R_{crit.}^{ideal}$ / 1/h	s / -
97/3/0	Alginate	3.1 ± 0.1	1.83	5.67	1.97
97/3/0	Kynar	4.3 ± 0.1	0.90	3.88	2.25
94/6/0	CMC/SBR 1/1	10.2 ± 0.3	0.57	5.83	2.09

It is noteworthy that for all electrode compositions the slope s of the capacity loss in Eq. 3 is close to 2 (see Table 3). By definition, the critical C-rate for the ideal electrode would correspond to a hypothetical electrode with a tortuosity of one (here somewhere between ~4-6 1/h). The reader is reminded that all cells are cycled at the same conditions, having the same thickness, porosity, and loading and that the same electrolyte is used. The constant value for $R_{crit.}^{ideal}$ thus shows that even for optimized graphite electrodes with, e.g., aligned particles,[7] higher charging rates than ~4-6 1/h may never be achieved for the given thickness, porosity, and electrolyte transport parameters. To

confirm that in the theoretical scenario of a tortuosity of one the critical C-rate would range somewhere between ~4-6 1/h, numerical modeling studies would have to be conducted. However, here we focus on estimating the influence of the tortuosity on the accessible capacity at a given C-rate, which may be done using Eq. 3 and Eq. 4 with the fit parameters from Table 3. We are aware that in general $R_{\mathrm{crit.}}^{\mathrm{ideal}}$ and s will depend in some way on the electrolyte transport parameters and the slope of the OCV curve of the analyzed active material and emphasize that in this context Eq. 3 may only be used to understand the estimated performance change as a result of a tortuosity variation. Nevertheless, a rough estimate to predict the relative C-rate capability of anodes which differ only by their tortuosity value (i.e., which have identical thickness, porosity, and areal capacity) is afforded by Eq. 4 (e.g., doubling the tortuosity reduces the critical C-rate by a factor of 2). Since thickness, porosity, and areal capacity are typically electrode design requirements, simple and fast tortuosity measurements of electrodes in an electrode optimization study (e.g., variation of ink mixing and drying procedures) should thus serve as a rough predictor for the C-rate capability of electrodes.

Conclusions

Graphite electrodes with binder contents between 1.5 and 10 wt.% of two water (CMC/SBR and alginate) and three NMP based (PVDF from Kynar, Kureha and Solef) binder systems have been prepared and analyzed in terms of their ionic tortuosities by analysis of the Nyquist plots of symmetric cell impedance measurements using a non-intercalating electrolyte with a simplified transmission line model equivalent circuit.[3] Although the slurry mixing and electrode preparation procedure was not optimized, we find clear trends, i.e., higher tortuosities for higher amounts of binder and, more importantly, a wide range of tortuosity values for graphite electrodes of similar porosity and loading (from 2.7 ± 0.1 to 10.2 ± 0.3) for different types of polymeric binder. By addition of high surface area conductive carbon, the tortuosity of the electrodes with a binder layer thickness above 6 nm decreases.

Electrochemical charge performance tests of selected anodes with different tortuosities were done in three electrode cells with lithium counter and reference electrodes and showed a clear improvement, i.e., lower overpotentials and thus higher charge capacities, for low tortuosity electrodes. This is in line with the theoretically expected, reduced concentration gradients due to fast ionic transport through the porous anodes at low tortuosities.[20,21] At last we describe an empirical expression which allows to estimate the accessible capacity for a given C-rate and tortuosity and suggest that even for an ideal electrode, i.e., tortuosity of unity, the highest C-rate at which 50% of the nominal capacity can be accessed without lithium plating is ~4-6 1/h for the here used anodes with a thickness of ~100 μm, a porosity of ~50%, and an areal capacity of ~3.4 ± 0.2 mAh/cm^2. The empirical expression introduced allows to roughly predict the dependence of the critical C-rate (at which 50 % of the capacity is accessible) on the tortuosity of the electrode and thus serves as a valuable tool for electrode optimization studies.

Acknowledgment

We gratefully acknowledge the funding by the BMBF (Federal Ministry of Education and Research, Germany) for its financial support under the auspices of the ExZellTUM II project (grant number 03XP0081).

References

1. T. DuBeshter, P. K. Sinha, A. Sakars, G. W. Fly, and J. Jorne, *J. Electrochem. Soc.*, **161**, A599–A605 (2014).
2. D. Cericola and M. E. Spahr, *Electrochim. Acta*, **191**, 558–566 (2016).
3. J. Landesfeind, J. Hattendorff, A. Ehrl, W. A. Wall, and H. A. Gasteiger, *J. Electrochem. Soc.*, **163**, A1373–A1387 (2016).
4. I. V. Thorat, D. E. Stephenson, N. a. Zacharias, K. Zaghib, J. N. Harb, and D. R. Wheeler, *J. Power Sources*, **188**, 592–600 (2009).
5. M. Ebner, D. W. Chung, R. E. García, and V. Wood, *Adv. Energy Mater.*, **4**, 1–6 (2014).
6. F. Tariq, V. Yufit, M. Kishimoto, P. R. Shearing, S. Menkin, D. Golodnitsky, J. Gelb, E. Peled, and N. P. Brandon, *J. Power Sources*, **248**, 1014–1020 (2014).
7. V. Wood and M. O. J. Ebner, *EP Pat. App.*, EP20,130,001,974 (2014).
8. J. S. Kim, W. Pfleging, R. Kohler, H. J. Seifert, T. Y. Kim, D. Byun, H. G. Jung, W. Choi, and J. K. Lee, *J. Power Sources*, **279**, 13–20 (2015).
9. S. Jaiser, M. Müller, M. Baunach, W. Bauer, P. Scharfer, and W. Schabel, *J. Power Sources*, **318**, 210–219 (2016).
10. V. Barsykov and V. Khomenko, *Sci. J. Riga Tech. Univ.*, **21**, 67–71 (2010).
11. D. Guy, B. Lestriez, R. Bouchet, V. Gaudefroy, and D. Guyomard, *J. Electrochem. Soc.*, **8**, 17–21 (2005).
12. R. Wang, L. Feng, W. Yang, Y. Zhang, Y. Zhang, W. Bai, B. Liu, W. Zhang, Y. Chuan, Z. Zheng, and H. Guan, *Nanoscale Res. Lett.*, **12**, 575 (2017).
13. S. Komaba, N. Yabuuchi, T. Ozeki, Z. J. Han, K. Shimomura, H. Yui, Y. Katayama, and T. Miura, *J. Phys. Chem. C*, **116**, 1380–1389 (2012).
14. J. Landesfeind, M. Ebner, A. Eldiven, V. Wood, and H. A. Gasteiger, submitted (2018).
15. T. Marks, S. Trussler, a. J. Smith, D. Xiong, and J. R. Dahn, *J. Electrochem. Soc.*, **158**, A51 (2011).
16. M. Müller, L. Pfaffmann, S. Jaiser, M. Baunach, V. Trouillet, F. Scheiba, P. Scharfer, W. Schabel, and W. Bauer, *J. Power Sources*, **340**, 1–5 (2017).
17. H. Keiser, K. D. Beccu, and M. a. Gutjahr, *Electrochim. Acta*, **21**, 539–543 (1976).
18. R. Morasch, B. Suthar, J. Landesfeind, and H. A. Gasteiger, in preparation (2018).
19. A. Ehrl, J. Landesfeind, W. A. Wall, and H. A. Gasteiger, *J. Electrochem. Soc.*, **164**, A826–A836 (2017).

20. K. G. Gallagher, S. E. Trask, C. Bauer, T. Woehrle, S. F. Lux, M. Tschech, P. Lamp, B. J. Polzin, S. Ha, B. Long, Q. Wu, W. Lu, D. W. Dees, and A. N. Jansen, *J. Electrochem. Soc.*, **163**, 138–149 (2016).

21. B. Suthar, P. W. C. Northrop, D. Rife, and V. R. Subramanian, *J. Electrochem. Soc.*, **162**, 1708–1717 (2015).

Chapter 5

In-Situ Impedance Analysis

Electrochemical impedance spectroscopy is a powerful tool to characterize lithium-ion batteries. The quality of impedance analyses is determined by the validity of the chosen equivalent circuit model and the measurement conditions, which may emphasize individual processes. The articles presented in this section serve as an example how impedance data of complex systems may be analyzed in a perhaps more rigorous fashion and how novel insights into cell aging may be obtained. As indicated by the brief introduction of impedance spectroscopy in Section 1.2, the significance of impedance measurements, i.e., the ability to assign processes unambiguously to an impedance feature, increases for simpler systems. For a small number of electrochemical effects the equivalent circuit becomes unique and allows for an unambiguous assignment of physical parameters. The innovative approach presented in the following sections is based on an in-situ deconvolution of the full-cell impedance (holding information of both electrodes simultaneously), into separate anode and cathode spectra using a three electrode setup employing a micro reference electrode (see Section 5.1), thereby reducing the number of processes which are reflected in an impedance spectrum by roughly a factor of two. In addition, a novel measurement protocol is introduced which is based on chosing measurement conditions at which one of the electrodes in a full-cell is driven in a blocking condition by completely delithiating the electrode of interest. This concept of a *blocking electrode* configuration is similar to the previously utilized *blocking electrolyte* concept for the determination of electrode tortuosities (see Section 4.1). Combination of the blocking electrode impedance spectra of an anode or a cathode in a full-cell with the commonly measured standard impedance (in non-blocking configuration, i.e., allowing for charge transfer reactions to occur) enables a novel simultaneous analysis which further reduces the complexity of the system and thus the uncertainty of the obtained parameters. This method is introduced in detail in Section 5.2 for the cathode impedance of an LNMO/-graphite full-cell and furthermore applied to the anode side in a subsequent work in Section 5.3.

5.1 Gold Wire Reference Electrode

In this section the article *A Gold Micro-Reference Electrode for Impedance and Potential Measurements in lithium-ion batteries*[86] is presented, which was submitted in June 2016 and published in the peer-reviewed Journal of the Electrochemical Society in August 2016. The article was presented as Paper 211 at the 230th meeting of The Electrochemical Society/PRIME 2016 in Honolulu (USA) in October 2016.

Although the majority of impedance analyses of lithium ion cells are based on full-cell configurations a great deal of laboratory work focuses on three-electrode cell configurations which allow to obtain anode and cathode impedance spectra separately. The three-electrode cell designs in the literature are based on lithium reference electrodes sitting outside the anode/separator/cathode stack,[113] reference electrode meshes, circular lithium reference rings, ring electrodes with centered circular reference electrodes,[114] or reference electrode wires.[115] However typical problems of the reported setups are artifacts in the impedance measurements[116] or unstable potentials of the reference electrode during long term operation.[115] In the presented article we introduce a novel reference electrode setup based on a 65 µm diameter, insulated gold wire reference electrode (GWRE) which is lithiated in-situ. The advantages of the setup are the thermodynamically defined potential of the formed lithium gold alloy (313 mV vs. metallic lithium) and its long term stability (>1000 h), whereby the GWRE may be regenerated easily in-situ by lithiation from the cell's lithium inventory. Due to the small dimensions of the wire and its insulation only the head of the wire is ionically connected and the necessary amount of lithium to charge and activate the GWRE is negligible. The geometric dimension of the wire, as well as its insulation further satisfy the requirements for well defined impedance measurements, as the potential of the active area of the reference electrode is only sensed at the tip of the wire. Due to the small wire dimensions the impedance of the reference electrode is high, which leads to distortions in the recorded impedance spectra at high frequencies (here ≈100 kHz, see Ref. [33]). By removing a larger portion of the insulation at the tip of the wire the active surface area is increased, which enables measurements to higher frequencies as recently shown in a numerical study.[117] In the manuscript we prove the validity of the proposed cell setup by comparing recorded impedances with symmetric cell measurements, a technique widely applied in the literature,[118] although requiring a large number of cells and individual measurements. We demonstrate how anode and cathode half-cell impedances of a LFP/graphite cell may be obtained in-situ and use this approach to study the effect of VC on the graphite and LFP impedance after formation.

Author Contributions

D.P. and J.L. developed the GWRE three-electrode cell design. D.P. and S.S. elaborated the concept of using an insulated gold wire and alloying it with lithium to obtain stable potentials. D.P., S.S. and E.K. performed all electrochemical measurements. Data analysis was done by S.S., D.P. and J.L. and the manuscript was written by S.S. and edited by H.G. All authors discussed the data and commented on the results.

A Gold Micro-Reference Electrode for Impedance and Potential Measurements in Lithium Ion Batteries

Sophie Solchenbach,[a,*,z] Daniel Pritzl,[a,*] Edmund Jia Yi Kong,[a,b] Johannes Landesfeind,[a,*] and Hubert A. Gasteiger[a,]**

[a]*Chair of Technical Electrochemistry, Department of Chemistry and Catalysis Research Center, Technische Universität München, D-85748 Garching, Germany*
[b]*Singapore Institute of Technology, Singapore*

Impedance measurements of lithium-ion batteries are a powerful tool to investigate the electrolyte/electrode interface. To separate the contributions of anode and cathode to the full-cell impedance, a reference electrode is required. However, if the reference electrode is placed inappropriately, the impedance response can easily be biased and lead to erroneous conclusions. In this study, we present a novel micro-reference electrode for Swagelok-type T-cells which is suitable for long-term impedance and reference potential measurements. The reference electrode consists of a thin insulated gold wire, which is placed centrally between cathode and anode and is in-situ electrochemically alloyed with lithium. The resulting lithium-gold alloy reference electrode shows remarkable stability (>500 h) even during cycling or at elevated temperatures (40°C). The accuracy of impedance measurements with this novel reference electrode is carefully validated. Further, we investigate the effect of different vinylene carbonate (VC) contents in the electrolyte on the charge transfer resistance of LFP/graphite full cells and demonstrate that the ratio of VC to active material, rather than the VC concentration, determines the impedance of the anode SEI.
 [DOI: 10.1149/2.0581610jes]

Manuscript submitted June 7, 2016; revised manuscript received July 26, 2016. Published August 19, 2016. This article is a version of Paper 211 from the Honolulu, Hawaii, Meeting of the Society, October 2–7, 2016.

The lifetime of lithium-ion batteries strongly depends on the properties of the interfaces between each electrode and the electrolyte. Electrochemical impedance spectroscopy (EIS) is a simple and non-destructive method to investigate the kinetics of active materials, the resistance of electrode/electrolyte interfaces, and the effect of electrolyte additives.[1,2] As impedance measurements of full-cells always reflect the sum of both electrodes, it is difficult to deconvolute the individual contributions by the cathode and the anode. To gain insight into the impedance of individual electrodes, measurements on symmetric cells have been proposed, where two cathodes or two anodes from nominally identical cells are reassembled to symmetric cells.[3,4] While this method leads to reliable results, it requires the disassembly and destruction of the original cells. Hence, for the impedance investigation of cells at different state-of-charge (SOC) values or at different points in their cycle life, a large number of nominally identical cells operated or aged at identical conditions is required.

An alternative approach is the use of a reference electrode, where the AC potential perturbation is measured between working and reference electrode, while the current is applied between working and counter electrode. A number of cell designs for impedance measurements with a reference electrode have been suggested, with the reference electrode either placed between anode and cathode,[5–9] or placed in-plane with anode or cathode through a central hole (also referred to as co-axial arrangement).[10–12] The more commonly used design, however, is a Swagelok T-cell design with the reference electrode (typically consisting of a lithium metal disc) being placed perpendicularly to the anode and cathode, outside the active area.[13] Yet, experiments and numerical simulations by Ender et al.[14] showed that the impedance measurements with the latter reference electrode placement can display significant distortions caused by small in-plane offsets between anode and cathode (referred to as geometrical asymmetry) and/or by large differences in the impedance response of anode and cathode (referred to as electrical asymmetry), consistent with earlier work by Dees et al.[15] This is also the case for coaxially located reference electrodes, for which the measured anode or cathode impedance is shown to be highly sensitive toward misplacements of the electrodes.[10,12,16] The impedance artefacts in both of these designs stem from the location of the reference electrode being *at the edge* of the working and the counter electrodes, where the current density is not homogeneous. If one electrode is now shifted slightly toward the reference electrode, the potential field around the reference electrode is dominated by this electrode, which leads to a biased impedance response. In contrast, if the reference electrode is placed *centrally between* the electrodes far away from their edges, small relative shifts of the electrodes do not affect the impedance response.[15] This geometry is typically realized by using a thin wire with an electronic insulator around its perimeter, being exposed only at its end, which is placed well inside the active area.[6–8] Yet, this location of the reference electrode can block parts of the working electrodes and thus alter the potential field between them. In order to minimize this effect, the reference electrode needs to be small compared to the size of the electrodes and the distance between them. Dees et al.[15] showed that a 25 μm thick reference electrode, between two electrodes separated by 100 μm, delivered sufficiently accurate potential and impedance measurements.

Unfortunately, the design of a micro-reference electrode, i.e., an insulated wire with small diameter (25–50 μm) imposes difficult requirements on the choice of material. Lithium metal, which is typically used as reference electrode in lithium ion cells, is difficult to accurately produce and handle in micron-sized dimensions. On the other hand, the potential of the reference electrode should be well-defined and stable in a lithium-ion electrolyte, as the reference electrode should (ideally) also be able to record the absolute potential of both electrodes during cycling. Additionally, potential drifts during impedance measurements can lead to a biased impedance response.[17] Zhou et al.[7] successfully plated lithium in-situ onto a thin, insulated copper wire as reference electrode. As the wire insulation was only removed at the very tip of the wire, the reference electrode active area was small and located far away from the electrode edges. However, they also showed that the potential stability of the reference electrode depends strongly on the plating parameters, as thin films of high surface area lithium can be completely dissolved or disconnected due to continuous SEI growth.

A similar approach has been followed by Abraham et al.[6] using an insulated tin-coated copper wire. Yet, instead of plating metallic lithium on a non-alloying copper wire like Zhou et al.,[7] lithium was in-situ electrochemically alloyed with the tin coating at the wire tip, where the insulation had been removed. While the long-term potential stability of this reference electrode is also limited, it can

*Electrochemical Society Student Member.
**Electrochemical Society Fellow.
[z]E-mail: sophie.solchenbach@tum.de

nevertheless be used for impedance measurements of individual electrodes during long-term cycling studies by short re-lithiation prior to the measurement.[8,18] The use of lithium alloys as reference electrode brings – in theory – a number of advantages: i) lithium forms alloys with a large number of metals, which are readily available as thin wires and at high purity;[19,20] and ii) the volume expansion and thus the specific surface area of lithium alloys is smaller compared to in-situ plated lithium, which means that the alloy should be less prone to self-delithiation surface reactions. Yet, only few lithium alloys have been employed as reference electrodes apart from Li-Sn:[6,8,18] a lithiated aluminum wire has been used as reference electrode by Verbrugge et al.;[9] and Gómez-Cámer and Novák[21] recently demonstrated the use of a lithium-bismuth alloy as reference electrode in their specifically designed impedance cell with a coaxial reference electrode.

So far, the viability of lithium-gold alloys as reference electrodes has not yet been examined. Studies on the electrochemical lithiation of gold are limited, as its poor capacity retention, high cost and low specific capacity compared to other alloys disqualify gold as a potential anode material. The Li_3Au phase is the most lithium-rich composition which can be obtained electrochemically, corresponding to a specific capacity of 408 mAh/g_{Au}.[19,22–26] The lithiation of gold proceeds in two main potential plateaus, with the first stage having an OCV potential of ∼0.3 V vs. Li/Li^+, and the second ∼0.2 V vs. Li/Li^+.[25] Surprisingly, the intermediate phases detected between α-Au and Li_3Au during electrochemical alloying could not be assigned to any of the known thermodynamic Li-Au phases.[27–30] Bach et al.[30] recently identified the metastable Li_3Au_2, Li_5Au_3, Li_3Au_5 and $LiAu_2$ phases by in-situ high energy X-ray diffraction during the electrochemical lithiation and delithiation of gold thin film electrodes.

Despite its drawbacks as an anode, several properties of the lithium-gold alloy make it an interesting reference electrode material: i) the potentials of both stages are very flat, and already low degrees of lithiation will result in an OCV of around 0.31 V vs. Li/Li^+; ii) it is difficult to completely delithiate a lithium-gold alloy by electrochemical or chemical means;[24,26] iii) gold is chemically resistant against HF and does not form any substantial surface oxide films;[31] and, iv) the high electrical conductivity of gold means that the potential drop along the length of the reference electrode wire is negligible.

In this study, we developed a novel micro-reference electrode based on a 50 μm thick, insulated gold wire, which we integrated into a conventional T-cell design. This gold wire reference electrode (GWRE) is placed centrally between both electrodes and two 200 μm thick glass fiber separators. Analogous to the approach used by Abraham et al.[6] for a tin-based reference electrode, we achieve a stable potential of the gold wire by in-cell electrochemical alloying with lithium. We show that the potential of the lithiated GWRE is stable for several weeks, even under elevated temperatures (40°C). With this lithiated GWRE, we are able to record the potential of both electrodes in LFP/graphite full-cells for more than 200 cycles. Further, we evaluate the capabilities of the lithiated GWRE to accurately measure the impedance of individual electrodes in full-cells, which we verify by symmetric cell measurements. As a proof of concept, we conduct a similar study as Burns et al.[32] on the impedance growth of anode and cathode in the presence of different concentrations of vinylene carbonate (VC) in LFP/graphite full-cells, using however our lithiated GWRE instead of a symmetric cell approach. We can reproduce the findings by Burns et al.[32] and further demonstrate that the total amount of VC per active material, rather than its concentration, is the key parameter for the electrolyte/anode interface resistance. This result is important when electrolyte additives are tested in laboratory cells, as these cells typically have a higher electrolyte to active material ratio than commercial lithium-ion cells.

Experimental

Electrode preparation.—Lithium iron phosphate ($LiFePO_4$, LFP) electrodes were prepared by mixing LFP (BASF SE, Germany), carbon black (Super C65, Timcal), and polyvinylene diflouride (PVDF, Kynar) in a mass ratio of 93:3:4 with NMP (N-methyl pyrrolidone, anhydrous, Sigma-Aldrich, Germany) in a planetary mixer (Thinky Corp.) for 15 min. The resulting ink was coated on carbon-coated aluminum foil (MTI) with a doctor blade mounted on an automatic coater and dried at 50°C in a convection oven for at least 3 h. The final LFP coating had a loading of 11.7 mg_{LFP}/cm^2 (≡ 2.0 mAh/cm^2 based on 170 mAh/g_{LFP}). Electrodes with a diameter of 11 mm were punched out and pressed to 35% porosity (2 × 60 s at 260 MPa) with a KBr press (Mauthe, PE-011). Graphite electrodes were prepared by mixing graphite (T311, SGL Carbon GmbH) and PVDF in a mass ratio of 95:5 with NMP, following the same procedure. The graphite ink was doctor-blade coated on copper foil (MTI) and dried in a convection oven at 50°C for at least 3 h. The final loading of the graphite coating was 5.9 $mg_{graphite}/cm^2$ (≡ 2.2 mAh/cm^2 based on 372 $mAh/g_{graphite}$) at a porosity of 40%. Both types of electrodes were dried under dynamic vacuum at 120°C overnight and transferred to an Argon-filled glove box (MBraun, Germany) without exposure to air.

Cell design and assembly.—The reference electrode current collector of a 3-electrode Swagelok T-cell (see Figure 1a) was modified to be able to host the GWRE. To this purpose, a small hole (1 mm diameter, 2.5 mm depth) was drilled into the flat front side of the reference current collector. To fix the GWRE wire, a thread was cut into the side of the reference current collector at approximately 2 mm distance from the front edge. For the actual reference electrode, a gold wire with a core diameter of 50 μm, coated with a 7 μm thick polyimide insulation (Goodfellow Cambridge Ltd., United Kingdom), was cut into pieces of ∼1.5 cm. The last 3 mm of one end of the wire was slightly scratched with a scalpel to allow good electrical contact of the wire to the reference electrode current collector. The scratched end of the wire was then inserted into the hole of the reference current collector and fixed with a small set screw. During cell assembly, the GWRE was inserted through a hole in the polymer lining of the T-cell (green lines in Fig. 1) and cushioned between two glassfiber separators (see Figure 1b); note that the insulation at the wire perimeter was not removed and that the only segment of the wire accessible to the electrolyte is the cut cross-section at the tip of the wire (see Figure 1c). The SEM image of the wire tip in Figure 1c shows that the polyimide insulation is almost completely intact around the edge of the cut cross-section, and that the exposed gold surface is relatively smooth. As the sealing and all other cell components are left unchanged compared to the conventional T-cell design, we could omit any benchmarking and air permeation tests that are normally required when developing a new electrochemical cell for the lithium ion chemistry. T-cells with GWRE were assembled with graphite as anode, LFP as cathode, and 2 glassfiber sheets (Whatman) as separator soaked with 60 μL electrolyte.

As standard electrolyte, 1 M lithium hexafluorophosphate ($LiPF_6$) in a mixture of ethylene carbonate (EC) and ethyl methyl carbonate (EMC) at a weight ratio of 3:7 was used (LP57, BASF SE, Germany). The water content of this electrolyte was determined via Karl-Fischer-Titration to be <10 ppm. Vinylene carbonate (VC, BASF SE, Germany) was added in weight ratios of 0.17% and 0.52% to the standard electrolyte. These concentrations were chosen as they yielded g_{VC}/Ah_{Cell} ratios equal to 2% and 6% VC additive (same solvent/salt) in 225 mAh full-cells used in a study on the anode and cathode impedance growth in the presence and absence of VC by Burns et al.[32] For stability measurements of the gold wire electrode, symmetrical lithium/lithium cells with a GWRE were built using 11 mm lithium discs (450 μm thickness, Rockwood, USA) as both cathode and anode.

Cell cycling and impedance measurements.—The gold wire reference was lithiated by applying a current of 150 nA between the working electrode (LFP or lithium) and the gold wire reference electrode using a potentiostat (VMP300, BioLogic, France). Please note that the selected current range of 10 μA has an accuracy of 0.1%, which leads to an error of ∼10 nA. LFP/graphite cells were cycled

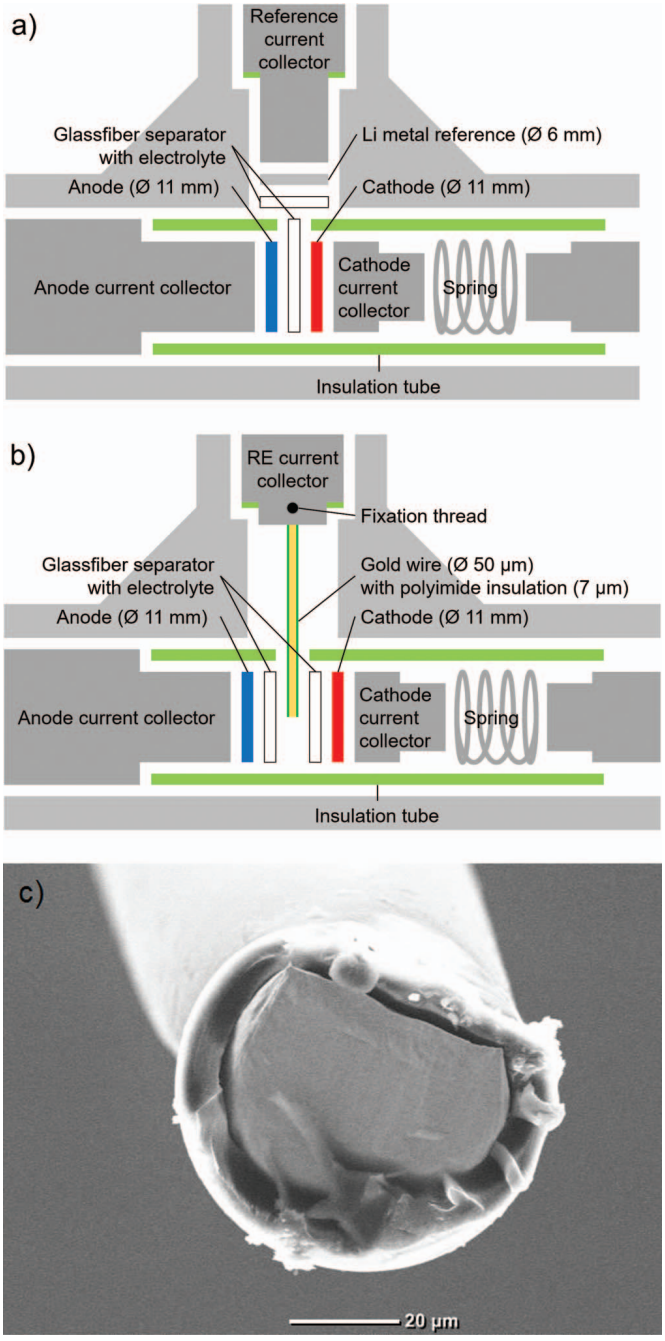

Figure 1. a) Conventional Swagelok T-cell design, b) modified T-cell design with gold wire reference electrode (GWRE), c) SEM image of the cut cross-section of gold wire tip prior to lithiation.

between cell voltages of 2 and 4 V using a BioLogic potentiostat and a CCCV charge/CC discharge procedure with a C/20 current cutoff to end the CV phase. During cycling, the cells were placed inside a climatic chamber with a constant temperature of 25°C or 40°C. Electrochemical impedance spectroscopy (EIS) measurements were conducted either potential controlled with a perturbation of 5 mV at OCV (referred to as PEIS, with the AC voltage perturbation applied between working and reference electrode) or current controlled with a perturbation of 0.5 mA (referred to as GEIS), both in a frequency range of 100 kHz–0.1 Hz. The impedance measurements were conducted at 50% SOC and 25°C or 10°C. Prior to the measurement, the cells were allowed to rest at OCV and thermally equilibrate for 15 min.

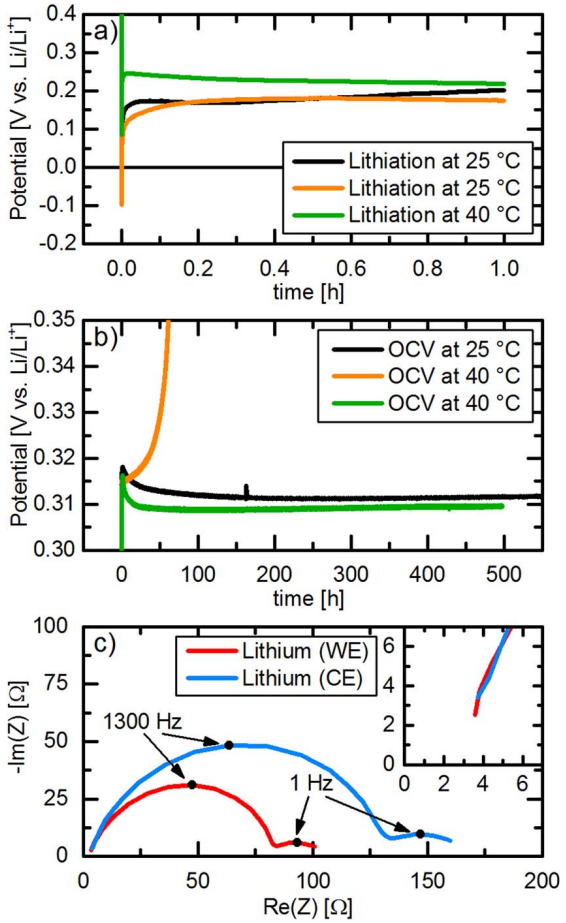

Figure 2. a) Potential of two GWREs during lithiation at 25°C (black and orange lines) and of one GWRE during lithiation at 40°C (green line) with 150 nA for 1 h. b) Potential of GWREs lithiated at 25°C during subsequent OCV at 25°C (black line) or at 40°C (orange line) as well as of the GWRE lithiated at 40°C during subsequent OCV at 40°C (green line). c) Nyquist plot of the lithium electrodes in a lithium/lithium cell at OCV at 25°C after lithiation of the GWRE at 25°C (PEIS, 100 kHz to 0.1 Hz, 5 mV AC perturbation). All potentials are given vs. Li/Li^+ and experiments were conducted in LP57 electrolyte.

Results and Discussion

Suitability of the GWRE to quantify individual electrode impedance in full-cells.—As a first step, the potential stability of a lithiated GWRE was investigated in symmetric lithium-lithium T-cells with our modified design (see Fig. 1b). The GWRE was lithiated by applying a current of 150 nA for 1 h between one of the lithium electrodes and the GWRE. The black curve in Figure 2a shows the potential of the GWRE vs. Li/Li^+ during galvanostatic lithiation at 25°C. The potential drops briefly below 0 V vs. Li/Li^+ and then stays constant at ~0.2 V vs. Li/Li^+ during the entire lithiation procedure, which is similar to the first potential plateau observed during the electrochemical lithiation of gold thin films.[25] The overpotential at the first moments of lithiation have been attributed to the reduction of surface oxides[19] or the nucleation of the lithium-gold alloy phase.[25] During the subsequent OCV at 25°C (see black curve in Figure 2b), the potential of the GWRE shoots up to 0.318 V and then quickly relaxes to ~0.311 V vs. Li/Li^+, which corresponds to the OCV potential of a Li_xAu alloy with $0 < x < \sim 1.2$.[25] The lithiated GWRE potential remains stable for more than 500 h, varying by less than 2 mV after the initial 20 h of the OCV period. This means that the lithiated GWRE might not be suitable for highly accurate potential measurements during initial cycles, but is sufficient for tracking electrode potentials during prolonged cycling. Further, no morphological

changes of the wire could be observed visually after disassembly of the cells.

As many battery cycling tests are performed at higher temperatures to accelerate aging and to reflect more realistic operating conditions, it is desirable that the GWRE also functions at higher temperatures. However, if the GWRE is lithiated at 25°C and the cell temperature is then increased to 40°C for OCV measurements, the gold wire potential starts to drift to more positive values after less than 10 hours (see orange curve in Figures 2a and 2b). This is in accordance with Abraham et al.,[6] who reported that the potential of a lithiated tin wire is substantially less stable at elevated temperatures, where the rate of SEI growth and the concomitant self-delithiation is generally enhanced. Once the cell is heated to 40°C, this effect must lead to a rather rapid depletion of lithium at the wire's tip, resulting in the observed potential drift. Interestingly, a re-lithiation of the wire with the same procedure at 25°C restored a stable GWRE potential of 0.311 V vs. Li/Li^+, as long as the cell was kept at 25°C. We also observed that the GWRE potential stability over long time was limited in combination with high voltage cathodes (>4.7 V vs. Li/Li^+), and also here the GWRE could be relithiated.[33]

After further investigations, we found that if the gold wire lithiation is conducted at 40°C (see green curve in Figures 2a and 2b), the GWRE shows the same stability during OCV at 40°C as was observed at 25°C, only shifted downwards by 1–2 mV. It is reported that an SEI formed at higher temperatures contains more inorganic species,[34] which we hypothesize might form a more effective surface film on the lithium-gold alloy. While high temperature SEI formation was shown to lead to inferior capacity retention on graphite anodes during cycling,[34] the more inorganic SEI could be advantageous in the absence of cycling-induced volume changes, i.e., for reference electrodes. However, the exact mechanism behind this enhanced stability by lithiation at higher temperatures is not clear at this point. We further believe that the stable potential of the GWRE for over hundreds of hours at up to 40°C is partly due to the fact that, contrary to previous micro-electrode designs,[6,7] the reference electrode area exposed to the electrolyte is limited to the cross-sectional area of the tip (see Figure 1c), minimizing side reactions with the electrolyte. The stable potential over 500 h indicates that the lithium diffusion along the wire (i.e., away from the tip) must be sufficiently slow to prevent a significant depletion of lithium at the tip.

To evaluate if the GWRE in the modified T-cell design is suitable for impedance measurements of individual electrodes, we also measured the impedance of a symmetrical lithium/lithium cell with a GWRE (see Figure 2c). Arbitrarily, one of the lithium electrodes was designated as working electrode (WE), while the other was designated as counter electrode (CE). Prior to the impedance measurement in the lithium/lithium cell, the GWRE was lithiated at 25°C as described above from the lithium electrode designated as WE. The high frequency resistance (see inset) is identical for both lithium electrodes, which indicates that the GWRE is located centrally between the electrodes. Hence, a first precondition for an artefact-free measurement is fulfilled.[14] Both lithium electrodes show a large semicircle in the high-frequency region (100 kHz–20 Hz, with the apex at ≈1.3 kHz), followed by a smaller semicircle at frequencies between 20 and 0.1 Hz (with the apex at ≈1 Hz), as reported previously for lithium metal electrodes.[35,36] While the high-frequency semicircle has been ascribed to the SEI resistance, the semicircle in the low-frequency region is thought to represent the charge transfer resistance.[36] Interestingly, both semicircles of the electrode used for the lithiation of the GWRE (designated as WE, see red line in Figure 2c) are about 35% smaller compared to the other electrode (≡ CE, s. blue line). We believe that this originates from the stripping of lithium from the WE electrode during lithiation of the GWRE, as this would cause a roughening of the lithium surface, leading to higher surface area and thus smaller impedance.

As a next step, the use of the GWRE in a LFP/graphite full-cell is tested and evaluated. Here, we also want to assess whether lithiation of the reference electrode is necessary for impedance measurements, i.e., whether the non-lithiated Au wire can be used as pseudo-GWRE.

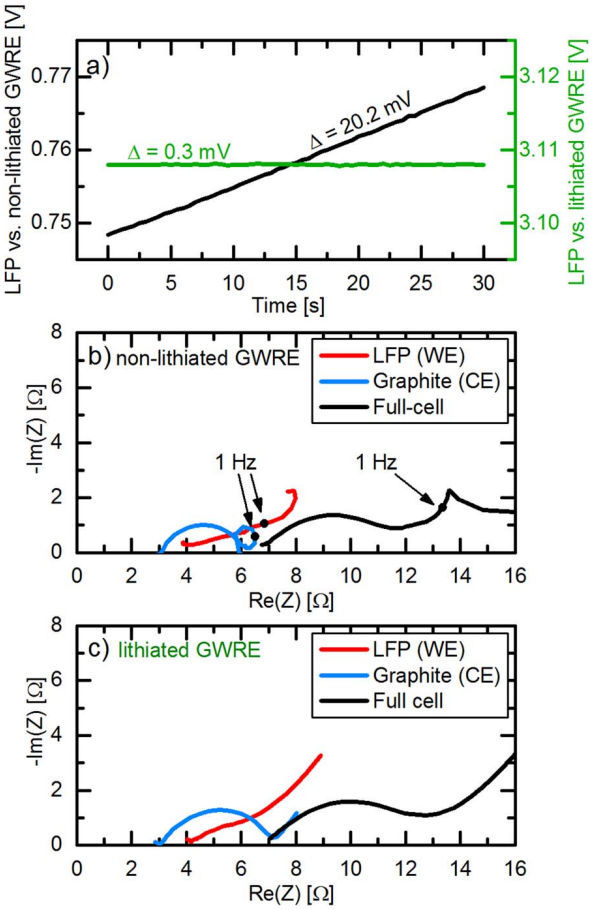

Figure 3. Comparison of voltage drift and impedance quality for a lithiated GWRE and a non-litiated pseudo-GWRE in LFP/graphite full-cells. a) Measured potential between the LFP working electrode (WE) and either the non-lithiated pseudo-GWRE (black line) or the lithiated GWRE (green line). b) Nyquist plot of an LFP/graphite full-cell obtained with a non-lithiated pseudo-GWRE before lithiation. c) Nyquist plot of an LFP/graphite full-cell obtained with a lithiated GWRE. Conditions: 25°C, LP57 electrolyte, PEIS with 5 mV amplitude at OCV (100 kHz–0.1 Hz).

To this purpose, we built identical LFP/graphite cells with GWRE: in one case, we lithiated the GWRE with 150 nA for 1 h at 25°C from the LFP electrode (note that the 150 nAh needed for lithiation of the GWRE are negligible compared to the LFP cathode capacity of 1.95 mAh); in the other case, we did not lithiate the GWRE. Subsequently, both cells underwent one formation cycle (at a rate of C/10) at 25°C and then were charged to 50% SOC. Figure 3a shows the potential of the LFP cathodes vs. the non-lithiated pseudo-GWRE and vs. the lithiated GWRE during 30 seconds of OCV prior to the impedance measurement. As the potential of the LFP electrode does not change significantly during the measurement, all potential changes can be ascribed to changes in the GWRE potential. While the LFP potential vs. the non-lithiated GWRE drifts about 20 mV during 30 seconds (black curve in Figure 3a), the LFP potential vs. lithiated GWRE remains stable within 0.3 mV (green curve in Figure 3a). In the subsequent potential-controlled impedance measurement (PEIS; 5 mV amplitude, 100 kHz–0.1 Hz) at OCV, the cell with the non-lithiated GWRE (see Figure 3b) shows significant distortions at frequencies near/below 1 Hz: i) the graphite impedance (blue line) displays an inductive loop; ii) the LFP impedance (red line) bends toward lower Re(Z) values; and, iii) even the full-cell impedance (black line) shows an irregular sharp peak. These distortions appear at frequencies near or below 1 Hz, where the average potential drift of 0.67 mV/s of the non-lithiated pseudo-GWRE (see black line in Figure 3a) is no longer significantly lower than the change of the AC voltage amplitude of

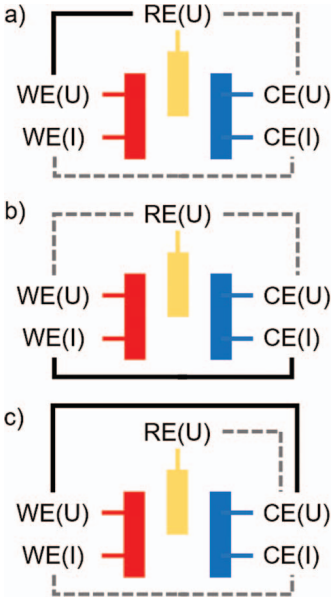

Figure 4. Systematic scheme of impedance measurements modes. a) Potential-controlled impedance spectroscopy (PEIS): The potential perturbation is controlled between WE and RE (black solid line), while current and potential between WE - CE are measured (gray dotted lines). A drift of the RE will lead to bias current between WE and CE. b) Current-controlled impedance spectroscopy (GEIS): The current perturbation is applied between WE and CE (black solid line), while potentials between WE - RE and CE - RE are measured. c) Modified potential-controlled impedance spectroscopy (PEIS): The potential perturbation is controlled between WE and CE (black solid line), while current between WE - CE and potential between RE - CE are measured (gray dotted lines).

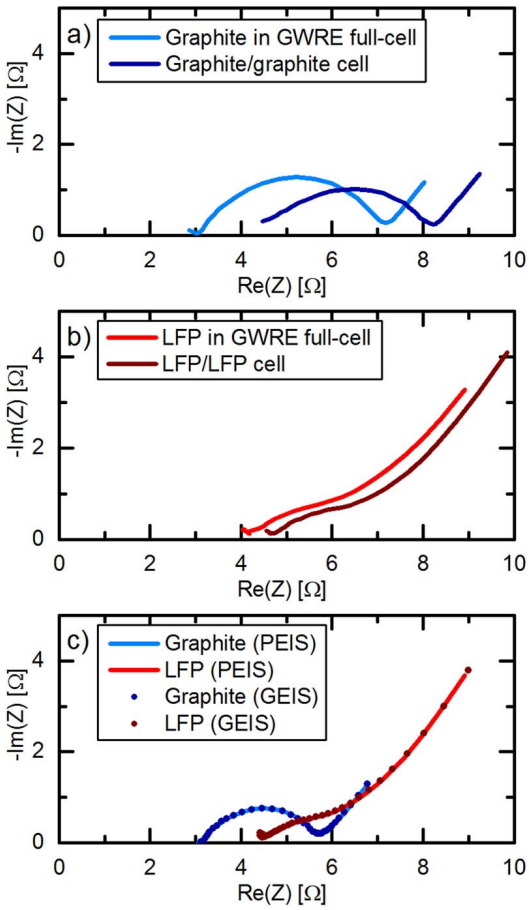

Figure 5. Impedance measurements on LFP and graphite electrodes after one C/10 formation cycle at 25°C and subsequent charge to 50% SOC. a) Nyquist plot of the graphite electrode of an LFP/graphite full-cell with lithiated GWRE (blue line) and of a symmetrical graphite/graphite cell divided by 2 (dark blue). b) Nyquist plot of the LFP electrode of an LFP/graphite full-cell with lithiated GWRE (red line) and of a symmetrical LFP/LFP cell divided by 2 (dark red). c) Comparison of the impedance response (100 kHz–0.1 Hz) of graphite and LFP electrodes under potential-controlled (PEIS at 5 mV amplitude, straight lines) and current-controlled (GEIS at 0.5 mA amplitude, dotted lines) conditions. All impedance measurements were conducted at 25°C.

5 mV. In contrast, the impedance spectra of the cell with the lithiated GWRE (Figure 3c) do not show these distortions, as the reference potential drift is almost two orders of magnitude lower in this case (0.01 mV/s). Our measurements are in agreement with simulations by Victoria et al.,[17] who showed that linear potential drifts on the order of 0.1 mV/s during impedance measurements can lead to these types of artefacts below 1 to 0.1 Hz, depending on the excitation amplitude. The potentiostatic impedance measurement mode used here (see Figure 4a), where the potential between WE and RE is controlled, leads to a particularly detrimental effect: As the base potential between RE and WE is fixed, the WE potential has to drift in the same way as the RE, which leads to a bias current between WE and CE. This continuously increasing current renders the full system nonlinear and time-variant, leading to the full cell impedance artefacts observed at low frequencies. While normally the full cell impedance should be unaffected by artefacts related to the reference electrode,[14] this comparison shows that it is crucial to use a reference electrode with a stable and defined potential for WE - RE potential controlled impedance measurements at low frequencies. To avoid the effects of a drifting pseudo-reference electrodes on the full cell impedance, one could either use a current-controlled measurement mode (GEIS, see Figure 4b), or control the potential between WE and CE during the impedance measurement (Figure 4c). Yet, artefacts of a non-stable RE will still be visible in the half cell impedance in these measurement setups.

Next, we take a closer look at the impedance spectra of the LFP and graphite electrodes recorded with a lithiated GWRE (Figure 3c). In contrast to the previous setup with two lithium electrodes, the HFR of both electrodes is not identical here. Gaberscek et al.[37] showed that the contact resistance between an aluminum current collector and an LFP electrode composite can be on the order of several Ωcm^2. Our own measurements confirm that the through-plane resistance of the used LFP electrodes is about 1 Ωcm^2 higher compared to the graphite electrodes (data not shown). Thus, the $\approx 1\ \Omega$ difference in HFR originates from the higher contact resistance between the LFP coating and the current collector (1 Ωcm^2 corresponds to $\approx 1\ \Omega$ for our electrode area of 0.95 cm^2). The charge transfer semicircle of the LFP electrode is small and almost invisible, which suggests the lack of a resistive cathode film.[38,39] At the same time, the graphite anode shows a clearly distinguishable semicircle. As this semicircle is not visible in graphite electrodes prior to cycling, we attribute it to a combined SEI/charge transfer resistance on the graphite surface.

To further validate the impedance data measured in a full-cell with a lithiated GWRE, we compare its impedance response with that of symmetric cells, which are commonly used for accurate impedance measurements.[4] Figures 5a and 5b show the comparison of the impedance spectra of a graphite and a LFP electrode measured in a full-cell with lithiated GWRE and in reassembled symmetric LFP/LFP and graphite/graphite cells, all after one C/10 formation cycle at 25°C and subsequent charge to 50% SOC. Note that the impedances of the symmetric cells have been divided by 2 in order to account for the two nominally identical electrodes in the symmetric cells. Apart from a slight shift in HFR, the impedance response of the symmetric cells and the full-cell with the lithiated GWRE are essentially identical for both graphite (Figure 5a) and LFP (Figure 5b) electrodes. The HFR shift is probably introduced by a weaker compression of the glassfiber seperators in the symmetric cells, caused by the slightly different assembly

procedure for cells with and without GWRE. The additional high frequency contact resistance feature visible in the impedance spectra of symmetric cells by Dahn's group,[4] which results from the contact resistance between the cell housing and the electrode coating on the back side, does not appear in our symmetric cell impedance spectra (see Figures 5a and 5b), as we use single-side coated electrodes for both symmetric cells and full cells.

As a final consistency check, we performed a potential-controlled impedance measurement (PEIS) followed by a current-controlled impedance measurement (GEIS) on the same LFP/graphite full-cell with a lithiated GWRE (see Figure 5c). Mathematically speaking, both measurements should give identical results in a Nyquist plot; hence any differences between them would indicate a biased impedance response.[21] However, Figure 5c shows that the two methods deliver completely identical impedance spectra. These results confirm that the presented cell setup with the lithiated GWRE is free of measurement artefacts and is suitable for the impedance investigation of individual electrodes in full-cells. In summary, our modified T-cell design with a lithiated GWRE is able to provide accurate impedance measurements of individual electrodes in full-cells in a wide frequency range (100 kHz–0.1 Hz). A stable potential of the GWRE is especially crucial for measurements at low frequencies. If lithiated at elevated temperature, the potential of the GWRE is stable for several weeks at up to 40°C, which we partially attribute to the small area exposed to the electrolyte.

Anode & cathode impedances during cycling in full-cells with GWRE.—In the following, we want to demonstrate the suitability of the lithiated GWRE to investigate the evolution of anode and cathode impedances during extended charge/discharge cycle tests in full-cells. To this purpose, LFP/graphite full-cells with lithiated GWRE were cycled at 25°C for 200 cycles at a rate of 1C after two initial formation cycles at C/10. Impedance measurements were performed at 50% SOC after 5, 10, and each subsequent 10th cycle at 25°C. Figures 6a and 6b show the potential of the cathode and anode vs. the lithiated GWRE potential (left y-axis) during cycles 10, 50, 100 and 200 (for the sake of clarity, cycles in between were omitted), which can easily be converted into the Li/Li$^+$ scale by adding 0.311 V (right y-axis). The LFP charge and discharge plateaus are centered around 3.11 V vs. the lithiated GWRE (see Figure 6a and also Figure 3a), corresponding to a calculated value of 3.42 V vs. Li/Li$^+$, which matches well with the true LFP equilibrium potential.[40] The LFP potential center vs. lithiated GWRE remains constant during cycling, meaning that the lithiated GWRE maintains its stable potential of 0.311 V vs. Li/Li$^+$. Throughout cycling, the overpotentials of both electrodes do not change, yet the maximum potential of the graphite anode at the discharge end point moves upwards (see dark blue to light blue lines in Figure 6b). At the same time, the minimum potential of the cathode also moves upwards (see dark red to light red lines in Figure 6a), which indicates that the SOC of both electrodes slip against each other. Figure 6c shows the impedance spectra of both cathode and anode after 10, 50, 100 and 200 cycles. Note that both the cathode and anode impedance decrease slightly from cycle 5 (data not shown) to cycle 10, which could be related to the dissolution of gasses evolved during formation and/or improved wetting over the first cycles. Between cycle 10 and 200, the high frequency resistance of both electrodes increases slightly by about 0.1–0.2 Ω. This could be due to an increased electrical resistance between the electrode coatings and the current collectors, implying a very slow delamination of the composite electrodes, or a higher ionic resistance within the bulk electrolyte. While the cathode impedance shows no further changes during cycling, the anode semicircle increases slightly from ~1.9 Ω after cycle 10 to ~2.2 Ω after cycle 200, which indicates a very slow SEI growth. Overall, the potential changes of both electrodes during cycling and the small but measureable impedance growth of the anode can be related to the loss of active lithium due to a slow but steady SEI growth, which has been identified as the dominant aging mechanism in LFP/graphite cells.[41–45]

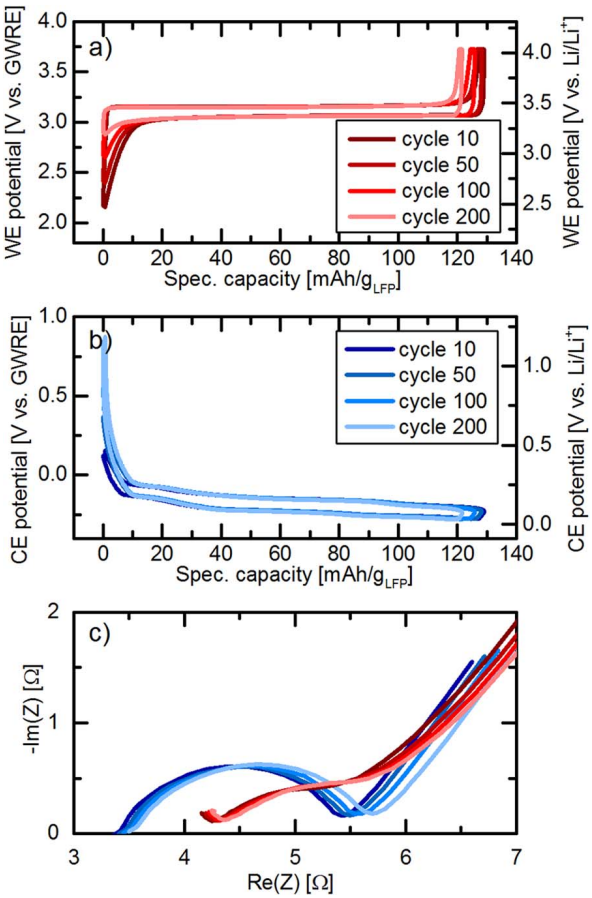

Figure 6. Charge/discharge of an LFP/graphite full-cell with a lithiated GWRE at a rate of 1C after two initial formation cycles at C/10 (LP57 electrolyte, 25°C). a) Cathode potential vs. the lithiated GWRE of cycles 10, 50, 100 and 200. b) Anode potential vs. the lithiated GWRE of cycles 10, 50, 100 and 200. The conversion to the Li/Li$^+$ scale (right axis in a and b) was done by adding 0.311 V to the GWRE potential. c) Nyquist plot of the PEIS (5 mV amplitude, 25°C) at 50% SOC of both the graphite anode (shown in the range from 100 kHz to 0.1 Hz) and the LFP cathode (shown in the range from 100 kHz to 0.3 Hz) after cycle number 10, 50, 100 and 200.

Application of the GWRE to anode & cathode impedance growth during full-cell formation.—Vinylene carbonate (VC) is one of the most commonly used electrolyte additives, as it leads to improved SEI stability at elevated temperatures and thus enhanced cycle life of lithium ion cells.[46,47] However, high concentrations of VC have shown to increase the impedance of both anode and cathode,[32] which in turn leads to higher overpotentials and heat generation during cycling. Freiberg et al.[48] recently indicated that the absolute amount of an additive per active material, instead of its concentration, is the crucial parameter when comparing larger cells (e.g. commercial cells) and small lab-scale cells (e.g. coin cells). Therefore, we want to compare the effect of different amounts of VC in LP57 electrolyte on both anode and cathode impedance in LFP/graphite full-cells obtained with a lithiated GWRE to the study by Burns et al.,[32] who used 225 mAh LCO/graphite pouch cells with the same electrolyte and examined the effect of VC on the impedance of the individual electrodes via symmetric cell measurements. In Burns' study, it was shown that the charge transfer resistance of a graphite anode decreases slightly from 0% to 0.5% VC in the electrolyte and increases roughly linearly with VC concentration between 1% and 6% VC (see Figure 9b in Ref. 32). At the same time, the impedance of the LCO cathode from Burns' study (see Figure 9a in Ref. 32) decreases about 50% from 0% to 2% VC and then gradually increases again up to VC concentrations of 6% to a value which is still below the 0% VC case. Unfortunately, the exact amount of active material in the cells used by Burns et al. was not

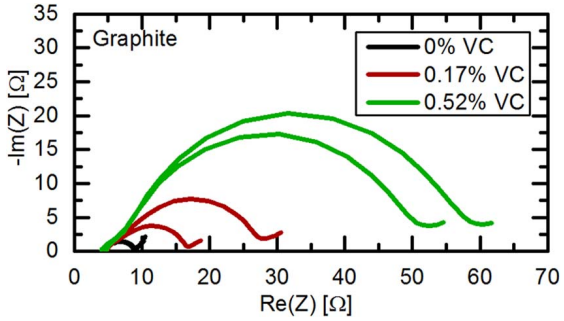

Figure 7. Nyquist plot of the graphite anode impedance after one formation cycle and recharge to 50% SOC at 40°C of LFP/graphite full-cells with a lithiated GWRE in LP57 electrolyte containing 0%, 0.17%, and 0.52% VC in the electrolyte. PEIS was measured at 10°C between 100 kHz–0.1 Hz with an amplitude of 5 mV.

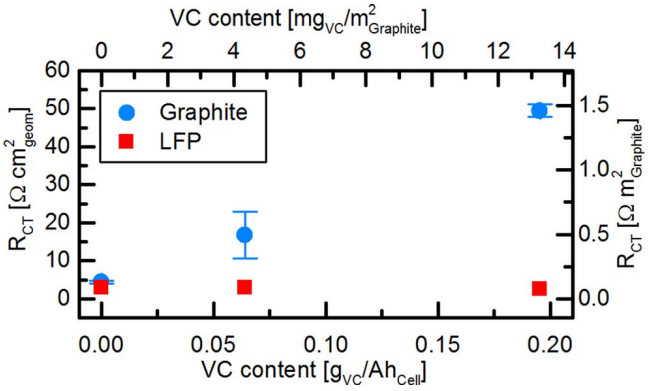

Figure 8. R_{ct} of the graphite anode and the LFP cathode after formation in LFP/graphite full-cells with different VC amounts added to LP57 electrolyte. Impedance data were obtained with a lithiated GWRE (PEIS at 5 mV amplitude and 10°C between 100 kHz and 0.1 Hz) and fitted by an equivalent circuit consisting of a resistor for the electrolyte, an RQ-element for the electrolyte/electrode interface resistance, and a Warburg element for solid-state diffusion. Note that the upper x-axis and the right y-axis display the VC content and charge transfer resistance normalized to the graphite BET surface area.

given. However, the specific capacities of LCO and LFP are similar, and our anode to cathode capacity ratio of 1.1 is close to a commercial balancing. Hence, we think it is reasonable to assume that the masses of both anode and cathode active materials are proportional to the respective cell capacity. As the ratio of electrolyte to cell capacity (and thus active material) in our lab-scale T-cell design is 11.6 times higher compared to Burns et al.[32] (38 $g_{electrolyte}/Ah_{Cell}$ vs. 3.3 $g_{electrolyte}/Ah_{Cell}$), we adjusted the amount of VC in the electrolyte accordingly. Thus, our chosen concentrations of 0.17% and 0.52% VC represent the same g_{VC}/Ah_{Cell} ratio, namely 0.06 g_{VC}/Ah_{Cell} and 0.2 g_{VC}/Ah_{Cell}, as cells with 2% and 6% VC in the study by Burns et al.[32] After lithiation of the GWRE and one formation cycle at 40°C, the LFP/graphite cells were charged to 50% SOC and the impedance measurements were then conducted at 10°C, i.e., under the same conditions as reported by Burns et al.[32]

Figure 7 shows the Nyquist plot of graphite electrodes after formation with different concentrations of VC. For each concentration, two cells are shown to assess the cell to cell variation. Quite clearly, the cells with 0.17% and 0.52% VC show an increased charge transfer resistance of the graphite anodes. These results already indicate that electrolytes cannot be compared without considering the amount of active material, as the anode charge transfer resistance decreases up to a VC concentration of 0.5% in the study by Burns et al.,[32] while Figure 7 shows that the anode charge transfer resistance increases substantially within the same VC concentration range.

To quantify the charge transfer resistances, the impedance spectra of cathode and anode of each cell were fitted using a simple electrochemical equivalent circuit composed of: i) a resistor for the electrolyte, ii) a resistor and a constant phase element in parallel to describe the electrolyte/electrode interface resistance, and, iii) a Warburg-type diffusion element in series representing solid state diffusion. This circuit is a simplified version of a model used by Illig et al.[35] for LFP electrodes; we omitted the electrode contact resistance and the low frequency capacitor, as both are not visible within our measurement range. Figure 8 shows the average fitted charge transfer resistances (left y-axis), normalized to the geometrical electrode area, of both electrodes at different g_{VC}/Ah_{Cell} ratios (lower x-axis). The anode charge transfer resistance is ~5 Ωcm^2 for cells without VC and increases to ~16 Ωcm^2 and ~47 Ωcm^2 for cells with 0.06 g_{VC}/Ah_{Cell} (≡0.17% VC) and 0.2 g_{VC}/Ah_{Cell} (≡0.52% VC), respectively. In comparison, Burns et al.[32] showed an anode charge transfer resistance of ~30 Ωcm^2, ~60 Ωcm^2 and ~150 Ωcm^2 for cells with identical g_{VC}/Ah_{Cell} ratios (0%, 2% and 6% VC in their study). The linear increase in charge transfer resistance from 0.033 to 0.2 g_{VC}/Ah_{Cell} that has been observed by Burns et al.[32] (corresponding to 1%-6% VC in their study) is also found in our results within the same g_{VC}/Ah_{Cell} range, although our absolute VC concentrations are completely different (0–0.52% VC). This further proves that the amount of additive per active material (here corresponding to the g_{VC}/Ah_{Cell} ratio) determines the effect of an additive on the surface of an electrode, and not its concentration. The differences in absolute resistance values between Burns' study[32] and ours could be explained by differences in active material loading and BET surface area of the used electrodes: As the impedance of an electrode is inversely proportional to the electrochemical active area, a higher roughness factor (i.e., electrode surface area per geometric area) will result in an overall lower impedance, even if the surface chemistry is identical. While our electrodes are loaded with 5.9 mg/cm^2 graphite having a BET surface area of ~5 m^2/g, we can estimate the anodes investigated by Burns et al.[32] to have a loading of ~10 mg/cm^2 graphite[49] with a BET surface area of ~0.7 m^2/g.[50,51] In total, this would give a ~5-fold higher roughness factor in our study, which would fit with the measured ~4 times lower absolute charge transfer resistance values. However, it is to note that the assumed values for loading and BET were taken from other publications by the Dahn group and not directly from Burns et al.,[32] and hence this is only an estimate. A different BET surface area would also affect the amount of additive per unit surface, and thus result in a different charge transfer resistance. To make our data more comparable to future studies, we therefore included the amount of VC per graphite BET surface area ($mg_{VC}/m^2_{Graphite}$, upper x-axis) and the charge transfer resistance normalized to the graphite BET surface area (Ω $m^2_{Graphite}$, right y-axis) in Figure 8. An additional difference between our cells and the study by Burns et al.[32] is the different cycling protocol: Our impedance data was recorded after one formation cycle, whereas the cells by Burns et al.[32] were disassembled for impedance measurements of symmetric cells after 23 cycles. However, further cycling and impedance measurements of our LFP/graphite cells showed that the impedances of both electrodes does not change significantly with cycle number once the formation cycle is completed.

The charge transfer resistance of the LFP cathode in our study does not show any dependency on the VC content (see Figure 8). In contrast, Burns et al.[32] found that the impedance of an LCO cathode decreases about half by the addition of low concentrations of VC (0.5–2%) and increases again slightly at higher VC concentrations (4–6%). This discrepancy can be understood considering the studies by El Ouatani et al.,[52,53] which showed that LCO cathodes form a surface film of poly(VC) in VC-containing electrolytes, while this film is lacking on LFP cathodes. Thus, the cathode charge transfer resistance remains constant and independent from the VC content in LFP/graphite cells. As VC reacts on the LCO surface,[52,53] one can imagine that slightly less VC is available for SEI formation in LCO/graphite than in LFP/graphite cells. This could in turn also partially explain the deviations of the absolute values for the anode charge

transfer resistance at points of equal g_{VC}/Ah_{Cell} in our study compared to Burns et al.[32] Hence, we can conclude that not only the ratio of additive to active material, but also the cell chemistry of cathode and anode and their reactivity toward the additive is an important aspect to consider when comparing additives across different cell types.

Conclusions

In this study, we introduce a novel micro-reference electrode in a Swagelok T-cell design, which is suitable for impedance and potential measurements of both working and counter electrode individually. The reference electrode consists of a thin, insulated gold wire and is placed centrally between both electrodes and two 200 µm thick glass fiber separators. By electrochemical alloying with lithium, we achieve a defined potential of 0.311 V vs. Li/Li^+ of the gold wire reference electrode (GWRE), which is stable for several weeks during cycling and even under elevated temperatures (40°C). In contrast to previous micro-reference designs, only the cut cross-section of the wire's tip is the electrochemically active area, which supposedly minimizes side reactions with the electrolyte and contributes to the long-term stable potential of the GWRE. The cell setup with GWRE was validated by impedance measurements of the corresponding symmetrical cells. Further, we demonstrated the suitability of the lithiated GWRE for impedance and potential measurements in LFP/graphite full-cells for up to 200 cycles. Based on these measurements, we could identify lithium inventory loss due to SEI growth as the dominant aging mechanism in LFP/graphite cells at room temperature, in agreement with literature.

As a proof of concept, we investigated LFP/graphite full-cells with a lithiated GWRE and different VC contents in the electrolyte. Using symmetrical cells, Burns et al.[32] showed that the charge transfer of a graphite anode depends almost linearly on the concentration of vinylene carbonate (VC) in the electrolyte. We can reproduce the findings by Burns et al.[32] using a lithiated GWRE, and further demonstrate that the ratio of mass VC to active material, rather than the VC concentration, is the key parameter for the electrolyte/anode interface resistance. This result needs to be considered when electrolyte additives are tested in laboratory cells, as these cells typically have a higher electrolyte to active material ratio than commercial lithium-ion cells.

Acknowledgment

This work is financially supported by the BASF SE Battery Research Network. J. L. gratefully acknowledges the funding by the Bavarian Ministry of Economic Affairs and Media, Energy, and Technology for its financial support under the auspices of the EEBatt project.

References

1. M. Klett, J. A. Gibson, S. E. Trask, B. J. Polzin, A. N. Jansen, D. W. Dees, and D. P. Abraham, *J. Electrochem. Soc.*, **163**, A875 (2016).
2. N. Ogihara, S. Kawauchi, C. Okuda, Y. Itou, Y. Takeuchi, and Y. Ukyo, *J. Electrochem. Soc.*, **159**, A1034 (2012).
3. C. H. Chen, J. Liu, and K. Amine, *J. Power Sources*, **96**, 321 (2001).
4. R. Petibon, C. P. Aiken, N. N. Sinha, J. C. Burns, H. Ye, C. M. VanElzen, G. Jain, S. Trussler, and J. R. Dahn, *J. Electrochem. Soc.*, **160**, A117 (2013).
5. T. S. Ong and H. Yang, *J. Electrochem. Soc.*, **149**, A1 (2002).
6. D. P. Abraham, S. D. Poppen, A. N. Jansen, J. Liu, and D. W. Dees, *Electrochim. Acta*, **49**, 4763 (2004).
7. J. Zhou and P. H. L. Notten, *J. Electrochem. Soc.*, **151**, A2173 (2004).
8. A. N. Jansen, D. W. Dees, D. P. Abraham, K. Amine, and G. L. Henriksen, *J. Power Sources*, **174**, 373 (2007).
9. M. W. Verbrugge, D. R. Baker, and B. J. Koch, *J. Power Sources*, **110**, 295 (2002).
10. S. Klink, E. Madej, E. Ventosa, A. Lindner, W. Schuhmann, and F. La Mantia, *Electrochem. commun.*, **22**, 120 (2012).
11. C. Bünzli, H. Kaiser, and P. Novák, *J. Electrochem. Soc.*, **162**, A218 (2015).
12. C. Delacourt, P. Ridgway, V. Srinivasan, and V. S. Battaglia, *J. Electrochem. Soc.*, **161**, A1253 (2014).
13. V. R. Koch, C. Nanjundiah, G. B. Appetecchi, and B. Scrosati, *J. Electrochem. Soc.*, **142**, L116 (1995).
14. M. Ender, A. Weber, and E. Ivers-Tiffée, *J. Electrochem. Soc.*, **159**, A128 (2012).
15. D. W. Dees, A. N. Jansen, and D. P. Abraham, *J. Power Sources*, **174**, 1001 (2007).
16. S. Klink, D. Höche, F. La Mantia, and W. Schuhmann, *J. Power Sources*, **240**, 273 (2013).
17. S. N. Victoria and S. Ramanathan, *Electrochim. Acta*, **56**, 2606 (2011).
18. D. P. Abraham, M. M. Furczon, S.-H. Kang, D. W. Dees, and A. N. Jansen, *J. Power Sources*, **180**, 612 (2008).
19. A. N. Dey, *J. Electrochem. Soc.*, **118**, 1547 (1971).
20. J. Wang, I. D. Raistrick, and R. A. Huggins, *J. Electrochem. Soc.*, **133**, 457 (1986).
21. J. L. Gómez-Cámer and P. Novák, *Electrochem. commun.*, **34**, 208 (2013).
22. T. L. Kulova, A. M. Skundin, V. M. Kozhevin, D. A. Yavsin, and S. A. Gurevich, *Russ. J. Electrochem.*, **46**, 877 (2010).
23. Y. J. Lee, Y. Lee, D. Oh, T. Chen, G. Ceder, and A. M. Belcher, *Nano Lett.*, **10**, 2433 (2010).
24. K. Nishio, K. Yuda, and H. Masuda, *ECS Electrochem. Lett.*, **2**, C1 (2012).
25. P. Bach, M. Stratmann, I. Valencia-Jaime, A. H. Romero, and F. U. Renner, *Electrochim. Acta*, **164**, 81 (2015).
26. G. Taillades, N. Benjelloun, J. Sarradin, and M. Ribes, *Solid State Ionics*, **152-153**, 119 (2002).
27. G. Kienast and J. Verma, *Zeitschrift für Anorg. und Allg. Chemie*, **310**, 143 (1961).
28. A. D. Pelton, *Bull. Alloy Phase Diagrams*, **7**, 228 (1986).
29. S. Misra, N. Liu, J. Nelson, S. S. Hong, Y. Cui, and M. F. Toney, *ACS Nano*, **6**, 5465 (2012).
30. P. Bach, I. Valencia-Jaime, U. Rütt, O. Gutowski, A. H. Romero, and F. U. Renner, *Chem. Mater.*, **28**, 2941 (2016).
31. B. D. Craig and D. S. Anderson, *Handbook of Corrosion Data*, p. 439, (1994).
32. J. C. Burns, R. Petibon, K. J. Nelson, N. N. Sinha, A. Kassam, B. M. Way, and J. R. Dahn, *J. Electrochem. Soc.*, **160**, A1668 (2013).
33. D. Pritzl, S. Solchenbach, and H. A. Gasteiger, Manuscript in preparation.
34. S. B. Lee and S. Il Pyun, *Carbon N. Y.*, **40**, 2333 (2002).
35. J. Illig, M. Ender, T. Chrobak, J. P. Schmidt, D. Klotz, and E. Ivers-Tiffée, *J. Electrochem. Soc.*, **159**, A952 (2012).
36. R. Mogi, M. Inaba, S.-K. Jeong, Y. Iriyama, A. Abouimrane, and Z. Ogumi, *J. Electrochem. Soc.*, **149**, A1578 (2002).
37. M. Gaberscek, J. Moskon, B. Erjavec, R. Dominko, and J. Jamnik, *Electrochem. Solid-State Lett.*, **11**, A170 (2008).
38. N. Dupré, J.-F. Martin, J. Degryse, V. Fernandez, P. Soudan, and D. Guyomard, *J. Power Sources*, **195**, 7415 (2010).
39. M. Cuisinier, N. Dupré, J.-F. Martin, R. Kanno, and D. Guyomard, *J. Power Sources*, **224**, 50 (2013).
40. A. Yamada, H. Koizumi, S.-I. Nishimura, N. Sonoyama, R. Kanno, M. Yonemura, T. Nakamura, and Y. Kobayashi, *Nat. Mater.*, **5**, 357 (2006).
41. L. Castro, R. Dedryvère, J.-B. Ledeuil, J. Bréger, C. Tessier, and D. Gonbeau, *J. Electrochem. Soc.*, **159**, A357 (2012).
42. M. Dubarry, C. Truchot, and B. Y. Liaw, *J. Power Sources*, **258**, 408 (2014).
43. M. Kassem, J. Bernard, R. Revel, S. Pélissier, F. Duclaud, and C. Delacourt, *J. Power Sources*, **208**, 296 (2012).
44. T. G. Zavalis, M. Klett, M. H. Kjell, M. Behm, R. W. Lindström, and G. Lindbergh, *Electrochim. Acta*, **110**, 335 (2013).
45. H. Zheng, L. Chai, X. Song, and V. S. Battaglia, *Electrochim. Acta*, **62**, 256 (2012).
46. D. Aurbach, K. Gamolsky, B. Markovsky, Y. Gofer, M. A. Schmidt, and U. Heider, *Electrochim. Acta*, **47**, 1423 (2002).
47. B. Zhang, M. Metzger, S. Solchenbach, M. Payne, S. Meini, H. A. Gasteiger, A. Garsuch, and B. L. Lucht, *J. Phys. Chem. C*, **119**, 11337 (2015).
48. A. Freiberg, M. Metzger, D. Haering, S. Bretzke, S. Puravankara, T. Nilges, C. Stinner, C. Marino, and H. A. Gasteiger, *J. Electrochem. Soc.*, **161**, A2255 (2014).
49. R. Petibon, E. C. Henry, J. C. Burns, N. N. Sinha, and J. R. Dahn, *J. Electrochem. Soc.*, **161**, A66 (2013).
50. A. J. Smith, J. C. Burns, X. Zhao, D. Xiong, and J. R. Dahn, *J. Electrochem. Soc.*, **158**, A447 (2011).
51. X. Xia, P. Ping, and J. R. Dahn, *J. Electrochem. Soc.*, **159**, A1834 (2012).
52. L. El Ouatani, R. Dedryvère, C. Siret, P. Biensan, and D. Gonbeau, *J. Electrochem. Soc.*, **156**, A468 (2009).
53. L. El Ouatani, R. Dedryvère, C. Siret, P. Biensan, S. Reynaud, P. Iratçabal, and D. Gonbeau, *J. Electrochem. Soc.*, **156**, A103 (2009).

5.2 Cathode Impedance Analysis

In this section the article *An Analysis Protocol for Three-Electrode Li-Ion Battery Impedance Spectra: Part I. Analysis of a High-Voltage Positive Electrode*[62] is presented, which was submitted in March 2017 and published in the peer-reviewed Journal of the Electrochemical Society in June 2017. The article was presented as Paper 534 at the 231st meeting of The Electrochemical Society in New Orleans (USA) in May/June 2017. http://dx.doi.org/10.1149/2.0131709jes.

Making use of the previously introduced gold wire micro reference electrode (see Section 5.1) we exemplarily analyze the impedance of an LNMO/graphite full cell in-situ. While the use of the micro reference electrode allows to obtain the impedance for anode and cathode separately, we additionally introduce an innovative measurement protocol which is based on the combination of two impedance measurements of an electrode in two different electrochemical configurations. Specifically, the analysis method is based on simultaneously fitting the impedance spectra of an individual electrode (enabled by the use of the micro reference electrode) in blocking and non-blocking condition. These conditions are obtained for a completely delithiated LNMO cathode (the diverging charge transfer resistance yields only capacitive coupling) or an LNMO cathode at mid state of charge (charge transfer resistance small), respectively. In the first part of this study the focus is on the introduction of the equivalent circuit model and the demonstration of simultaneous analysis method of two impedance spectra. The method is applied to the cathode impedance spectra recorded during 86 cycles of an LNMO/graphite cell to demonstrate the power of the technique.

The manuscript proves experimentally that indeed blocking conditions are obtained in-situ by delithiating the LNMO cathode completely and we furthermore show that this blocking electrode measurement corresponds to the blocking electrolyte condition employed for the determination of electrode tortuosities (see Section 4.1). With the physically motivated equivalent circuit model introduced in the article we obtain good agreement with the recorded impedance spectra in blocking and non-blocking conditions for all cycles. I.e., the physical and electrochemical parameters of the equivalent circuits can be obtained in-situ and with small uncertainties. In the literature the observed increase of the LNMO impedance is typically ascribed to an increased charge transfer resistance of the active material,[119] which, however, we could show unambiguously to remain fairly constant upon cycling. Instead we identify the increase of a contact resistance at the cathode/aluminum foil interface as the dominant aging mechanism of LNMO/graphite cells, cycled at 40 °C, which is currently analyzed in detail.[120]

Author Contributions

J.L., D.P. and H.G. developed the measurement procedure, which is based on obtaining blocking conditions in a full-cell configuration by fully delithiating the electrode of interest. All electrochemical measurements were conducted by D.P. J.L. developed the equivalent circuit model and analyzed the data. The manuscript was written by J.L., D.P. and edited by H.G. All authors discussed the data and commented on the results.

An Analysis Protocol for Three-Electrode Li-Ion Battery Impedance Spectra: Part I. Analysis of a High-Voltage Positive Electrode

Johannes Landesfeind,[=,*] Daniel Pritzl,[=,*,z] and Hubert A. Gasteiger[**]

Chair of Technical Electrochemistry, Department of Chemistry and Catalysis Research Center, Technical University of Munich, Munich, Germany

A key for the interpretation of porous lithium ion battery electrode impedance spectra is a meaningful and physically motivated equivalent-circuit model. In this work we present a novel approach, utilizing a general transmission line equivalent-circuit model to exemplarily analyze the impedance of a porous high-voltage $LiNi_{0.5}Mn_{1.5}O_4$ (LNMO) cathode. It is based on a LNMO/graphite full-cell setup equipped with a gold wire micro-reference electrode (GWRE) to obtain impedance spectra in both, non-blocking conditions at a potential of 4.4 V cell voltage and in blocking configuration achieved at 4.9 V cell voltage. A simultaneous fitting of both spectra enables the deconvolution of physical effects to quantify over the course of 85 cycles at 40°C: a) the true charge transfer resistance (R_{CT}), b) the pore resistance (R_{Pore}), and c) the contact resistance ($R_{Cont.}$). We demonstrate that the charge transfer resistance would be overestimated significantly, if the spectra are fitted with a conventionally used simplified *R/Q* equivalent-circuit compared to our full transmission line analysis.

 [DOI: 10.1149/2.0131709jes]

Manuscript submitted March 27, 2017; revised manuscript received June 6, 2017. Published June 16, 2017. This was Paper 534 presented at the New Orleans, Louisiana, Meeting of the Society, May 28–June 1, 2017.

Advanced analysis techniques for lithium ion batteries are a key requirement to deconvolute the complex interplay between the aging mechanisms occurring at the anode and the cathode. In principle, this can be accomplished by electrochemical impedance spectroscopy (EIS), if the individual contributions of anode and cathode to the overall cell impedance can be determined, and if this EIS response can be fitted unambiguously to physically motivated equivalent-circuit models. In general, the measured cell and/or electrode impedances are usually fitted with a serial connection of an ohmic resistor (*R*), with a parallel circuit of a resistor and a capacitor (*C*), commonly referred to as *R*/*C* element and often also modified to an *R*/*Q* element (*Q* representing a constant-phase element), as well as with a Warburg element (*W*).[1–5] Recently, more elaborate equivalent-circuits using a transmission line model are getting more and more attention.[6–8]

In order to independently obtain the impedance of anode and cathode, there are two possible options: i) the assembly of symmetric cells as shown by Chen et al.[9] or Petibon et al.,[10] where coin cells out of two anodes (impedance of the negative electrode) or two cathodes (impedance of the positive electrode) are assembled in a glove box or dry-room from two (aged) full-cells at a specified state-of-charge (SOC); ii) the use of three-electrode setups consisting of a working electrode (WE), a counter electrode (CE) and a reference electrode (RE), which allows to individually determine the impedance of the anode and the cathode of a lithium ion battery full-cell. The latter is a more convenient approach, as individual impedance spectra can be recorded continuously during battery cycling, so that anode and cathode impedance can be monitored during cycle-life studies on a full-cell instead of obtaining only one set of anode and cathode impedance spectra after disassembly of a full-cell via the symmetric cell approach. A main criterion for a micro-reference electrode suitable for high-quality EIS measurements is a centered position of the reference electrode between working and counter electrode.[11–13] Several approaches are presented in the literature, as for example, a copper wire, where lithium is in-situ plated from anode or cathode,[14] a reference electrode consisting of a lithium-tin alloy,[15] or consisting of a lithium-bismuth alloy.[16] Our group has recently developed a micro-reference electrode consisting of a polyimide-shrouded gold wire with a core diameter of 50 µm and an additional 7 µm polyimide insulation layer which enables the deconvolution of full-cell impedances into anode and cathode contributions after lithiation of the gold wire.[17] The latter was used in this study and will be referred to as gold wire reference electrode (GWRE).

Besides the deconvolution of individual electrode impedances, EIS measurements with the GWRE at different states-of-charge of the electrodes allow to get insight into different physical effects. If conducting EIS analysis at a so-called blocking condition for a specific electrode, where no charge transfer reactions (i.e., no faradaic reactions) can take place, the only impedance contribution from the solid-electrolyte interphase is via capacitive coupling. Blocking conditions of electrodes have been used in the literature before to address individual physical processes like the pore resistance and thus the effective ionic conductivity across the thickness of an electrode.[18,19]

In this work, by using a GWRE and by recording impedance spectra at both blocking and non-blocking conditions, we will demonstrate the ability to deconvolute and quantify the impedance contributions developing during the aging of a high-voltage spinel cathode ($LiNi_{0.5}Mn_{1.5}O_4$ or LNMO) in an LNMO/graphite full-cell cycled at 40°C. For this, we measure half-cell impedance spectra with our GWRE and fit the impedance spectra with a general transmission line model for two distinct points during cycling: i) at 4.4 V cell voltage, corresponding to ~7–12% SOC, where the charge transfer resistance has a typical and reasonably low value; ii) at 4.9 V, where the LNMO is fully delithiated (≡ 100% SOC) and where, as we will demonstrate, the LNMO cathode exhibits nearly perfect blocking behavior. The novelty of our approach lies in the fact that by recording both sets of impedance spectra, individual impedance contributions by the LNMO cathode (contact resistance, charge transfer resistance, and pore resistance) can be deconvoluted mathematically and allow for a rather rigorous quantitative analysis during the course of cycle-life experiments. While this is illustrated for the cycling of an LNMO/graphite cell, the general approach shown here is applicable to many other cell chemistries, and the presented analysis of the cathode impedance contributions is also being extended to the anode in our current work. In the following, we will first review the necessary theoretical impedance background, then provide the experimental data, and finally discuss the analysis of the cathode impedance contributions and their variation during cycling.

[=]These authors contributed equally to this work.
[*]Electrochemical Society Student Member.
[**]Electrochemical Society Fellow.
[z]E-mail: daniel.pritzl@tum.de

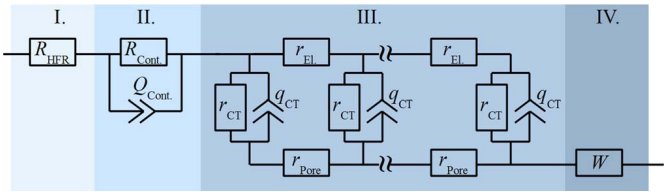

Figure 1. Cathode equivalent circuit model with four parts (from left to right): I. the high frequency resistances from the ionic resistance of the separator and the electronic resistance of the cell setup, II. the contact resistance at the interface between the cathode electrode and its current collector, III. the general transmission line model describing the porous coating, and IV. a Warburg diffusion element.

Theory

The impedance contributions from a porous cathode electrode can be described by a combination of four physical mechanism which are labelled with Roman numerals in the equivalent-circuit depicted in Figure 1 as well as in the simulated Nyquist impedance plot (Figure 2 with parameters given in Table I), using the following assignments: I) the high-frequency resistance (Z_{HFR}), which represents the sum of the ionic resistance of the separator and the electronic resistance of external, electronic cell contacts; II) the contact resistance between the porous electrode and the current collector ($Z_{Cont.}$); III) the impedance contribution from ion and electron conduction across the thickness of the porous cathode electrode (Z_{Pore}), described by the general transmission line model; and, IV) a Warburg diffusion element (Z_W), representing the impedance at very low frequencies. Thus, the overall

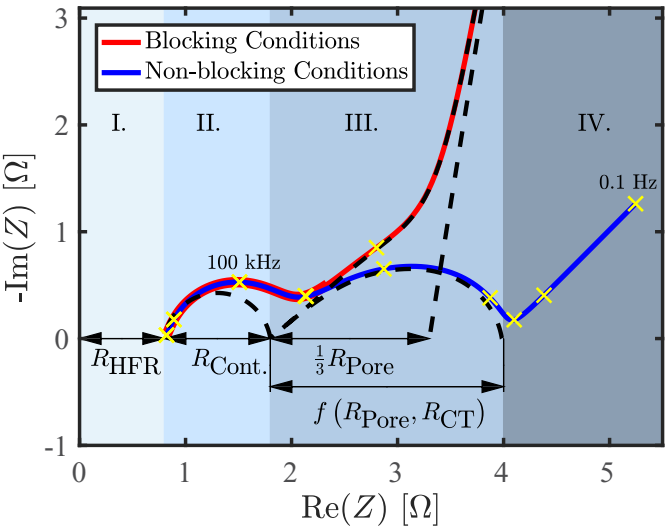

Figure 2. Simulated impedance response of a porous cathode electrode either under blocking conditions (red line) or under non-blocking conditions (blue line), using the parameters listed in Table I for a simulated frequency range from 10 Mhz–0.1 Hz. Each frequency decade is highlighted by a yellow cross. The arrows mark the values of the simulation parameters for the high-frequency resistance (R_{HFR}), the electronic contact resistance ($R_{Cont.}$), and of one third of the pore resistance (R_{Pore}), which are obtained by extrapolating the high- and low-frequency segments of the transmission line response under blocking conditions (dashed black lines). The dashed lines are the modelled impedance responses of only the equivalent-circuit elements in the corresponding region (compare Figure 1), a) the R/Q element due to the contact resistance (region II.), b) the blocking condition transmission line model extending to low frequencies (region III), and, c) the transmission line model in non-blocking condition (region III), and, d) the constant phase behavior of the transmission line model in blocking condition at low frequencies (region III.). The frequency range corresponding to the measurement, from 100 kHz to 0.1 Hz is labelled for the reader's convenience.

cathode impedances is:

$$Z_{cathode} = Z_{HFR} + Z_{Cont.} + Z_{Pore} + Z_W \quad [1]$$

In our following measurements with a GWRE (64 μm total diameter) placed in between two glass fiber separators (each with a compressed thickness of ≈200 μm) located between anode and cathode, the impedance at the highest frequencies is composed of the ionic electrolyte resistance in the separator between the cathode/separator interface and the GWRE ($R_{Sep.}$) as well as of the contact resistances from the cell setup (R_{Setup}), adding up to the overall high-frequency resistance, R_{HFR} (compare region I. in Figures 1 and 2):

$$Z_{HFR} = R_{Sep.} + R_{Setup} = R_{HFR} \quad [2]$$

In terms of an equivalent circuit, the overall cathode impedance can thus be described with the equivalent circuit model depicted in Figure 1. The first element starting from the left is R_{HFR}, which is connected in series to the impedance due to contact resistance between the current collector and the positive electrode, described by the $R_{Cont}/Q_{Cont.}$ element (compare region II. in Figures 1 and 2). The contact resistance circuit element between the cathode current collector and the cathode electrode is a parallel circuit between the interfacial resistance ($R_{Cont.}$) and the generally very small interfacial capacitance (expressed as constant phase element $Q_{Cont.}$), which, based on the definition of the impedance of a constant-phase element ($Z = [Q \cdot (i\omega)^{\alpha}]^{-1}$), equates to:

$$Z_{Cont.} = \frac{R_{Cont.}}{R_{Cont.} \cdot Q_{Cont.} \cdot (i\,\omega)^{\alpha_{Cont.}} + 1} \quad [3]$$

with the angular frequency $\omega = 2\pi f$. In this work constant phase elements rather than capacitors are used to account for the non-ideal capacitive behavior commonly observed for the double layer capacitance of porous electrodes.[20] The contact resistance is followed by a transmission line equivalent circuit, composed of incremental elements of the charge transfer resistance (r_{CT}), the interfacial double layer capacitance of the cathode (q_{CT}), the purely electronic resistance in the electrode ($r_{El.}$), and the purely ionic resistance in the electrode (r_{Ion}) in the mid frequency range (compare region III. in Figures 1 and 2). Thus, the overall charge transfer resistance, the overall electronic and ionic resistances as well as the overall capacitance of the electrode are described by ${R_{CT}}^{-1} = \Sigma({r_{CT}}^{-1})$, $Q_{CT} = \Sigma(q_{CT})$, $R_{El.} = \Sigma(r_{El.})$, and $R_{Pore} = \Sigma(r_{Pore})$. Please note, that the constant phase elements in region II. and region III., namely $Q_{Cont.}$ and $q_{CT.}$, both describe the electrochemical double layer capacitance, $Q_{Cont.}$ at the current collector interface and q_{CT} at the active material and carbon surface respectively.

In this mid-frequency range, the cathode electrode pores dominate the impedance response. In this work, the impedance of the pores is described with a general transmission line model, given by:[21]

$$Z_{Pore} = Z_{||} + Z^* \frac{1 + 2 \cdot p \cdot s\left[\sqrt{1 - \tanh(\nu)^2} - 1\right]}{\tanh(\nu)} \quad [4]$$

with

$$Z_{||} = \frac{Z_P \cdot Z_S}{Z_P + Z_S} \quad [5]$$

$$Z^* = \sqrt{(Z_P + Z_S) \cdot Z_Q} \quad [6]$$

$$p = \frac{Z_P}{Z_P + Z_S} \quad [7]$$

$$s = \frac{Z_S}{Z_P + Z_S} \quad [8]$$

$$\nu = \sqrt{\frac{Z_P + Z_S}{Z_Q}} \quad [9]$$

Here, Z_S, Z_P, and Z_Q represent the impedances of the electron conducting solid phase of the electrode, of the ionically conducting

pore phase of the electrode, and of the solid/electrolyte interface surfaces within the electrode, respectively. In this work, these elements are described by the electrical resistance throughout the electrode ($Z_S \equiv R_{El.}$), by the ionic resistance throughout the electrode ($Z_P \equiv R_{Pore}$), and by an *R/Q* element describing the coupling for the capacitive elements (Q_{CT}) and of the charge transfer resistance (R_{CT}) at the solid/electrolyte interface surface of the active material in the electrode:

$$Z_Q = \frac{R_{CT}}{R_{CT} \cdot Q_{CT} \cdot (i\,\omega)^{\alpha_{CT}} + 1} \quad [10]$$

For the commonly considered special case, where the electronic resistance of the electrode is negligible compared to the ionic resistance in the electrode pores (i.e., $R_{El.} \ll R_{Pore}$), the transmission line model for the pore impedance (Eqs. 4–9) in blocking conditions ($R_{CT} \rightarrow \infty$) simplifies to Ref. 19:

$$Z_{Pore} = \sqrt{R_{Pore} \cdot Z_Q} \cdot \coth\left(\sqrt{\frac{R_{Pore}}{Z_Q}}\right)$$

$$= \sqrt{\frac{R_{Pore}}{Q_{CT} \cdot (i\,\omega)^{\alpha_{CT}}}} \cdot \coth\left(\sqrt{R_{Pore} \cdot Q_{CT} \cdot (i\,\omega)^{\alpha_{CT}}}\right) \quad [11]$$

Finally, the last element represents a Warburg impedance, which generally becomes relevant at very low frequencies (compare region IV. in Figures 1 and 2) and which is connected serially to the transmission line model to account for the salt concentration gradients evolving at low frequencies inside the separator. Please note that this placement of a Warburg diffusion element is not in contradiction with the literature, where a diffusion element is generally connected in series to the charge transfer resistances in order to describe a slow solid-state diffusion process inside the active material particles.[20,22] In the literature, the solid-state diffusion is generally assumed to be the slowest step (i.e., the one with the longest characteristic time constant), however, as estimated in the Appendix, liquid diffusion through the separator can have a substantially larger impedance, depending on the experimental setup, e.g., the active area or the diffusion coefficient. Thus, with our placement of a Warburg diffusion element in series to the transmission line model we aim at describing the liquid concentration gradients inside the separator.

Only at the very lowest frequencies, a Warburg (*W*) behavior may be observed, which can be modelled with Ref. 20:

$$Z_W = \frac{W}{\sqrt{\omega}} - i \cdot \frac{W}{\sqrt{\omega}} \quad [12]$$

with the Warburg coefficient *W* as defined in the Appendix. Generally, the boundary conditions for ionic diffusion in the separator domain will yield a finite, transmissive diffusion behavior for very low frequencies (compare, e.g., Ref. 20, page 102 and following). In this work, no signs of a finite length diffusion were observed in the investigated frequency range (100 kHz to 0.1 Hz), i.e., the decline of the negative imaginary impedance toward the real axis at lowest frequencies in a Nyquist plot, which enables modelling of the separator diffusion with a semi-infinite Warburg diffusion element.

An exemplary evaluation of Equations 1–10 is shown in form of a simulated Nyquist plot in Figure 2 (10 MHz to 0.1 Hz), using the specific parameters for an LNMO cathode listed in Table I, whereby two cases are considered: a) blocking conditions (red line), where R_{CT} becomes very large (ideally going to infinity), here using a value of $R_{CT\text{-blocking}}$ of 1 kΩ; and, b) conditions where a typical value for the charge transfer resistance is observed (blue line), which applies throughout most of the SOC region and which here is given as $R_{CT\text{-non-blocking}}$ of 1 Ω. In the first case (red line), the semi-circle for the contact resistance (region II. in Figure 1) can be clearly seen at high frequencies as well as a roughly 45° line produced by the transmission line segment of the circuit shown in Figure 1 (region III.). From this, the value corresponding to one third of the pore resistance (R_{Pore}) can be determined as the difference between the Re(*Z*)-axis intercept of the two black dashed lines, which are the extensions of the high- and low-frequency segments of the transmission line part (region III.) of the equivalent circuit shown in Figure 1. This is derived from the low-frequency limit of Eq. 4, assuming a negligible electronic resistance ($R_{El.} \sim 0$), as explained, e.g., in Ref. 20 (p. 207, Eq. 9.11). The difference between the left dashed line intersecting with the Re(*Z*)-axis and the high-frequency resistance intersect is the value of the contact resistance ($R_{Cont.}$).

Table I. Parameters used in Equations 1–10 for the simulation of the two impedance responses shown in Figure 2, either under blocking conditions where the charge transfer resistance is very large ($R_{CT\text{-blocking}}$) or under normal conditions, where a typical value for the charge transfer resistance is used ($R_{CT\text{-non-blocking}}$; evaluated at 4.4 V_{FC}). Note that the here chosen values are very similar to the ones which will be found in our later cathode impedance analysis during cycling of an LNMO/graphite cell.

Parameter	Value
$R_{HFR.}$	0.8 Ω
$R_{Cont.}$	1.0 Ω
$Q_{Cont.}$	5 μF · $s^{(\alpha_{Cont.}-1)}$
$a_{Cont.}$	0.9
R_{Pore}	4.5 Ω
$R_{El.}$	1 mΩ
$R_{CT-non-blocking}$	1.0 Ω
$R_{CT-blocking}$	1 kΩ
Q_{CT}	1 mF · $s^{(\alpha_{CT}-1)}$
a_{CT}	0.9
W	1 Ω/$\sqrt{s}$

Under non-blocking conditions (blue lines), two semi-circles appear across regions II and III in Figure 2 (plus the onset of the Warburg diffusion branch at low frequencies in region IV), and the low-frequency semi-circle now corresponds to a complex convolution (not simply additive) of the pore ionic conduction and the charge transfer resistance (marked by the arrow labelled $f(R_{Pore}, R_{CT})$). In the most general case, also the magnitude of the electronic resistance influences the shape of the transmission line part (region III. in Figures 1 and 2) but can be neglected when it is much smaller than the ionic resistance inside the pore. The simulated transmission line segment under non-blocking conditions (see region III in Figure 1 with finite R_{CT}) is shown as the dashed semi-circle at low frequencies in Figure 2. Quite clearly, if one were to fit two semi-circles and a Warburg element to the blue EIS response under non-blocking conditions, the diameter of the semi-circle at low-frequencies, which is commonly ascribed to the charge transfer resistance,[23,24] would indeed be much larger than the actual charge transfer resistance (ca. 2.5 Ω as can be seen from Figure 2 in contrast to the 1 Ω (see Table I) which was used in the model). Therefore, as we will illustrate in the Results and discussion section, a quantification of the charge transfer resistance requires impedance spectra at both blocking and non-blocking conditions for an unambiguous assignment. For a better comparison with our experimental data, which were limited to an upper frequency of 100 kHz due to experimental reasons (see Experimental section), each frequency decade of the blocking and the non-blocking equivalent-circuit simulations (from 10 MHz to 0.1 Hz) in the simulations shown in Figure 2 is marked by a yellow cross (the maximum experimental frequency of 100 kHz is labeled in the figure).

Experimental

Electrode preparation.—Cathodes were prepared from $LiNi_{0.5}Mn_{1.5}O_4$ powder (LNMO, BASF SE, Germany), polyvinylene difluoride (PVdF HSV 900, Kynar), and carbon black (SuperC65, Timcal). The powders were mixed in a mass ratio of 92:3:5 (LNMO:PVdF:carbon black) and dissolved in NMP (N-methyl pyrrolidone, anhydrous, Sigma Aldrich, Germany), followed by three sequential mixing steps with a planetary mixer (Thinky Corp.) for a total of 15 minutes. The final ink, which had a solid content

of 60%, was coated on the rough side of an aluminum foil (MTI, thickness ∼18μm) at a wet film thickness of ∼200 μm with a doctor blade coating device (RK PrintCoat Instruments, UK). The resulting loading of the electrodes was ∼13 $mg_{LNMO}/cm^2_{Electrode}$ corresponding to ∼1.9 mAh/ $cm^2_{Electrode}$ based on a theoretical capacity of 140 mAh/g_{LNMO}. The electrodes were punched out with a diameter of 11 mm and afterwards compressed to a porosity of ∼32% using a KBr press (Mauthe, PE-011).

Anodes were prepared from Graphite powder (commercial, SGL Carbon GmbH) and PVdF with a mass ratio of 95:5. The mixing procedure was identical to the cathodes. The ink (60% solid content) was coated on the rough side of a copper foil (MTI, thickness ∼12 μm). The electrodes were punched out with a diameter of 11 mm and compressed to a porosity of ∼32%. The final loading was 6.6 $mg_{Graphite}/ cm^2_{Electrode}$, corresponding to ∼2.3 $mAh/cm^2_{Electrode}$ based on a theoretical capacity of ∼340 $mAh/g_{Graphite}$.

Anode and cathode coatings were dried in a convection oven at 50°C for at least 3 h. The as-prepared electrodes (graphite anodes and LNMO cathodes) were vacuum dried for at least 12 h at 120°C in a vacuum oven (Büchi, Switzerland) and transferred into an Argon-filled glove box without exposure to air.

Cell assembly and testing.—Spring-compressed (at ∼1 bar) T-cells (Swageklok, U.S) were assembled in an Argon-filled glove box (<0.1 ppm O_2 and H_2O, MBraun, Germany). The cell components were dried beforehand in a 70°C drying oven for at least 20 h. A gold wire micro-reference (core diameter of 50 μm and an additional 7 μm polyimide shrouding, Goodfellow Ltd., United Kingdom) is used as a reference electrode,[17] placed in between two glass fiber separators (glass microfiber filter, 691, VWR, Germany) with a compressed thickness of ∼200 μm each. During cell assembly, 60 μl of LP57 electrolyte (1 M $LiPF_6$ in EC:EMC 3:7 w:w, <20 ppm H_2O, BASF, Germany) was added. The GWRE was lithiated with a constant current of 150 nA for 1h and initially yielded a constant potential of 0.31 V vs. metallic lithium, which drifted toward the potential of an unlithiated gold wire within ca. 10 cycles (caused, we believe, by reaction of alloyed lithium with electrolyte oxidation products from the LNMO cathode at 4.9 V_{FC} cell voltage). However, as shown in our previous work, artefact-free impedance spectra (indicated by the absence of inductive loops at low frequency; see Figure 3 in Reference 17) can be obtained from micro reference electrodes as long as the potential drift of the RE over the course of the impedance measurement is smaller than the chosen voltage amplitude. In the present work the potential drift of the RE over the course of the impedance measurement with a lower limit of 0.1 Hz is ∼3–4 mV, which is sufficiently below the perturbation amplitude during the EIS measurement (in this case 15 mV). This is verified by the absence of inductive loops at low frequency and was furthermore verified by comparing the impedance measurement with the micro-reference electrode with a standard EIS measurement using a symmetrical cell configuration (for the LNMO cathode; see Figure 6). It is emphasized that while the potential value of the reference electrode is unstable (i.e., it deviates from 0.31 V vs. metallic lithium after ∼10 cycles), the reference electrode potential drift during the time period needed for an impedance measurement (∼5 minutes) is still small (<4 mV) compared to the potential perturbation. For details about the cell setup and the preparation of the gold wire, please refer to the original publication.[17]

The full-cells were cycled between 3.0 and 4.9 V cell voltage; for measurements with additional cells, the figure captions give the detailed experimental procedure (e.g., modified amplitudes or frequency ranges of impedance measurements). In the following, all potentials refer to the LNMO/graphite full cell voltage (indicated by the subscript FC) unless stated otherwise. Two formation cycles were carried out at 25°C at a C-Rate of C/10, while cycling was done at 40°C at a C-Rate of C/2. Potential-controlled impedance spectra (15 mV perturbation, from 100 kHz to 0.1 Hz; acquisition time of 10 min./spectrum) were recorded during discharge at 4.4 V_{FC} after a 1 h OCV (open-circuit voltage) phase as well as under blocking condition, which were achieved by fully delithiating the cathode by holding it at 4.9 V_{FC} until a current of <C/40 was obtained and then recording impedance spectra while holding the potential at 4.9 V_{FC}. Analogously, impedance spectra of the anode in blocking condition have been recorded by holding the potential at 3.0 V_{FC} at the end of discharge (completely delithiated graphite) until a current of <C/100 is reached. The cycling protocol was carried out on a potentiostat (VMP 300, BioLogic, France). It should be noted that due to the relatively high impedance of the reference electrode, individual impedance spectra for anode and cathode cannot be obtained at frequencies above 100 kHz.

Results and Discussion

LNMO/graphite cycling data.—First we verified that the charge and discharge potentials are not affected by the OCV holds during discharge at 4.4 V_{FC} and at the end of discharge/charge at 3.0 V_{FC} / 4.9 V_{FC}, which were required for the EIS measurements. Figure 3 exemplarily shows three selected cycles at the beginning, the middle, and the end of the cycling procedure of the LNMO/graphite cell. The peak during discharge (red lines) is caused by the OCV phase and the subsequent impedance measurement, once the cell potential reaches 4.4 V_{FC} (indicated by the black dashed line in Figure 3). From cycle 1 to 75 (at C/2 and 40°C), the capacity drops from ∼125 mAh/g to ∼90 mAh/g (compare also Figure 4), which is typical for LNMO/graphite cells, due to their high operating potential and instability at elevated temperatures.[25,26] At the same time, the cell polarization increases, which can be seen easily when comparing the potential plateau around 4.65 V_{FC} during charge (dark lines) and at approximately 4.55 V_{FC} during discharge (green lines).

The discharge capacities and the coulombic efficiencies over all 85 charge/discharge cycles are shown in Figure 4 (formation cycles not shown). Discharge capacities slightly above 120 mAh/g_{LNMO} (∼16% of the initial capacity are consumed by SEI formation during the first two cycles at C/10) are reached in the initial cycles, but owing to a rather poor coulombic efficiency which never reaches more than ∼99.3% (see Figure 4), the initial capacity decreases by ∼30% to ∼87 mAh/g after only 85 cycles. This compares reasonably well with literature data on LNMO/graphite cells operated at 45°C at a sequence of C-rates (first ten cycles at C/10, followed by 40 cycles at C/4, and another 40 cycles by C/2), which lost ∼20% of their initial capacity over the same number of cycles.[27] Our cycling data, capacity loss of 20–30 mAh/g at a cycling rate of C/2 at 40°C, also agrees well with

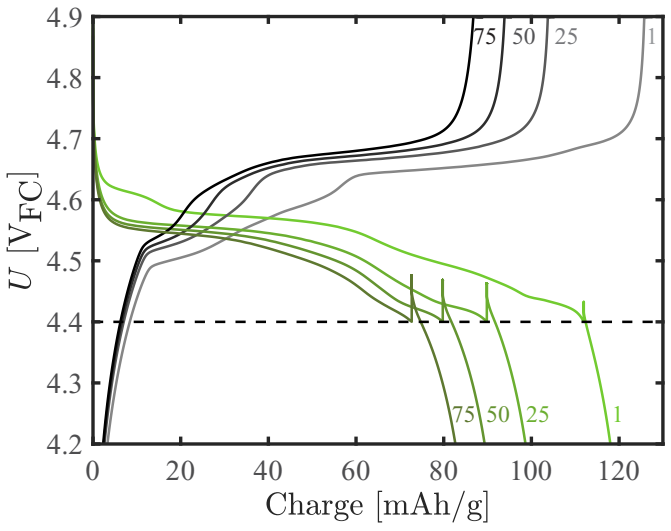

Figure 3. Exemplary charge (dark lines) and discharge (green lines) potential profiles for cycles 1, 25, 50, and 75 (marked in the figure) of the LNMO/graphite cell at 40°C, cycled at C/2 followed by a CV phase after charge until I <C/40 and a CV phase after discharge until I <C/100 between 3.0 and 4.9 V_{FC}. The peaks in the discharge curves are due to a 1 h OCV phase and a subsequent impedance measurement once the discharge potential reaches 4.4 V_{FC}.

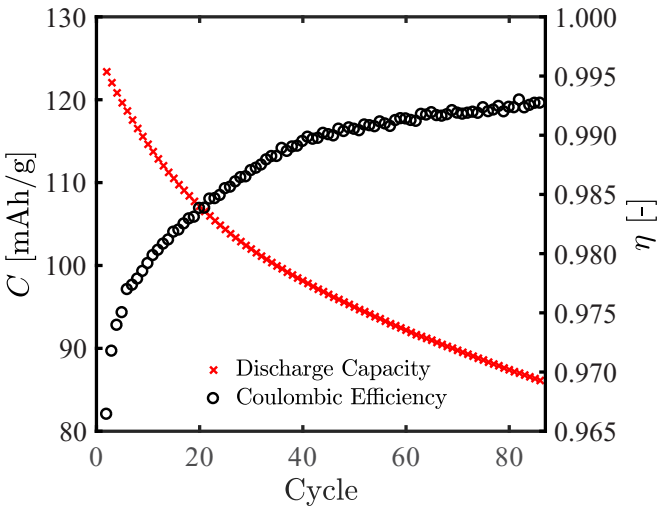

Figure 4. Discharge capacities for the LNMO/graphite cell cycled at 40°C and C/2 rate followed by a CCCV charge until I <C/40 and a CCCV discharge until I <C/100 in a potential window from 3.0 V_{FC} to 4.9 V_{FC} as well as the corresponding coulombic efficiencies.

the capacity loss of 30 mAh/g over 50 cycles at C/5 and 45°C, as reported by the group of Brett Lucht.[28] Thus, we conclude that the cycling data of the LNMO/graphite cells do not seem to be influenced significantly by the GWRE and the OCV periods required by for the EIS measurements. In the following we will focus our analysis to the impedance measurements performed during cycling of the cell.

Blocking conditions for the LNMO cathode in full-cells.—In the following, we will show that blocking conditions can indeed be achieved for the LNMO cathode in an LNMO/graphite full-cell by adding a constant voltage phase at the upper cutoff potential of 4.9 V_{FC} until the current decays below C/40, which leads to a condition where the cathode is fully delithiated so that the charge transfer resistance becomes very large (ideally, for perfect blocking conditions, R_{CT} would become infinitely large). For this purpose, an LNMO/graphite full-cell was built and charged galvanostatically at a C-Rate of C/10. Every 3 minutes during charge, the potential was held at its current value (no OCV phase), and an impedance spectrum with a perturbation of 50 mV was recorded in the frequency range from 100 kHz to 1 Hz (to obtain a short measurement time of ∼2 min per spectrum). After reaching the upper cutoff potential of 4.9 V_{FC}, impedance spectra were recorded continuously (taking ∼2 min each). Figure 5 demonstrates, how the cathode impedance spectra change upon approaching 100% SOC, showing exemplarily the EIS response at various potentials during the galvanostatic charge at potentials of 4.64 V_{FC}, 4.7 V_{FC}, 4.8 V_{FC}, and 4.9 V_{FC} as well as after increasingly long potential holds at the upper cutoff potential of 4.9 V_{FC}, after which EIS spectra are obtained potentiostatically while holding the potential. While the impedance spectra at 4.64 V_{FC} (blue line) resemble those simulated for non-blocking conditions (see blue line in Figure 2 between 100 kHz and 0.1 Hz), the impedance spectra after having held the cell potential at the upper cutoff potential approach those expected for blocking conditions, as is evident by comparing the red lines in Figure 5 with the red line in Figure 2.

To verify our above conclusions that the Nyquist plot of the cathode recorded in blocking conditions of an LNMO/graphite full-cell (i.e., after a 4.9 V_{FC} hold for 5 minutes) indeed follows the transmission line model for a blocking electrode, we prepared two additional cells, viz. one LNMO/graphite full-cell with GWRE and one LNMO/LNMO symmetric cell. The red data points in Figure 6 shows the impedance spectrum of the LNMO cathode of the LNMO/graphite full-cell, filled with the same electrolyte which was used for the cycling experiment (see Experimental), and subsequently charged at C/2 rate to 4.9 V_{FC}

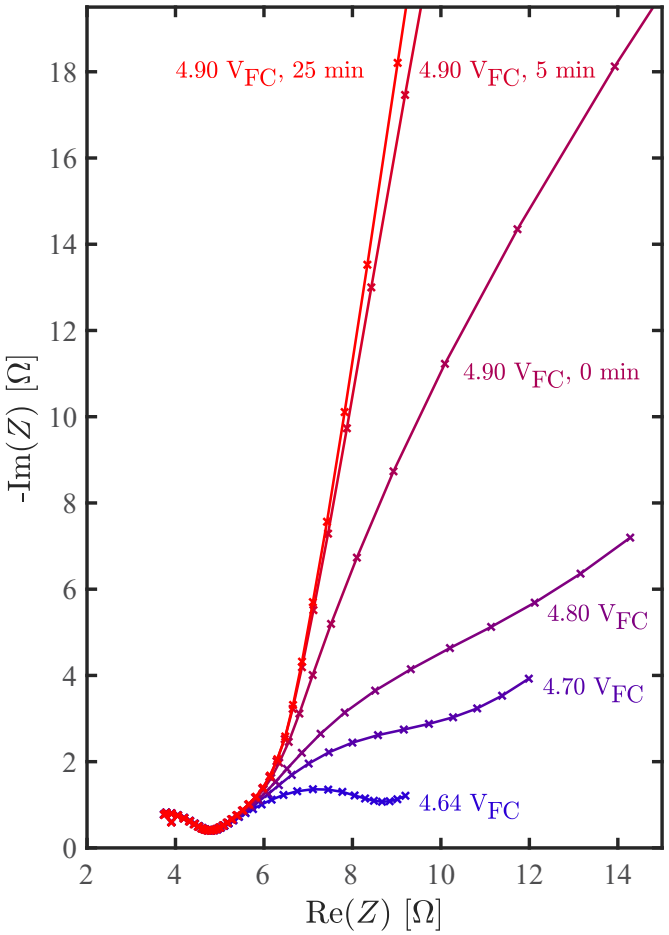

Figure 5. Evolution of the Nyquist plots of an LNMO cathode in an LNMO/graphite full-cell, obtained from EIS measurements (perturbation of 50 mV, 100 kHz–1 Hz) versus a GWRE. The data are recorded at a temperature of 25°C after two formation cycles at 25°C at C/10 followed by 5 C/10 cycles between 4.9 V_{FC} and 3.0 V_{FC}. Impedance spectra were obtained during galvanostatic charging of the cell at a charging rate of C/10 C and are shown from 4.64 V_{FC} up to 4.9 V_{FC}, followed by different holding times at 4.9 V_{FC}.

at 40°C and held at this potential for 5 minutes (after two formation cycles at 25°C and C/10), whereby the x- and y-axis values are multiplied by the conductivity of the electrolyte at the measurement temperature of 40°C ($\kappa = 11$ mS/cm). As can be seen in Figure 6 (red dashed line), the data can be fitted very well with a transmission line model without an $R_{Cont.}/Q_{Cont.}$ circuit element and with an infinitely large R_{CT} which is closely approached by a completely delithiated LNMO cathode. The resulting fit yields a value of 0.043 cm^{-1} for the product of $R_{Pore} \cdot \kappa$. In order to demonstrate that this approach yields reliable and meaningful physical-chemical parameters which describe ionic conductivity in the porous cathode electrode, a symmetric cell with two identical LNMO cathodes (albeit not cycled) and a non-intercalating electrolyte (10 mM $TBAClO_4$ in EC:EMC 3:7 w:w) was built. Its impedance response is shown by the black data in Figure 6 whereby it should be noted that the symmetric cell impedance was divided by two, as it represents the sum of two identical electrodes. The transmission line model for blocking conditions yields a very good fit of the data (see dashed black line) and a value of 0.033 cm^{-1} for $R_{Pore} \cdot \kappa$.

While the impedance spectra from both the LNMO cathode in the LNMO/graphite full-cell (measured with the GWRE) and from the LNMO/LNMO symmetric cell nicely fit the transmission line model for a blocking electrode, it remains to be determined whether the same pore resistance characteristics are observed for both nominally identical cathodes for these two different measurement

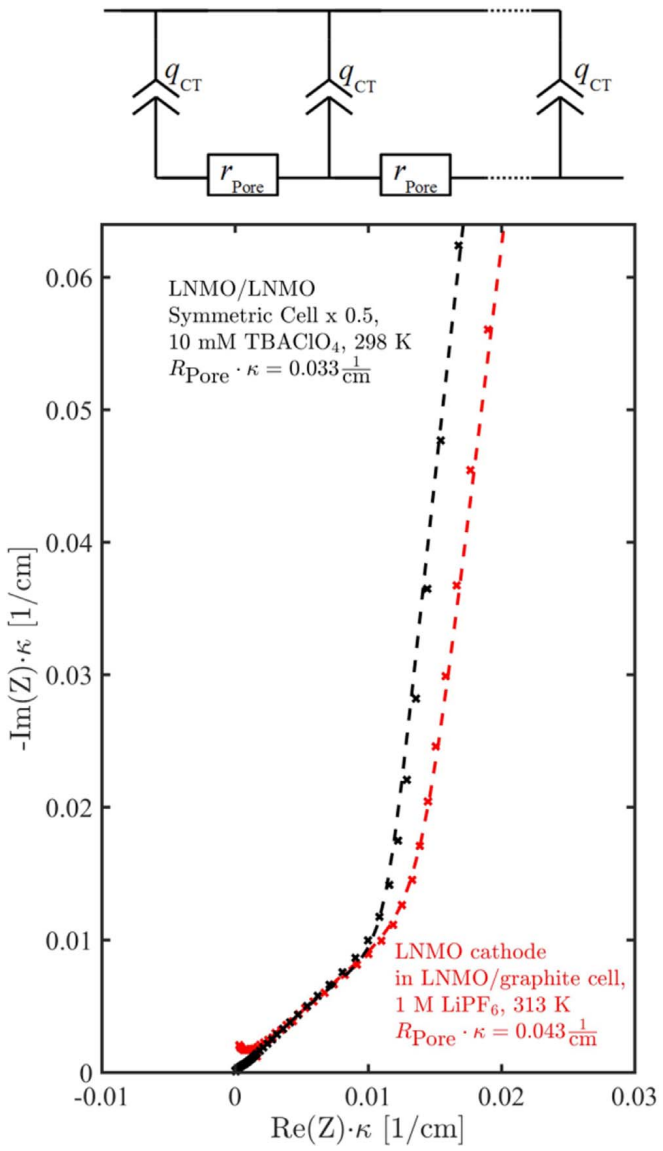

Figure 6. Comparison of the conductivity-scaled Nyquist spectra (i.e., real and imaginary impedances multiplied by the ionic conductivity) of an LNMO cathode in an LNMO/graphite cell (with GWRE) in blocking conditions (red data points) versus an LNMO/LNMO symmetric cell with non-intercalating electrolyte (black data points), whereby the latter impedance spectrum was divided by two in order to obtain the response of one LNMO cathode. The latter was measured after 12 h wetting by a non-intercalating electrolyte (10 mM $TBAClO_4$ in EC:EMC 3:7 w:w) at 25°C and using one CG2500 separator; the conductivity of this electrolyte at 25°C was determined to be $\kappa = 0.332$ mS/cm. The LNMO cathode impedance spectrum was obtained at 40°C after C/2 charging to 4.9 V_{FC} and holding that potential for 5 min (after two formation cycles); the electrolyte was 1 M $LiPF_6$ in EC:EMC (3:7, w:w) and had a conductivity at 40°C of $\kappa = 11$ mS/cm. Impedance spectra were recorded in the frequency range from 100 kHz to 0.1 Hz using an excitation amplitude of 15 mV and 20 mV for the LNMO/graphite cell and the symmetric cell, respectively. Both spectra were shifted to the origin for better comparability. The fit of the data to a simple transmission line model (shown in the figure) is represented by the dashed line and the resulting values of $R_{Pore} \cdot \kappa$ are given in the figure.

approaches. This can be checked by determining the corresponding MacMullin numbers (N_M), which would have to be the same for the nominally identical LNMO cathodes (i.e., having the same porosity (ε) and the same tortuosity (τ)) measured in the two different cell configurations:

$$N_M = \frac{\tau}{\varepsilon} = R_{Pore} \cdot \kappa \cdot \frac{A}{d} \quad [13]$$

where A is the area of the electrodes ($A = 0.95\,cm^2$) and d is their thickness ($d = 58\ \mu m$). The resulting MacMullin numbers obtained from the analysis of the data in Figure 6 are 7.0 ± 0.3 for the LNMO cathode measured in the LNMO/graphite full-cell with the GWRE under blocking conditions and 5.4 ± 0.3 for the nominally identical LNMO cathode measured in the LNMO/LNMO symmetric cell configuration, whereby the error results from the limited accuracy of the coating thickness measurement ($\pm 2\ \mu m$). More important than the measurement error for a given cell is the cell-to-cell variation (due minor differences in cell assembly and/or LNMO electrode coating), which was estimated by analyzing three more LNMO/LNMO symmetric cells and two more LNMO/graphite cells with GWRE (data not shown), yielding overall mean MacMullin numbers of 6.3 ± 0.6 for the LNMO electrodes measured in the LNMO/graphite full-cell setup (based on 3 repeat experiments) and 5.9 ± 0.6 for the LNMO cathode in the LNMO/LNMO symmetric cell setup (based on 4 repeat experiments). Thus, within the experimental error represented by the above standard deviations, both methods yield identical values for the MacMullin number. The fact that these values for the here used LNMO cathode with 5%wt conductive carbon are substantially lower than those we reported previously for an LNMO cathode with 2%wt conductive carbon ($N_M \approx 17$)[19] is simply related to the substantial lowering of the MacMullin number as the conductive carbon content is being increased (e.g., for lithium iron phosphate cathodes with comparable porosity, the MacMullin number decreases from 21 to 12 when the carbon content is increased from 5% to 15% wt.[19]). In summary, the above analysis demonstrates that blocking conditions are reached for an LNMO/graphite full-cell by holding the cell potential at 4.9 V_{FC} (Figure 5), and that reliable values for the ionic conduction characteristics of the LNMO cathode (i.e., its MacMullin number) can be obtained under these conditions via a simple transmission line model (Figure 6). In the following, we will now analyze the evolution of the impedance spectra over extended charge/discharge cycles and will utilize impedance measurements under blocking and non-blocking conditions in order to quantify the contributions derived from R_{Pore}, $R_{Cont.}$, and $R_{CT\text{-non-blocking}}$.

LNMO cathode impedance evolution in LNMO/graphite cells.— The cycle dependent Nyquist plots for the cathode in non-blocking condition at 4.4 V_{FC} and in blocking condition (i.e,. after a potential hold at 4.9 V_{FC} until I <C/40) are summarized in Figure 7 for every 25th cycle.

At the highest frequencies, a semi-circle can be observed, both, in non-blocking (Figure 7a) and in blocking conditions (Figure 7b), which is identical in magnitude and independent of the SOC and is thus ascribed to the contact resistance ($R_{Cont.}$, region II in Figure 1 and Figure 2). Over the course of charge/discharge cycling, this contact resistance clearly increases, evidenced by a shift of the spectra to larger real resistance values. It must be noted, however, that it is difficult to directly assess the value of the contact resistance, since in the experimentally accessible frequency range (100 kHz to 0.1 Hz; see Experimental section), only part of the contact resistance semi-circle can be obtained (this is illustrated by the modelled impedance response shown in Figure 2, where the 100 kHz data point is marked by the third yellow cross from the left). Therefore, the diameter of the semi-circle corresponding to the contact resistance cannot be determined visually from the acquired spectra without knowing the value of the high frequency resistance (R_{HFR}, region I in Figures 1 and 2). In non-blocking conditions (Figure 7a) the contact resistance semi-circle is followed by another distorted semi-circle, which increases in diameter from initially $\approx 1.5\ \Omega$ to $2\ \Omega$ in cycle 75, while at the lowest frequencies a Warburg type behavior can be observed (W, region IV in Figures 1 and 2). On the other hand, in blocking conditions (Figure 7b), an essentially straight line can be observed at medium frequencies (with an angle of close to 45 degrees in the first cycle), gradually turning into a nearly vertical line at the lowest frequencies, as one would expect for blocking conditions (compare the red line in region III marked in Figure 2). Thus, holding the cell potential at 4.9 V_{FC} does lead to the very large charge transfer resistance (R_{CT}) which is required to closely

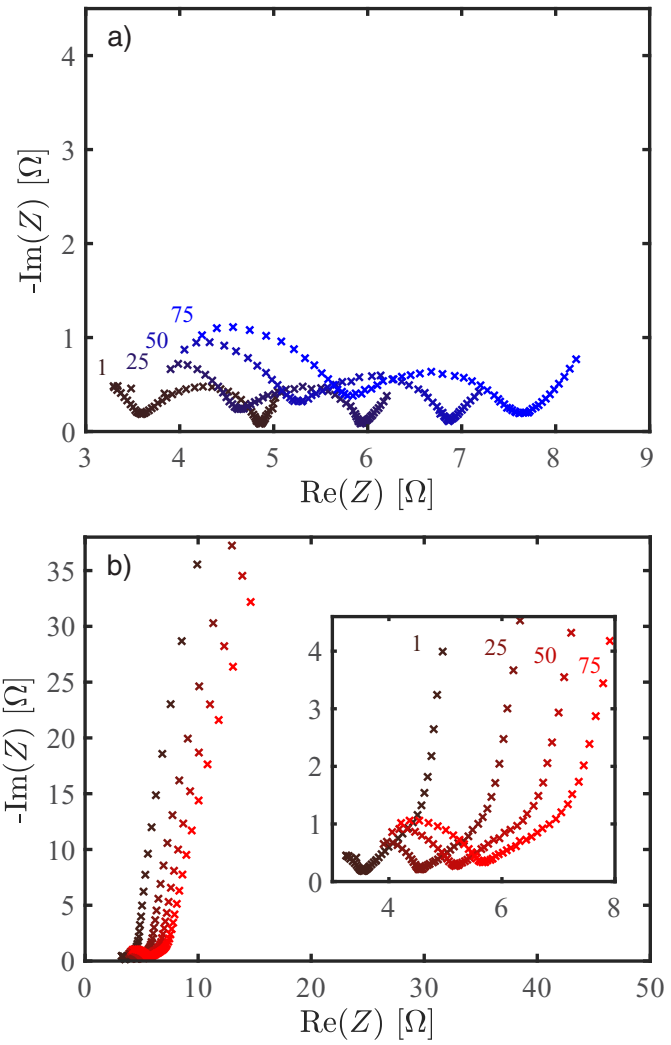

Figure 7. Evolution of the impedance spectra of the LNMO cathode (every 25th cycle; cycle numbers 1, 25, 50 and 75 are marked in the figure) during cycling of an LNMO/graphite cell at a rate of C/2 at 40°C: a) at 4.4 V_{FC} under non-blocking conditions (recorded at OCV after a 1 h OCV period); b) after potential hold at 4.9 V_{FC} under blocking conditions (recorded at a controlled potential of 4.9 V after a potential hold at 4.9 V until the current was below C/40). Potential-controlled EIS spectra were recorded with an amplitude of 15 mV in the frequency range from 100 kHz to 0.1 Hz.

approach blocking conditions. The decrease of the angle in the mid frequency region (initially close to 45 degrees) with cycling could be caused by electrolyte degradation products deposited in the cathode pores (see discussion after Figure 9), which change the pore structure inside the cathode.

In the following, the measured spectra of the half-cell cathode impedances are analyzed using Matlab (v. 2016b). Minimization of the sum of squares using a modulus weighing according to Lasia[20] was performed using Matlab's *fminsearch*[29] algorithm, and 95% confidence intervals are calculated via the Jacobian matrix obtained with the *jacobianest*[30] function. For each charge/discharge cycle, spectra in non-blocking condition at 4.4 V_{FC} and in blocking condition are fitted simultaneously using the equivalent circuit model shown in Figure 1. For the fitting of the spectrum in non-blocking conditions, 10 fitting parameters are required (viz., R_{HFR}, $R_{Cont.}$, $Q_{Cont.}$, $\alpha_{Cont.}$, R_{Pore}, $R_{El.}$, $R_{CT\text{-non-blocking}}$, Q_{CT}, α_{CT}, and W). In blocking conditions, the numerically identical parameters are used, except that a different value for the charge transfer resistance, referred to as $R_{CT\text{-blocking}}$ (in contrast to $R_{CT\text{-non-blocking}}$) is fitted and that the Warburg element is omitted. In summary the spectrum in non-blocking condition requires ten and the spectrum in blocking condition nine fitting parameters for an accurate description of the equivalent circuit model in Figure 1. However, since it is reasonable to assume that changes in the properties of the electrode and the active material are negligible within a single charge/discharge cycle, most of the parameters used to fit the blocking and non-blocking spectra within a given cycle are identical (viz., R_{HFR}, $R_{Cont.}$, $Q_{Cont.}$, $\alpha_{Cont.}$, R_{Pore}, $R_{El.}$, Q_{CT}, and α_{CT}), so that only eleven parameters are required to fit both spectra for a given cycle (see Table I).

Seeking to reduce the number of the free parameters in order to increase the accuracy of the fitted parameters, the following simplifications can be made. One is based on the assumption that the electronic resistance within the electrode ($R_{El.}$ in Figure 1) is small compared to the ionic resistance in the electrode and that its value does not change significantly over the course of the cycling experiment (to a good approximation, it would be sufficient that the ratio of $R_{Pore}/R_{El.}$ remains at $\gg$1).The maximum value of $R_{El.}$ for our pristine LNMO cathodes was obtained by a 2-point probe measurement, placing the LNMO electrode between two copper blocks, each equipped with a current and voltage lead (at a compression of 0.1 MPa using a static material testing machine zwickiLine from ZwickRoell, Ulm, Germany) and using a nanovoltmeter (Keithley 2182) in combination with a DC current source (Keithley 6221). This yielded a value of $R_{El.} \approx 0.1\ \Omega$, (≈30-fold lower than R_{Pore}, as will be shown later), so that $R_{El.} = 0.1\ \Omega$ was used as a fixed and constant resistance in the fitting of all impedance spectra. The other simplification in fitting the impedance spectra is related to the high-frequency resistance (R_{HFR} in Figure 1). While theoretically its value could be obtained from the overall fit of the impedance spectra, it would decrease the quality of the fit, because only a fraction of the contact resistance semi-circle can be observed with the experimentally accessible upper frequency limit of 100 kHz for the GWRE (see Figure 1 and Figure 7). The pure high-frequency resistance for the LNMO/graphite full-cell ($R_{HFR,full\text{-}cell}$), however, could be determined by measuring the *full-cell* impedance between anode and cathode after the cycling test, as in this case an upper frequency limit of 7 MHz could be used, so that despite the LNMO contact resistance the high-frequency real axis intercept can be obtained. This yielded a value of $R_{HFR,full\text{-}cell} = 4.8\ \Omega$, i.e., of 2.4 Ω for each half-cell. In addition, analysis of the graphite impedance data using the GWRE in the same setup (the detailed analysis of the anode data will be submitted soon), where the high frequency resistance even at an upper frequency limit of 100 kHz can be determined unambiguously, yielding a *cycle independent* value of $R_{HFR,anode} = 2.4\ \Omega$. As the GWRE sits in the center of two glass fiber separators, the high frequency resistance of the anode and the cathode half-cells are identical.[17] From this it can be concluded that the high frequency resistance (R_{HFR} in Figure 1), i.e., the resistance caused by the ionic resistance in the separator of the LNMO half-cell, remains essentially constant at a value of 2.4 Ω. Therefore, the value of R_{HFR} in the following impedance fits was kept constant at 2.4 Ω, reducing the number of final fitting parameters to nine (viz., $R_{Cont.}$, $Q_{Cont.}$, $\alpha_{Cont.}$, R_{Pore}, $R_{CT\text{-non-blocking}}$, $R_{CT\text{-blocking}}$, Q_{CT}, α_{CT}, and W), which are fitted simultaneously to each of the two impedance spectra (blocking and non-blocking conditions) per cycle.

Exemplary fits of the cathode impedance spectra of the LNMO/graphite full-cell after 30 cycles both in blocking condition (potential hold at 4.9 V_{FC}) and in non-blocking condition at 4.4 V_{FC} are shown in Figure 8. The fitted impedance spectra (lines in Figure 8) with the above listed set of 9 fitting parameters provide quite a good fit to the impedance data (black crosses) under both conditions over the entire frequency range (100 kHz to 0.1 Hz).

Figure 9 collects the values of the most relevant equivalent circuit model parameters for the LNMO cathode and depicts their evolution with cycling as well as their 95% confidence intervals. As discussed above, the high frequency resistance (R_{HFR}) and the electronic resistance ($R_{El.}$) are kept constant to allow for an explicit determination of the contact resistance. The contact resistance is found to increase from ≈1 Ω initially to ≈3 Ω after 85 cycles at C/2 at 40°C (yellow symbols in Figure 9a), which confirms the observation made in the discussion

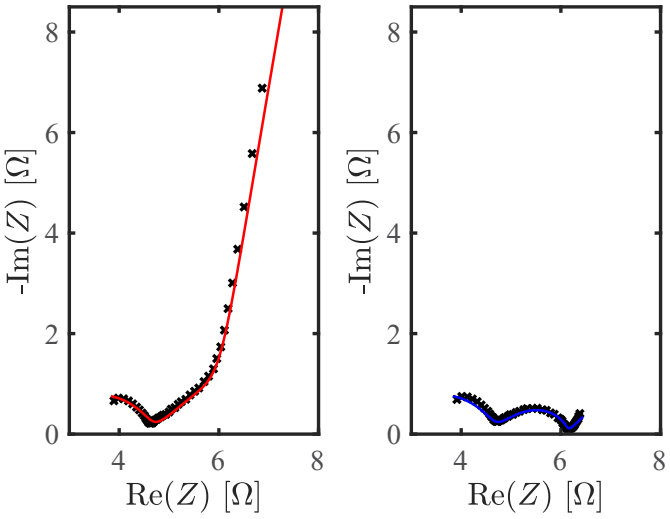

Figure 8. Exemplary fits (shown as solid lines) of the cathode impedance at cycle 30 obtained from the LNMO/graphite full-cell in blocking condition at 4.9 V_{FC} (left) and non-blocking conditions at 4.4 V_{FC} (right). Both spectra are fitted simultaneously, using the equivalent circuit model shown in Figure 1 with the same values for most parameters ($R_{Cont.}$, $Q_{Cont.}$, $\alpha_{Cont.}$, R_{Pore}, Q_{CT}, α_{CT}) and individual values for the charge transfer resistance in blocking condition ($R_{CT\text{-}blocking}$), the charge transfer resistance in non-blocking condition at 4.4 V_{FC} ($R_{CT\text{-}non\text{-}blocking}$), and the Warburg diffusion element (W) which is only used in non-blocking condition. AC impedance data (black crosses) were recorded at 40°C between 100 kHz and 0.1 Hz (15 mV voltage perturbation) after holding the cell potential at 4.9 V_{FC} (blocking condition, left) or at 4.4 V_{FC} after an 1 h OCV period (non-blocking condition, right).

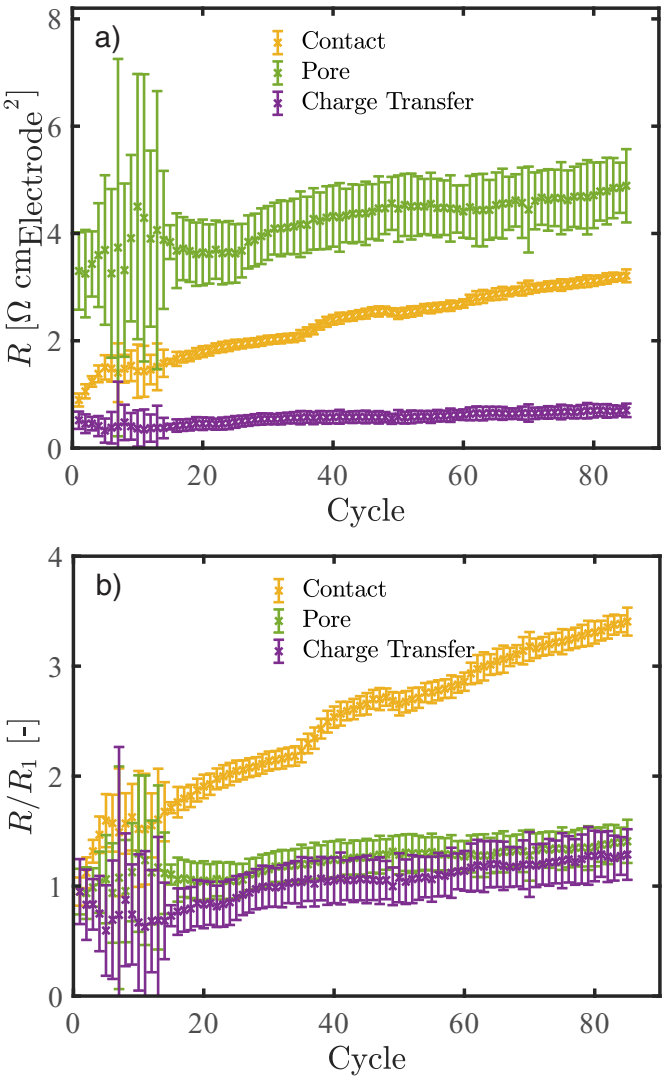

Figure 9. a) Evolution of the contact resistance ($R_{Cont.}$), the charge transfer resistance at 4.4 V_{FC} ($R_{CT\text{-}non\text{-}blocking}$, obtained under non-blocking conditions), and the pore resistance (R_{Pore}, obtained under blocking conditions) of the LNMO cathode, normalized to the electrode area, in the LNMO/graphite full-cell over extended charge/discharge cycling at 40°C at a rate of C/2 between 3.0 and 4.9 V_{FC} (the corresponding capacity vs. time plot and exemplary voltage vs. capacity plots are shown in Figure 4 and Figure 3, respectively; the formation cycles are not included). The shown values were determined by simultaneously fitting two impedance spectra per cycle, one in blocking condition and one in non-blocking condition as shown in Figure 8. The high frequency resistance contribution to the cathode (R_{HFR} in Figure 1) was set to a constant value of 2.4 Ω, and the electronic resistance in the cathode ($R_{El.}$ in Figure 1) was set to 0.1 Ω (see discussion in the text). b) Resistances normalized to their initial value after formation. Error bars indicate the parameters' 95% confidence interval from the fit.

of Figure 7, namely that the shift of the spectra to higher real resistance values is due to an increase of the high-frequency semi-circle representing the contact resistance. This increase of the LNMO cathode's contact resistance fits very well to the observation that a delamination of the LNMO electrode from the current collector occurs during cycling at elevated temperatures (60°C),[31] the underlying mechanism of which will be a subject of a future work.[32] Compared to the contact resistance, the pore resistance (R_{Pore}, green symbols) increases from an initial value of ≈3.5 Ω to ≈5 Ω after 85 cycles, while the charge transfer resistance at 4.4 V_{FC} ($R_{CT\text{-}non\text{-}blocking}$, purple symbols) starts at ≈0.5 Ω and increases to only ≈0.7 Ω after 85 cycles. Thus, the contact resistance shows the strongest increase over the 85 charge/discharge cycles of +300%, while the pore and charge transfer resistance at 4.4 V only increase by ≈45% and ≈30%, respectively (see Figure 9b). The charge transfer resistances in blocking-condition (not shown in Figure 9) is found to be ≈900 Ω, a very large value compared to the other resistances, as would be expected for the observed blocking electrode behavior, i.e., the nearly vertical line at lowest frequencies (see Figure 7b or the left panel of Figure 8). The error bars of all resistances shown in Figure 9 are mostly smaller than 25%, which is quite reasonable considering that two spectra were fitted simultaneously with a restricted parameter set for any given cycle, thus suggesting that the equivalent circuit representation of the LNMO cathode in Figure 1 captures most of the relevant processes. The irregularities observed for the fitted contact and pore resistance around cycles five to fifteen can be explained with the drift of the GWRE potential from its lithiated state to its unlithiated potential (see Experimental).

Over the course of the 85 charge/discharge cycles at 40°C, the overall resistance of the LNMO cathode ($R_{Cont.} + f(R_{Pore}, R_{CT\text{-}non\text{-}blocking})$) increases from an initial value of ≈5 Ω to ≈9 Ω (see Figure 9a). At the given charge/discharge current of ≈1 mA (based on a capacity of ≈2 mAh and a rate of C/2), this would predict an increase in cathode polarization of only ≈4 mV and would thus be rather negligible. As can be seen from the cell voltage vs. capacity data in Figure 3, the increase in the polarization of the LNMO/graphite cell seems to be much larger than 4 mV, which is due to the fact that the largest contribution to the cell polarization with cycling is caused by a substantial gain in the impedance of the anode (this analysis will be subject of a future publication).

Using the charge transfer resistances at 4.4 V of ≈0.5–0.7 Ω (see purple lines in Figure 9a), the linearized Butler-Volmer equation allows to estimate the exchange current density:

$$i_0 = \frac{RT}{F} \cdot \frac{1}{A_{LNMO} \cdot R_{CT-non-blocking}} \quad [14]$$

with R, T, and F being the gas constant (8.831 kJ/mol K), temperature (303 K), and the Faraday constant (96485 As/mol),

respectively. In addition, A_{LNMO} represents the active surface area of the LNMO, which can be estimated using the mass of LNMO (13.7 mg) in the cell and its BET surface area (0.9 m^2/g), equating to $A_{LNMO} = 123\ cm^2_{LNMO}$. Based on this, we find an exchange current density of 0.43–0.30 mA/cm^2_{LNMO} at 4.4 V_{FC} (i.e., at ≈7–12% SOC, s. Figure 3), which is within the range of exchange current densities for intercalation materials reported in the literature (0.02–0.3 mA/cm^2_{LNMO} for LNMO,[33] 0.17 mA/cm^2_{LFP} for $LiFePO_4$,[34] and 2.5 $mA/cm^2_{Graphite}$ for graphite[35]).

The observed increase in the pore resistance with cycling (see green lines in Figure 9) can be explained by a decrease of the effective electrolyte conductivity in the pores, likely caused by a partial blockage of the cathodes' pore volume by electrolyte oxidation fragments, thereby decreasing the cathode's void volume, which would probably also be accompanied by an increase in the cathode's tortuosity. In the literature, it is reported that the electrode/electrolyte interface at the LNMO cathode (often referred to as CEI) is not stable, compared to the solid electrolyte interface (SEI) on the graphite anode, so that electrolyte oxidation would happen at the surface of the LNMO particles.[2,25,26] This is consistent with the observation that both, charge transfer resistance at 4.4 V and the pore resistance, increase over the 85 charge/discharge cycle by 30% and 45% respectively.

The feasibility of the obtained fitting parameters for the impedance spectra can also be checked by examining the values the fit yielded for the capacitive constant phase elements related to both the LNMO cathode material (Q_{CT}, see Figure 1) and the contact resistance ($Q_{Cont.}$, see Figure 1). A rough order of magnitude estimate of the capacitances can be done by neglecting the constant phase factor, yielding values of $Q_{Cont.}$ ≈10 μF and Q_{CT} ≈1 mF. If normalized to the exposed areas of the current collector/electrode interface (≈1 cm^2) and the LNMO area ($A_{LNMO} = 123\ cm^2_{LNMO}$), the resulting area specific capacitance amounts to ≈10 $\mu F/cm^2_{surface}$ in either case, which is a reasonable value for the double layer capacitance.

The results obtained from this study suggest that the charge transfer resistance of the LNMO cathode is not increasing substantially during extended charge/discharge cycling, which is in disagreement with reports in the literature. For example, Aurbach et al. analyzed the impedance of LNMO/graphite cells by measuring the impedance of the LNMO electrode versus a lithium wire reference electrode, showing that the impedance in the high-to-medium frequency range increases during cycling, which they ascribed to an increase of a combination of a surface film (inferred from an increase in the LiF surface coverage measured by XPS) and a charge transfer resistance at the LNMO/electrolyte interface.[26] However, examining the semi-circle at high-to-medium frequencies in their measurements (apex-frequency = 1.58 kHz, $R_{semi\text{-}circle} = 126\ \Omega$), one obtains a capacitance value of ≈1 μF, which is more consistent with a contact resistance between the LNMO cathode and the current collector rather than with the capacitance of the high surface area of the porous LNMO cathode. This suggests that their reported increase in LNMO surface/charge transfer resistance is likely incorrect and that the impedance increase in their study is propably due to an increase in $R_{Cont.}$, analogous to what is shown in Figure 9. Similarly, Lu et al. analyzed the impedance of LNMO/graphite cells (full-cell impedance) and claimed that the observed increase of the high frequency semi-circle is related to an increase in the thickness of a resistive film on the LNMO surface.[25] In summary, these studies claim the formation of a resistive film and/or an increase in the charge transfer resistance during extended cycling of an LNMO cathode, contrary to our analysis shown in Figure 9, which we believe is due to an incorrect assignment of the impedance data, caused primarily by the interference from contact and/or pore resistances with the charge transfer resistance. Here it may be noted that similarly incorrect assignments were discussed previously for LFP/graphite electrodes by Gaberscek et al.[36]

By exemplary analysis of LNMO half-cell data we have demonstrated that it is possible to analyze the impedance of an LNMO cathode in an LNMO/graphite full-cell with a GWRE in both blocking and in non-blocking conditions over the course of cycling, which

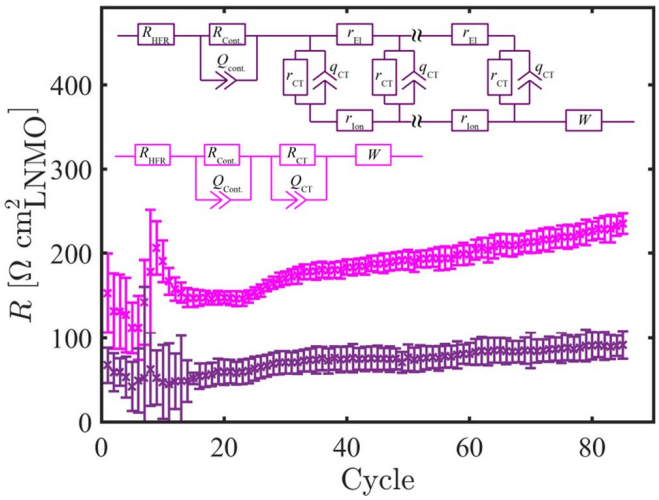

Figure 10. Comparison of the areal charge transfer resistances, normalized to the LNMO BET surface area (123 cm^2), obtained from the transmission line model including pore resistance (lilac) with the *apparent* charge transfer resistance extracted from the conventionally used simplified equivalent circuit (magenta) with one *R/Q* element to describe the mid frequency region (region III in Figure 1 and Figure 2), while one *R/Q* element is used to describe the high-frequency region semi-circle (region II in Figure 1 and Figure 2).

in turn allows for an unambiguous determination of all parameters in the general transmission line model with small errors. The obtained resistances are found to be of reasonable magnitude and in good agreement with the literature and can be monitored in-situ over the course of extended cell cycling. This minimizes the required number of cells compared to the rather cumbersome conventional approach, in which pairs of cells are cycled to a certain number of cycles and the impedances of the half-cells are obtained after cell disassembly and reassembly of anodes and cathodes into symmetric cells–clearly advantageous from an experimental point of view. Furthermore, in most impedance studies in the literature, the observed distorted semi-circle of the impedance spectra in non-blocking condition (compare Figure 7a) are fitted and interpreted in terms of a single *R/Q* equivalent circuit element in the mid frequency region, yielding an apparent charge transfer resistance,[10,26,37] even though this frequency region also contains the pore resistance (region III in Figure 1 and Figure 2). To highlight the difference in the charge transfer resistance values obtained by these two approaches, we compare the charge transfer resistance obtained from our simultaneous fit in blocking and non-blocking conditions (see data in Figure 9, fitted to the equivalent circuit shown in Figure 1) with the apparent charge transfer resistance obtained when the distorted semi-circle (see Figure 7a, second semi-circle from the left) is simply fitted with an *R/Q* element (i.e., using the conventionally applied simplified equivalent circuit depicted in Figure 10 (magenta)). The two different equivalent circuit models are depicted together with the resulting charge transfer resistances (including 95% confidence intervals) in Figure 10.

Figure 10 (magenta symbols) illustrates the stark overestimation of the apparent charge transfer resistance using the simplified equivalent circuit model, which neglects the ionic resistance within the porous electrode: the obtained apparent charge transfer resistance larger by a factor of two to three (magenta symbols) compared to the charge transfer resistance obtained from our transmission line model evaluated simultaneously in blocking and non-blocking conditions (lilac symbols), which is due to the fact that in the former approach the pore resistance (R_{Pore}) is added erroneously to the charge transfer resistance. Thus, in our opinion, the simplified equivalent circuit model is a coarse oversimplification for a porous electrode, and the true charge transfer resistance constitutes only a fraction of the observed mid-frequency semi-circle width.

Conclusions

We utilize a gold wire micro-reference electrode to separate anode and cathode spectra in an LNMO/graphite full-cell over the course of extended charge/discharge cycling. The LNMO cathode impedance spectra could be deconvoluted into individual resistance contributions by measuring in non-blocking conditions at 4.4 V_{FC} and in blocking conditions by holding the LNMO/graphite full-cell potential at 4.9 V_{FC}. This novel impedance analysis approach, i.e., the simultaneous fitting of impedance spectra measured in blocking and non-blocking condition, enables the in-situ quantification of the cycle dependent charge transfer, contact, and pore resistances, over the course of extended charge/discharge cycling, which is a powerful analysis tool for aging studies. We applied our approach exemplarily to an LNMO cathode, but generally the technique could also be applied to other active materials which can be brought into a blocking condition in a full-cell configuration, such as, e.g., lithium iron phosphate, graphite, or LTO.

Acknowledgment

J. L. gratefully acknowledges the funding by the Bavarian Ministry of Economic Affairs and Media, Energy, and Technology for its financial support under the auspices of the EEBatt project. D. P. acknowledges funding from BASF SE within the framework of the Network on Electrochemistry and Batteries. The authors thank Werner Strunz from Zahner for his helpful remarks regarding the general transmission line model and Andrzej Lasia for his comments on proper weighing of impedance spectra and his critical feedback on the equivalent circuit model.

Appendix

Diffusion impedances of solid diffusion and liquid diffusion.—As outlined in the Theory section, the imaginary part of the impedance of a diffusion process depends on the diffusion coefficient of the diffusing species as well as the cross sectional area, bulk concentration of the species in the medium, and the temperature. The diffusion coefficient of lithium in the liquid electrolyte is on the order of 10^{-10} m^2/s for typical lithium ion battery electrolytes at room temperature.[38] For the solid state diffusion coefficient, the range of reported diffusion coefficients in various cathode materials range from 10^{-12} m^2/s to 10^{-19} m^2/s.[39] Mohamedi et al. report an apparent solid state diffusion coefficient for LNMO of 10^{-14} m^2/s to 10^{-16} m^2/s.[33] In the following, we will present our own conservative estimate of the lower limit for the solid state diffusion coefficient of lithium in LNMO (for even larger solid state diffusion coefficients, the impact of the solid state diffusion on the impedance spectrum would be reduced further).

LNMO electrodes with a very small loading of 10 $\mu g/cm^2$ were cycled at 25°C versus metallic lithium in a three electrode configuration with a lithium reference electrode in the potential range from 3 V to 4.9 V vs. lithium using a standard electrolyte ($LiPF_6$ in EC:EMC 3:7, w:w) and two glass fiber separators. The LNMO was always deintercalated (charged) at a constant current of C/3 until the cutoff of 4.9 V vs. the lithium RE was reached. Constant current intercalation (discharge) was done at C-Rates from 1C to 500C until the lower cutoff potential of 3.0 V vs. lithium was reached. By minimizing the loading, the total current in the cell is small (at 500C, $I = 5\ mA$) and all overpotentials from separator resistances, contact resistances, and the concentration gradients in the liquid electrolyte play an insignificant role. The intercalation direction was chosen on purpose to allow large overpotentials. In these measurements, ~20% of the full (1C) capacity could be extracted from the low loaded LNMO cathodes at a C-Rate of 100C. Assuming, conservatively, that all limitations in this experiment are a result of the solid state diffusion inside the active material particles (s. above), i.e., neglecting all other resistances and/or a concentration buildup in the liquid phase, we can now estimate the lower limit of the solid state diffusion coefficient. 20% of the capacity of the LNMO particles (15 μm diameter, based on SEM images) can be extracted from the particle shell region between $r = 7.0\ \mu m$ to $r = 7.5\ \mu m$ (corresponding to 20% of the particle volume). During 20% of the time of a 100C intercalation ($t = 0.2 \cdot 36s = 7.2$ s), the lithium in the LNMO has to travel at least $\Delta r = 0.5\ \mu m$, equating to an estimated diffusion coefficient of $D = \Delta r^2/t = 3.5 \cdot 10^{-14}\ \frac{m^2}{s}$.

With the above estimates for the solid and the liquid diffusion coefficient,[38] the diffusion impedance can be estimated (strictly valid only for semi-infinite diffusion inside a film) with Equation 12 and the definition of the Warburg coefficient (compare Reference 40, Eq. 5–40 for the same kinetic rate constants for forward and backward reaction $k_f = k_b$)
;

$$W = \frac{4 \cdot RT}{z^2F^2\ A\ C\ \sqrt{2 \cdot D}} \qquad [A1]$$

The Warburg coefficient of the liquid electrolyte phase at a frequency of 0.1 Hz thus yields a value of

$$W_{Liquid} = \frac{4 \cdot RT}{z^2\ F^2 \cdot 0.95\ cm^2 \cdot 1000\frac{mol}{m^3}\sqrt{2 \cdot 10^{-10}\frac{m^2}{s}}} = 792\frac{m\Omega}{\sqrt{s}} \qquad [A2]$$

while for solid state diffusion the Warburg coefficient at a frequency of 0.1 Hz can be estimated as

$$W_{Solid-state} = \frac{4 \cdot RT}{z^2\ F^2 \cdot 123\ cm^2 \cdot 10700\frac{mol}{m^3}\sqrt{2 \cdot 3.5 \cdot 10^{-14}\frac{m^2}{s}}} = 31\frac{m\Omega}{\sqrt{s}} \qquad [A3]$$

Here, the lithium concentration in the solid (10700 $mole/m^3$) is calculated for an LNMO particle at 50% SOC ($\equiv$ 70 mAh/g_{LNMO} = 252 As/g_{LNMO}), using a bulk density of 4.4 g/cm^3 (252 As/g ·4.4 g/cm^3/96485 As/mol ·10^6 cm^3/m^3 = 10700 mol/m^3). With the above Warburg coefficients, Warburg impedances of $Z_W^{Liquid}(0.1\ Hz) = 1\ \Omega$ and $Z_W^{Solid-state}(0.1\ Hz) = 39\ m\Omega$ are obtained. This means that the contribution of the solid state diffusion impedance at the lowest frequency measured in this work (0.1 Hz) is 1.5 orders of magnitude smaller than the diffusion impedance caused by the liquid electrolyte. Based on this result, the solid state diffusion inside the active material is negligible, i.e., we can omit the Warburg element in series to the charge transfer resistance in the equivalent circuit model in Figure 1, but must place a Warburg element in series to the separator resistance to capture the effect of liquid diffusion.

References

1. K. Xu, *J. Electrochem. Soc.*, **154**, S9 (2007).
2. S. R. Li, C. H. Chen, X. Xia, and J. R. Dahn, *J. Electrochem. Soc.*, **160**, A1524 (2013).
3. T. R. Jow, M. B. Marx, and J. L. Allen, *J. Electrochem. Soc.*, **159**, A604 (2012).
4. J. P. Schmidt, T. Chrobak, M. Ender, J. Illig, D. Klotz, and E. Ivers-Tiffée, *J. Power Sources*, **196**, 5342 (2011).
5. J. Illig, M. Ender, T. Chrobak, J. P. Schmidt, D. Klotz, and E. Ivers-Tiffee, *J. Electrochem. Soc.*, **159**, A952 (2012).
6. D. W. Abarbanel, K. J. Nelson, and J. R. Dahn, *J. Electrochem. Soc.*, **163**, A522 (2016).
7. N. Ogihara, Y. Itou, T. Sasaki, and Y. Takeuchi, *J. Phys. Chem. C*, 150209102507001 (2015).
8. J. N. Illig, *Dr. Diss., Karlsruhe* (2014).
9. C. H. Chen, J. Liu, and K. Amine, *J. Power Sources*, **96**, 321 (2001).
10. R. Petibon, C. P. Aiken, N. N. Sinha, J. C. Burns, H. Ye, C. M. VanElzen, G. Jain, S. Trussler, and J. R. Dahn, *J. Electrochem. Soc.*, **160**, A117 (2012).
11. S. Klink, E. Madej, E. Ventosa, A. Lindner, W. Schuhmann, and F. La Mantia, *Electrochem. commun.*, **22**, 120 (2012).
12. M. Ender, A. Weber, and E. Ivers-TiffeÉe, *J. Electrochem. Soc.*, **159**, A128 (2012).
13. C. Bünzli, H. Kaiser, P. Novák, C. Bunzli, H. Kaiser, and P. Novak, *J. Electrochem. Soc.*, **162**, A218 (2014).
14. J. Zhou and P. H. L. Notten, *J. Electrochem. Soc.*, **151**, A2173 (2004).
15. D. P. Abraham, S. D. Poppen, A. N. Jansen, J. Liu, and D. W. Dees, *Electrochim. Acta*, **49**, 4763 (2004).
16. J. L. Gómez-Cámer and P. Novák, *Electrochem. commun.*, **34**, 208 (2013).
17. S. Solchenbach, D. Pritzl, E. J. Y. Kong, J. Landesfeind, and H. A. Gasteiger, *J. Electrochem. Soc.*, **163**, A2265 (2016).
18. N. Ogihara, S. Kawauchi, C. Okuda, Y. Itou, Y. Takeuchi, and Y. Ukyo, *J. Electrochem. Soc.*, **159**, A1034 (2012).
19. J. Landesfeind, J. Hattendorff, A. Ehrl, W. A. Wall, and H. A. Gasteiger, *J. Electrochem. Soc.*, **163**, A1373 (2016).
20. Andrzej Lasia, *Electrochemical Impedance Spectroscopy and its Applications*, Springer (2014).
21. H. Göhr, in *Electrochemical Applications*, p. 2, ZAHNER-elektrik GmbH & Co. KG (1997).
22. M. E. Orazem and B. Tribollet, *Electrochemical Impedance Spectroscopy*, WILEY A (2008).
23. J. A. Gilbert, J. Bareño, T. Spila, S. E. Trask, D. J. Miller, B. J. Polzin, A. N. Jansen, and D. P. Abraham, *J. Electrochem. Soc.*, **164**, A6054 (2017).
24. R. Petibon, J. Xia, L. Ma, M. K. G. Bauer, K. J. Nelson, and J. R. Dahn, *J. Electrochem. Soc.*, **163**, A2571 (2016).
25. D. Lu, M. Xu, L. Zhou, A. Garsuch, and B. L. Lucht, *J. Electrochem. Soc.*, **160**, A3138 (2013).
26. D. Aurbach, B. Markovsky, Y. Talyossef, G. Salitra, H. J. Kim, and S. Choi, *J. Power Sources*, **162**, 780 (2006).
27. B. Michalak, B. B. Berkes, H. Sommer, T. Bergfeldt, T. Brezesinski, and J. Janek, *Anal. Chem.*, **88**, 2877 (2016).
28. Y. Dong, J. Demeaux, and B. L. Lucht, *J. Electrochem. Soc.*, **163**, A2413 (2016).
29. *Matlab Ref.*, 2016b https://de.mathworks.com/help/matlab/ref/fminsearch.html.
30. *Matlab File Exch.*, 2016b http://de.mathworks.com/matlabcentral/fileexchange/13490-adaptive-robust-numerical-differentiation/content/DERIVESTsuite/jacobianest.m.
31. T. Yoon, S. Park, J. Mun, J. Heon, W. Choi, Y. Kang, J. Park, and S. M. Oh, *J. Power Sources*, **215**, 312 (2012).
32. D. Pritzl, M. Wetjen, J. Landesfeind, S. Solchenbach, and H. A. Gasteiger, in preparation.
33. M. Mohamedi, M. Makino, K. Dokko, T. Itoh, and I. Uchida, *Electrochim. Acta*, **48**, 79 (2002).

34. C. Heubner, M. Schneider, and A. Michaelis, *J. Power Sources*, **288**, 115 (2015).
35. Y.-C. Chang, J.-H. Jong, and G. T.-K. Fey, *J. Electrochem. Soc.*, **147**, 2033 (2000).
36. M. Gaberscek, J. Moskon, B. Erjavec, R. Dominko, and J. Jamnik, *Electrochem. Solid-State Lett.*, **11**, A170 (2008).
37. J. Xia, L. Ma, K. J. Nelson, M. Nie, Z. Lu, and J. R. Dahn, *J. Electrochem. Soc.*, **163**, 2399 (2016).
38. A. Ehrl, J. Landesfeind, W. A. Wall, H. A. Gasteiger, and W. A. Wall, *J. Electrochem. Soc.*, **164**, A826 (2017).
39. M. Park, X. Zhang, M. Chung, G. B. Less, and A. M. Sastry, *J. Power Sources*, **195**, 7904 (2010).
40. V. F. Lvovich, *Impedance Spectroscopy Applications to Electrochemical and Dielectric Phenomena*, p. 78, John Wiley & Sons, Ltd, New Jersey (2012).

5.3 Anode Impedance Analysis

In this section the article *An Analysis Protocol for Three-Electrode Li-Ion Battery Impedance Spectra: Part II. Analysis of a Graphite Anode Cycled vs. LNMO*[121] is presented, which was not yet submitted at the time of submission of this thesis.

This manuscript is the second part of the novel impedance analysis method introduced in the previous section (see Section 5.2). Here the focus is on the analysis of the impedance evolution of the graphite anode of an LNMO/graphite full-cell, cycled at 40 °C. As shown for the LNMO cathodes before, blocking electrode conditions can be obtained (purely capacitive coupling at the anode at low frequencies) by completely delithiating the graphite particles. Yet, in contrast to the LNMO cathodes, the recorded graphite half-cell impedance in blocking condition does not show a simple transmission line model behavior in the Nyquist plot. During cycling a distinct high frequency semi-circle evolves, a feature which was also observed for LNMO cathodes and could be ascribed to the formation of a contact resistance between the aluminum current collector and the porous electrode (see Section 5.2 and Ref. [120]). For graphite electrodes, coated on copper foils, the formation of a contact resistance however is unlikely (see Section 2.1 and 4.1). With the help of temperature dependent measurements we obtained an activation energy for the high frequency semi-circle, similar to an ionic process, ≈9 kJ/mol compared to ≈16 kJ/mol reported in the literature,[100] which is in stark contrast to an electronic resistance effect, ≈1 kJ/mol.[100] In the literature the dissolution of manganese from the LNMO cathode at elevated temperatures and during high voltage operation is suggested to lead to an ongoing formation of the solid electrolyte interface at the anode.[122] Supported by previous reports in the literature, as well as by systematic addition of manganese salt to the pristine electrolyte we successfully identified the main contribution of the anode impedance to a SEI layer at the anode/separator interface.

In summary, the use of a micro reference electrode enabled us to deconvolute anode and cathode impedances. The additional simultaneous analysis of each electrode impedance in two different states (blocking and non-blocking condition) allowed us to identify all parameters of the physically motivated equivalent circuit models with a small uncertainty. At last the full deconvolution of all the physical and electrochemical origins for the full-cell resistance and its evolution during cycling of the LNMO/graphite cell is shown. For the first time we could demonstrate that the impedance increase of a LNMO/graphite cell, cycled at 40 °C, is dominated by an electrical contact resistance at the LNMO cathode and an ionic contact resistance from SEI precipitates at the anode/separator interface.

Author Contributions

All electrochemical measurements were conducted by D.P. D.P., S.S. and J.L. developed the equivalent circuit model. Data analysis was done by J.L. and D.P. The manuscript was written by D.P. and J.L. All authors discussed the data and commented on the results.

An Analysis Protocol for Three Electrode Li-Ion Battery Impedance Spectra: Part II. Analysis of a Graphite Anode Cycled vs. LNMO

Daniel Pritzl[1, =], Johannes Landesfeind[1, #, =], Sophie Solchenbach[1] and Hubert A. Gasteiger[1]

[1] Chair of Technical Electrochemistry, Department of Chemistry and Catalysis Research Center, Technical University of Munich, Munich, Germany

[#]corresponding author

[=]equal contribution

Abstract

Li-Ion cells consisting of LNMO ($LiNi_{0.5}Mn_{1.5}O_4$) cathodes and graphite anodes show severe capacity fading at elevated temperatures due to a damage of the solid electrolyte interface (SEI) on the anode. Hence, a detailed investigation of the anode SEI with electrochemical impedance spectroscopy (EIS) can provide valuable insight into the phenomenon of anode degradation. In this study, we use a modified version of our novel impedance procedure (Part I of this study), where the anode impedance is measured at non-blocking conditions (10% SOC) and blocking conditions (0% SOC) with a gold wire reference electrode (GWRE). We show that during cycling an ionic contact resistance ($R_{\text{Cont. Ion}}$) at the separator/anode coating interface evolves which is most likely caused by manganese dissolution from the high-voltage cathode (LNMO). By simultaneously fitting EIS spectra in blocking and non-blocking conditions, we can deconvolute the anode impedance over 86 cycles at 40°C into contributions of: a) the separator resistance ($R_{\text{Sep.}}$), b) the true charge transfer resistance (R_{CT}) and c) the ionic contact resistance ($R_{\text{Cont. Ion}}$) between the separator and anode coating. We also show that the main contributor to a rising anode impedance is the ionic contact resistance ($R_{\text{Cont. Ion}}$).

Introduction

For future Li-Ion batteries – as for example graphite/$LiNi_{0.5}Mn_{1.5}O_4$ (LNMO) cells with an energy density of 624 Wh/kg[1] at the materials level – electrochemical impedance spectroscopy is a powerful tool to investigate degradation mechanisms. Graphite/LNMO cells do suffer from a drastic capacity decay when these cells are cycled at elevated temperatures (> 40°C)[1–3], which is related to electrochemical electrolyte oxidation[4] followed by transition metal dissolution (both manganese and nickel) from the spinel cathode[5] and thus leading to a loss of active lithium on the anode due to ongoing SEI formation.[2, 6] As the degradation of the graphite anode is a key failure mechanism of graphite/LNMO cells, a detailed impedance analysis of the anode is necessary to better understand the processes happening at elevated temperatures.

In the literature, there are several approaches in order to investigate the anode impedance. One type of studies focuses on the solid electrolyte interface (SEI) formation on graphite anodes.[7–10] The impedance is recorded at different potentials during lithiation of a graphite anode and the impedance response is generally fitted with two R/Q elements connected in series representing the charge transfer resistance and the SEI resistance. In these studies the graphite impedance is measured versus the lithium metal counter electrode in a two electrode configuration, however in this scenario the lithium metal anode dominates the EIS response due to its small surface area[11], and prevents a clear analysis of the graphite electrode impedance.

Another type of studies uses a symmetric cell approach in order to deconvolute the anode impedance from the full-cell impedance.[12,13] However, as the symmetrical cell approach is a destructive method, extensive studies over cycling or at different states-of charge would lead to numerous amount of cells. A third group of papers uses micro-reference electrodes, where a deconvolution of the anode impedance from the full-cell impedance is possible during cycling without disassembly of the cells (as for the symmetric cell approach).[11,14,15] Here the reference electrode has to fulfill certain criteria, as for example a centered position between two separators[16] and the wire should be thin relative to the separators.[17] Focus of these studies was the evolution of anode and cathode impedance over cycling and the effect of anode additives after battery formation.

In a previous study of our group[18] we analyzed the impedance of the LNMO cathode in graphite/LNMO cells where the impedance was analyzed in non-blocking conditions (4.4 V cell voltage, open-circuit conditions) and blocking conditions (4.9 V cell voltage, constant-voltage conditions) utilizing a micro-reference electrode (GWRE[11]). We were able to deconvolute the cathode impedance (R_{Cathode}) into contributions of: a contact resistance between current collector an LNMO coating ($R_{\mathrm{Cont.}}$), the true charge transfer resistance (R_{CT}) and the ionic resistance (R_{Pore}) of the porous cathode in-situ and over 86 cycles. This deconvolution was possible, as from the spectrum in blocking conditions (no faradaic reaction during the measurement, as the cathode does not contain lithium) the pore resistance could be obtained from the 45° transmission line and the charge transfer resistance (R_{CT}) was shifted two lowest frequencies in the spectrum. By fitting both the blocking and non-blocking spectra at the same time with a general transmission line model (TLM), a deconvolution with very low uncertainties was possible.

Now we apply this concept to the graphite anode. Therefore, we will measure the impedance of the graphite anode either in a graphite/LFP cell or in a graphite/LNMO cell at ≈1.9 V vs. Li/Li^+ (delithiated state) and show that blocking electrode behavior can be achieved. Further, a semi-circle is evolving in the blocking graphite impedance spectra (in graphite/LNMO cells over 86 cycles at 40°C), which we will correlate with the formation of an interface anode/separator induced by manganese dissolution from the cathode. Next, we will fit both blocking (3.0 V_{FC}) and non-blocking spectra (4.4 V_{FC}) at the same time with the general transmission line model and deconvolute the overall anode impedance. Last, we will show the overall full-cell impedance of a graphite/LNMO cell and show a detailed analysis of the contributions to anode and cathode impedance.

Experimental

Electrode Preparation – $LiNi_{0.5}Mn_{1.5}O_4$ (LNMO) electrodes were prepared by mixing LNMO (BASF SE, Germany), carbon black (Super C65, Timcal), and polyvinylene difluoride (PVdF, Kynar) at a mass ratio of 92/5/3 with NMP (N-methyl pyrrolidone, anhydrous, Sigma-Aldrich, Germany) in a planetary mixer (Thinky Corp.) for 15 min. The ink was coated onto aluminum foil (MTI, 18 µm) with a doctor blade coater and dried afterwards at 50°C in a convection oven for at least 3 h. The final LNMO coating had a loading of ≈13.6 mg_{LNMO}/cm^2, corresponding to ≈1.9 mAh/cm². Electrodes with a diameter of 11 mm (≡0.95 cm^2) were punched out and compressed to ≈32% porosity with a KBr press (Mauthe, PE-011). $LiFePO_4$ (LFP) electrodes with a composition of 93/4/3 (LFP/PVdF/carbon black) were assembled using the same mixing- and coating procedure as for the LNMO cathodes. The final loading was ≈2.0 mAh/cm² and the cathodes were compressed to a porosity of 30%. Graphite electrodes were prepared by mixing graphite (T311, SGL Carbon, Germany) and PVdF at a mass ratio of 95/5 with NMP by applying the same procedure as for the positive electrodes.

The graphite ink was coated onto copper foil (MTI, ~12 µm) and dried in a convection oven at 50°C for 3 h. The loading of the graphite coating was ≈6.6 $mg_{graphite}/cm^2$ corresponding to ≈2.3 mAh/cm². The electrodes were punched out with a diameter of 11 mm and compressed to a porosity of ≈32%. All electrodes were dried under dynamic vacuum at 120°C for at least 12 h in a vacuum oven (Büchi, Switzerland) and then transferred into an Argon-filled glovebox (MBraun, Germany) without exposure to air.

Cell Assembly and Battery Testing – T-Cells (Swagelok, U.S) were assembled in an Argon-filled glove box (< 0.1 ppm O_2 and H_2O, MBraun, Germany) and dried beforehand in a 70 °C convection oven. The graphite anode and LNMO or LFP cathode were sandwiched between two glassfiber separators (glass microfiber filter, 691, VWR Germany). As electrolyte, 60 µL of LP57 (1M $LiPF_6$ in EC/EMC 3:7 w:w < 20 ppm H_2O, BASF SE, Germany) were used. Between the separators a gold-wire reference electrode (GWRE) was placed (the detailed assembly procedure can be found in Reference [11]). The GWRE was lithiated with a constant current of 150 nA for 1 h at 40 °C. Due to the specific cell chemistry – electrochemical electrolyte oxidation on LNMO cathodes – protic species (e.g. HF) causes delithiation of the lithiated GWRE, leading to a loss of potential after several cycles. [19] However, as shown in Part I [18] of this publication, the potential drift after the chemical delithiation of the GWRE is smaller than < 0.4 mV/time scale of the impedance measurement, and hence the drift does not affect the EIS measurement with a perturbation of 15 mV. In order to convert the full cell potential (graphite/LNMO) into a half cell potential (graphite/Li) identical T-cells were assembled with a lithium metal reference electrode.

The full cells (graphite/LNMO) were cycled between 3.0 and 4.9 V_{FC} (full cell voltage). Formation cycles were carried out at 25 °C with a C-rate of C/10 (1/h) by applying a constant current constant voltage (CCCV) charge with a current limit of C/20 for the CV phase and a CC discharge. Extended charge/discharge cycling was carried out with C/2 at 40 °C with a CCCV charge to 4.9 V_{FC} (current limit for CV = C/40) and a CCCV discharge to 3.0 V_{FC} (current limit for CV = C/100). The impedance was recorded in non-blocking conditions at 4.4 V_{FC} after a 1 h OCV period under open-circuit conditions and in blocking conditions 3.0 V_{FC} during constant voltage hold and after the current dropped below C/100. The impedance was recorded from 100 kHz to 100 mHz with a perturbation of 15 mV (acquisition time of 10 min/spectrum).

Graphite/LFP cells were also equipped with a GWRE and cycled between 1.5 and 4.0 V_{FC}. Formation was carried out at C/10 at 25°C with a CCCV charge (current limit of C/20) and a CC discharge. Cycling was done at C/2 at 40°C with a CCCV charge (current limit of C/40) and a CCCV discharge (current limit of C/100). Impedance was recorded at non-blocking conditions (1 h of charge from upper cut-off (4.0 V_{FC}) at C/2) and under blocking conditions (1.5 V_{FC} at CV conditions after the current dropped below C/100). As electrolyte, 60 µL of either LP57 (1M $LiPF_6$ in EC/EMC 3:7 w:w < 20 ppm H_2O, BASF SE, Germany) or LP57 with 50 or 100 mM $Mn(TFSI)_2$ (Solvionic, France) were used.

Results & Discussion

Blocking conditions for a graphite anode cycled versus LFP or LNMO at elevated temperatures (40°C)

In Part I[18] of this study, we successfully deconvoluted the impedance contributions from contact resistance ($R_{Cont.}$), porous electrode resistance (R_{Pore}) and charge transfer resistance (R_{CT}) of an LNMO cathode by simultaneous analysis of recorded impedance spectra in blocking and non-blocking configuration. To apply this technique to any electrode it is necessary to check if blocking conditions can be obtained. In blocking conditions the charge transfer reaction has an enormous resistance and will thus occur at very low frequencies in EIS measurements, which allows for an unambiguous interpretation of the remaining physical effects.

To check at which potentials blocking conditions of the anode can be reached, a graphite/LNMO cell with a gold wire reference electrode (GWRE) was assembled and formation was done at C/10 at 25 °C. Afterwards the cell was discharged (at 40 °C) and the impedance was recorded either under open-circuit potential or constant voltage condition at defined potentials. The spectra are shown in Figure 1. At 3.9 V_{FC} (graphite at ≈0.9 V vs. Li/Li$^+$) the impedance spectrum consists of a suppressed semi-circle and a 45° Warburg branch. During subsequent discharge of the full-cell (delithiation of the anode) from 3.6 V_{FC} (graphite at ≈1.1 V vs. Li/Li$^+$) to 3.0 V_{FC} (graphite at ≈1.9 V vs. Li/Li$^+$) the points at low frequencies shift towards high imaginary values, which indicates a significantly increased charge transfer resistance. When the cell potential reaches 3.0 V_{FC} (graphite at ≈1.9 V vs. Li/Li$^+$) reintercalation into the graphite anode is hindered (as can be seen from the almost straight line at low frequencies), i.e., blocking conditions are achieved. At medium frequencies (3000 Hz - 300 Hz), a 45° transmission line (see inset in Figure 1) can be observed, whereas at higher frequencies (> 3000 Hz, left in the Nyquist plot) a depressed semi-circle is present in the anode blocking spectra. This semi-circle arises already after formation on the LNMO/graphite cells and will be analyzed in detail below. During the constant voltage phase at 3.0 V_{FC} of 5 minutes or 25 minutes does not change the behavior of the high- and medium frequency part. The points at lowest frequencies still shift towards high values on the imaginary axis (if a constant voltage phase is applied) what reflects still a changes in the capacitance of the graphite anode.

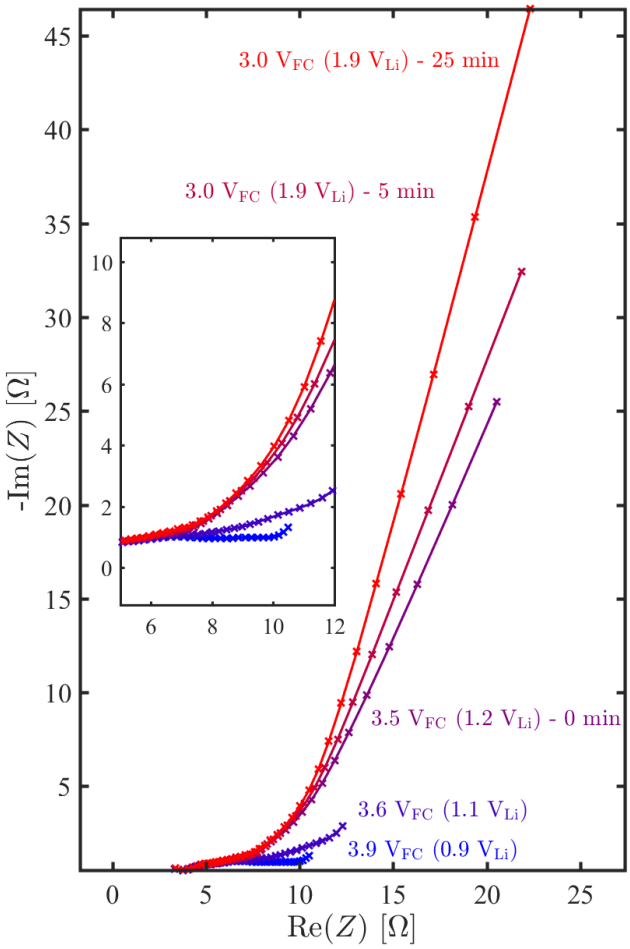

Figure 1: Impedance spectra of the graphite anode measured with a gold wire reference electrode (GWRE) in a graphite/LNMO cell. The impedance spectra are recorded at 3.9 V, 3.6 V, 3.5 V under open circuit conditions and at 3.0 V under constant voltage conditions with a CV phase of 5 or 25 minutes. The impedance is recorded at 40 °C from 100 kHz to 100 mHz with a perturbation of 15 mV. The full cell potential conversion into half-cell potentials was realized with an identical T-cell equipped with a lithium metal reference electrode.

To investigate the anode impedance in the absence of a LNMO cathode, a graphite/LFP cell was assembled and formation for 2 cycles at C/10 was carried out. Afterwards, the cell was discharged (delithiation of the graphite anode) and impedance spectra were recorded at different states of charge (SOC's). Figure 2 shows the anode impedance spectra of a graphite/LFP cell measured at different voltages either under open-circuit - or constant voltage conditions. The potential versus metallic lithium (V_{Li}) is recalculated from the known potential of the lithiated GWRE (≈ 0.31 V vs. Li/Li$^+$). [11] At a graphite potential of 0.45 V_{Li} and 0.55 V_{Li}, the impedance spectrum consists of one suppressed semi-circle, which reflects both charge transfer resistance and SEI resistance (R_{CT} and R_{SEI}), and a 45° Warburg diffusion branch representing lithium ion concentration gradients within the separator. By further delithiating the graphite anode (see spectra at 1.05 V_{Li}) the semi-circle turns into a ≈40° line and the points at lower frequencies show the typical onset for blocking conditions, as at 1.05 V_{Li}, reintercaltion of lithium into graphite is thermodynamically not possible.

By going to 1.87 V_{Li} (identical to blocking condition voltage (1.9 V vs. Li/Li^+, see Figure 1 of the graphite/LNMO cell) and recording the impedance spectra after a 5 minutes CV phase, a blocking electrode behavior is achieved for the graphite anode. The 45° transmission line reflects 1/3 [20] of the ionic resistance within the porous graphite (R_{Pore}) anode and at lowest frequencies, only capacitive coupling along the electrode is observed. After a potential hold of 5 minutes at 1.87 V vs. Li/Li^+ the transmission line is identical to the spectrum where the CV phase was carried out for 0 minutes. For the graphite anode in a graphite/LFP cell (see Figure 2) the 45° transmission line region is clearly visible, while in same procedure in the graphite/LNMO cells shows a depressed semicircle at high frequencies (compare Figure 1) which will be one of the main focuses of our following analysis.

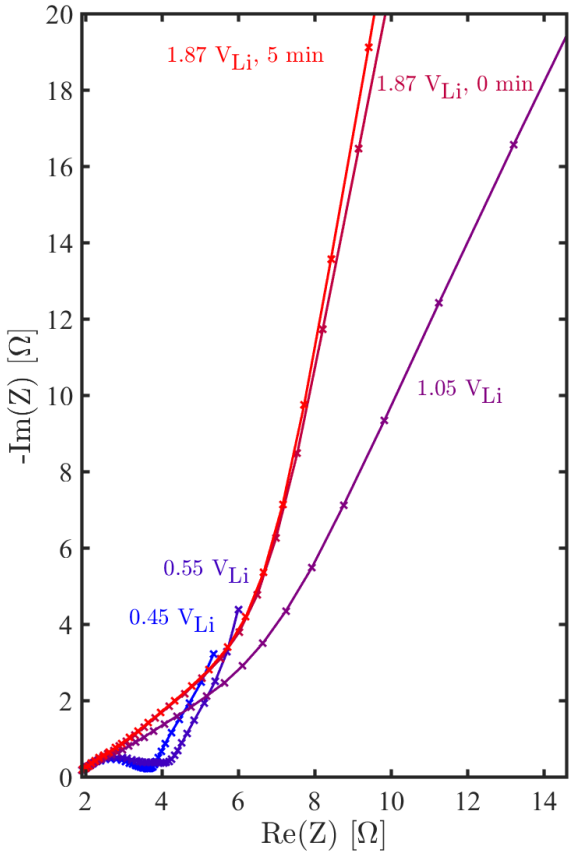

Figure 2: : Impedance spectra of a graphite anode measured versus a GWRE in a graphite/LFP cell. The spectra are recorded at 0.45 V, 0.55 V, 1.05 V versus lithium metal (calculated from the known potential of the GWRE) under open-circuit conditions and at 1.87 V versus lithium metal under constant voltage for 0 and 5 minutes. The impedance is recorded from 100 kHz to 100 mHz with a perturbation of 15 mV at 40°C.

Evolution of the graphite impedance during charge/discharge cycling at 40°C over 86 charge/discharge cycles at 40°C

In the following section, we want to analyze both blocking and non-blocking impedance spectra over the course of 86 charge/discharge cycles and investigate the evolution of the semi-circle at higher frequencies with cycling. The cycle dependent Nyquist plots for the anode in non-blocking (4.4 V_{FC}, Figure **3** a)) and blocking configuration (3.0 V_{FC}, Figure 3 b)) are shown for the 1st, 25th, 50th and 75th cycle. The capacity retention of this cell – cycled with C/2 (0.95 mA/cm²) at 40 °C – is shown in Reference 18 (see Figure 4 in that publication). For the spectra in non-blocking conditions (Figure 3 a)), the impedance spectrum consists of the separator resistance (high-frequency resistance, HFR) and a semi-circle, which is a convolution of the charge transfer resistance, SEI resistance and pore resistance. At lowest frequencies a 45° line for the warburg diffusion is observable. The diameter of the semi-cirlce increases from ≈2 Ωcm² (cycle 1) to ≈15 Ωcm² (cycle 75). The capacitance after 25 cycles is $8.9\,\mathrm{mF}\cdot \mathrm{s}^{(\alpha_{CT}-1)}/\mathrm{cm}^2_{\mathrm{geo.}}$ (normalized to the current collector area), which gives a reasonable value for the electrochemical double layer capacitance of $\approx 4.5\,\mu\mathrm{F}/\mathrm{cm}^2_{\mathrm{BET}}$, taking into account the roughness factor of the graphite anode (– 3 $m_{BET}^2/g \cdot 6.6$ mg/cm² $= 198\,\frac{\mathrm{cm}^2_{\mathrm{BET}}}{\mathrm{cm}^2_{\mathrm{geometric}}}$) while neglecting the constant phase factor.

The blocking spectra (Figure 3 b)) show a slightly distorted transmission line after the first cycle (convolution of a semi-circle at highest frequencies and a 45° line at medium frequencies) followed by the onset for the large charge transfer resistance which indicate a blocking behavior. After 25 cycles, the blocking spectra show a distinct semi-circle with a diameter of ≈10 Ωcm², which increases to ≈15 Ωcm² after 75 cycles. The capacitance after the 25th cycle is $\approx 73\,\mu\mathrm{F}\cdot \mathrm{s}^{(\alpha_{CT}-1)}/\mathrm{cm}^2_{\mathrm{geo.}}$ (normalized to the current collector area) which is two orders of magnitude lower compared to the semi-circle in the respective non-blocking spectrum. This suggests that the surface area where this resistance is located is small. A capacitance of $\approx 73\,\mu\mathrm{F}\cdot \mathrm{s}^{(\alpha_{CT}-1)}/\mathrm{cm}^2_{\mathrm{geo.}}$ corresponds to a surface area of $\approx 17\mathrm{cm}^2_{\mathrm{BET}}$ assuming a specific capacitance of $\approx 4.5\,\mu\mathrm{F}/\mathrm{cm}^2_{\mathrm{BET}}$. As the total electrode has a surface area of $198\,\mathrm{cm}^2_{\mathrm{BET}}$, this interface corresponds to ≈ 9% of the total surface are. In the next section, we will show where the interface is located and what might be the origin for this semi-circle in the blocking anode impedance spectra.

A semi-circle in a blocking spectrum (no fardaic process during the impedance measurement) has so far only been explained by a contact resistance ($R_{\mathrm{Cont.}}$) between an aluminum current collector and a cathode coating[18,21,22] However, for a graphite anode coated on a copper collector – both materials are good electronic conductors – we do not expect a contact resistance between the current collector and the anode coating. Also, in graphite/LFP cells cycled at 40 °C (data not shown in here), no semi-circle evolves in the blocking spectra.

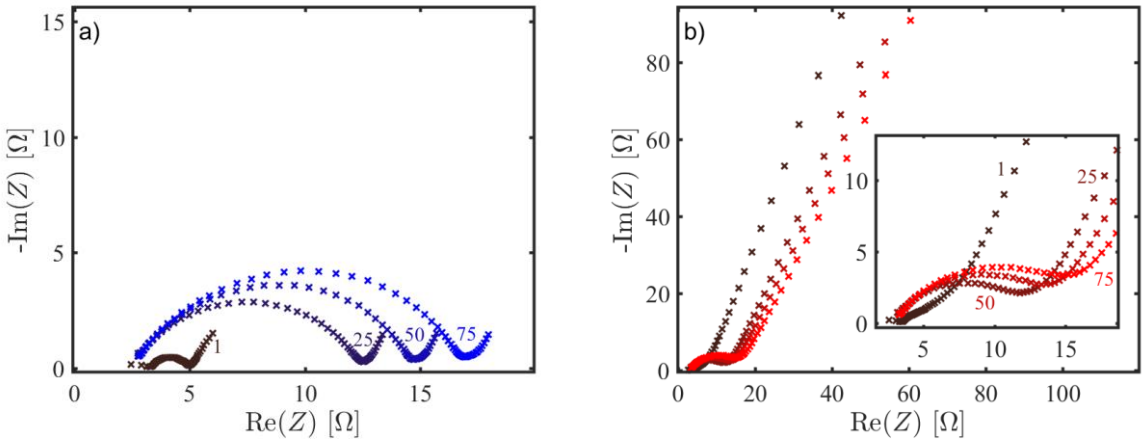

Figure 3: Evolution of the impedance spectra of the graphite anode (every 25th cycle; cycle numbers 1, 25, 50 and 75 are marked in the figure) during cycling of an LNMO/graphite cell at a rate of C/2 at 40°C: a) at 4.4 V_{FC} in non-blocking conditions (recorded at OCV after 1 h OCV period); b) after potential hold at 4.9 V_{FC} under blocking conditions (recorded at a controlled potential of 4.9 V_{FC} after a potential hold at 4.9 V_{FC} until the current dropped below C/100). Potential controlled EIS spectra were recorded with an amplitude of 15 mV in the frequency range from 100 kHz to 100 mHz.

Origin of the high frequency semi-circle in the graphite impedance spectra under blocking conditions in graphite/LNMO cells

In order to find the physical origin for the high frequency semi-circle visible in blocking conditions, temperature-dependent EIS measurements of a graphite/LNMO cell with a GWRE were recorded in blocking conditions (3.0 V_{FC}) after formation (C/10, 25 °C) and five subsequent C/2 charge/discharge cycles at 40 °C. The impedance was measured at 10 °C (blue points), at 25 °C (green points) and at 40 °C (red points) in order to discriminate its origin to be of electronic or ionic nature (see Figure 4). The diameter of the semi-circle increases from ≈9 Ωcm² at 40 °C to ≈14 Ωcm² at 25 °C and ≈22 Ωcm² at 10 °C. From this data, the apparent activation energy is calculated using the Arrehnius equation. A similar analysis for several type of resistances occuring in porous electrodes has been done by Ogihara et al.[23] We find an apparent activation energy of ≈9 kJ/mol, which is close to the value for ionic resistances according to Ogihara et al.[23] (≈16 kJ/mol) and differs largely from the expected activation energy of electronic processes (0.84 kJ/mol from Ogihara et al.[23]). Together with the small geometric interface area (9% of the total graphite surface area) we conclude that this ionic resistance most likely stems from the interface anode coating/separator.

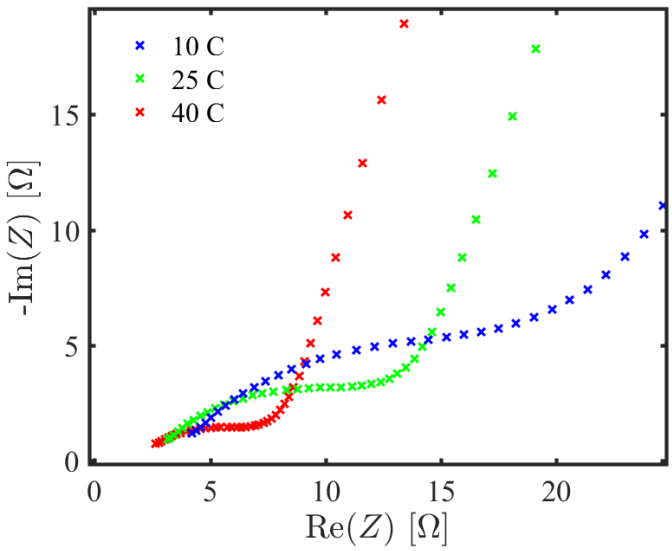

Figure 4: Impedance spectra of a graphite anode measured versus the GWRE in a graphite/LNMO cell after 5 cycles at C/2 (40°C). The impedance is recorded in blocking conditions (3.0 V_{FC} potential hold after a CV phase at 3.0 V_{FC} with a current limit of C/100) at 10°C, 25°C and 40°C. The impedance is recorded from 100 kHz to 100 mHz with a perturbation of 15 mV. Before starting the measurement, an open-circuit period (1 h) at the specific temperature is carried out to ensure thermal equilibration.

Burns et al.[24] explained the rapid capacity drop after extended cycling (> 700 cycles) of 18650-sized graphite/NMC111 cells with oxidation products of the cathode, which can be reduced on top of the graphite anode (interface anode/separator). When a certain amount of oxidation products was reduced there, the insulating layer becomes so thick that ion transport through to the bulk of the anode is hindered and the cells can no longer be cycled at the same C-rate. These conclusions were drawn from SEM pictures before and after cycling. For LNMO cathodes it is well known that transition metal dissolution[5] (e.g. manganese dissolution) and subsequent deposition on the anode is a key failure mechanism of these cells, especially when cycled at elevated temperatures. Hence, a deposition of manganese at the interface anode/separator could lead to a thick, ionically insulating layer, which could be the origin for the semi-circle in the blocking anode impedance spectra. In order to prove this hypothesis, graphite/LFP cells (where no transition metal dissolution occurs under typical cycling conditions) were prepared without and with a defined amount (50 or 100 mM) of deliberately added Mn(II)TFSI salt to mimic the transition metal dissolution in LNMO/graphite cells.

Formation of the graphite/LFP cells was done at C/10 and 25°C from 2.0 V to 4.0 V_{FC}. After formation, five cycles at C/2 and 40°C from 1.5 V_{FC} (1.9 V vs. Li/Li^+) and 4.0 V_{FC} were conducted and the impedance was recorded at 1.5 V_{FC} under constant voltage conditions after the current dropped below C/100. Three types of cells were investigated: (i) graphite/LFP cells cycled in pure LP57 electrolyte, (ii) graphite/LFP cells where formation was done in LP57 electrolyte; after formation, the cells were opened in an Ar-filled glovebox and reassembled with fresh separators and LP57 + 50 mM $Mn(TFSI)_2$ electrolyte, and (iii)

graphite/LFP cells which were handled as described in (ii) but with LP57 + 100 mM $Mn(TFSI)_2$ as the final electrolyte.

Figure 5 shows the spectra in blocking configuration (1.9 V vs. Li/Li^+) after the 5th cycle. The anode impedance spectrum of the cell with pure LP57 (in light blue) shows almost perfect blocking behavior – i.e., a transmission line followed by a capacitive branch (identical to the data in Figure 2). When 50 mM $Mn(TFSI)_2$ were added to a graphite/LFP cell (in purple) the 45° transmission line turns into a distinct semi-circle. When 100 mM $Mn(TFSI)_2$ are added to the electrolyte (in pink), a large semi-circle in the blocking spectra is observable. From these results we conclude that manganese deposition and a subsequent SEI formation are also the cause for the semi-circle in the blocking anode impedance spectra of the graphite/LNMO cells. This could imply that transition metals are deposited preferentially at the separator facing side of the graphite anode and lead to an enhanced SEI formation. Studies on the analysis of the SEI distribution across the thickness of graphite anodes are currently on the way to prove our impedance results.

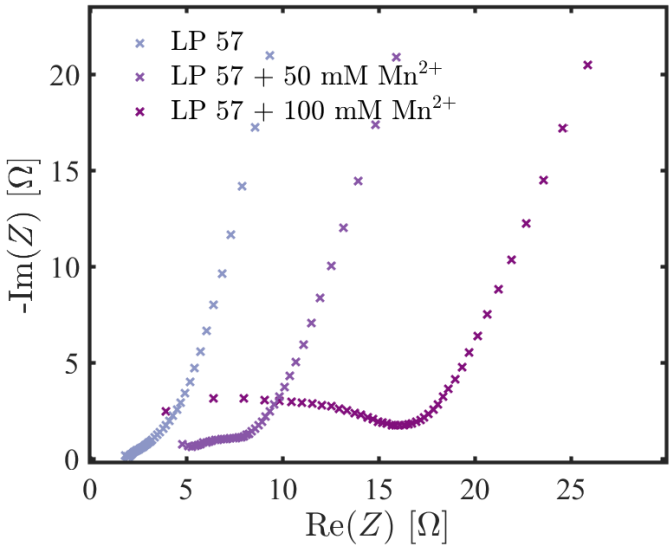

Figure 5: Impedance spectra of a graphite anode measured versus the GWRE in a graphite/LFP cell after formation (2 cycles at C/10 with a CCCV charge and a CC discharge at 25°C). The cells are refilled with a novel electrolyte after formation: LP57, LP57 + 50 mM $Mn(TFSI)_2$ or LP57 + 100 mM $Mn(TFSI)_2$ and the charged/discharge for 5 cycles between 1.5 – 4.0 V_{FC}. The impedance is recorded at 1.5 V_{FC} under blocking conditions after the current dropped below C/100 at 40°C.

Fitting anode impedance spectra of graphite/LNMO cells under blocking and non-blocking conditions

In the following, both the spectra in blocking and non-blocking conditions of the graphite/LNMO cell cycled at C/2 and at 40°C for 86 charge/discharge cycles (see Figure 3) are fitted at the same time using the equivalent circuit shown in Figure 6. The used equivalent circuit consists of: i) a separator resistance ($R_{Sep.}$) representing the ionic resistance with in the separator (section I in equivalent circuit representation in Figure 6), ii) an R/Q element for the ionic contact resistance ($R_{Cont.Ion}$) which accounts for the semi-circle evolving in the blocking anode impedance spectra due to transition metal dissolution (section II in Figure 6), iii) the general transmission line model composed of differential elements for the charge transfer resistance (r_{CT}) connected in parallel with the double layer capacitance (q_{CT}), the pure ionic (r_{Pore}) and electrical resistance ($r_{El.}$) in the porous anode (r_{Pore}), which is section III in Figure 6, and iv) a Warburg diffusion element (W, section IV) accounting for concentration gradients within the separator . The interested reader is referred to Ref 17 for details on the simultaneous fitting procedure.

As the 45° transmission line is only observable in the very first cycles (afterwards, the ionic contact resistance ($R_{Cont.Ion}$) dominates in the impedance spectra), the pore resistance is fitted from the spectrum of the first cycle (Figure 3b)) using a transmission line model (see Figure 6) without the R/Q element for the ionic contact resistance, and fixed for all the subsequent cycles to its 1st cycle value. The obtained 1st cycle pore resistance is ≈10.6 Ωcm² with an uncertainy of ± 17%, as determined by the jacobian matrix.

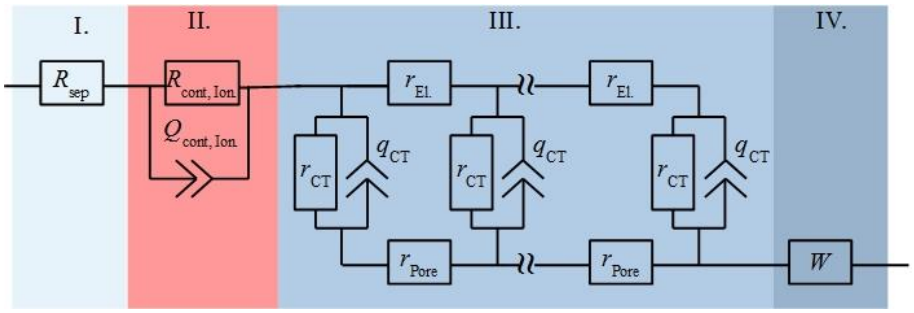

Figure 6: Anode equivalent circuit model with four section (from left to right): I. separator resistance (R_{Sep}) from ionic resistance of the separator and electronic/contact resistances of the cell setup, II. The ionic contact resistance at the interface separator/anode coating, III. The general transmission line model (TLM) describing the porous coating, and, IV. A Warburg diffusion element describing concentration gradients within the separator.

In Figure 7, two exemplary fits of the anode impedance from the 30th cycle are shown. Figure 7a) shows the spectrum under blocking conditions (3.0 V_{FC} recorded under CV conditions and after the current dropped below C/100, black crosses) and fitted line (in red). Figure 7b) shows the spectrum under non-blocking conditions with experimental data (black crosses) and the corresponding fit (blue line).

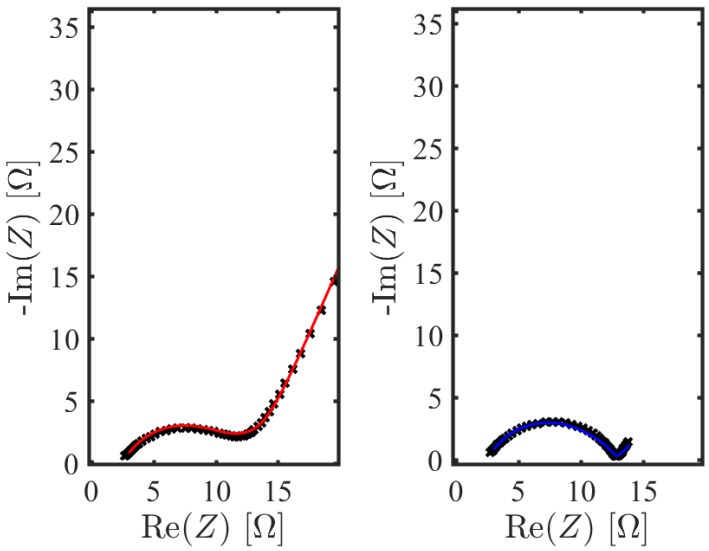

Figure 7: Exemplary fits (shown as solid lines) of the anode impedance after the 30th cycle from a LNMO/graphite cell in blocking condition (left) at 3.0 V_{FC} and non-blocking conditions at 4.4 V_{FC} (right). Both spectra are fitted at the same time using the equivalent circuit shown in Figure 6. AC impedance spectra (black crosses) were recorded at 40°C between 100 kHz and 100 mHz with a perturbation of 15 mV.

The following parameters are fitted from the blocking and non-blocking spectrum: $R_{Sep.}$, $R_{Cont.Ion}$, $Q_{Cont.Ion}$, $\alpha_{Cont.}$, $R_{CT\text{-}non\text{-}blocking}$, $R_{CT\text{-}blocking}$, Q_{CT}, α_{CT} and the Warburg element. The pore resistance (R_{Pore}) and the electronic resistance ($R_{El.}$, assumed as 1 mΩ for the graphite anode) are fixed for all cycles. Table I summarizes the fitting results obtained from simultaneous fitting of two spectra from cycle 30 at the same time.

Table 1: Fit parameters of the equivalent circuit in Figure 6 for a simultaneous fit of impedance spectra under blocking conditions ($R_{\text{CT-blocking}}$) and non-blocking conditions ($R_{\text{CT-non-blocking}}$) in cycle 30 (see Figure 7).

Parameter	**Value**
$R_{\text{Sep.}}$	$2.4\ \Omega\ \pm 16\%$
$R_{\text{Cont. Ion}}$	$7.3\ \Omega\ \pm 6.1\%$
$Q_{\text{Cont.}}$	$90\ \mu\text{F} \cdot \text{s}^{(\alpha_{\text{Cont.}}-1)}\ \pm 21\%$
$a_{\text{Cont.}}$	$0.74\ \pm 4.3\%$
R_{Pore}	$10.6\ \Omega$ (fixed)
$R_{\text{El.}}$	$1\ \text{m}\Omega$ (fixed)
$R_{\text{CT-non-blocking}}$	$0.8\ \Omega\ \pm 19\%$
$R_{\text{CT-blocking}}$	$9\ \cdot 10^{8}\Omega$
Q_{CT}	$6.7\ \text{mF}\ \cdot \text{s}^{(\alpha_{\text{CT}}-1)} \pm 3.4\%$
a_{CT}	$0.74\ \pm 0.50\%$
W	$0.9\ \Omega/\sqrt{s}\ \pm 31\%$

Figure 8 presents the fitting results from simultaneous fitting of blocking and non-blocking spectra over 86 cycles. Figure 8a) shows the absolute values of the fitted resistances normalized to the surface area of the current collector, whereasFigure 8b) shows the fitted resistances normalized to their value in the first cycle (R/R_1). The fitted ionic contact resistance, which we have previously related to the interface anode/separator ($R_{\text{Cont.Ion}}$), is small in the beginning and the increases steeply to ≈5 Ωcm² until cycle 18. Afterwards, the slope decreases gradually, and after 86 cycles $R_{\text{Cont.Ion}}$ is ≈10 Ωcm². The separator resistance ($R_{\text{Sep.}}$) has a value of ≈3 Ωcm² after formation and stays constant during cycling at ≈2.7 Ωcm² after 86 charge/discharge cycles at 40°C. The charge transfer resistsance (R_{CT}) increases from ≈0.2 Ωcm² after formation to ≈2 Ωcm² after 86 cycles which might be because of thick SEI layers covering the surface or insulating parts of the anode. The normalized values in Figure 8b show that while $R_{\text{Sep.}}$ stays constant during cycling, $R_{\text{Cont.Ion}}$ increases by a factor of 20 and the SEI/charge transfer resistance (R_{CT}) increases linearely by a factor of 5. The ionic contact resistance ($R_{\text{Cont.Ion}}$), i.e., the interface between separator and anode coating, increases very steep in the beginning and then flattens out, whichcould be explained that the following scenario: In the beginning, the deposited manganese ions lead to a strong SEI formation. After several charge/discharge cycles, the insulating layer (SEI) at the top of the graphite anode is sufficiently thickto stop the deposition of manganese ions deposited, as no more electrons are available from the graphite. Due to the dominating

$R_{\text{Cont. Ion}}$ a deconvolution of the SEI resistance (covered over the whole graphite electrode) from the charge transfer resistance is not possible. However we are currently trying this deconvolution in graphite/LFP cells with the same blocking/non-blocking approach.[25]

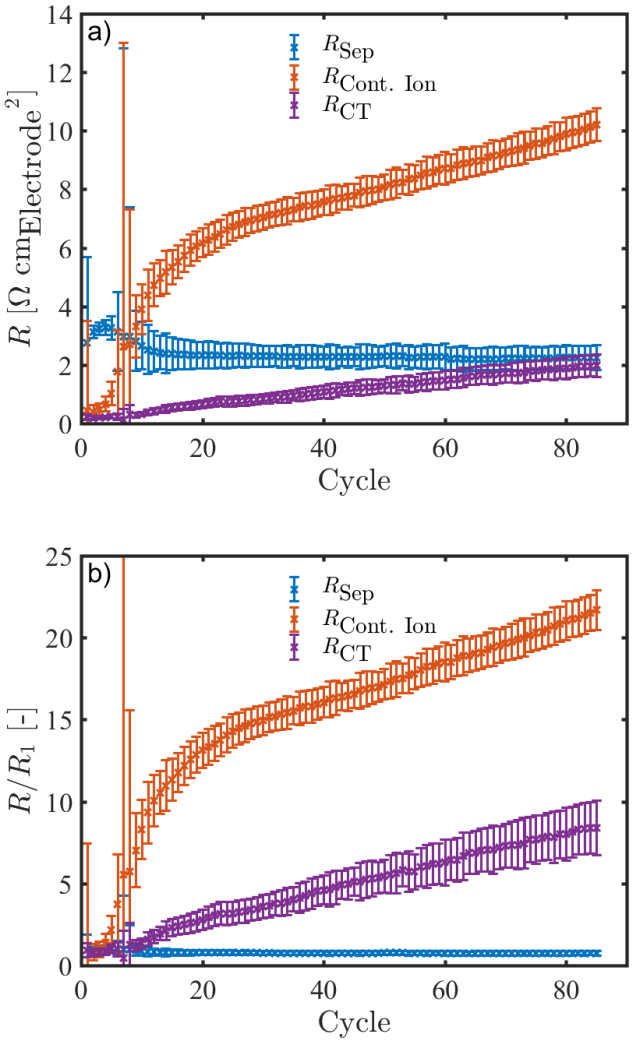

Figure 8: a) Evolution of the high frequency resistance ($R_{\text{Sep.}}$), the charge transfer resistance (R_{CT}.) and the ionic contact resistance ($R_{\text{Cont. Ion}}$) of the graphite anode normalized to the electrode area, in the LNMO/graphite full-cell over extended charge/discharge cycling at 40°C at a rate of C/2 between 3.0 and 4.9 V_{FC}. The values are obtained by fitting the two impedance spectra und blocking (4.4 V_{FC}) and non-blocking (3.0 V_{FC}) conditions at the same time as shown in Figure 7 for one cycle. b) Resistances normalized to their initial value after formation. The error bars represent the parameter's 95% confidence interval from the fit.

Overview – LNMO/graphite full cell impedance

Based on our previous analysis of the LNMO cathode of LNMO/graphite cells[18] and the above investigation of the graphite anode impedance contributions, we are now able to combine all impedance results and compare them to the full cell spectra.

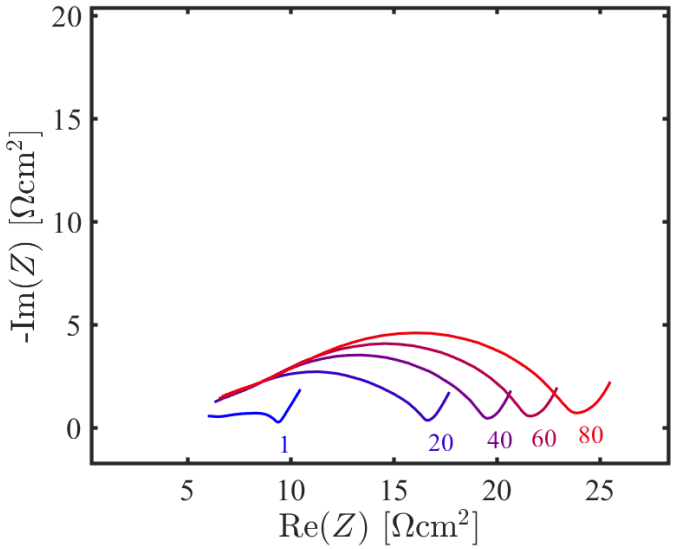

Figure 9: Full cell impedance spectra of LNMO/graphite cells at 40 °C from cycle 1 (blue) to cycle 80 (red, cycle numbers are given in the figure), measured at 4.4 V_{FC},in frequency range from 100 kHz to 0.1 Hz using an excitation amplitude of 15 mV.

Figure 9 shows the increase of the LNMO/graphite full cell impedance in non-blocking conditions, i.e., at a full cell potential of 4.4 V_{FC}, over the course of cycling. The scope of showing Figure 9 is to exemplify the ambiguity in impedance analysis of full-cell spectra, which include anode and cathode impedance signals. The full cell impedance mainly shows *one* smeared out semi-circle in the Nyquist plot, with a low frequency resistance (inflection point) of 10 Ohm in cycle 1 up to ~25 Ohm in cycle 80, followed by a Warburg like increase at lowest frequencies (compare Figure 9). From the analysis of full cells measured to higher frequencies (see text in previous publication, Ref 18), we could show that the full cell high frequency resistance equals ≈ 4.8 Ωcm². Based on this, known high frequency resistance one could argue that the full cell EIS response includes a second feature at high frequencies. Compared to the best case scenario of two discernable features of the full cell impedance spectra we could successfully disentangle not only the origin of the observed ≈ 4 fold increase of the full cell low frequency resistance (the separator resistance is invariant at ≈ 4.8 Ωcm²) but also attribute individual resistances to anode and cathode pores, charge transfer reactions and contact resistances. The underlying resistance contributions that were discerned successfully using the GWRE are summarized in Figure 10.

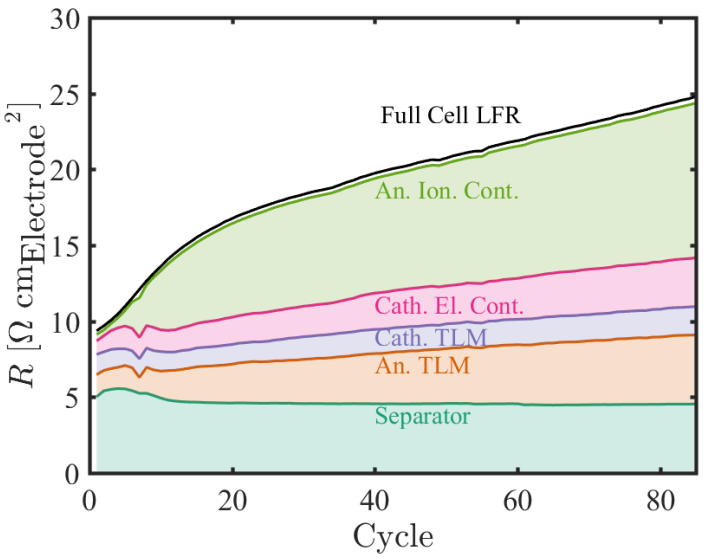

Figure 10: Cumulative resistance plot of LNMO/graphite full cell impedance at 40°C cycling at C/2. Individual contributions were determined using half-cell spectra combined with simultaneously fitting the electrode impedance responses in blocking and in non-blocking conditions. The full cell impedance at 3 Hz is also plotted as a reference and to show the good agreement between the half-cell analyses and the full cell data.

Figure 10 shows the separator resistance, mainly remaining constant over the course of 86 cycles, cathode electronic as well as anode ionic contact resistances (compare Ref. 18 as well as previous section) and the resistances of the simplified transmission line model for both electrodes which include the charge transfer and the pore resistance. It is emphasized that the resistance contributions of the electrode pores and their charge transfer resistance (including SEI at the anode in the present analysis) cannot be added as both elements are not serially connected in the transmission line model. I.e., rather than showing R_{Pore} (or 1/3 R_{Pore}) and R_{CT} Figure 10 shows the low frequency resistance of the simplified transmission line model ($R_{\mathrm{TLM}}(f \to 0)$, neglecting electronic resistances) instead of individual values for R_{Pore} and R_{CT}. In the low frequency limit the simplified transmission line model yields a low frequency resistance of

$$R_{\mathrm{TLM}}(f \to 0) = \frac{\sqrt{R_{\mathrm{Pore}} \cdot R_{\mathrm{CT}}}}{\tanh\left(\sqrt{\frac{R_{\mathrm{Pore}}}{R_{\mathrm{CT}}}}\right)} \qquad 1$$

which is independent of the surface capacitance. The reader is referred to the previous section as well as part I of this work regarding the absolute values for pore resistance and charge transfer. Figure 10 shows the full cell low frequency resistance (LFR), here we used intercept of the linear extrapolation of the last three frequency points (compare Figure 9) with the x-axis. The cumulative sum of individual resistance contributions is in very good agreement with the LFR obtained from the full cell spectra.

Analogous analysis of full cells cycled at various conditions, as exemplarily shown in part I of this work as well as the current study for LNMO/graphite cells using a gold wire micro-reference electrode, allows to get a profound understanding of the individual aging mechanism occurring, during in-situ operation. Figure

10 nicely summarizes the capabilities of minute impedance analysis using elaborate procedures (combining measurements in blocking and non-blocking conditions) and the use of a reference electrode, and proves the necessity to use reference electrodes, especially when compared to the full cell spectra shown in Figure 9, to understand the aging processes occurring in the cell. We are certain that application of the presented analysis techniques will help to get a better understanding of the cycling behavior of a variety of cell chemistries and setups.

Conclusions

Using a gold wire reference electrode (GWRE), the anode impedance of a graphite/LNMO is analyzed over the course of 86 charge/discharge cycles at 40°C. First we showed that blocking electrode behavior can be achieved for a graphite anode cycled versus an LFP electrode. When the cathode is replaced by LNMO, the blocking spectrum shows an additional semi-circle at higher frequencies. This feature evolves over 86 cycles in a graphite/LNMO cell and becomes the dominating contribution to the overall resistance. By temperature-dependent impedance measurements and the addition of manganese ions to the electrolyte in graphite/LFP cells, we showed that the semi-circle appears due to a resistive layer formed at the interface anode/separator. By fitting both blocking and non-blocking spectra at the same time with a general transmission line model (TLM), the anode impedance is deconvoluted into its contributions from separator ($R_{\mathrm{Sep.}}$) , pore resistance (R_{Pore}), and interface ionic resistance and SEI/charge transfer resistance.

Acknowledgment

Financial support by the BASF SE through its Research Network on Electrochemistry and Batteries is gratefully acknowledged. J. L. gratefully acknowledges the funding by the BMBF (Federal ministry of Education and research, Germany) for its financial support under the auspices of the ExZellTUM II project, grant number 03XP0081.

References

1. J.-H. Kim, N. P. W. Pieczonka, and L. Yang, *ChemPhysChem*, **15**, 1940–1954 (2014).
2. D. Lu, M. Xu, L. Zhou, A. Garsuch, and B. L. Lucht, *J. Electrochem. Soc.*, **160**, A3138–A3143 (2013).
3. L. Yang, B. Ravdel, and B. L. Lucht, *Electrochem. Solid-State Lett.*, **13**, A95 (2010).
4. S. R. Li, C. H. Chen, X. Xia, and J. R. Dahn, *J. Electrochem. Soc.*, **160**, A1524–A1528 (2013).
5. N. P. W. Pieczonka, Z. Liu, P. Lu, K. L. Olson, J. Moote, B. R. Powell, and J.-H. Kim, *J. Phys. Chem. C*, **117**, 15947–15957 (2013).
6. J. Wandt, A. Freiberg, R. Thomas, Y. Gorlin, A. Siebel, R. Jung, H. A. Gasteiger, and M. Tromp, *J. Mater. Chem. A*, **4**, 18300–18305 (2016).
7. P. Lu, C. Li, E. W. Schneider, and S. J. Harris, *J. Phys. Chem. C*, **118**, 896–903 (2014).
8. S. S. Zhang, K. Xu, and T. R. Jow, *Electrochim. Acta*, **51**, 1636–1640 (2006).
9. S. Zhang, M. S. Ding, K. Xu, J. Allen, and T. R. Jow, *Electrochem. Solid-State Lett.*, **4**, A206 (2001).
10. S. S. Zhang, *J. Power Sources*, **163**, 713–718 (2007).
11. S. Solchenbach, D. Pritzl, E. J. Y. Kong, J. Landesfeind, and H. A. Gasteiger, *J. Electrochem. Soc.*, **163**, A2265–A2272 (2016).
12. C. H. Chen, J. Liu, and K. Amine, *J. Power Sources*, **96**, 321–328 (2001).
13. R. Petibon, C. P. Aiken, N. N. Sinha, J. C. Burns, H. Ye, C. M. VanElzen, G. Jain, S. Trussler, and J. R. Dahn, *J. Electrochem. Soc.*, **160**, A117–A124 (2013).
14. M. Klett, J. A. Gilbert, S. E. Trask, B. J. Polzin, A. N. Jansen, D. W. Dees, and D. P. Abraham, *J. Electrochem. Soc.*, **163**, A875–A887 (2016).
15. J. Zhou and P. H. L. Notten, *J. Electrochem. Soc.*, **151**, A2173 (2004).
16. M. Ender, A. Weber, and E. Ivers-Tiffée, *J. Electrochem. Soc.*, **159**, A128 (2012).
17. A. N. Jansen, D. W. Dees, D. P. Abraham, K. Amine, and G. L. Henriksen, *J. Power Sources*, **174**, 373–379 (2007).
18. J. Landesfeind, D. Pritzl, and H. A. Gasteiger, *J. Electrochem. Soc.*, **164**, A1773 – A1783 (2017).
19. D. Pritzl, S. Solchenbach, M. Wetjen, and H. A. Gasteiger, *J. Electrochem. Soc.*, **164**, A2625–A2635 (2017).
20. J. Landesfeind, J. Hattendorff, A. Ehrl, W. A. Wall, and H. A. Gasteiger, *J. Electrochem. Soc.*, **163**, A1373–A1387 (2016).
21. M. Gaberscek, J. Moskon, B. Erjavec, R. Dominko, and J. Jamnik, *Electrochem. Solid-State Lett.*, **11**, A170 (2008).
22. D. Pritzl, A. Bumberger, M. Wetjen, J. Landesfeind, S. Solchenbach and H. A. Gasteiger, *Manuscr. prep.*
23. N. Ogihara, S. Kawauchi, C. Okuda, Y. Itou, Y. Takeuchi, and Y. Ukyo, *J. Electrochem. Soc.*, **159**, A1034–A1039 (2012).
24. J. C. Burns, A. Kassam, N. N. Sinha, L. E. Downie, L. Solnickova, B. M. Way, and J. R. Dahn, *J. Electrochem. Soc.*, **160**, A1451–A1456 (2013).
25. S. Solchenbach, D. Pritzl, J. Landesfeind and H. A. Gasteiger, *Manuscr. prep.*

Chapter 6

Sensitivity Analysis of Parameter Ranges

In this section the physical and electrochemical parameters of a lithium-ion battery on the electrode level are used in a numerical experiment using Comsol Multiphysics®. The discharge of a 1D NMC/graphite lithium-ion battery is simulated using the Newman model[24–26] at 0.1, 0.2, 0.5, 1, 2, 5, 10 and 20 C until the full cell potential reaches 2.7 V. For simplicity it is assumed that the charge/discharge is isothermal, which strictly speaking only applies for lab-scale single-electrode cells. All required parameters (see Figure 2.1) have been determined or estimated using the methods outlined in Chapter 2 as well as the articles presented in Chapters 3 to 5. Typical standard values for the parameters and their experimentally found upper and lower ranges (in brackets) are collected in Table 6.1. The aim of this chapter is to illustrate the sensitivity of the electrochemical performance of the simulated NMC/graphite cell on the experimental uncertainty of the found parameters. Therefore the simulation is done with a standard parameter basis set (see values in Table 6.1) and the results are compared with the simulation when always only one parameter is changed to its upper or lower boundary. For the electrolyte transport properties, the concentration dependent functions determined in Section 3.4 are scaled with the factors f_x (see Electrolyte section in Table 6.1 and Table 6.2), based on the observed experimental uncertainty. The concentration dependent electrolyte parameters are reprinted for reference in Table 6.2 and correspond to the functional description found in Section 3.4 for $LiPF_6$ in EC:EMC (3:7 w:w) at 25 °C. It is emphasized that the approach used here is not a sensitivity study for each parameter in the classic sense, as the parameters are not changed by a fixed percentage value, but that our estimated experimental uncertainty of each value is used.

To compare the influence of the physical and electrochemical parameters on the isothermal operation of the NMC/graphite cell, the discharge capacities and the overpotentials during operation are analyzed. Figure 6.1 demonstrates the analysis at a C-rate of 2 C and for the electrode tortuosity as a parameter. In the standard case, i.e., with the tortuosity of 3.5, the full capacity is obtained at a discharge rate of 0.1 C (see black line in Figure 6.1). For the higher discharge C-rate of 2 C, the capacity obtained when the discharge cut-off potential is reached reduces to ≈90 % (see purple line at end of discharge in Figure 6.1). At the same discharge C-rate of 2 C, a higher capacity is found for a smaller electrode tortuosity (≈95 %, see green line at end of discharge in Figure 6.1) and vice versa for a higher electrode tortuosity (≈70 %, see orange line at end of discharge in Figure 6.1). Although subsequently the overpotentials

Table 6.1: Overview of physical and electrochemical parameters (at 25 °C) required for the simulation of a lithium-ion battery (see Figure 2.1). Most of the parameters have been determined or estimated as a part of this thesis (see references given in the table, as well as Chapter 2 and the articles presented in Chapters 3 to 5). Parameters for anode and cathode are collected separately, while some parameters are used for both electrodes (see section Anode and Cathode) for the sake of simplicity. Standard values for each parameter are given. The experimentally obtained upper and lower boundary of some parameters are given in brackets and are used for the sensitivity analysis of parameter errors.

Parameter	Abbrev.	Value (Range)	Unit	Comment
Anode				
thickness Cu CC	t_{Cu}	9	µm	meas.
density copper	ρ_{Cu}	8.96	g/cm³	Ref. [38]
conductivity copper	σ_{Cu}	$5.9 \cdot 10^7$	S/m	Ref. [38]
density of graphite	ρ_{Gra}	2.26	g/cm³	Ref. [38]
BET of graphite	$\mathrm{BET}_{\mathrm{Gra}}$	3	m²/g	spec. sheet
OCV of graphite	$\mathrm{OCV}_{\mathrm{Gra}}$	see ref.	V	lit. Ref. [72]
loading an.	L_{A}	3	mAh/cm²	defined
thickness	$t_{\mathrm{A/C}}$	≈ 54	µm	calc. from $\varepsilon_{\mathrm{A/C}}$ and $L_{\mathrm{A/C}}$
film resistance	R_{SEI}	200 (100–400)	$\Omega\mathrm{cm}^2_{\mathrm{BET}}$	meas., Refs. [87, 88]
Separator				
thickness	$t_{\mathrm{Sep.}}$	20 (15–25)	µm	meas., Sec. 2.2/Ref. [41]
porosity	$\varepsilon_{\mathrm{Sep.}}$	0.47 (0.4–0.6)	-	meas., Sec. 2.2/Ref. [41]
tortuosity	$\tau_{\mathrm{Sep.}}$	3.2 (2.5–4.5)	-	meas., Sec. 2.2/Ref. [41]
density (bulk)	$\rho_{\mathrm{Sep.}}$	0.9	g/cm³	Ref. [38]
Cathode				
thickness Al CC	t_{Al}	12	µm	meas.
density aluminum	ρ_{Al}	2.70	g/cm³	Ref. [38]
conductivity aluminum	σ_{Al}	$3.8 \cdot 10^7$	S/m	Ref. [38]
density of NMC	ρ_{NMC}	4.7	g/cm³	Ref. [123]
BET of NMC	$\mathrm{BET}_{\mathrm{NMC}}$	0.3	m²/g	spec. sheet
OCV of NMC	$\mathrm{OCV}_{\mathrm{NMC}}$	see ref.	V	lit. Ref. [73]
loading cath.	L_{C}	$L_{\mathrm{A}} \cdot 0.95$	mAh/cm²	calc.
thickness	$t_{\mathrm{A/C}}$	≈ 50	µm	calc. from $\varepsilon_{\mathrm{A/C}}$ and $L_{\mathrm{A/C}}$
Anode and Cathode				
composition	$\%_{\mathrm{AM}}/\%_{\mathrm{BI}}/\%_{\mathrm{CA}}$	95/3/2	wt.%	defined
density of CA	ρ_{CA}	2.26	g/cm³	Ref. [38]
density of PVDF	ρ_{PVDF}	1.74	g/cm³	Ref. [38]
BET of CA	$\mathrm{BET}_{\mathrm{CA}}$	62	m²/g	spec. sheet
porosity	$\varepsilon_{\mathrm{A/C}}$	0.3 (0.25 - 0.35)	-	meas., Sec. 2.4/Ref. [41]
tortuosity	$\tau_{\mathrm{A/C}}$	3.5 (2–5)	-	meas., Sec. 2.4/Ref. [41]
contact resistance	$R_{\mathrm{Cont.,A/C}}$	0 (40)	$\Omega\mathrm{cm}^2_{\mathrm{geo}}$	meas., Sec. 4.1/Ref. [41]
conductivity (electrical)	$\sigma_{\mathrm{A/C}}$	100 (50–10000)	mS/cm	meas., Ref. [55]
radius	$r_{\mathrm{A/C}}$	5 (2–10)	µm	meas., Sec. 2.5
solid state diff. coeff.	$D_{\mathrm{SS,A/C}}$	10 (3.5–40)	10^{-10} cm²/s	lower bound., Sec. 2.5
kinetic rate constant	k	5 (1–10)	10^{-11} m/s	meas., Sec. 2.6/Ref. [99]
charge transfer coeff.	α	0.5	-	ass. (pulse symm.)
Electrolyte				
conductivity (ionic)	$f_{\kappa_{\mathrm{Ion}}}$	1 (0.97–1.03)	-	see Tab. 6.2
binary diff. coeff.	$f_{D_{\pm}}$	1 (0.90– 1.10)	-	see Tab. 6.2
transference number	f_{t_+}	1 (0.80–1.20)	-	see Tab. 6.2
thermodynamic factor	f_{TDF}	1 (0.50–1.50)	-	see Tab. 6.2
density	$\rho_{\mathrm{Elyt.}}$	conc. dep. fct.	g/cm³	see Sec. 3.4
double layer cap.	C_{DBL}	2.5 (1, 5)	µF/cm²	meas., Tab. I in Ref. [62]

Table 6.2: Overview of electrolyte transport properties for $LiPF_6$ in EC:EMC (3:7 w:w) at 25 °C as found in the article presented in Section 3.4. The scaling factors f_x are added to illustrate how the electrolyte parameters are varied in the sensitivity analysis of the parameter errors (see Table 6.1). The electrolyte salt concentration c_l is used in units of moles per liter.

Parameter		Unit	Reference
$\kappa_{\mathrm{Ion}}(c_l)$	$= f_{\kappa_{\mathrm{Ion}}} \cdot 37.0 \cdot c_l \cdot \frac{1-1.06\cdot\sqrt{c_l}+0.353\cdot(1-0.103\cdot c_l)}{1+0.0424\cdot c_l^4}$	mS/cm	see Sec. 3.4
$D_{\pm}(c_l)$	$= f_{D_{\pm}} \cdot 5.45 \cdot \exp -0.619 \cdot c_l$	10^{-6} cm²/s	see Sec. 3.4
$t_+(c_l)$	$= f_{t_+} \cdot \left(0.341 + 2.02 \cdot c_l - 0.710 \cdot c_l^2 + 0.235 \cdot c_l^3\right)$	-	see Sec. 3.4
$\mathrm{TDF}(c_l)$	$= f_{\mathrm{TDF}} \cdot \left(0.700 - 0.784 \cdot c_l + 0.377 \cdot c_l^2 - 0.0585 \cdot c_l^3\right)$	-	see Sec. 3.4

of the simulated 1 C discharge curves are analyzed, Figure 6.1 illustrates the analysis of the overpotential for the 2 C discharge case as it better visualizes the analysis. As indicated in Figure 6.1 the overpotential (vertical arrows) is obtained as the difference of the mean potential of a discharge curve (shown as dashed horizontal colored lines in Figure 6.1) and the 0.1 C discharge curve of the standard case, i.e., with the basis parameter set. Note that the mean potential of the standard case at 0.1 C (black line) is obtained only within the same capacity range as the discharge curve of the parameter (note different endpoints, indicated by the vertical lines), and therefore not only three different mean discharge potentials are shown for the three tortuosity values at a discharge C-rate of 2 C (dashed horizontal colored lines) but also three corresponding mean potentials of the standard discharge curve in the respective capacity ranges are shown (dashed horizontal black/colored lines). The rationale behind this approach is to avoid identical overpotentials for totally different potential transients. E.g., two cells which had the same initial potential and showed a perfectly linear potential decay during discharge, with one cell's potential fading twice as fast, will have the same arithmetic mean potential, until the lower potential cut-off potential is reached. Therefore both cells of this thought experiment would show the same overpotential if referenced to the mean discharge potential of the full discharge curve of the standard case at 0.1 C. Thus, to allow for a fair comparison the mean potential during discharge at a given C-rate is subtracted from the mean potential during discharge of the standard case at 0.1 C, calculated only for the same capacity range (see Figure 6.1).

The found dependence of the relative discharge capacities, normalized to the capacity at 0.1 C ($\mathrm{Cap_{A/C}}$) for each C-rate, are further analyzed by fitting them with

$$\frac{\mathrm{Cap_{A/C}}}{\%} = \frac{100}{1 + \left(\frac{\mathrm{C-rate}}{R_{\mathrm{crit.}}}\right)^s} \tag{6.1}$$

using two fitting parameters $R_{\mathrm{crit.}}$ and s. This approach is also used in the article in Section 4.3 and allows to obtain the so-called critical C-rate $R_{\mathrm{crit.}}$, which corresponds to the C-rate at which only half of the full capacity can be obtained during discharge.[65] Exemplary fits of the capacities obtained at the simulated discharge C-rates of 0.1 C to

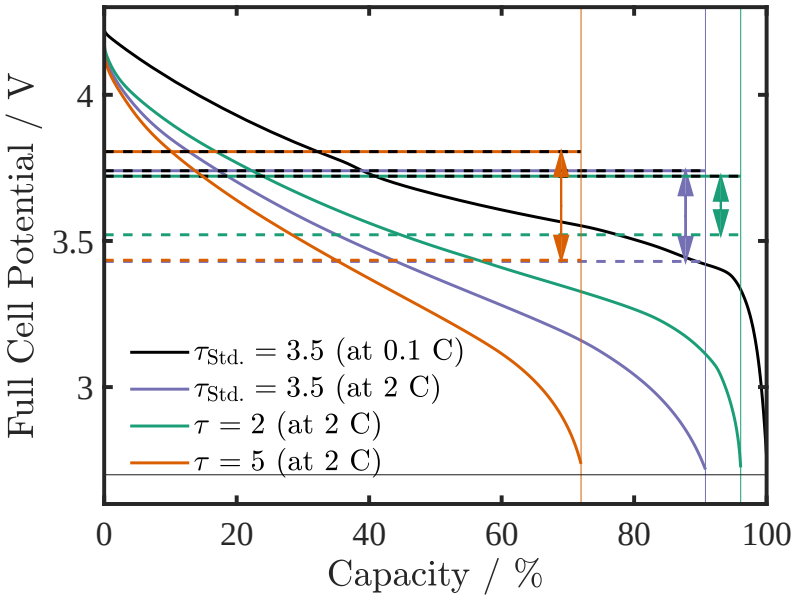

Figure 6.1: Simulation of constant current discharge curves of an isothermal ≈3 mAh/cm² 1D NMC/graphite cell until a lower cut-off potential of 2.7 V is reached, done using Comsol Multiphysics®. All parameters for the simulation are given in Tables 6.1 and 6.2, apart from the thermodynamic parameters of the active materials, which are taken from the literature.[72,73] The discharge capacities are taken as the point when the full-cell potential reaches the lower cell cut-off potential and is indicated by vertical lines in the figure. The exemplary analysis of the overpotentials (vertical arrows) is shown for a rate of 2 C and described in the main text.

20 C are shown in Figure 6.2 for different electrode tortuosities. Here, in addition to the capacities obtained for the simulation discharge C-rates (crosses in Figure 6.2) also the critical C-rate from the fit (solid line) is shown (dashed vertical lines). In Section 4.3 it was found empirically that the critical C-rate furthermore is inversely proportional to the electrode tortuosity. Similar to the analysis in Section 4.3 the critical C-rate for the ideal electrode ($R_{\text{crit.}}^{\text{ideal}}$) may be obtained from $R_{\text{crit.}} \cdot \tau$ and yields fairly similar $R_{\text{crit.}}^{\text{ideal}}$ values of 12, 14.5 and 15.7 for the critical C-rates of 6.00, 4.15 and 3.14 of the simulated NMC/graphite cells with electrode tortuosities of 2, 3.5 and 5, respectively.

The critical C-rates and the obtained overpotentials during a 1 C discharge are compared to the critical C-rate and the mean overpotential at 1 C of the standard case (basis set of parameter values). The normalized overpotentials and critical C-rates caused by all parameters are summarized in Figures 6.3 and 6.4. Upper and lower values for each parameter are given in the figures and correspond to the ranges given in Table 6.1. The parameters are collected in five groups, parameters describing the electrolyte, the kinetics at the interface between particles and electrolyte, the active materials, the electrodes, and the separator (see labels in 6.3 and 6.4). The critical C-rate of the reference case (≈4.2 C) and its overpotential at 1 C (146 mV) are shown right to the standard case lines in the figures.

It is emphasized, that the sensitivity analysis shown in Figure 6.3 and 6.4 does not

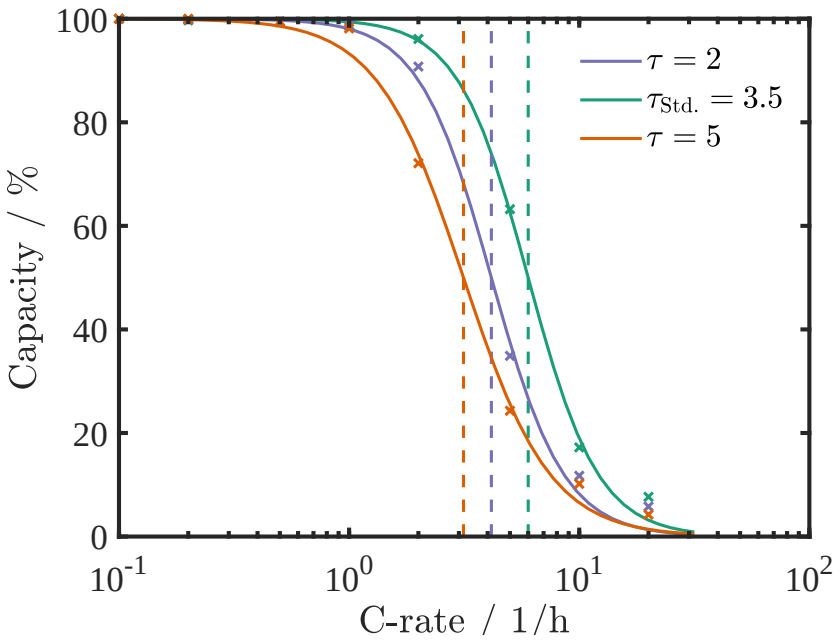

Figure 6.2: Capacities obtained from the simulated discharge curves shown in Figure 6.1 for C-rates from 0.1 C to 20 C (crosses) for the variation of the electrode tortuosity as a parameter. The discharge simulation of a ≈3 mAh/cm² 1D NMC/graphite cell (assumed to be isothermal) was done using a constant current until a lower cut-off potential of 2.7 V is reached. All parameters for the simulation are given in Tables 6.1 and 6.2, apart from the thermodynamic parameters of the active materials, which are taken from the literature.[72,73] The obtained capacity/C-rate relation is fitted using Eq. 6.1 (solid lines) and allows to extract the critical C-rate (dashed vertical lines), corresponding to the C-rate at which 50 % of the capacity can be obtained.

depict the sensitivity towards the same, e.g., percentual change of each parameter, but it represents the sensitivity of the critical C-rate and the overpotential at 1 C for the experimental uncertainty in each parameter. Thus, analysis of Figure 6.3 and 6.4 only allows to draw conclusions about the range of the critical C-rate and the overpotential at 1 C for the range of used values for each parameter. E.g., the ionic conductivity can be determined with a low uncertainty (here 3 % is assumed, see Section 2.3) and within this experimental uncertainty the critical C-rate and the overpotential at 1 C remain fairly constant (<1 % change). On the other hand, due to the high uncertainty of the thermodynamic factor (here 50 % is assumed, see Section 2.3), it has a high influence on the overpotential at 1 C (≈ ±25 %), while the effect would be negligible if the 3 % uncertainty found for the ionic conductivity would also be assumed for the TDF.

The sensitivity study shows that within the range of experimental values the ionic conductivity, the double layer capacity, the SEI resistance, the electrical conductivity of the electrode and the porosity of the separator have negligible influence on the critical C-rate and the overpotential at 1 C (all <3 %). The critical C-rate is mostly influenced by the uncertainty of the electrolyte parameters, the active material's solid state lithium transport and the geometric parameters, porosity and tortuosity, of the electrode. It is stressed, that the solid state diffusion coefficient as well as the particle radius both affect

the characteristic diffusion time within the solid and the found impact on the critical C-rate of 85 % to 105 % represents the same physical phenomena. The analysis of the overpotentials at 1 C for the lower and upper limits for each parameter show that the thermodynamic factor and the kinetic parameters have a strong impact, leading to a change of the overpotential by 80 % to 125 %.

From this sensitivity analysis it becomes clear that the key factors that can reduce the overpotentials at 1 C and that can enable higher critical C-rates are the electrolyte transport properties and the electrode tortuosity and porosity, as they represent the main factors yielding an increase of the critical C-rate in Figure 6.3 and a decrease of the overpotential at 1 C in 6.4.

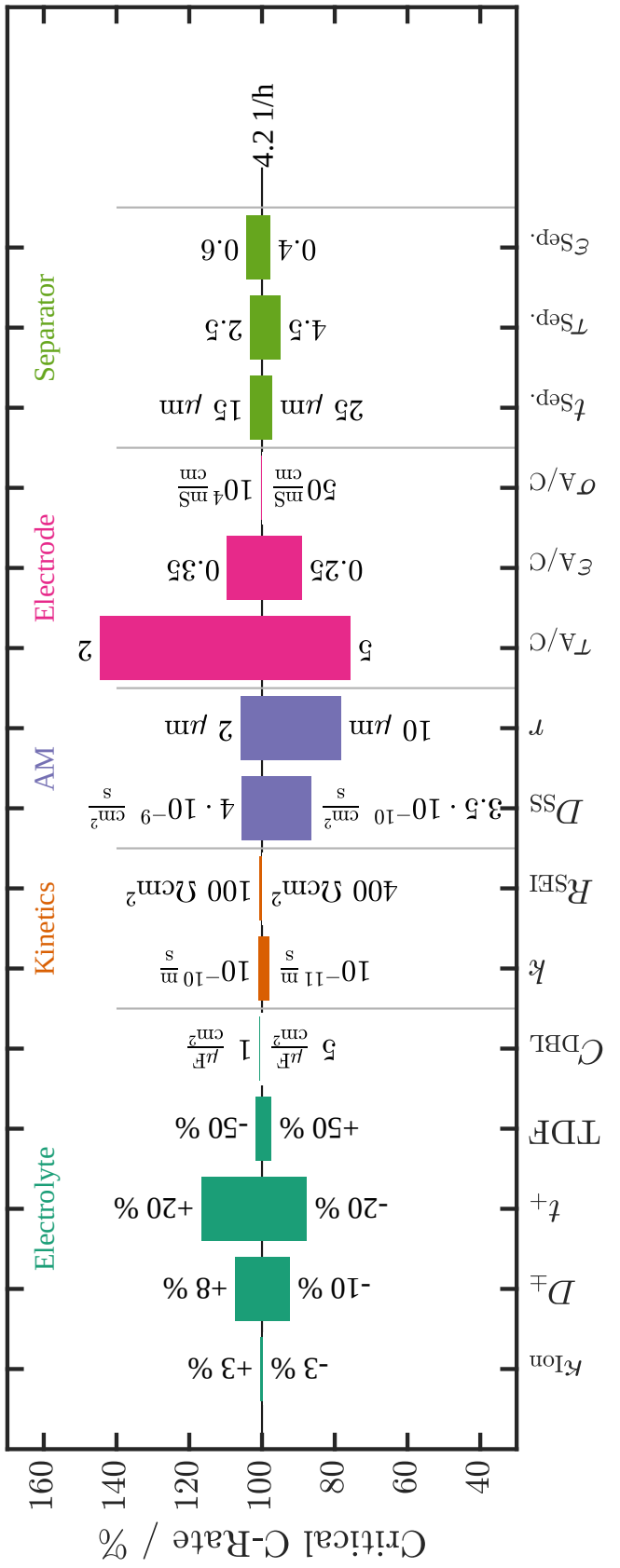

Figure 6.3: Sensitivity analysis of a range of experimentally obtained physical and electrochemical parameters for the numerical description of a 1D lithium-ion battery (assumed to be isothermal) and their impact on the critical C-rate during discharge operation of a NMC/graphite full-cell. All parameters for the simulation are given in Tables 6.1 and and 6.2, apart from the thermodynamic parameters of the active materials, which are taken from the literature.[72,73] The determination of the critical C-rates is described by Figures 6.1 and 6.2 and values for the lower and upper range of each studied parameter (according to Table 6.1) are normalized to the reference scenario with the standard values for each parameter.

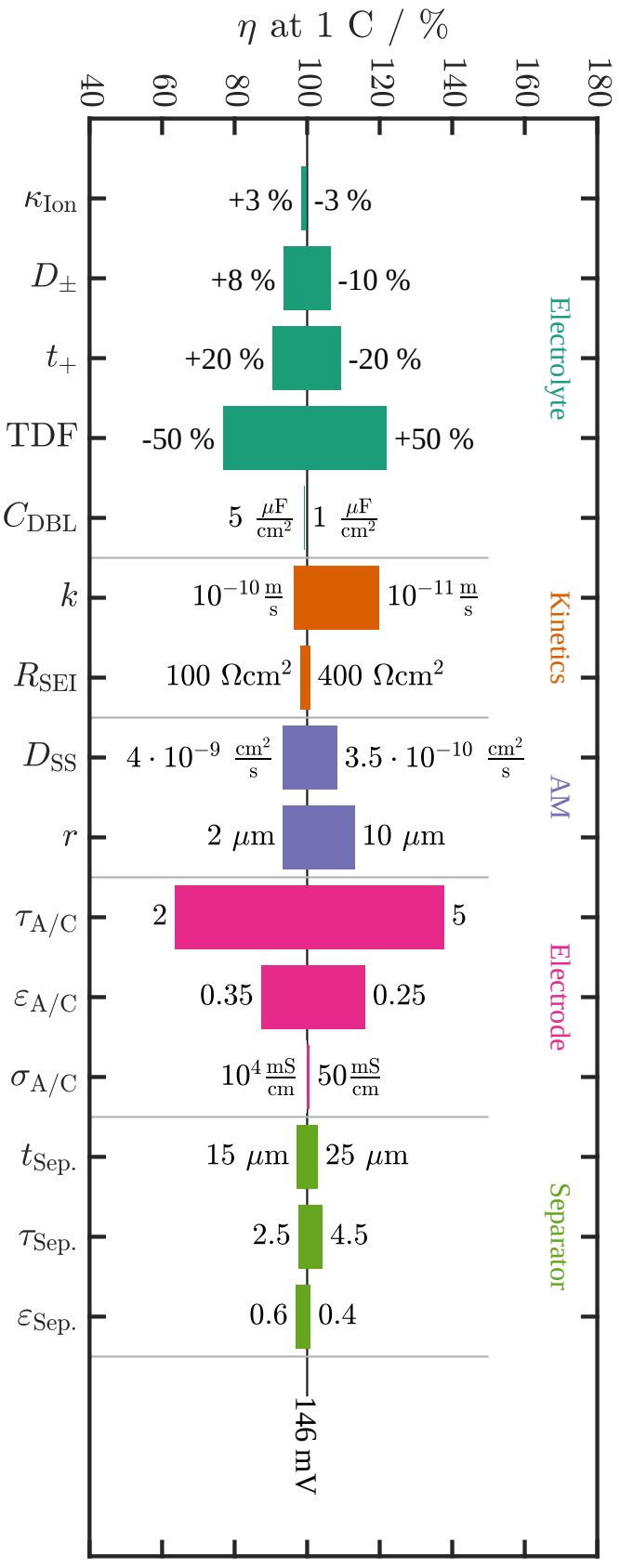

Figure 6.4: Sensitivity analysis of a range of experimentally obtained physical and electrochemical parameters for the numerical description of a 1D lithium-ion battery (assumed to be isothermal) and their impact on the overpotential during discharge operation of a NMC/graphite full-cell at 1 C. All parameters for the simulation are given in Tables 6.1 and and 6.2, apart from the thermodynamic parameters of the active materials, which are taken from the literature.[72,73] The determination of the overpotential is described by Figure 6.1 and values for the lower and upper range of each studied parameter (according to Table 6.1) are normalized to the reference scenario with the standard values for each parameter.

Chapter 7

Conclusion

In this thesis the fundamental parameters describing the ionic transport in lithium ion batteries, namely the electrolyte transport properties and the tortuosity of the porous electrodes and separators, are determined. In addition, using an innovative three-electrode setup with a novel gold wire micro reference electrode, impedance spectra are recorded in-situ, i.e., during cycling of an LNMO/graphite cell, allowing to obtain new insights into the resistance build-up at each of the electrodes. The key to obtain all parameters for the physically motivated equivalent circuits is the simultaneous analysis of impedance spectra recorded at two different states of charge, i.e., at non-blocking and at blocking conditions.

While the focus of this thesis was on the determination of electrode tortuosities, on the liquid electrolyte properties, and on the in-situ characterization of lithium-ion batteries using impedance spectroscopy, all other parameters necessary to describe a lithium-ion battery with the Newman model have been determined or estimated. An overview of all determination approaches and of typical parameters values and their reasonable ranges is given at the beginning of this thesis.

Electrolyte transport properties are determined in this thesis based on the analysis of pulse experiments in two-electrode lithium cells and concentration cell potential measurements. Multiple analytical approaches for the determination of the binary diffusion coefficient and the transference number of lithium ions in the electrolyte are investigated for their accuracy both numerically and experimentally. The obtained values were found to compare well with diffusion coefficients and transference numbers reported in the literature for similar electrolytes. One of the initial goals was also to find a method for the direct electrochemical determination of the thermodynamic factor, which unfortunately was found to be invalid later in this work. An alternative approach to find all electrolyte properties is not based on individual experiments for each parameter, yet it allows to obtain thermodynamic factor and transference numbers without the necessity of any assumptions on their functional concentration dependence. The latter methodology is introduced and described in great detail and will allow to determine electrolyte transport property measurements in laboratories working on lithium-ion batteries, as only commonly available cell setups are required. The study of electrolyte properties conducted in this thesis provides novel insights into the build-up of concentration gradients and accompanying electrolyte overpotentials during battery operation. Comparison of these electrolyte properties for currently used electrolytes with that of recently pro-

posed ethylene carbonate free electrolyte compositions allows to develop strategies for superior electrolytes for future batteries and is key to predict the power performance of lithium-ion batteries. Furthermore, comparing the electrolyte properties of an $LiPF_6$ and a $NaPF_6$ based electrolyte the superiority of sodium ion transport in the same solvent system (here EC:DEC (1:1 v:v)) is shown and provides a new perspective for sodium battery research.

The tortuosity of porous separators and electrodes are determined using impedance spectroscopy. Separator tortuosities were found readily by measurements of the ionic resistance of the porous polymer membranes using impedance spectroscopy, namely by positioning them between two copper electrodes and referencing the resistance versus the pristine ionic conductivity of the electrolyte. Here, as well as for the analysis of porous electrode tortuosities, the required porosities are calculated based on the composition of the material (separator or electrode), its mass, volume, and the bulk density of each component. Due to the high electrical conductivity of the porous electrodes, the ionic resistance has to be found using a different approach. In this study symmetric cells of nominally identical electrodes are assembled with a non-intercalating electrolyte, i.e., not containing lithium ions. The Nyquist plot of such a cell shows a characteristic transmission line model behavior and allows to unambiguously find the ionic resistance of the electrodes. Tortuosities are measured for a range of in-house prepared electrode compositions and active materials, and the distinct influence on the active material particle morphology (spherical or platelet) is demonstrated. More importantly, these *electrochemically* found tortuosities are larger than the values predicted by the Bruggeman relation (only valid for spheres and without binder and conductive additive) and larger than the tortuosity values found using 3D reconstructions based on FIB-SEM or X-ray tomography. To validate our first study on the impedance-based tortuosity of porous electrodes our key assumptions were checked rigorously in a follow-up study. The negligible influence of the electrical conductivity of the electrodes was demonstrated analytically and experimentally and it was shown that the ionic resistance obtained from the transmission line model analysis indeed allows to obtain the true tortuosity of a porous electrode. In consequence, the small volumetric fractions of the polymeric binder and conductive additives, which cannot be resolved using X-ray tomography, are identified as the root cause for the lower tortuosities found using this approach. The dominant influence of the binder type and amount is presented in a follow-up investigation and shows how the tortuosity of graphite anodes may change from 2 to 6-10, depending on the electrode composition, even if the binder content remains small (<10 %). In charge rate tests it is further demonstrated how electrodes of similar thickness, loading, and porosity can show large differences in their high power performance

The capacity fade of lithium-ion batteries, as well as possible safety hazards from lithium dendrite formation, are directly linked to the extent of ionic concentration gradients in the electrolyte phase within the electrode pores which evolve during operation, predominantly during fast charging. The lifetime of a lithium-ion battery is furthermore determined by unwanted side reactions occurring during battery operation and leading to the formation of additional resistances. Such effects make it necessary to use in-situ measurement techniques to understand the origin of these detrimental effects. In this work impedance spectroscopy is used to analyze the aging of an LNMO/graphite cell cycled at 40 °C. To avoid the ambiguity of full-cell impedance analysis a novel gold wire

micro reference electrode is developed and allows to separate the full-cell impedance into anode and cathode contributions. Combination of this GWRE with a new impedance analysis protocol enables to monitor all electrode resistances in-situ. The new measurement protocol is based on the simultaneous fitting of two impedance spectra of the same electrode but at different states of charge. While one spectrum is recorded at mid SOC, the other is determined in blocking conditions, here obtained by fully delithiating the electrode of interest. Thereby all parameters of the physically motivated equivalent circuit models for anode and cathode can be found with a low error. For the first time, all impedance contributions of the LNMO/graphite could be deconvoluted in-situ and it could be shown that the resistance increase of the cell is dominated by the formation of contact resistances between the porous LNMO electrode and the aluminum current collector as well as by the resistance of a layer of SEI precipitates at the separator/anode interface. This detailed understanding could not have been obtained using a two-electrode impedance analysis and explains why the resistance build-up for this cell chemistry has been wrongly assigned in the literature to an increasing charge transfer resistance.

The importance of reliable parameters for the numerical description of lithium-ion batteries is shown in a final sensitivity analysis for the obtained parameter ranges. Using Comsol Multiphysics® the 0.1 C to 20 C discharge curves of NMC/graphite cells are simulated using the standard values of all the relevant physical and electrochemical parameters summarized in the beginning of this work. Changing individual parameters within their typical range or experimental error allows to compare the critical C-rates (the C-rate at which only 50 % of the full capacity is obtained) and the mean overpotentials with the reference case including all the standard values for the parameters. It was shown graphically that the high power performance of lithium-ion batteries may be improved most prominently by reduction of the electrode tortuosity and improvement of the electrolyte transport properties.

Chapter 8

Acknowledgements

The mediocre teacher tells.
The good teacher explains.
The superior teacher demonstrates.
The great teacher inspires.

— William Arthur Ward

I thank Hubert Gasteiger, a true great teacher, for his demanding scientific passion, which I cherish tremendously. It was a great pleasure to work with him on pursuing a fundamental understanding of current lithium-ion battery technology. Most importantly it has always been a fun experience to challenge novel ideas and methods with seemingly endless and catching curiosity and I sincerely hope for many students to come to be enriched by his truly scientific nature.

Julia Kunze-Liebhäuser, Odysseas Paschos, Peter Lamp and Nikolaos Tsiouvaras are gratefully acknowledged for introducing me to the world of electrochemistry during my bachelor and master theses. I am indebted to my colleagues at the Chair for Technical Electrochemistry for the fruitful working atmosphere and the friendships evolved in the laboratory, the office or beyond the university campus. I am grateful for the enthusiastic work of my students Maximilian Graf, Dinesh Kumar Arumugam, Martin Frankenberger, Daniel Pritzl, Konstantin Weber and Askin Eldiven during their bachelor thesis or master thesis projects and beyond. I hope they had as much fun working with me as I did and remember they core of what I tried to teach them (just in case, *question the logic of everything*). Special thanks goes to Anna Freiberg for calmly and patiently showing the bull (me) a safe way out of the china shop (experimental chemistry) whenever I had a question.

I will always appreciate the fun and passionate working experience with Andreas Ehrl without whom the ionic transport in binary electrolytes would have likely remained a mystery and the friendship formed while working through the basics of electrochemical charge conduction. Furthermore I thank Daniel Pritzl and Sophie Solchenbach for valueable *EIS* meetings which finally allowed us to obtain a great understanding of the lithium-ion battery elephant.[32] I enjoyed working with Simon Erhard during his short hands-on experience at TEC and miss his (not only scientifically) spot on analyses. I am happy to see my work being continued and questioned by the young subgroup for

Physical **U**nderstanding of **RE**volutionary **L**ithium-**I**on **B**atteries (PURELIB), with its motivated members Robert Morasch, Bharatkumar Suthar and students.

I thank my collaborators from the Chair of Inorganic Chemistry with Focus on Novel Materials at the Technical University of Munich, Henrik Eickhoff, Lorenzo Toffoletti and Thomas Fässler as well as Wolfgang Wall and Rui Fang at the Institute for Numerical Mechanics. I enjoyed the open-minded scientific discussions with Martin Ebner from ETH Zürich/Battrion AG which has not only led to a valueable scientific contribution but also taught me to share the scientific team spirit, so vividly impersonated by Martin.

Special thanks goes to Prof. Shinichi Komaba at the Tokyo University of Science who made it possible for me to get an insight into sodium and potassium battery system research in Japan. I enjoyed working in his laboratories a lot and learned a great deal from his students and coworkers Tomooki Hosaka and Kei Kubota. I am also grateful for the financial support within the EEBatt, the SurfaLIB and the ExZellTUM II projects as well as the travel grants from the DAAD 2016 and the Electrochemical Society 2017 which enabled me to present my research to an international auditorium.

Last but not least I gratefully acknowledge the TUM Chemistry Department workshop and electronics crew, the glass blower Jürgen Höhn in Garching and the steady administrative support through the maze of German bureaucracy by Franziska Friebel and Veronika Pichler.

Bibliography

[1] J. M. Tarascon. "The Li-Ion Battery: 25 Years of Exciting and Enriching Experiences". *Interface magazine* 25.3 (2016), pp. 79–83.

[2] *Deepflight Super Falcon S*. 2018. URL: https://www.deepflight.com (visited on 03/12/2018).

[3] D. C. Bock, A. C. Marschilok, K. J. Takeuchi, and E. S. Takeuchi. "Batteries used to power implantable biomedical devices". *Electrochimica Acta* 84 (2012), pp. 155–164.

[4] M. C. Smart, B. V. Ratnakumar, R. C. Ewell, S. Surampudi, F. J. Puglia, and R. Gitzendanner. "The use of lithium-ion batteries for JPL's Mars missions". *Electrochimica Acta* 268 (2018), pp. 27–40.

[5] D. Hodges, ed. *The Guinness Book of Car Facts and Feats*. 4th editio. Guinness World Records Limited, 1994.

[6] J. Larminie and J. Lowry. *Electric Vehicle Technology Explained*. Vol. 42. 1. Chichester: John Wiley & Sons, Ltd, 2003, p. 303.

[7] *Detroit Electric Car*. 2018. URL: http://detroit-electric-group.com/en/company.html (visited on 03/12/2018).

[8] K. Möser. *Geschichte des Autos*. Frankfurt/new York: Campus Verlag, 2002.

[9] *Fahrzeugzulassungen - Bestand an Kraftfahrzeugen nach Umwelt-Merkmalen*. 2017. URL: https://www.kba.de.

[10] K. G. Gallagher, S. E. Trask, C. Bauer, T. Woehrle, S. F. Lux, M. Tschech, P. Lamp, B. J. Polzin, S. Ha, B. Long, Q. Wu, W. Lu, D. W. Dees, and A. N. Jansen. "Optimizing Areal Capacities through Understanding the Limitations of Lithium-Ion Electrodes". *Journal of The Electrochemical Society* 163.2 (2016), pp. 138–149.

[11] O. Gröger, H. A. Gasteiger, and J.-P. Suchsland. "Review—Electromobility: Batteries or Fuel Cells". *Journal of The Electrochemical Society* 162.14 (2015), A2605–A2622.

[12] U. Eberle, B. Müller, and R. von Helmolt. "Fuel cell electric vehicles and hydrogen infrastructure: status 2012". *Energy & Environmental Science* 5.10 (2012), p. 8780.

[13] EEA. "Monitoring CO2 emissions from new passenger cars and vans in 2016" (2017), p. 56. URL: http://www.eea.europa.eu/publications/term-report-2015.

[14] Bundesamt für Wirtschaft und Ausführkontrolle. *Förderung von elektrisch betriebenen Fahrzeugen*. 2017. URL: http://www.bafa.de/ (visited on 03/13/2018).

[15] BMW. *BMW i3*. 2018. URL: www.bmw.de/de/index.html (visited on 03/12/2018).

[16] Infomine. *Cobalt Price*. 2018. URL: http://www.infomine.com/investment/metal-prices/cobalt/5-year/ (visited on 03/12/2018).

[17] K. G. Gallagher, S. Goebel, T. Greszler, M. Mathias, W. Oelerich, D. Eroglu, and V. Srinivasan. "Quantifying the promise of lithium–air batteries for electric vehicles". *Energy & Environmental Science* 7.5 (2014), p. 1555.

[18] Bosch. *LEAP closed dow*. 2018. URL: http://www.bosch-presse.de/pressportal/de/de/lithium-energy-and-power-gmbh-und-co-kg-schliesst-forschungs-und-entwicklungsaktivitaeten-im-bereich-batterie-technologie-ab-146880.html (visited on 03/12/2018).

[19] F. T. Wagner, B. Lakshmanan, and M. F. Mathias. "Electrochemistry and the future of the automobile". *Journal of Physical Chemistry Letters* 1.14 (2010), pp. 2204–2219.

[20] G. Patry, A. Romagny, S. Martinet, and D. Froelich. "Cost modeling of lithium-ion battery cells for automotive applications". *Energy Science & Engineering* 3.1 (2015), pp. 71–82.

[21] X. G. Yang, Y. Leng, G. Zhang, S. Ge, and C. Y. Wang. "Modeling of lithium plating induced aging of lithium-ion batteries: Transition from linear to nonlinear aging". *Journal of Power Sources* 360 (2017), pp. 28–40.

[22] C. Daniel and J. O. Besenhard. *Handbook of Battery Materials*. Wiley-VCH, 2011.

[23] G. E. Blomgren. "The Development and Future of Lithium Ion Batteries". *Journal of The Electrochemical Society* 164.1 (2017), A5019–A5025.

[24] K. E. Thomas, J. Newman, and R. M. Darling. "Mathematical Modeling of Lithium Batteries". *Advances in Lithium-Ion Batteries SE - 13* (2002). Ed. by W. Schalkwijk and B. Scrosati, pp. 345–392.

[25] C. M. Doyle. "Design and Simulation of Lithium Rechargeable Batteries". *PhD Thesis* (1996), Berkeley.

[26] J. Newman and K. Thomas-Alyea. *Electrochemical Systems*. 3rd ed. Hoboken: Wiley Interscience, 2004.

[27] M. Ender, A. Weber, and E. Ivers-Tiffée. "A novel method for measuring the effective conductivity and the contact resistance of porous electrodes for lithium-ion batteries". *Electrochemistry Communications* 34 (2013), pp. 130–133.

[28] V. Zinth, C. Von Lüders, M. Hofmann, J. Hattendorff, I. Buchberger, S. Erhard, J. Rebelo-Kornmeier, A. Jossen, and R. Gilles. "Lithium plating in lithium-ion batteries at sub-ambient temperatures investigated by in situ neutron diffraction". *Journal of Power Sources* 271 (2014), pp. 152–159.

[29] J. Wandt, P. Jakes, J. Granwehr, R. A. Eichel, and H. A. Gasteiger. "Quantitative and time-resolved detection of lithium plating on graphite anodes in lithium ion batteries". *Materials Today* xx.xx (2017), pp. 1–10.

[30] D. Aurbach, E. Zinigrad, Y. Cohen, and H. Teller. "A short review of failure mechanisms of lithium metal and lithiated graphite anodes in liquid electrolyte solutions". *Solid State Ionics* 148.3–4 (June 2002), pp. 405–416.

[31] Andrzej Lasia. *Electrochemical Impedance Spectroscopy and its Applications*. Springer, 2014.

[32] M. E. Orazem and B. Tribollet. *Electrochemical Impedance Spectroscopy*. WILEY A, 2008.

[33] V. F.Lvovich. *Impedance Spectroscopy Applications to Electrochemical and Dielectric Phenomena*. New Jersey: John Wiley & Sons, Ltd, 2012, pp. 78–81.

[34] E. Barsoukov and J. R. Macdonald. *Impedance Spectroscopy Theory, Experiment, and Applications*. Ed. by E. Barsoukov and J. R. Macdonald. Second Edi. John Wiley & Sons, Inc., 2005.

[35] H. Göhr. "Impedance Modelling of Porous Electrodes". In: *Electrochemical Applications*. Ed. by D. H.-J. Schäfer and C. A. Schiller. ZAHNER-elektrik GmbH & Co. KG, 1997, pp. 2–3.

[36] Zahner. *SIM - Simulation and Fitting*. 2013. URL: http://zahner.de/pdf/SIM.pdf (visited on 03/14/2018).

[37] Zahner. *EIS - Electrochemical Impedance Spectroscopy*. 2015. URL: http://zahner.de/pdf/EIS.pdf (visited on 03/14/2018).

[38] W. M. Haynes. *CRC Handbook of Chemistry and Physics*. 95th editi. CRC Press, 2014.

[39] M. Park, X. Zhang, M. Chung, G. B. Less, and A. M. Sastry. "A review of conduction phenomena in Li-ion batteries". *Journal of Power Sources* 195.24 (Dec. 2010), pp. 7904–7929.

[40] M. Gaberscek, J. Moskon, B. Erjavec, R. Dominko, and J. Jamnik. "The Importance of Interphase Contacts in Li Ion Electrodes: The Meaning of the High-Frequency Impedance Arc". *Electrochemical and Solid-State Letters* 11.10 (2008), A170.

[41] J. Landesfeind, J. Hattendorff, A. Ehrl, W. A. Wall, and H. A. Gasteiger. "Tortuosity Determination of Battery Electrodes and Separators by Impedance Spectroscopy". *Journal of the Electrochemical Society* 163.7 (2016), A1373–A1387.

[42] Celgard. *Product Specification Sheet - Separators*. 2014.

[43] K. Xu. "Nonaqueous Liquid Electrolytes for Lithium-Based Rechargeable Batteries". *Chemical Reviews* 104.10 (Oct. 2004), pp. 4303–4418.

[44] A. V. Cresce, S. M. Russell, O. Borodin, J. A. Allen, M. A. Schroeder, M. Dai, J. Peng, M. P. Gobet, S. G. Greenbaum, R. E. Rogers, and K. Xu. "Solvation behavior of carbonate-based electrolytes in sodium ion batteries". *Phys. Chem. Chem. Phys.* 19.1 (2017), pp. 574–586.

[45] L. Yang, A. Xiao, and B. L. Lucht. "Investigation of solvation in lithium ion battery electrolytes by NMR spectroscopy". *Journal of Molecular Liquids* 154.2-3 (July 2010), pp. 131–133.

[46] K. L. Gering. "Prediction of Electrolyte Conductivity: Results from a Generalized Molecular Model Based on Ion Solvation and a Chemical Physics Framework". *Electrochimica Acta* 225 (Jan. 2017), pp. 175–189.

[47] M. R. Wright. *An Introduction to Aqueous Electrolyte Solutions*. Chichester: John Wiley & Sons, Ltd, 2007.

[48] M. S. Ding and T. R. Jow. "Conductivity and Viscosity of PC-DEC and PC-EC Solutions of LiPF[sub 6]". *Journal of The Electrochemical Society* 150.5 (2003), A620.

[49] K. Kuratani, N. Uemura, H. Senoh, H. Takeshita, and T. Kiyobayashi. "Conductivity, viscosity and density of MClO4 (M = Li and Na) dissolved in propylene carbonate and γ-butyrolactone at high concentrations". *Journal of Power Sources* 223 (2013), pp. 175–182.

[50] L. O. Valøen and J. N. Reimers. "Transport Properties of LiPF6-Based Li-Ion Battery Electrolytes". *Journal of The Electrochemical Society* 152.5 (2005), A882.

[51] H. S. Harned and D. M. French. "A Conductance Method for the Determindation of the Diffusion Coefficients of ELectrolytes". *Annals of the New York Academy of Sciences* 46.5 (Nov. 1945), pp. 267–284.

[52] W. S. Price. "Pulsed-Field Gradient Nuclear Magnetic Resonance as a Tool for Studying Translational Diffusion. Part 1. Basic Theory". *Concepts in Magnetic Resonance* 9.5 (Aug. 1997), pp. 299–336.

[53] J. Zhao, L. Wang, X. He, C. Wan, and C. Jiang. "Determination of Lithium-Ion Transference Numbers in LiPF6–PC Solutions Based on Electrochemical Polarization and NMR Measurements". *Journal of The Electrochemical Society* 155.4 (2008), A292.

[54] A. Ehrl, J. Landesfeind, W. A. Wall, and H. A. Gasteiger. "Determination of Transport Parameters in Liquid Binary Lithium Ion Battery Electrolytes I. Diffusion Coefficient". *Journal of The Electrochemical Society* 164.4 (Feb. 2017), A826–A836.

[55] J. Landesfeind and H. A. Gasteiger. "The Temperature and Concentration Dependence of Ionic Transport Properties" (2018), in preparation.

[56] A. Nyman, M. Behm, and G. Lindbergh. "Electrochemical characterisation and modelling of the mass transport phenomena in LiPF6–EC–EMC electrolyte". *Electrochimica Acta* 53.22 (Sept. 2008), pp. 6356–6365.

[57] H. Lundgren, M. Behm, and G. Lindbergh. "Electrochemical Characterization and Temperature Dependency of Mass-Transport Properties of LiPF6 in EC:DEC". *Journal of the Electrochemical Society* 162.3 (2014), pp. 3–10.

[58] P. Bruce and C. Vincent. "Steady state current flow in solid binary electrolyte cells". *Journal of Electroanalytical Chemistry* 225 (1987), pp. 1–17.

[59] A. Ehrl, J. Landesfeind, W. A. Wall, and H. A. Gasteiger. "Determination of Transport Parameters in Liquid Binary Electrolytes : Part II . Transference Number". *Journal of the Electrochemical Society* 164.12 (2017), pp. 2716–2731.

[60] M. Farkhondeh, M. Safari, M. Pritzker, M. Fowler, T. Han, J. Wang, and C. Delacourt. "Full-Range Simulation of a Commercial LiFePO4 Electrode Accounting for Bulk and Surface Effects: A Comparative Analysis". *Journal of the Electrochemical Society* 161.3 (2013), A201–A212.

[61] S. Stewart and J. Newman. "Measuring the Salt Activity Coefficient in Lithium-Battery Electrolytes". *Journal of The Electrochemical Society* 155.6 (2008), A458.

[62] J. Landesfeind, D. Pritzl, and H. A. Gasteiger. "An Analysis Protocol for Three-Electrode Li-Ion Battery Impedance Spectra: Part I. Analysis of a High-Voltage Positive Electrode". *Journal of The Electrochemical Society* 164.7 (June 2017), A1773–A1783.

[63] T. Marks, S. Trussler, a. J. Smith, D. Xiong, and J. R. Dahn. "A Guide to Li-Ion Coin-Cell Electrode Making for Academic Researchers". *Journal of The Electrochemical Society* 158.1 (2011), A51.

[64] L. Ma, S. L. Glazier, R. Petibon, J. Xia, J. M. Peters, Q. Liu, J. Allen, R. N. C. Doig, and J. R. Dahn. "A Guide to Ethylene Carbonate-Free Electrolyte Making for Li-Ion Cells". *Journal of The Electrochemical Society* 164.1 (2017), pp. 5008–5018.

[65] J. Landesfeind, A. Eldiven, and H. A. Gasteiger. "Influence of the Binder on Lithium Ion Battery Electrode Tortuosity and Performance". *Journal of The Electrochemical Society* 165.5 (2018), A1122–A1128.

[66] M. Ebner, D. W. Chung, R. E. García, and V. Wood. "Tortuosity anisotropy in lithium-ion battery electrodes". *Advanced Energy Materials* 4.5 (2014), pp. 1–6.

[67] M. Ender, J. Joos, T. Carraro, and E. Ivers-Tiffée. "Three-dimensional reconstruction of a composite cathode for lithium-ion cells". *Electrochemistry Communications* 13.2 (2011), pp. 166–168.

[68] S. J. Harris and P. Lu. "Effects of inhomogeneities -Nanoscale to mesoscale -on the durability of Li-ion batteries". *Journal of Physical Chemistry C* 117 (2013), pp. 6481–6492.

[69] J. Landesfeind, M. Ebner, A. Eldiven, V. Wood, and H. A. Gasteiger. "Tortuosity of Battery Electrodes – Validation of Impedance-Derived Values and Critical Comparison with 3D Tomography". *Journal of The Electrochemical Society* 165.3 (2018), A469–A476.

[70] R. Dominko, M. Gabers, J. Drofenik, M. Bele, and J. Jamnik. "Influence of carbon black distribution on performance of oxide cathodes for Li ion batteries". *Electrochimica Acta* 48 (2003), pp. 3709–3716.

[71] R. Dominko, M. Gaberscek, J. Drofenik, M. Bele, and S. Pejovnik. "A Novel Coating Technology for Preparation of Cathodes in Li-Ion Batteries". *Electrochemical and Solid-State Letters* 4.11 (2001), pp. 187–190.

[72] M. Safari and C. Delacourt. "Modeling of a Commercial Graphite / LiFePO 4 Cell". *Journal of The Electrochemical Society* 158.5 (2011), pp. 562–571.

[73] S. G. Stewart and J. Newman. "The Use of UV/vis Absorption to Measure Diffusion Coefficients in LiPF6 Electrolytic Solutions". *Journal of The Electrochemical Society* 155.1 (2008), F13.

[74] Software. *ImageJ/Fiji*. 2018. URL: https://imagej.net/Welcome (visited on 03/16/2018).

[75] J. Landesfeind. "Analysis and characterisation of olivine cathode materials for automotive lithium-ion batteries". *Technische Universität München* (2013), Master Thesis.

[76] R. Malik, A. Abdellahi, and G. Ceder. "A Critical Review of the Li Insertion Mechanisms in LiFePO4 Electrodes". *Journal of the Electrochemical Society* 160.5 (May 2013), A3179–A3197.

[77] P. Prosini, M. Lisi, D. Zane, and M. Pasquali. "Determination of the chemical diffusion coefficient of lithium in LiFePO 4". *Solid State Ionics* 148 (2002), pp. 45–51.

[78] M. Levi, E. Markevich, and D. Aurbach. "Comparison between Cottrell diffusion and moving boundary models for determination of the chemical diffusion coefficients in ion-insertion electrodes". *Electrochimica Acta* 51.1 (Oct. 2005), pp. 98–110.

[79] E. Markevich, M. Levi, and D. Aurbach. "Comparison between potentiostatic and galvanostatic intermittent titration techniques for determination of chemical diffusion coefficients in ion-insertion electrodes". *Journal of Electroanalytical Chemistry* 580.2 (July 2005), pp. 231–237.

[80] D. Y. W. Yu, C. Fietzek, W. Weydanz, K. Donoue, T. Inoue, H. Kurokawa, and S. Fujitani. "Study of LiFePO4 by Cyclic Voltammetry". *Journal of The Electrochemical Society* 154.4 (2007), A253.

[81] S. Malifarge, B. Delobel, and C. Delacourt. "Guidelines for the Analysis of Data from the Potentiostatic Intermittent Titration Technique on Battery Electrodes". *Journal of The Electrochemical Society* 164.14 (2017), A3925–A3932.

[82] S. Brunauer, P. H. Emmett, and E. Teller. "Adsorption of Gases in Multimolecular Layers". *Journal of the American Chemical Society* 60.2 (Feb. 1938), pp. 309–319.

[83] P. B. Balbuena and Y. Wang, eds. *Lithium-Ion Batteries - Solid-Electrolyte Interphase*. London: Imperial College Press, 2004.

[84] S. Zhang, M. S. Ding, K. Xu, J. Allen, and T. R. Jow. "Understanding Solid Electrolyte Interface Film Formation on Graphite Electrodes". *Electrochemical and Solid-State Letters* 4.12 (2001), A206.

[85] S. S. Zhang. "Electrochemical study of the formation of a solid electrolyte interface on graphite in a LiBC2O4F2-based electrolyte". *Journal of Power Sources* 163.2 (2007), pp. 713–718.

[86] S. Solchenbach, D. Pritzl, E. J. Y. Kong, J. Landesfeind, and H. A. Gasteiger. "A Gold Micro-Reference Electrode for Impedance and Potential Measurements in Lithium Ion Batteries". *Journal of The Electrochemical Society* 163.10 (Aug. 2016), A2265–A2272.

[87] X. Huang. “Investigation of SEI Formation by Electrochemical Impedance Spectroscopy”. *Technische Universität München* (2017), Bachelor Thesis.

[88] S. Solchenbach, X. Huang, J. Landesfeind, D. Pritzl, and H. A. Gasteiger. “SEI Formation Monitored and Understood using a GWRE” (2018), in preparation.

[89] M. D. Levi, G. Salitra, B. H. Markovsky Teller, D. Aurbach, U. Heider, and L. Heider. “Solid-State Electrochemical Kinetics of Li-Ion Intercalation into Li 1-x CoO 2 : Simultaneous Application of Electroanalytical Techniques SSCV, PITT, and EIS”. *Journal of The Electrochemical Society* 146.4 (1999), pp. 1279–1289.

[90] T. R. Jow, M. B. Marx, and J. L. Allen. “Distinguishing Li+ Charge Transfer Kinetics at NCAElectrolyte and GraphiteElectrolyte Interfaces, and NCAElectrolyte and LFPElectrolyte Interfaces in Li-Ion Cells”. *Journal of The Electrochemical Society* 159.5 (2012), A604.

[91] P. Bai and M. Z. Bazant. “Charge transfer kinetics at the solid-solid interface in porous electrodes.” *Nature communications* 5 (2014), p. 3585.

[92] M. Z. Bazant. “Theory of chemical kinetics and charge transfer based on nonequilibrium thermodynamics”. *Accounts of Chemical Research* 46.5 (2013), pp. 1144–1160.

[93] C. Heubner, M. Schneider, and A. Michaelis. “Investigation of charge transfer kinetics of Li-Intercalation in LiFePO4”. *Journal of Power Sources* 288 (2015), pp. 115–120.

[94] A. Hess, Q. Roode-Gutzmer, C. Heubner, M. Schneider, A. Michaelis, M. Bobeth, and G. Cuniberti. “Determination of state of charge-dependent asymmetric Butler–Volmer kinetics for LixCoO2 electrode using GITT measurements”. *Journal of Power Sources* 299 (2015), pp. 156–161.

[95] J. Illig, M. Ender, T. Chrobak, J. P. Schmidt, D. Klotz, and E. Ivers-Tiffee. “Separation of Charge Transfer and Contact Resistance in LiFePO4-Cathodes by Impedance Modeling”. *Journal of the Electrochemical Society* 159.7 (2012), A952–A960.

[96] K. J. Nelson, G. L. D’Eon, a. T. B. Wright, L. Ma, J. Xia, and J. R. Dahn. “Studies of the Effect of High Voltage on the Impedance and Cycling Performance of Li[Ni0.4Mn0.4Co0.2]O2/Graphite Lithium-Ion Pouch Cells”. *Journal of the Electrochemical Society* 162.6 (2015), A1046–A1054.

[97] R. Chandrasekaran. “Quantification of bottlenecks to fast charging of lithium-ion-insertion cells for electric vehicles”. *Journal of Power Sources* (2014), pp. 1–11.

[98] *Comsol Multiphysics*. 2017. URL: https : / / www . comsol . com/ (visited on 03/12/2018).

[99] A. D. Kumar. “Kinetic Parameter Estimation in Lithium-ion Batteries”. *Universität Ulm* (2016), Master Thesis.

[100] N. Ogihara, S. Kawauchi, C. Okuda, Y. Itou, Y. Takeuchi, and Y. Ukyo. “Theoretical and Experimental Analysis of Porous Electrodes for Lithium-Ion Batteries by Electrochemical Impedance Spectroscopy Using a Symmetric Cell”. *Journal of the Electrochemical Society* 159.7 (2012), A1034–A1039.

[101] J. Newman and T. W. Chapman. "Restricted diffusion in binary solutions". *AIChE Journal* 19.2 (Mar. 1973), pp. 343–348.

[102] J. Landesfeind, A. Ehrl, M. Graf, W. A. Wall, and H. A. Gasteiger. "Direct Electrochemical Determination of Thermodynamic Factors in Aprotic Binary Electrolytes". *Journal of The Electrochemical Society* 163.7 (2016), A1254–A1264.

[103] J. Barthel, R. Neueder, H. Poepke, and H. Wittmann. "Osmotic coefficients and activity coefficients of nonaqueous electrolyte solutions. Part 2. Lithium perchlorate in the aprotic solvents acetone, acetonitrile". *Journal of Solution Chemistry* 28.5 (1999), pp. 489–503.

[104] G. Gritzner. *Handbook of Reference Electrodes*. Ed. by G. Inzelt, A. Lewenstam, and F. Scholz. Springer, Berlin, Heidelberg, 2013, pp. 25–32.

[105] J. Landesfeind, T. Hosaka, M. Graf, K. Kubota, S. Komaba, and H. A. Gasteiger. "Comparison of Ionic Transport Properties of Non-aqueous Lithium and Sodium Hexafluorophosphate Electrolytes" (2018), in preparation.

[106] A. Ponrouch, D. Monti, A. Boschin, B. Steen, P. Johansson, and M. R. Palacín. "Non-aqueous electrolytes for sodium-ion batteries". *J. Mater. Chem. A* 3.1 (2015), pp. 22–42.

[107] K. Kubota and S. Komaba. "Review—Practical Issues and Future Perspective for Na-Ion Batteries". *Journal of The Electrochemical Society* 162.14 (2015), A2538–A2550.

[108] D. A. G. Bruggeman. "Calculation of various physics constants in heterogenous substances I Dielectricity constants and conductivity of mixed bodies from isotropic substances". *Ann. Phys* 24.7 (1935), pp. 636–664.

[109] B. Tjaden, S. J. Cooper, D. J. L. Brett, and D. Kramer. "On the Origin and Application of the Bruggeman Correlation for analysing Transport Phenomena in Electrochemical Systems". *Nanotechnology, Separation Engineering* 12 (2016), pp. 44–51.

[110] R. B. Macmullin and G. A. Muccini. "Characteristics of porous beds and structures". *AIChE Journal* 2.3 (1956), pp. 393–403.

[111] D. Cericola and M. E. Spahr. "Electrochimica Acta Impedance Spectroscopic Studies of the Porous Structure of Electrodes containing Graphite Materials with Different Particle Size and Shape". *Electrochimica Acta* 191 (2016), pp. 558–566.

[112] J. Landesfeind, J. Hattendorff, A. Ehrl, W. A. Wall, and H. A. Gasteiger. "Erratum: Tortuosity Determination of Battery Electrodes and Separators by Impedance Spectroscopy [J. Electrochem. Soc. , 163, A1373 (2016)]". *Journal of The Electrochemical Society* 164.4 (Mar. 2017), pp. X7–X7.

[113] V. R. Koch. "The Interfacial Stability of Li with Two New Solvent-Free Ionic Liquids: 1,2-Dimethyl-3-propylimidazolium Imide and Methide". *Journal of The Electrochemical Society* 142.7 (1995), p. L116.

[114] S. Klink, E. Madej, E. Ventosa, A. Lindner, W. Schuhmann, and F. La Mantia. "The importance of cell geometry for electrochemical impedance spectroscopy in three-electrode lithium ion battery test cells". *Electrochemistry Communications* 22.1 (2012), pp. 120–123.

[115] D. P. Abraham, S. D. Poppen, A. N. Jansen, J. Liu, and D. W. Dees. "Application of a lithium-tin reference electrode to determine electrode contributions to impedance rise in high-power lithium-ion cells". *Electrochimica Acta* 49.26 (2004), pp. 4763–4775.

[116] M. Ender, A. Weber, and E. Ivers-Tiffée. "Analysis of Three-Electrode Setups for AC-Impedance Measurements on Lithium-Ion Cells by FEM simulations". *Journal of The Electrochemical Society* 159.2 (2012), A128.

[117] L. H. Raijmakers, M. J. Lammers, and P. H. Notten. "A new method to compensate impedance artefacts for Li-ion batteries with integrated micro-reference electrodes". *Electrochimica Acta* 259 (2018), pp. 517–533.

[118] R. Petibon, C. P. Aiken, N. N. Sinha, J. C. Burns, H. Ye, C. M. VanElzen, G. Jain, S. Trussler, and J. R. Dahn. "Study of Electrolyte Additives Using Electrochemical Impedance Spectroscopy on Symmetric Cells". *Journal of the Electrochemical Society* 160.1 (2012), A117–A124.

[119] D. Aurbach, B. Markovsky, Y. Talyossef, G. Salitra, H. J. Kim, and S. Choi. "Studies of cycling behavior, ageing, and interfacial reactions of LiNi0.5Mn1.5O4 and carbon electrodes for lithium-ion 5-V cells". *Journal of Power Sources* 162.2 SPEC. ISS. (2006), pp. 780–789.

[120] D. Pritzl, A. Bumberger, M. Wetjen, J. Landesfeind, S. Solchenbach, and H. A. Gasteiger. "Identifying Contact Resistances in High-Voltage Cathodes by Impedance Spectroscopy" (2018), in preparation.

[121] D. Pritzl, J. Landesfeind, S. Solchenbach, and H. A. Gasteiger. "An Analysis Protocol for Three Electrode Li-Ion Battery Impedance Spectra: Part II. Analysis of a Graphite Anode Cycled vs. LNMO" (), in preparation.

[122] J. C. Burns, A. Kassam, N. N. Sinha, L. E. Downie, L. Solnickova, B. M. Way, and J. R. Dahn. "Predicting and Extending the Lifetime of Li-Ion Batteries". *Journal of the Electrochemical Society* 160.9 (2013), A1451–A1456.

[123] R. Dash and S. Pannala. "Theoretical Limits of Energy Density in Silicon-Carbon Composite Anode Based Lithium Ion Batteries". *Scientific Reports* 6.February (2016), pp. 6–12.